Complexity

Advanced Control and Optimization for Complex Energy Systems 2021

Lead Guest Editor: Chun Wei
Guest Editors: Xiaoqing Bai, Taesic Kim, Jianwu Zeng, and Wenjie Lu

Advanced Control and Optimization for Complex Energy Systems 2021

Complexity

Advanced Control and Optimization for Complex Energy Systems 2021

Lead Guest Editor: Chun Wei
Guest Editors: Xiaoqing Bai, Taesic Kim, Jianwu Zeng, and Wenjie Lu

Contents

Hindawi
Complexity
Volume 2021, Article ID 1863855, 9 pages
https://doi.org/10.1155/2021/1863855

WILEY | Hindawi

Research Article

Distributed Energy Management of the Hybrid AC/DC Microgrid with High Penetration of Distributed Energy Resources Based on ADMM

Yaling Chen,[1] **Luxi Hao**,[2] **and Gaowen Yin**[3]

[1]*Strategic Emerging Industries Development Research Centers, Business School of Hunan University, Changsha 410208, China*
[2]*State Grid Hunan Electric Power Company Limited Research Institute, Changsha 410000, China*
[3]*School of Electrical and Information Engineering, Hunan University, Changsha 410082, China*

Correspondence should be addressed to Yaling Chen; dorianchen@hnu.edu.cn

Received 25 August 2021; Accepted 3 September 2021; Published 15 September 2021

Academic Editor: Chun Wei

This paper aims to investigate energy management of the hybrid AC/DC microgrid with the high penetration of distributed energy resources (DERs), such as electrical vehicles, heat pumps, and photovoltaics. In the previous studies, energy management of the hybrid microgrid is usually carried out by the system operator in a centralized manner, which suffers from the compromise of privacy information protection and the risk of single-point failure. Therefore, this paper proposes a distributed energy management scheme of the hybrid microgrid using the projection function-based alternating direction method of multipliers (P-ADMM), which allows each subgrid, i.e., AC subgrid and DC subgrid, to make day-ahead schedules independently with information exchanges while obtaining the optimal energy management solution. The energy management problem of the hybrid microgrid is formulated as a mixed-integer quadratic programming (MIQP) model, considering DER and energy storage system operation constraints, system operation constraints, and converter operation constraints. Then, the MIQP model is decomposed and distributed into smaller-scale QP models between subgrids using the P-ADMM algorithm, which can handle binary variables through projection functions. The numerical results conducted on the hybrid microgrid demonstrate that the proposed distributed scheme can effectively achieve optimal energy management for the hybrid AC/DC microgrid in a distributed manner.

1. Introduction

The next-generation distribution system involves the massive deployment of distributed energy resources (DERs), such as electrical vehicles (EVs), heat pumps (HPs), and photovoltaics (PVs) [1]. Adopting the microgrid concept (a small-scale autonomous energy system) has become an effective and promising technology for the integration of DERs due to its technical and economic benefits including the lower operation cost, higher reliability, and stronger resiliency [2].

Generally, microgrids can be put into three main categories according to the voltage type: (1) AC microgrids, (2) DC microgrids, and (3) hybrid AC/DC microgrids [3]. The hybrid AC/DC microgrid separates the AC and DC power supplies and loads, with the AC bus and DC bus linked through a bidirectional converter (BC) [4]. Compared with the conventional AC microgrid requiring a number of AC/DC converters to convert power, the hybrid AC/DC microgrid has the lower equipment investment and can reduce the energy loss during power conversion. Therefore, the hybrid AC/DC microgrid has been considered as an important type of microgrids as more DC power sources and loads are connected [5].

Although the utilization of the microgrid brings about technical and economic benefits, there exist challenges on the microgrid operation, such as energy management. Energy management refers to the optimized operation of dispatchable resources within microgrids such as controllable generation units and loads in order to realize the best tech-economic operation of the microgrid based on system information and forecast data [6].

Energy management for AC or DC microgrids has been widely studied. In [6], a double-layer coordinated energy management approach was proposed for microgrids considering grid-connected and islanding modes, which consists of two layers: the schedule layer obtains an economic operation scheme based on forecast data, while the dispatch layer dispatches controllable units based on real-time data. A centralized optimal microgrid scheduling model which considers multiperiod islanding constraints was proposed in [7]. The optimal scheduling model is solved using the bender decomposition technique, and the obtained solution ensures the microgrid has sufficient capacity to switch to the islanded mode if needed by examining the solution with a proposed islanding criterion. In [8], a practical energy management model for microgrids which considers the operational constraints of DERs, active-reactive power balance, unbalanced system configuration, and voltage-dependent loads was formulated. Moreover, a novel linearization approach was used to reduce the computation complexity. In [9], a model predictive control-based microgrid energy management framework was proposed, which considers the demand response in smart loads and models power flow and unit commitment constraints simultaneously. A multiobjective optimal scheduling model for a DC microgrid considering PVs and EVs was formulated in [10] and solved by the NSGA-II algorithm. In [11], energy management of a DC microgrid with energy storage systems (ESSs) and EVs was studied. Moreover, the uncertainty of renewable energy resources was widely studied and modeled in the microgrid energy management problem in [12–14].

For hybrid AC/DC microgrids, the energy management problem of the hybrid microgrid was modeled in [14] considering multiple distributed ESSs. In [15], a decentralized power sharing method was proposed to share power demands between the AC and DC sources without requiring communication between power sources. A temporally coordinated energy management strategy for the hybrid microgrid was proposed in [16] to deal with uncertainties of the RESs, loads, and converters while considering the dynamic conversion efficiency model of the converter. A two-stage min-max-min robust optimal energy management for the hybrid microgrid was proposed in [17] to deal with the uncertainties of generation sources and loads. An up-down energy management scheme of the hybrid microgrid was proposed in [18], which consists of two levels: the generation and load balance are realized at the system level, while power converter-based resources are used to control the voltage variations at the device level. However, energy management of the hybrid microgrid in the aforementioned studies is carried out by the system operator in a centralized manner, which suffers from the compromise of privacy information protection and single-point failure risk.

To resolve the aforementioned issues, distributed methods, such as analytical target cascading (ATC) and alternating direction method of multipliers (ADMM), have been widely applied to solve optimization models in a distributed/decentralized manner in order to design distributed/decentralized schemes. For instance, in [19–22], the ATC method was used. In [19], a decentralized data-driven load restoration scheme was proposed for the coupled transmission and distribution system based on ATC. The uncertainty of wind power and load consumption was dealt with by formulating a data-driven robust model. In [20], an ATC-based decentralized generator startup sequence scheme was proposed for bulk system restoration considering the available black-start resources in the distribution system. In [21], a spatiotemporal decomposition and coordination scheme was proposed for load restoration in an AC/DC hybrid based on the ATC algorithm. In [22], the ADMM algorithm was used to solve the local flexibility market clearing problem and to design a distributed market clearing scheme.

For the energy management of the microgrid, in [23], a distributed energy management scheme was proposed for the AC microgrid based on the predictor-corrector proximal multiplier method. In the proposed scheme, the local controller of each unit (DERs and loads) optimizes its cost function and sends an optimal schedule to the centralized controller, and the centralized controller optimizes the total cost function based on the system operational constraints. However, the hybrid AC/DC configuration is not considered. In [24], a distributed robust energy management scheme for networked hybrid AC/DC microgrids was proposed, in which each hybrid AC/DC microgrid operator solves the adjustable robust optimization model to optimize its operational cost considering the uncertainty of the renewable generation and load demand. For the networked microgrids, the coordination of energy sharing is carried out to minimize the power loss based on the alternating direction method of multipliers (ADMM). However, in order to use the ADMM to solve the energy management model in a distributed manner, the model was reformulated as a convex model by removing nonlinear terms based on strict assumptions regarding the structure of the objective function, which makes the proposed distributed energy management only suitable for specific models. In order to resolve the aforementioned issues, we propose a distributed energy management scheme for the hybrid AC/DC microgrid based on the projection function-based alternating direction method of multipliers (P-ADMM) that can deal with binary variables efficiently. The P-ADMM algorithm has been widely used to solve nonconvex instances. In [25–28], the P-ADMM algorithm was used to solve the service restoration problem of distribution networks in a hierarchical/distributed manner. In [29], a P-ADMM-based distributed scheme was proposed to coordinate the fast dispatch of PV inverters with the slow dispatch of on-load tap changer and capacitor banks for voltage regulation in unbalanced distribution systems. The practical evidence in these studies denotes that the P-ADMM is an effective method to obtain quality solutions for mixed-integer quadratic programming (MIQP) and mixed-integer linear programming (MILP) models.

In this study, the energy management problem of the hybrid microgrid is firstly formulated as a MIQP model, considering DER and ESS operation constraints, system operation constraints, and converter operation constraints. Then, the MIQP model is decomposed and distributed into

smaller-scale submodels using the P-ADMM-based algorithm that can handle binary variables through projection functions. In the proposed scheme, each subgrid, i.e., AC subgrid and DC subgrid, can make day-ahead schedules independently with information exchanges while achieving optimal energy management.

The main contributions of this paper are summarized as follows: (1) proposes a distributed energy management scheme for the hybrid AC/DC microgrid, which allows each subgrid to make energy schedules independently with information exchanges while realizing optimal energy management and (2) proposes a P-ADMM-based algorithm to efficiently solve the MIQP energy management model in a distributed manner.

The rest of this paper is organized as follows. The framework of the proposed distributed energy management scheme and energy management model formulations are presented in Section 2. The P-ADMM-based algorithm to solve the energy management model is presented in Section 3. Case studies are presented and discussed in Section 4, followed by conclusions.

2. Framework and Model Formulations of the Distributed Energy Management Scheme

2.1. Framework of the Distributed Energy Management Scheme. Figure 1 illustrates the physical and communication architecture of the hybrid AC/DC microgrid, to which various sources and loads are connected. In the DC subgrid, photovoltaics (PVs), ESSs, EVs, and heat pumps (HPs) are connected, while diesel generators (DGs) and conventional AC loads are connected to the AC subgrid. AC subgrid and DC subgrid are tied by a BC.

In the proposed distributed scheme, the AC subgrid operator and DC subgrid operator communicate with each other to make day-ahead energy schedules for respective sources and loads independently.

2.2. Optimal Energy Management Model. In this section, the optimal energy management model of the hybrid microgrid is formulated.

2.2.1. Objective Function. For the energy management of microgrids, the objective function is to minimize operational costs during the scheduling period. The objective function is formulated as follows:

$$\min \sum_{t\in N_T} c_1^G\left(p_t^{\mathrm{DG}}\right)^2 + c_2^G p_t^{\mathrm{DG}} + \lambda_t p_t^{\mathrm{UG}} + b\left(p_t^{\mathrm{UG}}\right)^2. \quad (1)$$

The objective function costs of three terms are as follows: the first two terms are to minimize energy costs of DGs, where N_T is the set of scheduling periods, c_1^{G} and c_2^{G} are generation cost parameters, and p_t^{DG} is the DG generation; the last term is to minimize the cost of purchasing energy from the external grid, where λ_t is the energy sport price, b is the price sensitivity coefficient, and p_t^{UG} is the purchased power.

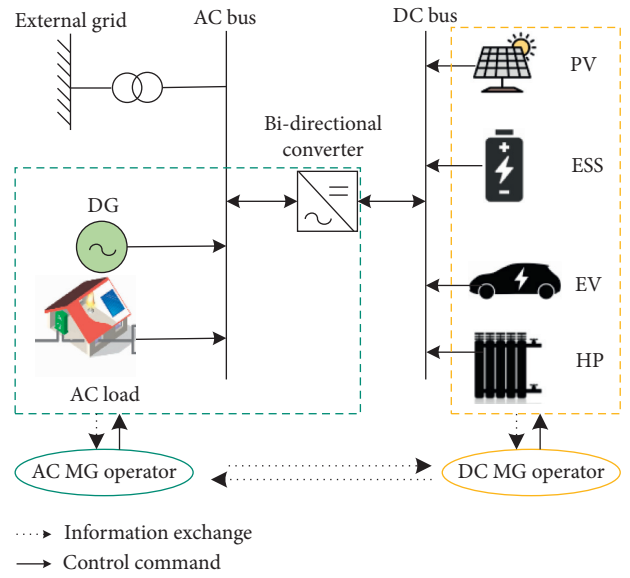

Figure 1: Physical and communication architecture of the hybrid AC/DC microgrid.

2.2.2. Power Balance Equations

$$p_t^{\mathrm{UG}} + p_t^{\mathrm{DG}} + \eta_{\mathrm{dta}} p_t^{\mathrm{dta}} = p_t^{\mathrm{AC\_L}} + p_t^{\mathrm{atd}}, \quad \forall t \in N_T, \quad (2)$$

$$p_t^{\mathrm{ed}} + p_t^{\mathrm{pv}} + \eta_{\mathrm{atd}} p_t^{\mathrm{atd}} = p_t^{\mathrm{ec}} + \sum_{i\in N_e} p_{i,t}^{\mathrm{ev}} + \sum_{i\in N_h} p_{i,t}^{\mathrm{hp}} + p_t^{\mathrm{dta}}, \quad \forall t \in N_T. \quad (3)$$

Equations (2) and (3) are active power balance equations of the AC subgrid and DC subgrid, respectively, where N_h and N_e are sets of HPs and EVs, respectively; p_t^{dta} is the power transferring from the DC side to the AC side at hour t and p_t^{atd} is the power transferring from the AC side to the DC side at hour t; $p_t^{\mathrm{AC\_L}}$ is the conventional AC load consumption; $p_{i,t}^{\mathrm{ev}}$ is the EV charging power of the ith EV at hour t; $p_{i,t}^{\mathrm{hp}}$ is the power consumption of the ith heat pump at hour t; p_t^{ec} and p_t^{ed} are the ESS charging and discharging power, respectively; p_t^{pv} is the PV generation power; and η_{dta} and η_{atd} are power transfer coefficients.

2.2.3. DG Operation Constraints

$$p_t^{\mathrm{DG,min}} \le p_t^{\mathrm{DG}} \le p_t^{\mathrm{DG,max}}, \quad \forall t \in N_T, \quad (4)$$

$$\begin{cases} p_t^{\mathrm{DG,dr}} \le p_t^{\mathrm{DG}} - p_{t-1}^{\mathrm{DG}} \le p_t^{\mathrm{DG,ur}} \\ p_{t_1}^{\mathrm{DG,dr}} \le p_{t_1}^{\mathrm{DG}} - p_0^{\mathrm{DG}} \le p_{t_1}^{\mathrm{DG,ur}} \end{cases}, \quad \forall t \in N_T. \quad (5)$$

Constraint (4) is the DG capacity constraint, where $p_t^{\mathrm{DG,max}}$ and $p_t^{\mathrm{DG,min}}$ are the maximum and minimum limits of the DG active power generation. Constraint (5) is the DG ramping constraint, where $p_t^{\mathrm{DG,ur}}$ and $p_t^{\mathrm{DG,dr}}$ are the upramping and downramping limits.

2.2.4. EV Operation Constraints

$$e_{i,t}^{\min} \le e_{i,0} + \sum_{t_- \le t} \left(p_{i,t_-}^{\text{ev}} - d_{i,t_-}^{\text{ev}} \right) \le e_{i,t}^{\max}, \quad \forall i \in N_e, t \in N_t, \tag{6}$$

$$p_{i,t}^{\text{ev,min}} \le p_{i,t}^{\text{ev}} \le a_{i,t} p_{i,t}^{\text{ev,max}}, \quad \forall i \in N_e, t \in N_t. \tag{7}$$

Constraint (6) is the EV SOC level constraint, where $d_{i,t}^{\text{ev}}$ is the power consumption of the ith EV at hour t due to driving, $e_{i,0}$ is the initial SOC level of the ith EV, and $e_{i,t}^{\min}$ and $e_{i,t}^{\max}$ are the minimum and maximum SOC level limits of the ith EV. Constraint (7) is the EV charging power constraint, where $p_{i,t}^{\text{ev,min}}$ and $p_{i,t}^{\text{ev,max}}$ are the minimum and maximum charging power limits of the ith EV at hour t and $a_{i,t}$ is the charging availability of the ith EV at hour t.

2.2.5. HP Operation Constraints

$$c_i^{\text{cop}} p_{i,t}^{\text{hp}} - k_1\left(K_{i,t}^h - K_{i,t}^u\right) - k_2\left(K_{i,t}^h - K_{i,t}^s\right) = k_3\left(K_{i,t}^h - K_{i,t-1}^h\right), \quad \forall t \in N_T, i \in N_h, \tag{8}$$

$$-k_4\left(K_{i,t}^s - K_{i,t}^u\right) + k_2\left(K_{i,t}^h - K_{i,t}^s\right) = k_5\left(K_{i,t}^s - K_{i,t-1}^s\right), \quad \forall t \in N_T, i \in N_h, \tag{9}$$

$$K_{i,t}^{h,\min} \le K_{t,i}^h \le K_{i,t}^{h,\max}, \quad \forall t \in N_T, i \in N_h, \tag{10}$$

$$p_{i,t}^{\text{hp,min}} \le p_{i,t}^{\text{hp}} \le p_{i,t}^{\text{hp,max}}, \quad \forall t \in N_T, i \in N_h. \tag{11}$$

Constraints (8) and (9) represent thermal equations of the house equipped with the HP [30, 31], where c_i^{cop} is the coefficient of performance; k_1, k_2, k_3, k_4, and k_5 are thermal efficiency coefficients; and $K_{i,t}^h$, $K_{i,t}^u$, and $K_{i,t}^s$ are the household inside temperature, outside temperature, and structure temperature, respectively. Constraint (10) represents the household temperature constraint, where $K_{i,t}^{h,\max}$ and $K_{i,t}^{h,\min}$ are the maximum and minimum limits of the household inside temperature. Constraint (11) represents the HP power consumption constraint, where $p_{i,t}^{hp,\max}$ and $p_{i,t}^{hp,\min}$ are the maximum and minimum limits of the ith heat pump power consumption at hour t.

2.2.6. ESS Operation Constraints

$$x_t^{\text{ec}} p_i^{\text{ec,min}} \le p_t^{\text{ec}} \le x_t^{\text{ec}} p_i^{\text{ec,max}}, \quad \forall t \in N_T, \tag{12}$$

$$x_t^{\text{ed}} p_i^{\text{ed,min}} \le p_t^{\text{ed}} \le x_t^{\text{ed}} p_i^{\text{ed,max}}, \quad \forall i \in N_e, t \in N_T, \tag{13}$$

$$x_{i,t}^{\text{ec}} + x_{i,t}^{\text{ed}} = 1, \quad t \in N_T, \tag{14}$$

$$E_t^{\text{es}} = E_{t-1}^{\text{es}} + \eta^c p_t^{\text{ec}} \Delta t - \frac{1}{\eta^d} p_t^{\text{ed}} \Delta t, \quad \forall t \in N_T, \tag{15}$$

$$E_t^{\text{es,min}} \le E_t^{\text{es}} \le E_t^{\text{es,max}}. \tag{16}$$

Constraints (12) and (13) are ESS charging and discharging power constraints, respectively, where $p_i^{\text{ec,min}}$ and $p_i^{\text{ec,max}}$ are the minimum and maximum limits of ESS charging power, respectively; $p_i^{\text{ed,min}}$ and $p_i^{\text{ed,max}}$ are the minimum and maximum limits of ESS discharging power, respectively; and x_t^{ec} and x_t^{ed} are the binary variables representing ESS charging/discharging status, ESS is in the charging mode if $x_t^{\text{ec}} = 1$, and ESS is in the discharging mode if $x_t^{\text{ed}} = 1$. Constraint (15) is the ESS energy balance constraint, where E_t^{es} is the ESS SOC level, Δt is the time interval of an hour, and η^c and η^d are the charging and discharging coefficients. Constraint (16) is the ESS SOC level constraint, where $E_t^{\text{es,min}}$ and $E_t^{\text{es,max}}$ are the minimum and maximum limits of the ESS SOC level.

2.2.7. Bidirectional Converter Operation Constraint

$$\begin{cases} 0 \le p_t^{\text{atd}} \le x_t^{\text{atd}} p_t^{\text{bc,max}}, & \forall t \in N_T, \\ 0 \le p_t^{\text{dta}} \le x_t^{\text{dta}} p_t^{\text{bc,max}}, & \forall t \in N_T, \\ x_t^{\text{atd}} + x_t^{\text{dta}} = 1, & \forall t \in N_T. \end{cases} \tag{17}$$

Constraint (17) represents the transferring power limit, where $p_t^{\text{bc,max}}$ is the maximum active power converted on the BC and x_t^{atd} and x_t^{dta} are binary variables representing the power conversion direction, power is transferred from the AC side to the DC side if $x_t^{\text{atd}} = 1$, and power is transferred from the DC side to the AC side if $x_t^{\text{dta}} = 1$ and also represents that the BC can operate either in the charging mode or the discharging mode.

Finally, the energy management problem is formulated as a MIQP problem in (1)–(17). It is noted that the AC subproblem and DC subproblem are coupled through the DC conversion power p_t^{atd} and p_t^{dta} in power balance equations (2) and (3) and constraint (17). In order to realize distributed energy management, the AC subgrid operator and DC subgrid operator should solve their own problems independently. Therefore, a P-ADMM-based algorithm is proposed to solve the energy management problem in a distributed manner, which will be detailed in the next section.

3. P-ADMM-Based Solution Method

In this section, the P-ADMM algorithm is used to solve the optimal energy management problem in a distributed manner. Firstly, the MIQP problem is reformulated for the

implementation of the P-ADMM algorithm. Then, the augmented Lagrangian of the problem is introduced. Finally, the P-ADMM-based algorithm is presented.

3.1. Decoupling of Coupled Constraints. To decouple power balance equations and BC operational constraints, a set of auxiliary variables are introduced as follows:

$$\begin{cases} p_t^{\mathrm{dta}} = \widehat{p}_t^{\mathrm{dta}}, p_t^{\mathrm{dta}} = \widetilde{p}_t^{\mathrm{atd}}, p_t^{\mathrm{atd}} = \widehat{p}_t^{\mathrm{atd}}, p_t^{\mathrm{atd}} = \widetilde{p}_t^{\mathrm{dta}}, \\ x_t^{\mathrm{atd}} = \widehat{x}_t^{\mathrm{atd}}, x_t^{\mathrm{dta}} = \widehat{x}_t^{\mathrm{dta}}, x_t^{\mathrm{dta}} = \widetilde{x}_t^{\mathrm{atd}}, x_t^{\mathrm{ec}} = \widehat{x}_t^{\mathrm{ec}}, x_t^{\mathrm{dc}} = \widehat{x}_t^{\mathrm{dc}}. \end{cases} \tag{18}$$

We replace original variables with auxiliary variables, and the model is reformulated.

Objective function of the reformulated model is (1).

Constraints of the reformulated model include original constraints (4)–(11), auxiliary constraint (18), and

$$\widehat{x}_t^{\mathrm{ec}} p_i^{\mathrm{ec,min}} \le p_t^{\mathrm{ec}} \le \widehat{x}_t^{\mathrm{ec}} p_i^{\mathrm{ec,max}}, \quad \forall t \in N_T, \tag{19}$$

$$\widehat{x}_t^{\mathrm{ed}} p_i^{\mathrm{ed,min}} \le p_t^{\mathrm{ed}} \le \widehat{x}_t^{\mathrm{ed}} p_i^{\mathrm{ed,max}}, \quad \forall i \in N_e, t \in N_T, \tag{20}$$

$$\widehat{x}_{i,t}^{\mathrm{ec}} + \widehat{x}_{i,t}^{\mathrm{ed}} = 1, \quad t \in N_T, \tag{21}$$

$$p_t^{\mathrm{UG}} + p_t^{\mathrm{DG}} + \eta_{\mathrm{dta}} \widetilde{p}_t^{\mathrm{atd}} = p_t^{\mathrm{AC\_}L} + \widehat{p}_t^{\mathrm{atd}}, \quad \forall t \in N_T, \tag{22}$$

$$p_t^{\mathrm{ed}} + p_t^{\mathrm{pv}} + \eta_{\mathrm{atd}} \widetilde{p}_t^{\mathrm{dta}} = p_t^{ec} + \sum_{i \in N_e} p_{i,t}^{\mathrm{ev}} + \sum_{i \in N_h} p_{i,t}^{\mathrm{hp}} + \widehat{p}_t^{\mathrm{dta}}, \quad \forall t \in N_T, \tag{23}$$

$$\begin{cases} 0 \le \widehat{p}_t^{\mathrm{atd}} \le \widehat{x}_t^{\mathrm{atd}} p_t^{\mathrm{bc,max}}, & \forall t \in N_T, \\ 0 \le \widehat{p}_t^{\mathrm{dta}} \le \widehat{x}_t^{\mathrm{dta}} p_t^{\mathrm{bc,max}}, & \forall t \in N_T, \end{cases} \tag{24}$$

$$\widehat{x}_t^{\mathrm{atd}} + \widetilde{x}_t^{\mathrm{atd}} = 1, \quad \forall t \in N_T. \tag{25}$$

It is assumed that variables with superscripts of "atd" are affiliated variables of the AC subgrid operator and variables with superscripts of "dta" are affiliated variables of the DC subgrid operator. Therefore, constraints (4)–(11) and (19)–(25) are fully decomposable between the AC and DC subgrids, whereas equality constraint (18) is still coupled.

3.2. Augmented Lagrangian. By adding equality constraint (18) into objective function (1) through dual variables $\Lambda =: \{\lambda_t, \widehat{\lambda}_t, \delta_t, \widehat{\delta}_t, \chi_t, \theta_t, \kappa_t, \psi_t\}$ and the penalty parameter ρ, the augmented Lagrangian of the MIQP model is formulated as follows:

$$\begin{aligned} &\min \sum_{t \in N_T} c_1^G \left(p_t^{\mathrm{DG}}\right)^2 + c_2^G p_t^{\mathrm{DG}} + \lambda_t p_t^{\mathrm{UG}} + \\ &\frac{\rho}{2} \left\{ \left\| p_t^{\mathrm{dta}} - \widetilde{p}_t^{\mathrm{atd}} + \lambda_t \right\|^2 - \left\| \lambda_t \right\|^2 + \left\| p_t^{\mathrm{dta}} - \widehat{p}_t^{\mathrm{dta}} + \widehat{\lambda}_t \right\|^2 - \left\| \widehat{\lambda}_t \right\|^2 \right. \\ &\quad + \left\| p_t^{\mathrm{atd}} - \widetilde{p}_t^{\mathrm{dta}} + \delta_t \right\|^2 - \left\| \delta_t \right\|^2 + \left\| p_t^{\mathrm{atd}} - \widehat{p}_t^{\mathrm{atd}} + \widehat{\delta}_t \right\|^2 - \left\| \widehat{\delta}_t \right\|^2 + \\ &\quad + \left\| x_t^{\mathrm{atd}} - \widehat{x}_t^{\mathrm{atd}} + \chi_t \right\|^2 - \left\| \chi_t \right\|^2 + \left\| x_t^{\mathrm{dta}} - \widehat{x}_t^{\mathrm{dta}} + \theta_t \right\|^2 - \left\| \theta_t \right\|^2 + \\ &\left\| x_t^{\mathrm{dta}} - \widetilde{x}_t^{\mathrm{atd}} + \xi_t \right\|^2 - \left\| \xi_t \right\|^2 + \left\| x_t^{ec} - \widehat{x}_t^{ec} + \kappa_t \right\|^2 - \left\| \kappa_t \right\|^2 + \\ &\left. \left\| x_t^{\mathrm{ed}} - \widehat{x}_t^{\mathrm{ed}} + \psi_t \right\|^2 - \left\| \psi_t \right\|^2 \right\}. \end{aligned} \tag{26}$$

Subject to (4)–(11) and (19)–(25).

The augmented Lagrangian is optimized over two groups of primal variables $\mathbf{X} =: \{p_t^{\mathrm{DG}}, p_t^{\mathrm{UG}}, p_{i,t}^{\mathrm{ev}}, p_{i,t}^{\mathrm{hp}}, p_t^{\mathrm{ec}}, p_t^{\mathrm{ed}}, \widetilde{p}_t^{\mathrm{atd}}, \widehat{p}_t^{\mathrm{dta}}, \widetilde{p}_t^{\mathrm{dta}}, \widehat{p}_t^{\mathrm{atd}}, \widehat{x}_t^{\mathrm{atd}}, \widetilde{x}_t^{\mathrm{atd}}, \widehat{x}_t^{\mathrm{dta}}, \widehat{x}_t^{\mathrm{ec}}, \widehat{x}_t^{\mathrm{ed}}\}$ and $\mathbf{Y} =: \{p_t^{\mathrm{dta}}, p_t^{\mathrm{atd}}, x_t^{\mathrm{atd}}, x_t^{\mathrm{dta}}, x_t^{\mathrm{ec}}, x_t^{\mathrm{ed}}\}$ and a group of dual variables Λ.

3.3. P-ADMM-Based Algorithm. For the ease of presentation, the objective function of the augmented Lagrangian is represented using a compact form $\mathbf{L}(\mathbf{X}, \mathbf{Y}, \Lambda)$. The augmented Lagrangian is solved by the P-ADMM-based algorithm with an iterative procedure, as shown in Algorithm 1, in which optimizations of two subproblems and the dual-variable update procedure are carried out iteratively.

3.4. Subproblem I. In the kth iteration, primal variables $\mathbf{X}^k$ are optimized in subproblem I, given by (26), subject to (4)–(11) and (19)–(25), with parameters $\mathbf{Y}^{*,k-1}$ and Λ^{*k-1} obtained in the $(k-1)$th iteration.

$$\mathrm{Subproblem} \cdot \mathrm{I} : \cdot L\left(\mathbf{X}^k, \mathbf{Y}^{*,k-1}, \boldsymbol{\Lambda}^{*,k-1}\right), \tag{27}$$

s.t. constraints (4)–(11) and (19)–(25).

Subproblem I is a QP problem, and its objective function and constraints can be fully decoupled between AC and DC subgrids. Therefore, subproblem I can be solved in a distributed manner between AC and DC subgrids.

3.5. Subproblem II. The primal variables $\mathbf{Y}^k$ are optimized in subproblem II, given by (27) with parameters $\mathbf{X}^{*,k}$ and Λ^{*k-1} obtained in the kth and $(k-1)$th iteration.

$$\mathrm{Subproblem} \cdot \mathrm{II} : \cdot L\left(\mathbf{X}^{*,k}, \mathbf{Y}^k, \boldsymbol{\Lambda}^{*,k-1}\right). \tag{28}$$

It is noted that subproblem II is a nonconstrained MIQP problem. Instead of directly solving the MIQP problem to optimize binary variables, the binary variables are optimized using the projection function in (28), where $\mathbf{P}_x$ denotes the projection function, which rounds each entry to its nearest binary value. The remaining primal variables are optimized by solving the QP problem after excluding binary variables, which can be fully decoupled between AC and DC subgrids. Therefore, subproblem II can be solved in a distributed manner as well.

$$\begin{cases} x_t^{\mathrm{atd}} = \mathbf{P}_x\left(\widehat{x}_t^{\mathrm{atd}} - \chi_t\right), \\ x_t^{\mathrm{dta}} = \mathbf{P}_x\left(\dfrac{\widehat{x}_t^{\mathrm{dta}} - \theta_t + \widetilde{x}_t^{\mathrm{atd}} - \xi_t}{2}\right). \end{cases} \tag{29}$$

3.6. Update of Dual Variables. After solving subproblems I and II, dual variables are updated in (29).

$$\begin{aligned} \boldsymbol{\Lambda}^k &= \boldsymbol{\Lambda}^{*,k-1} + \left(\mathbf{X}^{\mathrm{ex},*,k-1} - \mathbf{Y}^{*,k}\right), \\ \mathbf{X}^{\mathbf{ex}} &=: \left\{\widetilde{p}_t^{\mathrm{atd}}, \widehat{p}_t^{\mathrm{dta}}, \widetilde{p}_t^{\mathrm{dta}}, \widehat{p}_t^{\mathrm{atd}}, \widehat{x}_t^{\mathrm{atd}}, \widetilde{x}_t^{\mathrm{atd}}, \widehat{x}_t^{\mathrm{dta}}\right\}. \end{aligned} \tag{30}$$

3.7. Stop Criteria. The iterative procedure continues till primal and dual residuals are lower than specified thresholds, respectively, as follows:

$$\left\|\mathbf{X}^{\mathrm{ex},*,k} - \mathbf{Y}^{*,k}\right\|^2 \le \sigma_1, \left\|\mathbf{X}^{\mathrm{ex},*,k} - \mathbf{X}^{\mathrm{ex},*,k-1}\right\|^2 \le \sigma_2. \tag{31}$$

4. Case Studies

A case study was conducted on the hybrid AC/DC system shown in Figure 1 to demonstrate the effectiveness of the proposed distributed energy management scheme. In the system, one DG and conventional loads are connected to the AC bus, whereas one ESS, 200 EVs [30, 32], 200 HPs, and one PV are connected to the DC bus. Figures 2 and 3 show the forecasted spot price and PV active power generation profile. The key parameters of DGs, EVs, HPs, and ESSs are given in Table 1. The P-ADMM-based algorithm is implemented using GAMS [31, 33], and the solution is obtained with the CPLEX solver [34]. In the algorithm, convergence thresholds σ_1 and σ_2 are set as 0.01, and penalty parameter ρ is set as 50.

4.1. Computational Performance. Although the convergence of the P-ADMM-based algorithm cannot be guaranteed for the MIQP model, the algorithm shows good convergence performance. A convergence analysis is conducted by solving the MIQP model with different penalty parameter values between 10 and 150. Table 2 shows that the algorithm can converge within 650 iterations when the penalty parameter value varies within 10 and 150. It can be seen that the convergence performance of the algorithm highly depends on the selection of the penalty parameter value. For example, an improper value $\rho = 30$ would cause nonconvergence within the preset iteration limit (1000). Within the certain range, the algorithm with $\rho = 50$ has the best convergence performance. The convergence process of the P-ADMM-based algorithm with $\rho = 50$ is shown in Figure 4. It can be seen that the primal and dual residuals are lower than thresholds after 91 iterations.

The distributed solution $\mathbf{S}^{\mathrm{d}}$ is compared with the centralized solution $\mathbf{S}^{\mathrm{c}}$ in Table 3(take hour t_{12} as an example). The centralized solution is obtained by solving the MIQP model using the GAMS/CPLEX solver with a zero optimality gap. It is shown in Table 2 that the distributed solution is almost the same as the centralized solution. The maximum relative error (RE) between the centralized and distributed solutions is 1.28% (the RE is calculated by (31)), which is very small and demonstrates that the proposed P-ADMM-based algorithm can reproduce the optimal centralized solution.

$$\mathrm{RE} = \frac{\left\|\mathbf{S}^c - \mathbf{S}^d\right\|}{\left\|\mathbf{S}^c\right\|}. \tag{32}$$

4.2. Energy Management Results. Figures 5 and 6 show the optimal day-ahead energy schedules of the AC and DC subgrids, respectively. In the DC subgrid, the PV active

P-ADMM algorithm
(1) input: system and DER parameters
(2) output: AC and DC energy schedules and BC operation status
(3) while: $\|\mathbf{X}^{\mathrm{ex},*,k} - \mathbf{Y}^{*,k}\|^2 \le \sigma_1, \|\mathbf{X}^{\mathrm{ex},*,k} - \mathbf{X}^{\mathrm{ex},*,k-1}\|^2 \le \sigma_2$
do
Solve subproblem I to update primal variables $\mathbf{X}^k$
Solve subproblem I to update primal variables $\mathbf{Y}^k$
Update dual variables Λ^{k+1}using (30)
end

Algorithm 1: Pseudo-code of the P-ADMM algorithm.

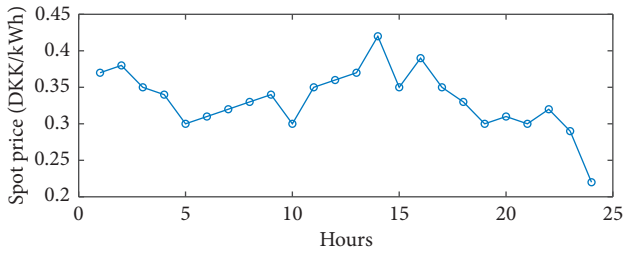

Figure 2: Forecasted spot prices.

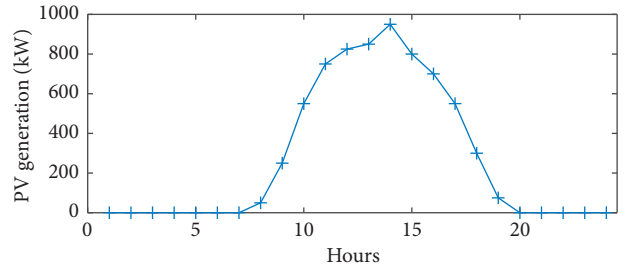

Figure 3: Forecasted PV active power generation.

power, ESS discharging power, and power converted from the AC subgird support the total power consumption of EVs and HPs. For load consumption, it can be seen that EVs and HPs tend to charge more power at hours with relatively low spot prices in order to minimize day-ahead energy costs. For power generations, in most hours, e.g., hours t_1–t_9 and t_{19}–t_{24}, AC power is converted into DC power to support EV and HP power consumption. At hours t_{10}–t_{16}, since there is sufficient PV active power, there is no need to convert AC power into DC power. Especially at hours t_{14} and t_{16}, the DC subgrid delivers surplus power to the AC grid. In addition, the ESS would store surplus power at hours with relatively low prices and discharge power at those hours with relatively high spot prices to minimize energy costs.

In the AC subgrid, the AC operator chooses to dispatch the DG unit or buy external electricity for AC load consumption according to DG energy costs and spot prices. In this case, since the DG energy cost is smaller than the energy cost of purchasing external electricity in most hours, the DG maximum capacity is almost used. In addition, the external purchased electricity profile has almost opposite variation

Table 1: Key parameters used in simulations.

ESS parameters	
ESS battery size $E_t^{\mathrm{es,max}}$	200 kWh
Min/max charging power limit $p_i^{\mathrm{ec,min}}/p_i^{\mathrm{ec,max}}$	0/50 kW
Min/max discharging power limit $p_i^{\mathrm{ed,min}}/p_i^{\mathrm{ed,max}}$	0/50 kW
Charing/discharging coefficients η^c/η^d	0.90/0.90
HP parameters	
COP of HP c_i^{cop}	2.3
Min/max temperature of the house $K_{i,t}^{h,\min}/K_{i,t}^{h,\min}$	20/24oC
Min/max HP power consumption $p_{i,t}^{\mathrm{hp,min}}/p_{i,t}^{\mathrm{hp,max}}$	0/6 kW
EV parameters	
Min/max HP power consumption $p_{i,t}^{ev,\min}/p_{i,t}^{\mathrm{ev,max}}$	0/11 kW
EV availability $a_{i,t}$	1
DG parameters	
Min/max DG active power generation $p_t^{\mathrm{DG,min}}/p_t^{\mathrm{DG,max}}$	0/200 kW
Down- and upramping limits $p_t^{\mathrm{DG,dr}}/p_t^{\mathrm{DG,ur}}$	80 kW
DG energy costs c_1^G/c_2^G	0.001/0.15
BC parameters	
Max. limit of active power converted $p_t^{\mathrm{bc,max}}$	1000 kW
Power transfer coefficients $\eta_{\mathrm{dta}}/\eta_{\mathrm{dta}}$	0.9/0.9

Table 2: Numbers of iterations with different penalty parameter values.

ρ	10	20	30	40	50	100	150
Num. of iterations	633	434	—	175	91	245	404

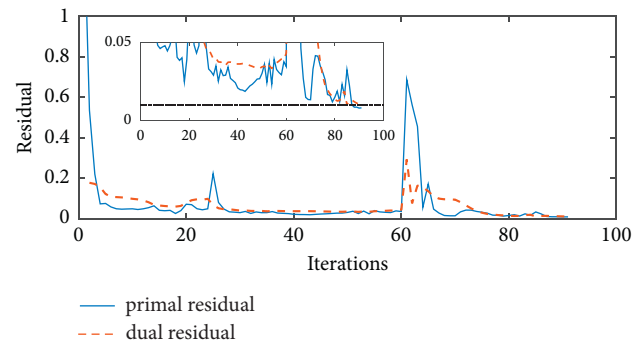

Figure 4: Convergence process of the P-ADMM-based algorithm ($\rho = 50$).

Table 3: Comparison between centralized and distributed solutions (take hour t_{12} as an example).

kW	P_t^{DG}	$\sum P_{i,t}^{ev}$	$\sum P_{i,t}^{hp}$	P_t^{ec}	P_t^{ed}	P_t^{atd}	P_t^{dta}
Centralized	139.9	219.2	559.5	46.2	0	0	0
Distributed	139.9	218.4	559.6	46.8	0	0	0

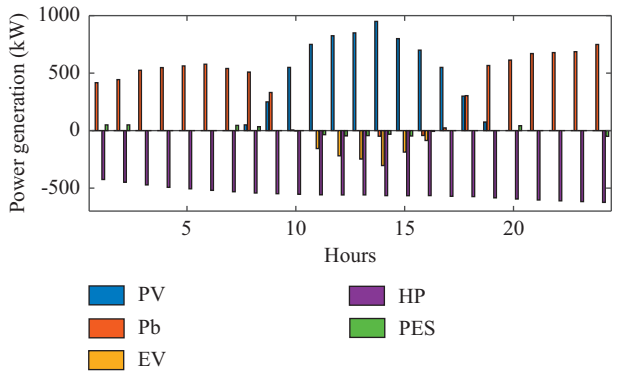

Figure 5: Day-ahead scheduling in the DC grid.

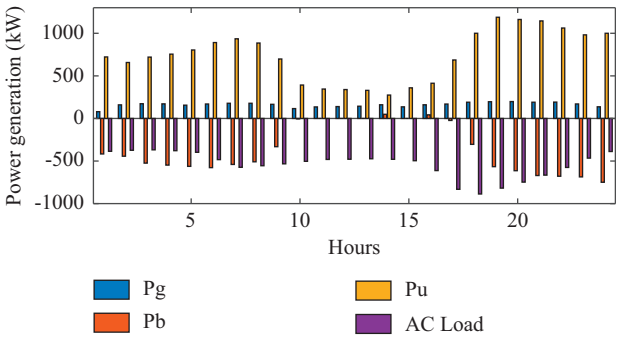

Figure 6: Day-ahead scheduling in the AC grid.

tendency as compared with the forecasted spot price profile in order to minimize energy costs.

5. Conclusions

To resolve the privacy information protection compromise and single-point failure issues when the centralized energy management scheme is applied, this paper proposes a distributed energy management scheme for the hybrid AC/DC microgrid based on the proposed P-ADMM-based algorithm. The energy management problem of the hybrid microgrid is formulated as a MIQP model, considering DER operation constraints, system operation constraints, and converter operation constraints. Then, the MIQP model is decomposed and distributed into smaller-scale submodels between subgrids using the P-ADMM-based algorithm. The numerical results demonstrate that the proposed algorithm can efficiently solve the MIQP model in a distributed manner and can deal with binary variables. The proposed distributed scheme allows each subgrid operator to make day-ahead schedules independently with information exchanges while acquiring the optimal energy management solution.

Data Availability

The data used to support the findings of this study are available from the corresponding author upon request.

Conflicts of Interest

The authors declare that there are no conflicts of interest regarding the publication of this paper.

References

[1] B. Kroposki, B. Johnson, Y. Zhang et al., "Achieving a 100% renewable grid: operating electric power systems with extremely high levels of variable renewable energy," *IEEE Power and Energy Magazine*, vol. 15, no. 2, pp. 61–73, 2017.

[2] C. Wei, Z. Shen, D. Xiao, L. Wang, X. Bai, and H. Chen, "An optimal scheduling strategy for peer-to-peer trading in interconnected microgrids based on RO and nash bargaining," *Applied Energy*, vol. 275, 2021.

[3] C. Gamarra and J. M. Guerrero, "Computational optimization techniques applied to microgrids planning: a review," *Renewable and Sustainable Energy Reviews*, vol. 48, pp. 413–424, 2015.

[4] H. M. A. Ahmed, A. B. Eltantawy, and M. M. A. Salama, "A planning approach for the network configuration of ac-dc hybrid distribution systems," *IEEE Transaction on Smart Grid*, vol. 9, no. 3, pp. 2203–2213, 2018.

[5] C. Zhao, S. Dong, C. Gu, F. Li, Y. Song, and N. P. Padhy, "New problem formulation for optimal demand side response in hybrid ac/dc systems," *IEEE Transactions on Smart Grid*, vol. 9, no. 4, pp. 3154–3165, 2018.

[6] Q. Jiang, M. Xue, and G. Geng, "Energy management of microgrid in grid-connected and stand-alone modes," *IEEE Transactions on Power Systems*, vol. 28, no. 3, pp. 3380–3389, 2013.

[7] A. Khodaei, "Microgrid optimal scheduling with multi-period islanding constraints," *IEEE Transactions on Power Systems*, vol. 29, no. 3, pp. 1383–1392, 2014.

[8] B. V. Solanki, C. A. Canizares, and K. Bhattacharya, "Practical energy management systems for isolated microgrids," *IEEE Transactions on Smart Grid*, vol. 10, no. 5, pp. 4762–4775, 2019.

[9] B. V. Solanki, A. Raghurajan, K. Bhattacharya, and C. A. Canizares, "Including smart loads for optimal demand response in integrated energy management systems for isolated microgrids," *IEEE Transactions on Smart Grid*, vol. 8, no. 4, pp. 1739–1748, 2017.

[10] X. Lu, N. Liu, Q. Chen, and J. Zhang, "Multi-objective optimal scheduling of a DC micro-grid consisted of PV system and EV charging station," in *Proceedings of the 2014 IEEE Innovative Smart Grid Technologies - Asia (ISGT ASIA)*, pp. 487–491, Kuala Lumpur, Malaysia, May 2014.

[11] M. I. Ghiasi, M. A. Golkar, and A. Hajizadeh, "Lyapunov based-distributed fuzzy-sliding mode control for building integrated-DC microgrid with plug-in electric vehicle," *IEEE Access*, vol. 5, pp. 7746–7752, 2017.

[12] M. Dabbaghjamanesh, A. Kavousi-Fard, S. Mehraeen, J. Zhang, and Z. Y. Dong, "Sensitivity analysis of renewable energy integration on stochastic energy management of automated reconfigurable hybrid AC-DC microgrid considering

DLR security constraint," *IEEE Transactions on Industrial Informatics*, vol. 16, no. 1, pp. 120–131, 2020.

[13] Z. Liang, H. Chen, X. Wang, S. Chen, and C. Zhang, "Risk-based uncertainty set optimization method for energy management of hybrid AC/DC microgrids with uncertain renewable generation," *IEEE Transactions on Smart Grid*, vol. 11, no. 2, pp. 1526–1542, 2020.

[14] M. Mahmoodi, P. Shamsi, and B. Fahimi, "Economic dispatch of a hybrid microgrid with distributed energy storage," *IEEE Transactions on Smart Grid*, vol. 6, no. 6, pp. 2607–2614, 2015.

[15] N. Eghtedarpour and E. Farjah, "Power control and management in a hybrid AC/DC microgrid," *IEEE Transactions on Smart Grid*, vol. 5, no. 3, pp. 1494–1505, 2014.

[16] B. Wei, X. Han, P. Wang, H. Yu, W. Li, and L. Guo, "Temporally coordinated energy management for AC/DC hybrid microgrid considering dynamic conversion efficiency of bidirectional AC/DC converter," *IEEE Access*, vol. 8, pp. 70878–70889, 2020.

[17] B. Zhao, H. Qiu, R. Qin, X. Zhang, W. Gu, and C. Wang, "Robust optimal dispatch of AC/DC hybrid microgrids considering generation and load uncertainties and energy storage loss," *IEEE Transactions on Power Systems*, vol. 33, no. 6, pp. 5945–5957, 2018.

[18] P. Teimourzadeh Baboli, M. Shahparasti, M. Parsa Moghaddam, M. R. Haghifam, and M. Mohamadian, "Energy management and operation modelling of hybrid AC-DC microgrid," *IET Generation, Transmission & Distribution*, vol. 8, no. 10, pp. 1700–1711, 2014.

[19] J. Zhao, Q. Wu, N. Hatziargyriou, F. Li, and F. Teng, "Decentralized data-driven load restoration in coupled transmission and distribution system with wind power," *IEEE Transactions on Power Systems*, vol. 36, no. 5, pp. 4435–4444, 2021.

[20] J. Zhao, H. Wang, Q. Wu, N. D. Hatziargyriou, and F. Shen, "Optimal generator start-up sequence for bulk system restoration with active distribution networks," *IEEE Transactions on Power Systems*, vol. 36, no. 3, 2021.

[21] J. Zhao, H. Wang, Q. Wu, N. D. Hatziargyriou, and W. Zhang, "Spatio-temporal decomposition and coordination for distributed load restoration in AC/DC hybrid system," *IEEE Transactions on Smart Grid*, vol. 12, no. 2, 2021.

[22] F. Shen, Q. Wu, X. Jin, B. Zhou, C. Li, and Y. Xu, "ADMM-based market clearing and optimal flexibility bidding of distribution-level flexibility market for day-ahead congestion management of distribution networks," *International Journal of Electrical Power & Energy Systems*, vol. 123, Article ID 106266, 2020.

[23] A. Silani and M. J. Yazdanpanah, "Distributed optimal microgrid energy management with considering stochastic load," *IEEE Transactions on Sustainable Energy*, vol. 10, no. 2, pp. 729–737, 2019.

[24] Q. Xu, T. Zhao, Y. Xu, Z. Xu, P. Wang, and F. Blaabjerg, "A distributed and robust energy management system for networked hybrid AC/DC microgrids," *IEEE Transactions on Smart Grid*, vol. 11, no. 4, pp. 3496–3508, 2020.

[25] F. Shen, Q. Wu, J. Zhao, W. Wei, N. D. Hatziargyriou, and F. Liu, "Distributed risk-limiting load restoration in unbalanced distribution systems with networked microgrids," *IEEE Transactions on Smart Grid*, vol. 11, no. 6, pp. 4574–4586, 2020.

[26] F. Shen, J. C. López, Q. Wu, M. J. Rider, T. Lu, and N. D. Hatziargyriou, "Distributed self-healing scheme for unbalanced electrical distribution systems based on alternating direction method of multipliers," *IEEE Transactions on Power Systems*, vol. 35, no. 3, pp. 2190–2199, 2020.

[27] J. C. López, M. J. Rider, F. Shen, and Q. Wu, "Distributed service restoration of active electrical distribution systems using ADMM," in *Proceedings of the 2019 IEEE Power & Energy Society Innovative Smart Grid Technologies Conference (ISGT)*, pp. 1–5, Washington, DC, USA, February 2019.

[28] F. Shen, Q. Wu, Y. Xu, F. Li, F. Teng, and G. Strbac, "Hierarchical service restoration scheme for active distribution networks based on ADMM," *International Journal of Electrical Power & Energy Systems*, vol. 118, Article ID 105809, 2020.

[29] Q. Zhang, K. Dehghanpour, and Z. Wang, "Distributed CVR in unbalanced distribution systems with PV penetration," *IEEE Transactions on Smart Grid*, vol. 10, no. 5, pp. 5308–5319, 2019.

[30] S. Huang, Q. Wu, S. S. Oren, R. Li, and Z. Liu, "Distribution locational marginal pricing through quadratic programming for congestion management in distribution networks," *IEEE Transactions on Power Systems*, vol. 30, no. 4, pp. 2170–2178, 2015.

[31] C. Wei, M. Benosman, and T. Kim, "Online parameter identification for state of power prediction of lithium-ion batteries in electric vehicles using extremum seeking," *International Journal of Control, Automation and Systems*, vol. 17, no. 11, pp. 2906–2916, 2019.

[32] P. Bacher and H. Madsen, "Identifying suitable models for the heat dynamics of buildings," *Energy and Buildings*, vol. 43, no. 7, pp. 1511–1522, 2011.

[33] GAMS. Language and Environment, https://www.gams.com/latest/docs/UG_MAIN.html#UG_Language_Environment.

[34] Overview of CPELX, https://www.gams.com/latest/docs/S_CPLEX.html.

Hindawi
Complexity
Volume 2021, Article ID 9695452, 9 pages
https://doi.org/10.1155/2021/9695452

Research Article

Numerical Simulation and Computational Flow Characterization Analyses of Centrifugal Pump Operating as Turbine

Du Jianguo,[1] Guanghui Chang,[1] Daniel Adu,[1,2] Ransford Darko,[3] Muhammad A. S. Khan,[1] and Eric O. Antwi[4]

[1]*School of Management Science & Eng., Jiangsu University, Zhenjiang 212013, China*
[2]*Faculty of Engineering, Accra Technical University, Barnes Road, Accra, Ghana*
[3]*Department of Agricultural Engineering, University of Cape Coast PMB 233, Cape Coast, Ghana*
[4]*Department of Energy and Environmental Engineering, University of Energy and Natural Resources Sunyani, Sunyani, Ghana*

Correspondence should be addressed to Daniel Adu; adudaniel39@yahoo.com

Received 29 April 2021; Revised 14 July 2021; Accepted 13 August 2021; Published 21 August 2021

Academic Editor: Xiaoqing Bai

Using a pump in reverse mode as a hydraulic turbine remains an alternative for hydropower generation in meeting energy needs, especially for the provision of electricity to remote and rural settlements. The primary challenge with small hydroelectric systems is attributed to the high price of smaller size hydraulic turbines. A specific commercial pump model, with a flow rate of 12.5 m^3/h, head 32 m, pressure side diameter of 50 mm, impeller out, and inlet diameters of 160 mm and 6 mm, respectively, was chosen for this research. This research aimed to investigate a pump's flow characteristics as a turbine to help select a suitable pump to be used as a turbine for micro- or small hydropower construction. Numerical methodologies have been adopted to contribute to the thoughtful knowledge of pressure and velocity distribution in the pump turbine performance. In this study, the unsteady flow relations amongst the rotating impeller and stationary volute of the centrifugal pump made up four blades and four splitters. Intermittent simulation results of pressure and velocity flow characteristics were studied considering diverse impeller suction angles. The study was conducted by considering a wide range of rotational speeds starting from 750 rpm to 3250 rpm. From the results, it was found that PAT operation was improved when operated at low speeds compared to high-speed operation. Thus, speeds between 1500 rpm and 2000 rpm were suitable for PAT performance. This research helps to realize the unsteady flow physiognomies, which provide information for future research on PAT. This study makes useful facts available which could be helpful for the pump turbine development. Future studies should focus on cost analysis and emission generation in energy generation.

1. Introduction

Centrifugal pumps are commonly used for domestic and industrial applications such as water supply, energy generation, flood control, irrigation for agricultural purposes, and transportation of liquid-solid mixtures. Designs of hydropower plants are based on its ability to function at all-out efficiency matching with acceptable speed. Hydroturbine performance rests on its speed; therefore, it is manufactured to function at the greatest attainable efficiency in a specific rapidity. The role head is to provide speed since the speed rests on its head. The ability of the head variation can affect the performance of the turbine. Therefore, it is essential for the adjustment of rotational speed to result in a possible all-out efficiency [1, 2]. PAT A can, in general, take care of higher flow rates, which sequentially could implicate higher output energy ranges [3]. Nevertheless, since pump producers have not made available pump performance curves in turbine mode, it is usually not easy to select an appropriate pump turbine to run suitably at specific operating conditions, which has become a significant challenge [4]. Several investigational and theoretical research studies were carried out on the performance of pumps running in reverse [5]. The easiest way is the pump model-based prediction since the

user only needs to have access to the necessary information of the pump performance studies, for example, QP, HP, and ηP, as it makes finding correspondent in turbine mode operation easier using simple scheming. As a result, much attention was given to pump mode performance parameters by theoretical researchers such as [6–8]. Many researchers like [9–11] have established some PAT relationships with precise pump speed. Various researchers have continually conducted several research pieces to provide a PAT general performance prediction method [12–14]. Comparative research was conducted by Hossain et al. [15], not forgetting [8, 16] methods to come out with a knowledge edge that is better than the others. The method of [16–18] was discovered to offer a deeper understanding of PAT performance characteristics; they consist of the "area ratio," which was a theoretical method developed in [19–21]. A study was conducted to investigate material consumption and carbon emissions in selected towns and provinces in China. The outcome was that total infrastructure building delivery in the selected towns was not leveled. Thus, infrastructure building supply remained steady along with economic growth [22]. Cao et al. carried out an experiment and numerical study on snowdrift on a typical large-span retractable roof utilizing the Euler-Euler technique. It was revealed that not one unchanging snow delivery on the roofs was different, which must be well thoughtout [23]. Other researchers also researched the various turbines for power generation, axial flow pumps, and energy conservation. [24–26]. A standardized pump can operate as a hydraulic turbine deprived of modifications to the casing or the impeller geometry. Consideration should only be given to the selection of appropriate flow rate (Q), head (H), and speed (n) for a site. It is conceivable to attain an equally high PAT efficiency level as that of pump mode operation in most cases. At best turbine mode operation, the impact of PAT on pressure movement is controlled. The dissimilarity of shared shock loss controls a major part of the energy from the fluid which is then transported open-air through the shaft by PAT. The power take out could be utilized again, either in a mechanical or electrical form. The dissimilarity between the turbine and the pump rests on their rotational bearing, which is indicated by an arrow, as shown in Figure 1. Additionally, the turbine head usually has a higher head and flow at BEP (best efficiency point) than the pump mode at equal speed. Table 1 shows the comparison of methods to obtain BEP for PAT proposed by previous researchers.

2. Centrifugal Pump Model

A specific commercial pump model, which has four main blades and four splitter, head at 16 m, flow rate of 12.5 m^3/h, and running at a speed of 2900 rpm, was carefully chosen for the paper. The pump is mainly composed of long straight pipes, as shown in [27]. The entire computational flow domains were generated using three-dimensional (3D) Pro/*E* 5.0 software. The long straight pipes at the impeller inlet and volute outlet were adequately extended to make the simulation more accurate. Figure 2 displays the complete model of the selected commercial pump.

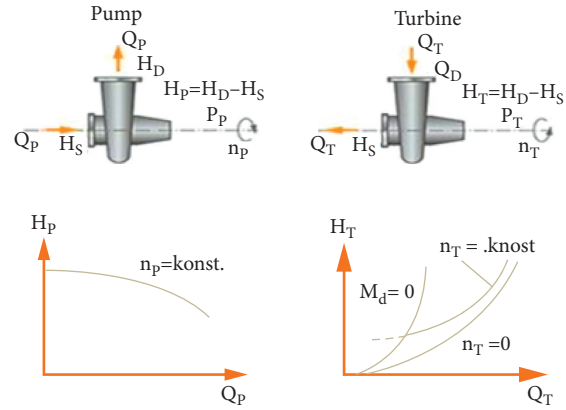

Figure 1: Structure of dissimilarity amongst pump and turbine modes.

Summary of the scheme parameters and hydraulic evaluation description of the selected centrifugal pump model under the study are presented in Table 2.

3. Numerical Simulations

3.1. Computational Domains. Meshing is the process of discretizing a region under consideration to a set of the control volume. Mesh for diverse PAT scheme parts such as volute covering, wearing the ring, and front plus back chambers is generated in ANSYS ICEM 14.5. The CFD calculation method was used. An unstructured grid with a tetrahedral mesh was selected to represent and create all the parts of PAT fluid domains. Since mesh of this type has outstanding compliance, particularly for flows which has complicated border situations. Mesh independence study was performed by Zhang et al. [28], and the results show that mesh size of 1.65 was selected for creating the computational domain, bearing in mind the structure of the applied computing, for which Figure 3 provides the pictures of the whole mesh areas.

3.2. Transient Simulation Setup. In carrying out a numerical study, ANSYS CFX code 16 was chosen for creating PAT geometry. The K-omega (k-ω) turbulence model was selected for the study [8]:

$$\frac{\partial \mathbf{k}}{\partial \mathbf{t}} + \mathbf{U_j}\frac{\partial \mathbf{k}}{\partial \mathbf{x_j}} = \mathbf{P_k} - \boldsymbol{\beta}^{*}\mathbf{k}\boldsymbol{\omega} + \frac{\partial}{\partial \mathbf{x_j}}\left(\mathbf{v} + \boldsymbol{\sigma}_\mathbf{k}\mathbf{v_T}\right)\frac{\partial \mathbf{k}}{\partial \mathbf{x_j}}, \quad (1)$$

Specific dissipation rate:

$$\frac{\partial \boldsymbol{\omega}}{\partial \mathbf{t}} + \mathbf{U_j}\frac{\partial \boldsymbol{\omega}}{\partial \mathbf{x_j}} = \propto \mathbf{s}^2 - \boldsymbol{\beta}\boldsymbol{\omega}^2 + \frac{\partial}{\partial \mathbf{x_j}}\left(\mathbf{v} + \boldsymbol{\sigma}_\boldsymbol{\omega}\mathbf{v_T}\right)\frac{\partial \boldsymbol{\omega}}{\partial \mathbf{x_j}} + 2\left(1 - \mathbf{F_1}\right)\boldsymbol{\sigma}_{\boldsymbol{\omega}2}\frac{1}{\boldsymbol{\omega}}\frac{\partial \mathbf{k}}{\partial \mathbf{x}}\frac{\partial \boldsymbol{\omega}}{\partial \mathbf{x_i}}. \quad (2)$$

The values $\mathbf{k}$ and $\boldsymbol{\omega}$ follow closely after the transport equations for turbulent kinetic energy as well as the dissipation range of turbulence [6].

Table 1: Comparison methods to obtain BEP for PAT.

N_s (m, m^3/s)	η_{Pmax} (%)	D (m)	h	q	h	q	h	q	h	q	h	q
14.6	65.5	0.250	2.05	1.56	1.63	1.28	1.78	1.45	2.20	2.09	2.14	1.48
14.7 (Williams, 1992)	46	0.125	2.87	1.63	2.17	1.47	2.54	1.86	2.84	2.4	2.71	1.72
20.7 (micro-hydropower development, 2003)	60	0.160	2.24	1.73	1.84	1.42	2.4	1.66	2.22	2.04	2.29	1.74
23.0	76	0.250	1.95	1.59	1.41	1.19	1.49	1.29	1.78	1.76	1.94	1.60
34.8 (Joshi S., 2005)	83	—	1.71	1.55	1.28	1.14	1.34	1.20	1.49	1.36	1.70	1.48
36.4 (Singh, 2005)	74.4	0.175	1.72	1.54	1.81	1.34	1.43	1.27	1.73	1.78	1.71	1.50
37.7	86.5	0.250	1.73	1.48	1.24	1.11	1.27	1.16	1.34	1.16	1.65	1.44
45.2 (Singh, 2005)	80	0.200	1.40	1.38	1.56	1.25	1.31	1.2	1.51	1.49	1.51	1.33
55.6	87	0.250	1.34	1.15	1.23	1.11	1.26	1.16	1.32	1.13	1.38	1.18

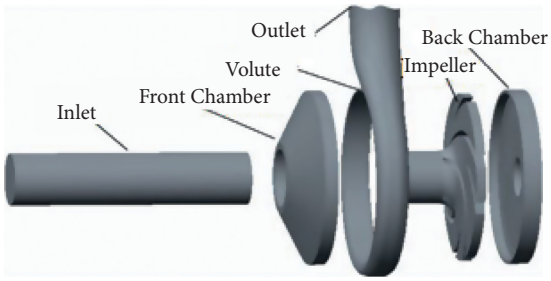

Figure 2: Complete 3D model of the selected centrifugal pump.

Table 2: Scheme parameters of the selected pump model.

Pressure side diameter, D_1	50 mm	Flow rate, qd	12.5 m3/h
Impeller out diameter, D_2	160 mm	Head, hd	32 m
Impeller out width, b_2	6 mm	Efficiency, η	56%
Long blades		4	4
Splitter		4	4
Splitter inlet diameter	di/mm	104 mm	
Power P	3 kW	Speed, n	2900 rpm

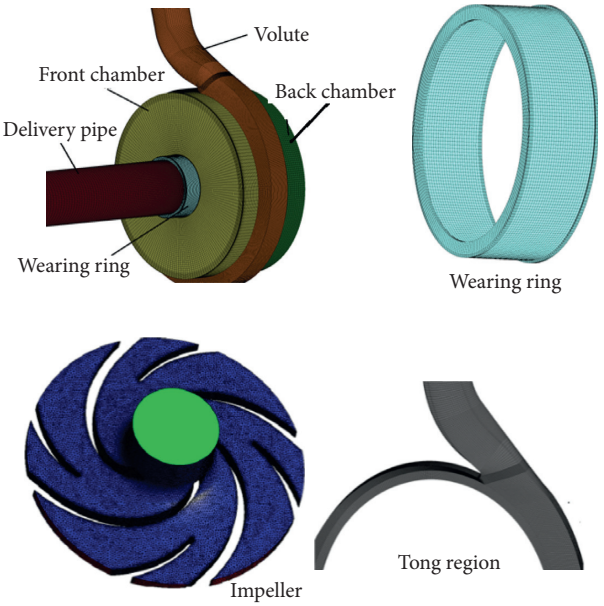

Figure 3: The whole created mesh areas of the selected centrifugal pump model.

All boundary conditions were set. The steady calculations were first performed to make an initial flow field available for the unsteady simulation. In each time step, 1×12^{-5} was set. The simulation was conducted for 12 complete impeller rotations to achieve a steady simulation outcome. Flow field, pressure, and absolute velocity data were further studied in the study. There was one interface between the two domains when simulating a PAT model. This interface was found between the stationary volute and the rotating impeller domain. The interface between domains is created using the "interface" icon on the toolbar. The entire interface was designed, and the interface type was set to a fluid-fluid interface. The general grid interface (GGI) connection option was selected as the interface model for the two separate individual rotary and stator fields. The stationary blade was used for frame change.

4. Results and Discussion

4.1. Hydraulic PAT Performs Characteristics Curves. The speed of a turbine is determined by the amount of load used. At constant flow rate and head, the turbine speed decreases when the turbine uses a higher load more than the design load; with the decrease of the burden placed on a turbine, whereas the head and flow rate remain constant, the turbine speed increases [29]. The same principle applies when hydraulic pumps are used as a turbine at a specified site with a continuous flow rate and contribute significantly to determining the turbine's performance characteristics. As the PAT load is further reduced, the PAT's speed reaches a maximum value at which the PAT can deliver no torque. This speed is called runaway speed. The PAT's runaway speed was obtained to be approximately 2250 rpm, as can be seen in Figure 4, while Figure 5 shows the relationship between speed and power. From the results, as the speed of PAT increases, the power output also rises until it reaches 1750 rpm (512 kw), after which the power began to drop progressively. Increase in PAT's efficiency with the increase in impeller's rotational speed, until it reaches 1500 rpm should be also mentioned, as shown in Figure 6. It means that when PAT operates beyond 1500 rpm, the efficiency of the PAT will decrease. PAT efficiency behaves equally as the power output of the PAT. Therefore, it can be concluded that the best-operating conditions for selected PAT could be achieved when it operates between 1000 and 1750 pm.

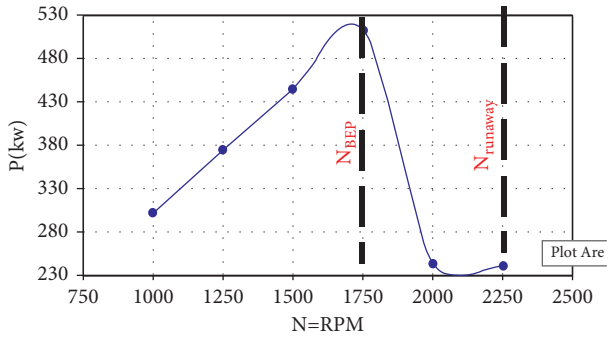

Figure 4: Power vs. rotational speed for selected PAT at $Q_t = 1.2\ m^3/s$.

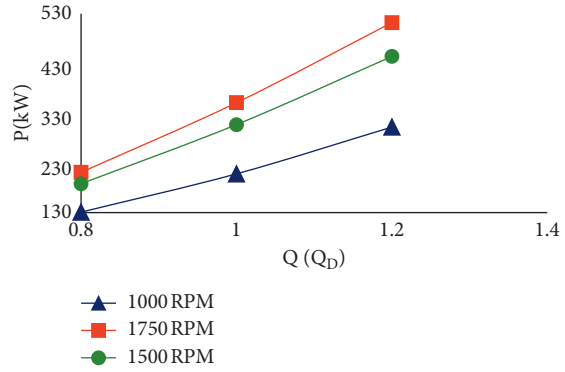

Figure 5: Power vs. rotational speed for selected PAT.

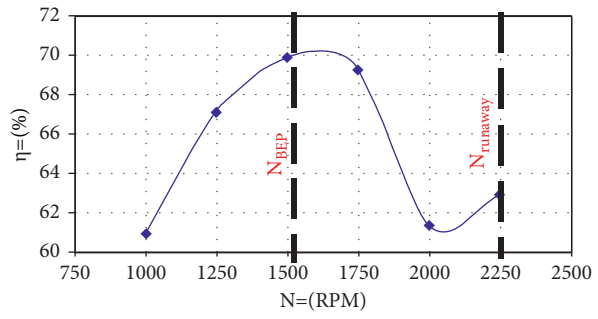

Figure 6: Power vs. efficiency for selected PAT at $Qt = 1.2\ m^3/s$.

4.2. Performance of PAT Predicted Based on Pump Performance. PAT simulation results acquired from ANSYS CFX was used to evaluate the performance parameters of the PAT. It is essential to recognise these parameters for PAT performance under different flow rate conditions. They consist of the head, power, and nondimensionless coefficients such as head, flow, and power coefficient. Pump mode data can predict PAT performance by using the pump BEP. This section will determine the PAT performance using the BEP of the pump and compare anticipated results with the CFD simulation result. The performance parameters of PAT could be predicted by considering pump mode performance. The public affinity laws are used to establish relationships between the performance parameters of similar machines operating under similar kinematic conditions. It is essential to know the following dimensionless parameters, which are vital in determining the turbine's performance characteristics. They consist of a head, flow, and power coefficient. The similarities between these parameters are that the variables with the particular coefficient are made dimensionless through normalising with a diameter (D) and rotation speed (N). Except for the flow coefficient, previous and latter parameters call for one additional variable to normalise. The dimensionless coefficients result realised from the PAT numerical simulation has also been plotted as displayed in Figure 5, showing the head coefficient, flow coefficient, and power coefficient. These results show the differences which exist among these coefficients. Thus, Figure 6 indicates the difference in the head coefficient at different flow coefficient levels and different rotational speeds. It can be witnessed from the results that the increase in the head coefficient increases the flow coefficient, but this occurs at a different rotational speed; thus, increase in rotational speed decreases the head coefficient as shown in Figure 7. Figure 8 shows the difference in the flow coefficient via the power coefficient. One can observe from the figure that the power coefficient performs comparably with the PAT flow coefficient under different flow rate conditions. It is characterised by reducing the value as the flow coefficient drops. Figure 9 shows the head coefficient vs. flow coefficient curves of a selected PAT at a different flow rates.

The nondimensional parameters at various rotational speeds have been studied (let us say $\phi = 0.8$), as tabulated in Table 3. The study discovered that an increase in speed increases power coefficient (π) and efficiency η. Nevertheless, their differences in ψ were not much except at higher speeds. The results are as shown in the curves below, with the BEP points at different rotational speeds also indicated. The power output and efficiency were found better in the speed range of 1000–1200 rpm. As PAT operates in the opposite direction of pump mode operation, the energy converted from hydraulic to mechanical might not be effectual at higher speeds, causing its better performance at the lower speed level.

4.3. Transient Static Pressure Supply under Diverse Flow Rate in Lieu of Centrifugal Pump Impeller. Pressure distribution under different flow conditions and rotational speed in pump as turbine fluid domain are displayed in Figure 10. From the results, pressure progressively intensified in a streamwise way with the pressure side recording the maximum. Flow parting could be observed at the impeller blade leading edge. The flow at the inlet is not at a tangent with a blade with uniformed flow observed near the blade, which causes flow parting to occur on the blade surface. Minimal pressure was found at the impeller inlet along the suction area, representing location cavitation which usually occurs in pumps.

It is observed from Figure 11 that static pressure was asymmetrically disseminated. The minimum pressure happens at the blade suction area. Pressure increases as the flow rate reaches the lowest values, while it decreases with increasing flow rates, as shown in Figure 11(b). Comparing the

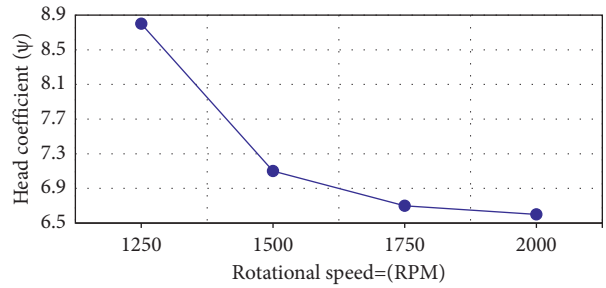

Figure 7: Rotational speed vs. head coefficient characteristics curve of selected PAT at $Qt = 0.8\ m^3/s$.

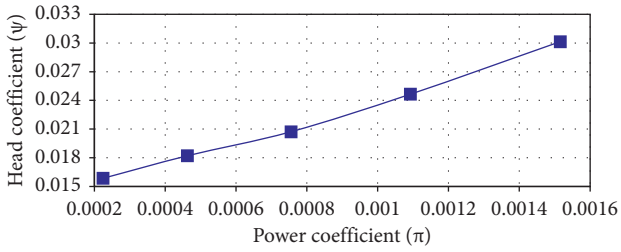

Figure 8: Power coefficient vs. flow coefficient curve of selected PAT at $Qt = 0.8\ m^3/s$ and $n = 1500$ rpm.

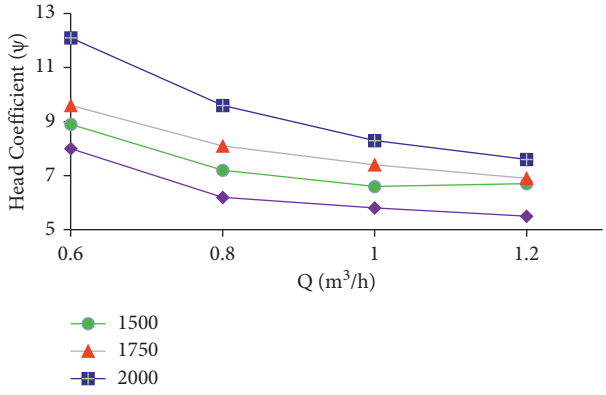

Figure 9: Head coefficient vs. flow coefficient curves of a selected PAT at a different flow rates.

Table 3: Parameters at $\phi = 0.8$ at different rotational speeds for the original impeller.

N (rpm)	ψ	π	ϕ	η (%)
1250	8.8	0.16	7.71	0.00202
1500	7.1	0.07	6.45	0.00207
1750	6.6	0.08	5.53	0.00184
2000	6.4	0.04	4.84	0.00106

two selected rotational speeds under three flow conditions from $Q = 0.08\ m^3/s$ to $Q = 1.2\ m^3/s$, a rise in the flow rate also brought about an increase in drop closer to the exit duct of the volute. Proper recirculation of flow could be observed at the impeller suction area due to lower flow rates, though the flow on the pressure side is smooth. On the contrary, as the flow rate increases, flow parting along the pressure side occurs, bringing about continuous flow movement in the pressure side. This movement in the suction side of the impeller blade drops as the flow rate rises.

4.4. Transient Velocity Distribution in the PAT Model for a Selected Centrifugal Pump. Hydrodynamics of flow in PAT was numerically calculated using CFD to find the supply of actual parameters defining hydrodynamics flow in the pump, which interconnects the PAT characteristics' geometric model. Figure 12 shows the velocity in the PAT colored by relative velocity distribution. Considering the volute shape, one could observe the velocity increase with a rise flow rate. Flow then moves smoothly in the volute region at a minimal flow rate. Moreover, it slows down after striking the trailing edge of the impeller, after which relative fluid velocity begins to once again increase to some extent. The CFD model shows a trend of velocity differences with changes in rotational speed. It was also observed that, as water enters the suction side, relative velocity intensified next to the curving of the blade in the streamwise direction as the passage bit by bit gets smaller. In summary, a portion of the simulation was performed by the PAT impeller as a feedback turbine as a result of reaction from the pressure drop, with a change in kinetic energy also playing a role.

4.5. Transient Static Pressure Distribution for Centrifugal Pump Impeller. In analysing flow features of the centrifugal pump in pump mode, pressure and velocity contour plots and vectors are employed. The streamlines of the 3D models are plotted to examine the flow design in a centrifugal pump. Figure 13 displays the static pressure transfer of the designated PAT model under a diverse flow rate at $n = 1750$ rpm. The results show that lower static pressure was observed at the blade leading edge. As kinetic energy flowed and transported to fluid, the static pressure progressively increases. The figure shows that maximum pressure was monitored on the blade side, whereas minimal pressure was also detected on the blade suction side at the same radial position. As the fluid leads, it is a way to the volute casing. The static pressure further increased, as shown in Figure 13, which could be attributed to the conversion of the fluid's kinetic energy to pressure energy because of the increasing casing cross-segment region. Figure 14 also displays the velocity delivery of the designated PAT model under diverse flow rate, $n = 1750$ rpm.

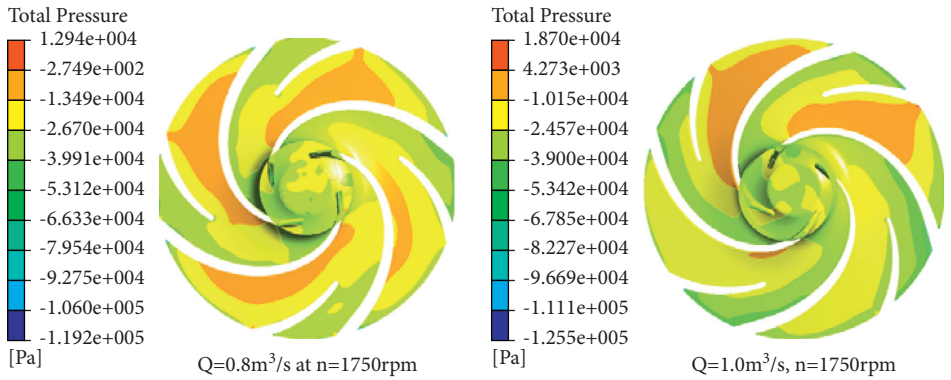

Figure 10: Total pressure distribution on the PAT impeller at a different flow rate.

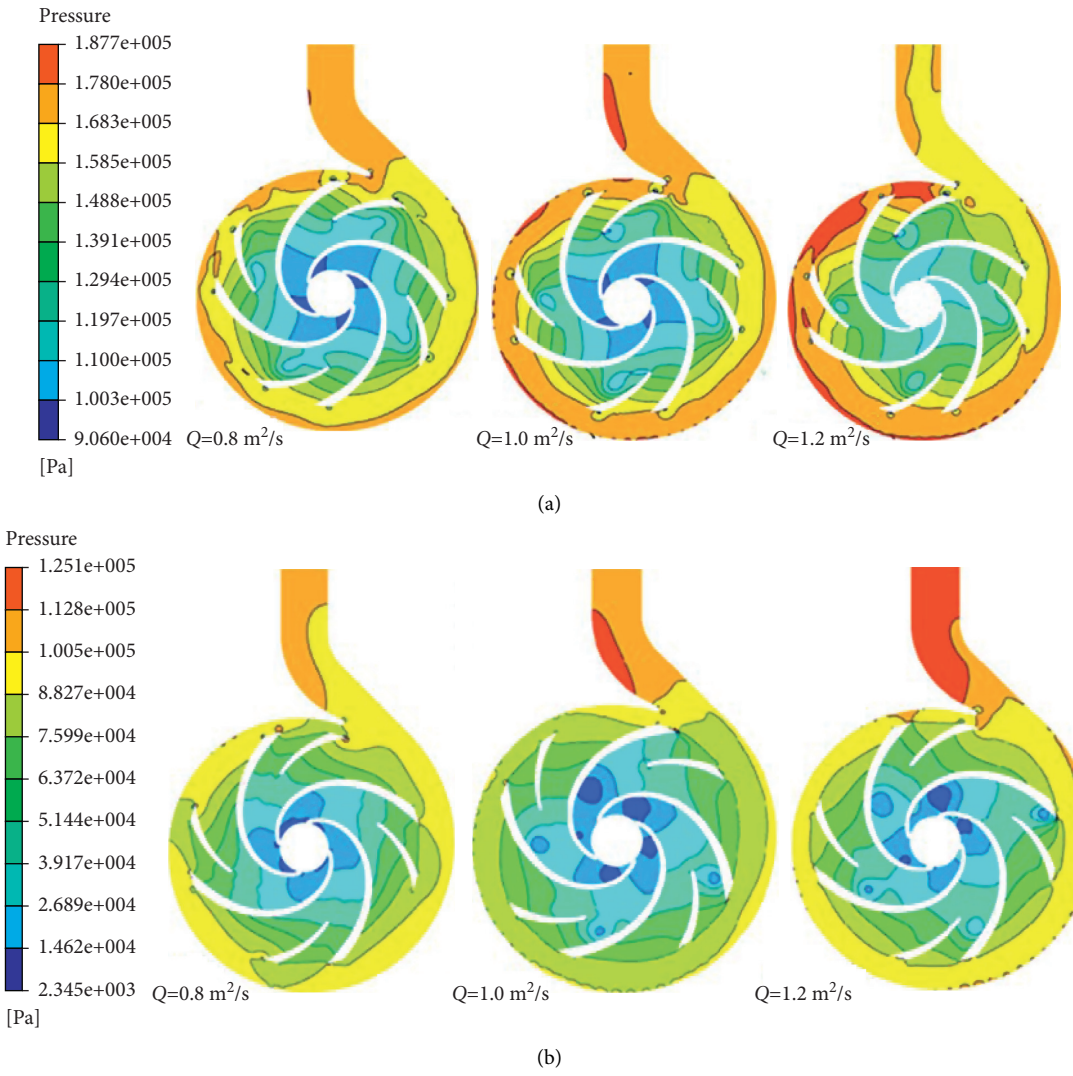

Figure 11: (a) 3D pressure dissemination for the PAT model under the dissimilar flow rate, $n = 1750$ rpm. (b) 3D pressure dissemination for the PAT model under different flow rates, $n = 1500$ rpm.

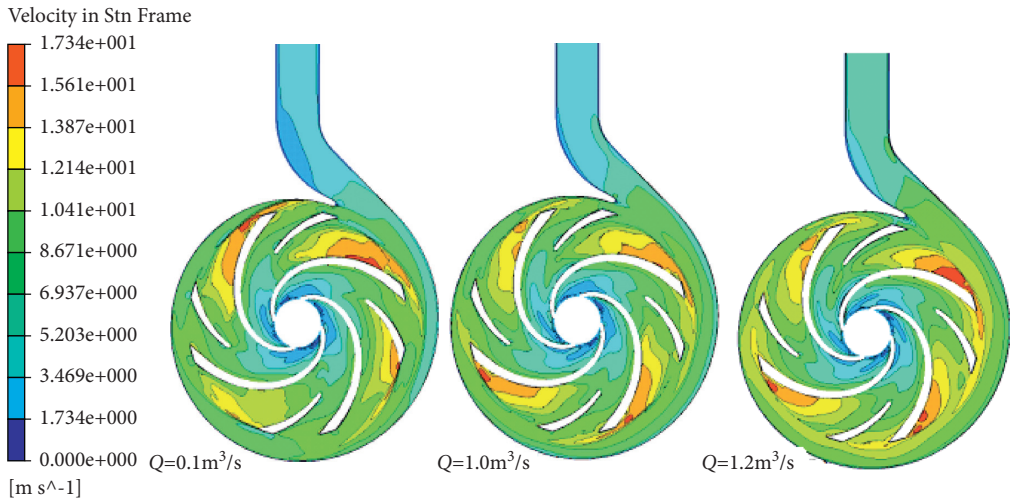

Figure 12: Absolute velocity delivery of the designated PAT model under diverse flow rate, $n = 1750$ rpm.

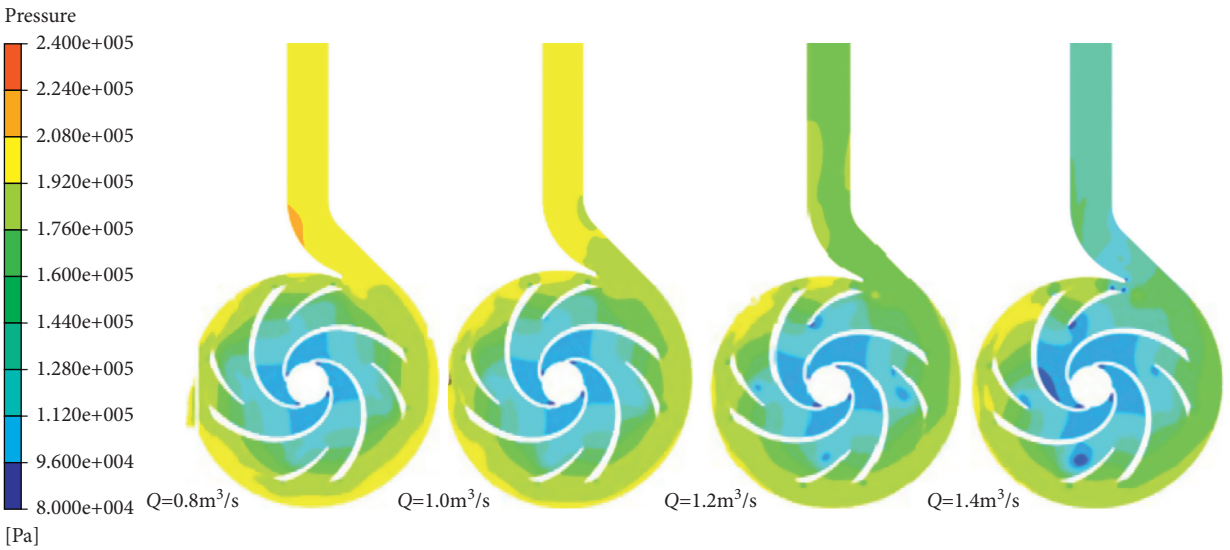

Figure 13: Static pressure delivery of the designated PAT model under diverse flow rate, $n = 1750$ rpm.

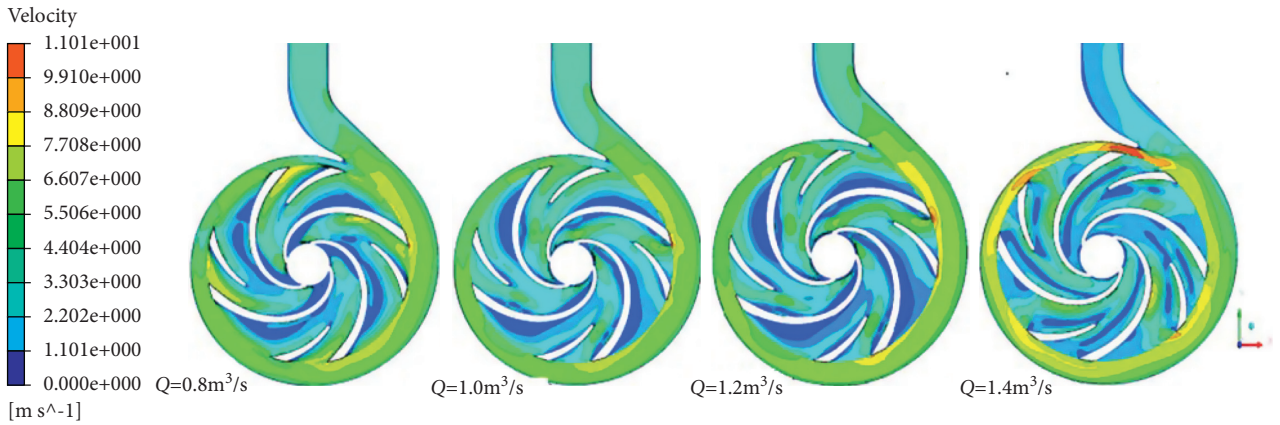

Figure 14: Velocity distribution for the selected centrifugal pump model at different flow rates, $N = 1750$ rpm.

5. Conclusion

In this study, the comparison of numerical studies results obtained under different flow and speed conditions was investigated. From the study, the following conclusions were made:

(A) The speed of a turbine is determined by the amount of load used. At constant flow rate and head, the turbine speed decreases when the turbine uses a higher load more than the design load; with the decrease of the burden placed on a turbine, whereas the head and flow rate remain constant, the turbine speed increases. The same principle applies when hydraulic pumps are used as a turbine at a specified site with a continuous flow rate and contribute significantly to determining the turbine's performance characteristics. As the PAT load is further reduced, the PAT's speed reaches a maximum value that the PAT can deliver no torque. This speed is called runaway speed. The runaway speed of the PAT was obtained to be approximately 2250 rpm.

(B) Increase in PAT's efficiency with the increased rotational speed of the impeller till it reaches 1500 rpm should also be mentioned. It means that when PAT operates beyond 1500 rpm, the efficiency of the PAT will decrease. In comparison with Figures 6 and 7, PAT efficiency behaves equally as the power output of the PAT. Therefore, it can be concluded that the best-operating conditions for selected PAT could be achieved when it operates between 1000 rpm and 1750 rpm.

(C) Pressure distribution under different flow conditions and rotational speed in the pump as turbine fluid domain. From the results, pressure progressively intensified in a streamwise way with the pressure side recording the maximum. Flow parting could be observed at the impeller blade leading edge. The flow at the inlet is not at a tangent with the blade with ununiformed flow observed near the blade, which causes flow parting to occur on the blade surface. Minimal pressure was found at the impeller inlet along the suction area, representing location cavitation typically occurs in pumps.

In summary, PAT simulation results acquired from ANSYS CFX have been used to evaluate the PAT's performance parameters. It is essential to recognise these parameters for PAT performance under different flow rate conditions. They consist of the head, power, and non-dimensionless coefficients such as head, flow, and power coefficient. Pump mode data can predict PAT performance by using the pump BEP.

Data Availability

The data are openly available in a public repository that issues datasets with DOIs. The authors confirm that the data supporting the findings of this study are available within the article and could be obtained upon request. The data, generated at a central, large-scale facility, are available upon request. Raw data were generated at Jiangsu University Lab. The derived data supporting the findings of this study are available from the corresponding author upon request.

Conflicts of Interest

The authors declare that they have no conflicts of interest.

Acknowledgments

This study was supported by the National Science Foundation of China, under Grant nos. 71974081, 71704066, and 71971100, and special funds of the National Social Science Fund of China (Grant no. 18VSJ038).

References

[1] J. González and C. Santolaria, "Unsteady flow structure and global variables in a centrifugal pump," *Journal of Fluids Engineering*, vol. 128, no. 5, pp. 937–946, 2006.

[2] B. K. Gandhi, S. N. Singh, and V. Seshadri, "Performance characteristics of centrifugal slurry pumps," *Journal of Fluids Engineering*, vol. 123, no. 2, pp. 271–280, 2001.

[3] H. Nautiyal, A. Varun, and A. Kumar, "Reverse running pumps analytical, experimental and computational study: a review," *Renewable and Sustainable Energy Reviews*, vol. 14, no. 7, pp. 2059–2067, 2010.

[4] S. V. Jain and R. N. Patel, "Investigations on pump running in turbine mode: a review of the state-of-the-art," *Renewable and Sustainable Energy Reviews*, vol. 30, pp. 841–868, 2014.

[5] H. Nautiyal, V. Varun, A. Kumar, and S. Y. S. Yadav, "Experimental investigation of centrifugal pump working as turbine for small hydropower systems," *Energy Science and Technology*, vol. 1, pp. 79–86, 2011.

[6] A. J. Stepanoff, *Centrifugal and Axial Flow Pumps, Design and Applications*, John Wiley & Sons, New York, NY, USA, 1957.

[7] S. Childs, "Convert pumps to turbines and recovers HP," *Hydrocarbon Processing and Petroleum Refiner*, vol. 41, pp. 173-174, 1962.

[8] R. K. Sharma, *Small Hydroelectric Projects—Use of Centrifugal Pumps as Turbines*, Kirloskar Electric Co, Bangalore, India, 1984.

[9] S. Gopalakrishnan, "Power recovery turbines for the process industry," in *Proceedings of the Third International Pump Symposium*, pp. 3–11, Texas A&M University, Houston, TX, USA, September 1986.

[10] H. Diederich, "Verwendung von kreiselpumpen als turbinen," *KSB Techn Ber*, vol. 12, pp. 30–36, 1967.

[11] K. Grover, *Conversion of Pumps to Turbines*, GSA Inter corporate, Katonah, NY, USA, 1982.

[12] A. Morabito and P. Hendrick, "Pump as turbine applied to micro energy storage and smart water grids: a case study," *Applied Energy*, vol. 241, pp. 567–579, 2019.

[13] M. Rossi, A. Nigro, and M. Renzi, "Experimental and numerical assessment of a methodology for performance prediction of pumps-as-turbines (PaTs) operating in off-design conditions," *Applied Energy*, vol. 248, pp. 555–566, 2019.

[14] B. Luo and X. C. L. Wang, "Numerical simulation of flow-induced vibration of double-suction centrifugal pump as turbine," *Journal Drainage Irrigation Mechanical Engineering*, vol. 37, pp. 313–318, 2019.

[15] I. M. Hossain, S. Ferdous, and T. Jamal, "Pump-as-turbine (PAT) for small-scale power generation: a comparative analysis," in *Proceedings of the 2014 3rd International Conference on the IEEE Developments in Renewable Energy Technology (ICDRET)*, pp. 1–5, Dhaka, Bangladesh, May 2014.

[16] J.-M. Chapallaz, P. Eichenberger, and G. Fischer, "Manual on pumps used as turbines," *Vieweg*, vol. 11, 1992.

[17] S. Derakhshan and A. Nourbakhsh, "Theoretical, numerical and experimental investigation of centrifugal pumps in reverse operation," *Experimental Thermal and Fluid Science*, vol. 32, no. 8, pp. 1620–1627, 2008.

[18] P. Vasanthakumar, J. Krishnaraj, S. Karthikayan, T. Vinoth, and S. K. Arun Sankar, "Investigation on reverse characteristics of centrifugal pump in turbine mode: a comparative study by an experimentation and simulation," *Materials Today: Proceedings*, vol. 4, no. 2, pp. 693–700, 2017.

[19] M. Gantar, "Propeller pumps running as turbines," in *Proceedings of the Conference on Hydraulic Machinery*, pp. 237–248, Ljubljana, Slovenia, August 1988.

[20] H. H. Anderson, "Borehole pumps," *Centrifugal Pumps and Allied Machinery*, vol. 4, pp. 177–185, 1993.

[21] D. Adu, J. Zhang, M. Jieyun, S. N. Asomani, and M. Osman Koranteng, "Numerical investigation of transient vortices and turbulent flow behaviour in centrifugal pump operating in reverse mode as turbine," *Materials Science for Energy Technologies*, vol. 2, no. 2, pp. 356–364, 2019.

[22] H. Wang, Y. Wang, C. Fan et al., "Material consumption and carbon emissions associated with the infrastructure construction of 34 cities in northeast China," *Complexity*, vol. 2020, Article ID 4364912, 20 pages, 2020.

[23] Z. Cao, M. Liu, and P. Wu, "Experiment investigation and numerical simulation of Snowdrift on a typical large-span retractable roof," *Complexity*, vol. 2019, Article ID 5984804, 14 pages, 2019.

[24] K. Ren, H. Li, S. Li, and H. Dong, "Voltage stability analysis of front-end speed controlled wind turbine integrated into regional power grid based on bifurcation theory," *Complexity*, vol. 2020, Article ID 8816334, 11 pages, 2020.

[25] D. Flórez-Orrego, I. B. Henriques, T.-V. Nguyen et al., "The contributions of prof. Jan Szargut to the exergy and environmental assessment of complex energy systems," *Energy*, vol. 161, pp. 482–492, 2018.

[26] Y. Zhang, Y. Xu, Y. Zheng et al., "Multiobjective optimization design and experimental investigation on the axial-flow pump with orthogonal test approach," *Complexity*, vol. 2019, Article ID 1467565, 14 pages, 2019.

[27] X. Xu, X. Yuan, M. Cui, Y. Yuan, and L. Qi, "Joint optimization of energy conservation and migration cost for complex systems in edge computing," *Complexity*, vol. 2019, Article ID 6180135, 14 pages, 2019.

[28] Y. L. Zhang, S. Q. Yuan, Z. Jinfeng et al., "Numerical investigation of the effects of splitter blades on the cavitation performance of a centrifugal pump," *IOP Conference Series: Earth and Environmental Science*, vol. 22, Article ID 052003, 2014.

[29] Z. Jinfeng, A. Daniel, S. Lv, and K. Majid, "Small hydropower by using pump as turbine for power generation in Southern Africa," *Current Science*, vol. 118, no. 3, 2019.

Hindawi
Complexity
Volume 2021, Article ID 2073332, 11 pages
https://doi.org/10.1155/2021/2073332

Research Article

Optimal Power Flow Algorithm Based on Second-Order Cone Relaxation Method for Electricity-Gas Integrated Energy Microgrid

Fan Zhang,[1] Zhuzheng Shen,[2] Wen Xu,[1] Guofeng Wang ,[2] and Biyi Yi[1]

[1]*Zhejiang Huayun Electric Power Engineering Design Consulting Co. Ltd, Hangzhou 310014, China*
[2]*College of Information Engineering, Zhejiang University of Technology, Hangzhou 310023, China*

Correspondence should be addressed to Guofeng Wang; gf_wang18@163.com

Received 21 May 2021; Revised 23 June 2021; Accepted 13 August 2021; Published 20 August 2021

Academic Editor: Abdellatif Ben Makhlouf

Due to the existence of nonlinear constraints, it is difficult to solve the power flow directly. This paper proposes a microgrid optimal scheduling strategy using second-order cone relaxation method to realize linear transformation, so as to minimize the total cost of the microgrid. Firstly, a microgrid system model of electricity-gas integrated energy is established, and the nonlinear constraints of branch power flow are transformed by the second-order cone relaxation method. Then, based on the microgrid model, the application conditions of the second-order cone relaxation transformation method are studied, and the optimal scheduling strategy with the total cost of microgrid as the objective function is proposed. In addition, in the case that the microgrid system does not meet the application conditions of second-order cone programming, the optimization problem is solved by increasing the line loss. Finally, an example is given to verify the effectiveness of the proposed method.

1. Introduction

In recent years, with the rapid development of the global economy, the energy demand has become larger, which leads to the rapid depletion of fossil fuels and the increasing global environmental pollution [1, 2]. As a small system including distributed energy, energy storage system, thermal and electrical load, protection, and monitoring devices, microgrid will play an important role in the future energy network. It can give full play to the economic and environmental benefits of distributed generation and has great social and economic significance. At the same time, it is also of great significance for maintaining system stability, improving the efficiency of energy management and environmental protection [3, 4], so the research on microgrid system is increasingly important.

Nowadays, most of the researches focus on the structure and algorithm of microgrid. In the aspect of microgrid structure, it mainly involves the types and coupling relationships of various energy sources in microgrid. Related researches include the establishment of combined cooling heating and power (CCHP) system model based on electricity cooling heating structure [5]. Considering the coupling relationship between wind turbine and photovoltaic, an integrated energy microgrid optimization model is established [6]. In addition, energy storage system plays an important role in energy storage optimization because of its advantages of flexible regulation, so the research on microgrid including energy storage system is also very extensive. In reference [7], an analogue energy storage model is proposed to represent the time-dependency characteristics of energy transfer processes. In reference [8], the microgrid consists a rooftop photovoltaic (PV) system, a battery energy storage system (BESS), an ice-thermal energy storage system (ice-TESS), and loads. On the basis of the above, hydrogen energy, as a clean energy, is more and more widely used in microgrid systems. The integrated energy system dominated by hydrogen energy provides the direction for the future development of integrated energy system [9]. There are some researches on the optimization algorithm of micro network.

The common methods are to minimize the total cost of the system and to solve the problem by using mixed-integer programming method [10]. In order to meet the needs of new energy sources, an approximate dynamic programming algorithm is proposed to better meet the daily scheduling demand of the independent microgrid with the new power generation as the main power source [11]. For specific micro networks, particle swarm optimization and artificial swarm optimization are introduced to solve the problem of optimal scheduling of micro networks [12–14]. Nowadays, stochastic optimization technology [15] and bilevel optimization technology [16, 17] are more and more common in the selection of optimization algorithm because of their practicability. In addition, the traditional centralized optimization scheduling method is difficult to fully reflect the interest demands of different agents in the integrated energy microgrid, and the application of artificial intelligence technology in integrated energy scheduling needs to be further explored. Artificial intelligence algorithm is becoming a new research direction [18, 19]. In the related research, adaptive neural network is introduced in reference [20]. The main contribution of this paper is the design and the validation of an innovative online-trained artificial neural network-based control system for a hybrid microgrid.

When modeling microgrid system, because of the existence of nonlinear constrains of microgrid power flow, linear transformation is needed. In the past, the linearization method has been widely used in solving nonlinear optimal scheduling problems due to its advantages of simplicity [21–23]. However, these methods still have obvious shortcomings in solving nonlinear models, such as slow solving speed, easy to fall into local optimum, and being unable to guarantee global optimum. These problems urge researchers to explore more effective solving algorithms to meet the requirements of global optimum and fast solving speed. The second-order cone relaxation method is proposed due to its advantages of high efficiency and comprehensive solution. The second-order cone relaxation method is mostly applied to the linear transformation of power flow constraints in distribution networks [24–26]. In order to solve the problem of integrated energy system, an improved second-order cone relaxation method was proposed in reference [27]. A second-order cone programming (SOCP) method is utilized to solve the optimization problem, which is actually a mixed-integer nonconvex and nonlinear programming issue. Reference [28] presents an alternative mixed-integer nonlinear programming formulation of the reactive optimal power flow (ROPF) problem and utilizes a mixed-integer second-order cone programming (MISOCP) based approach to find global optimal solutions of the proposed ROPF problem formulation.

The internal grid structure of microgrid is very close to the distribution network in the actual power system, and in the steady-state operation, they are mostly radial network operation [29], so the research results of the second-order cone relaxation method in the distribution network are also applicable to the microgrid system with similar structure. In this paper, the nonlinear power flow constraints in microgrid model are linearly transformed by using the second-order cone relaxation method, and the second-order cone program (SOCP) is obtained. Based on the microgrid model, the application conditions of the second-order cone relaxation method are discussed; at the same time, the problem solving of microgrid model without meeting the application conditions of SOCP is studied, and the method to solve the problem by increasing the line loss is proposed; finally, an example is given to verify the effectiveness and accuracy of the proposed method.

2. Scheduling Model of Integrated Energy Microgrid

The microgrid model established in this paper is an electricity-gas integrated energy microgrid system considering hydrogen energy, natural gas, and hybrid energy storage, and its structure diagram is shown in Figure 1.

2.1. Objective Function. In this paper, the optimization objective of microgrid system operation is the lowest comprehensive operation cost, which includes system operation cost and environmental cost. From the point of view of the whole microgrid system, hydrogen energy is consumed inside the microgrid system and is not exchanged with the outside. Only electricity and natural gas are exchanged with the outside. Therefore, the operation cost of the whole microgrid system consists of electricity exchange cost between the microgrid and the main network and energy exchange cost with natural gas. At the same time, we also hope that the energy loss of the system during energy conversion is as small as possible, so the energy loss penalty cost should be added to the system operation cost to control the energy loss. The time step is set to Δt. The scheduling time is T.

2.1.1. System Operation Cost

$$f1 = f11 + f12 + f13. \tag{1}$$

(1) Cost and benefit of energy exchange between microgrid and main grid.

In (1), $f11$ is the cost and benefit of energy exchange between microgrid system and main network, expressed as

$$f11 = \sum_{t=1}^{T} \Delta t\left(C_{e1}P_{\text{in}}^{E} - C_{e2}P_{\text{out}}^{E}\right), \tag{2}$$

where C_{e1} is the time of use price of microgrid purchasing electricity through the main grid, while C_{e2} is the time of use price of electricity from microgrid to main grid, P_{in}^{E} is the active power of microgrid purchasing power through main grid in t period, and P_{out}^{E} is the active power of the microgrid selling electricity to the main grid in t period.

(2) Energy exchange cost and benefit of microgrid and natural gas network.

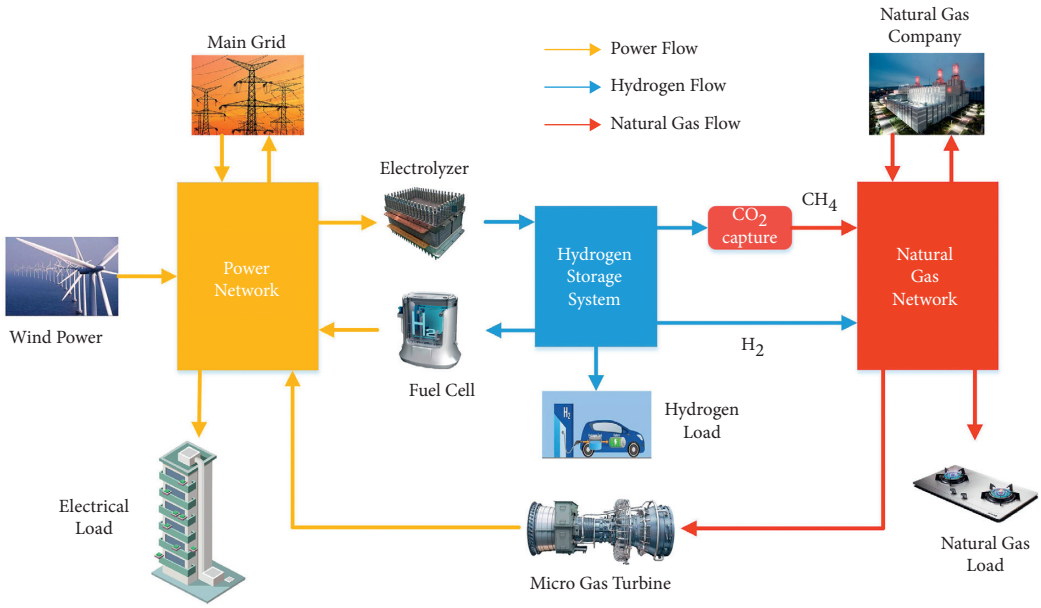

Figure 1: Structure of electricity-gas integrated energy microgrid.

In (1), $f12$ is the cost and benefit of purchasing and selling natural gas from the microgrid to the natural gas network, expressed as

$$f12 = \sum_{t=1}^{T} \frac{\left(C_{g1}P_{\text{in}}^{G} - C_{g2}P_{\text{out}}^{G}\right)\Delta t}{H}, \tag{3}$$

where C_{g1} is the purchase price of natural gas, C_{g2} is the selling price of natural gas, P_{in}^{G} represents the CH4 power purchased by the microgrid from the gas network in t period, P_{out}^{G} represents the CH4 power sold by the microgrid in t period, and H is the high calorific value of natural gas.

(3) Penalty cost of energy loss in system operation.

In (1), $f13$ is the penalty cost of energy loss in microgrid system operation, expressed as

$$f13 = K_{\text{Loss}}\left(f_{\text{Loss}}^{EL} + f_{\text{Loss}}^{FC} + f_{\text{Loss}}^{H2G} + f_{\text{Loss}}^{\text{MT}}\right), \tag{4}$$

where K_{Loss} is the weight coefficient, which indicates the importance of the system for energy loss ($0 \le K_{\text{Loss}} \le 1$); f_{Loss}^{EL}, f_{Loss}^{FC}, f_{Loss}^{H2G}, and $f_{\text{Loss}}^{\text{MT}}$ represent the energy loss of electrolyzer, fuel cell, hydrogen to gas device, and micro gas turbine (MT) in energy conversion.

2.1.2. Environmental Cost. In order to simplify the treatment, the conversion of various forms of energy in this microgrid system is considered not to produce harmful gases, so the environmental cost is mainly composed of CO_2 emissions. The expression of environmental cost is as follows:

$$f2 = \rho_{\text{CO}_2}^{G}P_{t}^{G} + \rho_{\text{CO}_2}^{\text{MT}}\sum_{t=1}^{T}\sum_{i=1}^{N_{\text{MT}}}P_{i,t}^{\text{MT}} - \rho_{\text{CO}_2}^{\text{CH}_4}\sum_{t=1}^{T}\sum_{i=1}^{N_{\text{H}_2\text{G}}}P_{i,t}^{\text{H}_2\text{G}}, \tag{5}$$

where $\rho_{\text{CO}_2}^{G}$ is the average CO_2 emission coefficient per unit power supply of the regional power grid, $\rho_{\text{CO}_2}^{\text{MT}}$ is the CO_2 emission coefficient of MT power generation, and $\rho_{\text{CO}_2}^{\text{CH}_4}$ is the CO_2 capture coefficient of CH_4.

2.1.3. Comprehensive Operation Cost. Combined with the above mathematical expressions, the objective function of comprehensive operation cost considering economy and environmental protection is as follows:

$$f = \omega_1\frac{f_1}{f_1^{\max}} + \omega_2\frac{f_2}{f_2^{\max}},$$
$$\begin{cases} \omega_1 + \omega_2 = 1, \\ 0 \le \omega_1, \quad \omega_2 \le 1, \end{cases} \tag{6}$$

where $f_1^{\max}$ and $f_2^{\max}$ are the maximum operating cost and the maximum environmental cost of the micro network system and ω_1 and ω_2 are the respective weight coefficients of the system operation cost and environmental cost. In this paper, the multiobjective optimization problem is transformed into a single-objective optimization problem by giving different weight coefficients to the system operation cost and environmental cost according to the degree of attention.

2.2. Power Flow Constraints of Microgrid. Because this paper focuses on the application of second-order cone relaxation method in solving microgrid power flow, only the microgrid power flow constraints are listed here, and the constraints in other microgrid systems, such as gas grid power flow constraints, output constraints of various energy conversion devices, and energy storage device constraints, are not discussed here. The basic model of microgrid power flow is as follows:

$$\begin{cases} p_j = \sum_{k\epsilon\delta(j)} P_{jk} - \sum_{i\epsilon\pi(j)} \left(P_{ij} - I_{ij}^2 r_{ij}\right) + g_j V_j^2, & \forall j \in B, \\ q_j = \sum_{k\epsilon\delta(j)} Q_{jk} - \sum_{i\epsilon\pi(j)} \left(Q_{ij} - I_{ij}^2 x_{ij}\right) + b_j V_j^2, & \forall j \in B, \end{cases} \tag{7}$$

$$V_j^2 = V_i^2 - 2\left(P_{ij} r_{ij} + Q_{ij} x_{ij}\right) + I_{ij}^2\left(r_{ij}^2 + x_{ij}^2\right), \quad \forall ij \in E, \tag{8}$$

$$I_{ij}^2 = \frac{P_{ij}^2 + Q_{ij}^2}{V_i^2}, \quad \forall ij \in E, \tag{9}$$

$$\underline{I}_{ij} \le I_{ij} \le \overline{I}_{ij}, \forall ij \in E, \tag{10}$$

$$\underline{V}_j \le V_j \le \overline{V}_j, \quad \forall j \in B^+, \tag{11}$$

$$\begin{cases} p_j \in R_j^p \\ q_j \in R_j^q \end{cases}, \quad \forall j \in B. \tag{12}$$

In (7)–(12), branch impedance r_{ij}, x_{ij}, node admittance g_j, and b_j are constant. Because the internal voltage level of microgrid system is 400 V (as shown in Figure 2), the influence of admittance g_j and b_j on microgrid power flow is very small. For simple calculation, $g_j V_j^2$ and $b_j V_j^2$ in (7) can be ignored. Node voltage V, branch current I, branch power flow P-Q, and node injection power p-q are optimization variables, which are obviously nonlinear. This nonlinear constraint condition will be transformed by the second-order cone relaxation method in Section 3. Equations (7)–(11) are the common constraint equation of general power flow; equation (12) is the unique constraint condition of each microgrid system, which is determined by its own power load, micro source, and other internal structures of the microgrid.

3. Nonlinear Constraint Transformation of Microgrid Power Flow

3.1. Second-Order Cone Relaxation Transformation. In this paper, the nonlinear constraints in this model are linearized by the second-order cone relaxation method, and the nonlinear programming problem of the system is transformed into SOCP. For conversion of equation (9), first define $\widetilde{I}_{ij} = I_{ij}^2$, $\widetilde{V}_j = V_j^2$, and then the second-order cone relaxation transformation is carried out to obtain

$$\widetilde{V}_j \widetilde{I}_{ij} \ge P_{ij}^2 + Q_{ij}^2, \quad \forall ij \in E, \tag{13}$$

and equation (13) can be equivalent to the standard form of second-order cone relaxation expressed by type 2 norm. Then, by substituting $\widetilde{I}_{ij} = I_{ij}^2$ and $\widetilde{V}_j = V_j^2$ into equations (7)–(8), the optimal power flow constraint equation after second-order cone relaxation can be obtained:

$$p_j = \sum_{k\epsilon\delta(j)} P_{jk} - \sum_{i\epsilon\pi(j)} \left(P_{ij} - \widetilde{I}_{ij} r_{ij}\right) + g_j \widetilde{V}_j, \quad \forall j \in B, \tag{14}$$

$$q_j = \sum_{k\epsilon\delta(j)} Q_{jk} - \sum_{i\epsilon\pi(j)} \left(Q_{ij} - \widetilde{I}_{ij} x_{ij}\right) + b_j \widetilde{V}, \quad \forall j \in B, \tag{15}$$

$$\widetilde{V}_j = \widetilde{V}_i - 2\left(P_{ij} r_{ij} + Q_{ij} x_{ij}\right) + \widetilde{I}_{ij}\left(r_{ij}^2 + x_{ij}^2\right), \quad \forall ij \in E, \tag{16}$$

$$\left\| \begin{matrix} 2P_{ij} \\ 2Q_{ij} \\ \widetilde{I}_{ij} - \widetilde{V}_j \end{matrix} \right\| \le \widetilde{I}_{ij} + \widetilde{V}_j, \quad \forall ij \in E, \tag{17}$$

$$\underline{I}_{ij}^2 \le \widetilde{I}_{ij} \le \overline{I}_{ij}^2, \quad \forall ij \in E, \tag{18}$$

$$\underline{V}_j^2 \le \widetilde{V}_j \le \overline{V}_j^2, \quad \forall j \in B^+. \tag{19}$$

3.2. Analysis of Second-Order Cone Relaxation Model. The nonconvex feasible region C_{original} of the original problem is transformed into a convex feasible region C_{SOC} by SOC relaxation. If the optimal solution S obtained by the second-order cone relaxation transformation model is still a point in C_{original}, then the second-order cone relaxation transformation is strictly effective; that is, the optimal solution S is also the optimal solution of the original problem. The second-order cone in this paper is actually a rotating second-order cone; the standard form is as follows:

$$K = \left\{ x_i \in R_n | 2x_1 x_2 \ge \sum_{j=3}^{n} x_j^2, x_1, x_2 \ge 0 \right\}. \tag{20}$$

Because $\widetilde{I}_{ij} = I_{ij}^2$, $\widetilde{V}_j = V_j^2$, it is obvious that equation (13) satisfies the condition of $x_1, x_2 \ge 0$ in equation (20), and the form is exactly the same. Figure 2 is the structure diagram of microgrid system, which is obviously a radial power network. For the radial power network, the second-order cone relaxation model established is strictly accurate; that is, the optimal solution calculated by the second-order cone relaxation model is also the optimal solution of the original problem. At the same time, if the optimal scheduling objective function of microgrid operation is convex and is a strictly increasing function of branch current, then the second-order cone relaxation transformed model is accurate convergence.

For the microgrid system in this paper, the objective of system optimization cost is the strict increasing function of branch current. The analysis is as follows: under the condition of (13), the node voltage $\widetilde{V}_j$ in microgrid is basically unchanged due to the constraints of upper and lower limits of voltage (voltage loss is ±5%). The branch current $\widetilde{I}_{ij}$ (actually the square of the branch current) can have a wide range of values under the

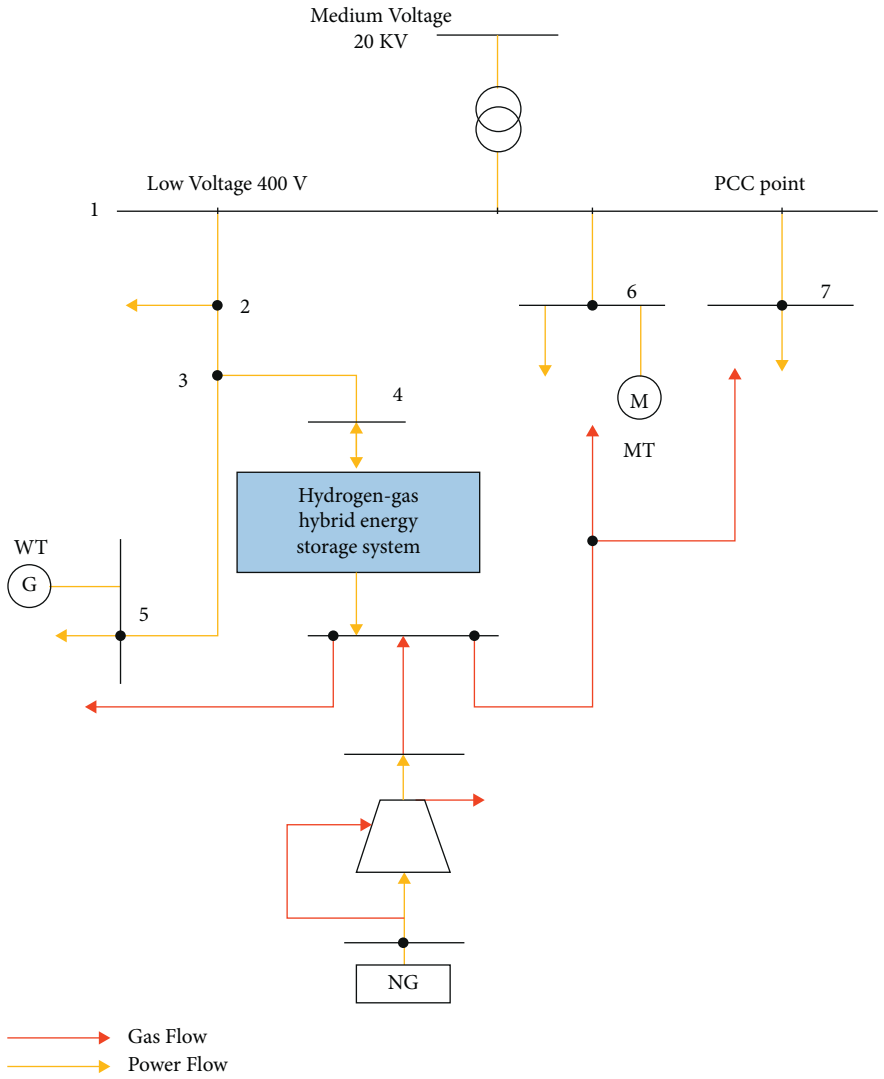

Figure 2: Structure diagram of microgrid system.

constraints of the upper and lower limits of the current. However, the greater the difference between $\widetilde{I}_{ij}$ and the actual value of the branch current, the greater the loss $\widetilde{I}_{ij}r_{ij}$ on the branch of the microgrid, so that the power supply needs to provide more active power to meet the active power balance constraints in (15), which leads to the increase of the system cost target. Therefore, the cost objective of microgrid system is a strictly increasing function of branch current $\widetilde{I}_{ij}$. In the process of seeking the lowest cost objective of the system, $\widetilde{I}_{ij}$ converges to the equal sign of (13) and finally makes $\widetilde{I}_{ij}$ equal to the actual value of branch current. Therefore, the system model obtained by second-order cone relaxation for power flow constraints is effective and accurate.

4. Simulation Analysis

In order to verify the validity and accuracy of the model, a simulation example of the microgrid system is analyzed, and the time step Δt is taken as 1 h, and the scheduling time T is 24 h. The simulation results are based on MATLAB programming. For convenience, Gurobi solver is used to solve the optimization problem.

4.1. Basic Data. The load distribution of microgrid 24 hours a day is shown in Figure 3.

The forecast output of the wind turbine in one day is shown in Figure 4, the TOU price is shown in Figure 5, and the natural gas price is given as 2.5 yuan/m^3.

4.2. Second-Order Cone Transformation Model for Microgrid without Abandoned Wind. When the wind turbine output is normal, the wind power of microgrid system and the loss of microgrid branch are shown in Figure 6, while the current of microgrid branches L23 and L36 is shown in Figure 7.

It can be seen from Figures 6 and 7 that, in the case without abandoned wind in the microgrid, the microgrid power flow obtained by the model after the second-order cone transformation is completely consistent with the actual value. At this time, the second-order cone transformation method is effective and accurate, and the above conclusion

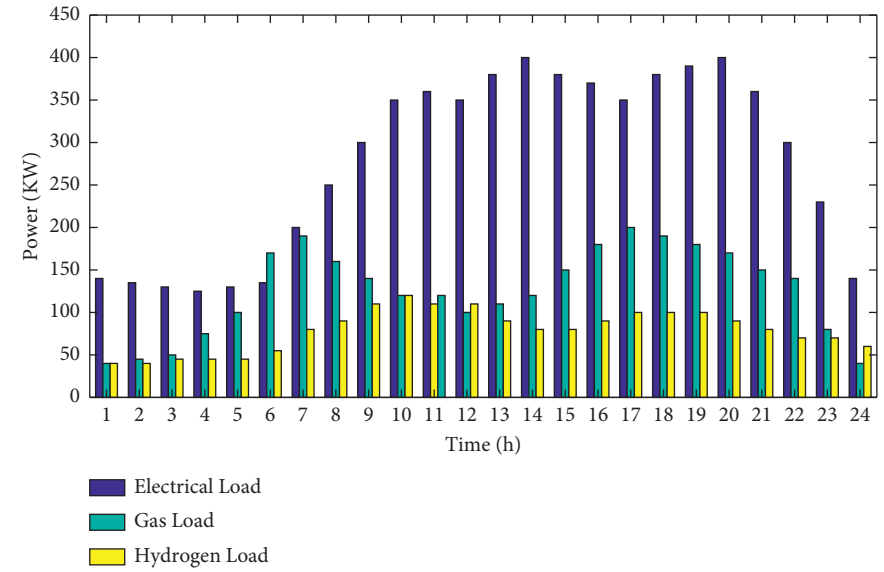

Figure 3: Microgrid load.

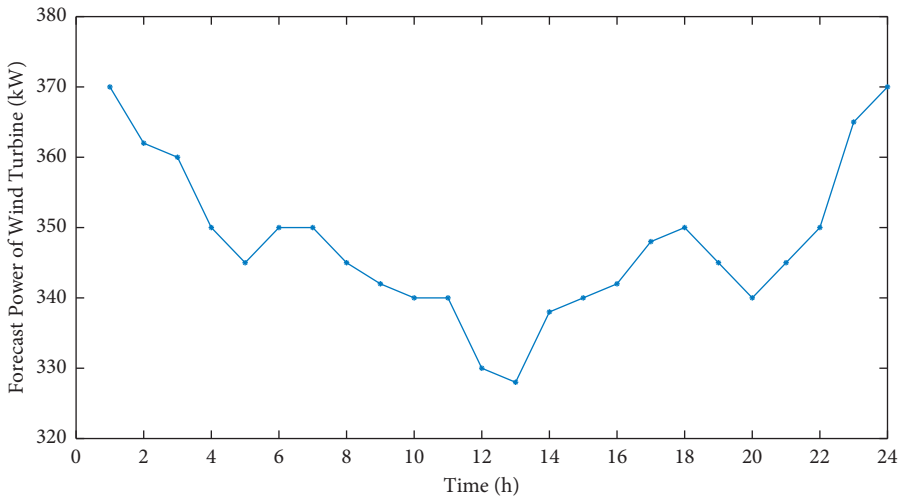

Figure 4: Wind power forecast output.

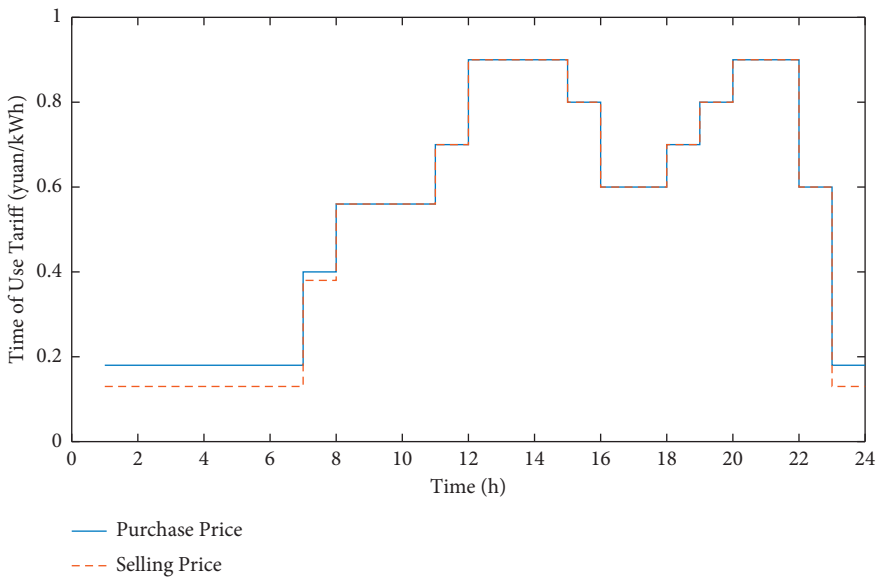

Figure 5: Electricity price.

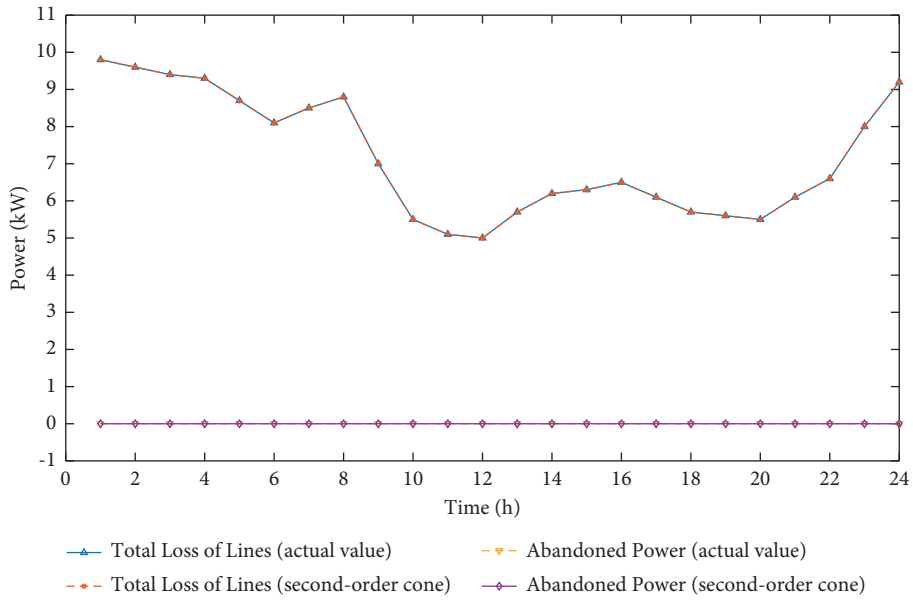

Figure 6: Total line loss and abandoned wind volume without abandoned wind.

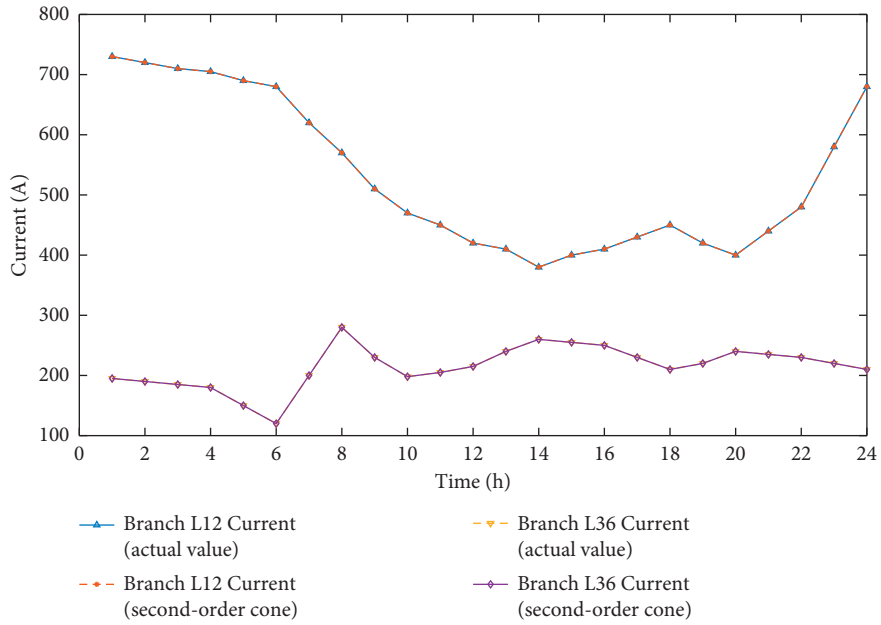

Figure 7: Current of branches L12 and L36 without abandoned wind.

that the objective function is the strictly increasing function of branch current $\tilde{I}_{ij}$ is also completely correct. The actual value of branch current in Figure 7 is obtained by equation (21) according to node voltage V and line power flow P-Q checking calculation.

$$\tilde{I}_{ij} = \frac{P_{ij}^2 + Q_{ij}^2}{\tilde{V}_i}, \quad \forall ij \in E. \tag{21}$$

4.3. Second-Order Cone Transformation Model for Microgrid with Abandoned Wind. When the wind turbine output is 1.5 times the normal condition, the wind abandonment appears in the microgrid system. At this time, the power of the abandoned wind and the loss of the branch of the microgrid are shown in Figure 8, while the current of branches L23 and L36 is shown in Figure 9.

When the wind abandonment occurs in the microgrid, the current of each branch calculated by the transformation model is different from the actual value, and the wind abandonment is also different from the actual value. It can be seen from Figure 8 that the abandoned wind volume of microgrid calculated by the second-order cone relaxation transformation model is less than the actual abandoned wind volume, and the difference is large, while it can be seen from Figure 9 that the branch current of microgrid calculated by the second-order cone relaxation transformation

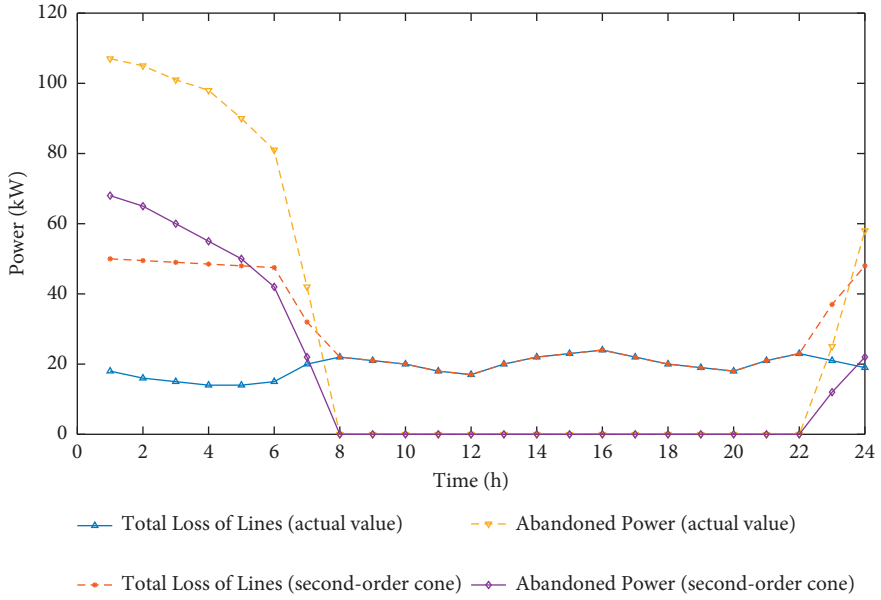

Figure 8: Total line loss and abandoned wind volume with abandoned wind.

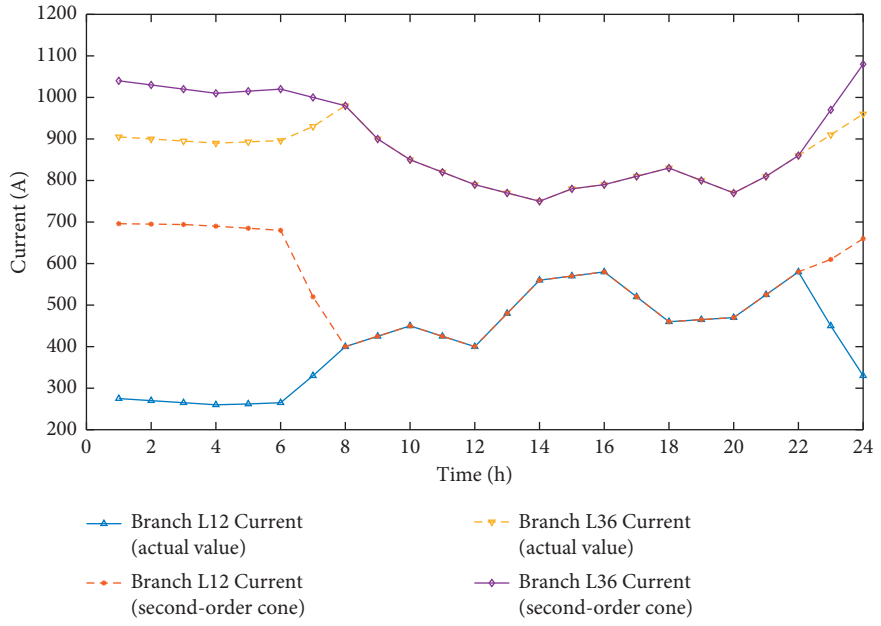

Figure 9: Current of branches L12 and L36 with abandoned wind.

model is greater than the actual branch current, and the difference is also large. At the same time, the results obtained by the second-order cone relaxation transformation model are very different from the actual value in the periods of 0: 00–7:00 and 23:00–24:00, that is, the period when the microgrid has abandoned wind at night, while in the daytime, when there is no abandoned wind in the microgrid, there is no difference with the actual value, so it is accurate. For this problem, the explanation can be given by analyzing equations (13) and (14).

In the case of no wind abandonment in microgrid, the above conclusion that the objective function is the strictly increasing function of branch current $\widetilde{I}_{ij}$ is correct. However, in the case of wind abandonment in microgrid system, when $\widetilde{I}_{ij}$ is greater than the actual value, the loss $\widetilde{I}_{ij}r_{ij}$ on the branch of microgrid "increases," and the power output further increases, but at this time, the wind turbine is used as the power supply, The increased branch loss power is compensated by the abandoned wind power. Therefore, in the process of solving the optimal cost objective function, this part of "increased" loss power will not increase the system cost, but cause a false appearance of reducing the abandoned wind volume of microgrid system. The final results are shown in Figures 7 and 8; by solving the second-order cone relaxation transformation model, the abandoned wind power of microgrid system

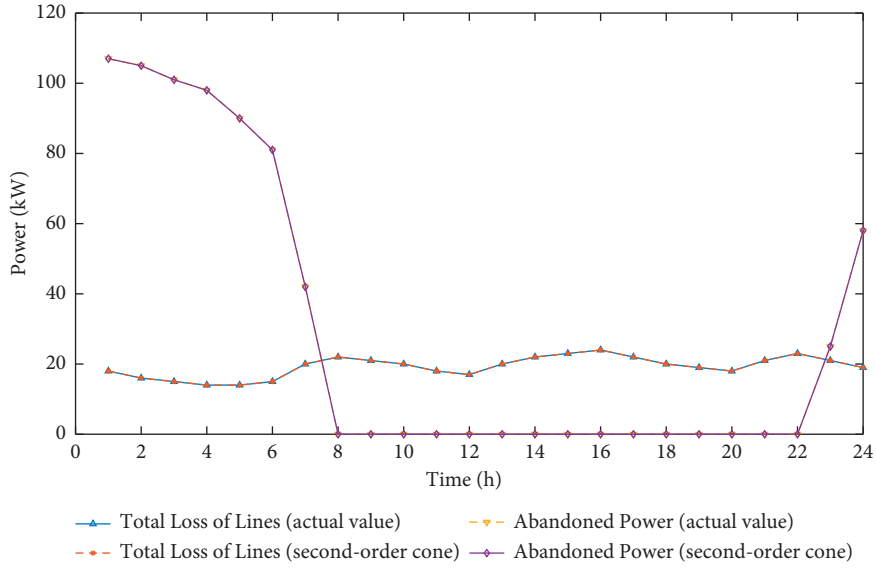

Figure 10: Total line loss and abandoned wind volume with abandoned wind after improvement.

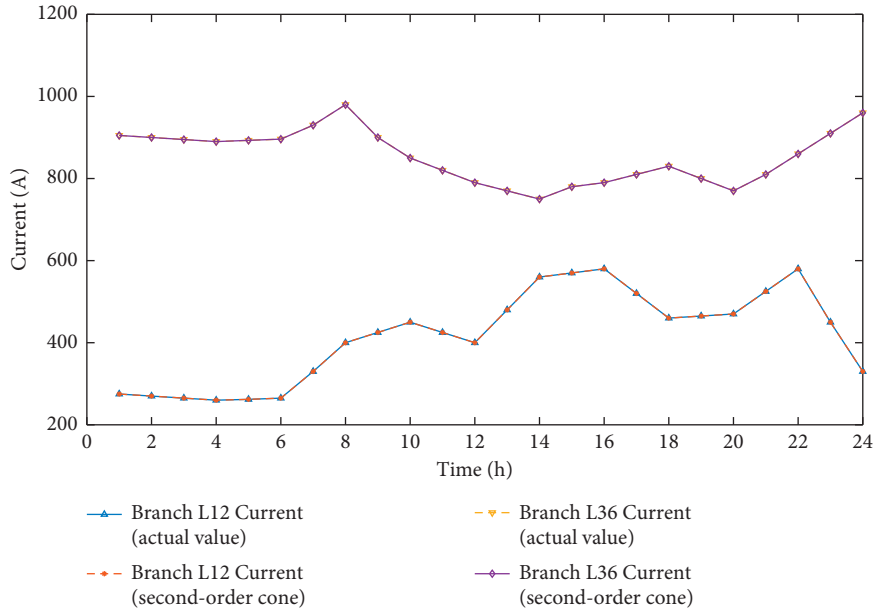

Figure 11: Current of branches L12 and L36 with abandoned wind after improvement.

decreases and the branch current increases. Therefore, it can be seen from the above analysis that when the microgrid system has abandoned wind, the system cost target is no longer a strictly increasing function of branch current $\widetilde{I}_{ij}$.

4.4. Solving the Deviation Problem of Second-Order Cone Transformation Model. It can be seen from the above analysis that when the microgrid system abandons the wind, the constraints of equations (13) and (15) are insufficient to make the branch current $\widetilde{I}_{ij}$ converge to the actual value, because at this time the objective cost function is no longer a strictly increasing function of $\widetilde{I}_{ij}$. In the night time with wind abandonment, there is a large deviation between the second-order cone conversion value and the actual value at 0 : 00–7:00 and 23 : 00–24 : 00. The maximum deviation of total line loss is 34.5 kW, the maximum deviation of wind abandonment power is 43 kW, the maximum deviation of branch L12 current is 430 A, and the maximum deviation of branch L36 current is 135 A. These deviations are obviously not allowed in practical application. In order to solve the above problem, it is necessary to add a strictly increasing function of $\widetilde{I}_{ij}$ in the objective cost function, Obviously, the active power loss of microgrid branch is the strict increasing function of $\widetilde{I}_{ij}$, and it is also practical to add the branch loss cost to the objective function. Equation (22) is

the increased cost function of active power loss of microgrid branch:

$$f_{\text{Line}} = K_{\text{Line}} \sum_{t=1}^{T} \sum_{ij \in E} \widetilde{I}_{ij} r_{ij} \Delta t, \tag{22}$$

where K_{Line} is the branch loss cost coefficient, which is very small. Its function is to ensure that the objective cost function is a strictly increasing function of the branch current $\widetilde{I}_{ij}$ of the microgrid at any time, and it almost does not affect the optimal scheduling of the microgrid system. After adding the branch loss cost function of microgrid into the objective cost function, the optimal scheduling problem of microgrid system is solved again, as shown in Figures 10 and 11. The results show that when the microgrid system has abandoned wind, the solution result of the second-order cone relaxation transformation model is still the actual effective value, which verifies the effectiveness of the method.

5. Conclusion

This paper mainly studies the application of the second-order cone relaxation method in solving the optimal power flow of microgrid. Through the second-order cone relaxation method, the nonlinear constraints in microgrid power flow are transformed into the second-order cone programming problem (SOCP), and the application conditions of the second-order cone relaxation method are further discussed. In the microgrid operation optimization scheduling problem, if the microgrid structure is a radial power network and the system cost objective is a strictly increasing function of the branch current of the microgrid, then the microgrid model after second-order cone transformation is accurate and effective. When there is no abandoned wind in the microgrid system, the branch current is a strict increasing function of the system cost objective, and the second-order cone relaxation method is accurate. However, when the microgrid system has abandoned wind, the branch current is no longer the strict increasing function of the optimization objective, and the second-order cone relaxation method is biased. This problem can be solved by increasing the line loss cost function. Simulation results show the effectiveness of this method. Although this method can effectively improve the application scope of second-order cone programming, there are still some problems, such as slow solution speed and complex operation. The next research direction should be to study the improved second-order cone relaxation method which can solve the problem quickly.

Data Availability

The data used to support the findings of this study are included within the article.

Conflicts of Interest

The authors declare no conflicts of interest.

Acknowledgments

This work was supported in part by the National Natural Science Foundation of China under Grant no. 51777193.

References

[1] T. Morstyn, B. Hredzak, and V. G. Agelidis, "Control strategies for microgrids with distributed energy storage systems: an overview," *IEEE Transactions on Smart Grid*, vol. 9, no. 4, pp. 3652–3666, 2018.

[2] C. Wei, M. Benosman, and T. Kim, "Online parameter identification for state of power prediction of lithium-ion batteries in electric vehicles using extremum seeking," *International Journal of Control, Automation and Systems*, vol. 17, no. 11, pp. 2906–2916, 2019.

[3] J. Wu, X. Y. Xing, C. Wu, and B. L. Li, "Cyber-enabled intelligence control and security optimization for complex microgrid networks transient frequency stability analysis of power systems considering photovoltaic grid connection," *Complexity*, vol. 2020, Article ID 5641596, 10 pages, 2020.

[4] W. H. Li, G. Zhang, X. Yang, and Z. Tao, "Sizing a hybrid renewable energy system by a coevolutionary multiobjective optimization algorithm," *Complexity*, vol. 2021, Article ID 8822765, 9 pages, 2021.

[5] Z. Luo, W. Gu, Z. Wu, Z. Wang, and Y. Tang, "A robust optimization method for energy management of CCHP microgrid," *Journal of Modern Power Systems and Clean Energy*, vol. 6, no. 1, pp. 132–144, 2018.

[6] Y.-Y. Hong and R.-C. Lian, "Optimal sizing of hybrid wind/pv/diesel generation in a stand-alone power system using markov-based genetic algorithm," *IEEE Transactions on Power Delivery*, vol. 27, no. 2, pp. 640–647, 2012.

[7] L. Tian, L. Cheng, J. Guo, and K. Wu, "System modeling and optimal dispatching of multi-energy microgrid with energy storage," *Journal of Modern Power Systems and Clean Energy*, vol. 8, no. 5, pp. 809–819, 2020.

[8] B. Mohandes, S. Acharya, M. S. E. Moursi, A. S. Al-Sumaiti, H. Doukas, and S. Sgouridis, "Optimal design of an islanded microgrid with load shifting mechanism between electrical and thermal energy storage systems," *IEEE Transactions on Power Systems*, vol. 35, no. 4, pp. 2642–2657, 2020.

[9] Y. Tao, J. Qiu, S. Lai, and J. Zhao, "Integrated electricity and hydrogen energy sharing in coupled energy systems," *IEEE Transactions on Smart Grid*, vol. 12, no. 2, pp. 1149–1162, 2021.

[10] A. Heidari, Z. Y. Dong, D. Zhang, P. Siano, and J. Aghaei, "Mixed-integer nonlinear programming formulation for distribution networks reliability optimization," *IEEE Transactions on Industrial Informatics*, vol. 14, no. 5, pp. 1952–1961, 2018.

[11] H. Shuai, J. Fang, X. Ai, Y. Tang, J. Wen, and H. He, "Stochastic optimization of economic dispatch for microgrid based on approximate dynamic programming," *IEEE Transactions on Smart Grid*, vol. 10, no. 3, pp. 2440–2452, 2019.

[12] A. Raghavan, P. Maan, and A. K. B. Shenoy, "Optimization of day-ahead energy storage system scheduling in microgrid using genetic algorithm and particle swarm optimization," *IEEE Access*, vol. 8, pp. 173068–173078, 2020.

[13] H. U. R. Habib, U. Subramaniam, A. Waqar, B. S. Farhan, K. M. Kotb, and S. Wang, "Energy cost optimization of hybrid renewables based v2g microgrid considering multi objective

function by using artificial bee colony optimization," *IEEE Access*, vol. 8, pp. 62076–62093, 2020.

[14] P. Li, D. Xu, Z. Zhou, W.-J. Lee, and B. Zhao, "Stochastic optimal operation of microgrid based on chaotic binary particle swarm optimization," *IEEE Transactions on Smart Grid*, vol. 7, no. 1, pp. 66–73, 2016.

[15] M. K. AlAshery, D. Xiao, and W. Qiao, "Second-order stochastic dominance constraints for risk management of a wind power producer's optimal bidding strategy," *IEEE Transactions on Sustainable Energy*, vol. 11, no. 3, pp. 1404–1413, 2020.

[16] D. Xiao, J. C. do Prado, and W. Qiao, "Optimal joint demand and virtual bidding for a strategic retailer in the short-term electricity market," *Electric Power Systems Research*, vol. 190, Article ID 106855, 2021.

[17] D. Xiao, M. K. AlAshery, and W. Qiao, "Optimal price-maker trading strategy of wind power producer using virtual bidding," *Journal of Modern Power Systems and Clean Energy*, 2021.

[18] T. A. Jumani, M. W. Mustafa, A. S. Alghamdi, M. M. Rasid, A. Alamgir, and A. B. Awan, "Swarm intelligence-based optimization techniques for dynamic response and power quality enhancement of AC microgrids: a comprehensive review," *IEEE Access*, vol. 8, pp. 75986–76001, 2020.

[19] W. Liu, P. Zhuang, H. Liang, J. Peng, and Z. Huang, "Distributed economic dispatch in microgrids based on cooperative reinforcement learning," *IEEE Transactions on Neural Networks and Learning Systems*, vol. 29, no. 6, pp. 2192–2203, 2018.

[20] N. Chettibi, A. Mellit, G. Sulligoi, and A. Massi Pavan, "Adaptive Neural network-based control of a hybrid AC/DC microgrid," *IEEE Transactions on Smart Grid*, vol. 9, no. 3, pp. 1667–1679, 2018.

[21] Z. Yang, K. Xie, J. Yu, H. Zhong, N. Zhang, and Q. X. Xia, "A general formulation of linear power flow models: basic theory and error analysis," *IEEE Transactions on Power Systems*, vol. 34, no. 2, pp. 1315–1324, 2019.

[22] B. Zargar, A. Monti, F. Ponci, and J. R. Martí, "Linear Iterative power flow approach based on the current injection model of load and generator," *IEEE Access*, vol. 9, pp. 11543–11562, 2021.

[23] P. Pareek and A. Verma, "Piecewise linearization of quadratic branch flow limits by irregular polygon," *IEEE Transactions on Power Systems*, vol. 33, no. 6, pp. 7301–7304, 2018.

[24] S. Huang, Q. Wu, J. Wang, and H. Zhao, "A sufficient condition on convex relaxation of AC optimal power flow in distribution networks," *IEEE Transactions on Power Systems*, vol. 32, no. 2, pp. 1359–1368, 2017.

[25] A. F. Soofi, S. D. Manshadi, G. Liu, and R. Dai, "A SOCP Relaxation for cycle constraints in the optimal power flow problem," *IEEE Transactions on Smart Grid*, vol. 12, no. 2, pp. 1663–1673, 2021.

[26] S. Huang, Q. Wu, J. Wang, and H. Zhao, "A sufficient condition on convex relaxation of AC optimal power flow in distribution networks," *IEEE Transactions on Power Systems*, vol. 32, no. 2, pp. 1359–1368, 2017.

[27] Y. Sun, B. Zhang, L. Ge, D. Sidorov, J. Wang, and Z. Xu, "Day-ahead optimization schedule for gas-electric integrated energy system based on second-order cone programming," *CSEE Journal of Power and Energy Systems*, vol. 6, no. 1, pp. 142–151, 2020.

[28] S. E. Kayacık and B. Kocuk, "An MISOCP-based solution approach to the reactive optimal power flow problem," *IEEE Transactions on Power Systems*, vol. 36, no. 1, pp. 529–532, 2021.

[29] C. Wei, Z. Shen, D. Xiao, L. Wang, X. Bai, and H. Chen, "An optimal scheduling strategy for peer-to-peer trading in interconnected microgrids based on RO and Nash bargaining," *Applied Energy*, vol. 275, 2021.

Hindawi
Complexity
Volume 2021, Article ID 4014362, 12 pages
https://doi.org/10.1155/2021/4014362

Research Article

Economic Feasibility Analysis of PVAC and TAC of Three Typical Application Cases in China

Dan Zhou,[1] **Haoran Wang**,[1] **Cheng Zhang**,[1] **Ke Sun**,[2] **Hanyun Wang**,[3] **Lihua Zhou**,[3] **Jian Wu**,[4] **and Yaojie Hu**[4]

[1]*College of Information Engineering, Zhejiang University of Technology, Hangzhou 310023, China*
[2]*State Grid Zhejiang Electric Power Company, Ltd., Hangzhou 310008, China*
[3]*State Grid Huzhou Power Supply Company, Huzhou 313000, China*
[4]*Huzhou Xinlun Comprehensive Energy Service Co, Ltd., Huzhou 313000, China*

Correspondence should be addressed to Dan Zhou; zhoudan@zjut.edu.cn

Received 6 May 2021; Revised 20 June 2021; Accepted 23 July 2021; Published 5 August 2021

Academic Editor: Xiaoqing Bai

Solar photovoltaic driven air conditioning (PVAC) system with electricity storage is proposed as a good solution to help shifting peak load and consuming solar energy. In this paper, a grid-connected PVAC system using the TRNSYS simulation model consisting of PV panels, traditional air conditioners (TAC), power conditioning units, inverters, and grid connection equipment is proposed to investigate the economic feasibility compared with the traditional air conditioner. In the PVAC system, the electricity, firstly generated by PV panels and then stored in battery, is consumed by a DC inverter air conditioner to maintain the temperature of the room and the surplus electricity is sold to the grid. A life cycle cost comparison between PVAC system, traditional air conditioning system, and decomposed PV and air conditioning systems of three typical application cases is conducted, in which the operation conditions are based on the present circumstances of China. The results show that, in comparison with conventional air conditioners, better economic benefits can be achieved when the peak load of the air conditioning system is over a certain value. Sensitivity analysis is conducted to evaluate the effects caused by variation of economic assumptions. At last, a new operation model is proposed to achieve more benefits for the system.

1. Introduction

Nowadays, peak load reduction, carbon emission reduction, and renewable energy curtailment reduction are three main problems threatening the progress and development of the electricity department in China [1].

Peak load reduction can be achieved by strategic conservation, load shifting, and flexible load shape [2]. Thus, an increase in the capacity factors of devices of the grid can be achieved. However, in China, base load is produced by coal power plants, whereas peak load is provided by nuclear, hydro-, or renewable power [3]. Thus, electricity generation during the peak period is more expensive than that during the off-peak period. Besides, installed power capacity should be larger than peak load to ensure the security of the power supply [4]. Based on these two reasons, there is great significance for reducing peak electricity load not only for reducing capital cost but also for higher capacity factor.

Solar energy is known to be clean energy and without carbon emission in power generation. It has been widely used in the combination with buildings for cooling in the previous years. Ai-Alili et al. [5] reported an experimental investigation of a hybrid solar air conditioner system. The experimental results show that the hybrid AC is more effective than the standalone AC in maintaining indoor conditions within the comfort zone. Zapalowicz and Opiela [6] presented an air conditioning system that consists of a conventional air conditioner, ground heat exchanger (GHE), and PV installation, mounted on the vertical, south-exposed wall of the building. The results showed that the efficiency of PV is improved. Goldsworthy [7] reported a building thermal design method for solar photovoltaic air

conditioning; the results showed that, in tropical climates, there are certain building thermal designs that lead to indoor temperatures < 25°C at all times with a modest size PV-battery system. Huang et al. [8] studied a solar air conditioning system directly driven by standalone solar PV. They found that if solar photovoltaic power generation is not large enough, there will be power loss in the air conditioning system, and an appropriate system design is needed to match the power consumption of the air conditioning system with the appropriate photovoltaic size. Aguilar et al. [9, 10] analyzed the viability of the use of photovoltaic systems to supply energy to air conditioning equipment without batteries or regulators. Fischer et al. [11] studied the impacts of PV and variable prices on optimal system sizing for heat pump and thermal storage. Liu et al. [12] studied the composition and principle of an air conditioner driven by a grid-connected photovoltaic (PV) system and analyzed the working principle of quasigrid-connected energy-saving technology. Wei et al. [13] designed a direct current (DC) air conditioning system powered by a solar photovoltaic module (PV) to solve the problem of temperature increase inside the vehicle when it stops in the summer.

However, with the ever-increasing penetration rate of renewable electricity power generation, problems of intermittence and fluctuation threaten the security of the grid significantly [14]. Though the introduction of the smart grid can solve these problems partly, the origin cannot be solved [15]. To offset the effects of intermittence and fluctuation caused by the increase in renewable electricity, the best technical route is consuming as much renewable electricity itself as it can [16].

According to [17], 19.5% of total energy is consumed as building energy consumption in 2013. It is known that building energy consumption mainly comes from cooling and heating. Thus, meeting the requirement of building load by consuming as much renewable electricity as possible is a good solution consuming renewable electricity and decreasing peak load, thus increasing the capacity factor of the grid. PV air conditioning is thus proposed as one of the solutions to meet the balance between electricity generation and consumption.

Because the cooling/heating load and the energy consumption of air conditioning system in buildings like supermarkets and office buildings are in phase with solar radiation intensity, solar PVAC thus becomes an ideal variable load generating device, which better suits the balance of electricity supply and demand especially when combined with electricity storage [8].

In the early stage, the cost of PV panels is very high, so Bolocan and Boian [18] thought that the high initial cost of a solar air conditioning system is the major obstacle for large-scale implementation. In that circumstance, some researchers have made an economic comparison between PV air conditioning system and other solar-driven chillers. Lazzarin [19] made an investment cost comparison and efficiency comparison between solar thermal driven sorption and PV-driven compression chillers. They anticipate that the PV-driven compression chillers have a better application prospect due to the lowering of the investment cost of PV panels and to the progress of their efficiency. Based on previous studies, Infante Ferreira and Kim [20] made a techno-economic review to investigate the most promising and attractive alternatives when solar energy is used to meet the cooling demands. Finally, they concluded that the PV-driven vapor compression cycles are the most attractive technical route.

In recent years, with great cost reduction of PV panels, PV air conditioning becomes a practical technical route. Allouhi et al. [21] investigated the potential of solar air conditioning in Morocco in hot climates assessing its economic and environmental impacts. Their major finding is that though solar air conditioning is an attractive alternative to mitigate greenhouse gas emissions and increase energy savings, however, the high capital cost is the major obstacle for their implementation. To solve this problem, Tarigan et al. [22] made a cost analysis of the proposed grid-connected system, which includes total capital cost, payback period, and standardized costs. The simulation result showed that the most cost-efficient way to connect PV panels and air conditioning for a classroom of a university is through a grid-connected system. To reduce the capital cost of battery and any inverter regulators, Aguilar et al. [23] carried out an experimental study and analyzed the possibility of using PV panels to power the compressor of DC inverter air conditioning without batteries or any inverter regulators. The experimental result showed that during summer days the solar contribution of PV panels is about 65% and during heating days the solar contribution of PV panels is about 50%. Li et al. [24] studied the performance of a solar PVAC system in the hot summer and cold winter zone. Based on the experimental results, they concluded that the PVAC can be a good solution to reduce the peak load of electrical grid in the areas where weather condition is similar to Shanghai.

However, to the best of the authors' knowledge and according to the comprehensive literature review, there is no research on the influence of the price differences between peak electricity and valley electricity, centralized PV power generation, and distributed power generation, and individual user and business user were neglected in the previous studies. In fact, economic factors especially price differences are decisive factors for development of PV industry. Moreover, some special application cases of PVAC were studied, but the more general application cases such as using in supermarket and office building were never discussed. Thus, this paper studies the economic feasibility of PVAC system considering three application cases. By making economic comparison between PVAC, TAC, and decomposed PV and AC system of three typical application cases, the economic feasibility of PVAC is verified.

2. System Description and Methods

2.1. System Description and Process. The block diagram of the PVAC system is shown in Figure 1. The system consists of PV panels, a commercial variable frequency split type air conditioner, a DC/DC converter, a PEM controller, a DC/AC inverter, and battery packs. In this system, the air

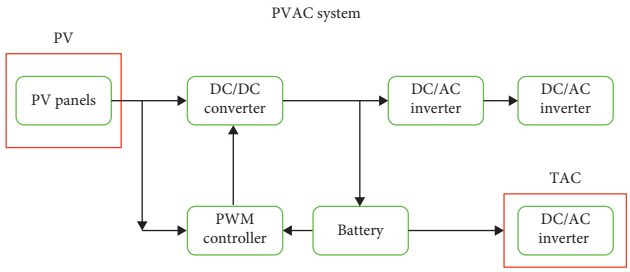

Figure 1: Block diagram of the PVAC system.

conditioner can be connected to the grid in case of lacking electricity powered by the PV arrays and the battery packs. Furthermore, the redundant PV electricity can be sent to the grid to achieve better economic benefits. Due to the issue of intermittence and unsteady electricity generated by PV arrays, a DC/DC converter and a PWM controller are applied to stabilize the output voltage. Then, the direct current is converted into alternating current by a DC/AC inverter to meet the air conditioning load or sent to the grid. In order to increase the reliability of powering PV panels, battery packs are usually used as an electricity storage device. When lacking electricity, the battery packs will work.

The existing electricity pricing schemes include time of use, critical peak price, real-time price, and so on. Time of use (TOU) refers to the different electricity prices set by the power sector for different types of users according to time periods, dates, and seasons. Critical peak price (CPP) is based on the time of use (TOU) price, which adds a new price for an extreme peak period, namely, critical peak price. Real-time price is a kind of dynamic electricity price, electricity price, and electricity cost linkage, reflecting the real-time supply and demand situation of the electricity market. Users can respond to real-time changes in electricity prices. This paper adopts the time of use price, which will be introduced in detail in Section 3.1.

2.2. Operation Case of Air Conditioning System. LCC (life cycle cost) refers to all costs related to the product during its effective use, including product design cost, manufacturing cost, procurement cost, use cost, maintenance cost, and waste disposal cost.

The LCC analysis studies the total cost over the lifespan of the PVAC system, which includes the capital cost of PV arrays and air conditioning, greenhouse gas emission, electricity consumption, operation and maintenance cost, and residual value. The economic analysis is carried out by comparing the key economic indicator of LCC using PVAC and TAC under three typical cases. Case 1 is a typical application in a supermarket with a working period from 08:00 to 21:00. In case 2, the air conditioning system runs in an office building, where the operation period is from 07:00 to 18:00. For the 3rd case, the system is run in residential in rural areas; thus, the working time for the air conditioning system is assumed to be 19:00 to next 06:00.

2.3. Life Cycle Cost Calculation Methods

2.3.1. Life Cycle Cost. Based on the LCC methodology evaluating the potential economic impact on an air conditioning system throughout its lifespan, the economic efficiency of the system is evaluated. The model is developed by grouping the cost into four categories and comprises capital cost (C_C), operation and maintenance cost ($C_{O\&M}$), residual value (C_{RV}), and greenhouse gas emissions cost (C_{GGE}). The relationship of these factors is combined as

$$\mathrm{LCC} = C_C + C_{O\&M} - C_{RV} + C_{GGE}. \tag{1}$$

Generally, the LCC is converted into a present value, which is widely applied when comparing cash flows at different times. Expressed in the form of a present value, LCC is calculated as

$$\mathrm{LCC} = C_C + \sum_{i=1}^{n} \frac{C_{O\&M,i}}{(1+r)^i} - \frac{C_{RV}}{(1+r)^n} + C_{GGE}, \tag{2}$$

where n refers to the lifetime calculated by year. In this study, the lifetime of n is 25; a constant value of $r = 6\%$ is adopted as the discount rate during the lifespan of the system.

In the PVAC system, capital cost mainly refers to the sum of the cost of land, building construction, instruments, and equipment. Considering the fact that most PV arrays are installed in roofs of buildings, the cost of land can be neglected when compared with the TAC system. In this study, the capital cost is paid off by investors.

For the PVAC system, the cost of operation and maintenance is mainly formed by the cost of labor and maintenance. The PV arrays need to be cleaned every week and the air conditioning system needs to be inspected every month. Maintenance cost contains the cost of regular maintenance and disaster recovery. According to the experience of the PV system and air conditioning system, the cost of labor and maintenance is estimated to be 2% of the capital cost every year. Besides, the cost of electricity is another significant part of this cost. The compound present worth of operation and maintenance cost is calculated:

$$C_{O\&M} = \sum_{i=1}^{n} \frac{2\% \times C_C + C_{\mathrm{ele},i}}{(1+r)^i}, \tag{3}$$

where $C_{\mathrm{ele},i}$ refers to the cost of electricity yearly and r is the discount rate.

The value of residual of fixed assets means the expected value at the end of the life of the assets. According to [25], a residual rate of $d = 5\%$ of the total price of fixed assets is commonly adopted. The residual value of the PVAC system lies in the worth of reusable units of PV arrays and air conditioning system. The residual value is calculated by applying

$$C_{RV} = \frac{d \times C_C}{(1+r)^n}. \tag{4}$$

The environmental impact that needs to be considered includes four categories: greenhouse gases emission, eutrophication effect, acidification effect, and winter smog

effect. Compared to the environmental impact caused by the manufacture of air conditioning system, PV arrays is the major source of pollution.

However, only carbon dioxide is under consideration in China currently. Other pollutions, like nitrogen oxides, sulfur dioxide, and so on, are not considered. Thus, the environmental impact cost mainly comes from equivalent carbon dioxide emission. The environmental impact inventory for multi-Si PV power production is shown in Table 1. The tax is estimated to be \$7.5/ton eq-CO_2 [26].

2.4. Economic Indicators. LCC, an important economic indicator in many economic analyses, provides a comprehensive understanding of the economics of the PVAC system. It provides decision makers with a set of references on which project planning decisions can be made [28].

Besides LCC, the discount rate is another key economic parameter to evaluate the economic behavior. A discount rate of 6% is adopted in this study for economic analysis.

2.5. Sensitivity Analysis. The objective of sensitivity analysis is to understand how uncertainties in input parameters impact important economic indicators. Besides, the sensitivity results will also find out the most important parameters, which have significant impacts on the economic benefit index of the investment project among these uncertain parameters. In this study, the capital costs of equipment including PV system and air conditioning system, price of peak electricity and valley electricity, on-grid price of PV power generating, and operating hours of air conditioning system and PV system are investigated as the main uncertainties. Besides these parameters, the perturbation of discount rate, which shows the present value of future expenses is also investigated.

3. Economic Life Cycle Inventory (ELCI)

The ELCI describes the whole process included in the system boundaries, which can be seen in Section 2.1. The LCC is typically divided into three phases: construction, utilization, and decommissioning. Of course, the cost of construction and utilization for the air conditioning system is the major cost-consuming phase. The economic data and technical parameters of equipment are collected in the following section. The case is divided into three cases: case 1, case 2, and case 3. The case analysis will be carried out by making a comparison between the PV air conditioning system and the TAC system.

3.1. Economic Data Collection. As power conditioning units, the DC/DC converter, PWM controller, and DC/AC inverter are used in this system. The price of PV arrays, DC/AC inverter, DC/DC converter, battery bank, and PWM controller is assumed to be \$1000/kWp, \$85/kW, \$120/kW, \$150/kWh, and \$25/kW. For the cost of electric power distribution, an addition of \$460/kW is adopted for the increase of power distribution equipment. The cost of an air conditioning system is about \$540/kW for which the cooling capacity is calculated based on the Coefficient of Performance (COP) and environmental conditions. These costs of equipment are listed in Table 2. The price of electricity for industrial and commercial customers during the period of peak electricity, valley electricity, and the other is \$0.1926/kWh, \$0.0569/kWh, and \$0.1203/kWh, respectively. The price of electricity for residential customers during the period of peak electricity and valley electricity is \$0.0949/kWh and \$0.0472/kWh, respectively. Dividing different types of electricity is based on the time segments, which are shown in Tables 2–4.

Table 1: Environmental impact inventory for multi-Si PV power production [27].

Item	Value	Unit
Carbon dioxide emissions	132.91	kg/kWp
Carbon monoxide emissions	1.70	kg/kWp
Nitrogen oxide emissions	279.61	kg/kWp
Sulfur dioxide emissions	0.79	kg/kWp

3.2. Technical Parameters of Equipment Collection and Case Analysis

3.2.1. Air Conditioning System. Generally, the construction cycle is less than several weeks; therefore, the construction cycle is assumed to be 0 in this study. The efficiency of the combination of DC/DC converter and PWM controller is assumed to be 93%. When the system is connected to the grid, a DC/AC inverter with a rated efficiency of 93% is necessary to output the excessive PV electricity especially during the spring and the autumn. For the lead-carbon battery packs, the efficiency and lifespan are varied inversely with the DOD (depth of discharge). The efficiency of 93% and the number of 4200 or nearly 15 years of charge-discharge cycles are adopted at the DOD of 70% [19]. The detailed technical data can be shown in Table 5. Since the COP of the air conditioning system is determined not only by the performance of equipment but also by the conditions of the ambient, it is hard to calculate the exact efficiency over the lifespan of the system. In this study, a simulation platform is constructed using Transient Systems (TRNSYS) to calculate the energy flow of an air conditioning system in Shanghai, a city in the typical climate of hot summer and cold winter in China.

A room with an area of 23.5 m^2 and a volume of 75 m^3 is adopted as the tested room. The cooling load is assumed to be 150 W/m^2; thus, the total cooling load is 3.5 kW. The detailed structural parameters of the tested room are listed in Table 6. According to the total cooling load, a frequency conversion air conditioner with a rated power of 0.62 kW is suited for the cooling needs. The main parameters of the air conditioner are shown in Table 7.

3.2.2. Lead-Carbon Battery Pack. Choosing the battery pack is based on the voltage of the system and the required powering days. The voltage is 48 V, and the capacity can be estimated by

Table 2: Summary of cost of different equipment [29].

Item	Data	Units
Air conditioning	540	$/kW
Lead-carbon battery packs	150	$/kWh
DC/AC inverter	85	$/kVA
DC/DC converter	120	$/kVA
On-grid price of centralized PV electricity	0.151	%/kWh
On-grid price of PV electricity for business user	0.103	$/kWh
On-grid price of PV electricity for personal user	0.126	$/kWh
Power distribution equipment	460	$/kW
PV panels	1000	$/kWp
PWM controller	25	$/kW

Table 3: Electricity price for industrial and commercial customers [30].

Item	Time	Price ($/kWh)
Peak electricity	08:00–11:00	0.1953
	13:00–15:00	0.1953
	18:00–21:00	0.1953
Valley electricity	22:00–06:00	0.0519
Others	—	0.123

Table 4: Different stages of electricity for residential customers [31].

Item	Time	Price ($/kWh)
Peak electricity	06:00–22:00	0.0949
Valley electricity	22:00–06:00	0.0472

Table 5: Summary of detailed technical data of equipment.

Item		Data
Battery voltage		48 V
DC/DC converter capacity		2 kVA
DC/AC inverter capacity		2 kVA
Rated efficiency	Battery bank	93%
	DC/AC inverter	90%
	DC/DC converter	90%
	PWM controller	95%

Table 6: Structural parameters of the tested room.

Item	East	South	West	North
Area of the wall (m^2)	16.5	14.9	16.4	14.9
Window to wall ratio (%)	18	28	0	3

Table 7: Parameters of the frequency conversion air conditioner.

Item	Data (kW)
Rated (min/max) cooling capacity	2.8 (0.8/3.6)
Rated (min/max) heating capacity	3.6 (0.8/5.2)
Rated (min/max) cooling input power	0.62 (0.17/1.10)
Rated (min/max) heating input power	0.85 (0.17/1.50)

$$C_{\text{battery}} = \frac{E_{\text{daily}}}{V} \times \frac{T}{\eta_{\text{inverter}} \cdot \text{DOD}}, \quad (5)$$

where E_{daily} refers to the daily electricity consumption of the system, Wh. To meet the requirements on most days, the larger rated power between cooling and heating of 0.85 kW is adopted. To calculate E_{daily} precisely, a simulation has been carried out to determine the required electricity and the results are shown in Figure 2. V is the system voltage, 48 V. T is the rainy days, and 1 day is assumed in this study. η_{invertor} is the rated efficiency of DC/AC inverter, it is assumed to be 93% in this study. The rated DOD of the battery pack is assumed to be 70%. When the capacity is calculated, the real capacity is chosen based on the nearest value from the product series. The results are shown in Table 8.

3.2.3. PV Panels. To make the balance between supplying sufficient power electricity and minimizing the capital investment, the capacity of panels is calculated by applying [32]

$$N_{\text{PV}} = \frac{E_{\text{daily}} \cdot f_\theta}{m \cdot I_m \cdot \eta_{\text{battery}} \cdot f_e \cdot S_P}, \quad (6)$$

where f_θ refers to the inclination correction factor and is assumed to be 0.99 [32]. m is the average daily sunshine hours under standard testing conditions; it is 4.134 in Shanghai [33]. I_m is the current of maximum power point under standard testing conditions, 6.86 A. η_{Battery} is the rated efficiency of the battery, 93%. f_e refers to the loss compensation coefficient of PV panels; it is assumed to be 0.9. And S_P is dust blocking factor, 0.96. The peak power of a panel under standard conditions is 120 W_p; thus, the peak power of PV panels can be accumulated. The result of the three cases is shown in Table 8.

3.3. Systems' Simulation to Calculate the Electricity Consumption and Generation of PV Air Conditioning System. Based on the information, a simulation is carried out to calculate the accurate energy flow for the system. Considering the response character, the time step is chosen as 5 minutes. The results are shown in Table 9 and Figure 3. For case 1, the annual electricity generation is 2175.2 kWh, and the surplus electricity is 1200.8 kWh, which is less than the difference between electricity output and consumption. The reason mainly lies in the power loss coming from equipment like batteries and invertors. However, the remaining electricity can be sold to the grid for shortening the payback period. For all three cases, the annual electricity output will go up in proportion to the PV installed capacity; however, the electricity consumption varies differently. On the one hand, the temperature during different periods causes different electricity consumption. On the other hand, the energy consumption of long-time continuous running of an air conditioning system is less than the energy consumption of intermittent running because of the heat capacity of the air and the room.

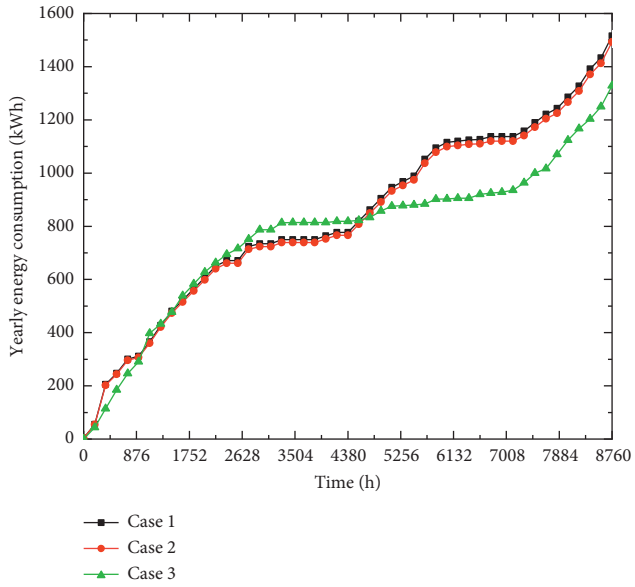

Figure 2: Theoretical yearly electricity consumption of three cases.

Table 8: Annual electricity consumption and technical parameters of three cases.

Item	Case 1	Case 2	Case 3
Running period	08:00–21:00	07:00–18:00	19:00–06:00
Cooling temperature (°C)	25	26	26
Heating temperature (°C)	18	20	18
Electricity consumption (kWh/year)	1515.9	1493.6	1328.0
Daily electricity consumption (Ah)	86.5	85.3	75.8
Battery capacity (Ah)	140	140	80
PV installed capacity (kWp)	1.92	1.92	1.92

Table 9: The simulation results of energy flow of three cases.

Item (kWh)	Data		
	Case 1	Case 2	Case 3
Annual electricity generated	2175.2	2175.2	2175.2
Annual electricity remaining	1200.8	1141.9	1661.6

4. Results

4.1. LCC Analysis of Case 1, Case 2, and Case 3. Once the parameters of costs of equipment, operation and maintenance, and residual are input, the LCC analysis is carried out to render all costs converting to the present value, so that the three typical cases can be compared. According to equations (1) and (2), we can get the following results. The LCC analysis results of three cases of both PVAC and air conditioning are shown in Table 10.

Table 10 shows the LCC of three cases of both PVAC system and air conditioning system. It can be concluded that the PVAC system shows more economic viability compared with the TAC system for case 1 but shows less economic viability compared with the TAC system for case 2. For case 3, although it is about individual PV users, the PVAC system also shows more economic viability compared with the TAC system. The LCC of PVAC is \$1986.1 and the TAC's is \$2620.1. The LCC of PVAC is 24% less than that of TAC. Meanwhile, case 1 is 17% and case 2 is 9.2%. In three cases, PVAC in case 3 shows the most obvious economy. To analyze the reason for the high LCC of the PVAC system and find a solution to reduce the LCC, Figure 3 collects the costs of each stage. Notice that the costs of capital and electricity account for about 82% of PVAC and over 91% of air conditioning of all three cases. For PVAC, the cost of the sum of PV panels and battery packs takes account of 79%, 79%, and 76% of capital cost for three cases, respectively. The LCC is the life cycle cost, which means that the smaller the LCC of one system is, the smaller the money it costs. So, smaller LCC means more economic performance. Therefore, Table 10 indicates that there is a great possibility for capital cost reduction because of the continuous technological progress of PV panels and battery causing substantial cost reduction. Besides, by design optimization of the capacity, better economic benefits can be gained without sacrificing the reliability of the electricity supply.

The cost of electricity is the second significant factor, which accounts for about one-fourth to one-third of the LCC of the PVAC system. Since the surplus electricity is sold to the grid, it seems that there are more economic benefits and lower LCC when the amount of electricity increases, as shown in Figure 4. However, considering the difference of on-grid PV electricity between commercial user, personal user, and centralized power station (the on-grid price of them progressively increases), outputting more electricity means greater economic losses. Thus, reducing electricity output and increasing electricity meet peak valley electricity requirements and reduce the design capacity of PV panels and battery packs.

4.2. Sensitivity Analysis of PVAC System

4.2.1. Sensitivity Analysis considering Economic Aspects of Three Cases. To better understand how these economic factors impact the LCC analysis and make comparisons of three cases of PVAC system, sensitivity analysis is conducted. The parameters investigated are the cost of equipment, on-grid price, and the discount rate. The LCC analysis is repeated with all parameters perturbed by 20%. The results are shown in Figure 5.

It can be seen that, among the parameters being investigated, the cost of equipment causes more significant impacts on the LCC of the PVAC system of all three cases. This is not surprising because it accounts for over 52% of total LCC, which implies that there is plenty of room for reducing the LCC because of the cost reduction caused by technical progress. Besides, these economic parameters that investigated especially on-grid price and discount rate have more impacts on case 3 than the other two cases. This is mainly because case 3 has a higher ratio of electricity price to

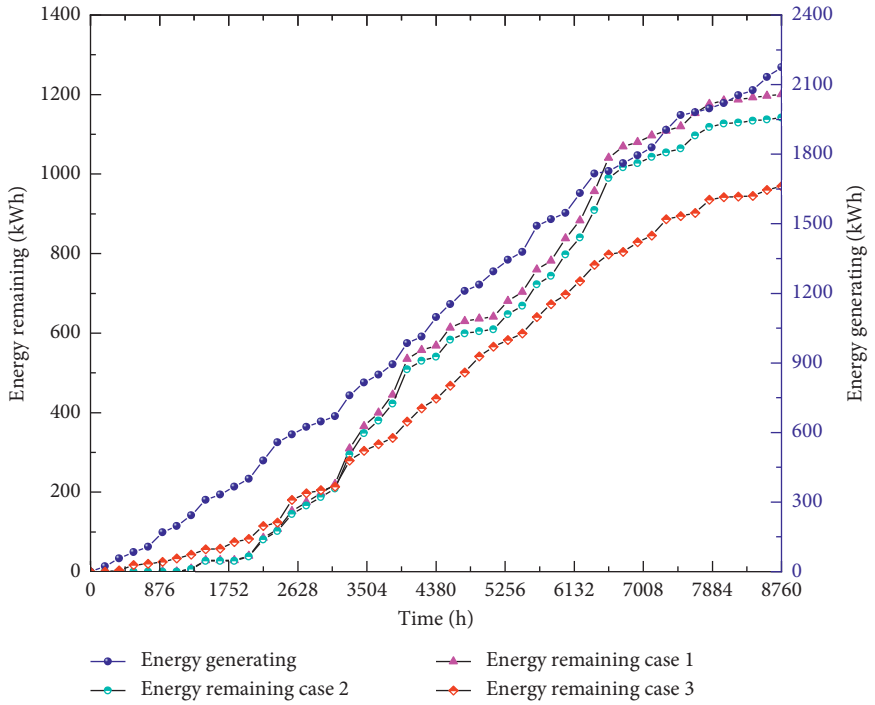

Figure 3: The simulation results of PVAC of three cases.

Table 10: Results of LCC analysis of three cases.

Item	Case 1		Case 2		Case 3	
	PVAC	TAC	PVAC	TAC	PVAC	TAC
LCC ($)	3810.1	4571.4	3885.3	4281.1	1986.1	2620.1

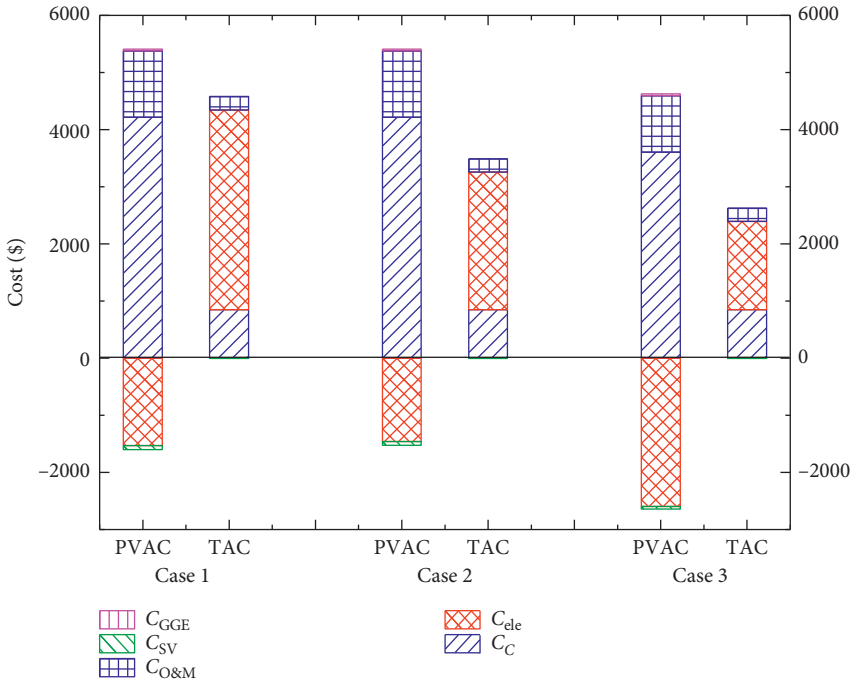

Figure 4: LCC analysis of three cases.

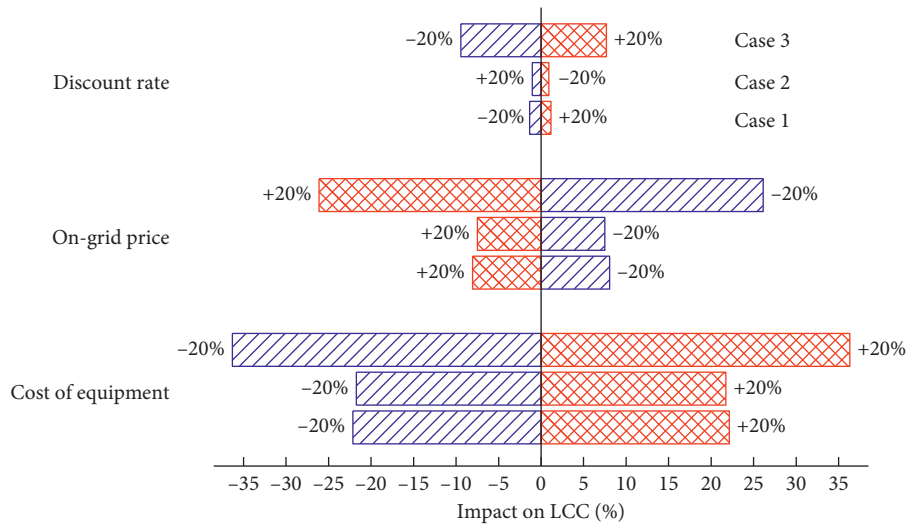

Figure 5: Sensitivity analysis considering economic aspects of three cases.

LCC for higher government subsidies for personal users based on incentive policies, though much more electricity is output in case 1. Of course, the LCC of all three cases is more economic than TAC. Therefore, the economic viability comparison between PVAC and TAC will be fully discussed in the next section on three cases.

4.2.2. Sensitivity Analysis considering Technical Aspects of Three Cases. In the former section, the impact of economic factors on LCC has been investigated; however, the economic viability is also influenced significantly by technical aspects. Thus, the sensitivity analysis is conducted to determine how these technical aspects impact the LCC analysis results. The parameters investigated are annual power generation capacity caused by enhancement of PV efficiency, battery capacity, battery efficiency, and efficiency of DC/DC converter. The LCC analysis is repeated with all parameters perturbed by 20% except the efficiency of the battery. Considering that their rated efficiency is as high as 90%, the perturbation ratio is +5% and −20%. The sensitivity analysis results are shown in Figure 6.

It can be seen from Figure 6 that battery efficiency shows the least impact on LCC while two others have significant impacts; thus, the technical progress of battery cannot promote the commercialization of PVAC. Of course, the LCC decreases with increasing PV efficiency because more electricity is generated. The improvement of PV efficiency and decrease of battery capacity influence the LCC obviously. Particularly, the latter has more significance. A decrease of 20% battery capacity causes a reduction of nearly 10% of total LCC because of the high capital cost of the battery. There is still big potential for cost reduction for the PVAC system with the technical progress resulting in cost reduction.

Decreasing the capacity of PV panels and battery capacity makes the PVAC become economical and more competitive. However, decreasing battery capacity can decrease the reliability for system operation and body comfort, which should be avoided in system design.

4.2.3. Economic Viability Comparison between PVAC and TAC in Cases 1 and 2. To better determine the economic boundaries between PVAC and TAC systems, economic viability comparison is carried out in this section. Considering that the peak electricity consumption ratio is low, the impact is discussed in the following section. Since there is little possibility for the on-grid price of PV electricity increasing and the price of peak electricity is expected to be higher in China because of electricity market reform [33], choosing peak electricity price as the variable for LCC is appropriate. The analysis results are shown in Figure 7 of cases 1 and 2.

It can be seen that the LCC of air conditioning increases with the peak electricity price linearly. From left to right, the first value of the x-axis of dot refers to the present LCC under the current price of the value of valley electricity price, which is \$0.1230/kWh. For case 1, when the price of peak electricity increases to the critical point, which is \$0.1360/kWh, both PVAC and air conditioning have the same LCC and economic benefits. So more benefits can be gained when the price of peak electricity is over \$0.1360/kWh. Particularly, the difference of LCC between PVAC and air conditioning is as large as \$761.3 when the price of peak electricity is \$0.1953/kWh, which is the present price of peak electricity. When the price of peak electricity exceeds the critical value of case 2 that is \$0.1529/kWh, there are economic benefits for PVAC. It can be expected that more benefits can be achieved with the increase of peak electricity in the near future because of electricity market reform boosting the development of renewable electricity power generation. The reform is implementing gradually by National Development and Reform Commission and has achieved preliminary results [34].

4.3. LCC Analysis of Case 1 and Case 2 considering the Curtailed Electricity. Since renewable electricity curtailment hardly happens to individual PV users, the discussion will not include case 3. To investigate the economic feasibility

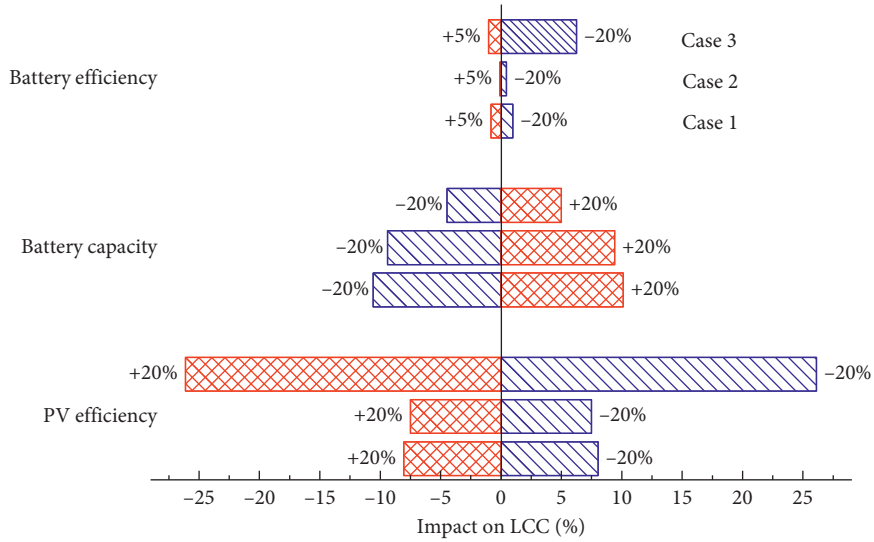

Figure 6: Sensitivity analysis considering technical aspects of three cases.

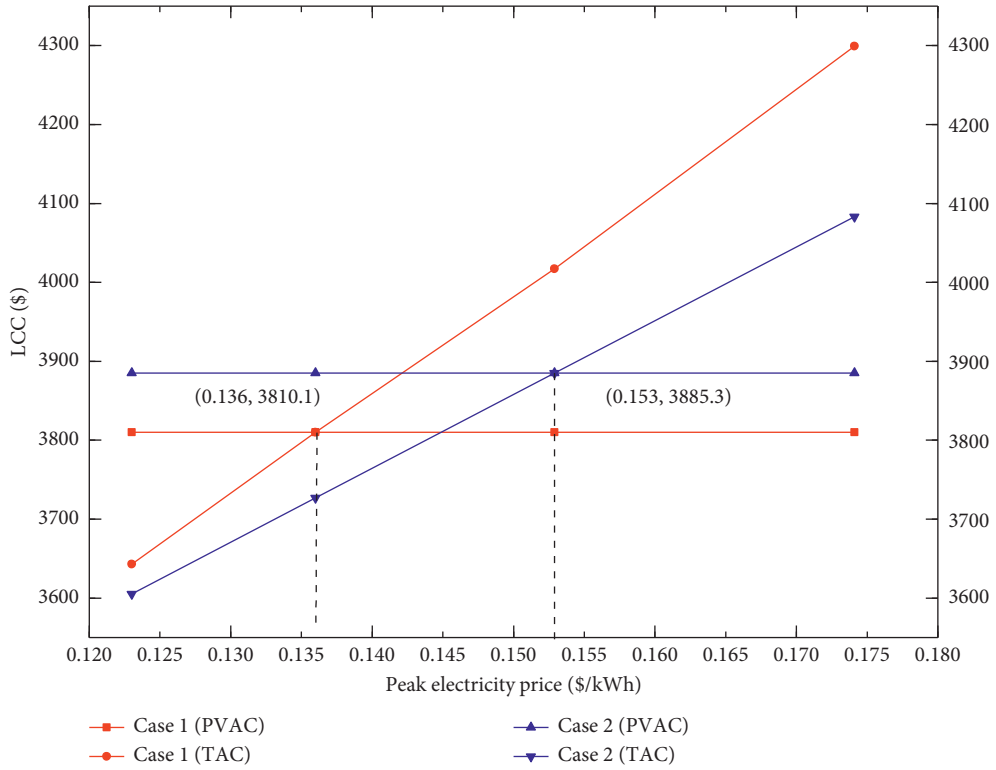

Figure 7: The impact of peak electricity price on LCC of cases 1 and 2.

when compared with the decomposed LCC of centralized PV power generation and TAC, an LCC comparison is conducted in this section. Because the PVAC system consumes a great large amount of electricity itself, no electricity is curtailed. However, when carrying out the decomposed LCC, the fact of an average PV electricity curtailment rate of 12.6% should be considered correspondingly based on the statistical data in China [35]. The detailed flowchart of three ways to use PV electricity is shown in Figure 8.

Because of the obvious disadvantage of PVAC of cases 2 and 3, the decomposed LCC will be carried out only for case 1. The results are shown in Table 11.

It can be concluded from Table 11 that the LCC from high to low is air conditioning, decomposed PV and air conditioning, and PVAC. Although higher income from selling electricity is achieved, more electric charge is paid for the high cost of peak electricity especially during summer and winter. To investigate the difference between PVAC and

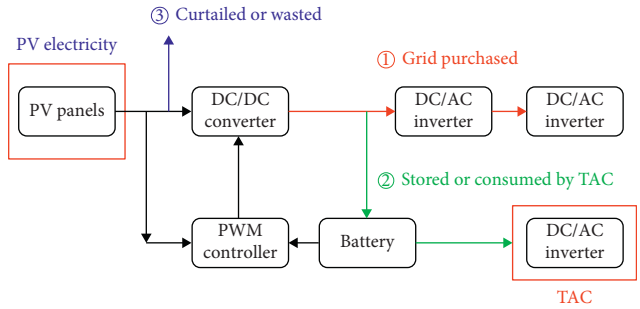

Figure 8: Flowchart of three ways to use PV electricity.

Table 11: The results of the LCC when considering a curtailment rate of 12.6%.

Item ($)	Case 1	Case 2
LCC of PVAC	3810.1	3885.3
LCC of TAC	4571.4	4281.1
LCC of decomposed PV and air conditioning	4282.2	3991.9

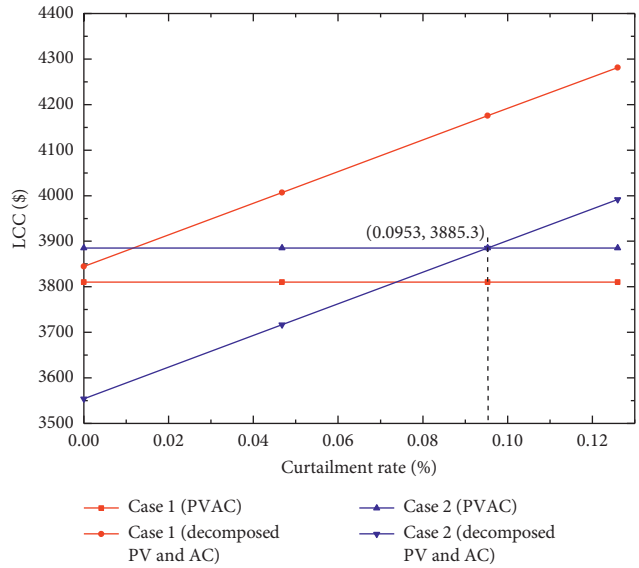

Figure 9: LCC comparison between decomposed PV and air conditioning and TAC considering the curtailment rate of case 1.

decomposed PV and air conditioning when the curtailment rate is changing, an analysis is carried out and the result is shown in Figure 9.

Figure 9 leads to the conclusion that, to compete with decomposed PV and air conditioning, the curtailment rate should be over 9.53% for case 2, which occurs in many areas of China; thus, the PVAC can be economically feasible. However, for case 1, PVAC is more competitive even if the price of selling electricity is cheaper. Compared with decomposed PVAC, an increase in the cost of power distribution equipment partly offsets the economic benefits coming from higher electricity selling prices for decomposed PV and air conditioning systems. More importantly, a large cost increase of consuming peak electricity brings more negative effects than positive effects of higher electricity selling price for cases consuming much peak electricity like case 1. However, when peak electricity consumption is reduced, there is a possibility that decomposed PV and air conditioning can achieve more benefits like case 2.

Although this could lead to the conclusion that PCAV can be economic when faced with cases consuming much peak electricity, it can also be seen that the decomposed PV and air conditioning is economic when the curtailment rate is low enough. To achieve more benefits, a new operation model is proposed in this study combining the advantage of both PVAC of avoiding peak electricity consumption and no curtailment rate and decomposed PV and air conditioning of higher electricity selling price. In the new operation model, the system operates the "PVAC model" during the electricity consuming period (from July to August and from

Table 12: LCC of PVAC operating on the mode of shifting peak electricity load for the grid.

Item ($)	Case 1	Case 2
Cost of surplus electricity	−607.8	−455.8
Cost of selling electricity	−666.0	666.0
Cost of consuming electricity	59.62	134.3
LCC	3794.3	4165.8

December to next April) and operates the "decomposed PV and air conditioning model" during other days, which will be discussed in the next section.

4.4. Economic Feasibility of a New Operation Model of PVAC System. Though the PVAC system contributes to clip peak and fill valley for the grid, the high LCC limits its commercialization seriously. To explore the development of the PVAC system, a new operation model is proposed. During summer and winter days, the system operates the "PVAC mode," which consumes electricity itself and sells surplus electricity to the grid. During other days, because the air conditioning system operates occasionally, the system sells its total generated electricity and purchases electricity from the grid when it requires. The LCC can be decreased and the results are shown in Table 12.

It can be concluded that case 1 has better economic benefits compared with the "PVAC model," while case 2 shows poor economic performance. Thus, we can conclude that when there is a large peak electricity requirement, it is better to operate the system in this "new model." In fact, this also helps the grid clip the peak load and fill the valley load during the peak time of summer and winter. But for cases like case 2, which has a lesser ratio of peak electricity, it is better to run the "PVAC model" both for users and the grid than decomposed PV and air conditioning and TAC system.

5. Conclusions

This paper presents economic feasibility comparisons between PVAC system, TAC system, and decomposed PV and air conditioning system of the three typical application cases for distributed PV air conditioning. Case 1 refers to the typical operation model of a supermarket, case 2 presents the application case of an office building, and case 3 is a typical residence in most rural areas of China. To obtain more accurate results, a TRNSYS simulation model is built to calculate the annual electricity generation, consumption, and surplus, which is sold to the grid.

According to the results of the simulation, LCC, and sensitivity analysis, the costs of equipment and peak electricity are the main costs, which are expected to decrease a lot in the near future with technological progress. When the system operates in all three cases, the PVAC system shows better economic benefits even when the peak electricity price is lower than the present value. In the three cases, the LCC of PVAC is $761.3, $395.8, and $634 less than the LCC of TAC, for an average of 16.7% less. The PVAC of all three cases shows a better economy than the LCC of TAC, even when the parameters of equipment cost, interconnection price, and discount rate are perturbed by 20%.

Considering that the on-grid price of the centralized PV electricity is higher than the distributed price, economic benefit comparison between PVAC and decomposed PV and air conditioning is carried out. The PVAC shows better economic performance for case 2 when the curtailment rate is over 9.53%. For case 1, there is an always economic advantage of PV air conditioning regardless of curtailment rate.

However, a lesson can be learned from the decomposed PV and air conditioning. By operating on a new model, more benefits can be achieved for case 1. But for case 2 consumes less peak electricity compared with case 1, the economic advantage caused by higher on-grid price is offset by an equipment cost increase of electricity distribution.

In the future, we will have a corresponding research on the operation model about PVAC, TAC, and decomposed PV and AC systems. Although we have proposed a simple model about it in this paper, we will propose a detailed operation model to minimize the value of LCC.

Data Availability

The data used to support the findings of this study are included within the article.

Conflicts of Interest

The authors declare that there are no conflicts of interest regarding the publication of this paper.

Acknowledgments

This work was supported by the National Key R & D Program of China (2018YFB0905200) and the science project of State Grid Sichuan Electric Power Corporation (SGTYHT/18-JS-199).

References

[1] X. Su, X. Bai, C. Liu, R. Zhu, and C. Wei, "Research on robust stochastic dynamic economic dispatch model considering the uncertainty of wind power," *IEEE Access*, vol. 7, pp. 147453–147461, 2019.

[2] C. Wei, M. Benosman, and T. Kim, "Online parameter identification for state of power prediction of lithium-ion batteries in electric vehicles using extremum seeking," *International Journal of Control, Automation and Systems*, vol. 17, no. 11, pp. 2906–2916, 2019.

[3] F. Cheng, L. Qu, W. Qiao, C. Wei, and L. Hao, "Fault diagnosis of wind turbine gearboxes based on DFIG stator current envelope analysis," *IEEE Transactions on Sustainable Energy*, vol. 10, no. 3, pp. 1044–1053, 2019.

[4] S. Afşar, L. Brotcorne, P. Marcotte, and G. Savard, "Achieving an optimal trade-off between revenue and energy peak within a smart grid environment," *Renewable Energy*, vol. 91, pp. 293–301, 2016.

[5] A. Al-Alili, Y. Hwang, and R. Radermacher, "A hybrid solar air conditioner: experimental investigation," *International Journal of Refrigeration*, vol. 39, pp. 117–124, 2014.

[6] Z. Zapalowicz and A. Opiela, "Boundary value of the air distribution coefficient that ensures working effectivity of the air-condition system connected with ground heat exchanger and with PV installation," *Sustainable Cities and Society*, vol. 42, pp. 93–99, 2018.

[7] M. J. Goldsworthy, "Building thermal design for solar photovoltaic air-conditioning in Australian climates," *Energy and Buildings*, vol. 135, pp. 176–186, 2017.

[8] B.-J. Huang, T.-F. Hou, P.-C. Hsu et al., "Design of direct solar PV driven air conditioner," *Renewable Energy*, vol. 88, pp. 95–101, 2016.

[9] F. J. Aguilar, S. Aledo, and P. V. Quiles, "Experimental analysis of an air conditioner powered by photovoltaic energy and supported by the grid," *Applied Thermal Engineering*, vol. 123, pp. 486–497, 2017.

[10] F. Aguilar, D. Crespí-Llorens, and P. V. Quiles, "Techno-economic analysis of an air conditioning heat pump powered by photovoltaic panels and the grid," *Solar Energy*, vol. 180, pp. 169–179, 2019.

[11] D. Fischer, K. B. Lindberg, H. Madani, and C. Wittwer, "Impact of PV and variable prices on optimal system sizing for heat pumps and thermal storage," *Energy and Buildings*, vol. 128, pp. 723–733, 2016.

[12] Z. Liu, A. Li, and Q. Wang, "Performance study of a quasi grid-connected photovoltaic DC air conditioner in the hot summer zone," *Applied Thermal Engineering*, vol. 121, pp. 1102–1110, 2017.

[13] P. Wei, Y. Hongwen, Z. Yongzhe, and Y. Hui, "Solar photovoltaic based air cooling system for vehicles," *Renewable Energy*, vol. 130, pp. 25–31, 2018.

[14] C. Wei, X. Xu, Y. Zhang, and X. Li, "A survey on optimal control and operation of integrated energy systems," *Complexity*, vol. 2019, Article ID 9462158, 14 pages, 2019.

[15] H. H. Chen, S. Chen, and Y. Lan, "Attaining a sustainable competitive advantage in the smart grid industry of China using suitable open innovation intermediaries," *Renewable and Sustainable Energy Reviews*, vol. 62, pp. 1083–1091, 2016.

[16] C. Wei, Z. Shen, D. Xiao, L. Wang, X. Bai, and H. Chen, "An optimal scheduling strategy for peer-to-peer trading in interconnected microgrids based on RO and Nash bargaining," *Applied Energy*, vol. 275, Article ID 117024, 2021.

[17] Building Energy Research Center of Tsinghua University, *Annual Development Report of China Building Energy Efficiency*, China Architecture & Building Press, Beijing, China, [in Chinese], 2015.

[18] S. Bolocan and I. Boian, "Solar cooling for energy saving. can we afford not to use the heat of the sun?" *Bulletin of the Transilvania University of Braşov*, vol. 3, p. 52, 2010.

[19] R. M. Lazzarin, "Solar cooling: PV or thermal? a thermodynamic and economical analysis," *International Journal of Refrigeration*, vol. 39, no. 4, pp. 38–47, 2014.

[20] C. Infante Ferreira and D.-S. Kim, "Techno-economic review of solar cooling technologies based on location-specific data," *International Journal of Refrigeration*, vol. 39, no. 1, pp. 23–37, 2014.

[21] A. Allouhi, T. Kousksou, A. Jamil, T. El Rhafiki, Y. Mourad, and Y. Zeraouli, "Economic and environmental assessment of solar air-conditioning systems in Morocco," *Renewable and Sustainable Energy Reviews*, vol. 50, pp. 770–781, 2015.

[22] E. Tarigan, F. D. Kartikasari, M. Fleicher, and B. Howley, "Study of PV powered air conditioning for a classroom of university of surabaya," in *Proceedings of the 2015 International Conference on Technology, Informatics, Management, Engineering & Environment (TIME-E)*, pp. 121–126, Samosir, Indonesia, September 2015.

[23] F. J. Aguilar, P. V. Quiles, and S. Aledo, "Operation and energy efficiency of a hybrid air conditioner simultaneously connected to the grid and to photovoltaic panels," *Energy Procedia*, vol. 48, pp. 768–777, 2014.

[24] Y. Li, G. Zhang, G. Z. Lv, A. N. Zhang, and R. Z. Wang, "Performance study of a solar photovoltaic air conditioner in the hot summer and cold winter zone," *Solar Energy*, vol. 117, pp. 167–179, 2015.

[25] The State Council, *Regulations for the Implementation of the PRC Enterprise Income Tax Law*, China Legal Publishing House, Beijing, China, 2007.

[26] Z. Yanju, H. U. Fengying, Z. Zhenglong, Z. Xiongwei, S. O. Business, and C. S. University, "Impact of optimal carbon tax rate on supply chain structure and social welfare," *Systems Engineering-Theory & Practice*, vol. 37, no. 4, pp. 886–900, 2017.

[27] Y. Fu, X. Liu, and Z. Yuan, "Life-cycle assessment of multi-crystalline photovoltaic (PV) systems in China," *Journal of Cleaner Production*, vol. 86, pp. 180–190, 2015.

[28] J. Ally and T. Pryor, "Life cycle costing of diesel, natural gas, hybrid and hydrogen fuel cell bus systems: an Australian case study," *Energy Policy*, vol. 94, pp. 285–294, 2016.

[29] L. Qiangqian, "Performance of lead-carbon batteries and their applications in electricity storage," *Power Construction*, vol. 35, no. 11, pp. 117–121, 2014, [in Chinese].

[30] State Grid Shanghai Municipal Electric Power Company, Shanghai Sales Tariff, [EB/OL]. 2016, http://www.sh.sgcc.com.cn/html/main/col7/2016-06/21/20160621144920167955047_1.html.

[31] T. Zhanlian and J. Chen, "Lead carbon ultrabatteries for energy storage," *Energy Storage Science and Technology*, vol. 4, no. 6, pp. 546–555, 2015, [in Chinese].

[32] G. Lv, "Research on Independent Photovoltaic Air Conditioning System," *Shanghai Jiaotong University*, Shanghai, China, 2012, (in Chinese).

[33] NEA (National Energy Administration), *Give Full Play to the Role of Price Leverage to Help Supply-Side Structural Reforms*, National Energy Administration, Beijing, China, 2016, http://www.nea.gov.cn/2016-05/04/c_135333301.htm.

[34] Nation Development and Reform Commission, Circular of the national development and Reform Commission on improving the on grid tariff mechanism for photovoltaic power generation, [EB/OL], 2019, https://www.ndrc.gov.cn/xxgk/zcfb/tz/201904/t20190430_962433.html.

[35] W. Zhao, N. Zhang, C. Kang, Y. Wang, P. Li, and S. Ma, "Estimation method of conditional prediction error probability distribution of photovoltaic power generation output," *Power system automation*, vol. 39, no. 16, pp. 8–15, 2015.

Hindawi
Complexity
Volume 2021, Article ID 9636383, 13 pages
https://doi.org/10.1155/2021/9636383

Research Article

On-Site Engineering Test of Active Support Control for the PV Station and Wind Farm in the AC-DC Hybrid Power Grid under Extreme Fault Conditions

Xiao-ling Su,[1,2] **Lai-jun Chen**,[2] **Jun Yang**,[3] **Zhengxi Li**,[3] **Peng Zhou**,[3] **and Hui Chen**[3]

[1]*School of Water Resources and Electric Power, Qinghai University, Xining 810016, China*
[2]*Qinghai Key Lab of Efficient Utilization of Clean Energy (Tus-Institute for Renewable Energy), Qinghai University, Xining 810016, China*
[3]*State Grid Qinghai Electric Power Company, Xining 810016, China*

Correspondence should be addressed to Lai-jun Chen; chenlaijun@qhu.edu.cn

Received 4 June 2021; Revised 20 June 2021; Accepted 7 July 2021; Published 5 August 2021

Academic Editor: Chun Wei

Power systems have developed significantly because of the increasing share of renewable energy sources (RESs). Despite the advantages, they also bring inevitable challenges to power system stability, especially under extreme fault conditions. This paper presents a practical active support control strategy for RESs to support the power grid under extreme fault conditions. The proof process is taken in an AC-DC hybrid power grid integrated with large capacity of PV stations and wind farms. The on-site engineering test results reflect that RESs bring potential risks in the AC-DC hybrid power grid operation and validate the excellent engineering practical features of the proposed control strategy. In addition, test results also reveal predisposing factors of power system instability which are missing in the simulation and fault simulation device-based testing results. They prove the outstanding advantages of on-site engineering tests.

1. Introduction

Power systems see more and more photovoltaic (PV) and wind generation integration. Within increasing renewable energy source (RES) penetration level, despite the advantages such as environmental friendly and sustainable development, it also brings problems to the utility grid [1–3]. Adjusting the power source structure brings an inevitable impact on the power system primary frequency response due to the conventional generators' reduction and consequent loss of inertia [4]. Therefore, the provision of ancillary services is becoming an increasingly challenging task to this new generation power system operation.

The power source structure has developed significantly because of the increasing share of RESs in the power system, and the coupling interaction between RESs and the power grid is becoming significant which reduces delivery capability and power accommodation capacity of the power system [5]. In addition, within disturbance rejection ability and robust stability, low overload capacity, insufficient tolerance to voltage changes, and all these characteristics of power electronic equipment may also deteriorate the power system operation environment even further.

Most of the PV stations and wind farms do not participate in power grid control at the present stage. Some large-scale grid-connected PV stations or wind farms adjust output power according to the automatic generation control (AGC) and automatic voltage and reactive power control (AVC) system to regulate voltage and frequency as power system requirements [6, 7]. Consequently, the conventional control or operation mode is no longer efficient in the new generation power system [8, 9]. Zhang et al. [10] studied the control performance of AGC for wind power ramping based on deep reinforcement learning. Prasad and Padhy [11] proposed the synergistic frequency regulation control mechanism for DFIG wind turbines with optimal pitch dynamics. Complicated stochastic AGC modeling causes high computational burdens concurrently. Chen et al. [12]

used the Itô-theory-based model to reduce the computational burden of optimization considering non-Gaussian wind power uncertainty. However, random communication delay and noise disturbance in the AGC/AVC control network usually cause the control system performance degradation or even system destabilization.

To address these challenges, the PV station and wind farm should provide active support to the power system in external faults and other transient processes. Using ESSs to add regulation capacity and improve the dynamic performance of AGC, particularly at the high RES penetration power systems, is a feasible solution [13–16]. Su et al. [17] proposed an adaptive robust sliding-mode control for energy storage system integrated PV and wind station to provide frequency and voltage control functionality for RESs. Wang et al. [18] used the supercapacitor in the large-scale hybrid wind-PV farm to improve stability in the multimachine power system. The large-scale grid-connected PV station or wind farm requires a large-capacity energy storage system which is not available at present. Therefore, it is more practical to use existing equipment such as the PV inverter and wind power generator and also conventional reactive power compensators such as static VAR compensator (SVC) or static VAR generator (SVG) to provide active support to the power grid. Karbouj et al. [19] proposed a self-adaptive voltage controller to enable solar PV power plant participation in voltage control ancillary service. STATCOM is used in large PV stations for fault-induced delayed voltage recovery alleviation in [20]. A coordinated damping optimization control strategy for wind power generators and their reactive power compensators is proposed in [21]. Wang et al. [22] analyzed the interval overvoltage risk caused by the impacts of load uncertainties and SVC.

Simulation and laboratory tests based on theoretical deduction are the most frequently used method in RES control strategy validation or power system. The performance of the proposed controller in [9] is demonstrated using simulation studies of an interconnected power system which are conducted within the DIgSILENT Power Factory platform. Case studies in [17] were developed based on MATLAB, while Varma and Mohan [20] presented the validation process by PSCAD/EMTDC. A three-phase four-wire hybrid simulation platform integrating the advantages of both digital simulation and physical simulation is developed in [23] which combines the physical simulation system and real-time digital simulator. Wang et al. [24] built laboratory platforms for experimental verification. Zimmerman et al. [25] presented the details of the network modeling and problem formulations used by MATPOWER. Reshikeshan et al. [26] verified the proposed autonomous voltage regulation scheme by power flow simulations on the EPRI Circuit 24 test feeder in an open-source distribution system simulation platform.

The large-scale PV station or wind farm is connected to the power grid with long electrical distance, and the reactive power control capability is relatively insufficient which makes voltage stability a challenging task for the power system, especially during large disturbances [27–30]. Laboratory tests only validate the operation performance of PV inverters or wind generators in the islanding mode, and some proof processes are taken in the microgrid. The power system is a very complicated, nonlinear, and strong coupling dynamic system, and experimental results based on islanding or grid-connecting setup are inadequate when it comes to a large-scale grid-connected PV station or wind farm.

On the contrary, the fault simulation device is the common option in RES on-site testing. However, because of the maximum voltage and current limitation, its capacity is also limited; consequently, it is almost impossible to simulate the power system. Fault simulation device is applied to PV inverter and wind generator onsite experiments; however, it is inadequate for large RESs station onsite engineering test, as it is impossible to simulate voltage waveform at grid connection point of RESs station by fault simulation device.

Therefore, the on-site engineering tests are necessary in the PV station and wind farm active support control study. The power system with large-scale RES and power electric device-based projects such as high-voltage direct current (HVDC) have much more possibility of voltage and frequency instability.

This paper proposes a practical active support control for the PV station and wind farm to support the power grid under extreme fault conditions. The excellent engineering practical features of the proposed control strategy are important since active support capability is an obligation for the PV station and wind farm in the future, and upgrading the RES with the large-capacity energy storage system is uneconomical, plus for some PV stations or wind farms, there is no space for ESSs. In addition, their control capability is verified through on-site engineering test in an AC-DC hybrid power grid integrated with large capacity of the PV station and wind farm. The on-site test includes three categories, and each has fifteen grounding faults at different sites.

2. Proposed Active Support Control for the PV Station and Wind Farm

In this section, the construction of the proposed active support control strategy for the PV station and wind farm is presented. Figure 1 gives the topology of the PV station. The PV inverters are connected to the power grid through a 10 kV/35 kV transformer; then, it is integrated to a 110 kV collection substation through a 35 kV/110 kV transformer with a long transmission line.

The topology of the wind farm is presented in Figure 2. The wind power generators are connected to the power grid through a 0.69 kV/35 kV transformer; then, it is integrated to a 110 kV collection substation through a 35 kV/110 kV transformer with a long transmission line.

2.1. High-Frequency Resistance Control. Primary frequency regulation is insufficient in a weak AC/DC hybrid power system, which makes high frequency problem an ineluctable challenge for RESs operation. Under this condition, the PV inverter, wind power generator, SVC, SVG in the PV station, and wind farm should maintain grid-connected operation

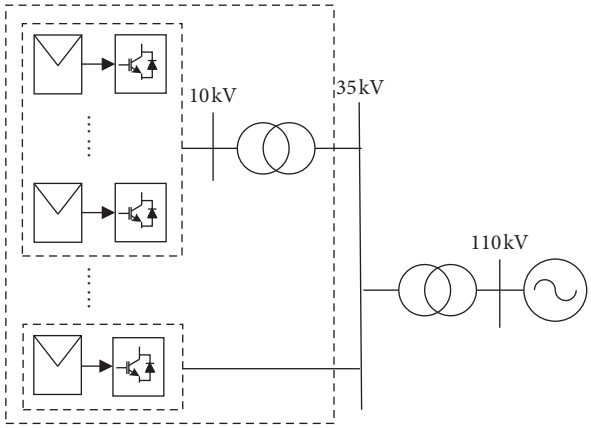

Figure 1: PV station topology.

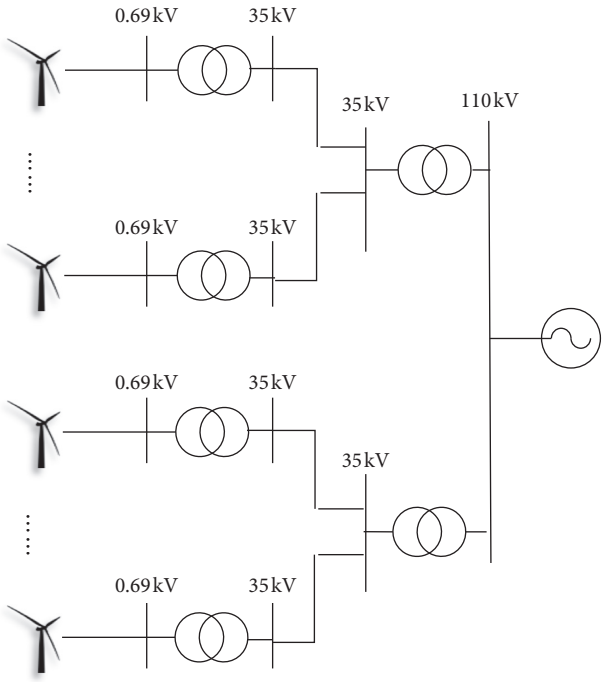

Figure 2: Wind farm topology.

and provide dynamic support to the power system simultaneously. The high-frequency resistance control strategy is designed as

$$\begin{cases} 49.5\,\text{Hz} \le f_T < 50.5\,\text{Hz}, & \text{continuous}, \\ 50.5\,\text{Hz} \le f_T < 51.0\,\text{Hz}, & t_T \ge 3\,\text{min}, \\ 51.0\,\text{Hz} \le f_T < 51.5\,\text{Hz}, & t_T \ge 10\,\text{s}, \\ 51.5\text{Hz} < f_T, & t_T \ge 2\,\text{s}, \end{cases} \tag{1}$$

where f_T is the frequency at the access point and t_T is the operation time requirement. Take a PV inverter for example; by adopting this control law, it remains in the grid-connected mode when the power system frequency is greater than or equal to 49.5 Hz and less than 50.5 Hz. When the frequency is greater than or equal to 50.5 Hz and less than 51.0 Hz, the PV inverter will remain in the grid-connected mode for over 3 min.

2.2. High-Voltage Resistance Control. Insufficient voltage control ability of the power system brings high-voltage challenge to RESs. In the steady state, the PV inverter, wind power generator, SVC, SVG in the PV station, and wind farm operate in the grid-connected mode, and they provide dynamic support to the power system during the transient state. High-voltage resistance control is designed as

$$\begin{cases} 0.9\,\text{p.u.} \le U_T < 1.1\,\text{p.u.}, & \text{continuous}, \\ 1.1\,\text{p.u.} \le U_T < 1.2\,\text{p.u.}, & t_T \ge 10\,\text{s}, \\ 1.2\,\text{p.u.} \le U_T < 1.3\,\text{p.u.}, & t_T \ge 0.5\,\text{s}, \end{cases} \tag{2}$$

where U_T is the voltage per unit value at the access point and t_T is the operation time requirement. Take the PV inverter for example; by adopting this control law, it remains in the grid-connected mode no less than 10 seconds when its access point voltage is greater than 1.1 p.u. and less than 1.2 p.u..

2.3. Low-Voltage Ride-Through Control. Low-voltage ride-through (LVRT) technology is one important indicator for the PV station and wind farm; the control logic is divided into 3 parts.

2.3.1. Current Coefficient for Reactive Power Control. The PV station and wind farm provide dynamic reactive power support for the grid during LVRT. The control strategy for dynamic reactive current increment $\Delta I_{q\text{LVRT}}$ of the PV inverter and direct-drive permanent magnet generator is

$$\begin{cases} \Delta I_{q\text{LVRT}} \ge K_1 (U_{\text{LV}} - U_T) I_N, & (0.2\,\text{p.u.} \le U_T \le 0.9\,\text{p.u.}), \\ \Delta I_{q\text{LVRT}} \ge 1.05 I_N, & (U_T < 0.2\,\text{p.u.}), \\ \Delta I_{q\text{LVRT}} = 0, & (U_T \ge 0.9\,\text{p.u.}), \end{cases} \tag{3}$$

where U_{LV} is the threshold of LVRT, U_T is the voltage per unit value at the access point, K_1 is the current coefficient for reactive power control, and I_N is the rated current of the equipment. $I_{q\text{LVRT}}$ reduces to zero in 10 ms after power grid voltage recovery.

2.3.2. Current Coefficient for Active Power Control. The PV station and wind farm generate reactive power during LVRT in the first instance, and the active current $I_{p\text{LVRT}}$ remains as the current before faults if its current is less than the current threshold; otherwise,

$$I_{P\text{LVRT}} = K_2 I_{P0}, \tag{4}$$

where I_{p0} is the current before faults or before voltage drop and K_2 is the current coefficient for active power control during LVRT. K_2 is equal to 1 if output current is less than the current threshold and current coefficient K_1 meets the requirements in equation (3).

2.3.3. Active Power Recovery Rate. The active power returns to its value before fault, and recovery speed is

$$\Delta P_{\mathrm{LVRT}} = K_P P_N, \tag{5}$$

where P_N is the rated power of the equipment and K_P is the recovery coefficient for active power, and its recommended value is 3.

2.4. High-Voltage Ride-Through Control. High-voltage ride-through (HVRT) is another important indicator for the PV station and wind farm. The PV station and wind farm absorb dynamic reactive power from the grid during HVRT. The control strategy for dynamic reactive current increment $\Delta I_{q\mathrm{HVRT}}$ of the PV inverter and direct-drive permanent magnet generator is

$$\begin{cases} \Delta I_{q\mathrm{HVRT}} \le K_3 (U_{\mathrm{HV}} - U_T) I_N, & (U_T \ge 1.1\ \mathrm{p.u.}), \\ \Delta I_{q\mathrm{HVRT}} = 0, & (U_T < 1.1\ \mathrm{p.u.}), \end{cases} \tag{6}$$

where U_{HV} is the threshold of HVRT, U_T is the voltage per unit value at the access point, K_3 is the current coefficient for reactive power control and its recommended value is over 1.5, and I_N is the rated current of the equipment.

With sufficient primary energy, the output active power remains as its value before fault if its output current is less than the current threshold and current coefficient K_3 meets the requirements in equation (6).

2.5. Continuous Ride-Through Control. Continuous occurrence of commutation failure in the HVDC system causes alternating high voltage and low voltage; the control strategy is designed in Figure 3 to cope with these operating conditions. When high/low voltage occurs, the PV station and wind farm not only can remain in grid-connected operation but also meet the requirements above.

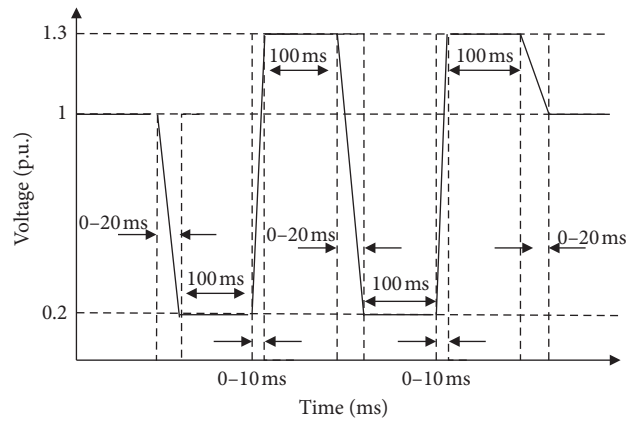

Figure 3: Continuous ride-through control strategy.

3. AC-DC Hybrid Power Grid within Large-Scale RESs

Voltage and frequency control is more challenging in the power system when the penetration level of the RES is relatively high. HVDC is another disturbance factor when it comes to power system stability. In order to validate the active support control under extreme conditions, on-site engineering tests are performed in an AC-DC hybrid power grid as shown in Figure 4. The main voltage class of this grid is 750/330/110 kV, and it has 194 substations (110 kV and above) and two HVDC transmission projects in this system. It covers an area of 622,000 square kilometers which is characterized as long-distance and large-capacity transmission.

3.1. Long Distance. PV and wind power generated in the west of this power system transmit to the load center through 800 km 750 kV AC transmission lines. PV, wind power, and hydropower from the south part of this power system transmit to the load center through 150 km 750 kV AC transmission lines.

3.2. Large Capacity. By the end of 2020, the total installed capacity is 40.3 million kW, hydropower, thermal power, wind power, photovoltaic, and solar thermal power accounting for 29.6%, 9.8%, 20.9%, 39.2%, and 0.5%, respectively, as shown in Figure 5. The renewable sources accounted for 60.7%, which is the largest installed power in this power grid.

3.3. Power Fluctuation and Stochastic Characteristic. Power fluctuation and stochastic characteristic of PV and wind generation bring uncontrollable problems to this power system. In addition, synchronous compensator, energy storage systems, and solar thermal power station make the operation mode of the power grid complex and changeable both in time domain range and geographical scope.

3.4. Small Load Scale. First, 86% of the power system load is connected to Station 2 and Station 6; meanwhile, only 0.5% of the power system load is connected to Station 3, Station 4, and Station 5. This type of load distribution is seriously uneven. Second, most of the load is large industrial load, accounted for 84%, which brings harmonics and voltage surges. Third, the load variation ratio is relatively small, with the average load rate equal to 95.7%, and a maximum peak-valley difference is 10%. Fourth, the total load is small compared to its total installed capacity; the historical maximum load is 10 million kW.

3.5. Insufficient Stable Power Source near the HVDC Converter Station. There is only one hydropower station near the ±800 kV HVDC converter station and over the PV station and wind farm. So, the coupling effect between the HVDC transmission system and AC power system is significant. In addition, disturbance from the PV station and wind farm is also remarkable for this HVDC converter station.

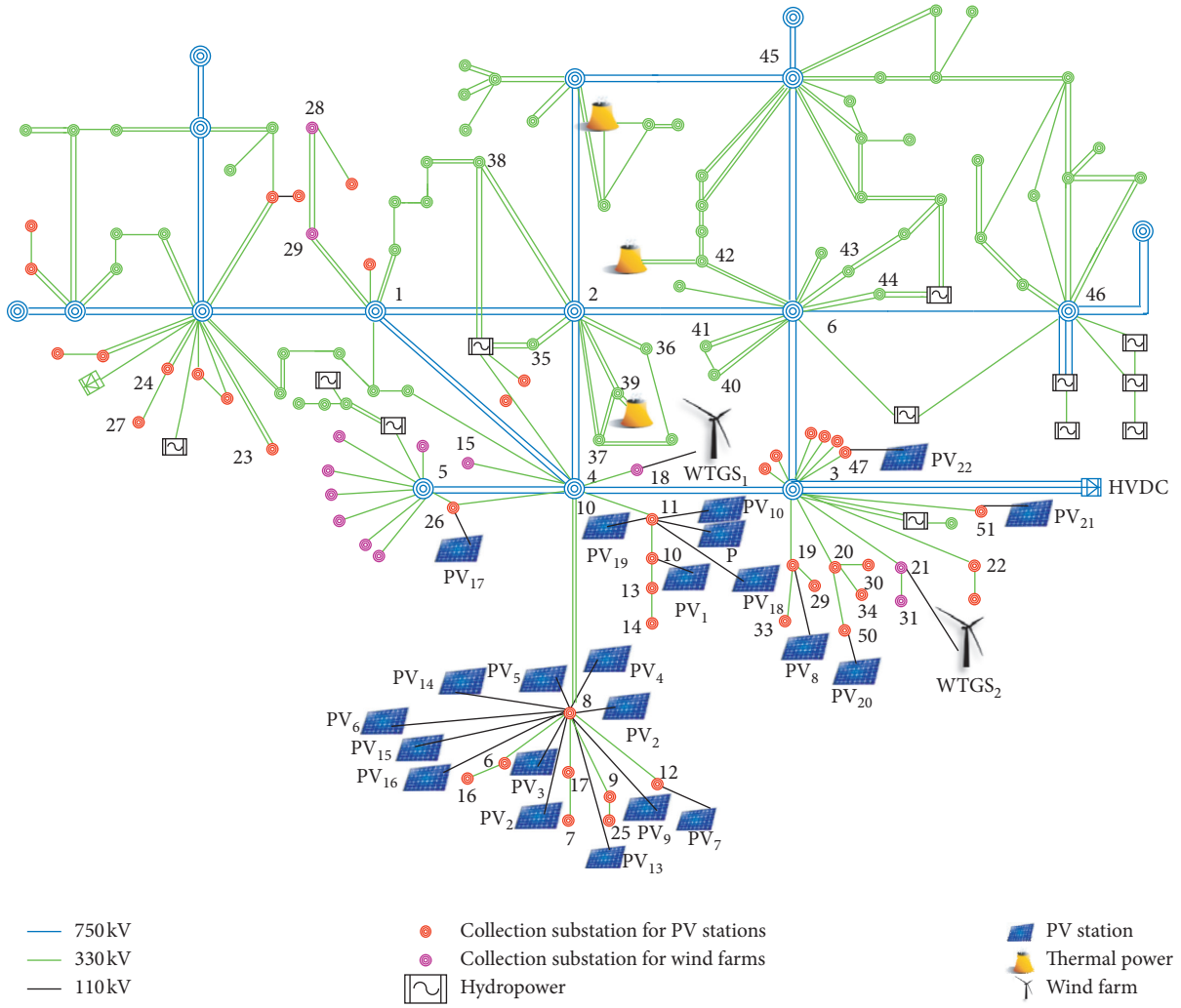

Figure 4: AC-DC hybrid power grid.

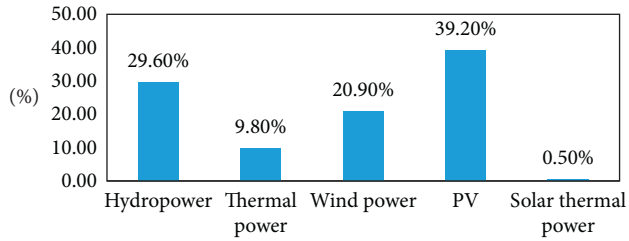

Figure 5: Installed capacity.

The AC power system near the ±800 kV HVDC converter station is a weak AC/DC hybrid power system. In this power system, insufficient voltage control and primary frequency regulation ability make RESs face problems such as overvoltage or low voltage constantly. It is the best on-site engineering test platform to verify the proposed active support control for the PV station and wind farm.

4. On-Site Experiments

The control strategy for the PV station and wind farm is test through on-site artificial fault tests which can be divided into three categories, and each category has fifteen grounding faults at different sites. There are over 200 PV stations and 30 wind farms that participated in these experiments. 54 of the PV stations and 5 of the wind farms adopt the proposed active support control strategy. Recommended control parameters for the PV inverter and direct-drive wind generator are given in Table 1.

To deal with the large-scale experimental data and waveform in the on-site engineering test, the monitoring location is chosen according to simulation analysis results and power grid operation experience. The chosen monitoring locations are (1) PV inverter, wind power

Table 1: Recommended control parameters.

Parameter	Value	Parameter	Value	Parameter	Value
U_{LV}	0.9	K_1	1.5–2	K_3	≥1.5
U_{HV}	1.1	K_2	=1	K_P	≥3

(a) (b)

Figure 6: PV inverters in PV station 8. (a) Series-connected PV inverter. (b) Centralized PV inverter.

generator, SVC, and SVG in the PV station and wind farm; (2) PMU and fault recording device in all 750 kV substations and some 330 kV substations; (3) ±800 kV HVDC converter station; (4) PMU and fault recording device in the 110 kV collection substation near the ±800 kV HVDC converter station; (5) 750 kV/330 kV/110 kV transmission line and some 35 kV transmission lines in the PV station and wind farm.

4.1. Inverter Parameters in PV Station 8. This paper presents testing results of PV station 8. Its capacity is 100 MW and connects to collection station 19. There are two types of PV inverters, series-connected PV inverter and centralized PV inverter, which are shown in Figure 6. The key parameters of the series-connected PV inverter are given in Table 2, and Table 3 gives key parameters of the centralized PV inverter.

The original and modified control parameters of series-connected PV inverters and centralized PV inverters in PV station 8 are given in Table 4. In order to avoid SVC or SVG disconnection during experiments, the voltage protection setting value of the SVC and SVG is adjusted to 0.6 U_N and 1.2 U_N, where U_N is its rated voltage.

Table 2: Parameters of the series-connected PV inverter.

DC max. input voltage	1500 VDC
DC max. input current	9 × 40 A
Isc	9 × 40 A
DC MPP range	500–1500 VDC
AC output nominal voltage	800 VAC
AC nominal operating frequency	50 Hz
AC output rated power	175 kW
AC output max. apparent power	193 kVA
AC output max. current	140.7 A
Power factor	−0.8–0.8

Table 3: Key parameters of the centralized PV inverter.

DC max. input voltage	1500 VDC
DC max. input current	3062 A
Isc	4200 A
DC MPP range	1150–1500 VDC
DC input channel	17
AC output nominal voltage	800 VAC
AC nominal operating frequency	50 Hz
AC output rated power	3150 kW
AC output max. apparent power	3465 kVA
AC output max. current	2273 A
Power factor	−0.8–+0.8
Transformer ratio	37/0.8 kVAC

4.2. Experimental Results. There is a grounding fault on phase A of 330 kV transmission line 3-19 near station 3. The voltage and current waveform of this transmission line from PMU is given in Figures 7 and 8. Figure 9 is the power and frequency waveform. The experiment result shows that the voltage on phase A of this line drops significantly because of the grounding fault, and instantaneous short circuit occurs when the fault occurs.

Figures 10 and 11 present output voltage and current waveforms of the centralized PV inverter in PV station 8. And its output active and reactive power is given in Figure 12.

Figures 13 and 14 present output voltage and current waveforms of the series-connected PV inverter in PV station 8. And its output active and reactive power is given in Figure 15.

Figures 16 and 17 present voltage and current waveforms at one point of common coupling (PCC) in PV station 8. The power flow value of this PCC is given in Figure 18.

Figures 19 and 20 present voltage and current waveforms at another point of common coupling (PCC) in PV station 8. The power flow value of this PCC is given in Figure 21.

Table 5 gives the voltage value at the high voltage side of main transformer #1 in 750 kV and 330 kV substations; the

Table 4: Control parameters of PV inverters in PV station 8.

PV station	Original		Modified	
	K_1	K_2	K_1	K_2
Centralized PV inverter	0.4	1.32	1.56	1.01
Series-connected PV inverter	1.31	0	1.21	0

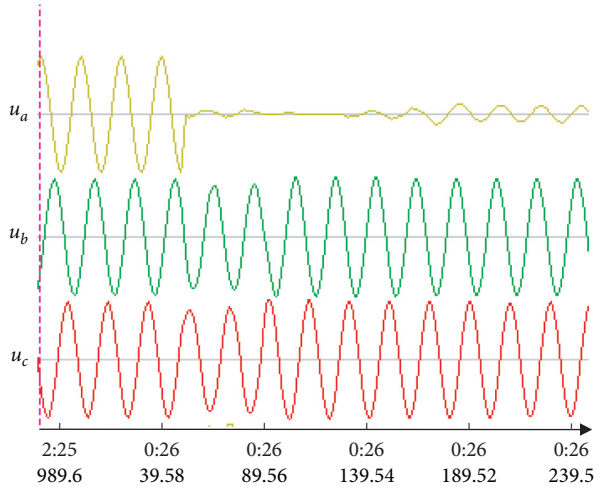

Figure 7: Voltage waveform of transmission line 3-19.

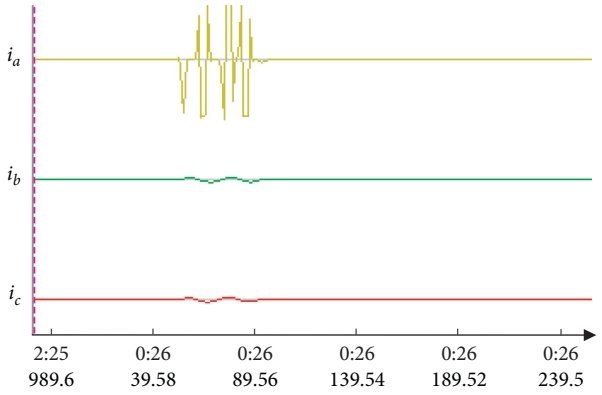

Figure 8: Current waveform of transmission line 3-19.

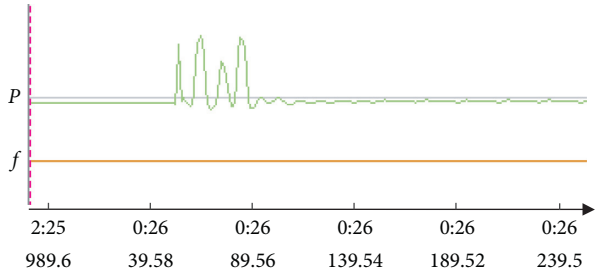

Figure 9: Power and frequency waveform on line 3-19.

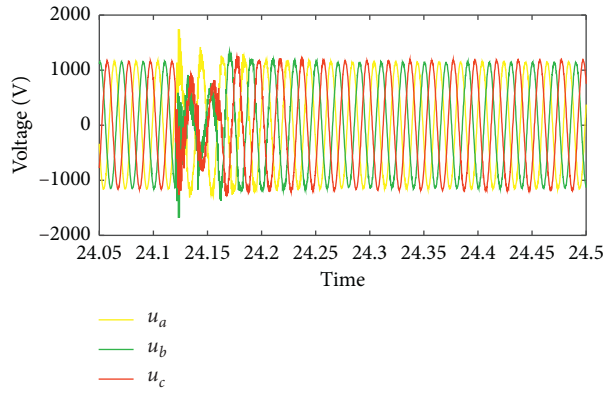

Figure 10: Output voltage waveforms of the centralized PV inverter.

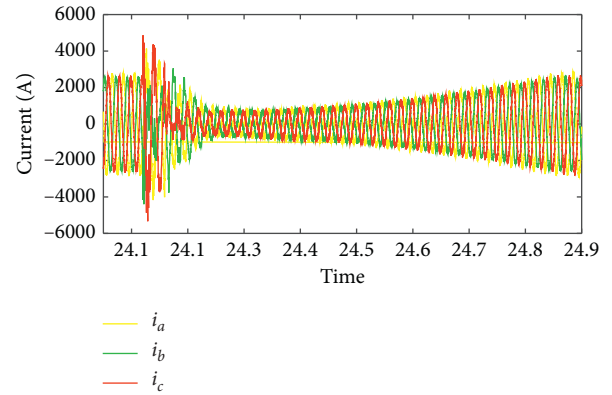

Figure 11: Output current waveforms of the centralized PV inverter.

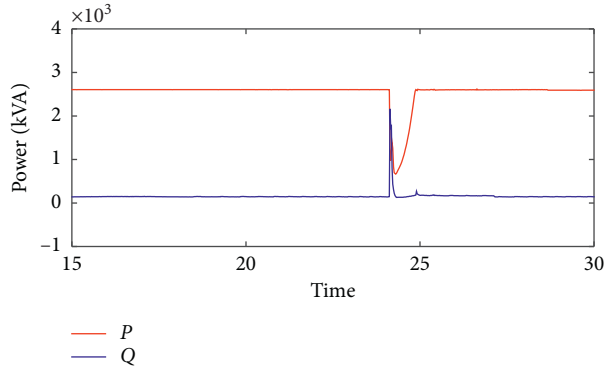

Figure 12: Output power of the centralized PV inverter.

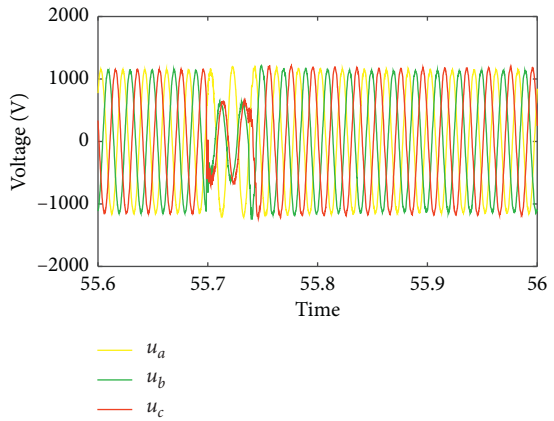

Figure 13: Output voltage waveforms of the series-connected PV inverter.

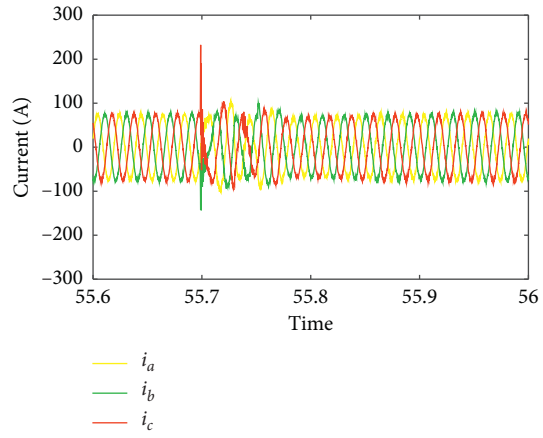

Figure 14: Output current waveforms of the series-connected PV inverter.

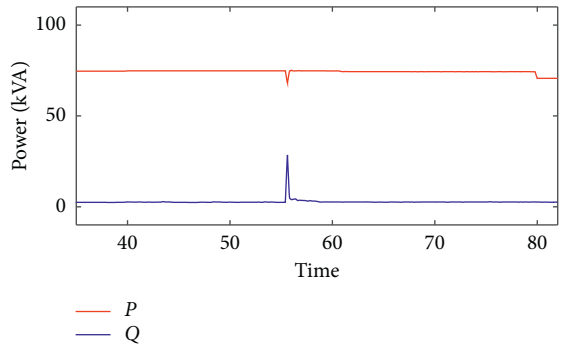

Figure 15: Output power of the series-connected PV inverter.

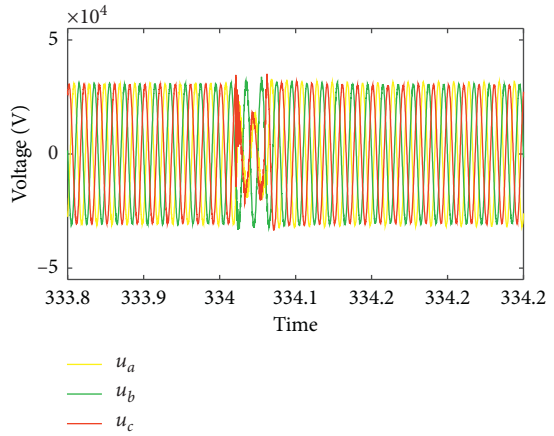

Figure 16: Voltage waveforms at PCC_1.

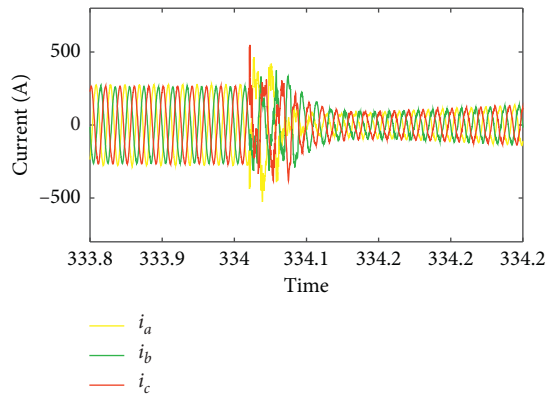

Figure 17: Current waveforms at PCC_1.

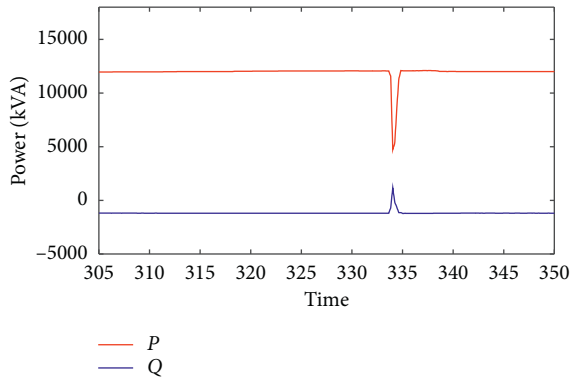

Figure 18: Power flow at PCC_1.

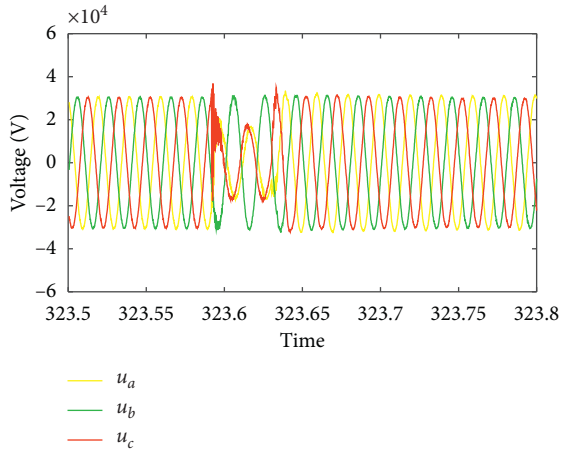

Figure 19: Voltage waveforms at PCC_2.

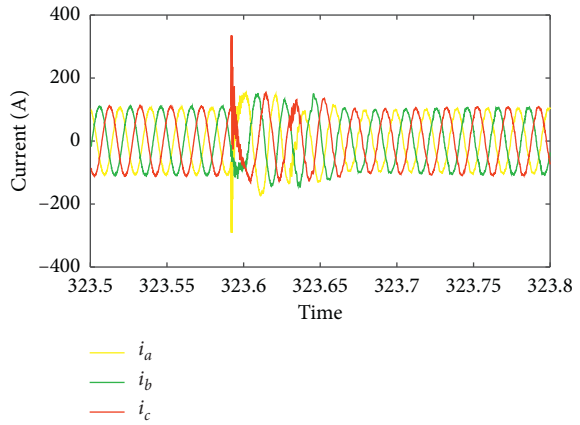

Figure 20: Current waveforms at PCC_2.

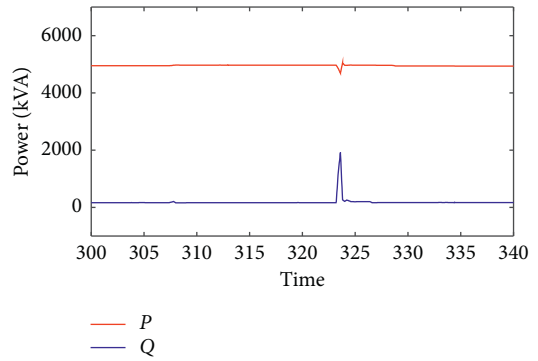

Figure 21: Power flow at PCC_2.

Table 5: Voltage value at 750 kV substations.

Station	u_{before} (kV)	u_{after} (kV)	Voltage drop (%)
Station 2	446.505	344.051	22.95
Station 3	447.42	277.349	38.01
Station 4	439.684	291.556	33.69
Station 6	438.422	354.295	19.19
Station 8	201.137	137.614	31.58
Station 11	195.322	133.143	31.23
Station 19	199.053	37.915	86.61
Station 22	200.141	39.249	86.17

Table 6: Transmission line voltage value.

Station	Line	u_{before} (kV)	u_{after} (kV)	Voltage drop (%)
Station 2	2-6	446.963	344.375	22.95
	2-1	446.532	344.078	22.94
	2-4	446.855	344.092	23.00
	2-35	203.175	167.189	17.71
	2-36	202.523	166.642	17.72
	2-37	203.029	167.096	17.70
	2-38	203.018	167.079	17.70
Station 3	3-6	445.532	276.217	38.00
	3-4	445.727	276.327	38.01
	3-14	200.112	11.951	91.35
	3-19	200.541	11.195	94.42

Table 6: Continued.

Station	Line	u_{before} (kV)	u_{after} (kV)	Voltage drop (%)
Station 4	4-1	437.51	289.99	33.72
	4-2	438.806	290.989	33.69
	4-3	437.28	290.908	33.47
	4-5	439.117	291.03	33.72
	4-8	200.377	137.554	31.35
	4-11	201.233	138.107	31.37
	4-26	200.716	137.75	31.37
	4-15	200.663	137.738	31.36
	4-18	200.734	137.75	31.38
Station 6	6-3	437.09	353.268	19.18
	6-4	437.34	353.407	19.19
	6-45	436.66	352.894	19.18
	6-46	436.993	353.185	19.18
Station 8	8-4	201.166	138.347	31.23
Station 11	4-11	193.102	132.145	31.33
Station 20	3-20	200.203	30.123	84.95
Station 19	3-19	199.938	37.820	86.63
Station 22	3-22	200.986	36.296	87.22

voltage value on transmission lines is given in Table 6. u_{before} is the voltage before the fault, and u_{after} is the voltage when the fault occurs.

5. Conclusions

The dynamic performance of PV inverters in PV station 8 during artificial grounding faults verifies the proposed active support control strategy, which means RES has the capability of disturbance rejection under extreme fault conditions, so it is practical for the RES to regulate voltage and frequency. There are several results seen only during on-site engineering tests:

(1) Through the on-site tests, it is clear that numbers of PV inverters are disconnected when a short circuit fault occurs. However, it did not occur in the fault simulation device experiments.

(2) Blocking and disconnection of the SVC and SVG are found in both PV stations and substations. Therefore, parameter modification or equipment upgrading is the reasonable solution for them.

(3) The test results reflect potential risks in the power grid operation and reveal predisposing factors of power system instability which is not shown in simulation experiments.

(4) Electromechanical simulation and electromagnetic simulation are practical methods in the power system and RES study, but they cannot fully reflect the electromagnetic characteristics during extreme conditions such as grounding faults and transient voltage sag.

(5) The outstanding benefits of on-site engineering tests are proved.

Data Availability

The data used to support the findings of this study are included within the article.

Conflicts of Interest

The authors declare that there are no conflicts of interest regarding the publication of this paper.

Acknowledgments

This work was supported by the Qinghai Science and Technology Program (Grant no. 2018-GX-A6) and State Grid Jibei Electric Power Company Zhangjiakou Chongli District Power Supply Branch Technology Project.

References

[1] W. Liu, G. Geng, Q. Jiang, H. Fan, and J. Yu, "Model-free fast frequency control support with energy storage system," *IEEE Transactions on Power Systems*, vol. 35, no. 4, pp. 3078–3086, 2020.

[2] Y. Wang, Y. Xu, Y. Tang et al., "Aggregated energy storage for power system frequency control: a finite-time consensus approach," *IEEE Transactions on Smart Grid*, vol. 10, no. 4, pp. 3675–3686, 2019.

[3] F. Cheng, L. Qu, W. Qiao, C. Wei, and L. Hao, "Fault diagnosis of wind turbine gearboxes based on DFIG stator current envelope analysis," *IEEE Transactions on Sustainable Energy*, vol. 10, no. 3, pp. 1044–1053, 2019.

[4] V. Knap, S. K. Chaudhary, D.-I. Stroe, M. Swierczynski, B.-I. Craciun, and R. Teodorescu, "Sizing of an energy storage system for grid inertial response and primary frequency reserve," *IEEE Transactions on Power Systems*, vol. 31, no. 5, pp. 3447–3456, 2016.

[5] H. Luo, Z. Hu, H. Zhang, and H. Chen, "Coordinated active power control strategy for deloaded wind turbines to improve regulation performance in AGC," *IEEE Transactions on Power Systems*, vol. 34, no. 1, pp. 98–108, 2019.

[6] D. Ganger, J. Zhang, and V. Vittal, "Forecast-based anticipatory frequency control in power systems," *IEEE Transactions on Power Systems*, vol. 33, no. 1, pp. 1004–1012, 2018.

[7] Z. Li, W. Wu, B. Zhang, and B. Wang, "Adjustable robust real-time power dispatch with large-scale wind power integration,"

IEEE Transactions on Sustainable Energy, vol. 6, no. 2, pp. 357–368, 2015.

[8] C. Wei, Z. Shen, D. Xiao, L. Wang, X. Bai, and H. Chen, "An optimal scheduling strategy for peer-to-peer trading in interconnected microgrids based on RO and Nash bargaining," *Applied Energy*, vol. 295, Article ID 117024, 2021.

[9] R. Patel, C. Li, L. Meegahapola, B. McGrath, and X. Yu, "Enhancing optimal automatic generation control in a multi-area power system with diverse energy resources," *IEEE Transactions on Power Systems*, vol. 34, no. 5, pp. 3465–3475, 2019.

[10] D. Zhang, H. Zhang, X. Zhang et al., "Research on AGC performance during wind power ramping based on deep reinforcement learning," *IEEE Access*, vol. 8, pp. 107409–107418, 2020.

[11] R. Prasad and N. P. Padhy, "Synergistic frequency regulation control mechanism for DFIG wind turbines with optimal pitch dynamics," *IEEE Transactions on Power Systems*, vol. 35, no. 4, pp. 3181–3191, 2020.

[12] X. Chen, J. Lin, F. Liu, and Y. Song, "Optimal control of AGC systems considering non-Gaussian wind power uncertainty," *IEEE Transactions on Power Systems*, vol. 34, no. 4, pp. 2730–2743, 2019.

[13] K. Doenges, I. Egido, L. Sigrist, E. Lobato Miguélez, and L. Rouco, "Improving AGC performance in power systems with regulation response accuracy margins using battery energy storage system (BESS)," *IEEE Transactions on Power Systems*, vol. 35, no. 4, pp. 2816–2825, 2020.

[14] F. Zhang, Z. Hu, K. Meng, L. Ding, and Z. Dong, "HESS sizing methodology for an existing thermal generator for the promotion of AGC response ability," *IEEE Transactions on Sustainable Energy*, vol. 11, no. 2, pp. 608–617, 2020.

[15] Y. Wang, C. Wan, Z. Zhou, K. Zhang, and A. Botterud, "Improving deployment availability of energy storage with data-driven AGC signal models," *IEEE Transactions on Power Systems*, vol. 33, no. 4, pp. 4207–4217, 2018.

[16] C. Wei, M. Benosman, and T. Kim, "Online parameter identification for state of power prediction of lithium-ion batteries in electric vehicles using extremum seeking," *International Journal of Control, Automation and Systems*, vol. 17, no. 11, pp. 2906–2916, 2019.

[17] X. L. Su, Z. K. Zhao, S. Yang, and Y. Q. Guo, "Adaptive robust SMC-based AGC auxiliary service control for ESS-integrated PV/wind station," *Complexity*, vol. 2020, no. 2, 10 pages, Article ID 8879045, 2020.

[18] L. Wang, Q.-S. Vo, and A. V. Prokhorov, "Stability improvement of a multimachine power system connected with a large-scale hybrid wind-photovoltaic farm using a supercapacitor," *IEEE Transactions on Industry Applications*, vol. 54, no. 1, pp. 50–60, 2018.

[19] H. Karbouj, Z. H. Rather, and B. C. Pal, "Adaptive voltage control for large scale solar PV power plant considering real life factors," *IEEE Transactions on Sustainable Energy*, vol. 12, no. 2, pp. 990–998, 2021.

[20] R. K. Varma and S. Mohan, "Mitigation of fault induced delayed voltage recovery (FIDVR) by PV-STATCOM," *IEEE Transactions on Power Systems*, vol. 35, no. 6, pp. 4251–4262, 2020.

[21] X. Tian, Y. Chi, Y. Li, H. Tang, C. Liu, and Y. Su, "Sub-synchronous oscillation coordinated damping optimization control of DFIG and SVG and self-optimization parameter tuning method," *CSEE Journal of Power and Energy Systems*, vol. 7, no. 1, pp. 140–149, 2021.

[22] S. Wang, Y. Dong, L. Wu, and B. Yan, "Interval overvoltage risk based PV hosting capacity evaluation considering PV and load uncertainties," *IEEE Transactions on Smart Grid*, vol. 11, no. 3, pp. 2709–2721, 2020.

[23] C. Mao, F. Leng, J. Li et al., "A 400-V/50-kVA digital-physical hybrid real-time simulation platform for power systems," *IEEE Transactions on Industrial Electronics*, vol. 65, no. 5, pp. 3666–3676, 2018.

[24] L. Wang, Y. Shi, Y. Shi, R. Xie, and H. Li, "Ground leakage current analysis and suppression in a 60-kW 5-level T-type transformerless SiC PV inverter," *IEEE Transactions on Power Electronics*, vol. 33, no. 2, pp. 1271–1283, 2018.

[25] R. D. Zimmerman, C. E. Murillo-Sánchez, and R. J. Thomas, "MATPOWER: steady-state operations, planning, and analysis tools for power systems research and education," *IEEE Transactions on Power Systems*, vol. 26, no. 1, pp. 12–19, 2011.

[26] S. S. M. Reshikeshan, S. L. Matthiesen, M. S. Illindala, A. A. Renjit, and R. Roychowdhury, "Autonomous voltage regulation by distributed PV inverters with minimal inter-node interference," *IEEE Transactions on Industry Applications*, vol. 57, no. 3, pp. 2058–2066, 2021.

[27] S. Rahman, S. Saha, S. N. Islam et al., "Analysis of power grid voltage stability with high penetration of solar PV systems," *IEEE Transactions on Industry Applications*, vol. 57, no. 3, pp. 2245–2257, 2021.

[28] S. B. Q. Naqvi, S. Kumar, and B. Singh, "Weak grid integration of a single-stage solar energy conversion system with power quality improvement features under varied operating conditions," *IEEE Transactions on Industry Applications*, vol. 57, no. 2, pp. 1303–1313, 2021.

[29] J. Ma, S. Wang, Y. Qiu, Y. Li, Z. Wang, and J. S. Thorp, "Angle stability analysis of power system with multiple operating conditions considering cascading failure," *IEEE Transactions on Power Systems*, vol. 32, no. 2, pp. 873–882, 2016.

[30] P. N. Korovesis, G. A. Vokas, I. F. Gonos, and F. V. Topalis, "Influence of large-scale installation of energy saving lamps on the line voltage distortion of a weak network supplied by photovoltaic station," *IEEE Transactions on Power Delivery*, vol. 19, no. 4, pp. 1787–1793, 2004.

Hindawi
Complexity
Volume 2021, Article ID 7069193, 13 pages
https://doi.org/10.1155/2021/7069193

Research Article

Research on the Influence of Volatility of International Energy Commodity Futures Market on CPI in China

Keyao Lin,[1] Chao Xun ,[1] Fei Wang,[2] Angela Chi Chao,[3] and Zhenyu Du[3]

[1]*State Grid Fujian Electric Power Company, Fu Zhou 350003, Fu Jian, China*
[2]*National Tax Institute of STA, Yangzhou 210023, Jiangsu, China*
[3]*School of Economics and Management, Southeast University, Nanjing 211189, Jiangsu, China*

Correspondence should be addressed to Chao Xun; cclinda@yandex.ru

Received 21 May 2021; Accepted 28 July 2021; Published 3 August 2021

Academic Editor: Xiaoqing Bai

This article analyses the transmission path of the international commodity futures market's impact on the Chinese economy. We use the MIDAS model and daily data to predict China's CPI in real time. Empirical analysis results show that (1) the influence of high-frequency explanatory variables on low-frequency CPI is different. The optimal lag orders of domestic high-frequency variables are all around 23, which can be regarded as one month in practice, indicating that their CPI influence takes one month to show. (2) Both the univariate MIDAS model and the multivariate MIDAS combined prediction model have good performance in prediction accuracy. (3) The predicted results of the multivariate MIDAS combined prediction model for CPI in China's normal months are relatively excellent. However, when exceptional circumstances occur, the prediction results will show a specific deviation, and the prediction accuracy will also be reduced. Finally, some feasible suggestions are put forward according to the research results.

1. Introduction

The stability of energy commodity markets is crucial to the global economy. On the one hand, energy commodities provide the industrial materials necessary for economic development and guarantee sustainable expansion and reproduction. On the other hand, speculative investments in energy commodities have caused abnormal volatility in financial markets and consequently affected economic stability. COVID-19 epidemic in 2020 has had a significant negative impact on all countries and the global economy has been struck hard. Although the epidemic is gradually being brought under control in all countries with vaccination, the recovery rate globally, except China, is still weak. In this context, a stable and reliable energy supply has drawn sufficient attention from China. To address this issue, scholars have conducted studies from multiple perspectives [1, 2]. At the moment, the global economy is underperforming and various economies are trying their best to seek recovery measures. Therefore, it is increasingly critical to analyze the impact of international energy commodities on the domestic economy.

International commodity markets have been the focus of scholars in the study of shocks from external financial markets. The commodity market has a long history and plays a vital role in contemporary economic life. Bulk commodities have financial and commodity attributes. They are the basic raw materials used in industrial production and can be used as a tool to predict global economic development trends [3, 4]. In recent years, as commodities' financial attributes have become stronger and stronger, people have also regarded commodity futures as a financial investment tool. Especially, when the major economies have not fully recovered and the global stock market has not performed well, hot money is flowing in and out of the stock market and the commodity futures market rapidly, which has a significant impact on the economic and financial development of other regions.

Since joining the WTO, China has played an increasingly prominent role in global economic growth, and its ties with

other regions have become increasingly close [5]. In recent years, China's relatively high economic growth rate has made its dependence on imports of bulk commodities remain high. The global share of domestic consumption of several major bulk commodities has shown an upward trend. In 2017, China's coal and steel consumption accounted for 65.2% and 46.7% of the world's total consumption, respectively, making China the world's largest coal and steel consuming country, showing a relatively apparent demand in short supply [6]. Therefore, studying the bulk commodity market has an essential guiding role in economic growth. In addition, discovering the frequency and magnitude of price fluctuations in the international commodity futures market, exploring how price fluctuations in the international commodity futures market affect China's economy, and analyzing the transmission mechanism between different markets are all very valuable issues. Finally, reasonable predictions of future fluctuations based on the research results, and then formulating measures to deal with commodity price fluctuations to curb the economic downturn, are of great significance for maintaining national economic security and stability.

2. Literature Review

The research on the international commodity market's impact on China's economy is mainly divided into price channel transmission and financial channel transmission. The former refers to the direct transmission of international commodity prices to the domestic macro economy, such as through price levels and industrial chains; the latter refers to the transmission of the domestic macro economy through the intermediate variable of China's financial market, such as the capital market and currency market.

2.1. Price Channel

2.1.1. Price Level. Most scholars believe that fluctuations in international commodity markets are transmitted through the domestic price level and that different regions are affected differently. The transmission of oil price changes to inflation is relatively low in CEE countries [7]. Moreover, there is an asymmetric behavior between oil spot prices and inflation rates [8], and deviations in oil price forecasts may affect deviations in inflation forecasts [9]. Joshi and Acharya established a VAR model and found that the co-integration relationship between commodity prices and India's domestic inflation data is becoming stronger [10]. Estrades and Terra used the DSGE model to find that the increase in commodity prices positively affects domestic economic development [11]. Filis believes that fluctuations in international oil prices can significantly affect the inflation levels of importing and exporting countries [12].

2.1.2. Industry Chain. Price changes in the international bulk commodity market can be directly transmitted to the material economy through the industrial chain and cause changes in the price level. Rising international oil prices increase the production cost of energy-intensive products using petroleum-related products as raw materials, which is not conducive for the export of such products [13] and the international commodity prices' transmission effect is from the upstream to the downstream of the industrial chain [14]. Fluctuations in the international bulk commodity market can also be transmitted between industries, thereby affecting a country's macroeconomics. Oil price fluctuations have been transmitted to various countries' macroeconomics through the industrial chain linkages under economic integration [15]. Price fluctuations in the international bulk commodity market will also affect a country's foreign trade situation. Blattman et al. analyzed the data of 35 commodity exporting countries and believed that trade fluctuations caused by the violent fluctuations of commodity prices would reduce foreign investment and thereby affect the economic growth of these countries [16].

2.2. Financial Channel

2.2.1. Capital Market Channel. Volatility in the international bulk commodity market will be transmitted to the material economy through the linkage effect of domestic and foreign financial markets. Many scholars have researched this transmission channel. Rudiger and Fischer believed that by influencing a country's import and export and international trade balances, the exchange rate would affect the country's economy and corporate investment, and ultimately affect the company's stock price on the stock market [17]. Buyuksahin and Robe found that the strength of the spillover effect between the international commodity market and the stock market is related to the strength of the commodity's financial attributes [18]. Quadrini believes that the material economy sector will be affected by asset price fluctuations, and this impact needs to be achieved through the credit path [19]. Hammersland et al. used two mutually reinforcing financial accelerator mechanisms to explain that financial accelerators can magnify asset prices' effect on the material economy [20].

2.2.2. Currency Market Channel. In terms of currency transmission channels, many scholars have discussed from the perspective of interest rates and credit. In the neoclassical price mechanism proposed by Jorgenson and Tobin [21, 22], monetary policy can affect the material economy by adjusting short-term interest rates. Jain and Ghosh found that international commodity prices significantly impact a country's currency exchange rate [23]. Credit has also played a vital role in economic development. Oliner and Rudebusch explained the credit mechanism's role in the transmission of monetary policy by studying the relationship between corporate investment and financing, in which small firms are the main transmission carriers of the credit mechanism [24]. Hume and Sentence studied the relationship between global credit peaks and the macroeconomic environment [25]. They believed that the credit peaks since the mid-1990s had no significant impact on high-speed economic growth and inflation.

2.3. Literature Summary. It can be seen from the above that most scholars study the impact of commodity market price fluctuations on China's macroeconomic variables such as prices and output. In addition, the generalization of the transmission channels is not the same, and most scholars have not fully considered the transmission of the international commodity market to the material economy with the Chinese commodity futures market as an intermediate variable. Based on this, this article reclassifies the transmission channels. In addition, in terms of research methods, commodity futures markets are high-frequency daily data, while many economic variables are low-frequency data published monthly, quarterly, and annually. Such frequency differences will lead to forced frequency reduction in research by many scholars. Such processing methods will lose the information in the high-frequency data and reduce the credibility of the research. Therefore, it is necessary to seek new models to process data of different frequencies. Thus, this article adopts the MIDAS model and introduces the mediation effect and the moderating effect, which is a supplement to the research on the mixing data model and an innovation in macroeconomic forecasting. On the one hand, MIDAS can overcome the errors and limitations caused by studying variables of different frequencies, and the results obtained are more accurate. On the other hand, prediction research based on mixed frequency data helps to make reasonable expectations and inferences about current and future economic trends, and assists in the formulation of national macroeconomic policies.

3. Transmission Path

After sorting out previous studies, this article reorganizes the transmission path and summarizes the impact of the international commodity futures market on the Chinese economy into three routes as seen in Figure 1: the material economy, the financial market, and the exchange rate. The first is that the international commodity futures market affects different sectors of the domestic industrial chain. The second is the link between domestic and international commodity futures markets. The third is to affect trade prices through changes in RMB's exchange rate against the US dollar.

3.1. Material Economy Route. This route refers to the fact that international commodity futures directly affect domestic consumer prices through international trade, affect domestic producer prices, and ultimately transmit to domestic consumer prices. Therefore, the domestic production sector plays an intermediary role. As China imports a large amount of bulk commodities, domestic bulk commodities' prices will be directly affected by international market prices and are extremely sensitive to fluctuations in international commodity futures prices. Specifically, when a certain commodity price increases and is imported into the country, the price of industrial products in the domestic industrial chain will also increase.

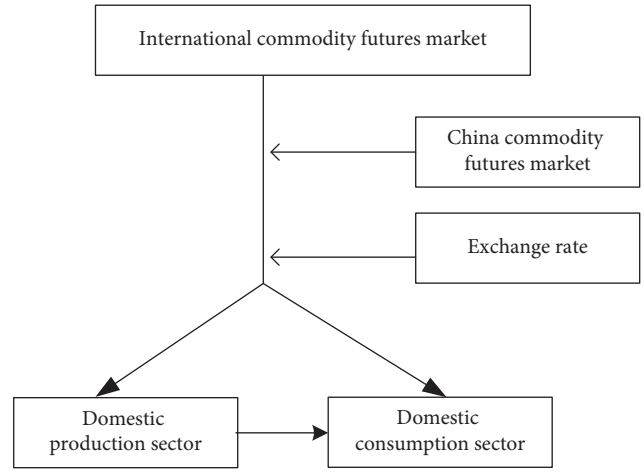

Figure 1: The path of international commodity futures market impact on CPI in China.

3.2. Financial Market Route. This route means that the prices of international commodity futures affect the domestic commodity futures market and the domestic economy. Due to the close links between global financial markets, price changes in the international commodity futures market will be quickly transmitted to the domestic commodity futures market, which is a short-term impact. In this process, due to the existence of capital controls in China's financial market, actual transmission may be lagging and insignificant compared to theory. In addition, futures play the role of price discovery. When prices in the international commodity futures market fluctuate, the domestic commodity futures market will change accordingly, which will then be transmitted to the material economy through price channels and affect the domestic consumer sector. This stage involves macro factors such as price levels, so the impact is relatively long term and indirect.

3.3. Exchange Rate Route. This route means that international commodity futures prices will affect various domestic production and consumption fields through the exchange rate. Generally speaking, the extent to which the international market price of a certain type of commodity can impact the domestic economy through a country's exchange rate is closely related to the proportion of imports of that type of commodity in the total supply. If the import proportion is large, then the fluctuation of its international price will have a greater impact through the exchange rate, otherwise it will not. At present, China belongs to the former situation. As China has a strong import dependence on bulk commodities, the transmission of rising international bulk commodity prices to the domestic economy will be affected mainly by the RMB exchange rate fluctuation.

To sum up, when the price of the international commodity futures market fluctuates, its impact will be directly transmitted to the domestic consumer sector on the one hand. On the other hand, it will be transmitted to the domestic consumer sector through the domestic production sector's intermediary variable.

4. Data and Model

4.1. Data. The variables used in this paper include international commodity futures price index, Nanhua futures commodity index, average daily coal consumption of six major power plants, exchange rate, and consumer price index (CPI). This paper selects the daily and monthly data of relevant variables from January 2010 to January 2020 as the research object.

International commodity futures market: there are many international commodity futures market indicators, and the most representative one is the CRB series price index, including spot price index and the futures price index. Since the international commodity futures trading volume is much larger than the spot trading volume and the fluctuations are more significant, it is more suitable to use the futures index as a variable. Therefore, this paper selects the RJ/CRB futures price composite index to measure the international bulk commodity price.

China's commodity futures market: we chose Nanhua Futures Commodity Index to represent the domestic commodity futures market. It was launched by the Nanhua Futures Exchange in 2004 and optimized from a price index to an investment index in 2008. The index provides investors with a more scientific and reasonable reference standard for futures investment returns.

Domestic production sector: we chose the average daily coal consumption of the six major power generation groups to represent the domestic production sector. Power generation has a very direct connection with industrial production. The average daily coal consumption of the six major power generation groups is often used to track industrial production. The coal consumption of the six power generation groups is the sum of the six power plants' coal consumption located in the southeast coastal area. The coal consumption of the six major power generation groups is daily high-frequency data, which can predict the changes in the country's total power generation to a certain extent, reflecting the changes in macro-industrial economic indicators.

Exchange rate: exchange rate is one of the most easily affected variables. The international bulk commodities are generally priced in US dollars, and the impact of exchange rates must be considered when influencing China's price level. Considering the availability of data, this article adopts the daily data of the US dollar against the RMB central parity.

Domestic consumption sector: we chose the consumer price index to represent the domestic consumption sector. The consumer price index is selected as the proxy variable of the national downstream price level. Its statistical scope covers all aspects of the national urban and rural residents' consumption. Simultaneously, it has good stability and can better reflect the domestic downstream consumption price level.

According to the sample frequency and availability, the sample window selected for model estimation is from January 2010 to January 2020, with 2367 observations for each set of high-frequency daily data and 121 observations low-frequency monthly data. We chose data from January 2010 to December 2018 for the in-sample forecast and January 2019 to January 2020 for the out-of-sample forecast. Given that CPI is monthly data, seasonal effects are excluded from the original data. The above data are from Wind and China Economic Network database.

4.2. MIDAS Model. The Mixed Data Sampling (MIDAS) model proposed by Ghysels can make full use of the information of the original data without processing the mixed frequency data. The MIDAS model has been studied and applied by many scholars, and the model form has been more expanded. At first, the MIDAS model was used to predict financial market fluctuations. Now, the MIDAS model has been widely used in analyzing and predicting future macroeconomic trends. The existing research mainly uses the MIDAS model to forecast macroeconomic variables of a country.

5. Empirical Analysis

In this part, six weight function regression models of Beta-Midas, Beta-nonzero-MIDAS, Exp-Almon-Midas, Stepfun-Midas, and Almon-Midas are used to study the prediction effect of each high-frequency explanatory variable on CPI, and the lag order of high-frequency variables starts from the first order to the optimal order. In parameter estimation, the optimal weight function is selected according to the principle that the smaller the error is, the greater the goodness of fit is. The errors include Root Mean Square Error (RMSE), Mean Squared Error of Forecast (MSFE), and Discounted Mean Squared Error of Forecast (DMSFE). RMSE, MSFE, and DMSFE of each model are used to reflect the prediction accuracy when making the in-sample forecast. The optimal weight function and the optimal lag order are selected according to the model's output and prediction accuracy. In the empirical analysis, we compare the models' fitting results and prediction accuracy with and without autoregressive terms. The results show that the fitting results and prediction accuracy of the model are better with an autoregressive term.

5.1. Univariate MIDAS Model. When the explanatory variable is the RJ/CRB International Commodity Futures Index, the goodness of fit and in-sample and out-of-sample prediction accuracies at different lag orders are shown in Table 1 (due to limited space, only part of the lag order results and the selected mixing model are shown in this paper). We found that the RMSE of Beta-AR(1)-MIDAS, Beta non-zero-AR(1)-MIDAS, and Exp Almon-AR(1)-MIDAS are more stable compared to the others. When the lag order equals 13, the RMSE, MSFE, and DMSFE of Almon-AR(1)-MIDAS model are 0.5046, 0.2546, and 0.0868, respectively, which is a better prediction accuracy than other models. After the lag order increases, the goodness of fit and prediction accuracy are both higher than that of lag order 13. Therefore, the Almon-AR(1)-MIDAS (13) has the highest in-sample prediction accuracy for the low-frequency CPI. As shown in Figure 2, the fluctuation range of the 13 coefficients

Table 1: RJ/CRB International Commodity Futures Index: the goodness of fit and in-sample and out-of-sample prediction accuracy at different lag orders.

Model	Index	Lag order					
		13	20	25	30	35	40
Beta-MIDAS	R^2	0.8629	0.8629	0.8629	0.8630	0.8675	0.8680
	RMSE	0.6430	0.6407	0.6430	0.6445	0.6300	0.6359
	MSFE	0.4134	0.4105	0.4134	0.4154	0.3969	0.4044
	DMSFE	0.1044	0.1041	0.1044	0.1046	0.1026	0.1044
Beta-nonzero-MIDAS	R^2	0.8628	0.8631	0.8633	0.8633	0.8677	0.8675
	RMSE	0.6382	0.6408	0.6421	0.6458	0.6331	0.6327
	MSFE	0.4073	0.4107	0.4123	0.4171	0.4009	0.4003
	DMSFE	0.1032	0.1042	0.1047	0.1053	0.1034	0.1031
Exp Almon-MIDAS	R^2	0.8629	0.8629	0.8629	0.8629	0.8675	0.8675
	RMSE	0.6429	0.6429	0.6429	0.6429	0.6324	0.6324
	MSFE	0.4133	0.4133	0.4133	0.4133	0.4000	0.4000
	DMSFE	0.1044	0.1044	0.1044	0.1044	0.1031	0.1031
U-MIDAS	R^2	0.8908	0.8937	0.9011	0.9038	0.9120	0.9201
	RMSE	0.7368	0.7863	0.8514	0.8703	0.8488	0.8936
	MSFE	0.5429	0.6183	0.7249	0.7575	0.7204	0.7986
	DMSFE	0.1336	0.1412	0.1661	0.1773	0.1826	0.1799
Stepfun-MIDAS	R^2	0.8796	0.8803	0.8858	0.8852	0.8897	0.8916
	RMSE	0.7100	0.7160	0.7483	0.7358	0.7004	0.7181
	MSFE	0.5041	0.5127	0.5600	0.5414	0.4906	0.5156
	DMSFE	0.1370	0.1348	0.1463	0.1459	0.1470	0.1487
Almon-MIDAS	R^2	0.8716	0.8682	0.8717	0.8695	0.8751	0.8750
	RMSE	0.5046	0.5868	0.7108	0.6905	0.6276	0.5997
	MSFE	0.2546	0.3443	0.5052	0.4768	0.3939	0.3597
	DMSFE	0.0868	0.0942	0.1342	0.1319	0.1216	0.1068

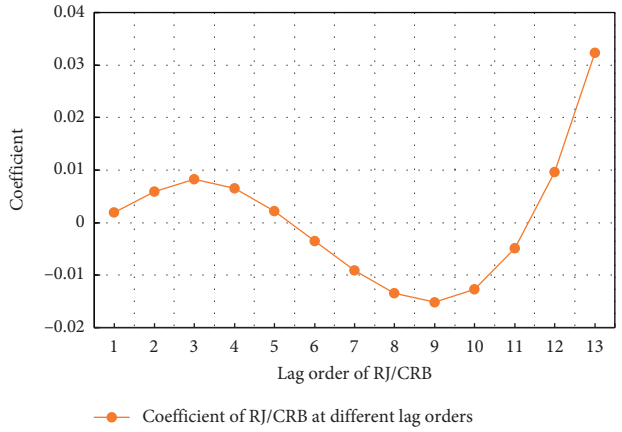

Figure 2: The coefficient fluctuation of Almon-MIDAS at lag order 13.

estimated by the Almon-AR(1)-MIDAS (13) is (−0.02, 0.04), that is, the RJ/CRB International Commodity Futures Index has both positive and negative effects on the CPI. The first-order delay effect is −0.0019, that is, the RJ/CRB International Commodity Futures Index on the previous trading day will cause the CPI to fall this month by 0.0019 units. The impact of the RJ/CRB International Commodity Futures Index on the CPI this month will last for 13 trading days.

When the explanatory variable is average daily coal consumption of six power plants, the goodness of fit and in-sample and out-of-sample prediction accuracy at different lag orders are shown in Table 2. Table 2 shows that Stepfun-AR(1)-MIDAS has the highest goodness of fit among the six models when the lag order increases to 20 or higher, indicating that when the lag order increases, the fitting effect of Stepfun-AR(1)-MIDAS has gradually become prominent. Moreover, when the lag order reaches 22, the RMSE, MSFE, and DMSFE of Stepfun-MIDAS are 0.5055, 0.255, and 0.0793, respectively, which are all the lowest. Therefore, Stepfun-AR(1)-MIDAS (22) has the best fitting effect and prediction accuracy, indicating that the impact of the average daily coal consumption of the six major power plants on the CPI is relatively long term and durable, and the duration is about one month. Figure 3 shows that the 22 coefficients estimated by the Stepfun-AR(1)-MIDAS (22) model fluctuate randomly between −0.006 and 0.01. The lagging influence of the six major power plants' average daily coal consumption on the CPI presents both positive and negative effects. At first, the average daily coal consumption of the six major power plants positively affected the CPI. The increase in the average daily coal consumption of the six major power plants would increase the CPI this month, but the effect gradually turned negative as it approached the end of the month. The impact of the average daily coal consumption of the six major power plants on the CPI will extend to 22 trading days.

When the explanatory variable is Nanhua Futures Commodity Index, the goodness of fit and in-sample and out-of-sample prediction accuracy at different lag orders are shown in Table 3. When the lag order increases to 15, the prediction effect of Almon-AR(1)-MIDAS is better than

Table 2: Average daily coal consumption of six power plants: the goodness of fit and in-sample and out-of-sample prediction accuracy at different lag orders.

Model	Index	Lag order					
		15	22	25	30	35	40
Beta-MIDAS	R^2	0.8727	0.8728	0.8728	0.8685	0.8709	0.8709
	RMSE	0.5778	0.5829	0.5831	0.5444	0.5451	0.5451
	MSFE	0.3339	0.3398	0.3400	0.2964	0.2972	0.2972
	DMSFE	0.0947	0.0946	0.0946	0.0834	0.0840	0.0840
Beta-nonzero-MIDAS	R^2	0.8619	0.8599	0.8598	0.8598	0.8655	0.8652
	RMSE	0.5691	0.5496	0.5439	0.5396	0.5373	0.5412
	MSFE	0.3239	0.3021	0.2959	0.2912	0.2887	0.2929
	DMSFE	0.0972	0.0888	0.0865	0.0852	0.0858	0.0867
Exp Almon-MIDAS	R^2	0.8728	0.8728	0.8728	0.8728	0.8740	0.8740
	RMSE	0.5824	0.5824	0.5824	0.5824	0.5745	0.5745
	MSFE	0.3392	0.3392	0.3392	0.3392	0.3301	0.3301
	DMSFE	0.0945	0.0945	0.0945	0.0945	0.0924	0.0924
U-MIDAS	R^2	0.9034	0.9066	0.9093	0.9177	0.9302	0.9325
	RMSE	0.6375	0.5952	0.6266	0.5850	0.5734	0.5657
	MSFE	0.4064	0.3543	0.3927	0.3422	0.3288	0.3200
	DMSFE	0.1001	0.0936	0.1000	0.0506	0.0564	0.0700
Stepfun-MIDAS	R^2	0.8879	0.8896	0.8899	0.8898	0.9065	0.9059
	RMSE	0.5181	0.5055	0.5217	0.5231	0.5237	0.5171
	MSFE	0.2684	0.2555	0.2722	0.2736	0.2743	0.2674
	DMSFE	0.0806	0.0793	0.0858	0.0828	0.0790	0.0758
Almon-MIDAS	R^2	0.8862	0.8874	0.8873	0.8873	0.8987	0.8972
	RMSE	0.5168	0.5187	0.5202	0.5234	0.5184	0.5295
	MSFE	0.2671	0.2690	0.2706	0.2740	0.2688	0.2804
	DMSFE	0.0756	0.0791	0.0810	0.0758	0.0606	0.0772

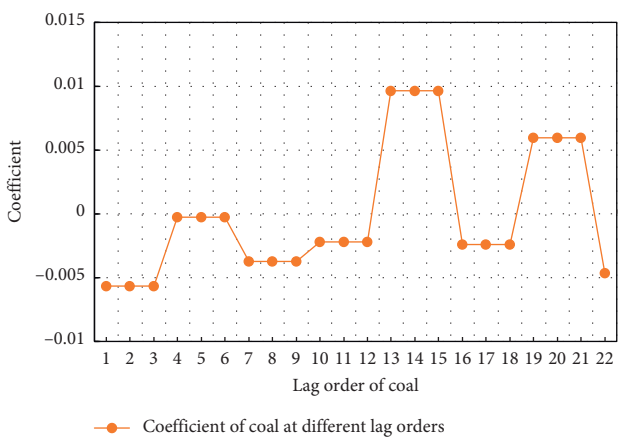

Figure 3: The coefficient fluctuation of Stepfun-MIDAS at lag order 22.

other models. When the lag order further increases, each model's goodness of fit also shows an increasing trend, and the RMSE generally changes in the same direction as the goodness of fit. In terms of prediction accuracy, the prediction accuracy of Exp-Almon-AR(1)-MIDAS model has been maintained at a relatively stable level. The RMSE is stable between 0.49 and 0.50, and the prediction effect is more stable than other models. When the lag order changes to 23, RMSE, MSFE, and DMSFE of the Almon-AR(1)-MIDAS are 0.4715, 0.2223, and 0.0876, respectively, which are lower than other models. When the lag order increases again, the prediction accuracy of the Almon-AR(1)-MIDAS model begins to decrease. After comparing different models and comparing different lag orders, when the lag order changes to order 23, the fitting effect and prediction accuracy of the Almon-AR(1)-MIDAS(23) model are relatively better. It can be seen from Figure 4 that the 23 coefficients estimated by the Almon-AR(1)-MIDAS model fluctuate randomly between −0.001 and 0.002. The lagging influence of the Nanhua Commodity Index on the CPI also has positive and negative situations, but the total delay effect is positive. The first-order delay effect of the Nanhua Futures Commodity Index on the CPI is 0.0016, that is, the growth of the Nanhua Futures Commodity Index will increase the CPI, and the impact on the CPI will extend to 23 trading days, that is, the CPI this month happened to be affected by the fluctuation of the Nanhua Futures Commodity Index.

When the explanatory variable is the exchange rate, the goodness of fit and in-sample and out-of-sample prediction accuracy at different lag orders are shown in Table 4. Table 4 shows that the goodness of fit and prediction accuracy of Beta-AR(1)-MIDAS, Beta-nonzero-AR(1)-MIDAS, and Exp Almon-AR(1)-MIDAS models are close at each order, with no significant difference. The goodness of fit of the U-MIDAS model is slightly better than other models, but the prediction accuracy is inferior to other models at higher orders. When the lag order reaches 20, the values of U-AR(1)-MIDAS prediction accuracy indicators RMSE, MSFE, and DMSFE are 0.4669, 0.2180, and 0.1210, respectively which

Table 3: Nanhua futures commodity index: the goodness of fit and in-sample and out-of-sample prediction accuracy at different lag orders.

Model	Index	Lag order					
		15	20	23	25	30	35
Beta-MIDAS	R^2	0.8653	0.8652	0.8651	0.8650	0.8649	0.8691
	RMSE	0.4999	0.5002	0.5003	0.5004	0.5006	0.5059
	MSFE	0.2499	0.2502	0.2503	0.2504	0.2506	0.2560
	DMSFE	0.0775	0.0775	0.0774	0.0774	0.0773	0.0779
Beta-nonzero-MIDAS	R^2	0.8644	0.8641	0.8641	0.8640	0.8641	0.8685
	RMSE	0.5020	0.5024	0.5025	0.5026	0.5019	0.5079
	MSFE	0.2520	0.2524	0.2525	0.2526	0.2519	0.2579
	DMSFE	0.0771	0.0767	0.0765	0.0763	0.0759	0.0766
Exp Almon-MIDAS	R^2	0.8657	0.8657	0.8657	0.8657	0.8657	0.8699
	RMSE	0.4986	0.4986	0.4986	0.4986	0.4986	0.5038
	MSFE	0.2486	0.2486	0.2486	0.2486	0.2486	0.2538
	DMSFE	0.0777	0.0777	0.0777	0.0777	0.0777	0.0782
U-MIDAS	R^2	0.8872	0.8941	0.8944	0.8955	0.9009	0.9086
	RMSE	0.5172	0.5581	0.5680	0.5851	0.6180	0.6347
	MSFE	0.2675	0.3115	0.3227	0.3424	0.3820	0.4029
	DMSFE	0.0878	0.0912	0.0959	0.1047	0.1184	0.1344
Stepfun-MIDAS	R^2	0.8709	0.8758	0.8761	0.8762	0.8816	0.8902
	RMSE	0.5130	0.5491	0.5395	0.5486	0.5625	0.5866
	MSFE	0.2631	0.3015	0.2911	0.3009	0.3165	0.3441
	DMSFE	0.0866	0.0948	0.0909	0.0961	0.0925	0.1073
Almon-MIDAS	R^2	0.8694	0.8683	0.8685	0.8688	0.8696	0.8723
	RMSE	0.4785	0.4736	0.4715	0.4775	0.5803	0.4907
	MSFE	0.2290	0.2243	0.2223	0.2280	0.3368	0.2408
	DMSFE	0.0835	0.0895	0.0876	0.0835	0.0919	0.0808

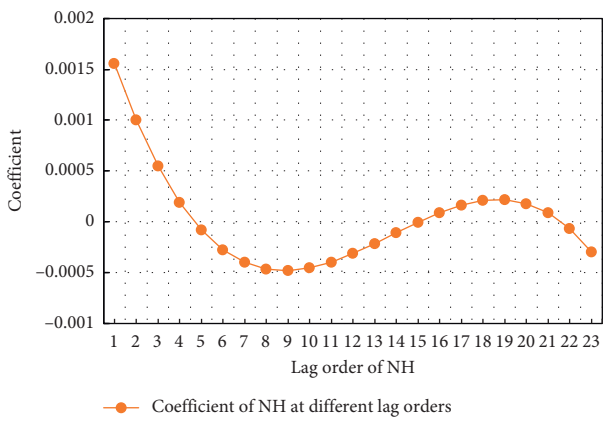

Figure 4: The coefficient fluctuation of Almon-MIDAS at lag order 23.

are the lowest among all models and lag order. Therefore, it can be seen from Table 3 that when the exchange rate lag order is 20, the U-AR(1)-MIDAS (20) model has the best prediction performance and can extract the potential information of high-frequency data to the maximum. Figure 5 shows that the 20 coefficients estimated by the U-AR(1)-MIDAS (20) model make random fluctuations in the positive and negative directions between −20 and 15. The first-order effect of delay is 1.26, that is, the rise in the exchange rate of USD/RMB on the previous trading day will drive the CPI increase of this month by 1.26 units. The influence of USD/RMB's exchange rate on the CPI of this month will last 20 trading days.

5.2. Multivariate MIDAS Model. In the univariate MIDAS model, the prediction results obtained by different high-frequency explanatory variables will be different. And, there are multiple routes through which price fluctuations can be transmitted, so it is impossible to use a univariate model to predict the CPI accurately. In this part, we consider combining univariate models from different routes to reduce prediction errors. By combining the information contained in different variables, the forecast accuracy of the model can be optimized. The combined prediction model can refer to [26]. In addition, we chose four different weight functions as follows:

Equal weight function:

$$\omega_{i,t} = \frac{1}{n}. \tag{1}$$

AIC weight function:

$$\omega_{i,t} = \frac{\exp\left(-\mathrm{AIC}_i\right)}{\sum_{i=1}^{n} \exp\left(-\mathrm{AIC}_i\right)}. \tag{2}$$

BIC weight function:

$$\omega_{i,t} = \frac{\exp\left(-\mathrm{BIC}_i\right)}{\sum_{i=1}^{n} \exp\left(-\mathrm{BIC}_i\right)}. \tag{3}$$

Table 4: Exchange rate: the goodness of fit and in-sample and out-of-sample prediction accuracy at different lag orders.

Model	Index	Lag order					
		15	20	25	30	35	40
Beta-MIDAS	R^2	0.8617	0.8621	0.8619	0.8619	0.8664	0.8668
	RMSE	0.4903	0.4863	0.4873	0.4877	0.5004	0.4938
	MSFE	0.2404	0.2364	0.2375	0.2378	0.2504	0.2439
	DMSFE	0.0770	0.0778	0.0779	0.0777	0.0797	0.0793
Beta-nonzero-MIDAS	R^2	0.8616	0.8617	0.8617	0.8617	0.8663	0.8664
	RMSE	0.4938	0.4916	0.4907	0.4896	0.5018	0.5007
	MSFE	0.2438	0.2417	0.2408	0.2397	0.2518	0.2507
	DMSFE	0.0781	0.0780	0.0779	0.0778	0.0798	0.0798
Exp Almon-MIDAS	R^2	0.8618	0.8620	0.8619	0.8620	0.8666	0.8668
	RMSE	0.4887	0.4875	0.4871	0.4837	0.4972	0.4929
	MSFE	0.2388	0.2377	0.2373	0.2340	0.2472	0.2430
	DMSFE	0.0770	0.0782	0.0780	0.0778	0.0803	0.0793
U-MIDAS	R^2	0.8810	0.8843	0.8918	0.9054	0.9230	0.9302
	RMSE	0.5246	0.4669	0.5415	0.7292	0.7439	0.8527
	MSFE	0.2752	0.2180	0.2932	0.5318	0.5534	0.7271
	DMSFE	0.1430	0.1210	0.1751	0.3701	0.3777	0.4827
Stepfun-MIDAS	R^2	0.8627	0.8641	0.8661	0.8700	0.8813	0.8829
	RMSE	0.4763	0.4839	0.4977	0.5728	0.6078	0.6080
	MSFE	0.2268	0.2342	0.2477	0.3281	0.3694	0.3696
	DMSFE	0.0736	0.0996	0.0990	0.1826	0.1980	0.1986
Almon-MIDAS	R^2	0.6872	0.6935	0.6976	0.7051	0.7103	0.7221
	RMSE	0.4906	0.4909	0.5023	0.5012	0.4973	0.4986
	MSFE	0.2407	0.2410	0.2523	0.2512	0.2473	0.2486
	DMSFE	0.0780	0.0780	0.0796	0.0794	0.0810	0.0796

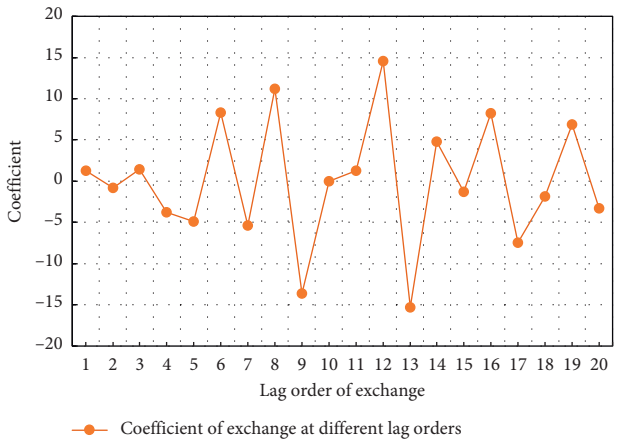

Figure 5: The coefficient fluctuation of U-MIDAS at lag order 20.

MSFE weight function:

$$\omega_{i,t} = \frac{m_{i,t}^{-1}}{\sum_{i=1}^{n} m_{i,t}^{-1}},$$
$$m_{i,t} = \sum_{i=T_0}^{i} \delta^{t-i}\left(y_{s+h}^{h} - \hat{y}_{i,s+h|s}^{h}\right)^2, \tag{4}$$

$\delta = 1$ when using MSFE weight function, $\delta = 0.9$ when using DMSFE weight function.

We introduced control variables and intermediate variables into the model. We selected the average daily coal consumption of the six power plants as the intermediate variables, and the Nanhua Futures Commodity Index, and the exchange rate as the control variables. We introduce the cross-multiplication of RJ/CRB International Commodity Futures Index, Nanhua Futures Commodity Index, and exchange rate to reflect the moderating effect. We introduce the cross-multiplication of the average daily coal consumption of the six power plants, the Nanhua Futures Commodity Index, and the exchange rate to reflect the mediating effect. According to each high-frequency explanatory variable's optimal weight function and optimal lag order, we construct a combined forecasting model to make out-of-sample forecasts for the CPI from January 2019 to January 2020. Table 5 shows the goodness of fit and prediction accuracy at the optimal lag order of each cross-multiplication variable.

5.2.1. Combined Forecast of the International Commodity Futures Market and the Domestic Production Sector. According to the univariate model results in Table 6, the AR(1)-MIDAS(13) model with MSFE weight function is better than other models in the goodness of fit and prediction accuracy. Therefore, this model is more suitable for out-of-sample CPI forecast under the material economy transmission route.

5.2.2. Combined Forecast of the International Commodity Futures Market, Chinese Commodity Futures Market, and Domestic Production Sector. According to the results in

Table 5: The goodness of fit and prediction accuracy at the optimal lag order of each cross-multiplication variable.

Model	Index	CRB × coal Lag = 36	NH × coal Lag = 24	Exchange × coal Lag = 22	CRB × NH Lag = 37	CRB × exchange Lag = 24
Beta-MIDAS	R^2	0.8652	0.8602	0.8696	0.8740	0.8657
	RMSE	0.5542	0.5567	0.6349	0.6626	0.6733
	MSFE	0.3072	0.3100	0.4031	0.4390	0.4534
	DMSFE	0.0882	0.0901	0.1044	0.1017	0.1099
Beta-nonzero-MIDAS	R^2	0.8668	0.8582	0.8598	0.8735	0.8665
	RMSE	0.5792	0.5502	0.5404	0.6665	0.6772
	MSFE	0.3355	0.3028	0.2921	0.4442	0.4586
	DMSFE	0.0947	0.0893	0.0853	0.1018	0.1116
Exp Almon-MIDAS	R^2	0.8659	0.8615	0.8706	0.8742	0.8659
	RMSE	0.5222	0.5662	0.6259	0.6646	0.6794
	MSFE	0.2727	0.3206	0.3917	0.4417	0.4616
	DMSFE	0.0837	0.0920	0.1034	0.1024	0.1111
U-MIDAS	R^2	0.9316	0.9095	0.9070	0.9220	0.9020
	RMSE	0.5205	0.5288	0.5906	0.8027	0.8192
	MSFE	0.2710	0.2796	0.3488	0.6443	0.6711
	DMSFE	0.0626	0.0769	0.0981	0.1264	0.1475
Stepfun-MIDAS	R^2	0.9096	0.8919	0.8907	0.8940	0.8868
	RMSE	0.5118	0.4745	0.4944	0.7087	0.7423
	MSFE	0.2619	0.2252	0.2444	0.5022	0.5509
	DMSFE	0.0742	0.0722	0.0798	0.1295	0.1378
Almon-MIDAS	R^2	0.9043	0.8870	0.8885	0.8778	0.8731
	RMSE	0.4911	0.4863	0.5091	0.6344	0.5910
	MSFE	0.2412	0.2365	0.2592	0.4024	0.3493
	DMSFE	0.0613	0.0679	0.0809	0.1054	0.0933

Table 6: The goodness of fit and prediction accuracy of RJ/CRB and coal.

Weight function	The goodness of fit and prediction accuracy	Lag = 13	Lag = 22	Lag = 36
MSFE	R^2	0.8389	0.8303	0.8320
	RMSE	0.5346	0.5644	0.5552
	MSFE	0.2858	0.3186	0.3083
DMSFE	R^2	0.8373	0.8315	0.8273
	RMSE	0.5359	0.5691	0.5539
	MSFE	0.2872	0.3238	0.3068
AIC	R^2	0.7736	0.7681	0.8225
	RMSE	0.5821	0.5585	0.5346
	MSFE	0.3388	0.3120	0.2858
BIC	R^2	0.7736	0.7977	0.8225
	RMSE	0.5821	0.5472	0.5346
	MSFE	0.3388	0.2995	0.2858
Equal weight	R^2	0.8380	0.8338	0.8387
	RMSE	0.5353	0.5757	0.5597
	MSFE	0.2865	0.3314	0.3133

Table 7, the AR(1)-MIDAS(22) model with AIC weight function is better than other models in the goodness of fit and prediction accuracy. Therefore, this model is more suitable for out-of-sample CPI forecasts under the financial market route.

5.2.3. Combined Forecast of the International Commodity Futures Market, Exchange Rate, and Domestic Production Sector. According to the results in Table 8, the AR(1)-MIDAS(22) model with MSFE weight function is better than other models in the goodness of fit and prediction accuracy. Therefore, this model is more suitable for out-of-sample forecasts of CPI under the exchange rate route.

5.2.4. Comparison of the Predicted and the Observed CPI. Table 9 shows the goodness of fit and prediction accuracy of combined forecasting model under three routes. The forecast CPI under the three routes is weighted and averaged to obtain a total predicted CPI. The comparison of the predicted and the observed CPI is shown in Figure 6. As shown in Figure 6, observed and predicted CPI are consistent in most months, except for February, March, October, November 2019, and January 2020. Changes in CPI in recent months may be ascribed to expected shocks such as price rise during the Chinese Lunar New Year, higher pork prices due to African swine fever, and the COVID-19 epidemic.

5.3. Conclusion. In this paper, four kinds of high-frequency daily data are used to predict China's CPI by using the MIDAS model. The four variables have different effects on China's CPI, and each high-frequency variable has different influence route on China's CPI forecast. Judging from the fit and prediction effect of a single variable, the RJ/CRB commodity price index's optimal lag order is 13. The optimal lag order of the other three high-frequency day variables representing domestic conditions is 22, 23, and 20. Considering that the data samples selected are all data from

Table 7: The goodness of fit and prediction accuracy of RJ/CRB, NH, and coal.

Weight function		The goodness of fit and prediction accuracy				
		Lag = 13	Lag = 22	Lag = 23	Lag = 24	Lag = 37
MSFE	R^2	0.8328	0.8253	0.8206	0.8215	0.8333
	RMSE	0.5428	0.5270	0.5403	0.5611	0.5543
	MSFE	0.2946	0.2777	0.2920	0.3148	0.3073
DMSFE	R^2	0.8318	0.8256	0.8221	0.8248	0.8312
	RMSE	0.5472	0.5439	0.5548	0.5695	0.5549
	MSFE	0.2994	0.2958	0.3078	0.3244	0.3079
AIC	R^2	0.7791	0.7807	0.7695	0.7685	0.7398
	RMSE	0.5716	0.5184	0.5310	0.5297	0.5658
	MSFE	0.3267	0.2687	0.2820	0.2805	0.3202
BIC	R^2	0.7791	0.8463	0.8462	0.8464	0.7398
	RMSE	0.5716	0.6954	0.6979	0.6941	0.5658
	MSFE	0.3267	0.4836	0.4870	0.4818	0.3202
Equal weight	R^2	0.8339	0.8308	0.8261	0.8278	0.8383
	RMSE	0.5534	0.5514	0.5632	0.5799	0.5617
	MSFE	0.3062	0.3040	0.3172	0.3363	0.3155

Table 8: The goodness of fit and prediction accuracy of RJ/CRB, exchange, and coal.

Weight function		The goodness of fit and prediction accuracy			
		Lag = 13	Lag = 20	Lag = 22	Lag = 24
MSFE	R^2	0.8408	0.8260	0.8240	0.8254
	RMSE	0.5455	0.5385	0.5322	0.5594
	MSFE	0.2975	0.2900	0.2833	0.3130
DMSFE	R^2	0.8374	0.8231	0.8231	0.8280
	RMSE	0.5535	0.5589	0.5537	0.5645
	MSFE	0.3063	0.3124	0.3066	0.3187
AIC	R^2	0.7673	0.7530	0.7578	0.7516
	RMSE	0.5824	0.5617	0.5523	0.5631
	MSFE	0.3391	0.3155	0.3050	0.3171
BIC	R^2	0.7673	0.7579	0.7583	0.7996
	RMSE	0.5824	0.5636	0.5524	0.5669
	MSFE	0.3391	0.3177	0.3052	0.3214
Equal weight	R^2	0.8402	0.8291	0.8298	0.8289
	RMSE	0.5582	0.5568	0.5483	0.5696
	MSFE	0.3116	0.3100	0.3007	0.3244

Table 9: The goodness of fit and prediction accuracy of combined forecasting model under three routes.

The goodness of fit and prediction accuracy	Route 1	Route 2	Route 3	Weighted sum
R^2	0.8389	0.7807	0.8240	0.8214
RMSE	0.5346	0.5184	0.5322	0.5208
MSFE	0.2858	0.2687	0.2833	0.2713

domestic trading days, we can consider 23 trading days consisting of a month, excluding holidays and other factors. Therefore, the three high-frequency daily variables in China can predict CPI more perfectly with the current month's data.

In the material economy route, the RJ/CRB commodity price index's direct impact on the CPI fluctuates, but the overall effect is positive. However, the optimal lag order is significantly smaller than other high-frequency explanatory variables, which indicates that the impact of the international commodity futures market on China's CPI is mainly short term. After adding the intermediary variable, the optimal lag order has increased significantly, indicating that the impact of international commodity futures prices on China's industrial output needs a longer time. Therefore, its impact on China's CPI will also have a time lag effect, and RJ/CRB commodity price index has a long-term effect on the CPI.

In the financial market route, after adding the Nanhua Commodity Futures Index as a regulatory variable to the model, the effects of moderating effect and mediating effect are alternating between the positive and the negative. The mediating effect of the Nanhua Commodity Futures Index

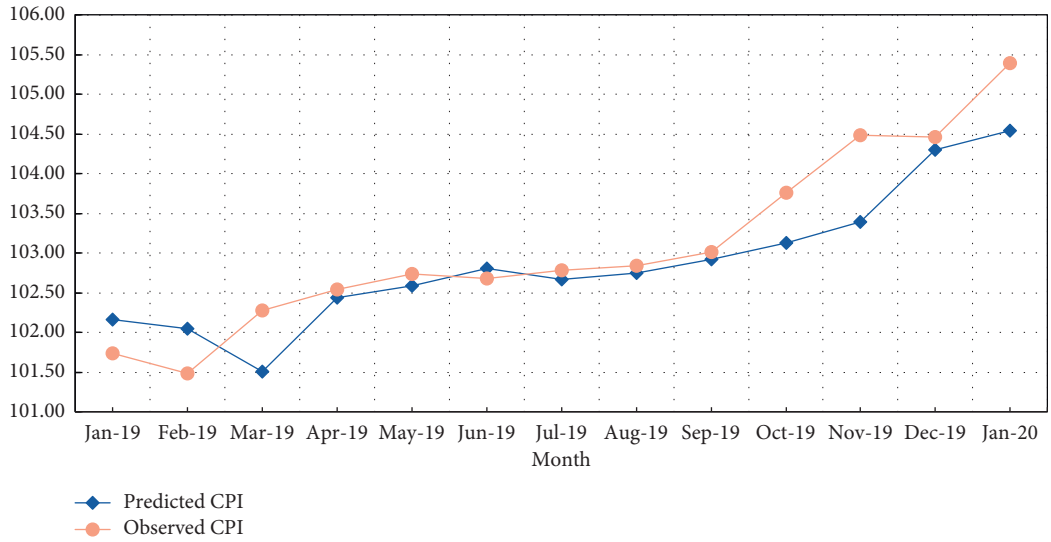

Figure 6: Predicted CPI vs. observed CPI.

and the average daily coal consumption of the six power plants are unstable for the CPI. The optimal lag order of the moderating effect of the RJ/CRB Commodity Price Index and Nanhua Commodity Futures Index is greater, and their influence on the CPI is longer.

The US dollar to the RMB exchange rate is added as the adjustment variable in the exchange rate route. The optimal lag order of the adjustment variable and the intermediary variable is the same. The effect on the CPI lasts about one month, indicating that this route conducts the domestic CPI more rapidly. The reason may be that exchange rate changes can more directly affect domestic purchasing power, and the real-time effect is more pronounced. In contrast, domestic and foreign financial markets' linkage effect has a short-term time lag, which takes longer to transmit to the domestic production and consumption side.

Based on the univariate model's fit and prediction results, we further construct the combined prediction model and analyze its prediction accuracy and effect. The results show that the combined prediction model with MSFE as the weight in the material economic route, the combined prediction model with AIC as the weight in the financial market route, and the combined prediction model with MSFE as the weight in the exchange rate route have high precision in China's CPI forecast. Finally, integrating the three routes can effectively predict the CPI in a normal month.

6. Policy Suggestions

China's strong dependence on international commodities will undoubtedly make the fluctuation of international commodity futures market and domestic economy interrelated. Its price increase will affect China's economic growth and promote inflation, thus affecting the economy's stability. Therefore, preventing and eliminating the risk of external shocks and effectively defusing the shocks caused by price fluctuations in the international commodity market must be considered. This article gives the following suggestions.

First of all, it is necessary to monitor the price change in real time and pay attention to the conduction effect of international commodity futures price fluctuation. Real-time monitoring and capturing the volatility of the international market is the prerequisite for proposing follow-up measures. The previous research and analysis makes it known that the international market price fluctuations will impact domestic industrial and consumer price levels. Simultaneously, the linkage of domestic and foreign futures market is a conduction route that cannot be ignored, and the change of international market price will increase the domestic financial risk. Therefore, real-time monitoring and early warning of international commodity futures prices are indispensable to develop timely and effective strategies to deal with financial uncertainty without risk.

Secondly, identify the main factors that cause fluctuations in international commodity futures prices and effectively resolve different channels' impact. The influence factors of international commodity futures price are very complicated. At different times and under different conduction routes, international commodities' conduction effect on China's economy will be different. Therefore, in dealing with the impact of international prices, it is essential to establish monitoring and early warning mechanisms. Relevant departments should improve the ability to collect and process information on the futures market and make reasonable predictions on important commodities' future trends. In addition, we should improve the ability to identify the dominant factors. According to domestic and foreign economy and finance, the corresponding policy means should be formulated for different transmission channels, monetary policy, and fiscal policy, and administrative intervention should be effectively adopted to guide enterprises to adopt flexible financial instruments to resolve risks.

Third, we must develop the domestic commodity futures market and strive for pricing power. China has a great demand for resources, and bulk commodities such as iron ore and crude oil account for a large proportion of world

demand. However, under the current trade background, China can only trade following the requirements of foreign exchange, has no right to speak in the process of commodity pricing, and has no advantage in import and export trade. From the research of this article, the fluctuation of international commodity futures prices will be carried out through the linkage of domestic and foreign markets. Therefore, China's futures market needs to be further improved. In terms of countermeasures, China's participation in the formation of international commodity futures prices mainly includes: perfecting the commodity varieties of China's futures market, reasonably exploring the reasons for price changes in the international commodity futures market, combining the background of domestic and foreign markets to forecast its future trends, while guarding against potential imported inflation risks.

Finally, the government should establish a strategic commodity reserve system. Changes in international commodity prices depend on supply and demand factors and are also affected by political factors. Since bulk commodities have strategic reserves, the establishment of a strategic reserve system is of great significance. When prices fluctuate sharply or frequently, the country can use strategic reserves to alleviate the shock caused by price fluctuations. On the one hand, it is necessary to reduce the degree of dependence on imports of bulk commodities. Relevant departments use policy measures to encourage domestic cultivation of agricultural products that are highly dependent on imports and control the industrial sector's demand for bulk commodities to reduce unnecessary consumption. On the other hand, in conjunction with the national development plan, actively expand the overseas sources of commodities, encourage enterprises to invest in overseas resources, and establish strategic cooperative relations with those that produce strategic resources and commodities.

Data Availability

The data used to support the findings of this study are available from the corresponding author upon request.

Conflicts of Interest

The authors declare that they have no conflicts of interest regarding the publication of this article.

Acknowledgments

This research was funded by the National Social Science Fund of China (grant no. 19BJL024).

References

[1] L. Hong, W. Shu, J. Wang, and R. Mian, "Harmonic resonance investigation of a multi-inverter grid-connected system using resonance modal analysis," *IEEE Transactions on Power Delivery*, vol. 34, no. 1, pp. 63–72, 2019.

[2] C. Wei, Z. Shen, D. Xiao, L. Wang, X. Bai, and H. Chen, "An optimal scheduling strategy for peer-to-peer trading in interconnected microgrids based on RO and Nash bargaining," *Applied Energy*, vol. 295, Article ID 117024, 2021.

[3] C. Zhang, J. Fu, and Z. Pu, "A study of the petroleum trade network of countries along "The Belt and Road Initiative"" *Journal of Cleaner Production*, vol. 222, pp. 593–605, 2019.

[4] C. Zhang, Z. Pu, and Q. Zhou, "Sustainable energy consumption in northeast asia: a case from China's fuel oil futures market," *Sustainability*, vol. 10, no. 1, p. 261, 2018.

[5] Z. Pu, J. Fu, C. Zhang, and J. Shao, "Structure decomposition analysis of embodied carbon from transition economies," *Technological Forecasting and Social Change*, vol. 135, no. 10, pp. 1–12, 2018.

[6] C. Wei, M. Benosman, and T. Kim, "Online parameter identification for state of power prediction of lithium-ion batteries in electric vehicles using extremum seeking," *International Journal of Control, Automation and Systems*, vol. 17, no. 11, pp. 2906–2916, 2019.

[7] D. Zivkov, J. Uraskovic, and S. Manic, "How do oil price changes affect inflation in Central and Eastern European countries? a wavelet-based Markov switching approach," *Baltic Journal of Economics*, vol. 19, no. 1, pp. 84–104, 2019.

[8] L. T. Goh, S. H. Law, and I. Trinugroho, "Do oil price fluctuations affect the inflation rate in Indonesia asymmetrically?" *The Singapore Economic Review*, vol. 7, no. 1, pp. 1–21, 2020.

[9] F. Bec and A. De Gaye, "How do oil price forecast errors impact inflation forecast errors? an empirical analysis from US, French and UK inflation forecasts," *Economic Modelling*, vol. 53, no. 2, pp. 75–88, 2016.

[10] A. R. Joshi and D. Acharya, "Commodity prices and domestic inflation in India," *Global Journal of Emerging Market Economies*, vol. 3, no. 2, pp. 223–246, 2011.

[11] C. Estrades and M. I. Terra, "Commodity prices, trade, and poverty in Uruguay," *Food Policy*, vol. 37, no. 1, pp. 58–66, 2012.

[12] G. Filis and I. Chatziantoniou, "Financial and monetary policy responses to oil price shocks: evidence from oil-importing and oil-exporting countries," *Review of Quantitative Finance and Accounting*, vol. 42, no. 4, pp. 709–729, 2014.

[13] T. R. Govinda, "Oil prices and the global economy," *Energy Economics*, vol. 49, no. 5, pp. 669–675, 2015.

[14] T.-H. Le, Y. Chang, and D. Park, "Oil price fluctuations and energy commodity prices: an analysis of asymmetric effects," *The Singapore Economic Review*, vol. 8, no. 3, pp. 1–23, 2020.

[15] A. M. Herrera, M. B. Karaki, and S. K. Rangaraju, "Oil price shocks and U.S. economic activity," *Energy Policy*, vol. 129, no. 6, pp. 89–99, 2019.

[16] C. Blattman, J. Hwang, and J. G. Williamson, "Winners and losers in the commodity lottery: the impact of terms of trade growth and volatility in the periphery 1870-1939," *Journal of Development Economics*, vol. 82, no. 1, pp. 156–179, 2007.

[17] R. Dornbusch and S. Fischer, "Exchange rates and the current account," *The American Economic Review*, vol. 70, no. 5, pp. 960–971, 1980.

[18] B. Büyükşahin and M. Robe, "Speculators, commodities and cross-market linkages," *Journal of International Money and Finance*, vol. 42, pp. 38–70, 2014.

[19] J. V. Quadrini, "Macroeconomic effects of financial shocks," *Social Science Electronic Publishing*, vol. 102, no. 1, pp. 238–271, 2012.

[20] R. Hammersland and C. B. Træe, "The financial accelerator and the real economy: a small macroeconometric model for Norway with financial frictions," *Economic Modelling*, vol. 36, no. 1, pp. 517–537, 2014.

[21] D. W. Jorgenson, "Capital theory and investment behaviour," *American Economic Review*, vol. 53, no. 2, pp. 247–259, 1963.
[22] J. Tobin, "A general equilibrium approach to monetary theory," *Journal of Money, Credit and Banking*, vol. 1, no. 1, pp. 15–29, 1969.
[23] A. Jain and S. Ghosh, "Dynamics of global oil prices, exchange rate and precious metal prices in India," *Resources Policy*, vol. 38, no. 1, pp. 88–93, 2013.
[24] S. Oliner and G. Rudebusch, "Is there a broad credit channel for monetary policy?" *Economic Review*, vol. 1, pp. 3–13, 1996.
[25] M. Hume and A. Sentance, "The global credit boom: challenges for macroeconomics and policy," *Journal of International Money and Finance*, vol. 28, no. 8, pp. 1426–1461, 2009.
[26] E. Andreou, E. Ghysels, and A. Kourtellos, "Should macroeconomic forecasters use daily financial data and how?" *Journal of Business and Economic Statistics*, vol. 31, no. 2, pp. 240–251, 2013.

Hindawi
Complexity
Volume 2021, Article ID 9564583, 9 pages
https://doi.org/10.1155/2021/9564583

Research Article

Optimal Setting Method of Inverse Time Overcurrent Protection for the Distribution Networks Based on the Improved Grey Wolf Optimization

Bo Yang,[1] Jun Tang,[1] Changsen Feng,[2] Chen Yang,[1] and Xiaofeng Dong[1]

[1]*State Grid Suzhou Power Supply Company, Suzhou 215004, China*
[2]*College of Information Engineering, Zhejiang University of Technology, Hangzhou 310023, China*

Correspondence should be addressed to Changsen Feng; fcs@zjut.edu.cn

Received 12 May 2021; Accepted 22 July 2021; Published 30 July 2021

Academic Editor: Xiaoqing Bai

The setting of protection parameters is vital to the large-scale application of reverse time overcurrent protection in the distribution networks. A fixed value optimization method of inverse time overcurrent protection for the distribution networks with distributed generation based on the improved Grey Wolf algorithm is proposed, which takes the protection action equation and the sensitivity, speed, and selectivity into consideration. Subsequently, four strategies, including good point set initialization, convergence factor exponential decay strategy, mutation strategy, and heuristic parameter determination strategy, are introduced to improve the Grey Wolf algorithm on the premise of retaining fewer adjustable parameters. Simulation results verify the feasibility and superiority of the proposed model in case of the two-phase and three-phase faults and discuss the influence of time differential on parameters setting and the research direction of algorithm optimization and engineering application.

1. Introduction

Distributed generation (DG), such as wind power, photovoltaic, fuel cell, and energy storage, is increasing access to the distribution networks along with China's nonignorable energy and environmental problems and the intelligent level of the power grid [1–4]. The widespread utilization of DG not only can ease the energy crisis and improve the utilization rate of energy but also will change the original grid structure and affect the sensitivity of protection. Therefore, the risk of refusing action or misoperation of the protection may be increased [5–7].

By far, research efforts mainly focused on two solutions:

(1) Collecting the electric parameters information of the critical nodes and processing them comprehensively to improve the protection of adjacent coordination characteristics and promoting the sensitivity of protection [8, 9]: according to the control strategy and fault current output characteristics of the inverter distributed power supply, an adaptive current velocity break protection scheme for the distribution networks is proposed in [8], and the power reference and control parameters can be obtained based on the MMS service of IEC61850 communication protocol. Literature [9] proposed a communication-based inverse time-limit overcurrent protection scheme, in which the upstream line protection receives the fault current data of the branch of the distributed generation by the communication channel to ensure the coordination between the upstream and the downstream protection. However, this method relies too much on the communication system, and if the communication system crashes, the protection will fail.

(2) The protection method suitable for large-scale DG distribution networks is improved to realize the adaptive protection setting. Inverse time overcurrent protection is widely applied in the distribution network protection scheme due to the characteristic of the short protection action time and stable

operation [10–13]. Some researchers introduced the artificial intelligence algorithm to optimize the fixed value setting of the inverse time overcurrent protection. In [11], a fixed value optimization model of inverse time overcurrent protection based on an improved particle swarm algorithm is established, which considers the uncertainty of fault line, fault type, and fault point location. Nevertheless, the particle swarm optimization algorithm has too many adjustable parameters, and the parameters have a direct impact on the search quality and efficiency of the algorithm. In [12], two settings of fixed values are obtained by distinguishing two scenarios of two-phase short circuit and three-phase short circuit, and the numerical example verifies that the sensitivity of a separate setting is more robust than that of a single setting. However, the method is restricted by too many parameters of particle swarm optimization (PSO). Literature [13] introduces the Grey Wolf algorithm to solve the fixed value setting of the inverse time overcurrent protection problem. The results show that the Grey Wolf algorithm has more advantages than the particle swarm algorithm in a high-dimensional nonlinear nonconvex optimization problem with inequality constraints. However, the Grey Wolf algorithm is easy to rapid convergence and needs to be improved.

Given the consideration above, a protection setting optimization method of inverse time overcurrent for distribution networks with DG based on the improved Grey Wolf algorithm is proposed. The good point set initialization strategy, convergence factor attenuation strategy, mutation strategy, and heuristic parameters strategy are introduced to develop the Grey Wolf algorithm, improving the algorithm accuracy without introducing a new parameter and retaining the advantages of the less adjustable parameter of the Grey Wolf algorithm. The simulation verified that the proposed model could effectively improve the selectivity and quick action of the inverse time overcurrent protection for the distribution networks with DG, guiding the corresponding scenario engineering practice.

2. Setting Value Optimization of Inverse Time Overcurrent Protection for Distribution Networks

2.1. Action Characteristic Equation. The inverse time overcurrent protection is widely used in the distribution network [14, 15]. The characteristic equation of the inverse time overcurrent protection operation is as follows:

$$t_{ij} = \frac{0.14T_{pi}}{\left[\left(I_{ij}/I_{pi}\right)^{0.02} - 1\right]}, \tag{1}$$

where i is the number of the equipment, j is the number of fault lines, t_{ij} is the action time of the protection equipment, T_{pi} is the time setting coefficient of the protection equipment, I_{ij} represents the current flowing through the equipment, and I_{pi} denotes the starting current of the equipment i. T_{pi} and I_{pi} are the value to be set.

2.2. Objective Function. Like other protection, the purpose of inverse time protection is to match the action time and short circuit current and timely remove the fault line in case of failure. In this study, the selectivity, reliability, and sensitivity are considered, and the matching of the action time and the short circuit current are guaranteed through the motion equation and constraint conditions. Given this premise, the least the total action time is, the better the protection sensitivity will be. Therefore, the protection setting can be formulated as a nonlinear optimization problem.

In [11–13], the objective function is minimizing the sum of all the action time of the relay. The target function of the setting value optimization of the inverse time overcurrent protection can be described as follows:

$$O = \min\left[\sum_{i=1}^{M}\sum_{a=1}^{B}\sum_{j=1}^{L}\left(t_{ij}^{p} + t_{aj}^{b}\right)\right], \tag{2}$$

where M is the total number of the primary protection, B is the number of backup protection, and L represents the number of fault lines. t_{ij}^{p} and t_{aj}^{b} denote the action time of primary protection i and backup protection a in case of line failure, during which the relay must send a tripping signal.

2.3. Coordinate Constraint. Cooperation of primary protection and backup protection is crucial to the safe and stable operation of the power system. The time limit of protection should be determined step by step to guarantee the selectivity of protection operation at all levels. The primary protection and backup protection action time must have a reasonable interval to ensure the coordination and selectivity of relay protection.

Therefore, the protection coordination time interval should be satisfied:

$$t_{ij}^{p} - t_{aj}^{b} \geq \mathrm{CTI}, \quad \forall i, \{j, k\}, \tag{3}$$

where CTI represents the coordinate interval for protection, also known as the time differential. Shortening the time differential can effectively increase the resection rate of the fault and reduce equipment damage.

2.4. Constraints. Firstly, the protection action time must meet the following constraints to ensure the sensitivity and quick action of the relay:

$$t_{ij,\min} \leq t_{ij} \leq t_{ij,\max}, \tag{4}$$

where $t_{ij,\min}$ and $t_{ij,\max}$ are the minimum and maximum action time of the relay.

Secondly, the time setting coefficient and current setting coefficient must be within the scope of allowed values:

$$T_{p\min} \le T_{pi} \le T_{p\max}, \quad \forall i, \tag{5}$$

$$I_{p\min} \le I_{pi} \le I_{p\max}, \quad \forall i, \tag{6}$$

where $T_{p\min}$ and $T_{p\max}$ are the maximum and minimum values of the time setting coefficient and $I_{p\min}$ and $I_{p\max}$ are the maximum and minimum starting current of the protection equipment.

To sum up, equations (1) and (2) are the objective function of the optimization model and equations (3)–(6) are the constraints.

2.5. Influence of Large-Scale DG Access on Reverse Time Overcurrent Protection in the Distribution Networks. As the large-scale DG access to the distribution networks, the bidirectional power appears. It needs to invest spare capacity and take control measures to compensate the intermittent power, which imposes a significant challenge on the protection setting and coordination operation of the distribution system. Moreover, the inverse time overcurrent protection may be affected by many aspects, such as the type of DG, access points, and distribution network mode.

2.5.1. The Impact of DG Type. Different kinds of DG, such as wind, solar, synchronous generator, fuel cell, and energy storage system, have different characteristics. Different types of DG regulate the active and reactive power in different ways. For example, wind power, usually asynchronous generators, needs to absorb reactive power from the grid without voltage regulation ability.

2.5.2. The Impact of DG Access Points. The short circuit current and the action time of the distribution network inverse time overcurrent protection depend on the access points and fault locations. DG access points have less impact on the upstream of the failure but affect the current downstream. If the downstream of the main protection action is faster, the upstream backup protection action time will be longer and may even refuse to move.

2.5.3. The Influence of DG Operation Mode. DG can parallel operation or run island, and there are many island schemes in DG island mode when switching. Different operation modes correspond to different grid topology structures and power flow, and the inverse time overcurrent protection may also be influenced.

The value setting is determined by solving optimization problems based on the distribution network topology structure containing DG access. It should be pointed out that the different topologies have covered most of the influencing factors. That is to say, no matter what type of the DG, what kind of DG operation mode from where the access points, and what the access scale, the setting optimization problem can be formulated by the similar mathematical optimization model, and this makes the optimization algorithm in this paper with general significance. In addition, when the capacity of DG access is over a specific value, the above optimization problem may not find the solution, which means that the inverse time overcurrent protection is not suitable for this scenario, and other suitable protection types should be introduced.

3. Grey Wolf Algorithm

Grey Wolf Optimizer (GWO), which has the advantages of stability and less regulating parameters, is a swarm intelligence algorithm presented by Mirijili in 2014 [16–18]. GWO can achieve an optimization search through the simulation of the Grey Wolf population hierarchy and hunting behavior. As shown in Figure 1, wolves can be divided into four types according to the status in the social structure of the Grey Wolf, including types α, β, δ, and ω. Type α represents the group leader. Types β and δ are in the middle level, and they assist type α and manage ω. Type ω is at the bottom, and its function is to detect and prey. The four types are corresponding to the optimal solution, suboptimum solution, third optimal solution, and search populations of the intelligent algorithm, respectively.

Wolves find the optimal route of hunting by way of surrounding the prey, and the behavior can be modeled as

$$\vec{D} = \left|\vec{C} \cdot \vec{X}_p(m) - \vec{X}(m)\right|, \tag{7}$$

$$\vec{X}(m+1) = \vec{X}_p(m) - \vec{A} \cdot \vec{D}, \tag{8}$$

where $\vec{X}_p$ represents the current position of the prey, $\vec{X}$ denotes the location of the Grey Wolf, and m is the number of iterations. $\vec{A}$ and $\vec{C}$ are the collaborative vector, and $\vec{D}$ is the distance between wolves and prey. The updated position of the Grey Wolf in the hunting process is formulated in equation (8).

Collaborative vectors $\vec{A}$ and $\vec{C}$ should be satisfied as follows:

$$\begin{aligned} \vec{A} &= 2\vec{a} \cdot \vec{r}_1 - \vec{a}, \\ \vec{C} &= 2 \cdot \vec{r}_2, \end{aligned} \tag{9}$$

where the modulus values of $\vec{r}_1$ and $\vec{r}_2$ are a random number between [0, 1], $\vec{a}$ is a convergence factor, and its value decreases linearly from two to zero with the increasing number of iterations.

The wolf hunting behavior is dominated by type α, followed by type ω. Type ω gradually moves to the high-grade wolf with ongoing hunting. Given these hunting behavior characteristics, the iterative optimization process of the Grey Wolf algorithm can be further described as follows:

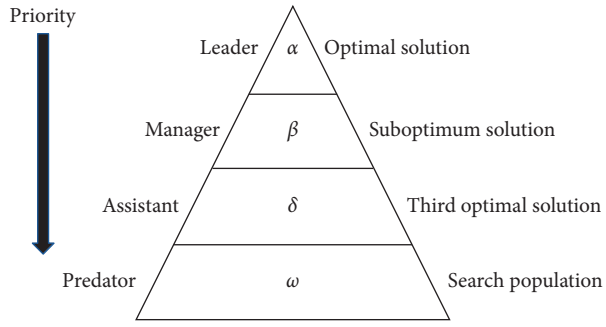

Figure 1: Hierarchy of GWO.

$$\begin{cases} \vec{D}_\alpha = \left|\vec{C}_1 \cdot \vec{X}_\alpha - \vec{X}\right|, \\ \vec{D}_\beta = \left|\vec{C}_2 \cdot \vec{X}_\beta - \vec{X}\right|, \\ \vec{D}_\delta = \left|\vec{C}_3 \cdot \vec{X}_\delta - \vec{X}\right|, \end{cases} \tag{10}$$

$$\begin{cases} \vec{X}_1 = \vec{X}_\alpha - \vec{A}_1 \cdot \vec{D}_\alpha, \\ \vec{X}_2 = \vec{X}_\beta - \vec{A}_2 \cdot \vec{D}_\beta, \\ \vec{X}_3 = \vec{X}_\delta - \vec{A}_3 \cdot \vec{D}_\delta, \end{cases}$$

$$\vec{X}(m+1) = \frac{\vec{X}_1 + \vec{X}_2 + \vec{X}_3}{3}, \tag{11}$$

where $\vec{X}_\alpha$, $\vec{X}_\beta$, and $\vec{X}_\delta$ represent wolf's position of types α, β, and δ in the current iteration, respectively. $\vec{X}$ denotes the location of type ω. $\vec{D}_\alpha$, $\vec{D}_\beta$, and $\vec{D}_\delta$ represent the distance between types α, β, and δ with ω in the current iteration, respectively. $\vec{A}_1$, $\vec{A}_2$, $\vec{A}_3$, $\vec{C}_1$, $\vec{C}_2$, and $\vec{C}_3$ are the coordination coefficient and $\vec{X}(m+1)$ denotes wolf's location of type ω in the next iteration.

4. Improved Grey Wolf Algorithm

Like other intelligent algorithms, the Grey Wolf algorithm also faces prematurity and falling into local optimum [19, 20], limiting the accuracy of the algorithm, and has a large room for improvement. Therefore, the good point set initialization strategy, the convergence factor exponential decay strategy, the mutation strategy, and the heuristic parameter determination strategy are introduced to improve the Grey Wolf algorithm. While improving the accuracy of the algorithm, the improvement preserves the advantage of less adjustable parameters of the Grey Wolf algorithm.

4.1. Good Point Set Initialization Strategy. For the swarm intelligence optimization algorithm, the quality of the initial population greatly influences the global optimization effect and convergence speed. Generally, the initial population is generated based on random initialization, making it difficult to guarantee good population diversity. Therefore, the good point set strategy [21] is adopted to initialize the population distribution. Under the premise of taking the same number of points, the sequence initialized by the good point set is more uniform, and the generated initial population is more ergodic than others. It should be pointed out that it is conducive to the global optimization of the algorithm without increasing new algorithm parameters. The good point set was put forward by Hua Luogeng et al. It can be defined as follows.

Assume that G_s is a unit cube of s-dimensional Euclidean space; the mathematical formulation can be described as follows:

$$P_n(k) = \left\{\left(\left\{r_1^{(n)} * k\right\}, \left\{\left\{r_1^{(n)} * k\right\}, \ldots, \left\{r_s^{(n)} * k\right\}\right), 1 \le k \le n\right\} r \in G_s \varphi(n) = C(r,\varepsilon) n^{-1+\varepsilon}, \tag{12}$$

where $\varphi(n)$ is the deviation of $P_n(k)$ and $C(r,\varepsilon)$ is a constant that only depends on γ and ε. $P_n(k)$ is called the good point set and r is the good point.

4.2. Convergence Factor Exponential Decay Strategy. Convergence factor $\vec{a}$ affects the global search ability of the algorithm, and the exponential function is introduced to calculate $\vec{a}$. The convergence factor exponential decay strategy can replace the linear attenuation strategy of the basic GWO algorithm [22]:

$$\vec{a} = 2\left(1 - \frac{m^2}{M^2}\right), \tag{13}$$

where m is the current iteration number and M is the maximum iteration number. It can be seen from equation (13) that the convergence factor decreases nonlinearly with the increase of iterations, which helps to balance the global search ability and local optimization ability of the GWO algorithm.

4.3. Mutation Strategy. In order to solve the problems of prematurity and low convergence accuracy of GWO algorithm without introducing new parameters and increasing the complexity of parameter initialization, the Gaussian mutation strategy is adopted, and corresponding Gaussian mutation operator is given to the position iteration of Grey Wolf in equation (11), as shown in the following equation:

$$\vec{X}(m+1) = \vec{X}(m+1) \cdot \left[1 + \frac{|\vec{a}|}{2} \cdot N(0,1)\right], \tag{14}$$

where $N(0, 1)$ is the standard Gaussian distribution. This setting enables GWO to obtain enough perturbation at the initial stage of the algorithm to increase the global search ability of the algorithm and reduce the perturbation at the end of the algorithm to avoid the turbulence of the optimal solution and accelerate the convergence process.

4.4. Heuristic Parameter Determination Strategy. The parameters of the GWO algorithm (population size, maximum number of iterations) often have a direct impact on the

search quality and efficiency of the algorithm. However, there is no simple, intuitive, and universal parameter determination method for the whole heuristic search strategy algorithm. In [23], the prior empirical setting method is utilized to directly give the parameters of the Grey Wolf algorithm and the comparison algorithm. Although the superiority of the target algorithm can be verified, the prior empirical setting method may be arbitrary when the target algorithm is applied to solve specific problems, and the comparison under different parameter settings is lacking. A heuristic parameter determination strategy is adopted to determine the parameters in two stages:

(1) According to the parameter range suggested in other literature, the population size is set to 10–50, and the maximum number of iterations is set as 100–1000. Randomly select a set of parameters and perform optimization calculation.

(2) According to the influence of parameters on the GWO, the heuristic parameter determination strategy is adopted to adjust the initial parameters. The comparative analysis under different parameters is conducted, among which the parameters corresponding to the optimal result are the optimal parameters. The larger the population size and the more the maximum number of iterations, the greater the possibility of finding the optimal global solution will be, but the optimization time is longer.

One of the advantages of the improved GWO proposed in this paper is that no new parameters are introduced in the improvement process. The advantage of the Grey Wolf algorithm with fewer adjustable parameters is retained. Compared with the PSO algorithm and harmony search algorithm (HSA) with more parameters, the workload in the process of heuristic parameter determination is greatly reduced.

5. Modeling

In this study, equations (1) and (2) are taken as the objective function, and equations (3)–(6) are taken as the constraint conditions. Based on a specific distribution network topology structure, a setting value optimization model of inverse time-limit overcurrent protection for the distribution networks with DG based on the improved GWO is established. The structure of the improved GWO model is depicted in Figure 2, and the modeling process is as follows:

(1) Heuristic initialization of the population size and maximum iteration times.

(2) Initialize the population distribution by the good point set strategy.

(3) Calculate the fitness of individual Grey Wolf and save the information of wolf types α, β, and δ with the best fitness.

(4) Update the location of Grey Wolf according to the convergence factor exponential attenuation strategy and mutation strategy.

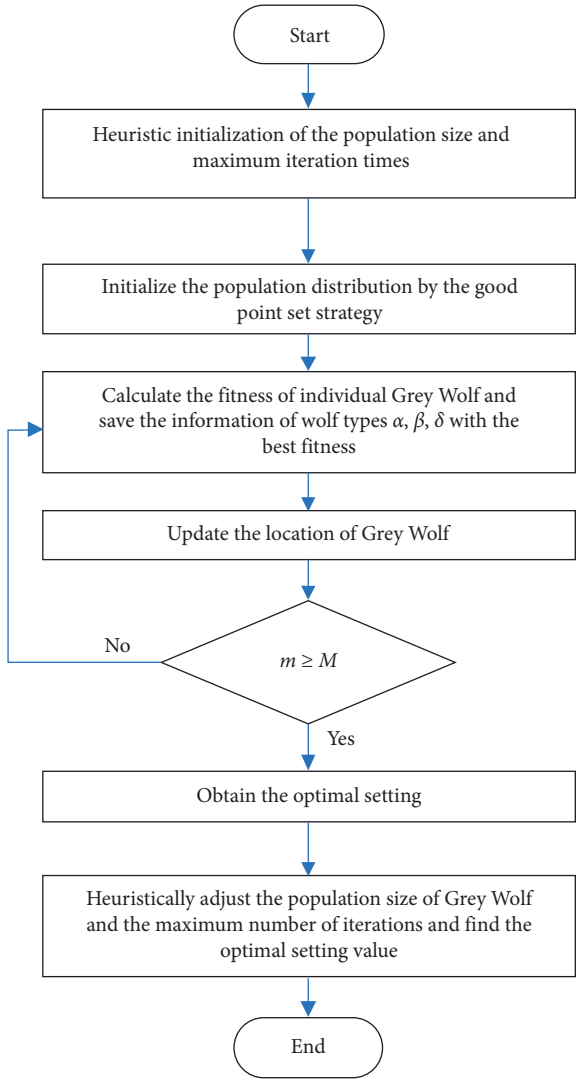

Figure 2: Improved GWO algorithm flowchart.

(5) If the maximum number of iterations is not reached, skip to Step 3 to continue optimization. Otherwise, the optimization ends, and the optimized setting is obtained.

(6) Heuristically adjust the population size of Grey Wolf and the maximum number of iterations and find the optimal setting value after several attempts and comparisons

6. Case Study

6.1. Example Description. In order to verify the effectiveness of the method presented in this paper, an example proposed in [12] is selected, and the improved GWO method is compared with the proposed setting method and other methods. The following IEEE 15-node distribution network with DG is employed to conduct the comparison analysis, as shown in Figure 3.

The parameter settings are listed in Table 1, the maximum power of DG is 480 kVA, and the DG is at the

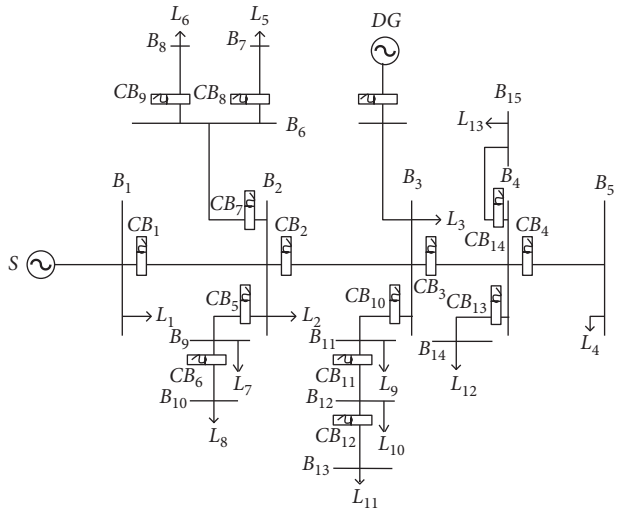

Figure 3: IEEE 15-bus distribution network with DG.

Table 1: Parameter settings.

Parameter	Value	Parameter	Value
DG maximum power	480 kVA	$T_{p\min}$	0.1
CTI	0.5 s	$T_{p\max}$	0.4
$t_{ij,\ \min}$	0.1 s	$I_{p\min}$	100 A
$t_{ij,\ \max}$	4 s	$I_{p\max}$	500 A

maximum output state. When CB1 is the primary protection, there is no backup protection. In other cases, there is one backup protection for each primary protection. The load parameters are shown in Table 2.

The improved PSO in [11], the improved HSA in [12], and the basic GWO and Cuckoo linear programming optimization algorithm (COA-LP) in [13] are selected to provide a comparative analysis. Two-phase short circuit and three-phase short circuit scenarios are distinguished in the optimization, and the protection value is set according to the terminal short circuit current. The system topology, protection method, objective function, and constraint conditions are all the same, and the quality of the optimization result mainly depends on the quality of the optimization algorithm. If the optimization results of the proposed method are superior to those of the control group, the effectiveness and superiority of the improved GWO algorithm in solving the problem of inverse time overcurrent protection setting can be verified.

6.2. Comparison Analysis. The results of the two-phase short circuit scenario are shown in Table 3. It can be seen from Table 3 that the total action time of the optimal solution obtained by the improved GWO algorithm is 23.162 seconds when a two-phase short circuit occurs, which is less than the other four algorithms.

In the case of the two-phase short circuit scenario, the setting values of each protection obtained by the improved GWO algorithm are listed in Table 4, and the action time results of each protection are shown in Table 5. As can be seen from Tables 3 and 5, the action time of protection obtained by the GWO algorithm satisfies the constraint of the time difference, which ensures selectivity and reliability of the protection and reduces the fault duration compared with other algorithms.

Table 2: Load parameters.

Load	Active power (MW)	Reactive power (MVar)
1	0.4	0.15
2	0.1	0.2
3	0.25	0.1
4	0.3	0.2
5	0.1	0.05
6	0.3	0.07
7	0.1	0.05
8	0.05	0.02
9	0.2	0.08
10	0.1	0.1
11	0.25	0.09
12	0.1	0.05
13	0.3	0.2

Table 3: Results of five algorithms when a two-phase short circuit occurs.

Algorithms	Total action time (s)
PSO	30.812
HSA	24.573
Basic GWO	26.298
COA-LP	28.720
Improved GWO	23.162

Table 4: Protection setting value when a two-phase short circuit occurs.

Relay	T_p	I_p (A)
CB_1	0.379	276.1
CB_2	0.301	193.2
CB_3	0.172	203.5
CB_4	0.099	104.7
CB_5	0.202	182.0
CB_6	0.108	106.9
CB_7	0.143	246.6
CB_8	0.101	113.7
CB_9	0.109	114.1
CB_{10}	0.203	232.5
CB_{11}	0.192	126.2
CB_{12}	0.105	103.9
CB_{13}	0.112	102.3
CB_{14}	0.097	101.9

Similarly, the results of the three-phase short circuit scenario are shown in Table 6. It can be found from Table 6 that the total action time of all protection obtained by the improved GWO algorithm in this paper is still the minimum in the case of a three-phase short circuit, which is better than the other four algorithms. The following conclusions can be drawn from the analysis:

(1) The good point set initialization strategy, convergence factor exponential decay strategy, mutation

Table 5: Protection action time when a two-phase short circuit occurs.

Fault location	Action time of primary protection (s)	Action time of backup protection (s)
B_1–B_2	1.119	—
B_2–B_3	1.027	1.539
B_3–B_4	0.623	1.238
B_4–B_5	0.326	0.879
B_2–B_9	0.602	1.411
B_9–B_{10}	0.310	0.851
B_2–B_6	0.656	1.932
B_6–B_7	0.344	0.909
B_6–B_8	0.357	0.868
B_3–B_{11}	0.832	1.376
B_{11}–B_{12}	0.773	1.271
B_{12}–B_{13}	0.446	0.958
B_4–B_{14}	0.359	0.913
B_4–B_{15}	0.307	0.826

Table 6: Results of five algorithms when a three-phase short circuit occurs.

Algorithms	Total action time (s)
PSO	31.272
HSA	23.579
Basic GWO	25.195
COA-LP	28.209
Improved GWO	21.923

strategy, and heuristic parameter determination strategy proposed in this paper can effectively improve the accuracy of the Grey Wolf algorithm

(2) No matter the two-phase short circuit or three-phase short circuit occurring, the improved GWO algorithm has a better optimization effect than the other four comparison algorithms

6.3. Heuristic Parameter Adjustment Analysis. The parameter settings of the optimization algorithm directly affect the search quality and efficiency of the algorithm. It should be pointed out that the Grey Wolf algorithm has only two adjustable parameters, which can save much work compared with PSO, HSA, and other methods in the parameter adjustment.

The population and the maximum number of iterations are adjusted based on the heuristic parameters optimization strategy. The number of wolves is set to 10, 20, 30, 40, and 50, respectively, and the maximum number of iterations of each group is set to 1000. The optimizations are carried out to ensure the searching ability of the algorithm at the expense of time efficiency, and the optimal number of wolves can be determined. At the same time, the decreasing rate of the target value under the optimal number of wolves is observed to obtain the optimal iteration number.

The optimization results for the two-phase short circuit are shown in Table 7. When the population size is 30, the minimum value, average value, and standard deviation of the total operation time of protection are all the minimum, indicating that the population size of 30 is the most appropriate and has the best robustness.

The decline rate of the optimization target value is observed when the population size is 30. It could be found that the algorithm converged when the average number of iterations reached 112 times, and therefore the maximum number of iterations is set as 150.

Similarly, the population is set as 30 in the case of the three-phase short circuit. The average number of iterations is 73 as the population converges, and the maximum number of iterations is set to 100. After the heuristic parameter adjustment, the algorithm parameters have better effectiveness and robustness, which can further improve the optimization quality.

6.4. Analysis of Time Differential. The CTI is simplified in this study, which is uniformly set as 0.5 s. It should be noted that although 0.5 s is a typical time differential setting for protection, it is not optimal. Relay protection should speed up the operation time and shorten the time differential as far as possible under the condition of satisfying selectivity. Different time differentials can be selected for different protection coordination relationships. In engineering practice, it is necessary to set different time differential according to the actual system structure and protection type, combined with the experience of protection manufacturers and engineers.

The protection action results of the two-phase short circuit under different time differential are described in Table 8. It can be seen from Table 8 that reducing the time differential can shorten the total operation time of the protection. Besides, the delay error depends on the type of protection device and the characteristics of the time relay. The settings should refer to engineering experience.

Table 7: Results of heuristic parameter adjustment when a two-phase short circuit occurs.

Population size	Maximum number of iterations	Minimum total action time (s)	Average total action time (s)	Standard deviation of the total action time
10	1000	23.118	26.682	7.091
20	1000	23.561	25.780	4.219
30	1000	22.977	23.561	0.762
40	1000	23.201	24.975	3.803
50	1000	23.379	24.683	3.625

Table 8: Protection action results of the two-phase short circuit under different time differential.

CTI (s)	Total action time (s)
0.4	22.381
0.45	22.739
0.5	23.162
0.55	24.073
0.6	24.833
0.65	25.690
0.7	27.196

7. Conclusions

An optimization method based on the improved GWO is proposed to optimize the parameters setting of inverse time-limit overcurrent protection in the distribution networks with DG. According to the protection action characteristic equation and the sensitivity, speed, and selectivity of protection, the fixed value optimization model of inverse time-limit overcurrent protection for the distribution networks is established. The good point set initialization strategy, convergence factor attenuation strategy, mutation strategy, and heuristic parameters determination strategy are introduced to overcome the low convergence precision of the traditional GWO algorithm. Due to the few adjustable parameters, the workload in heuristic parameter determination is significantly reduced compared to the PSO algorithm and the HSA algorithm. Simulation results show that the proposed method has better effectiveness and robustness for both two-phase short circuits and three-phase short circuits and has good application value.

In the future, further research can be carried out from three directions: improving the action equation of inverse time limit protection, taking the time level difference as a part of the constraint conditions and optimization parameters, and exploring the better objective function.

Data Availability

All the data used in this study are presented in the manuscript. There are no extra data to be provided.

Conflicts of Interest

The authors declare that they have no conflicts of interest.

Acknowledgments

This work was supported by the World Class Urban Distribution Network Demonstration Project in Suzhou Historic District.

References

[1] C. Wei, Z. Shen, D. Xiao, L. Wang, X. Bai, and H. Chen, "An optimal scheduling strategy for peer-to-peer trading in interconnected microgrids based on RO and Nash bargaining," *Applied Energy*, vol. 275, 2021.

[2] A. M. Tsimtsios, G. N. Korres, and V. C. Nikolaidis, "A pilot-based distance protection scheme for meshed distribution systems with distributed generation," *International Journal of Electrical Power & Energy Systems*, vol. 105, pp. 454–469, 2019.

[3] S.-E. Razavi, E. Rahimi, M. S. Javadi et al., "Impact of distributed generation on protection and voltage regulation of distribution systems: a review," *Renewable and Sustainable Energy Reviews*, vol. 105, pp. 157–167, 2019.

[4] S. Beheshtaein, R. Cuzner, M. Savaghebi, and J. M. Guerrero, "Review on microgrids protection," *IET Generation, Transmission & Distribution*, vol. 13, no. 6, pp. 743–759, 2019.

[5] S. Mirsaeidi, D. M. Said, M. W. Mustafa, M. H. Habibuddin, and K. Ghaffari, "Fault location and isolation in micro-grids using a digital central protection unit," *Renewable and Sustainable Energy Reviews*, vol. 56, pp. 1–17, 2016.

[6] C. Wei, M. Benosman, and T. Kim, "Online parameter identification for state of power prediction of lithium-ion batteries in electric vehicles using extremum seeking," *International Journal of Control, Automation and Systems*, vol. 17, no. 11, pp. 2906–2916, 2019.

[7] M. N. Alam, "Adaptive protection coordination scheme using numerical directional overcurrent relays," *IEEE Transactions on Industrial Informatics*, vol. 15, no. 1, pp. 64–73, 2018.

[8] D. H. Zeng, G. Wang, J. M. Guo et al., "Adaptive current protection scheme for distribution network with inveter-interfaced distributed generators," *Automation of Electric Power Systems*, vol. 41, no. 12, pp. 86–92, 2017.

[9] Y. H. Guo, J. Jiang, C. J. Fan et al., "Improved inverse-time over-current protection for distribution network," *Electric Power Automation Equipment*, vol. 41, no. 12, pp. 86–92, 2017.

[10] V. R. Mahindara, D. F. C. Rodriguez, M. Pujiantara et al., "Practical challenges of inverse and definite-time overcurrent protection coordination in modern industrial and commercial power distribution system," *IEEE Transactions on Industry Applications*, vol. 57, no. 1, pp. 187–197, 2020.

[11] R. Guo, *Research on Optimization of Inverse Time Overcurrent Protection Based on Improved Particle Swarm Optimization Algorithm*, Yanshan University, Qinghuangdao, China, 2019.

[12] K. J. Yang and C. Huang, "Optimal setting method of inverse time over-current protection for distribution network," *Electric Power Automation Equipment*, vol. 39, no. 3, pp. 163–168, 2019.

[13] J. Yi, *Research on Optimal Coordination of Directional Over-current Relays in Microgrids Considering Different Network Topologies*, Huazhong University of Science & Technology, Wuhan, China, 2019.

[14] R. Jalilzadeh Hamidi, A. Ahmadian, R. Patil et al., "Optimal time-current graded coordination of multistage inverse-time overcurrent relays in distribution networks," *International Transactions on Electrical Energy Systems*, vol. 29, no. 5, Article ID e2841, 2019.

[15] E. C. Piesciorovsky and N. N. Schulz, "Fuse relay adaptive overcurrent protection scheme for microgrid with distributed generators," *IET Generation, Transmission & Distribution*, vol. 11, no. 2, pp. 540–549, 2017.

[16] S. Mirjalili and A. Lewis, "Grey wolf optimizer," *Advances in Engineering Software*, vol. 69, no. 3, pp. 46–61, 2014.

[17] M. H. Nadimi-Shahraki, S. Taghian, and S. Mirjalili, "An improved grey wolf optimizer for solving engineering problems," *Expert Systems with Applications*, vol. 166, 2021.

[18] Q. Al-Tashi, S. J. Abdul Kadir, H. M. Rais, S. Mirjalili, and H. Alhussian, "Binary optimization using hybrid grey wolf optimization for feature selection," *IEEE Access*, vol. 7, pp. 39496–39508, 2019.

[19] H. Faris, I. Aljarah, M. A. Al-Betar, and S. Mirjalili, "Grey wolf optimizer: a review of recent variants and applications," *Neural Computing and Applications*, vol. 30, no. 2, pp. 413–435, 2018.

[20] Z. Feng, D. Pei, and W. Wang, "Face recognition by support vector machine optimized by an improved grey wolf algorithm," *Computer Engineering & Science*, vol. 41, no. 6, pp. 1057–1063, 2019.

[21] H. N. Zhang, X. M. You, S. Liu et al., "Ant colony algorithm based on dynamic evolution and interactive learning mechanism," *Information and Control*, vol. 49, no. 3, pp. 297–305, 2020.

[22] N. Mittal, U. Singh, and B. S. Sohi, "Modified grey wolf optimizer for global engineering optimization," *Applied Computational Intelligence and Soft Computing*, vol. 2016, no. 4598, 16 pages, Article ID 7950348, 2016.

[23] F. M. Tan, J. J. Zhao, and Q. Wang, "A grey wolf optimization algorithm with improved nonlinear convergence," *Microelectronics & Computer*, vol. 36, no. 5, pp. 89–95, 2019.

Hindawi
Complexity
Volume 2021, Article ID 2396929, 14 pages
https://doi.org/10.1155/2021/2396929

Research Article

Modeling and Control Strategy for Multiterminal Flexible DC Distribution Network with Echelon Utilization Power Battery

Min Mou,[1] **Yuhao Zhou**,[1] **Wenguang Zheng**,[1] **Yurong Xie**,[1] **Shipeng Wang**,[1] **Lili Liu**,[1] **and Chengzhi Wei**[2]

[1]*Huadian Electric Power Research Institute Co, Ltd, Hangzhou 310000, Zhejiang, China*
[2]*Electric Power Research Institute of CSG, Guangzhou 510080, Guangdong, China*

Correspondence should be addressed to Min Mou; min-mou@chder.com

Received 8 June 2021; Revised 2 July 2021; Accepted 17 July 2021; Published 27 July 2021

Academic Editor: Xiaoqing Bai

With the integration of distributed renewable energy to the distribution network and the development of multiterminal flexible DC transmission technology, multiterminal flexible DC distribution network has broad application prospects. At the same time, with the rapid development of new energy vehicles, the echelon utilization of power battery has become a research hotspot. By analyzing the characteristics of flexible DC distribution network and echelon utilization battery, the structure and control strategy of modular multilevel converter (MMC), DC solid-state transformer, photovoltaic power generation, wind power generation, and echelon utilization battery energy storage system are established, respectively, in this paper. To achieve a DC network connection of various types of power supply and load, this paper proposes a starting method of multiterminal flexible DC distribution network and a cooperative control strategy of the wind-solar-storage system. A six-terminal ring-shape DC distribution network model is built in real-time digital simulation (RTDS) platform. The simulation results show that the modeling methods and control strategies of each component in the real-time simulation model meet the operation requirements of the multiterminal flexible DC distribution network, which provides a reference for the construction and research of the flexible DC distribution network.

1. Introduction

With the development of renewable energy technology and energy storage technology, modern distribution network will contain more and more distributed power and energy storage. The common distributed power sources include photovoltaic cells, fuel cells, wind turbines, and gas turbines, and the power generated by these power sources is DC or can be converted into DC after simple rectification. At the same time, the modern load situation has changed. More and more loads need to use DC power supply mode, such as LCD TV, LED lighting, electric vehicle, personal computer, and mobile phone; the development of DC power grid can greatly reduce the flow change link, reduce the load access cost, improve the power conversion efficiency and power quality, improve the energy utilization efficiency, and fully demonstrate the economic benefits and utilization value of distributed energy. With the increase in new energy generation rate, DC distribution will play an increasingly important role in the future power grid [1].

At present, the research on the flexible DC distribution network system is in the experimental exploration stage at home and abroad [2, 3]. For the simulation design of DC distribution network, the paper [4] based on the demonstration project of Shenzhen MMC-DCDS proposes the starting and control strategy for the flexible DC distribution network, which is based on the system operation characteristics. The document [5] proposes the protection control system design scheme and corresponding control protection strategy of the converter station in the DC distribution network, but neither of them involves the research of the control strategy of the distributed power supply. The paper [6] studies the control and protection strategy of DC distribution network and builds the offline simulation model of the flexible DC distribution system based on MATLAB, which is used to verify the correctness of control strategy and the

reliability of protection scheme, but offline simulation is not suitable for simulating high switching frequency power electronic devices. The papers [2, 7] study and analyze the modeling and real-time simulation technology of the flexible DC distribution network with multiterminal, in which the real-time simulation model of DC distribution network based on the real-time Lab (RT-Lab) is established. The above research studies that involve the modeling of key equipment of the DC distribution system with wind-solar-storage and the coordination control strategy of the system are relatively few.

Based on the analysis of the key equipment of DC distribution network (including distributed generation, DC transformer, converter, and other components), this paper establishes a variety of load types of DC distribution network, such as modular multilevel converter, echelon utilization battery storage system, wind power generation device, photovoltaic power generation device, and synchronous motor, which are based on the control modes of vdc-q, P-Q, VF, and so on, so as to realize the DC network of multiple types of power supply and load. Based on the RTDS simulation platform, a six-terminal "ring" DC distribution network model is built to study the start-up and multisource coordinated control strategy of multiterminal DC distribution network. Finally, the simulation validation is carried out.

2. Modeling of Components in Flexible DC Distribution System

The multiterminal flexible DC distribution system is mainly composed of converter, DC transformer, distributed power supply (such as photovoltaic power generation system, wind power generation system, and energy storage device), and DC load.

2.1. Modular Multilevel Converter. At present, there are three kinds of voltage source converters used in flexible DC transmission projects: two-level voltage source converter (VSC), three-level VSC, and modular multilevel converter (MMC) [8]. MMC converter has the advantages of easy expansion, small harmonic distortion, low switching loss, no commutation failure, and strong fault handling ability [9–12]. It has been widely used in recent years.

The main circuit topology of three-phase MMC is shown in Figure 1(a). Each phase contains two arms of upper and lower bridge, and there are six bridge arms in all three phases. Each bridge arm is composed of N submodules (SM) and a circulation reactor in series. The structure of SM is shown in Figure 1(b), which consists of a half bridge with switching element IGBT and a DC energy storage capacitor.

MMC modeling is mainly divided into three modules: MMC control module, valve module, and main circuit. The MMC control module is mainly responsible for the active and reactive power control of the converter and then outputs the voltage amplitude and phase of the modulated wave corresponding to the power instruction value [13, 14]. The valve module uses the number of submodule corresponding to the former modulation waveform to control the state of each submodule by a set of optimization algorithm so as to realize commutation. In addition, the control of MMC converter also includes some auxiliary control, such as start-up, phase-locked, internal circulation suppression, and negative sequence voltage suppression. The control strategy structure of MMC is shown in Figure 2.

2.2. DC Solid-State Transformer. DC solid-state transformer (DCSST) based on power electronics technology can realize the matching of different voltage levels in DC distribution network. In order to improve the power density, a dual-active-bridge (DAB) structure can be used for the applications requiring bidirectional power transmission. DCSST is mainly composed of N identical DAB converters; each DAB converter consists of two full Bridges and one high-frequency isolation transformer, as shown in Figure 3. N DAB converters are connected in series at the high voltage end to connect with the high voltage DC bus and connected in parallel at the low voltage end to connect with the low voltage DC bus so as to increase the voltage level of the high voltage side by n times and the current level of the low voltage end by n times.

DAB in DCSST is controlled by phase shift, and energy transmission is realized by the size of phase shift between two cell bridges. The control block diagram of DAB with constant voltage and low voltage is shown in Figure 4. Among them, V^*_{sec} and V_{sec} represent the standard and measured values of the DC voltage on the secondary side of DAB, respectively; δ_1 represents the voltage phase angle at the midpoint of the bridge arm on the primary side; δ_2 represents the voltage phase angle at the midpoint of the bridge arm on the secondary side; and $\Delta\delta$ is the phase angle difference between two commutator bridge elements.

2.3. Photovoltaic Power Generation Device. Photovoltaic power generation device is a kind of power generation device that converts light energy into electric energy. The photovoltaic power generation in the flexible DC distribution system is mainly composed of photovoltaic panels and Boost links, as shown in Figure 5.

The output voltage and current of photovoltaic panels change with the change of light intensity and cell junction temperature, which has strong nonlinear characteristics, and there is a maximum power output point under a specific working condition. When the light intensity and the cell junction temperature change, the output voltage and output current of the photovoltaic array will also change, so the output power will also change. In order to make full use of solar energy, it is necessary to make the working point of the photovoltaic cell fall to the maximum power point, that is, maximum power point tracking (MPPT) control under the circumstances of light intensity and temperature change [15]. The MPPT algorithm was used to calculate the voltage V^*_{pv} of the maximum power point under the corresponding lighting and temperature. The control block diagram of the photovoltaic power generation device is shown in Figure 6. V_{pv} represents the DC voltage output by the photovoltaic

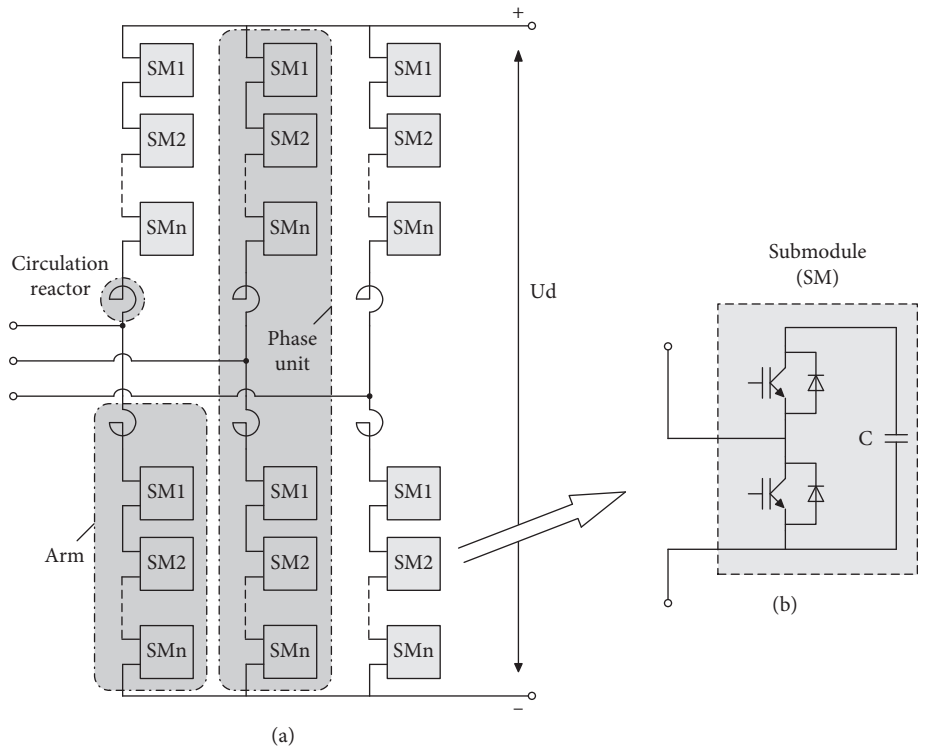

Figure 1: Main circuit structure of three-phase MMC.

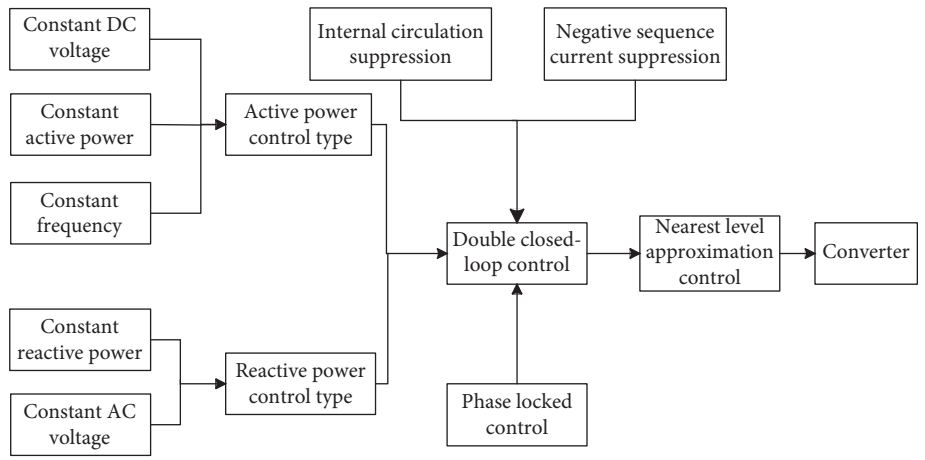

Figure 2: Control strategy of modular multilevel converter.

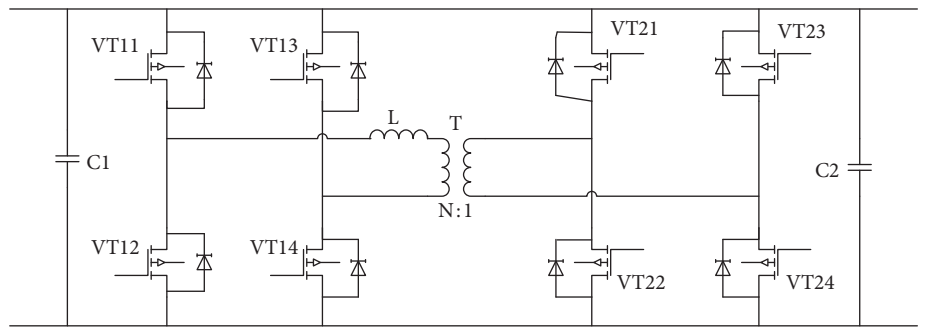

Figure 3: Circuit of dual-active-bridge.

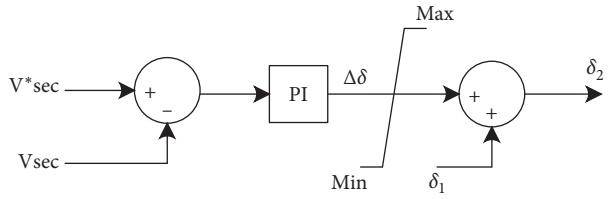

Figure 4: Control strategy of dual-active-bridge.

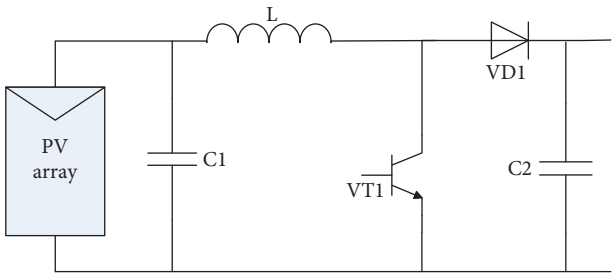

Figure 5: PV generation system with Boost converter.

power generation device, and Duty is the on-time DUTY ratio of the controllable device in the Boost circuit [16].

2.4. Wind Power Generation Device. Wind power generation equipment mainly includes wind turbine, gearbox, generator, and converter. The common wind turbines are mainly doubly fed wind turbines and permanent magnet synchronous generators (PMSGs). PMSG has no rotor winding, no excitation power supply, no collector ring, and carbon brush, which simplifies the structure and improves the conversion efficiency. The structure of PMSG in the flexible DC distribution system is shown in Figure 7.

PMSG is a full power converter. Under different wind speeds, the maximum power output speed of the fan is unique. Therefore, the maximum mechanical power can be obtained by adjusting the fan speed; that is, MPPT control is adopted to improve the energy utilization rate of the system. The control strategy of PMSG is shown in Figure 8. Among them, ω^* and ω, respectively, represent the reference value and measured value of wind turbine speed, i_{sa}, i_{sb}, and i_{sc}, respectively, represent the three-phase current on the generator side, u_{sa}, u_{sb}, and u_{sc}, respectively, represent the converter three-phase reference voltage, ω_e represents the angular speed of synchronous motor, L_s represents the stator inductance, Ψ_f represents the rotor permanent magnet flux, i_{sd}^* and i_{sd} represent D-axis reference current and actual current, respectively, i_{sq}^* and i_{sq} represent q-axis reference current and actual current, respectively, u_{sd}^* and u_{sd} represent d-axis reference voltage and actual voltage, respectively, and u_{sq}^* and u_{sq} represent q-axis reference voltage and actual voltage, respectively [17].

2.5. Energy Storage of Echelon Utilization Battery. At present, the commonly used energy storage device is lithium battery, which depends on the concentration difference of Li+ to complete the charge and discharge [18]. The architecture model of echelon utilization battery energy storage in the flexible DC distribution system is shown in Figure 9. In the echelon battery energy storage system, the voltage of each battery pack is inconsistent, so the DC/DC converter is needed to increase or decrease the voltage, and then the energy storage system can be connected to the grid. The DC/DC converter in this architecture adopts multichannel interleaving technology, and each battery pack can be equipped with a DC/DC branch to realize the independent charge and discharge, thus reducing the short board effect and safety problems caused by the poor consistency of battery pack in echelon utilization [19]. The working principle of DC/DC converter in the energy storage system is as follows: when discharging, the buck circuit IGBT turns off, the Boost circuit IGBT works, the DC/DC circuit acts as the Boost circuit, and the current flows from the battery to the load or grid; when charging, IGBT of Boost circuit is off, IGBT of buck circuit works, DC/DC circuit is buck circuit, and current flows from power supply to battery.

The operation mode that the energy storage system is connected to grid is constant power control mode [20]. The energy storage converter sends the received output power command to DC/DC converter. The controller of DC/DC converter obtains the SOC of each branch battery pack and sends power command to each DC/DC branch according to the SOC of each branch battery pack. The DC/DC branch power system realizes the command tracking accurately through the power closed-loop control [21].

3. Modeling and Control Strategy of Six-Terminal "Ring" Flexible DC Distribution System

3.1. Modeling of Flexible DC Distribution System. The six-terminal "ring" flexible DC distribution system is shown in Figure 10 [22–25]. Terminal 1 and terminal 3 are connected to 10 kV AC distribution network, terminal 2 is connected to AC load, terminal 4 is connected to photovoltaic power generation and energy storage device, terminal 5 is connected to 0.38 kV AC microgrid composed of load and synchronous generator, and terminal 6 is connected to DC load, wind power, and energy storage device. Considering the operation characteristics of each terminal, MMC converter is used for terminals 1, 2, 3, and 5, while DC transformer is used for terminals 4 and 6. The load at terminal 2 is AC resistive load, and the load at terminal 6 is DC load for the plant. The parameters and operation mode of each terminal are shown in Table 1 [26].

3.2. Control Strategy of Multiterminal DC Distribution System

3.2.1. Start-Up Control Strategy. In the start-up process of the flexible direct current system, appropriate start-up control and current limiting measures must be taken to

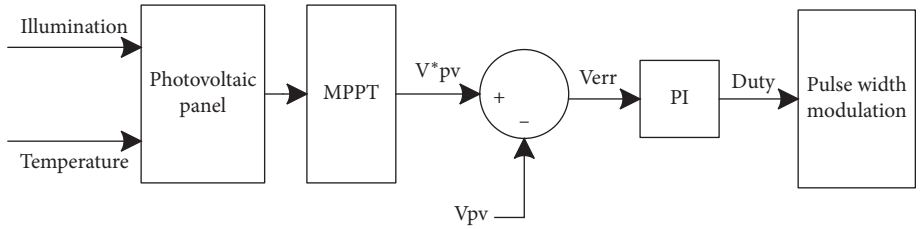

Figure 6: Control strategy diagram of the PV generation system with Boost converter.

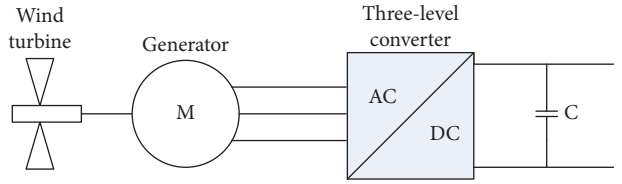

Figure 7: Structure of PMSG-based wind turbine.

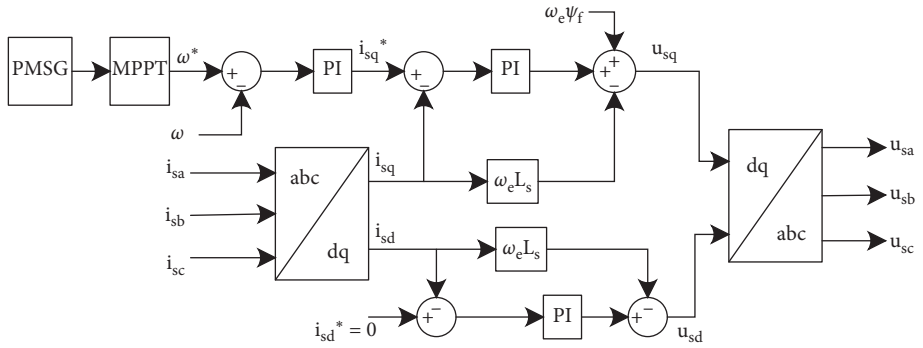

Figure 8: Control strategy of PMSG.

suppress the phenomenon of overvoltage and overcurrent. The goal of starting control is to make the DC voltage of the flexible DC system rise quickly to the normal working voltage by means of control methods and auxiliary measures but cannot produce the excessive charging current and voltage overshoot phenomenon.

A feasible scheme is to connect the starting resistor in series in the charging loop at start-up, charge the DC capacity through the AC side system voltage, and remove the starting resistor at the end of start-up to reduce the loss, as shown in Figure 11.

The whole starting process of the converter station is divided into two areas: uncontrollable current and controllable current, as shown in Figure 12. In the area where the current is not controllable, the converter station realizes current limit through series starting resistor. In the controlled area, the converter station realizes current limiting by controlling the limiting link of the outer loop controller of the system.

The starting control flow of a six-terminal "ring" DC distribution system is shown in Figure 13.

3.2.2. Multisource Coordinated Control Strategy. Multisource coordination is a kind of power supply method which adopts multiple types of distributed power supply and utilizes the complementary characteristics of different distributed power supplies to improve the output characteristics of distributed power supply [27, 28]. For example, solar energy and wind energy have strong intermittency and fluctuation, respectively, so the output power of solar power generation device and wind power generation device also has intermittency and fluctuation. This kind of distributed power generation device with unstable output will affect the stable and reliable operation of the distribution system. Therefore, photovoltaic power generation and wind power generation devices equipped with an appropriate amount of the energy storage system can improve the output characteristics of distributed power generation, making photovoltaic power generation and wind power generation into controllable and stable power supply.

4. Simulation Results and Analysis

Based on the real-time digital simulation platform RTDs, a six-terminal "ring" DC distribution system model is built. RTDS has an MMC valve model based on FPGA, which is conducive to simulate the MMC valve with a large number of switching elements and the internal pressure balancing problem of the analog valve. In this six-terminal model, the

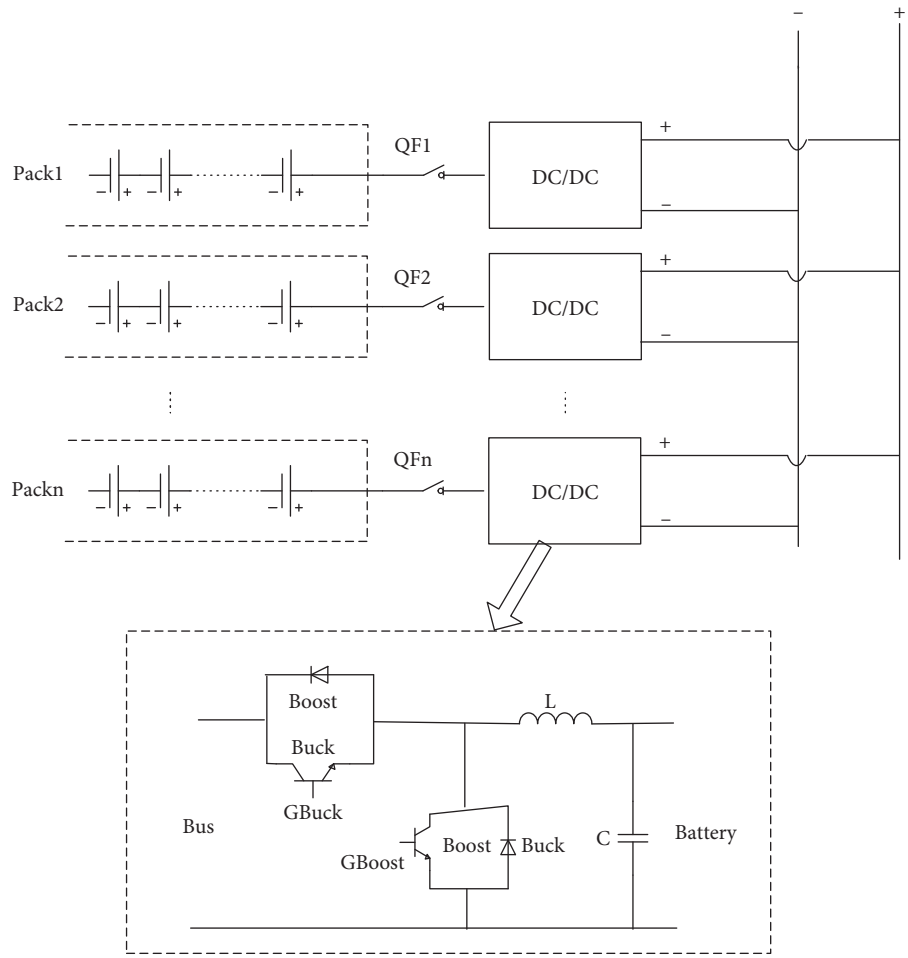

Figure 9: Architecture diagram of the echelon utilization battery energy storage model.

1-terminal and 3-terminal converter valves run in FPGA-based hardware, and the other parts run in RTDS.

4.1. The Simulation of Start-Up. When the system starts up, the auxiliary switches at terminal 1, 2, 3, and 5 are closed to charge the MMC of the whole DC distribution network; when the DC voltage reaches 0.73 p.u. (the reference value is 10 kV), the converter station at the first end unlocks and continues to charge the DC network. Until the DC voltage reaches 1 p.u., the main switch at the first end is closed and the other ends are unlocked so that the system enters the no-load operation stage. During system start-up, the waveform of DC voltage and charging current at terminal 1 of constant DC voltage is shown in Figure 14. According to the simulation waveform, it takes about 40°s for terminal 1 voltage to rise from 0 p.u. to 1 p.u., and the maximum charging current peak is 0.04 p.u. (the reference value is 1 kA).

When the terminal 2 that is constant frequency voltage (VF) terminal is merged into the DC system, the main switch at the terminal 2 is closed and the AC side voltage is raised according to the established slope to realize the grid-connected control of the two-terminal converter station. The simulation waveforms of at terminal 1 and 2 are shown in Figure 15. The simulation results show that the voltage of terminal 1 is basically stable at 1 p.u., and the DC power of terminal 1 is 0~−1 p.u. (the reference value is 10 MW). The effective value of the terminal 2 AC voltage varied from 0 to 0.99 p.u. (AC voltage reference value was 10 kV), and the terminal 2 DC power varied from 0 to 0.94 p.u., which is lasting for 5 s.

4.2. Power Step. Assume that the operation state of the DC distribution network supplied by this double-ended power source is as follows: (1) terminal 1 is the constant voltage terminal; (2) terminal 5 is AC microgrid that includes 3 MW load and 1 MW synchronous generator, which needs to absorb 2 MW active power from the grid; (3) terminal 3 is the constant power terminal, and the output power is 0 MW; (4) terminal 4 is the optical storage access terminal, which is set to transmit 3 MW active power to the power grid; (5) terminal 6 is connected to wind power and energy storage device; and (6) terminal 2 is in the no-load operation stage at this time.

4.2.1. Power Step of Converter Valve. Suppose that at this time, the power of terminal 3 which is the constant power terminal will step from 0 MW to 6 MW and terminal 6

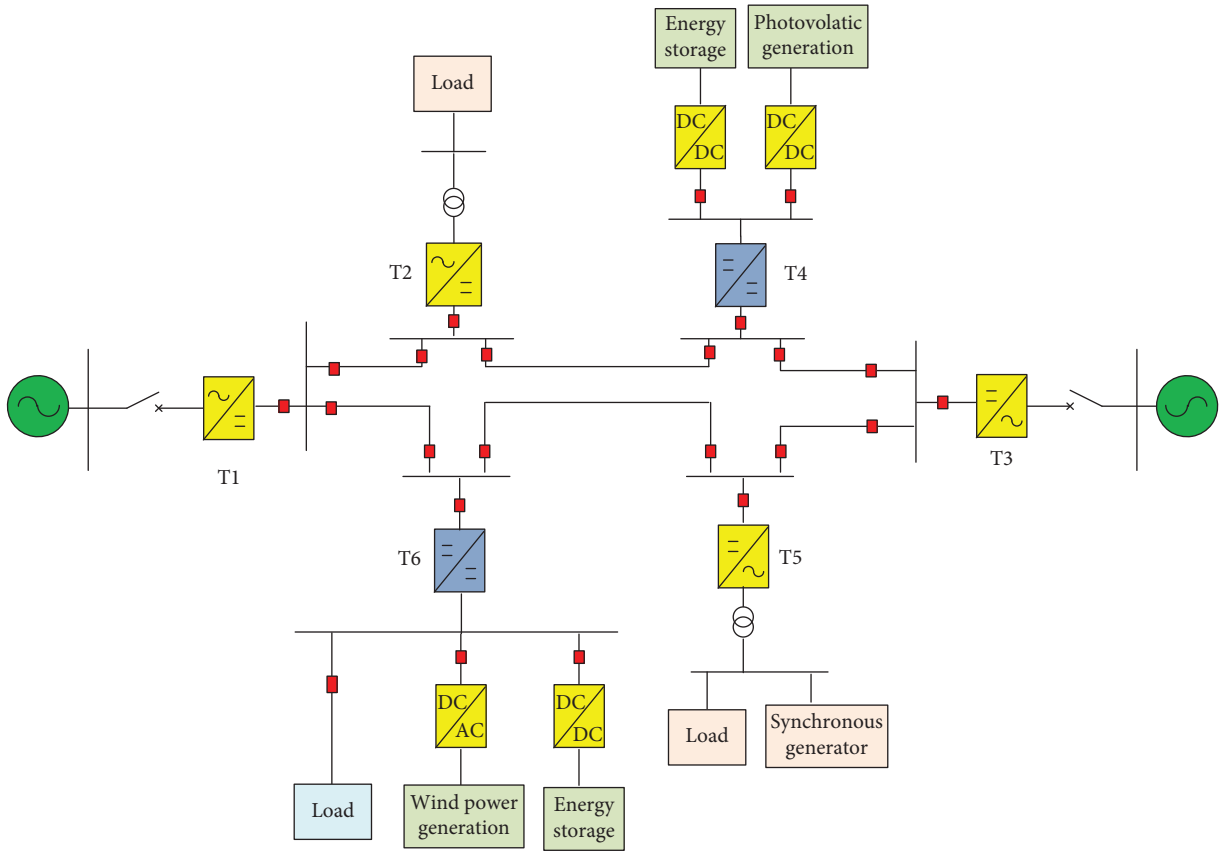

Figure 10: The topology of six-terminal ring-shape DC distribution network.

Table 1: The parameters and control mode of six-terminal ring-shape DC distribution network.

Terminal	Control mode	Load type	Voltage grade (kV)	Capacity (MW or MVA)	Comments
1	Constant DC voltage and constant reactive power	AC power grid	AC: 10 DC: ±10	Converter: 10	Connect to infinity power supply
2	Constant frequency, constant AC voltage	Load	AC: 0.38 DC: ±10	AC load: 3	Connected to AC resistive load
3	Constant active power, constant reactive power	AC power grid	AC: 10 DC: ±10	Converter: 10	Connect to infinity power supply
4	Constant low voltage DC voltage or constant power	Photovoltaic power generation, energy storage	DC: ±1.5	Photovoltaic power generation: 4 Energy storage: 4	Photovoltaic output according to the light curve
5	Constant frequency, constant AC voltage	Synchronous generator, load	AC: 0.38 DC: ±10	Load: 3 Synchronous generator: 1	The load is variable
6	Constant low voltage DC voltage or constant power	Wind power generation, energy storage, load	DC: ±1.5	Wind power generation: 3 Energy storage: 4 Load: 1	The fan control mode is changed from constant speed to constant power

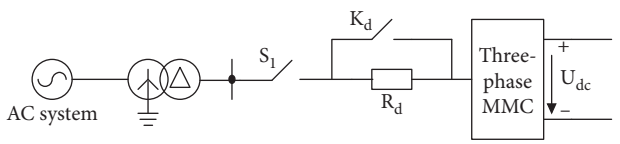

Figure 11: Structure of AC side converter station with start-up circuit.

transmits 0 MW active power to the power grid. The system simulation waveform is shown in Figure 16. The simulation results show that the DC voltage of the system is stable at 1 p.u. after 3 s. The secondary side voltage (reference value 1.5 kV) of DC transformers at terminal 4 and terminal 6 is basically stable at 1 p.u. The DC power transmission at each terminal can also be stable in a short time.

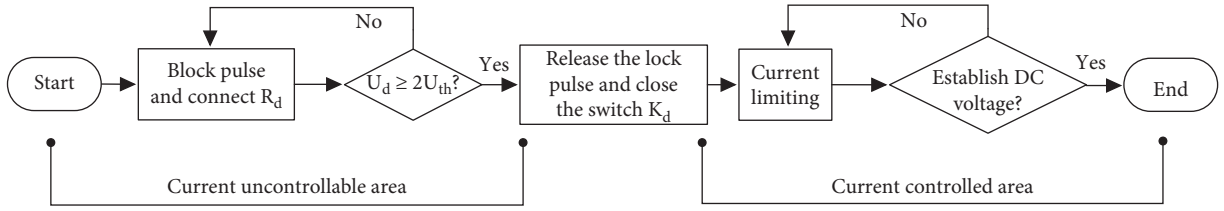

Figure 12: Diagram of start-up control strategy of VSC-HVCD.

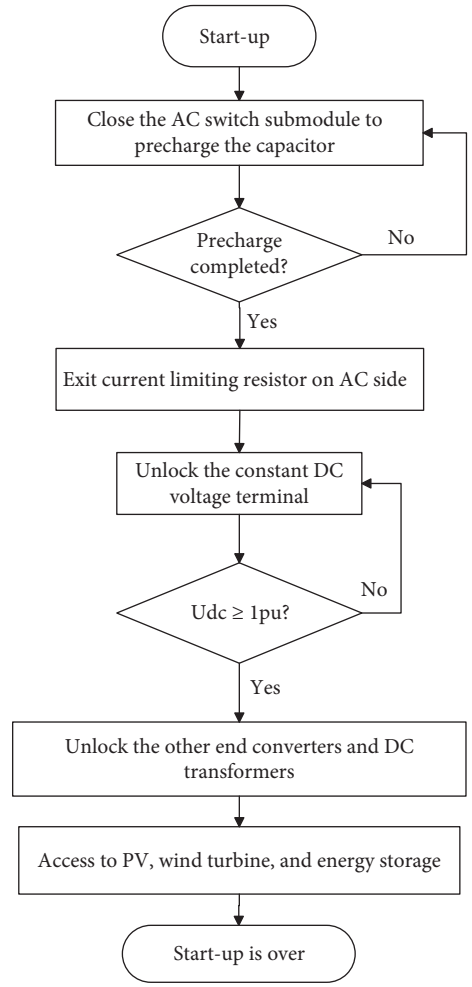

Figure 13: Start-up flow chart of the DC distribution system.

4.2.2. Power Step of Load. Based on the above experiments, the load switching experiment is carried out at terminal 5, and the 3 MW load carried by the terminal 5 is switched off and put into operation within 10 s. The simulation waveform is shown in Figure 17. According to the simulation waveform, when the load switching experiment is carried out at terminal 5, each terminal can quickly return to the stable operation state.

4.3. Multisource Coordinated Control Strategy. When the DC distribution system starts the coordinate control strategy of photovoltaic power generation, energy storage, wind power generation, and energy storage, the terminal 4 and terminal 6 are a stable power source for the whole system. This paper sets the power transmitted to the system at terminal 4 as 3 MW and the temperature as 25°C. The power output of the photovoltaic device changes with the illumination intensity. The output power waveform of the photovoltaic and energy storage at terminal 4 is shown in Figure 18. It can be seen from Figure 18 that the energy storage device can quickly respond to the power change of the photovoltaic device so that the output power of the terminal 4 is stable.

This paper sets the power transmitted to the system at terminal 6 as 4 MW. The output power of the wind power generation device changes with the wind speed and

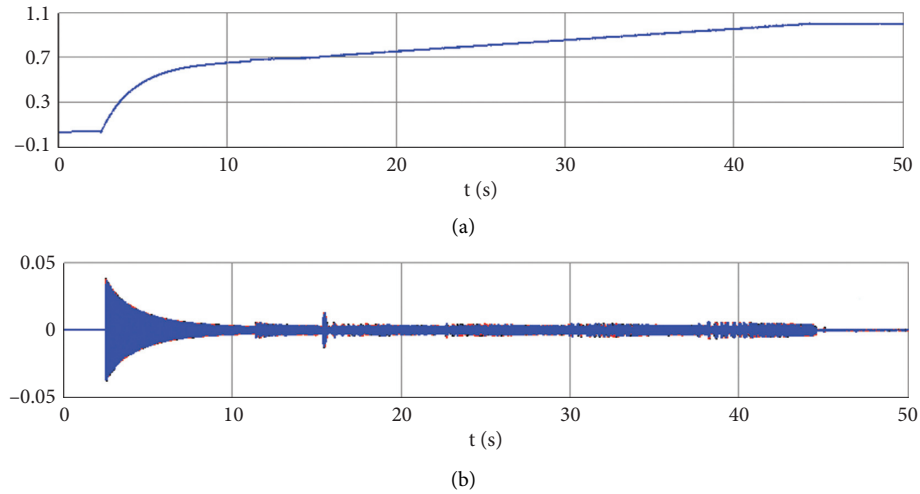

Figure 14: DC voltage and AC charging current waveform of terminal 1 during start-up: (a) DC voltage unit value at terminal 1; (b) AC side charging current unit value at terminal 1.

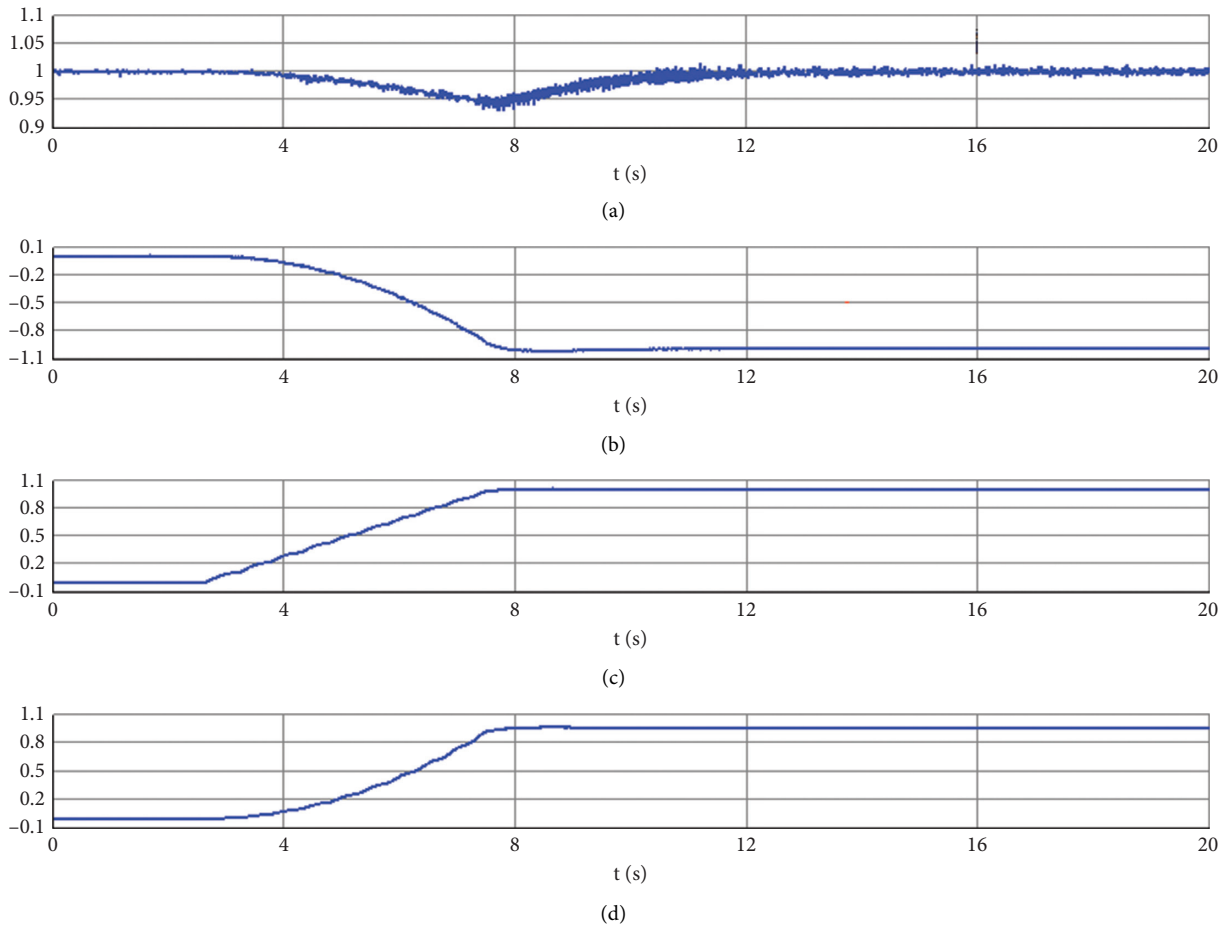

Figure 15: Voltage and power wave form of terminal 1 and terminal 2 when terminal 2 is put into operation: (a) DC voltage unit value at terminal 1; (b) active power unit value at terminal 1; (c) AC voltage RMS unit value at terminal; (d) active power unit value at terminal 2.

direction. The output power waveform of the wind power and energy storage at terminal 6 is shown in Figure 19. As can be seen, the output power of the energy storage device can quickly track the output power of the wind power generation device, thus ensuring that the output power at terminal 6 is constant.

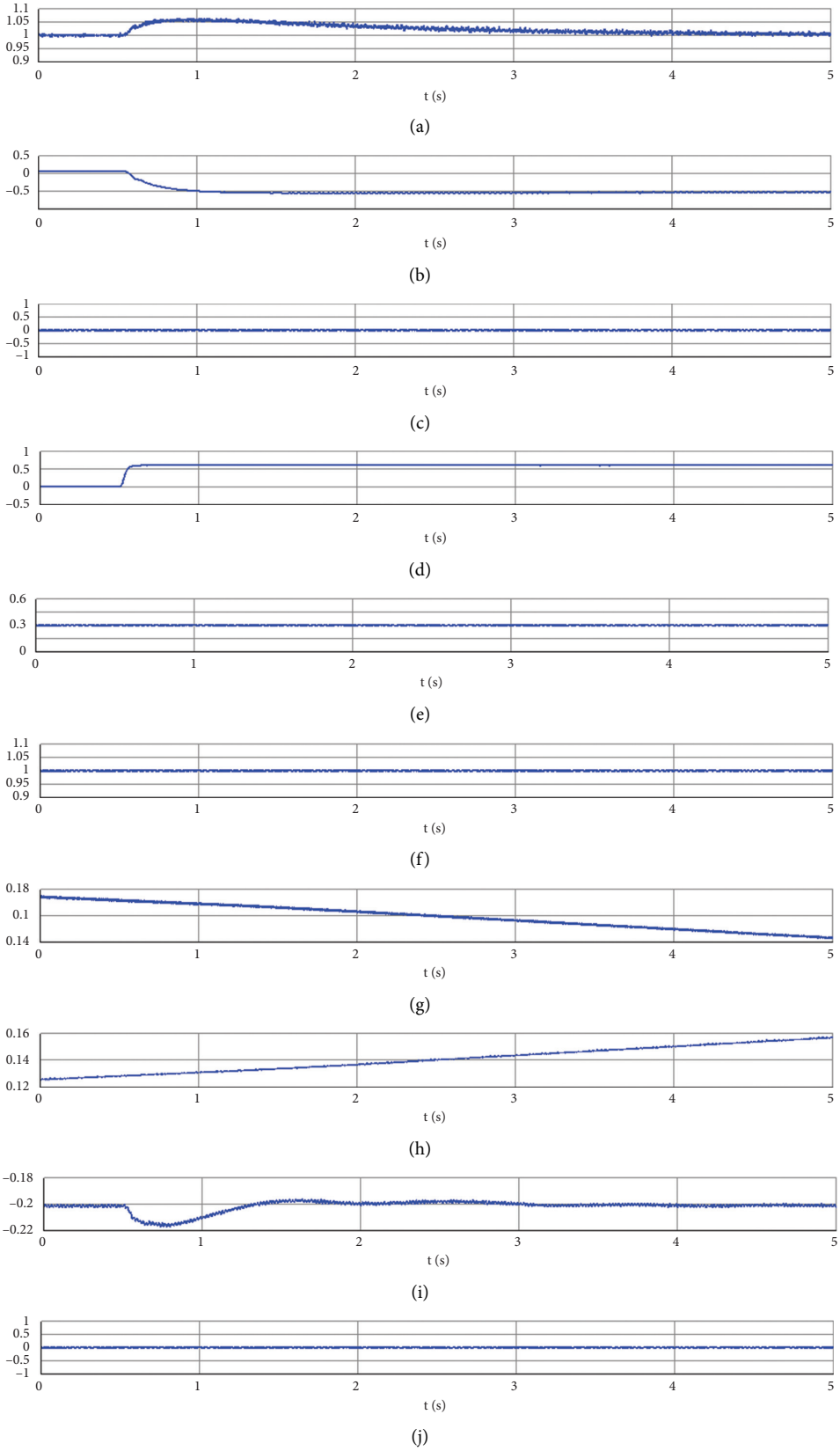

Figure 16: Continued.

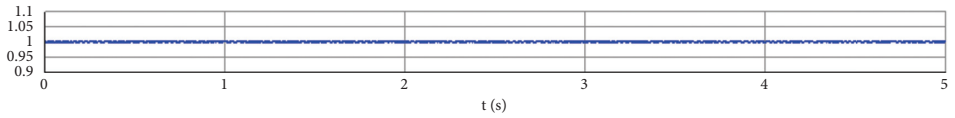

(k)

Figure 16: DC voltage and power waveform of the system when power of commutation valve step changes: (a) DC voltage unit value at terminal 1; (b) active power unit value at terminal 1; (c) active power unit value at terminal 2; (d) active power unit value at terminal 3; (e) active power unit value at terminal 4; (f) DC voltage unit value of the DC transformer secondary side at terminal 4; (g) output power unit value of photovoltaic device at terminal 4; (h) output power unit value of energy storage at terminal 4; (i) active power unit value at terminal 5; (j) active power unit value at terminal 6; (k) DC voltage unit value of the DC transformer secondary side at terminal 6.

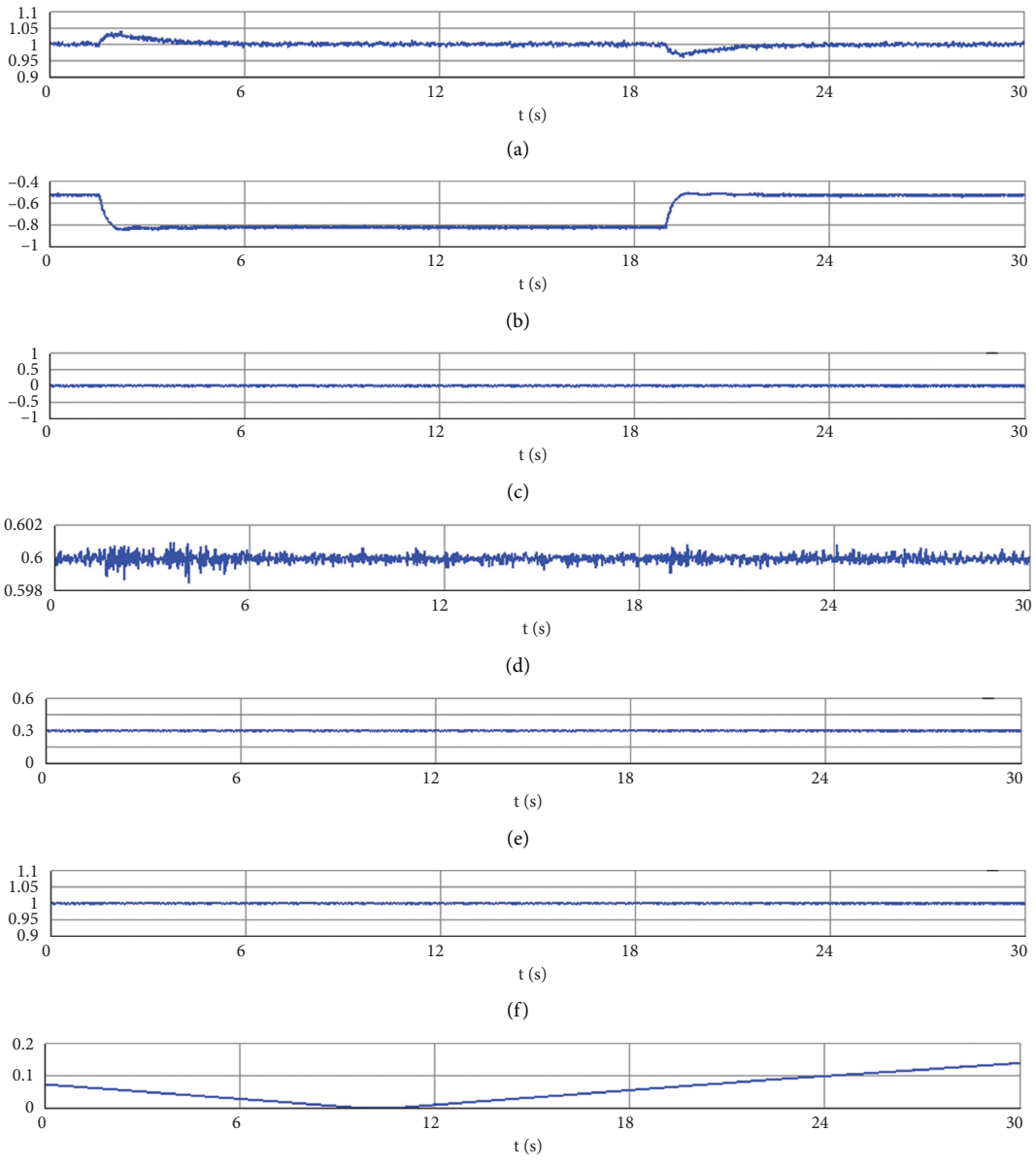

Figure 17: Continued.

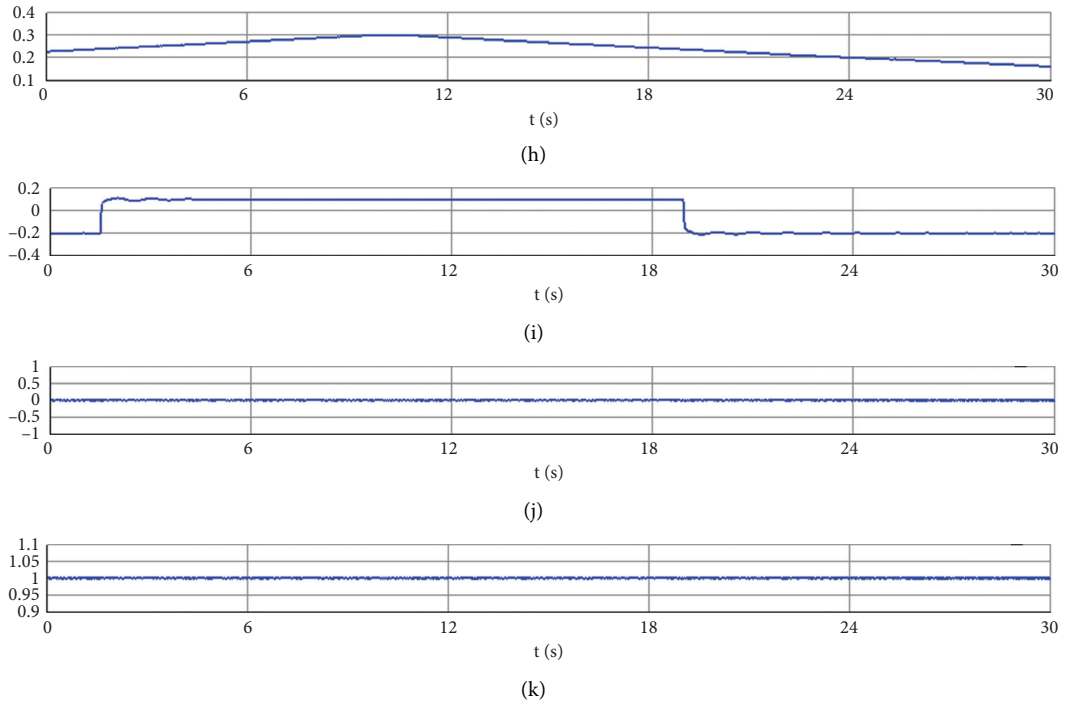

Figure 17: DC voltage and power waveform of the system when load changes at terminal 5: (a) DC voltage unit value at terminal 1; (b) active power unit value at terminal 1; (c) active power unit value at terminal 2; (d) active power unit value at terminal 3; (e) active power unit value at terminal 4; (f) DC voltage unit value of the DC transformer secondary side at terminal 4; (g) Output power unit value of photovoltaic device at terminal 4; (h) Output power unit value of energy storage at terminal 4; (i) Active power unit value at terminal 5; (j) active power unit value at terminal 6; (k) DC voltage unit value of the DC transformer secondary side at terminal 6.

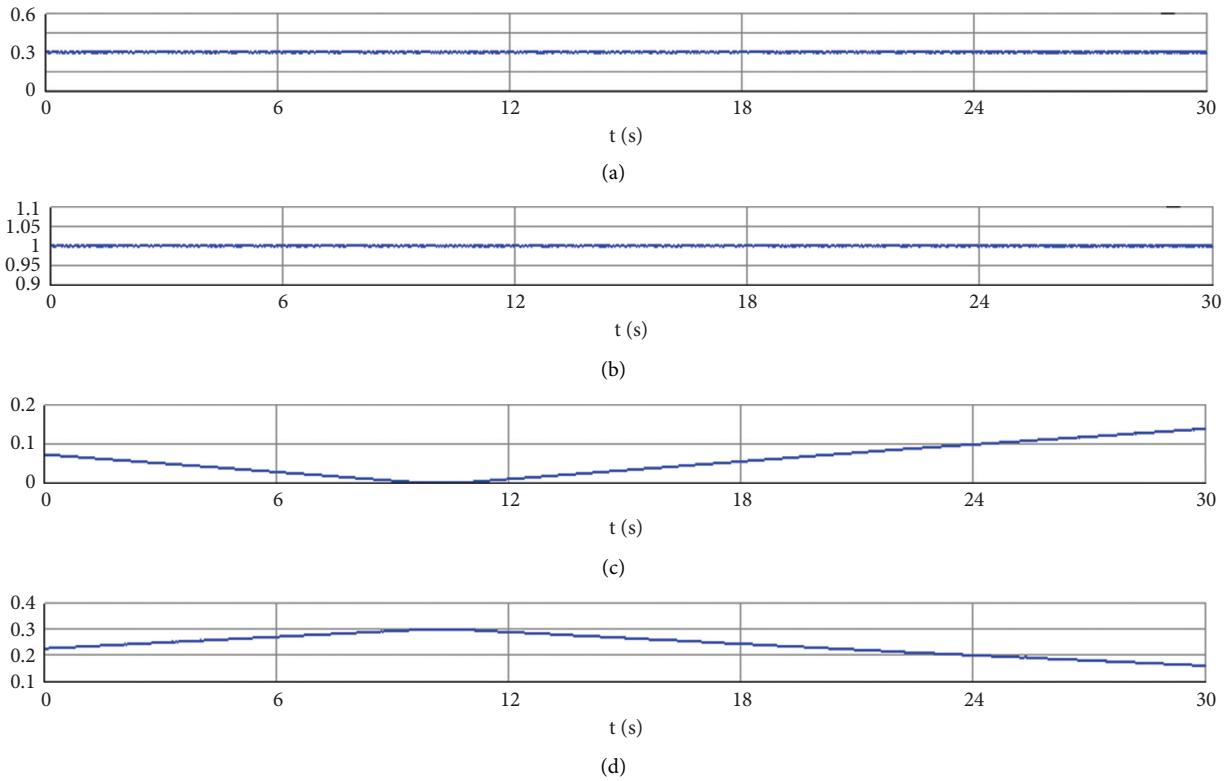

Figure 18: Waveforms of coordinating control of PV generation and energy storage systems at terminal 4: (a) active power unit value at terminal 4; (b) DC voltage unit value of the DC transformer secondary side at terminal 4; (c) output power unit value of photovoltaic device at terminal 4; (d) output power unit value of energy storage at terminal 4.

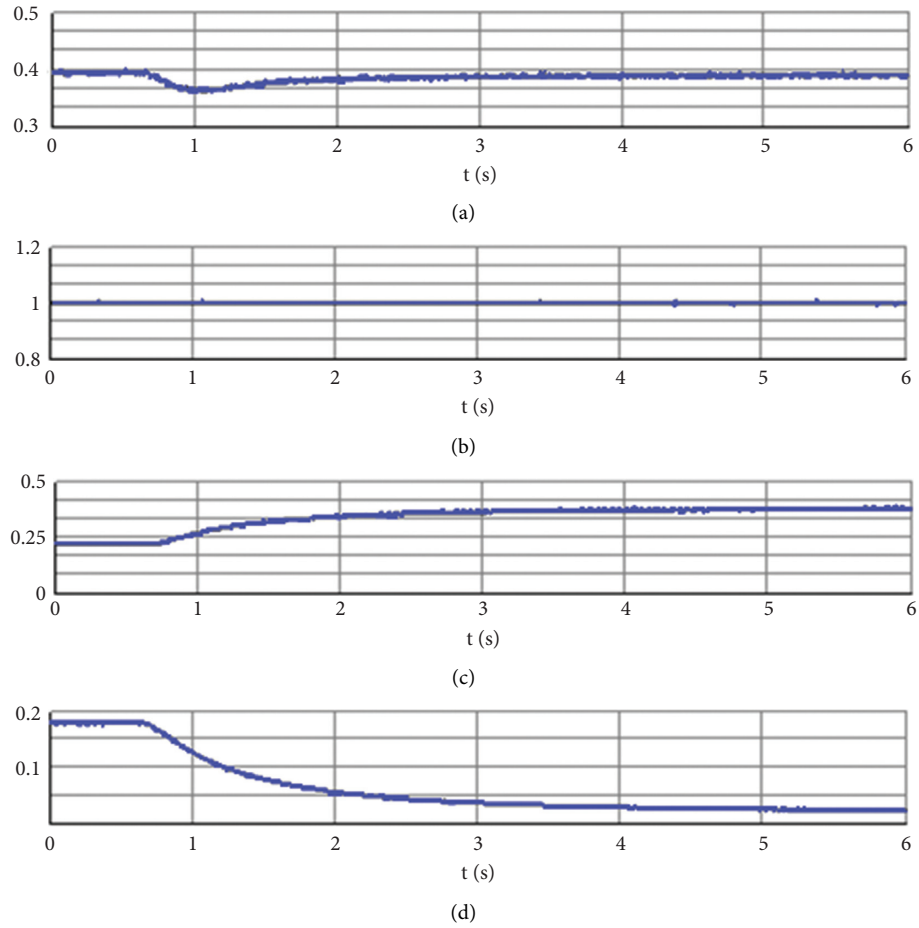

Figure 19: Waveforms of coordinating control of wind power generation and energy storage systems at terminal 6: (a) active power unit value at terminal 6; (b) DC voltage unit value of the DC transformer secondary side at terminal 6; (c) output power unit value of energy storage at terminal 6; (d) output power unit value of wind turbine generator at terminal 6.

5. Conclusion

The DC distribution system is the key link to ensure power quality, improve operation efficiency, and innovate service content. The models of modular multilevel converter, DC solid-state transformer, photovoltaic power generation device, wind power generation device, and energy storage device established in this paper are consistent with the basic characteristics of the actual device. The start-up strategy can make the multiterminal DC distribution system put into operation quickly and smoothly. Multisource coordinated control strategy can greatly improve the economic benefits of the DC distribution system operation and make the system operate stably. Therefore, the structure and control strategy of each component as well as the system start-up and multisource coordinated control strategy adopted in this paper are correct and effective, which lays a solid foundation for the subsequent control and protection research of the complex DC distribution system. The theoretical and technical problems of planning and design, dispatching control, and relay protection in the DC distribution network need to be further studied.

Data Availability

The data used to support the findings of this study are included within the article.

Conflicts of Interest

The authors declare that there are no conflicts of interest.

Acknowledgments

This work was supported in part by National Natural Science Foundation of China (51807179) and by S&T Major Project of Inner Mongolia Autonomous Region in China (2020ZD0018).

References

[1] Q. Song, B. Zhao, W. Liu et al., "An overview of research on smart DC distribution power network," *Proceedings of the CSEE*, vol. 33, no. 25, pp. 9–19, 2013.

[2] Y. Yu, Y. Jin, Q. Jiang et al., "RT-LAB based modeling and simulation analysis of flexible DC distribution network,"

Power System Protection and Control, vol. 43, no. 19, pp. 125–130, 2015.

[3] G. Tang, Z. He, and H. Pang, "Research, application and development of VSC-HVDC engineering technology," *Automation of Electric Power Systems*, vol. 37, no. 15, pp. 3–14, 2013.

[4] B. T. Ooi and X. Wang, "Voltage angle lock loop control of the boost type PWM converter for HVDC application," *IEEE Transactions on Power Electronics*, vol. 5, no. 2, pp. 229–235, 1990.

[5] L. Shu, Z. Yuming, C. Li et al., "Research on control and protection strategy and design scheme of VSC-DC distribution network control and protection system," *Distribution & Utilization*, vol. 35, no. 1, pp. 21–27, 2018.

[6] S. Li, *Study on Control Strategy and Protection Scheme of VSC Based Distribution Network*, North China Electric Power University, Beijing, China, 2016.

[7] W. W. Li, C. Jun, C. Ming et al., "RT-LAB real-time simulation research for multi-terminal VSC-DC power distribution network," *Guangdong Electric Power*, vol. 28, no. 10, pp. 78–82, 2015.

[8] X. Zheng, *Flexible Direct Current Transmission System*, Machine Press, Beijing, China, 2013.

[9] G. Li, L. Pengfei, Z. Ming et al., "Development and prospects for HVDC light," *Automation of Electric Power Systems*, vol. 27, no. 4, pp. 1–5, 2003.

[10] Q. Tu, X. Zheng, W.-Z. Yao et al., "Selecting number of voltage levels for modular multilevel converter based HVDC," *Power System Protection and Control*, vol. 38, no. 20, pp. 33–38, 2010.

[11] X. Zhai and C. Zhao, "Study of modular multilevel dynamic voltage restorer," *Power System Protection and Control*, vol. 41, no. 12, pp. 86–91, 2013.

[12] M. Guan and X. Zheng, "Modeling and control of modular multilevel converter based VSC-hvdc system connected to passive networks," *Transactions of China Electrotechnical Society*, vol. 28, no. 2, pp. 255–263, 2013.

[13] J. Lago and M. Heldwein, "Operation and control-oriented modeling of a power converter for current balancing and stability improvement of DC active distribution networks," *IEEE Transactions on Power Electronics*, vol. 26, no. 3, pp. 877–885, 2011.

[14] A. Radwan and Y. Mohamed, "Linear active stabilization of converter-dominated DC microgrids," *IEEE Transactions on Smart Grid*, vol. 3, no. 1, pp. 203–216, 2012.

[15] G. Hsieh, H. Hsieh, C. Tsai et al., "Photovoltaic power-increment-aided incremental-conductance MPPT with two-phased tracking," *IEEE Transactions on Power Electronics*, vol. 28, no. 6, pp. 2895–2911, 2013.

[16] X. Zhou, D. Song, and Y. Ma, "Control strategy of photovoltaic grid-connected inverter," *East China Electric Power*, vol. 38, no. 1, pp. 81–83, 2010.

[17] X. Wu, D. Tongzhen, X. Wenjing et al., "Real time simulation of grid side converter in wind power generation system based on RT-LAB," *Southern Power System Technology*, vol. 47, no. 10, pp. 17–19, 2013.

[18] C. Wei, M. Benosman, and T. Kim, "Online parameter identification for state of power prediction of lithium-ion batteries in electric vehicles using extremum seeking," *International Journal of Control, Automation and Systems*, vol. 17, no. 11, pp. 2906–2916, 2019.

[19] F. Li, "Cascade utilization battery energy storage system Architecture and control strategy," *Electrical Appliances and Energy Efficiency Management Technology*, vol. 4, pp. 81–84, 2021.

[20] H. Liu and Y. Lei, "Dual-passivity-based control strategy of energy storage converter under microgrid operation mode switching," *Electric Power*, 2021, https://kns.cnki.net/kcms/detail/11.3265.TM.20210513.1510.008.html.

[21] Y. Li, P. Peng, and B. Liu, "Research on the integration and control strategy of echelon use battery energy storage system," *Power Electronics*, vol. 55, no. 3, pp. 13–16, 2021.

[22] G. Jiang, Z. Li, H. Yang et al., "Research review on topological structure of flexible HVDC system," *Power System Protection and Control*, vol. 43, no. 15, pp. 145–154, 2015.

[23] B. Zhao, Y. Wang, Y. Zhao et al., "Energy internet based on flexible medium-voltage DC distribution," *Proceedings of the CSEE*, vol. 35, no. 19, pp. 3391–3403, 2015.

[24] G. Liu, Y. Zhao, Z. Yuan et al., "Study on demonstration project technical scheme of VSCDC distribution system in Shenzhen," *Southern Power System Technology*, vol. 10, no. 4, pp. 1–7, 2016.

[25] B. Zhao, Q. Song, W. Liu et al., "High-frequency-link DC solid state transformers for flexible DC distribution," *Proceedings of the CSEE*, vol. 34, no. 25, pp. 4295–4303, 2014.

[26] C. Wei, Z. Shen, D. Xiao, L. Wang, X. Bai, and H. Chen, "An optimal scheduling strategy for peer-to-peer trading in interconnected microgrids based on RO and nash bargaining," *Applied Energy*, vol. 275, 2021.

[27] M. Mou, D. Lin, Y. Zhou, W. Zheng, J. Ruan, and D. Ke, "An optimal allocation strategy for multi-energy networks based on double-layer non-dominated sorting genetic algorithms," *Complexity*, vol. 2019, Article ID 5367403, 11 pages, 2019.

[28] M. Mou, Y. Zhou, W. Zheng, D. Ke, Z. Zhang, and D. Lin, "Real-time optimal control strategy for multi-energy complementary microgrid system based on double-layer non-dominated sorting genetic algorithm," *Complexity*, vol. 2020, Article ID 8852186, 12 pages, 2020.

Hindawi
Complexity
Volume 2021, Article ID 9967577, 11 pages
https://doi.org/10.1155/2021/9967577

Research Article

A Study of a DC/AC Conversion Structure for Photovoltaic System Connected to the Grid with Active and Reactive Power Control

Houda Brahmi[1] **and Rachid Dhifaoui**[2]

[1]*University Tunis El Manar, Higher Institute of Medicals Technologies of Tunis (ISTMT), Rue Zouhair Essafi, 1006 Tunis, Unit of Research ERCO-INSAT, Tunisia*
[2]*Unit of Research (ERCO), INSAT, Centre Urbain Nord, B.P. N°676, 1080 Tunis Cedex, Tunisia*

Correspondence should be addressed to Houda Brahmi; houda.brahmi@istmt.utm.tn

Received 18 March 2021; Revised 18 June 2021; Accepted 26 June 2021; Published 7 July 2021

Academic Editor: Chun Wei

DC/AC conversion of photovoltaic energy is in great demand for AC applications; the supply of electrical machines and transfer energy to the distribution network is a typical case. This work is realized in this context and presents a new structure for the transfer of photovoltaic energy to the electricity grid. This structure is based on a push-pull converter connected to a three-phase DC/AC inverter. In particular, a great interest is focused on the steady operating conditions of energy transfer. The study also develops the limits and the feasibility of the PV energy transfer to the grid of the proposed structure. Injecting photovoltaic energy into the grid with maximum active power and zero reactive power is also considered for the dynamic regime. Support simulations are carried out to validate the proposed control strategy.

1. Introduction

Renewable energies are inexhaustible and clean and have the additional advantage of complementing each other. This favours and encourages their integration in the AC grid. Among these sources, photovoltaic solar energy offers a very promising alternative [1–5]. It is experiencing a wide development, favoured by the awareness of governments and other organizations seriously calling to preserve the environment.

Relatively for a long time, photovoltaic solar energy was used as a power source only for certain loads, such as satellites and/or rural areas situated far from conventional electricity transmission lines [6–9]. Nowadays, from the environmental concern of modern society, economical point of view, and technology advances, the interest in solar energy and associated conversion systems has emerged as good future solution. Furthermore, photovoltaic solar energy has the greatest potential for use in various ways. Due to its modular nature, it can be used in the country side and in the city, in small and large places [10–12].

Basically, there are two types of solar energy applications: isolated systems and grid connected systems [13, 14]. For the first case, we found a lot of applications: isolated and independent houses or equipment, rural power plants, telecommunication networks, water pumping, lighting systems, computers or cell phones, cameras, calculators, etc. Surely, photovoltaic solar energy can offer a more significant contribution in many countries where electrification levels are close to saturation [15–17]. Furthermore, many countries in Europe and Africa have great chance to produce photovoltaic energy in very high quantities. This is why the second case dealing with connexion of solar photovoltaic energy to the electricity grid shows a high growing rate during the last decades. At present, the governments of various European countries, Japan and the United States, among others, are promoting economic incentives for renewable energies to try to cope with climate change [18–20]. In this sense, there are special credits to finance photovoltaic installations for connection to the grid and remuneration per kWh sold to the electricity company.

To generate photovoltaic solar electricity, a photovoltaic generator is needed; that is, a set of solar panels are connected in series and/or in parallel to produce the desired direct current. Then, to produce alternating current (at rated voltage 220 V and rated frequency 50 Hz, for example), a DC/AC inverter is required. Thus, photovoltaic inverters are installed between the photovoltaic generator and the point of connection to the grid. Energy transfer from the DC side to the AC side is submitted to various constraints such as secure operating conditions, economical efficiency, and environmental benefits [21, 22].

As part of the specific grid-related operation requirements, the PV inverter must also operate within the output voltage and frequency ranges satisfying the tolerated harmonic distortion of the grid voltage wave. From a signal quality point of view, main technical issues to consider in an inverter are in fact power factor and harmonic distortion. The inverter must also have admissible galvanic insolation level between the network and the photovoltaic installation [23–26]. On the other hand, the global efficiency of a grid connected photovoltaic system depends largely on the efficiency of the inverter that in turn depends on circuit topology and control scheme. Generally speaking, this control must ensure various active power operating points at minimum possible reactive power [27, 28].

The study realized in this paper is organized as follows. Section 2 deals with the studied energy transfer structure. It gives a general view and a simplified description of main components of this structure. Section 3 details the used mathematical model of solar cells forming the photovoltaic generator. This model is relatively an enhanced one because it includes internal series and parallel resistors and is described by a unique nonlinear equation to solve by iterative numerical process. The first part of Section 4 defines the mathematical model connecting photovoltaic generator to a simple electrical circuit describing the grid bus bar. Then, it presents the steady-state regime and determines useful constraint to ensure the existence of realistic energy transfer solution. The system to solve is also presented and commented. The second part of Section 4 describes the control structure to solve in dynamic regime. The dynamic model of the grid is detailed and the procedure to impose active and reactive powers reference values is outlined. It also introduces how to incorporate corrective terms in voltage reference value. Finally, Section 5 presents and comments on obtained dynamic response signals. The degree of acceptance of the results and their accuracy are also discussed.

2. Presentation of the Proposed Structure

The studied structure is shown in Figure 1 and it is composed of the following:

(i) A photovoltaic generator whose voltage and current are denoted, respectively, in the usual way by V_p and I_p. Thus, its output power is

$$P_{\text{pv}} = V_p I_p. \tag{1}$$

(ii) A DC/DC push pull voltage converter with a fixed ratio m. It is assumed that it delivers a sufficiently smooth and constant voltage V_{dc} proportional to input voltage V_p such that

$$V_{\text{dc}} = mV_p. \tag{2}$$

(iii) A DC/AC three-phase inverter considered with a large inductance to sufficiently smooth the current supplied by the high voltage DC side of the DC/DC inverter

(iv) A three-phase voltage source representing the grid (distribution network)

Some working hypotheses are here considered. Surely, the goal is first to facilitate the study. On the other side, we keep in mind that the final target is focused on control feasibility and not to study detailed models of structure components. Thus, we assume that the two power inverters are lossless and alternative current signals are very close to a sinusoidal wave form so that they are treated within the framework of the first harmonic. This hypothesis can be validated by insertion of a filter circuit. Finally, we consider that the input impedance of the grid is very low to ovoid inadmissible voltage drop. In this context, the rms voltage V of the grid is linked to photovoltaic input voltage V_p by the following expression where ρ holds for the adjustable duty cycle that varies between 0 and 1:

$$\begin{aligned} V &= \frac{\rho V_{\text{dc}}}{\sqrt{2}} = \frac{m\rho V_p}{\sqrt{2}} = \gamma V_p, \\ \gamma &= \frac{m\rho}{\sqrt{2}}. \end{aligned} \tag{3}$$

3. PV Array Modelling

Figure 2 presents the refined model of a PV cell [29–32]. The equivalent electrical circuit is formed by a current source depending on the solar radiation, a diode characterized by a saturation current I_0 and an idealistic factor q, and two resistors modelling the joule losses in the cell R_s and R_{sh}, respectively. Current I_{ph} emitted by the cell under the effect of solar radiation (the current of photons) is strongly related to the intensity of the solar radiation but it depends very slightly on the temperature variation. The current I_D of the diode is strongly related to the temperature and to the energy of the gap of the junction. It also depends on the voltage across the diode. The shunt current I_{sh} corresponds to the current flowing through the shunt resistance R_{sh} usually considered very high.

Within the meaning of this electrical model given in Figure 2 and the considered notations listed in Abbreviations, we can write the following relations:

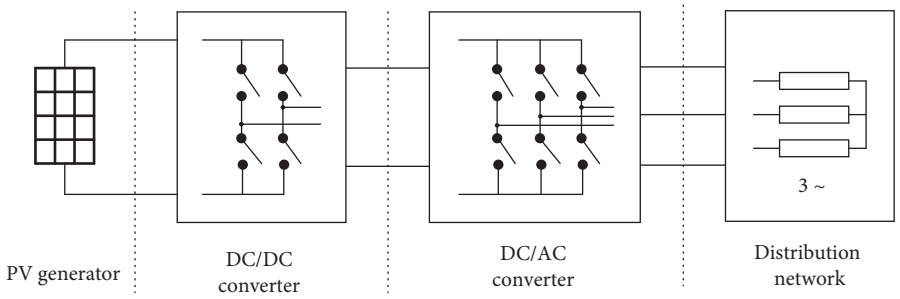

Figure 1: The studied energy conversion structure.

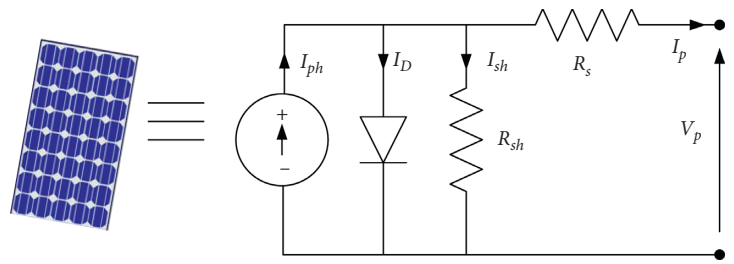

Figure 2: Electrical model of a solar cell.

$$I_{\text{ph}} = I_D + I_p + I_{\text{sh}} = I_d + I_p + \frac{V_p + R_s I_p}{R_{\text{sh}}},$$
$$I_D = I_s\left(\exp\left(\frac{V_p + R_s I_p}{V_T}\right) - 1\right), \tag{4}$$
$$V_T = \frac{\mathcal{K}_I \mathcal{K}_B}{q} T_j.$$

The electrical behaviour under load of the solar cell will be described by the following relation:

$$f\left(I_p, I_p\right) = I_p - I_{\text{ph}} + I_s\left(\exp\left(\frac{V_p + R_s I_p}{V_T}\right) - 1\right) + \frac{V_p + R_s I_p}{R_{\text{sh}}} = 0. \tag{5}$$

This system being nonlinear, we solved it by the iterative Newton–Raphson method which is the most appropriate tool for this case of systems.

4. Transfer of Photovoltaic Energy to the Grid

4.1. Study of Transfer Conditions in Steady State. In a general and simplified way, we deal with the circuit of Figure 3 representing a voltage source $v(t)$ supplying a AC load composed by a second voltage source $e(t)$ placed behind an internal impedance. Such a circuit could correspond to a portion of an electrical energy distribution network [33, 34]. The most important thing here is to consider that the short-circuit power of this load is very important compared to the limit power of the source, that is to say, the conversion chain formed by the photovoltaic generator and the two static converters. This assumption makes it possible to consider the voltage source constant in amplitude and frequency whatever the operating point.

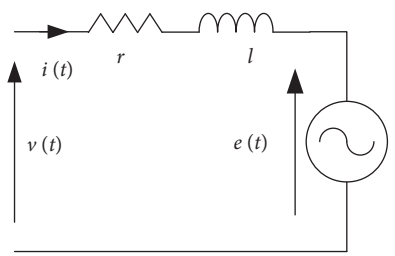

Figure 3: Single-phase equivalent diagram of the studied load.

During the steady state, Park's vectors merge with Fresnel's ones. Thus, for such a regime, we establish vector diagram of Figure 4 and consequently deduce the relations below. It is to be noted that these equations are generated in a synchronously rotating reference frame associated with voltage vector $\overline{E}$. In this situation, direct and quadrature voltage and current components are noted by capital characters.

$$V_d = rI_d - xI_q + E,$$
$$V_q = rI_q + xI_d. \tag{6}$$

Moreover, taking into account relation (1) and the power conservation imposed by the assumption of ideal static converters, system (7) is established where P holds for the power delivered by the photovoltaic generator:

$$V^2 = \gamma^2 V_p^2 = \left(rI_d - xI_q + E\right)^2 + \left(rI_q + xI_d\right)^2,$$
$$P_g = V_p I_p + rI^2 = EI_d + r\left(I_d^2 + I_q^2\right). \tag{7}$$

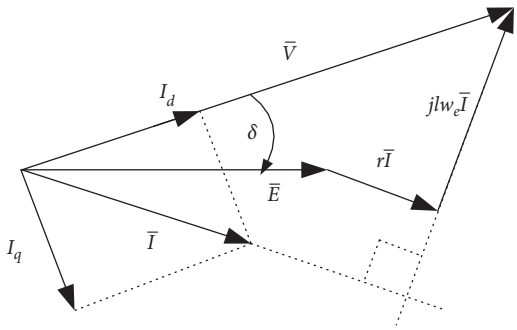

Figure 4: Vector diagram of the load in steady state.

For a (V_p, I_p) point taken on the $P = f(V)$ curve of the photovoltaic generator and for a specified value of the control variable γ, the two equations above are sufficient to determine the two variables I_d and I_q and to deduce from them the values of active power and reactive power at the source bus bar $\overline{E}$ and at the inverter output terminals. At the source bus bar $\overline{E}$, the active power P and the reactive power Q are calculated by

$$P = EI_d, \tag{8}$$

$$Q = -EI_q. \tag{9}$$

The choice of the control value γ plays a crucial role in the existence of a solution; this is on one hand, and on the other hand, it plays a crucial role in the degree of satisfaction with the solution if it exists. In fact, we could find a solution which would correspond, for example, to an inadmissible balance in reactive power and in this case the selected value is rejected. When the photovoltaic generator works in current generator mode, that is to say, when its voltage is low, the voltage at the output of the inverter would also be low and the load would be called upon to supply reactive power to the conversion chain. This is of course an undesirable regime on several levels: current overload, drop in voltage, and active power.

The strategies largely preferred in the field of integrating photovoltaic energy into the network consist in imposing zero reactive power on the bus bar of this network. It is precisely this type of control that we are interested in, in this study. A control structure is developed to impose a reference active power value P_{ref}, which is as high as possible, and a zero reference reactive power Q_{ref} at the point where the source E representing the electrical network is located. According to (8), to obtain null reactive power at the input of the electrical network, the quadrature component I_q of the current must also be zero. So, by imposing this condition in (7)–(9), we obtain

$$\gamma^2 V_p^2 = z^2 I_d^2 + 2rEI_d - 2xI_qE + E^2, \tag{10}$$

$$P_g = V_pI_p = EI_d + rI_d^2. \tag{11}$$

By multiplying (10) by (r/z^2) and subtracting (11), we get

$$I_d = \frac{z^2 V_p I_p - r\left(\gamma^2 V_p^2 - E^2\right)}{\left(x^2 - r^2\right)E}. \tag{12}$$

Then, by combining (11) and (12) and thus eliminating the current component I_d, one obtains the following unique equation:

$$\begin{aligned}\left(x^2 - r^2\right)^2 P_g = &\left(x^2 - r^2\right)\left[z^2 P_g - r\left(\gamma^2 V_p^2 - E^2\right)\right] \\ &+ \frac{r}{E^2}\left[z^2 P_g - r\left(\gamma^2 V_p^2 - E^2\right)\right]^2.\end{aligned} \tag{13}$$

For a set of parameters (r, x, E) chosen suitably, this equation defines in the plane (V_p, P_g) a curve branch which could cut the characteristic of the photovoltaic generator at a certain operating point as illustrated in Figure 5.

If we place at the point of the no-load regime, that is to say, $V_p = V_{\text{oc}}$ and $P = Q = 0$, the preceding equation implies the trivial solution:

$$\gamma V_p = \gamma V_{\text{oc}} = E. \tag{14}$$

It follows that the minimum theoretical value of γ guaranteeing the existence of an operating point of the photovoltaic generator for the climatic working conditions is

$$\gamma_{\min} = \frac{E}{V_{\text{oc}}}. \tag{15}$$

Any voltage ratio inferior to this critical value makes it impossible to transfer active power to the source E while respecting the zero reactive power. However, it is obvious that the best choice of γ is the one allowing the transfer of the maximum power. Let us say, for example, that we are at the optimum operating point of the photovoltaic generator where voltage, current, and power are, respectively, V_m, I_m, and P_m. From (10), we can calculate the value of the direct current I_d and deduce the optimum power. Substituting the result found in (10) allows us to deduce the value of the control variable γ to be used. If the short-circuit impedance of the network is low enough, which is usually the case, this value would almost correspond to the optimal value:

$$\gamma_m = \frac{E}{V_m}. \tag{16}$$

As the global voltage ratio includes the turns ratio m of the push pull transformer, it is evident that the feasibility condition (15) turns into a constraint on m. This means that a particular attention must then be given to the sizing of the minimum value of the DC/DC inverter. If such a precaution is not taken into account, the duty cycle of the inverter checking the operating point would be greater than 1 and the control structure would also fail because this ratio is of course saturated at 1. From this we understand that it is important to carry out a preliminary scan taking into account the limiting climatic variations in order to decide on the minimum value of the DC/DC converter ratio m. In a formal way, we pose the constraint below where γ_c is a value verifying the transfer of the optimal power within the largest variation in climatic conditions:

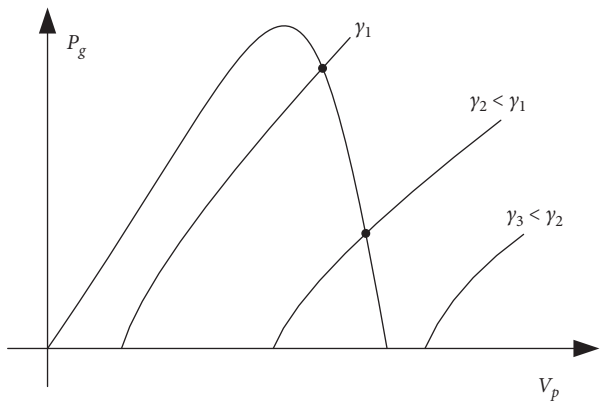

Figure 5: Zero reactive power control solutions.

$$m > \sqrt{2}\gamma_c. \tag{17}$$

The consideration of grid parameters (r, x, E) in the analysis of the possibilities of integrating photovoltaic energy is an aspect of great importance. To be able to transfer the power available in the photovoltaic source to the grid, it is essential to know in advance the limit level of this power and to check the effective possibility of transferring it. By this we mean that a preliminary calculation of the transmissible power is very necessary to ensure the transfer properly. In the case, for example, where the capacity for transferring power to the network is less than the power to be transferred, the control structure would regain certain failure. In terms of the power limit, and therefore in terms of the existence of a transfer solution, the following condition must be respected:

$$P < \frac{E^2}{2(z-r)} - rI^2. \tag{18}$$

Finally, the operating point corresponds to the simultaneous resolution of the three equations of the system (19) below by the Newton–Raphson method in terms of the three variables V_p, I_p, and I_d, for a specified value of γ. The details of this method are given in Figure 6. From the obtained value of I_d, one easily deduces the value of the power P transmitted to the source E of the network.

$$\begin{cases} I_p - I_{\text{ph}} + I_s\left(\exp\left(\dfrac{V_p + R_s I_p}{V_T}\right) - 1\right) + G_{\text{sh}}\left(V_p + R_s I_p\right) = 0, \\ z^2 I_d^2 + 2rEI_d + E^2 - \gamma^2 V_p^2 = 0, \\ EI_d + rI_d^2 - V_p I_p = 0. \end{cases} \tag{19}$$

4.2. Control Structure in Dynamic Regime. It is important to show the feasibility of the problem in variable regime through a control strategy. This is where the objective of this section lies. To approach this problem in the simplest and clearest way possible, only the dynamics of the control loop of the inverter and that of the load are here taken into account. It is assumed that the dynamics of the DC/DC converter upstream of the inverter is relatively slow because of its output large filter capacitor.

The proposed control structure is indicated by Figure 7. This structure comprises a set of modules associated with the necessary mathematical models. Module 1 relates to the photovoltaic generator. Its inputs are the variables illustrating the climatic conditions: ambient temperature T_a and solar radiation E_s. Its outputs are current I_p and voltage V_p which depend on the power level of the load and input variables T_a and E_s. Module 2 represents the DC/DC push pull converter, its output voltage is linked to photovoltaic generator voltage by equation (2). Module 3 generates reference voltage $\overline{v}_{\text{ref}}$ vector with a module ρ_{ref} and phase δ_{ref} with respect to the grid synchronous angle. These two quantities come from module 7 where the control part resides. Module 4 realises space pulse width modulation (SPWM) signals corresponding to switching times of power transistor of the inverter schematised by module 5. Output signals of this module are two quadratic voltage components in Concordia's representation. Module 6 solves the differential equation (20) below written in the stationary Concordia's reference frame. When they appear, Concordia's voltage and current components are noted with small characters. Relation (21) is to consider that the voltage at grid bus bar is purely sinusoidal.

$$\frac{\mathrm{d}\overline{i}}{\mathrm{d}t} = \frac{\overline{v} - r\overline{i} - \overline{e}}{\ell}, \tag{20}$$

$$\overline{e} = E\,\exp(j\omega t). \tag{21}$$

In Park's rotating reference frame synchronized with the network voltage source $\overline{E}$, the dynamics of the components of the current transmitted is expressed by

$$\begin{aligned} \frac{\mathrm{d}I_d}{\mathrm{d}t} &= \frac{V_d - E - rI_d + xI_q}{\ell}, \\ \frac{\mathrm{d}I_q}{\mathrm{d}t} &= \frac{V_q - rI_q - xI_d}{\ell}. \end{aligned} \tag{22}$$

These current components must converge in steady state towards their reference values imposed by the required active power P_{ref} and reactive power Q_{ref}:

$$\begin{aligned} I_{\text{dref}} &= \frac{P_{\text{ref}}}{E}, \\ I_{\text{qref}} &= \frac{Q_{\text{ref}}}{E} = 0. \end{aligned} \tag{23}$$

The output voltage components of the inverter are also known in steady state:

$$\begin{aligned} V_{\text{dref}} &= E + rI_{\text{dref}}, \\ V_{\text{qref}} &= xI_{\text{dref}}. \end{aligned} \tag{24}$$

For the transient state, one uses these relations to introduce corrective terms compensating the effect of the dynamic variation of the current components. The added

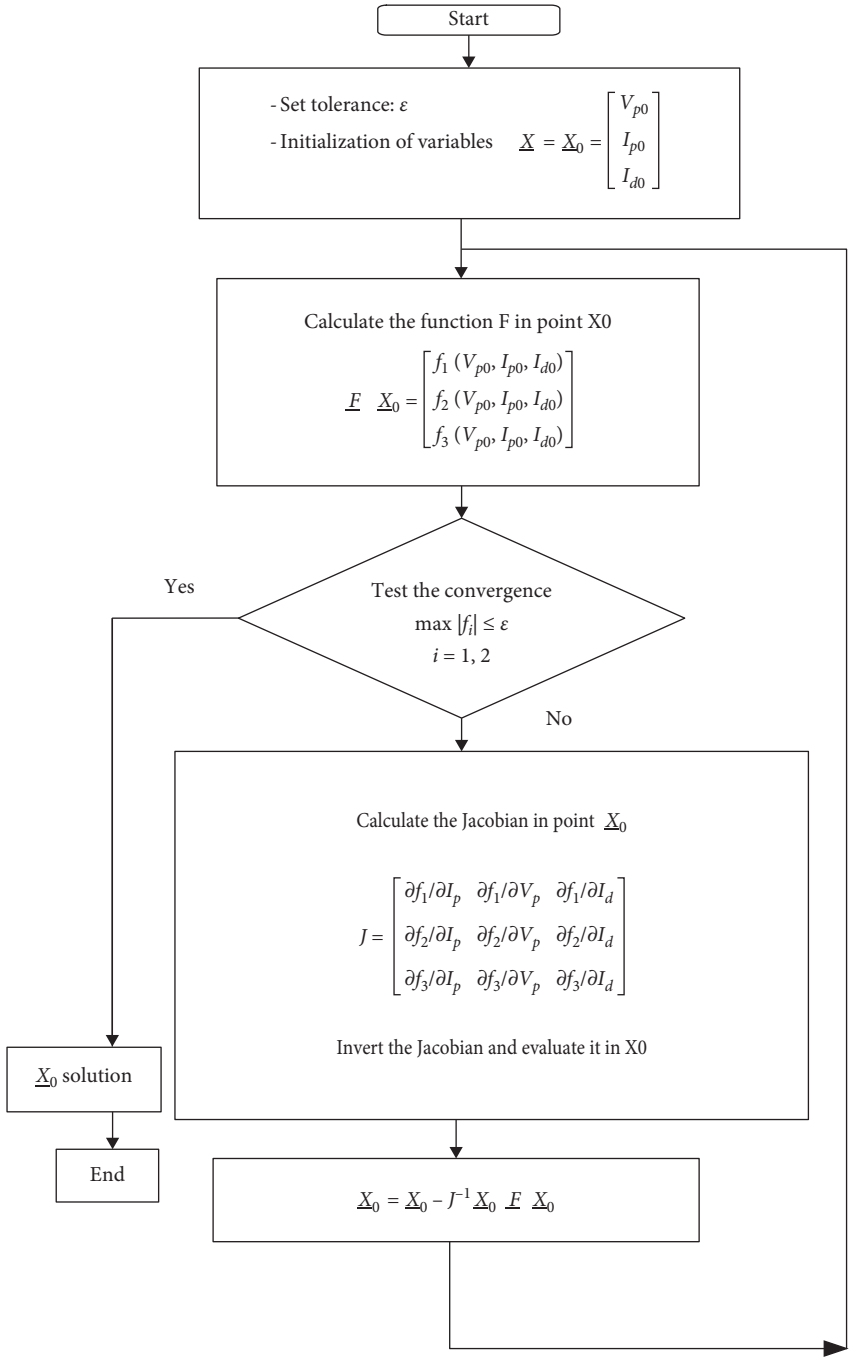

Figure 6: Chart diagram of Newton–Raphson method.

corrective terms are as follows, where r_c is a constant whose value will be provided in the part reserved for the simulation:

$$\begin{aligned} \Delta V_{\text{dref}} &= r_c\left(I_{\text{dref}} - I_d\right), \\ \Delta V_{\text{qref}} &= -r_c I_q. \end{aligned} \tag{25}$$

We then consider a reference voltage such as

$$\begin{aligned} V_{\text{dref}} &= E + rI_{\text{dref}} + r_c\left(I_{\text{dref}} - I_d\right), \\ V_{\text{qref}} &= xI_{\text{dref}} - r_c I_q. \end{aligned} \tag{26}$$

This fully defines the inputs of the inverter control module which are the voltage duty cycle ρ_{ref} and its phase δ_{ref} in the grid synchronous frame:

$$\begin{aligned} \rho_{\text{ref}} &= \frac{\sqrt{2\left(V_{\text{dref}}^2 + V_{\text{qref}}^2\right)}}{mV_p}, \\ \delta_{\text{ref}} &= t_g^{-1}\left(\frac{V_{\text{qref}}}{V_{\text{dref}}}\right). \end{aligned} \tag{27}$$

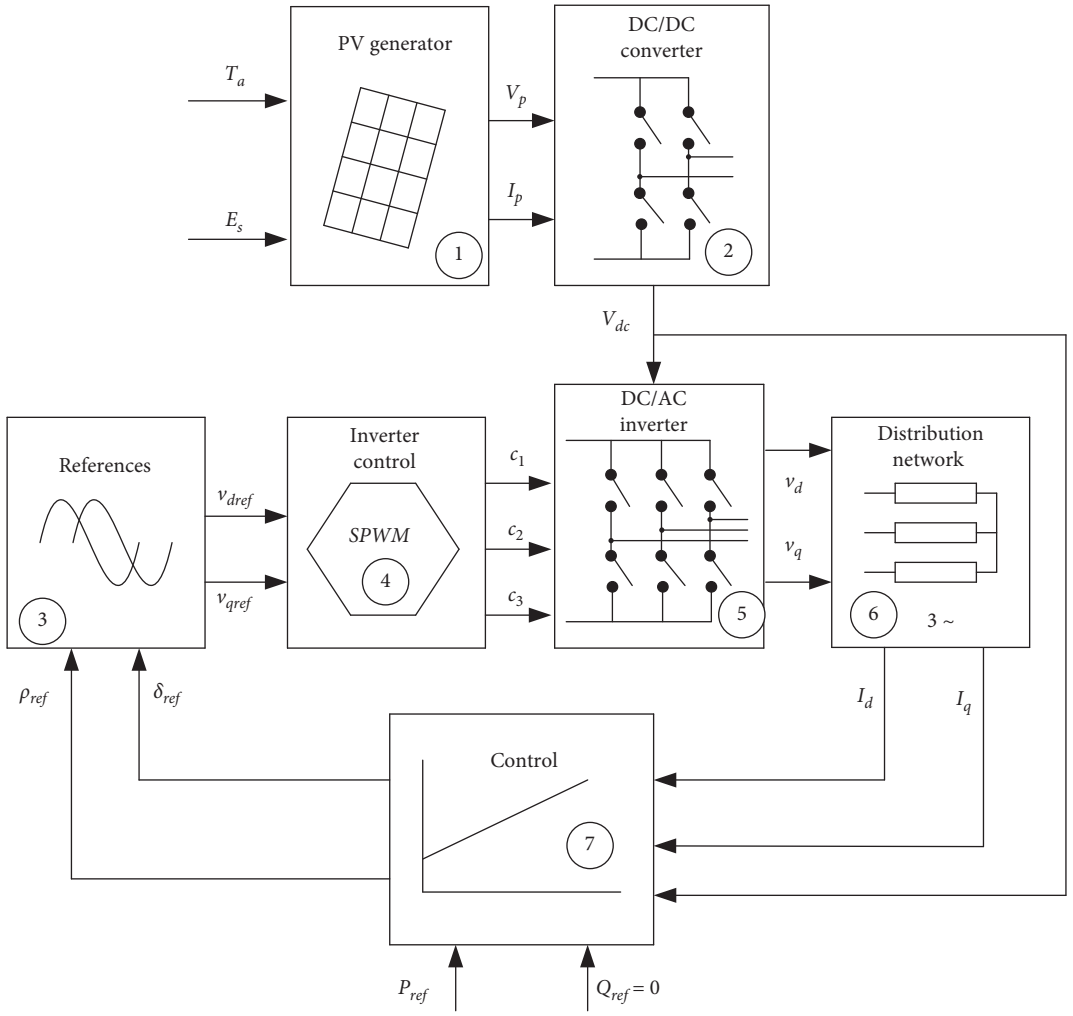

Figure 7: The developed control structure.

5. Simulations and Results

To check the performance of the proposed command in dynamic regime, a MATLAB/Simulink model of the PV system was initially developed. The parameters to be used are inspired from a practical project now under development in our research laboratory ERCO (Energy, Robotics, Control and Optimisation) situated at INSAT, Tunis.

The photovoltaic generator has been described in a previous work [31]. It is formed by 10 solar panels referenced TITAN STP-12-50, Multi-Cristallin technology. Table 1 reports the necessary parameters at standard climatic conditions.

The DC/DC inverter is a part of a real camping power supply. The reference of this device is KEBO IPS 1200. It is a rated 12 V/240 volts and a rated 500 W power device. This inverter is designed to be connected to a car battery of 12 volts. To meet this voltage constraint, solar panels are connected in parallel. In addition, the DC/DC inverter has being modified in our laboratory so that some input chemical capacitors support 25 dc volts. At a very low load, close to open circuit, we have verified that the voltage ratio is $m = 22.2$.

The global structure given by Figure 7 is simulated under the following conditions:

(i) Climatic conditions: temperature $T_a = 25^{\circ}\text{C}$ and a solar radiation $E_s = 1000\,\text{W/m}^2$

(ii) Push-pull converter with fixed ratio: $m = 22.2$

(iii) PWM frequency: 5 kHz

(iv) Reference reactive power $Q_{\text{ref}} = 0$

(v) Reference active power $P_{\text{ref}} = 408\,\text{W}$: this equals 97% of the maximum power of the photovoltaic generator

(vi) Filtering period: $m = 200\,\mu\text{s}$

(vii) Grid parameters: $r = 1\,\Omega$, $x = 5\,\Omega$

Figures 8 and 9 show the structure dynamic response in terms of active power and reactive power control. These variables suitably converge towards the requested references in a sufficiently short response time. Active power convergence is good. However, reactive power oscillates around zero. This is due to the fact that the internal impedance of the source representing the network is low, which generates a phenomenon of permanent current ripple around its

Table 1: Parameters of the PV generator used in simulation.

Solar panel TITAN-12-50 cell type: EFG Multi-Cristallin	
Number of series cells: **ns**	36
Number of parallel PV arrays: Np	10
Number of series PV arrays: Ns	1
Open circuit voltage in STC (per one PV array)	21 V
Short-circuit current en STC (per one PV array)	3.2 A
Optimal voltage in STC (per one PV array)	17.2 V
Optimal current in STC (per one PV array)	2.9 A
Optimal power in STC	45 W per module
Temperature	25°C
Radiation	1000 W/m^2

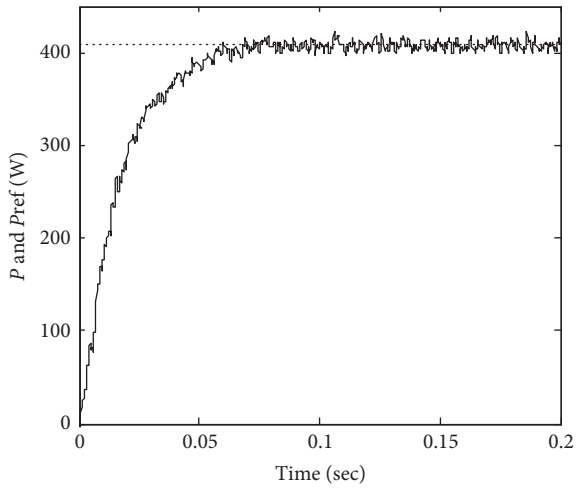

Figure 8: Dynamic evolution of active power.

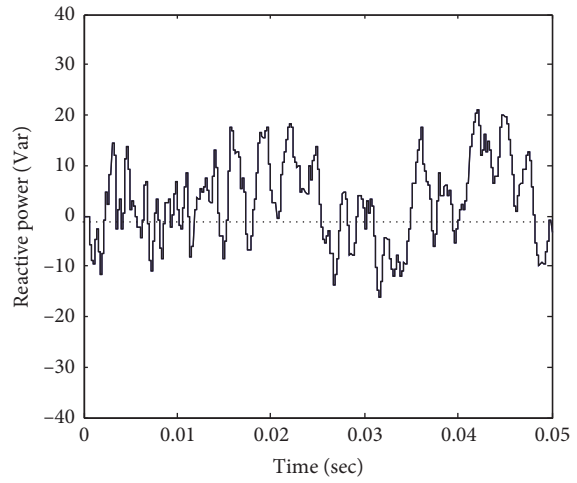

Figure 9: Dynamic evolution of reactive power.

fundamental sinusoidal component. We can easily observe that absolute reactive power variation remains within 20 vars that is inferior to 10% of final active power value. In general point of view, this performance gives full satisfaction. In theoretical point of view, oscillations can be justified by the fact that the reference voltage is defined in a pseudostatic form on one hand and the value of the compensation resistor r_c is sufficiently large on the other hand.

Figure 10 shows the evolution of the control variable γ which is proportional to the duty cycle of the inverter. We can easily see that this value remains within the range specified by the steady-state study. In fact, it converges to a value around $\gamma \simeq 15$ which means that the voltage ratio is about $\rho \simeq 95\%$.

The phase shift of the voltage of the inverter with respect to the synchronous axis of the network is of the order of $\delta = 2.5^\circ$ in steady state as indicated by Figure 11. This value, which seems very low, is well justified. The maximum power that can be transmitted to the network is inversely proportional to its internal impedance; see expression (27). This power is here very large as compared to the power requested.

Figure 12 gives a zoom on the instantaneous waveform of the current. Although the average value of the current remains generally sinusoidal, we observe the chopping due to the sudden switching of the output voltage of the inverter. Surely, this waveform is not of sufficient degree of acceptance. But we are also sure that the result can be enhanced. Three factors can contribute to reaching this goal. In fact, adding a filter circuit, realising accurate calculation of the transfer impedance, and finding optimal switching frequency could be a real solution.

Figure 13 gives a zoom on the steady state of the voltage signals. The central curve of this figure indicates the instantaneous average value which naturally characterizes the reference voltage. Figures 14 and 15 correspond, respectively, to the evolution of the current and the voltage of the photovoltaic generator. We can also prove through these curves the convergence of the power delivered towards the requested reference.

We have previously shown that is possible to obtain a steady-state operating point characterized by an active power $P_{\text{ref}} = 408$ W and null reactive power with a global voltage ratio of $\gamma \simeq 15$. Imposing $\gamma = 12$ in an open loop simulation case leads to inadmissible oscillations and shows impossibility to transfer the requested power. This result is summarised in Figures 16 and 17.

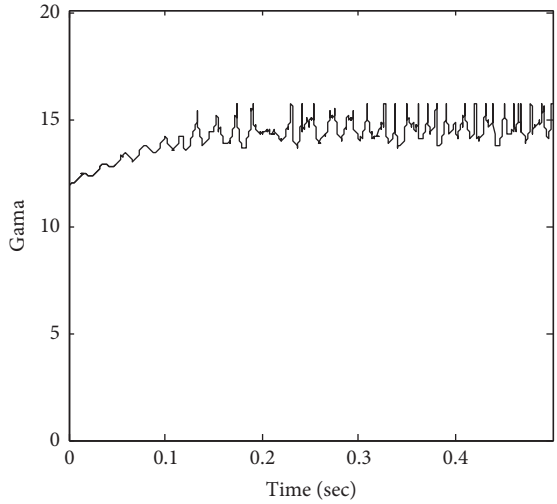

Figure 10: Evolution of the variable control γ.

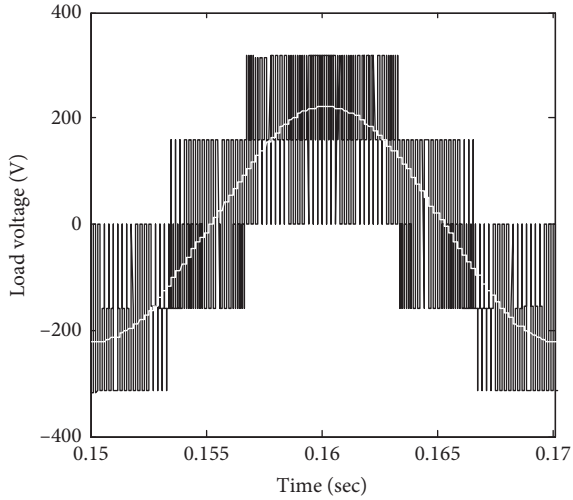

Figure 13: The steady state of the load voltage.

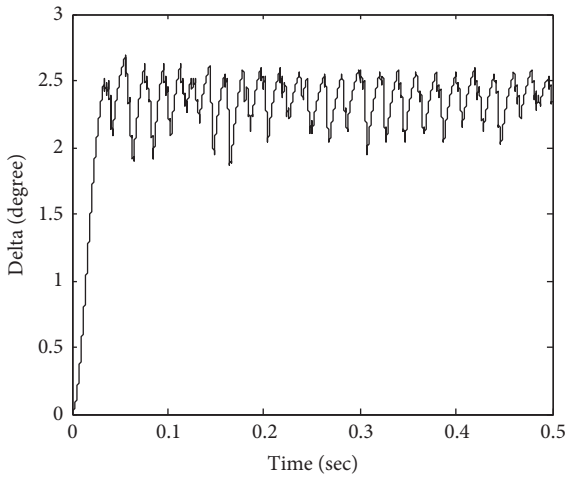

Figure 11: Dynamic evolution of the angle δ.

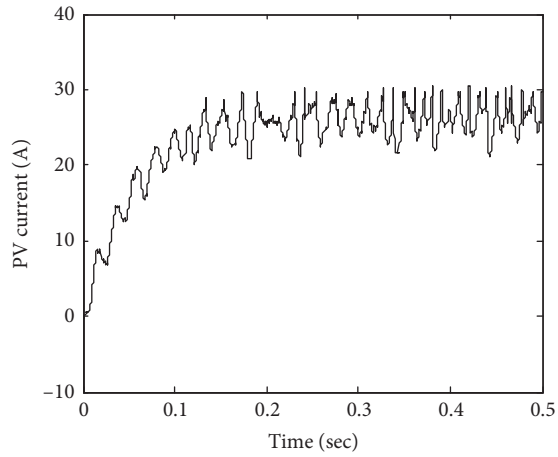

Figure 14: The steady state of the load current.

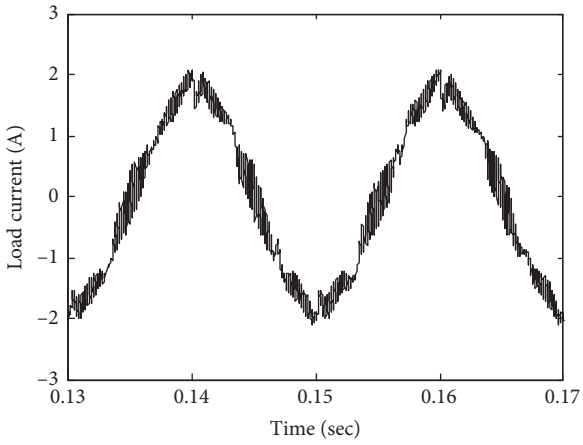

Figure 12: The steady state of the load current.

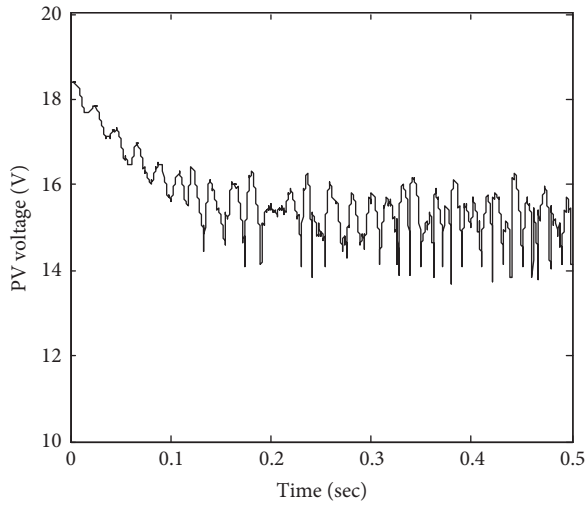

Figure 15: Evolution of the voltage of the photovoltaic generator.

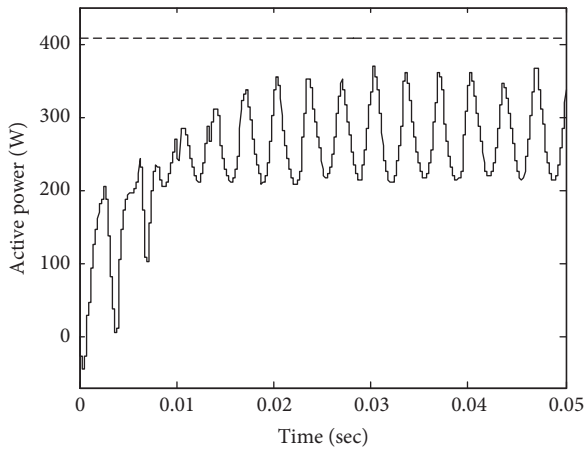

Figure 16: Dynamic evolution of the active power for $\gamma = 12$.

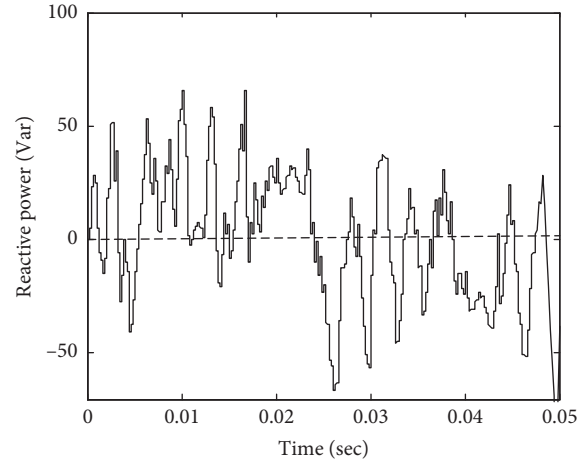

Figure 17: Dynamic evolution of the reactive power for $\gamma = 12$.

6. Conclusion

The aim of this analysis was to show the feasibility of transferring photovoltaic energy to the electrical grid with control of active and reactive powers. The proposed structure is based on a push-pull converter connected to three-phase AC-DC inverter. The steady-state study of the structure in question showed the limits of the energy transfer. Indeed, for a point (V_p, I_p) considered on the characteristic of the photovoltaic generator and for a specified value of the control variable γ, we can deduce the value of the active power and of the reactive power both at the level of the alternative current bus bar and at the output terminals of the inverter.

The choice of the value of γ plays a crucial role on one hand in the existence of a solution and on the other hand in the degree of satisfaction of the solution if it exists. Indeed, one could find a solution which would correspond, for example, to an inadmissible balance in reactive power. When the photovoltaic generator works in current generator mode, the voltage at the output of the inverter would also be low and the load would be called upon to supply reactive power to the conversion chain. This is obviously an undesirable regime on many levels: current overload, drop in voltage and active power, and being very profitable on the network side of the distribution. On the contrary, when the photovoltaic generator works in voltage generator mode, with the contribution of the adjustment on the converter side, we could have an output voltage greater than the voltage E of the network. In such a case, the conversion chain would produce reactive power. The mathematical model of the whole system with a three nonlinear equations describing the behaviour in static mode was formulated. The method of Newton–Raphson was used in order to solve this system numerically. The last point addressed in this work is the study of the dynamic regime during energy transfer. The command developed aims to ensure the transfer of maximum active power and zero reactive power. We have detailed the control strategy adopted; simulations in dynamic regime have shown the effectiveness of the control law.

Abbreviations

E_e: Solar radiation (W/m^2)
T_j: Temperature of diode junction (K°)
ω_g: Energy gap of the junction (ev)
q: Electronic charge $(1.610 - 13\,C)$
$\mathcal{K}_B$: Boltzmann's constant (J/K°)
$\mathcal{K}_I$: Diode quality factor
R_s: Series resistor (Ω)
R_{sh}: Shunt resistor (Ω)
I_{cc}: Short-circuit current (A)
I_{ph}: Photo current diode (A)
I_s: Saturation current diode (A)
T_a: Ambient temperature $(^\circ C)$
V_T: Thermal voltage of the diode (V)
V_{co}: Open circuit voltage (V).

Data Availability

The parameters of the photovoltaic panel used to support the findings of this study are included within the article.

Conflicts of Interest

The authors declare that they have no conflicts of interest.

References

[1] N. Kittner, F. Lill, and D. M. Kammen, "Energy storage deployment and innovation for the clean energy transition," *Nature Energy*, vol. 2, no. 9, Article ID 17125, 2017.

[2] M. Xiao, J. Tobias, J. Haas, and M. Klein, "Plummeting costs of renewables-are energy scenarios lagging?" *Energy Strategy Reviews*, vol. 35, Article ID 100636, 2021.

[3] S. Teske, S. Sawyer, O. Schaefer, T. Pregger, S. Simon, and T. Naegler, "Energy," *Evolution-A Sustainable World Energy Outlook 2015*, Greenpeace International, Amsterdam, Netherlands, 2015.

[4] K. Branker, M. J. M. Pathak, and J. M. Pearce, "A review of solar photovoltaic levelized cost of electricity," *Renewable and Sustainable Energy Reviews*, vol. 15, no. 9, pp. 4470–4482, 2011.

[5] M. Ram, D. Bogdanov, A. Aghahosseini et al., *Global Energy System Based on 100% Renewable Energy-Power, Heat, Transport and Desalination Sectors*, Lappeenranta University of Technology, Energy Watch Group, Berlin, Germany, 2019.

[6] J. Page, *The Role of Solar-Radiation Climatology in the Design of Photovoltaic Systems' Part II-1-A, McEvoy's Handbook of Photovoltaics'*, Elsevier Academic Press, Cambridge, MA, USA, 3rd edition, 2018.

[7] D. Yang, H. Latchman, D. Tingling, and A. A. Amarsingh, "Design and return on investment analysis of residential solar photovoltaic systems," *IEEE Potentials*, vol. 34, no. 4, pp. 11–17, 2015.

[8] S. K. Yadav and U. Bajpai, "Performance evaluation of a rooftop solar photovoltaic power plant in northern India," *Energy for Sustainable Development*, vol. 43, pp. 130–138, 2018.

[9] A. K. Akella, M. P. Sharma, and R. P. Saini, "Optimum utilization of renewable energy sources in a remote area," *Renewable and Sustainable Energy Reviews*, vol. 11, no. 5, pp. 894–908, 2007.

[10] R. Ramakumar, "Energizing rural areas of development countries using IRES," in *Proceedings of the 31st Intersociety Energy Conversion Engineering Conference*, vol. 3, pp. 1536–1541, Washington, DC, USA, August 1996.

[11] A. Y. Saber and G. K. Venayagamoorthy, "Efficient utilization of renewable energy sources by gridable vehicles in cyber-physical energy systems," *IEEE Systems Journal*, vol. 4, no. 3, pp. 285–294, 2010.

[12] J. Tomic and W. Kempton, "Using fleets of electric-drive vehicles for grid support," *Journal of Power Sources*, vol. 168, no. 2, pp. 459–468, 2007.

[13] V. K. Sood and H. Abdelgawad, "Power converter solutions and controls for green energy," in *Distributed Energy Resources in Microgrids*, R. K. Chauhan and K. Chauhan, Eds., Academic Press, Cambridge, MA, USA, 2019.

[14] E. S. N. Raju and T. Jain, "Chapter 2-distributed energy resources and control," in *Distributed Energy Resources in Microgrids*, R. K. Chauhan and K. Chauhan, Eds., Academic Press, Cambridge, MA, USA, 2019.

[15] Academic Press, *Energy*, Academic Press, Cambridge, MA, USA, 2014.

[16] O. S. Ohunakin, "Energy utilization and renewable energy sources in Nigeria," *Journal of Engineering and Applied Sciences*, vol. 5, no. 2, pp. 171–177, 2010.

[17] T. Adefarati and R. C. Bansal, "Chapter 2-energizing renewable energy systems and distribution Generation," in *Pathways to a Smarter Power System*, A. Taşcıkaraoğlu and O. Erdinç, Eds., Academic Press, Cambridge, MA, USA, 2019.

[18] B. Brand and K. Blok, "Renewable energy perspectives for the North African electricity systems: a comparative analysis of model-based scenario studies," *Energy Strategy Reviews*, vol. 6, pp. 1–11, 2015.

[19] NEPCO, *Annual Report 2012*, National Electric Power Company (NEPCO), Amman, Jordan, 2012.

[20] IEA, *Energy Balances of Non-OECD Countries*, International Energy Agency, Paris, France, 2012 edition, 2013.

[21] E. Roman, R. Alonso, P. Ibanez, S. Elorduizapatarietxe, and D. Goitia, "Intelligent PV module for grid-connected PV systems," *IEEE Transactions on Industrial Electronics*, vol. 53, no. 4, pp. 1066–1073, 2006.

[22] A. Q. Al-Shetwi, M. A. Hannan, K. P. Jern, A. A. Alkahtani, and A. E. Abas, "Power quality assessment of grid-connected PV system in compliance with the recent integration requirements," *Electronics*, vol. 9, no. 2, p. 366, 2020.

[23] J. Nömm, S. Rönnberg, and M. Bollen, "An analysis of voltage quality in a nanogrid during islanded operation," *Energies*, vol. 12, no. 4, p. 614, 2019.

[24] S. Y. Mousazadeh Mousavi, A. Jalilian, M. Savaghebi, and J. Guerrero, "Flexible compensation of voltage and current unbalance and harmonics in microgrids," *Energies*, vol. 10, no. 10, p. 1568, 2017.

[25] B. Fan, J. Peng, J. Duan, Q. Yang, and W. Liu, "Distributed control of multiple-bus microgrid with paralleled distributed generators," *IEEE/CAA Journal of Automatica Sinica*, vol. 6, no. 3, pp. 676–684, 2019.

[26] B. Ali, B. Mohamed Lokmane, and D. Mohamed, "Grid connected photovoltaic system, for a 800 W," *Energy Procedia*, vol. 74, pp. 414–422, 2015.

[27] S. Chatterjee, P. Kumar, and S. Chatterjee, "A techno-commercial review on grid connected photovoltaic system," *Renewable and Sustainable Energy Reviews*, vol. 81, pp. 2371–2397, 2018.

[28] A. Amir, A. Amir, H. S. Che, A. Elkhateb, and N. A. Rahim, "Comparative analysis of high voltage gain DC-DC converter topologies for photovoltaic systems," *Renewable Energy*, vol. 136, pp. 1147–1163, 2019.

[29] M. M. Fouad, L. A. Shihata, and E. I. Morgan, "An integrated review of factors influencing the performance of photovoltaic panels," *Renewable and Sustainable Energy Reviews*, vol. 80, pp. 1499–1511, 2017.

[30] H. Brahmi and R. Dhifaoui, "Dynamic characteristics and improved MPPT control of PV generator," *Frontiers in Energy*, vol. 7, no. 3, pp. 342–350, 2013.

[31] G. M. Tina and S. Scrofani, "Electrical and thermal model for PV module temperature evaluation," in *Proceedings of the 14th IEEE Mediterranean Electrotechnical Conference*, pp. 585–590, Ajaccio, France, May 2008.

[32] R. Gammoudi, H. Brahmi, and R. Dhifaoui, "Estimation of climatic parameters of a PV system based on gradient method," *Complexity*, vol. 2019, Article ID 7385927, 10 pages, 2019.

[33] H. Brahmi and D. Rachid, "On UPFC application in interconnected power system including wind energy," in *Proceedings of the ICESE 2011: International Conference on Energy Systems Engineering*, Venice, Italy, April 2011.

[34] H. Brahmi, H. Othman, and D. Rachid, "Direct voltage stability assessment of large power systems," in *Proceedings of the 6ème Conférence Internationale des Sciences et Techniques de l'Automatique STA'05*, Sousse, Tunisie, December 2005.

Hindawi
Complexity
Volume 2021, Article ID 3459427, 13 pages
https://doi.org/10.1155/2021/3459427

Research Article

A Causal and Correlation Analysis between China Energy Futures and China Energy-Related Companies Stock Market

Yufang Liu,[1] Chi Zhang ,[2] and Wang Zhang[1]

[1]*State Grid Jiangsu Electric Power Co., Ltd., Nanjing 210000, Jiangsu, China*
[2]*School of Economics, Nanjing University of Posts and Telecommunications, Nanjing 210023, Jiangsu, China*

Correspondence should be addressed to Chi Zhang; anhuizhc@njupt.edu.cn

Received 27 April 2021; Revised 22 May 2021; Accepted 16 June 2021; Published 30 June 2021

Academic Editor: Chun Wei

Taking the opportunity of China's launch of Shanghai crude oil futures (INE), this study empirically examined the information transmission in this immature financial market, investigating this issue from a new perspective. To identify the impact of INE on the related stock market, we collected high-frequency trading data of oil futures and 22 stocks owned by listed companies in the upstream and downstream of China's oil-related industry chains, constructed a causal chain through Directed Acyclic Graph, and used MFDCCA-MODWT to perform multifractal analysis on the chain. Research shows that INE does have a causal relationship with the stock market of the related industry chain, and there is a multifractal correlation between its transaction time series. Subsequently, the source of fractal correlation was analysed with shuffled and surrogated sequences. We conclude that long memory plays a leading role and is the main reason for multifractal features.

1. Introduction

After the signing of the Paris Climate Agreement, most signatories took the development of green finance as one of the important means for the domestic financial industry to respond to global climate change. In China, the focus of the work of the financial sector has included issuing green bonds and green credit, and establishing a regional green finance pilot system. For example, the People's Bank of China announced in August 2019 that since 2016, China's green bond market has ranked first in the world in terms of issuance, with annual issuance and inventory ranking among the top in the world. The balance of green loans has increased year by year, accounting for nearly 10% of total domestic corporate loans.

The effective use of green finance depends on the effective operation of international financial markets, especially those closely related to climate change. The trading of oil-based energy products is one of the most important markets. For developing countries, the development of their financial markets is often not perfect, but their energy consumption is huge, and traditional analysis methods are doubtful when analysing relevant markets [1, 2]. How to better identify the development status of imperfect financial markets but closely related to green finance? The use of data-driven analysis methods has become an option.

Regarding the analysis of the impact of the futures market on the spot market, scholars mostly proceed from the perspective of information efficiency. In classic literature, Fama divides information into historical information, publicly disclosed information, and all unknown related information [3]. The information efficiency of the market refers to the ability of market prices to digest and absorb the information when a new information shock occurs and to guide investors through the market price to predict another market price, and the increase in transaction time and transaction volume can strengthen information transmission [4]. That is, information efficiency can be the basis of market price efficiency, and the measurement of information efficiency is theoretically a test of market efficiency. But in developing economies' financial markets, due to the high appearance of false transactions and falsified financial data, some traditional models are not effective in studying these markets [5]. Since in markets, a transaction is a transaction,

and the data that appear every moment bring useful information; therefore, this study looks forward to considering the problem in a purely data-driven way. To explore the information transmission efficiency of China's crude oil future, this paper collects the high-frequency data of Shanghai oil futures (INE) price and the stock prices of several listed companies. Furthermore, we use DAG and Multifractal Detrended Cross-correlation Analysis (MFDCCA) to study the information transmission path and the multifractal relationship between these two markets and then analyse the multifractal sources.

Different from the previous research, we analyse the information transmission between INE and related stock markets from a data-driven perspective. Since the scholars have disputes over whether the market is effective, we choose not to make any prior logical assumptions, but to investigate the problem from a pure data perspective. Such methods can be used not only in the financial markets of immature developing countries but also in the analysis of relevant topics in mature markets. On the one hand, the research provides ideas for investigating the relationship between the energy market and energy-related stock markets in China. On the other hand, research provides a basis for investigating market linkages in the immature financial markets of developing countries, and it also provides a framework for investigating related content in other markets around the world.

In this paper, Section 2 reviews the literature. Section 3 introduces the data and methodology. Section 4 initials empirical research and talks about result implications, Section 5 discusses and puts forward policy suggestions.

2. Literature Review

2.1. Energy Futures. Energy futures play an important role in ensuring global energy supply and maintaining economic stability [6, 7]. On the one hand, energy futures influence the global economic development by influencing the price of energy products [8, 9]; on the other hand, the financialization of energy products also has an impact on the economy through financial markets [10, 11]. Among them, oil futures are the most attractive. At present, the researchers have carried out a large number of studies on several major oil futures contracts, including the linkage with other financial markets [12, 13], the influence on oil spot prices and stock prices of downstream industries [14, 15], and the prediction of macroeconomic indicators. INE has been listed for a short time, and relevant researches on them also follow the above directions [16]. Scholars found a clear-tail dependence between the INE, equities, foreign exchange, and gold markets [17]. Moreover, there is a significant and continuous two-way volatility spillover effect between INE, WTI, and Brent [18, 19], and its yield is also in equilibrium with the yield of Daqing, Shengli, Oman, WTI, and Brent crude oil spot prices, which supports the pricing efficiency of crude oil futures prices in the Asia–Pacific region [20]. At the moment, global financial uncertainty will closely affect the volatility of the INE [21]. In some extreme environments, there is a strong causal relationship between oil futures prices and investor sentiment [22, 23]. After several years of development, INE prices now have short-term and medium-term independence and conductivity. However, compared with international benchmark oil prices, INE has limited pricing power and lacks long-term influence on the international crude oil market [24, 25]. With the introduction of INE, it will promote the balance of China's and European and North American crude oil market price systems, help to improve the world crude oil price system, and research on crude oil prices and capital markets is increasingly relevant. Compared with international research, there is a relative lack of research on China's oil price volatility spillover effect and less attention to the complex impact of oil price volatility types on capital markets. The correlation between economic sectors and oil prices also needs to be further deepened.

2.2. Directed Acyclic Graph (DAG). In mathematics, particularly graph theory, a DAG is a finite directed graph with no directed cycles. This means that it is impossible to traverse the entire graph starting at one edge. The edges of the directed graph only go one way. The graph is a topological sorting, where each node is in a certain order. Based on this idea, Spirtes proposed the DAG analysis method in 2000 [26]. This method can effectively identify the causal relationship among high-dimensional variables and determine the conduction path and direction of information. Compared to the traditional methods like Granger causality test, DAG does not need to apply any theoretical assumptions. It can derive the causal relationship only according to the residual variance-covariance matrix of the data, which makes itself a purely data-driven method. Besides, the employment of data-driven methods such as machine learning for analysis and prediction in the field of energy finance is also a hot topic in recent years [27, 28]. DAG was first applied to the economic analysis in 2003 [29] and has been widely used in several fields until now. Liang et al. analyses the internationalization trend of China's stock market from the perspective of information spillover and finds that though there are significant differences in the dynamic path between return and volatility spillover, the international integration process of China's stock market is steadily advancing [30]. Yang et al. combined DAG and VAR to study the international transfer of inflation among G7 countries and found that US inflation has become less vulnerable to foreign shocks since the early 1990s [31]. Awokuse studied the relationship between Japanese exports and economic growth and found a bidirectional relationship [32]. In these studies, DAG can not only identify the causal relationship in the overlap period [33] but also solve the problem of nonsynchronization between different markets by applying constraints and restrictions [29]. According to what is mentioned above, DAG can not only analyse the domestic market that overlaps with the trading time of Shanghai crude oil futures but also the overseas market with the overnight time difference, which makes this article and subsequent research possible.

2.3. MFDCCA-MODWT (Multifractal Detrended Cross-Correlation Analysis-Maximal Overlap Discrete Wavelet Transform). The idea of fractal first appeared in the 19th century, such as Weierstrass function and the Cantor set [34]. According to Britannica, fractal, in mathematics, any of a class of complex geometric shapes that commonly have "fractional dimension," a concept was first introduced by the mathematician Felix Hausdorff in 1918. And the term fractal, derived from the Latin word fractus, was coined by the Polish-born mathematician Benoit B. Mandelbrot [35], and now fractal has been applied in several fields [7]. The fractal method consists of single-fractal and multifractal. Single-fractal is mainly used to analyse the long memory of sequences, also known as persistence or antipersistence. Later, scholars have gradually found that the multi-scale and complexity of financial time series poses a challenge to the single-fractal. Mandelbrot pointed out that multifractal can better quantify the complex wave characteristics of financial markets compared to the single-fractal and has wider application in the empirical research [36]. However, both single-fractal and multifractal can only characterize the fractal features of a single time series and not capable of the correlation between two time series. Referring to time-series correlation analysis, Podobnik et al. introduced the detrended fluctuation analysis method to correlation analysis and proposed a detrended cross-correlation analysis (DCCA) which can measure the long memory of two nonstationary time series [37]. On this basis, Zhou combines DCCA and multifractal and proposes the MFDCCA to study the cross-correlation multifractal of two time series with the same observations [38]. Subsequently, scholars proposed MFDMA [39], MFADCCA [40], DMF-ADCCA [41], and MFDCCA-MODWT [42] according to different purposes and achieved certain results [43]. Nowadays, correlation analysis based on multifractal has now been widely used in energy [44, 45], meteorology [46], and financial markets [47–49]. MFDCCA-MODWT performs better than MFDCCA when measuring long memory features of sequences of different lengths and different Hurst exponents because it does not need to select different polynomial orders to fit to eliminate trend items in the time series. Hence, this paper will use MFDCCA-MODWT to measure the multifractal correlations between the sequences.

Therefore, the contribution of this paper is to use the DAG for the first time to examine the influence path of INE on the industry chain and, on this basis, analyse the source of the multifractal correlation between INE and related stocks.

3. Data and Method

3.1. Data. We searched all related industries upstream and downstream following the industry chain and found the stock with the largest market value in each industry. The sample includes INE and 22 other stocks selected according to the industry chain, covering oil and gas, coal, energy, and downstream sectors, respectively. In the crude oil futures market, multiple contracts are traded at the same time. To make the sample representative, we have selected continuous data on the main contract of INE. The sample period is from March 26 to August 23, 2018, and the data type is 1-minute high-frequency data. The details can be seen in Table 1. Column 1 is the acronym for the Chinese Pinyin of the stock names (i.e., zgsh stands for Zhong Guo Shen Hua in Chinese and China Shenhua Energy Company Limited in English), Column 2 is the stock codes, and the remaining two columns are the industry to which the stock belongs and the role of enterprises in the industrial chain.

After the data matching process, 193 price observations per day multiply 103 days, and at last 19,879 observations are obtained for each stock/futures.

3.2. Method

3.2.1. DAG. DAG is composed of nodes and vector edges. Nodes represent variables and directed edges connect these nodes to represent the synchronic relationship. By analysing the correlation coefficient and the partial correlation coefficient of the variables, the synchronic relationship between variables is identified. The identification steps are divided into "edge removal" and "orientation." In the "edge removal" stage, DAG starts from an "undirected complete graph," first tests the unconditional correlation coefficients between variables, removes the edges with significantly zero coefficients, and then analyses the first-order partial correlation coefficients. In the above analysis, the Fisher's z test is normally used to determine the significance level. For the two variables x and y, there are five possible results for the casual relationship: $x\,y$ (independent and unconnected), $x \longrightarrow y$ (x causes y), $y \longrightarrow x$ (y causes x), $x \leftrightarrow y$ (two-way causality), and $x-y$ (a causality but the relationship cannot be clarified). In this paper, the above operations can be implemented by PC algorithm in the TETRAD 6.6.0 software.

3.2.2. MFDCCA-MODWT. First, suppose there are two time series $\{x(i)\}$ and $\{y(i)\}$, $i = 1, 2, ..., N$, where N represents the length of the time series, and then construct a contour sequence:

$$X(i) = \sum_{t=1}^{i} (x(t) - \overline{x}), Y(i) = \sum_{t=1}^{i} (y(t) - \overline{y}), \tag{1}$$

where $\overline{x}$ and $\overline{y}$ are the mean of the time series $\{x(t)\}$ and $\{y(t)\}$.

Then, divide time series $\{X(i)\}$ and $\{Y(i)\}$ equally into $N_s = [N/s]$ nonoverlapping intervals of length s. And the sequence is inversely processed in consideration of the fact that the total length N may not be an integer multiple of s. The same processing is performed on the reverse order of the time series to obtain $2N_s$ subintervals to avoid information loss.

According to MODWT, a sequence $x(t)$ can be calculated by wavelet.

$$x(t) = S_{J,i} + D_{J,i} + D_{J-1,i} + \ldots + D_{1,i}, \tag{2}$$

where J and i are integers that represent the maximum level of scale s and the number of coefficients in the specified component, respectively. $D_{J,i}$ and $S_{J,i}$ respectively represent

Table 1: Details of 22 selected stocks.

Acronym	Code	Industry	Role in the industry chain
cjdl	600900	Hydropower	Upstream/energy alternatives
czmz	002108	Plastic products	Downstream/petroleum user
dhny	002221	Oil and gas	Upstream/energy alternatives
dxlt	000040	Photovoltaic	Upstream/energy alternatives
gjny	000096	Oil sales	Midstream/sales
hlgf	600346	Chemical fiber	Downstream/petroleum user
hlhs	600426	Fertilizer	Downstream/petroleum user
hngj	600011	Thermal power	Upstream/energy alternatives
jnfd	601016	Wind energy	Upstream/energy alternatives
kpd	603798	Lubricating oil	Midstream/petroleum intermediate products
lmkg	600167	Thermoelectric	Upstream/energy alternatives
lxkj	300487	Synthetic resin	Downstream/petroleum user
qxtd	002408	Chemical raw materials	Downstream/petroleum user
shsh	600688	Refined oil refining	Upstream/oil production
slda	000553	Pesticide	Downstream/petroleum user
sls	002224	Synthetic rubber	Downstream/petroleum user
strq	002267	Oil and gas	Midstream/oil restore and transportation
sxjh	600740	Coking	Upstream/energy alternatives
zghd	601985	New energy	Upstream/energy alternatives
zgsh	601088	Raw coal mining	Upstream/energy alternatives
zgsy	601857	Oil and gas	Upstream/oil production
zjjk	002061	Polyurethane	Downstream/petroleum user

the wavelet and smooth trend of the sequence in the interval. By this method, a local trend for each interval v is calculated: $\widehat{y}_v(i) = S_{J,i}$. Then, construct the sequence residual:

$$\varepsilon_v(i) = y_v(i) - S_{J,i}\ 1 \le i \le s. \tag{3}$$

Thus, for each interval v, we can obtain wave function for two time series as follows:

$$F^2(s,v) = \frac{1}{s}\sum_{t=1}^{s}\left|\varepsilon_v^{(1)}(i)\right| \cdot \left|\varepsilon_v^{(2)}(i)\right|. \tag{4}$$

Fourth, construct a q-order wave function:

$$\text{when } q \neq 0, F_q(s) = \left\{\frac{1}{2N_s}\sum_{v=1}^{2N_s}\left[F^2_{(s,v)}\right]^{q/2}\right\}^{1/q},$$
$$\text{when } q = 0, F_q(s) = \exp\left\{\frac{1}{4N_s}\sum_{v=1}^{2N_s}\ln\left[F^2_{(s,v)}\right]\right\}. \tag{5}$$

Last, given any real number q, The scaling behavior of fluctuations can be described by a log-log graph between $F_q(s)$ and s. If $\{x(i)\}$ and $\{y(i)\}$ have a long-term correlation, then $F_q(s)$ changes by the power law:

$$F_q(s) \sim s^{H_{xy}(q)}. \tag{6}$$

Take the logarithm of two sides of equation (6):

$$logF_q(s) = H_{xy}(q)\log(s) + logA. \tag{7}$$

The scaling index $H_{xy}(q)$ is the Hurst exponent, which is the slope of the function diagram of $\ln F_q(s) \sim \ln s$. It could measure the power-law relationship between time series. If $H_{xy}(q)$ is independent of q, the correlation is single-fractal; if $H_{xy}(q)$ changes with q, the correlation has multifractal characteristics. When $q > 0(<0)$, $H_{xy}(q)$ exhibits the scaling behavior of the correlation between large (small) fluctuations of two time series.

The relationship between $H(q)$ and the multifractal index $t(q)$ is as follows:

$$t(q) = qH(q) - 1. \tag{8}$$

If $t(q)$ is a nonlinear function of q, it shows that series has multifractal characteristics.

With Legendre transform, we can obtain the relationship between the multifractal spectrum $D(q)$ and $h(q)$:

$$h(q) = \frac{dt(q)}{dq}, \tag{9}$$

$$D(q) = qh(q) - t(q), \tag{10}$$

where $h(q)$ is a singularity index that describes the singularity of a time series. $D(q)$ is a multifractal spectrum reflecting the fractal dimension with a singular exponent $h(q)$. To better reflect the multifractal characteristics, we use a financial risk index:

$$\Delta H = H_{\max}(q) - H_{\min}(q), \tag{11}$$

where ΔH is the range of $H_{xy}(q)$. The larger the span, the more obvious the multifractal feature and the higher the risk. According to equation (10), $\Delta H_{xy}(q)$ will be an index of the multifractal degree.

4. Empirical Analysis

4.1. Causality Analysis. We first import the processed 23 sets of data into TETRAD 6.6.0, and set the display mode as "causal order" and obtain Figure 1. In Figure 1, there are

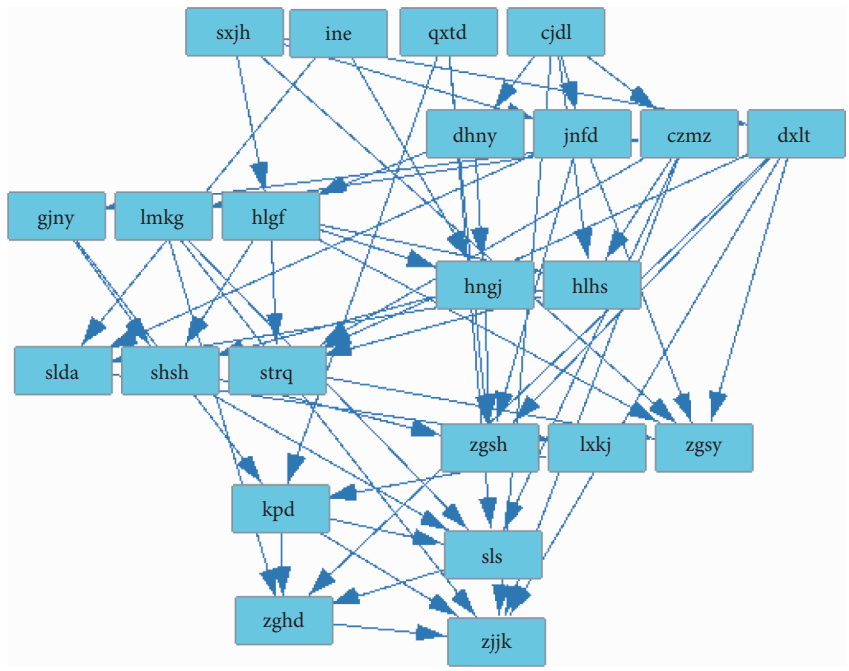

Figure 1: Causality diagram of INE and 22 stocks.

eight levels, of which INE and the other three stocks are in the first level, indicating that INE does have an impact on the relevant industries from the source, but the impact is not single, some stocks below in the hierarchy are affected by multiple sources. Since this paper mainly examines the correlation between INE and related industries, to simplify the subsequent analysis, we only select the causality chain containing INE for analysis. Based on this idea, we simplified Figure 1 to obtain Figure 2. In Figure 2, we can see that the causal relationship of volatility is roughly transmitted along the industrial chain: INE ⟶ Oil and gas exploration and sales ⟶ Downstream products. In addition, INE also directly affects the stock price fluctuation of downstream products.

4.2. Correlation Analysis. In this section, we will analyse the multifractal correlation between INE and stocks based on the causal relationships shown in Figure 2 and examine the sources of correlation.

Figure 3 shows the plot of the log $F_q(s) - \log(s)$ obtained by MFDCCA-MODWT. The curves in each subgraph from bottom to top correspond to $q = -10, -9, -8 \ldots, 8, 9, 10$. In Figure 3, we find that the slope of the curve is different for different q. The bigger the q, the flatter the curve. When q approaches −10, the curve fluctuates to a certain extent, but the values of the coefficient H(q) and the constant term log(A) obtained by OLS are significant at the 1% significance level. Therefore, for different q, each curve is linear, which indicates that there is a power–law correlation between the volatility of two products with a causal relationship.

Figure 4 shows the Hurst exponent Hq calculated by MFDCCA-MODWT. It can be seen from the figure that Hq decreases gradually as the q increases, indicating that the scaling index is not a constant, that is, the cross-correlation between the volatility has the multifractals. In addition, when $q = 2$, H(q) is greater than 0.5, indicating long-term memory. The scale index is approximately greater than 0.5 in the interval of $-10 < q < 7$, indicating that the correlation of volatility in this interval has long-range persistence; and less than 0.5 in the interval of $7 < q < 10$, indicating that the volatility correlation has an inverse persistence in this interval. That is to say, the cross-correlation of the volatility of the selected samples is characterized by multiple fractals. In general, H(q) decreases as q increases, indicating that the cross-correlation of volatility with small fluctuations is more persistent than the cross-correlation when large fluctuations occur. In short, when there is a small fluctuation occurs in one market compared to large fluctuations, the persistence of the cross-price correlation between the two markets is stronger.

4.3. Multifractal Analysis. The multifractal strength of the financial system is expressed by the degree of nonlinearity of the scale index. It can be seen from the second column of Figure 5 that the curve has a certain degree of curvature but is not obvious, indicating that the cross-correlation between the price of selected products has weak multifractal characteristics. The third column of Figure 5 is a singular spectral function of the multifractal spectrum that describes the complex dynamics of financial markets. In general, the multifractal spectral width is used to estimate the fractal strength. According to the study of Chen and He [50], the multifractality can be expressed by the width of the multifractal spectrum: Δhq and Δhq can measure the absolute magnitude of the price fluctuation of time series.

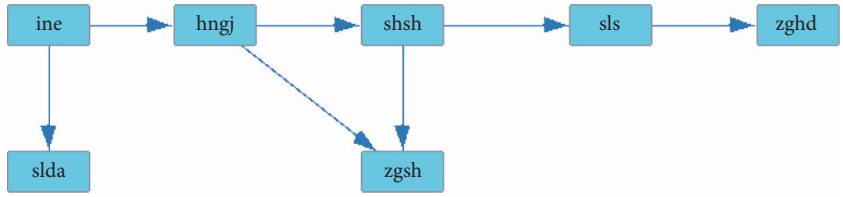

Figure 2: Simplified causality diagram of INE and 6 stocks.

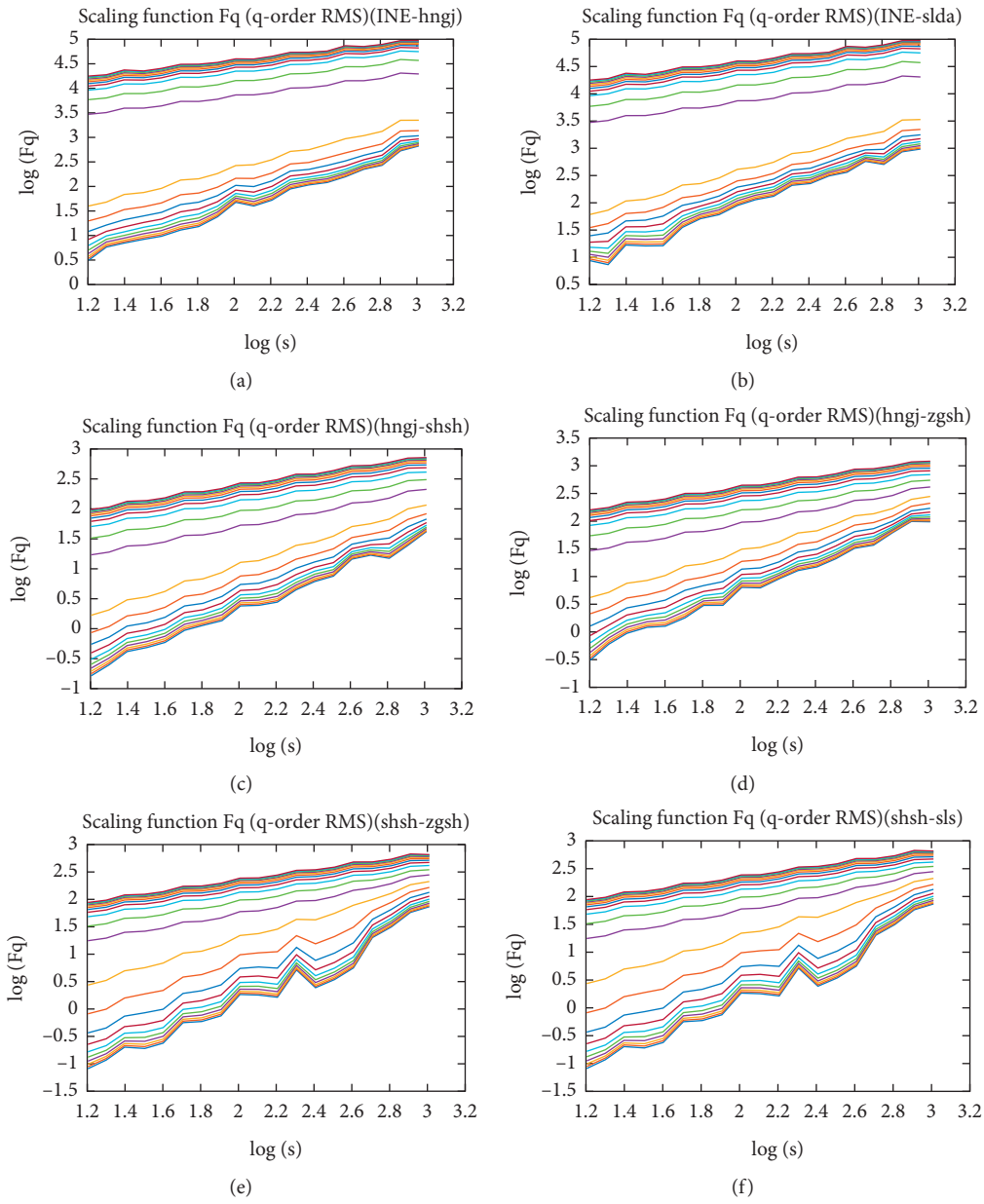

Figure 3: Continued.

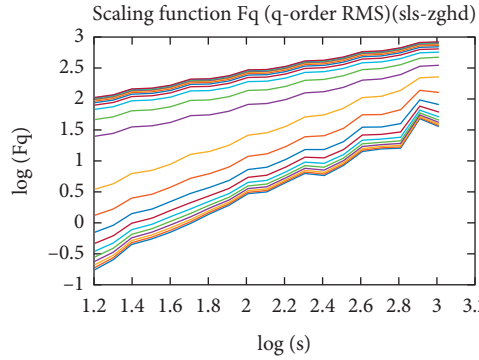

(g)

Figure 3: $\log F_q(s) - \log(s)$ of seven pairs of causality among INE and other six stocks.

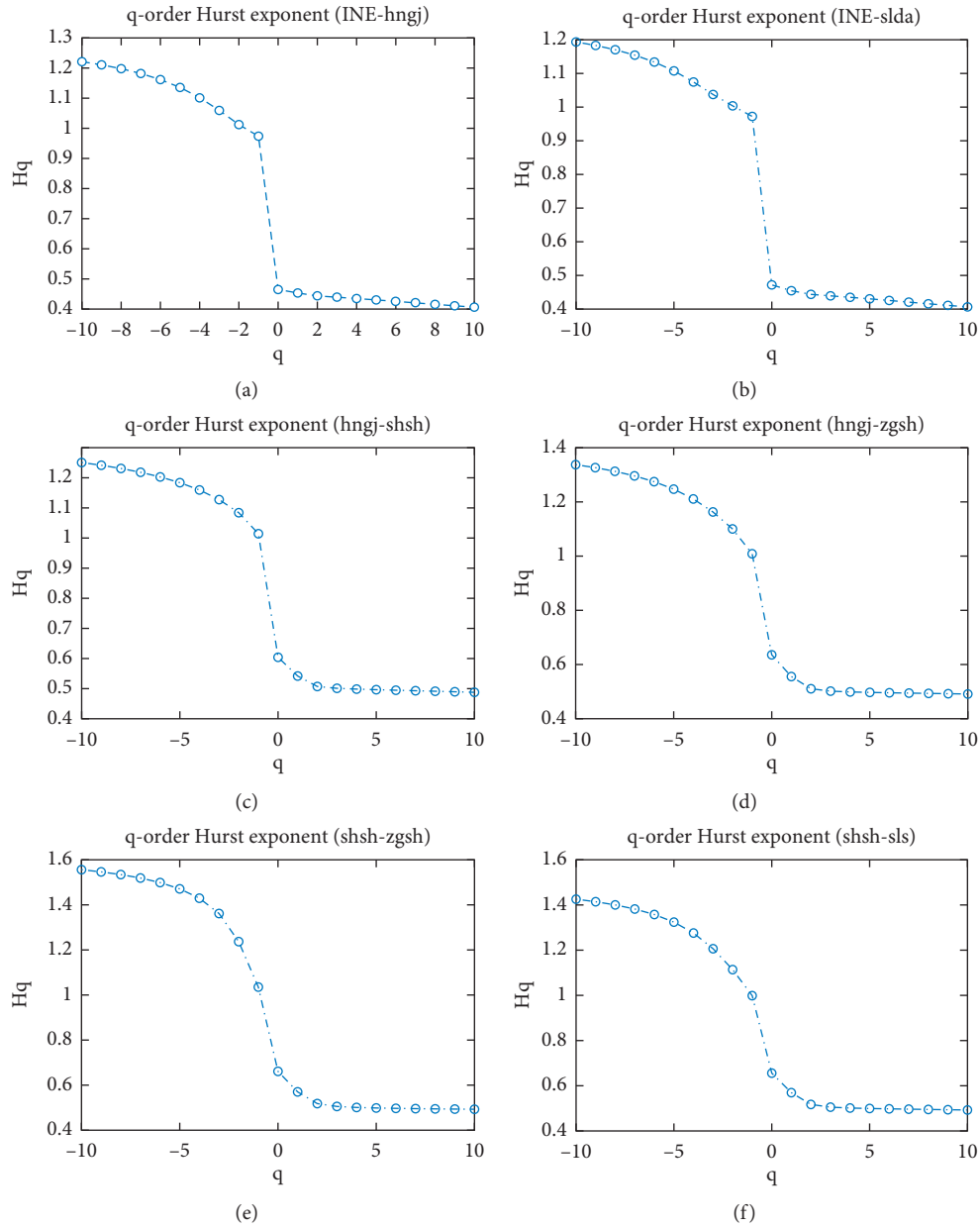

Figure 4: Continued.

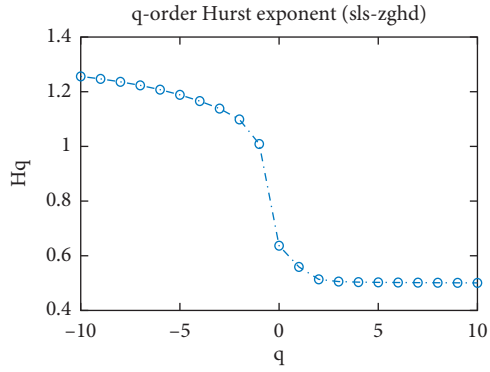

(g)

Figure 4: Hq – q of seven pairs of causality among INE and other six stocks.

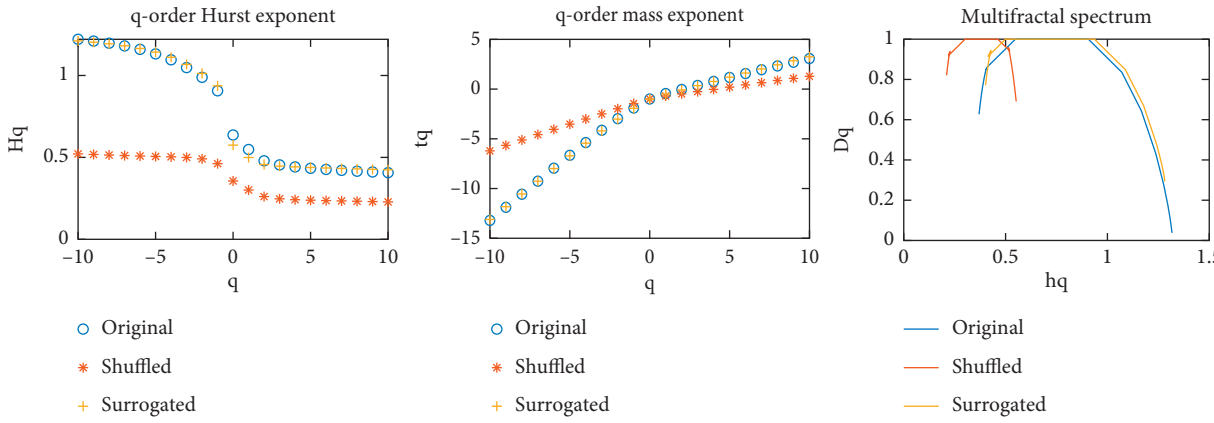

(a)

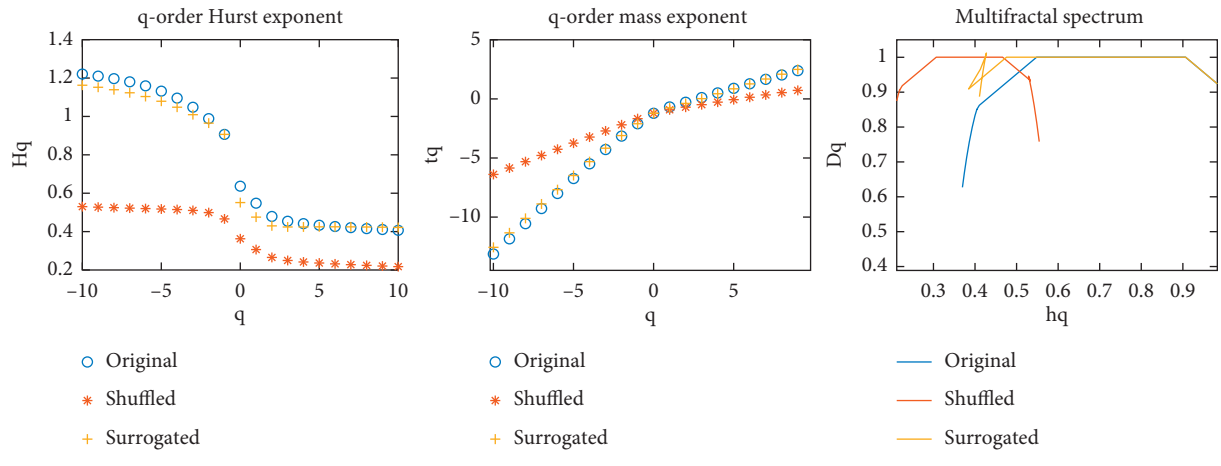

(b)

Figure 5: Continued.

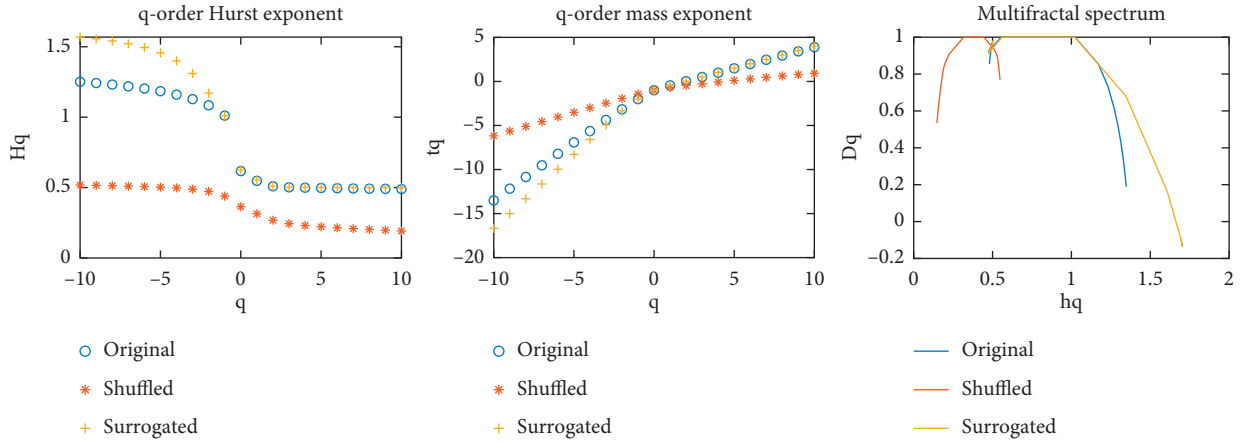

(c)

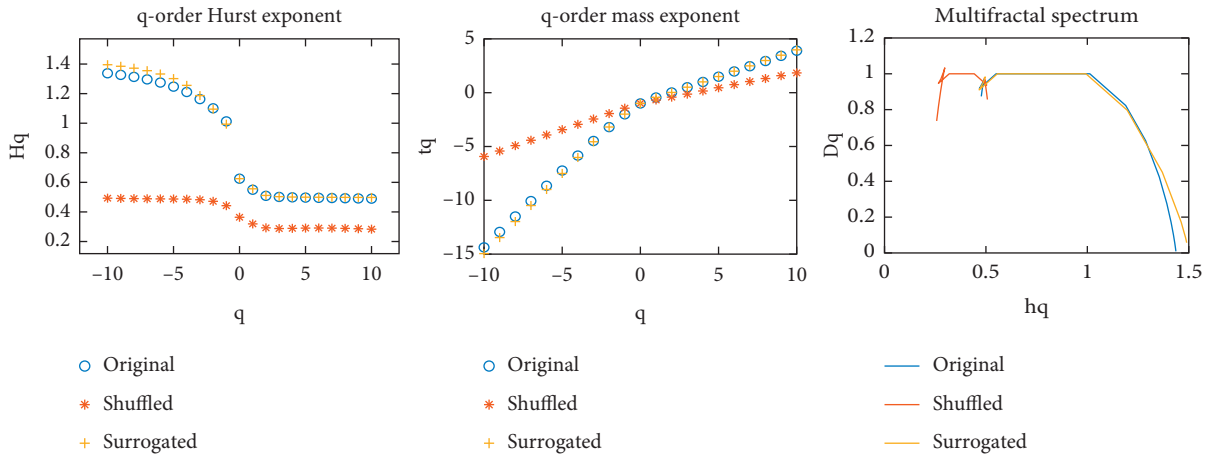

(d)

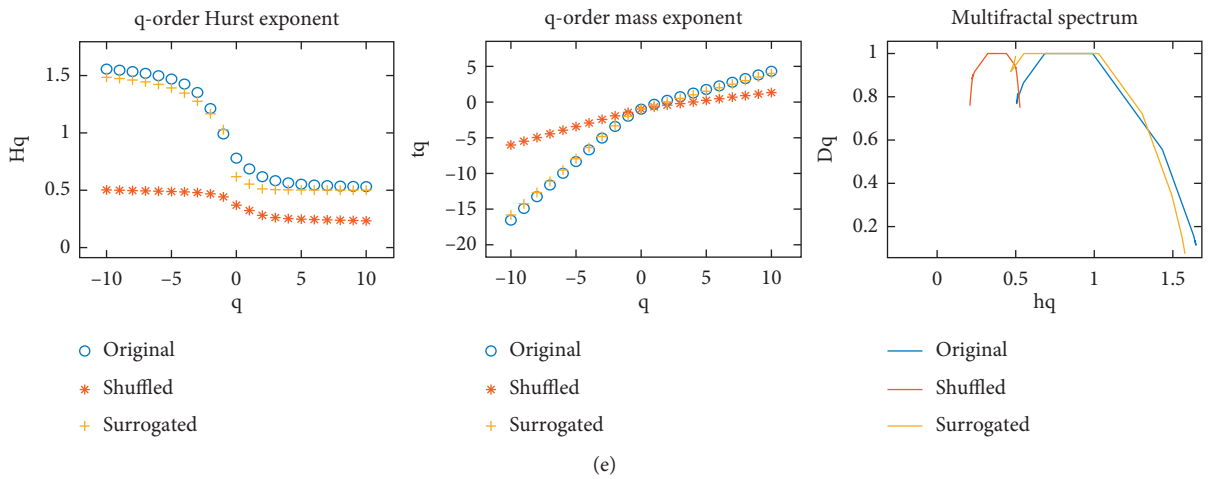

(e)

Figure 5: Continued.

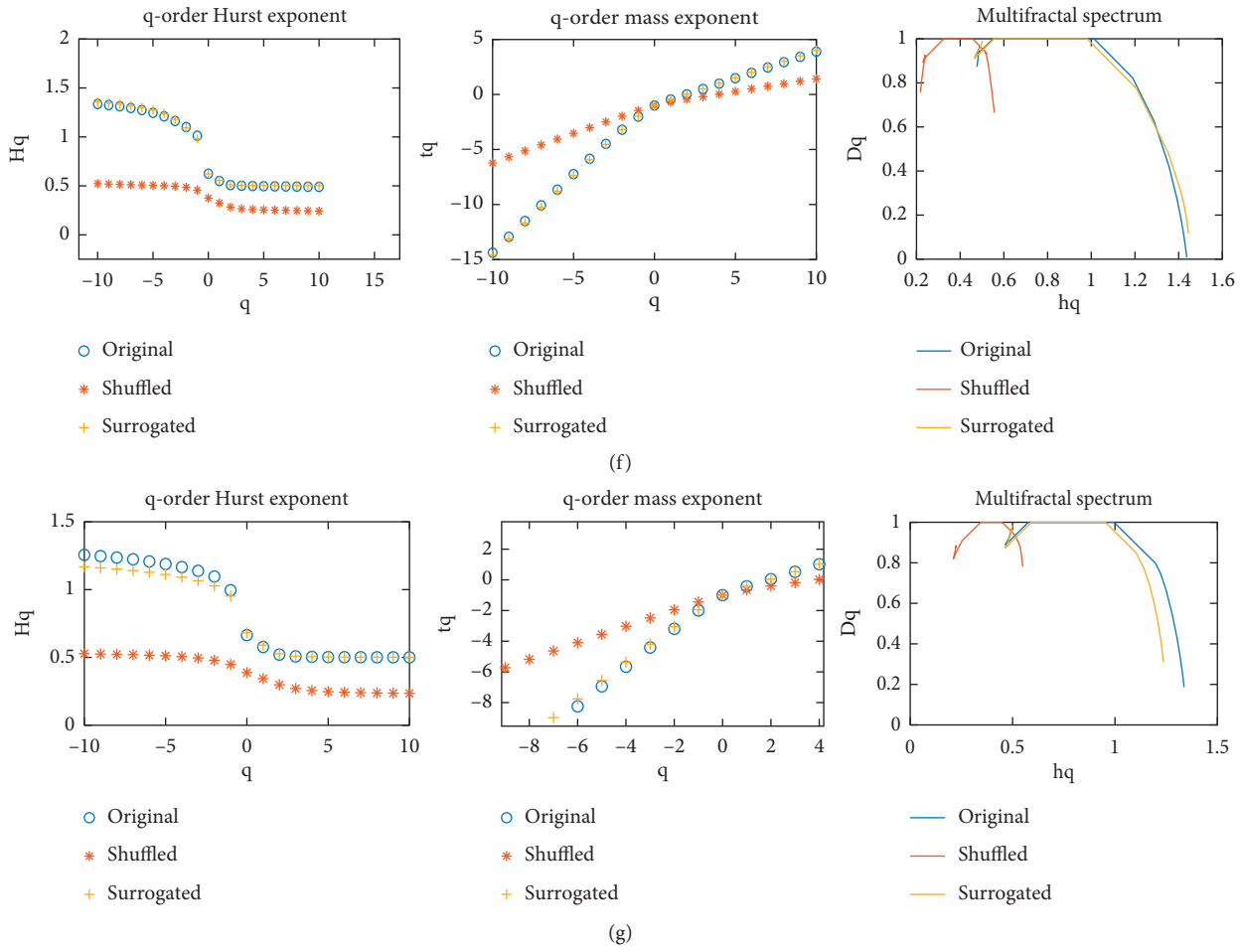

Figure 5: Comparison of Hurst exponent, mass exponent, and multifractal spectrum of original, shuffled, and surrogated series. (a) INE-hngj. (b) INE-slda. (c) hngj-shsh. (d) hngj-zgsh. (e) shsh-zgsh. (f) shsh-sls. (g) sls-zghd.

In the above, we found that the cross-correlation between INE and selected stocks price volatility has strong multifractal characteristics. Based on this, we will further explore the source of multifractal features. From the existing literature, there are many different methods used to characterize the implicit behavior of different financial variables, such as wave scale analysis, structure-function, wavelet transform method, and so on. It is generally believed that the thick tail distribution and the long memory are two possible sources of multifractal properties in financial time series [51]. First, by comparing the degree of multifractal between the original and the shuffled series, we can quantify the contribution of long memory. In this paper, the shuffled sequence can be achieved by the randperm command in the Matlab software. We repeat 100 times to ensure that the original series is completely disrupted. Second, the classical method of quantifying the contribution of thick-tailed distributions in sequence with multifractal features is to compare the multifractal degree between the original sequence and surrogated sequence. Here, the surrogate sequence is achieved by Fourier phase randomization. The procedure creates a surrogate data with the same correlation properties as the original signal [52]. Following the procedure, one performs a Fourier transform on the original time series, preserving the Fourier amplitudes but randomizing the Fourier phases. Finally, one performs an inverse Fourier transform to create surrogate data [53]. The results are shown in Figure 5 and Table 2.

From Table 2 we can see that the ΔHq and Δhq calculated with a shuffled and surrogated sequence is smaller than the original sequence, indicating that the multifractal feature between the volatility sequences is caused by the long memory and thick tail distribution. Figure 5 provides the span of Hurst exponent H(q) and the fractal spectrum between the original, shuffled, and surrogated series. It can be seen that the range of ΔH and Δhq of the original sequence was significantly reduced after shuffled and surrogated, indicating that that long memory and thick tail distributions play a role in multifractals. However, after comparing shuffled and surrogated sequences, we found that the shuffled sequence has a narrow opening in Figure 5, indicating that long memory plays a leading role and is the main reason for multifractal features.

For the empirical tests, we focused on the price correlation between China's first mature crude oil futures product and several key stocks in the crude oil industry chain in the

Table 2: ΔHq and Δhq of original, shuffled, and surrogated series.

	ΔHq			Δhq		
	Original	Shuffled	Surrogated	Original	Shuffled	Surrogated
INE-hngj	0.82	0.30	0.78	0.95	0.34	0.88
INE-slda	0.75	0.32	0.74	0.89	0.37	0.78
hngj-shsh	0.77	0.32	1.01	0.86	0.40	1.22
hngj-zgsh	0.85	0.18	1.10	0.97	0.25	1.02
shsh-zgsh	1.02	0.24	0.98	1.14	0.32	1.11
shsh-sls	0.93	0.31	0.85	1.06	0.34	0.98
sls-zghd	0.75	0.32	0.66	0.87	0.33	0.77

domestic stock market and obtained the following three findings: First, DAG ascertains the price causal relationship among INE and key stocks. From the simplified DAG, it can be seen that the price of INE has affected the market prices of oil and gas exploration and sales companies in China's financial market, and further affecting the stock price of downstream industry companies. Second, based on MFDCCA-MODWT with high-frequency data, we verified that there is a multifractal correlation among INE and selected stocks and the correlation between small fluctuations is higher than that between the large fluctuations. Third, by using shuffled and surrogated sequences, we prove that this multifractal is caused by long memory and thick tail distribution, and long-term memory is the main source of the multifractal features.

5. Discussion

Following the above results, the conclusion for the research could be drawn from two aspects. On one hand, for the financial market, the results of DAG and MFDCCA-MODWT show that INE could bring stable expectations and guidance to the market performance of China's key crude oil industry-related companies during trading hours. These results prove that INE has a good ability to reduce the risk of related products in the financial market. This indicator is especially crucial for high-frequency traders. Also, the correlation between the price of crude oil futures and the stock price of listed companies can be a piece of useful supplementary information for green finance tools using. If a listed company does have a green technology promotion, its stock price can usually find its value quickly. At this time, the auditing institution focuses on the correlation fluctuation between the company and the price of crude oil futures as double insurance to evaluate the authenticity of the declaration materials.

On the other hand, for Chinese policymakers, we suggest that China can better sort out its market linkages, and on this basis, promote its green financial policies more effectively. In addition, considering that the spillover effects of fluctuations between different financial sub-markets in China are more complex, decision-making departments should take into account the development trend of each financial sub-market and the information spillover and risk dissemination among the sub-markets, and strengthen structural governance to enhance the suitability of China's financial market system. Besides China, this research provides a basis for investigating market linkages in the immature financial markets of developing countries, and it also provides a framework for investigating related content in other markets around the world. At the same time, we can also use the linkages between the markets to design a check and balance mechanism to better regulate the energy market and implement precise policies to make more contributions to the control of global warming.

Data Availability

The data used to support the findings of this study are available from the corresponding author upon request.

Conflicts of Interest

The authors declare that they have no conflicts of interest.

Acknowledgments

This research was funded by Nanjing University of Posts and Telecommunications (grant no. NYY219004).

References

[1] Jacobs and Heiko, "Market maturity and mispricing," *Journal of Financial Economics*, vol. 122, no. 2, pp. 270–287, 2016.

[2] R. F. Stambaugh and Y. Yuan, "Mispricing factors," *The Review of Financial Studies*, vol. 30, no. 4, pp. 1270–1315, 2017.

[3] E. F. Fama, "Efficient capital markets: a review of theory and empirical work," *Journal of Finance*, vol. 25, no. 2, pp. 383–417, 1970.

[4] B. Ben Sita and P. J. Westerholm, "The role of trading intensity estimating the implicit bid-ask spread and determining transitory effects," *International Review of Financial Analysis*, vol. 20, no. 5, pp. 306–310, 2011.

[5] B. Yang, "Is informational inefficiency priced in stock markets? A comparison between the U.S. and Chinese cases," *Pacific-Basin Finance Journal*, vol. 55, pp. 222–238, 2019.

[6] C. Zhang, Z. Pu, and Q. Zhou, "Sustainable energy consumption in Northeast Asia: a case from China's fuel oil futures market," *Sustainability*, vol. 10, no. 1, p. 261, 2018.

[7] C. Zhang, Z. Pu, and J. Fu, "The recurrence interval difference of power load in heavy/light industries of China," *Energies*, vol. 11, no. 1, p. 106, 2018.

[8] C. Wei, "An optimal scheduling strategy for peer-to-peer trading in interconnected microgrids based on RO and Nash bargaining," *Applied Energy*, vol. 295, Article ID 117024, 2021.

[9] C. Zhang, J. Fu, and Z. Pu, "A study of the petroleum trade network of countries along "The Belt and Road Initiative," *Journal of Cleaner Production*, vol. 222, pp. 593–605, 2019.

[10] Z. Pu, "Structure decomposition analysis of embodied carbon from transition economies," *Technological Forecasting and Social Change*, vol. 135, no. 10, pp. 1–12, 2018.

[11] Z. Pu, S. Yue, and P. Gao, "The driving factors of China's embodied carbon emissions," *Technological Forecasting and Social Change*, vol. 153, Article ID 119930, 2020.

[12] E. M. Diaz, J. C. Molero, and F. Perez de Gracia, "Oil price volatility and stock returns in the G7 economies," *Energy Economics*, vol. 54, pp. 417–430, 2016.

[13] W. Mensi, "Modeling systemic risk and dependence structure between oil and stock markets using a variational mode decomposition-based copula method," *Journal of Banking & Finance*, vol. 75, pp. 258–279, 2017.

[14] Q. Li, K. Cheng, and X. Yang, "Response pattern of stock returns to international oil price shocks: from the perspective of China's oil industrial chain," *Applied Energy*, vol. 185, pp. 1821–1831, 2017.

[15] R. G. Cong, "Relationships between oil price shocks and stock market: an empirical analysis from China," *Energy Policy*, vol. 36, no. 9, pp. 3544–3553, 2008.

[16] Q. Ji and D. Zhang, "China's crude oil futures: introduction and some stylized facts," *Finance Research Letters*, vol. 28, pp. 376–380, 2019.

[17] H. Chaohua, "Correlation between Shanghai crude oil futures, stock, foreign exchange, and gold markets: a GARCH-vine-copula method," *Applied Economics*, vol. 53, no. 11, pp. 1249–1263, 2021.

[18] W. Liang, "The price volatility spillover effect and its sustainability between Chinese crude oil future and international crude oil futures-based on the BEKK-MGARCH model," *Systems Engineering*, vol. 12, pp. 1–22, 2020.

[19] D. Zhang and Q. Ji, "Studies on the dynamic risk spillovers for China's crude oil futures," *Chinese Journal of Management Science*, vol. 11, pp. 1–8, 2018.

[20] Y. Chen, "The pricing efficiency of crude oil futures in the Shanghai international exchange," *Finance Research Letters*, vol. 36, Article ID 101329, 2020.

[21] Y. Kun, "Global financial uncertainties and China's crude oil futures market: evidence from interday and intraday price dynamics," *Energy Economics*, vol. 96, Article ID 105149, 2021.

[22] C. Rongda, B. Weiwei, and J. Chenglu, "Investor sentiment and predictability for volatility on energy futures Markets: evidence from China," *International Review of Economics and Finance*, vol. 75, 2021.

[23] W. Lu, "The importance of extreme shock: examining the effect of investor sentiment on the crude oil futures market," *Energy Economics*, vol. 99, Article ID 105319, 2021.

[24] T. Hongzhi, Y. Feng, and L. Hui, "Does China have the international pricing power for crude oil?-based on a perspective of independence and conductivity between oil prices," *China Management Science*, vol. 28, no. 11, pp. 90–99, 2020.

[25] Z. Qi, D. Peng, and F. Arash, "Study on the impacts of Shanghai crude oil futures on global oil market and oil industry based on VECM and DAG models," *Energy*, vol. 223, Article ID 120050, 2021.

[26] P. Spirtes, *Causation, Prediction, and Search*, MIT Press, Cambridge, MA, USA, 2000.

[27] B. Zhu, "Forecasting carbon price using empirical mode decomposition and evolutionary least squares support vector regression," *Applied Energy*, vol. 191, no. APR.1, pp. 521–530, 2017.

[28] W. Sun and C. Zhang, "Analysis and forecasting of the carbon price using multi—resolution singular value decomposition and extreme learning machine optimized by adaptive whale optimization algorithm," *Applied Energy*, vol. 231, pp. 1354–1371, 2018.

[29] D. A. Bessler and J. Yang, "The structure of interdependence in international stock markets," *Journal of International Money and Finance*, vol. 22, no. 2, pp. 261–287, 2003.

[30] Q. Liang, Z. Li, and X. Hao, "The internationalization of Chinese stock market:based on information spillover," *Economic Research Journal*, vol. 4, pp. 150–164, 2015.

[31] J. Yang, H. Guo, and Z. Wang, "International transmission of inflation among G-7 countries: a data-determined VAR analysis," *Journal of Banking & Finance*, vol. 30, no. 10, pp. 2681–2700, 2006.

[32] T. O. Awokuse, "Export-led growth and the Japanese economy: evidence from VAR and directed acyclic graphs," *Applied Economics Letters*, vol. 12, no. 14, pp. 849–858, 2005.

[33] J. Yang and Y. Zhou, "Credit risk spillovers among financial institutions around the global credit crisis: firm-level evidence," *Management Science*, vol. 59, no. 10, pp. 2343–2359, 2013.

[34] C. C. Leary, D. A. Ruppe, and G. Hartvigsen, "Fractals, average distance and the cantor set," *Fractals-complex Geometry Patterns & Scaling in Nature & Society*, vol. 18, no. 3, pp. 327–341, 2010.

[35] B. B. Mandelbrot, "The fractal geometry of nature," *American Journal of Physics*, vol. 51, no. 3, p. 286, 1983.

[36] B. B. Mandelbrot, "The variation of certain speculative prices," in *Fractals and Scaling in Finance*, pp. 371–418, Springer, Berlin, Germany, 1997.

[37] B. Podobnik and H. E. Stanley, "Detrended cross-correlation analysis: a new method for analyzing two nonstationary time series," *Physical Review Letters*, vol. 100, no. 8, Article ID 084102, 2008.

[38] W.-X. Zhou, "Multifractal detrended cross-correlation analysis for two nonstationary signals," *Physical Review E*, vol. 77, no. 6, Article ID 066211, 2008.

[39] G.-F. Gu and W.-X. Zhou, "Detrending moving average algorithm for multifractals," *Physical Review E*, vol. 82, no. 1, Article ID 011136, 2010.

[40] G. Cao, "Detrended cross-correlation analysis approach for assessing asymmetric multifractal detrended cross-correlations and their application to the Chinese financial market," *Physica A: Statistical Mechanics and Its Applications*, vol. 393, pp. 460–469, 2014.

[41] G. Cao, "Asymmetric MF-DCCA method based on risk conduction and its application in the Chinese and foreign stock markets," *Physica A: Statistical Mechanics and Its Applications*, vol. 468, pp. 119–130, 2017.

[42] G. Cao and W. Xu, "Nonlinear structure analysis of carbon and energy markets with MFDCCA based on maximum overlap wavelet transform," *Physica A: Statistical Mechanics and Its Applications*, vol. 444, pp. 505–523, 2016.

[43] Z. Q. Jiang, "Multifractal analysis of financial markets: a review," *Reports on Progress in Physics*, vol. 82, no. 12, Article ID 125901, 2019.

[44] S. Fang, "Multifractal detrended cross-correlation analysis of carbon emission allowance and stock returns," *Physica A: Statistical Mechanics and Its Applications*, vol. 509, pp. 551–566, 2018.

[45] W. Xu, "Asymmetric volatility spillovers between oil and stock markets: evidence from China and the United States," *Energy Economics*, vol. 80, pp. 310–320, 2019.
[46] C.-H. Shen and C.-L. Li, "An analysis of the intrinsic cross-correlations between API and meteorological elements using DPCCA," *Physica A: Statistical Mechanics and Its Applications*, vol. 446, pp. 100–109, 2016.
[47] J. Huang and D. Gu, "Multiscale multifractal detrended cross-correlation analysis of high-frequency financial time series," *Fluctuation and Noise Letters*, vol. 18, no. 3, Article ID 1950014, 2019.
[48] R. Gu and B. Zhang, "Is efficiency of crude oil market affected by multifractality? Evidence from the WTI crude oil market," *Energy Economics*, vol. 53, pp. 151–158, 2016.
[49] W. Kristjanpoller and E. Bouri, "Asymmetric multifractal cross-correlations between the main world currencies and the main cryptocurrencies," *Physica A: Statistical Mechanics and Its Applications*, vol. 523, pp. 1057–1071, 2019.
[50] L.-Y. He and S.-P. Chen, "A new approach to quantify power-law cross-correlation and its application to commodity markets," *Physica A: Statistical Mechanics and Its Applications*, vol. 390, no. 21-22, pp. 3806–3814, 2011.
[51] J. W. Kantelhardt, "Multifractal detrended fluctuation analysis of nonstationary time series," *Physica A: Statistical Mechanics and Its Applications*, vol. 316, no. 1-4, pp. 87–114, 2002.
[52] J. Theiler, "Testing for nonlinearity in time series: the method of surrogate data," *Physica D: Nonlinear Phenomena*, vol. 58, no. 1-4, pp. 77–94, 1992.
[53] B. Podobnik, "Power-law autocorrelated stochastic processes with long-range cross-correlations," *The European Physical Journal B*, vol. 56, no. 1, pp. 47–52, 2007.

Hindawi
Complexity
Volume 2021, Article ID 4249152, 11 pages
https://doi.org/10.1155/2021/4249152

Research Article

Multistep Finite Control Set Model Predictive Control of Photovoltaic Power Generation System with Harmonic Compensation

Xuejiao Gong, Shifeng Hu, and Ruijin Zhu

College of Electrical Engineering, Tibet Academy of Agriculture and Animal Husbandry, Lhasa, Tibet Autonomous Region 860000, China

Correspondence should be addressed to Shifeng Hu; sushe11203@126.com

Received 14 April 2021; Revised 19 May 2021; Accepted 9 June 2021; Published 18 June 2021

Academic Editor: Chun Wei

Photovoltaic (PV) power generation is the main aspect of new energy power generation, and it is an important means to achieve the goal of carbon neutrality. When the PV system is connected to the grid, the nonlinear load of the grid will affect the power quality and consume reactive power. This paper proposes a PV power generation grid-connected system to improve power quality, with an active power filter (APF) function. Through the maximum power point tracking (MPPT) method, PV power generation can operate at the maximum power point and play the function of harmonic and reactive power compensation at the load side. To improve the dynamic performance of the grid-connected PV system and harmonic compensation simultaneously, multistep finite control set model predictive control (FCS-MPC) is adopted for the grid-connected module. The whole system does not need additional equipment, as it plays the role of two devices and effectively reduces the input cost. In this paper, the proposed structure and multistep FCS-MPC are verified in MATLAB/Simulink. The results show that the system injects the maximum power into the power grid at the same time when the load changes and compensates the harmonic generated by the nonlinear load of the power grid so that the total harmonic distortion of the power grid can meet the operation standard, and the system has good dynamic performance and steady-state performance.

1. Introduction

Renewable energy power generation is the primary means to solve the global environmental problems and energy crisis. It includes photovoltaic (PV) power generation, wind power generation, biological power generation, and other new energy power generation methods, which are the inevitable trend of grid-connected power generation [1, 2]. Photovoltaic power generation is becoming more popular because of its convenience, strong reliability, and low use conditions, which can meet the needs of large power grids and ordinary residents. Because of the randomness of photovoltaic power generation system, [3] realizes machine learning to accurately predict the photovoltaic power generation, which ensures the stable operation of power grid. In previous work [4], a support vector machine (GASVM) model based on genetic algorithm is proposed. SVM classifier is used to optimize the historical weather data, which improves the accuracy of prediction. The direct current generated by the PV power generation array is controlled by MPPT to keep the maximum power output, and then the PV grid-connected system supplies the direct current to the grid or load through the inverter [1, 5–8]. Due to the characteristics of converters and the existence of many nonlinear loads in the grid, harmonic pollution is inevitable in the grid-connected system. In this paper, a method of the grid-connected PV power generation and harmonic compensation is proposed. Through the control of the inverter, the active power of the grid is guaranteed, and the power quality is improved [9, 10].

General PV devices meet the needs of the home and industry, and all kinds of loads will inevitably flow harmonics into the grid, which will reduce the power quality of the grid and affect the safe operation of the grid. At present, the main ways of harmonic control include improving the

converter topology [11, 12], reducing the generation of harmonics from the harmonic source, and using an active power filter (APF), static var generator, unified power quality conditioner, and other devices to supplement. APF is widely used because it can compensate for reactive power and harmonic current simultaneously [13–15]. However, adding an APF to a grid-connected PV system requires additional costs, increasing the cost of PV utilization. Therefore, it is crucial to find a way to achieve grid connection and improve power quality simultaneously without adding other equipment. This idea was initiated in 1996 by Kim et al. [16]. The structure put forward at that time needed energy storage components, which will increase the cost. Based on the control technology at that time, the development of this technology was limited to a certain extent. However, with the development of control technology and the progress of microprocessor performance, this method began to develop in recent years. Previous work [17] proposes a photovoltaic-active power filter (PV-APF) system used in utility side. It uses fuzzy logic controller to reduce the harmonic content of photovoltaic system, but this control method does not have good dynamic performance.

Concerning the problems that existed in the control method of finite control set model predictive control (FCS-MPC), many scholars in related fields have proposed different methods [11]. Studies [18] have considered an MPC method with time-delay compensation. The reference current is predicted by Lagrange interpolation. In the future, multiple prediction periods will be calculated. Due to the irregular and rapid variation of harmonics, the prediction corresponding to the predicted reference value has a large error at the change. Previous work [19] has pointed out that FCS-MPC was applied to an APF to compensate for the harmonic current and reactive power.

In recent research, a nonlinear control system based on the Lyapunov stability theory is designed for a three-level NPC inverter in [20], which ensures the grid connection of a PV system and the improvement of power quality. The new system consists of a DC and bus voltage controller, a capacitor voltage controller, and an AC side controller. The instantaneous reactive power theory is used to extract harmonics. This controller's design is computationally complex and depends on the precise mathematical model. In [21], a grid-connected PV system used as a passive power filter is studied, and the direct power control method is applied to this kind of system. When the harmonic compensation is carried out, the reference value changes rapidly, and the dynamic response of the proposed control method is slow, which affects the compensation effect in some cases. In [22], an indirect current control strategy is proposed. In the current loop control, the hysteresis controller is used to gate and extract the signal. This control method has low precision.

In this paper, a strategy of joint use of a PV system and APF is proposed. First, the harmonic and reactive power of the microgrid load current of distributed PV system nodes is detected by the instantaneous reactive power method (i_p–i_q) as part of the command current, and the other part of the command current is the reference current of the grid-connected inverter. In this paper, the multistep FCS-MPC is used to reduce the error caused by the prediction delay of the system. The grid-connected system of the PV system combined with an APF is studied, which improves the utilization rate of light energy, improves the power quality of the power grid system, and reduces the cost of the PV power generation system.

2. PV System Combined with APF System (PV + APF)

The PV + APF system proposed in this paper is shown in Figure 1. The DC generated by the PV system passes through MPPT and the DC/DC plant to make it work at the maximum power point. Stable DC voltage is generated by the PV system and connected to the power grid through a three-phase inverter. For the current inner loop, a multistep FCS-MPC algorithm is used to control the PV + APF system to realize system functions [14, 19].

2.1. Mathematical Model of the PV + APF System. For the PV grid-connected inverter part, assuming the voltage balance of a three-phase power grid, according to Kirchhoff voltage law, the following can be obtained:

$$\begin{cases} u_{an} = L\dfrac{\mathrm{d}i_a}{\mathrm{d}t} + e_a + Ri_a, \\ u_{bn} = L\dfrac{\mathrm{d}i_b}{\mathrm{d}t} + e_b + Ri_b, \\ u_{cn} = L\dfrac{\mathrm{d}i_c}{\mathrm{d}t} + e_c + Ri_c. \end{cases} \tag{1}$$

In equation (1), the output voltage of the inverter is $u_{an} = u_{aN} - u_{nN}$, PCC is the common node, L is the filter inductor, and R is the equivalent resistance of the line and the filter inductor. i_a, i_b, and i_c are the three-phase grid current, and e_a, e_b, and e_c are the grid voltage. From equation (1), the three-phase voltage, current, and inverter output can be written in the vector form.

$$\mathbf{u} = L\frac{\mathrm{d}\mathbf{i}}{\mathrm{d}t} + R\mathbf{i} + \mathbf{e}, \tag{2}$$

where

$$\begin{cases} \mathbf{u} = \dfrac{2}{3}\left(u_{an} + \mathbf{a}u_{bn} + \mathbf{a}^2u_{cn}\right) = u_\alpha + ju_\beta, \\ \mathbf{i} = \dfrac{2}{3}\left(i_a + \mathbf{a}i_b + \mathbf{a}^2i_c\right) = i_\alpha + ji_\beta, \\ \mathbf{e} = \dfrac{2}{3}\left(e_a + \mathbf{a}e_b + \mathbf{a}^2e_c\right) = e_\alpha + je_\beta, \\ \mathbf{a} = e^{j(2/3)\pi} = -\dfrac{1}{2} + j\dfrac{\sqrt{3}}{2}, \end{cases} \tag{3}$$

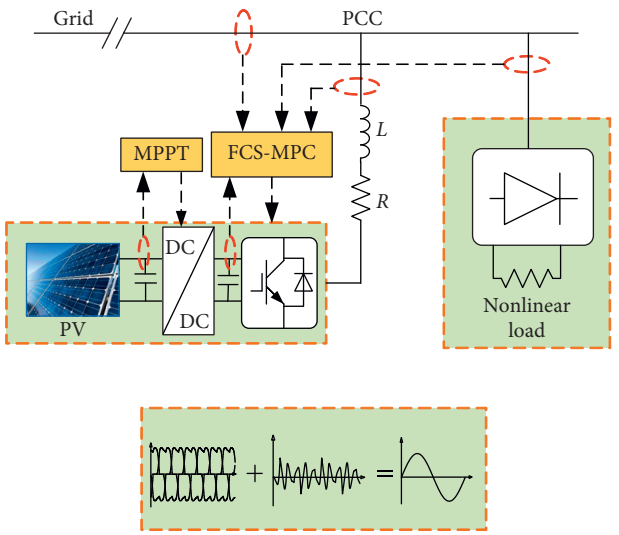

Figure 1: PV-APF system model.

where **u** is the output voltage vector of the inverter, **i** is the grid current vector, and **e** is the grid voltage vector.

2.2. MPPT. In this paper, the variable compensation disturbance observation method is used to realize the maximum power point tracking of PV power generation. This method can obtain the maximum power point voltage reference value of PV cells under certain external environments. The difference between the reference value and the actual output of PV cells is used as part of the reference value of the grid-connected active current after passing through the PI controller.

$$I_{dc}^{*} = k_p\left(u_{\text{ref}} - u_{dc}\right) + k_i \int \left(u_{\text{ref}} - u_{dc}\right)\mathrm{d}t, \tag{4}$$

where u_{ref} is the working voltage corresponding to the maximum power point under the disturbance observation method, u_{dc} is the DC voltage, and k_p and k_i are the proportional and integral coefficients of the DC side voltage controller.

In this paper, variable step maximum power tracking is adopted, and the threshold values of power variation and voltage variation are introduced to make the voltage disturbance zero when the system tracks near the maximum power point to ensure that the system has no oscillation in steady-state operation. When the external environment changes, a larger compensation disturbance is adopted to accelerate the dynamic response of the system. The flowchart of the variable step disturbance observation method is shown in Figure 2, and the reference value of the DC bus voltage in each sampling period is shown in the following equation:

$$u_{\text{ref}} = u(k) + \lambda\frac{\mathrm{d}P}{\mathrm{d}u} = u(k) + \lambda\frac{P(k) - P(k-1)}{u(k) - u(k-1)}. \tag{5}$$

When λ is fixed, and the actual working condition is far from the maximum power point, the voltage disturbance step becomes larger. When it is close to the maximum power point, the disturbance step decreases. When dP and du reach the set threshold, the disturbance step is zero; that is, there is no power fluctuation in the steady state.

3. Calculation of Reference Current

3.1. Calculation of Harmonic Reference Current. Since the theory of instantaneous reactive power of a three-phase circuit was put forward in the 1980s, it has been successfully applied in many aspects. Based on this theory, the real-time detection method of harmonic and reactive current for APF can be obtained. This paper uses i_p-i_q method based on instantaneous reactive power theory as shown in Figure 3 [23].

In the figure,

$$C_{32} = \sqrt{\frac{2}{3}}\begin{bmatrix} 1 & \frac{-1}{2} & \frac{-1}{2} \\ 0 & \frac{\sqrt{3}}{2} & \frac{-\sqrt{3}}{2} \end{bmatrix}, \tag{6}$$

$$C = \begin{bmatrix} \sin\omega t & -\cos\omega t \\ -\cos\omega t & -\sin\omega t \end{bmatrix}.$$

This method needs to use sine signal sinωt and cosine signal cosωt which are in phase with A-phase grid voltage e_a. They are obtained by phase locked loop (PLL) and sine-cosine signal-generating circuit.

3.2. Calculation of Grid-Connected Reference Current. The maximum power point voltage reference value of PV cells in a certain external environment can be obtained using the variable step disturbance observation method. The difference between the reference value and the actual output value of PV cells passes through the PI controller, which is a part of the given value of the grid-connected active current, and the amplitude of this part of the command current is zero in the d–q coordinate system.

$$\begin{bmatrix} i_d^{*} \\ i_q^{*} \end{bmatrix} = \begin{bmatrix} k_p\left(u_{\text{ref}} - u_{dc}\right) + k_i \int \left(u_{\text{ref}} - u_{dc}\right)\mathrm{d}t \\ 0 \end{bmatrix}, \tag{7}$$

where u_{ref} is the reference voltage of the grid-connected inverter on the DC side, u_{dc} is the current voltage of the grid-connected inverter on the DC side, and k_p and k_i are the proportional coefficient and integral coefficient of PI controller.

4. Predictive Control of the Inverter System

To compensate for the power grid harmonic pollution caused by the nonlinear load, the control schematic diagram is shown in Figure 4. The PV + APF system proposed in this paper uses light as the inverter and compensates for harmonics. At night or in the absence of light, it is used as an APF to compensate for the harmonics of the power grid. This paper does not discuss its use as an APF alone [24].

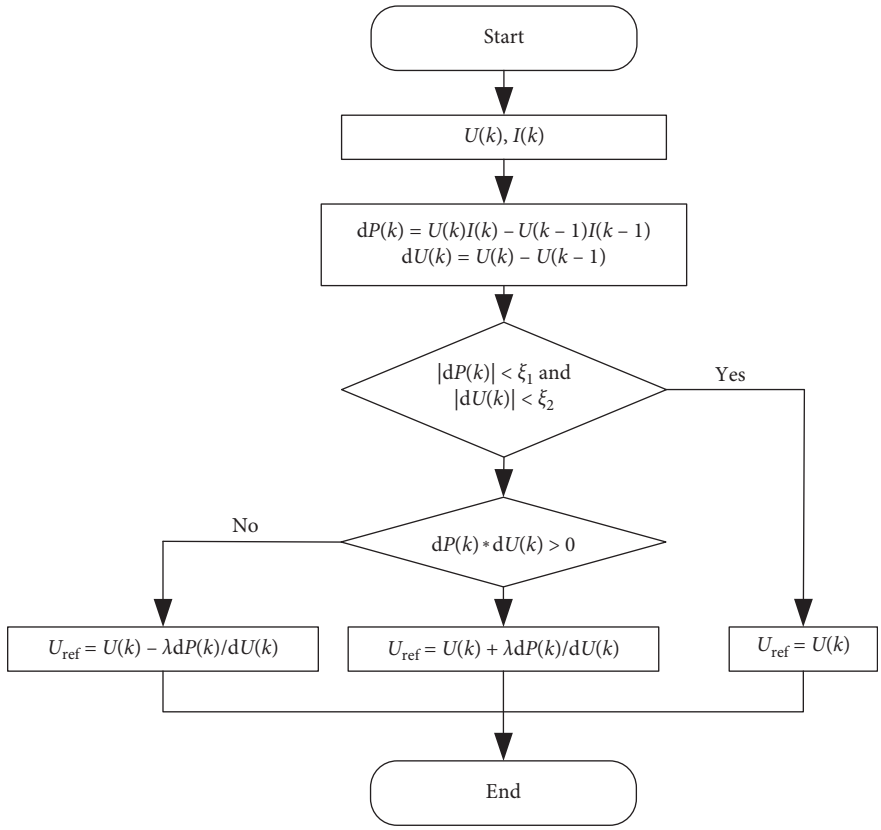

Figure 2: Variable step perturbation observation method.

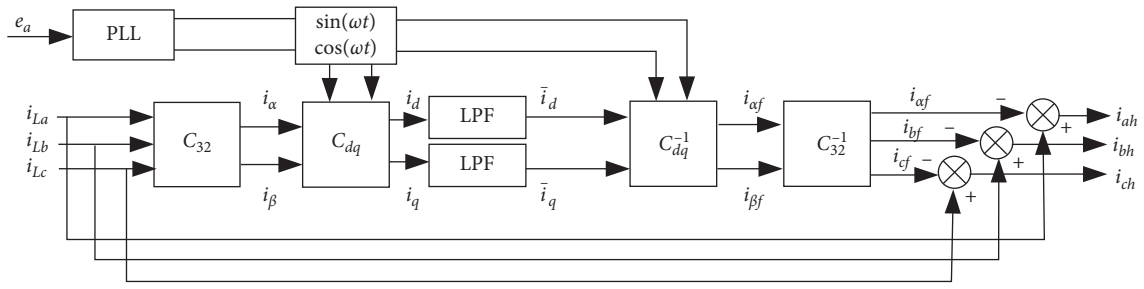

Figure 3: i_p-i_q method for harmonic detection of the reference current.

4.1. Model of Predictive Control. Equation (2) is the dynamic current equation of grid connection, which can be transformed into an α-β coordinate system to obtain

$$\begin{cases} u_\alpha = L\dfrac{\mathrm{d}i_\alpha}{\mathrm{d}t} + Ri_\alpha + e_\alpha, \\ \\ u_\beta = L\dfrac{\mathrm{d}i_\beta}{\mathrm{d}t} + Ri_\beta + e_\beta. \end{cases} \tag{8}$$

Equation (8) performs differential discretization to obtain

$$\begin{cases} u_\alpha(k) = L\dfrac{i_\alpha(k+1) - i_\alpha(k)}{T_s} + Ri_\alpha(k) + e_\alpha(k), \\ \\ u_\beta(k) = L\dfrac{i_\beta(k+1) - i_\beta(k)}{T_s} + Ri_\beta(k) + e_\beta(k). \end{cases} \tag{9}$$

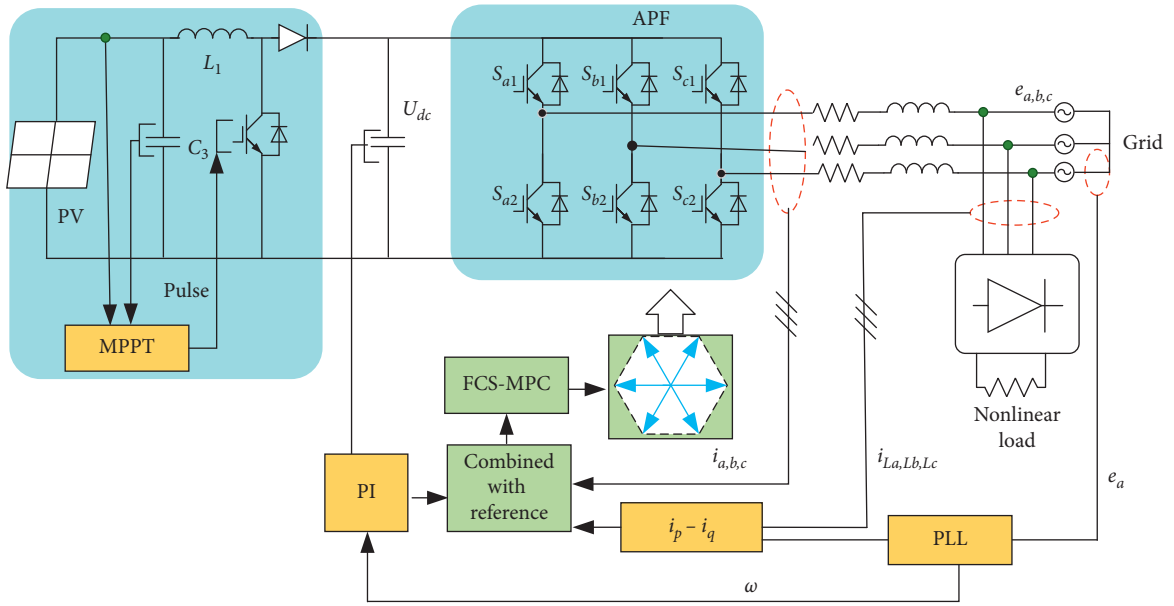

Figure 4: Predictive control of PV + APF.

T_s is the sampling period, which can be obtained from equation (9).

$$\begin{cases} i_\alpha(k+1) = \left(1 - \dfrac{RT_s}{L}\right) i_\alpha(k) + \dfrac{T_s}{L}\left[u_\alpha(k) - e_\alpha(k)\right], \\ i_\beta(k+1) = \left(1 - \dfrac{RT_s}{L}\right) i_\beta(k) + \dfrac{T_s}{L}\left[u_\beta(k) - e_\beta(k)\right]. \end{cases} \tag{10}$$

In equation (10), u_α and u_β are the output of the converter. In the three-phase two-level inverter structure, as shown in Figure 5, there are eight groups of vectors.

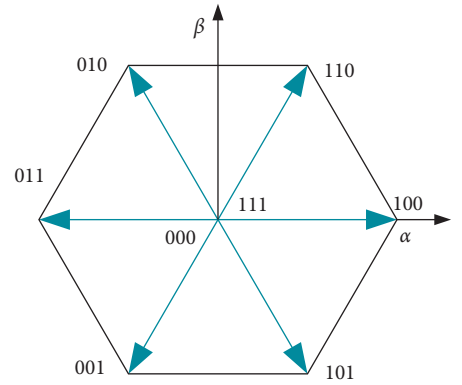

Figure 5: Eight groups of vectors of output.

4.2. FCS-MPC. The FCS-MPC of the current will have an error in the sinusoidal signal tracking, and the higher the frequency, the greater the error. Therefore, it is convenient and intuitive for the APF to track the reference predictive signal in an α-β coordinate system after the output of the predictive model. As shown in Figure 6, in the α-β coordinate system, V_x is eight voltage vectors and $J_{\min}$ is the voltage vector with the smallest objective function. Taking the tracking principle of an FCS-MPC algorithm at a certain sampling time, the objective function is calculated by synthesizing the switching frequency and tracking error, and the optimal target is derived to obtain the combined state of the switching signal and directly control the APF output.

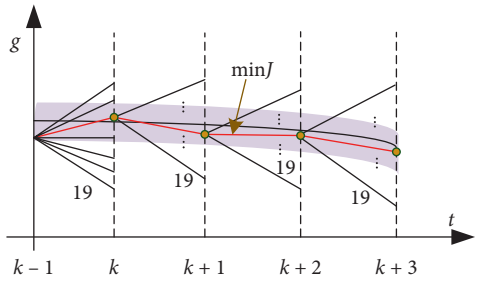

Figure 6: FCS-MPC method.

4.3. The Establishment of Objective Function. In the third section, the i_p-i_q method based on the instantaneous reactive power theory is used to detect the harmonics generated by the nonlinear load, which are i_{ah}, i_{bh}, and i_{ch}, and the reference current of the grid-connected inverter is i_d^* and i_q^*. In order to reduce the tracking error, the detected harmonics are transformed into an α-β coordinate system:

$$\begin{bmatrix} i_\alpha^{\text{ref}} \\ i_\beta^{\text{ref}} \end{bmatrix} = \sqrt{\frac{2}{3}} \begin{bmatrix} 1 & -\dfrac{1}{2} & -\dfrac{1}{2} \\ 0 & \dfrac{\sqrt{3}}{2} & \dfrac{-\sqrt{3}}{2} \end{bmatrix} \begin{bmatrix} i_{ah} \\ i_{bh} \\ i_{ch} \end{bmatrix} + \begin{bmatrix} \cos\theta & -\sin\theta \\ \sin\theta & \cos\theta \end{bmatrix} \begin{bmatrix} i_d^* \\ i_q^* \end{bmatrix}. \tag{11}$$

In the harmonic detection, there is a delay from the PLL to the harmonic reference current; that is, the output of the APF follows the reference current of the previous time. When establishing the objective function, the following current is the predicted value of the next time. In this process, the delay will produce certain errors. In this paper, to reduce the delay caused by the detection link, the Lagrange interpolation prediction method is used to predict the reference current. Equation (11) is the reference current value at the next time after interpolation. In order to reduce the amount of calculation, this paper uses the second-order interpolation prediction; that is, $n = 2$.

$$i_{\alpha,\beta}^{\mathrm{ref}}(k+1) = \sum_{i=0}^{n} (-1)^{n-i} \frac{(n+1)!}{i!\,(n+1-i)!} \cdot i_{\alpha,\beta}^{\mathrm{ref}}(k+i-n), \tag{12}$$

$$\begin{aligned} i_{\alpha,\beta}^{\mathrm{ref}}(k+1) = {} & 4i_{\alpha,\beta}^{\mathrm{ref}}(k) - 6i_{\alpha,\beta}^{\mathrm{ref}}(k-1) \\ & + 4i_{\alpha,\beta}^{\mathrm{ref}}(k-2) - i_{\alpha,\beta}^{\mathrm{ref}}(k-3). \end{aligned} \tag{13}$$

Through equations (9), (12), and (13), the objective function can be established:

$$\begin{aligned} J = {} & \left\| i_{\alpha}(k+1) - i_{\alpha}^{\mathrm{ref}}(k+1) \right\| + \left\| i_{\beta}(k+1) - i_{\beta}^{\mathrm{ref}}(k+1) \right\| \\ & + h_{\lim}(i) + \gamma_i s^2(i). \end{aligned} \tag{14}$$

In equation (14), the first two terms are the tracking of the predicted current to the harmonic reference current in the α-β coordinate system. $h_{\lim}(i)$ imposes the current constraint, while $s^2(i)$ penalizes the switching effort which can be controlled by the associated weighting factor g. Their terms are defined as follows:

$$\begin{aligned} h_{\lim}(i) &= \begin{cases} 0, & \text{if } i(k+1) \le i_{\max}, \\ \infty, & \text{if } i(k+1) > i_{\max}, \end{cases} \\ s(i) &= \sum \left| i_{a,b,c}(k+1) - i_{a,b,c}(k) \right|. \end{aligned} \tag{15}$$

For the three-phase two-level inverter, there are seven possible different switching vectors, which can be substituted into equation (10) to obtain the predicted value of the next time, and then the objective function J corresponding to the vector can be obtained. At each sampling point, all the vectors are cycled to obtain the switch vector that makes J minimum. This switch vector is the optimal vector. The optimal output can be obtained by using the switch combination corresponding to the optimal vector to control the inverter.

4.4. Multistep FCS-MPC. The single-step FCS-MPC can select the optimal switch combination in a sampling period, but the optimal switch combination at the current sampling time has some conservation problems because it is only the optimal solution at $k+1$ time. The processor has a certain delay in the actual process, and the optimal solution at the current time cannot be obtained for two or more cycles. Even though the calculation of the single-step prediction is low, and the structure is simple, the optimal situation at time stamp $k+2$ and $k+3$ is not considered. This method ignores the optimal control information that the suboptimal switch may contain; that is, the suboptimal switch at the current time may be beneficial to the selection of the optimal vector at the next time. In the case of measurement error or parameter mismatch, the conservatism of one-step prediction will affect the control effect. In the subsequent several cycles, eight switch vectors cannot select the appropriate state. This problem will make the inverter output unable to follow the reference value, thus making the control result more erroneous [25].

To solve the conservatism problem of one-step prediction, a multistep prediction method is proposed in this paper. The inverter output is also predicted in the next cycle. The multistep FCS-MPC combines the optimal state and suboptimal state at the current moment as the candidate vector to obtain the optimal state at the next moment to determine the switch combination that needs to act on the inverter. If the Euler forward difference is continued for equation (10), the following equation can be obtained:

$$\begin{cases} i_{\alpha}(k+2) = \left(1 - \dfrac{RT_s}{L}\right) i_{\alpha}(k+1) + \dfrac{T_s}{L}\left[u_{\alpha}(k+1) - e_{\alpha}(k+1)\right], \\ i_{\beta}(k+2) = \left(1 - \dfrac{RT_s}{L}\right) i_{\beta}(k+1) + \dfrac{T_s}{L}\left[u_{\beta}(k+1) - e_{\beta}(k+1)\right]. \end{cases} \tag{16}$$

In equation (16), $i_{\alpha}(k+1)$ and $i_{\beta}(k+1)$ are the predicted currents in the α-β coordinate system at time $k+1$; $e_{\alpha}(k+1)$ and $e_{\beta}(k+1)$ are the grid currents at time $k+1$, and $e(k+1) = e(k)$ in a very small sampling period; $u_{\alpha}(k+1)$ and $u_{\beta}(k+1)$ are the outputs of the inverter, which are obtained by cycling all switch vectors in the multistep prediction method.

In Section 4.2, the optimal vector and the suboptimal vector can be obtained. Substituting them into equation (9), the corresponding optimal predictive current $i_1^p(k+1)$ and suboptimal predictive current $i_2^p(k+1)$ can be obtained. Substituting them into equation (16), all the switching vectors are cycled again and the switching vector of the first step is selected under the minimum objective function of the second step to control the inverter through the objective function of the following equation:

$$\begin{aligned} J = {} & \left\| i_{\alpha}(k+2) - i_{\alpha}^{\mathrm{ref}}(k+1) \right\| + \left\| i_{\beta}(k+2) - i_{\beta}^{\mathrm{ref}}(k+1) \right\| \\ & + h_{k+1}^{\lim}(i) + \gamma_i s_{k+1}^2(i), \end{aligned} \tag{17}$$

where

$$\begin{aligned} h_{k+1}^{\lim}(i) &= \begin{cases} 0, & \text{if } i(k+2) \le i_{\max}, \\ \infty, & \text{if } i(k+2) > i_{\max}, \end{cases} \\ s_{k+1}(i) &= \sum \left| i_{a,b,c}(k+2) - i_{a,b,c}(k+1) \right|. \end{aligned} \tag{18}$$

The control algorithm of multistep FCS-MPC in each sampling period is shown in Figure 7.

The principle is as follows:

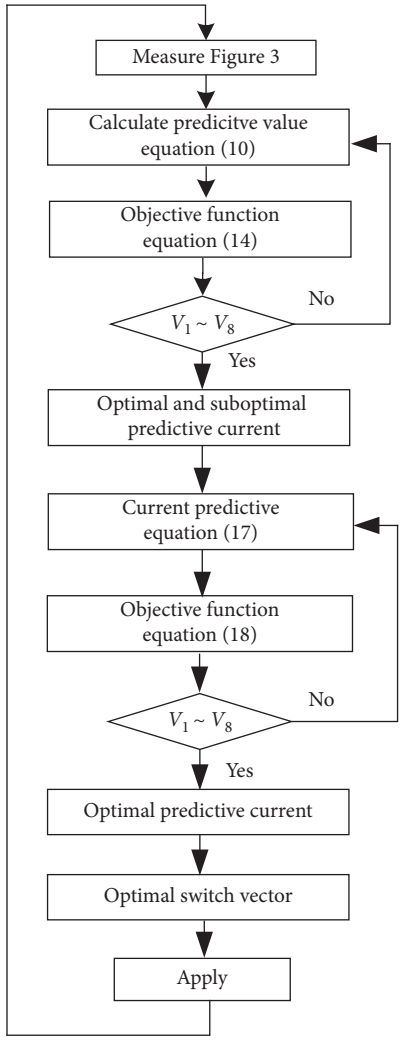

Figure 7: Multistep FCS-MPC method.

(a) At time k, according to the current value, the reference current at the next time is obtained by Lagrange interpolation.

(b) The objective function is constructed, eight groups of switch combinations are cycled, and the switch combinations which make the objective function minimum and the second smallest are selected. The two groups of switch states which make the objective function minimum are calculated. The optimal current prediction values $i_1^p(k+1)$ and $i_2^p(k+1)$ are obtained, and the corresponding switching states are recorded.

(c) Using the two groups of predicted values corresponding to the objective function at $k+1$ obtained in the second part, 8 groups of vectors are recycled again to display the switch state corresponding to the minimum objective function at $k+2$. The same method is also applied to the current prediction equation (16) to obtain two objective functions at $k+2$.

(d) The objective function at time $k+1$ and the smaller one at time $k+2$ is selected as the final prediction results, and the corresponding switch state at time $k+1$ is taken as the application state at time $k+1$ and applied to the APF.

From the above analysis, the advantage of the multistep FCS-MPC proposed in this paper over the traditional model prediction algorithm is that it seeks the optimal solution at the current time and in the subsequent multiple cycles by solving the objective function through multiple rolling optimization algorithms to solve the conservative problem of the traditional algorithm. Due to the increase of computation, the processor's performance is sacrificed in exchange for the optimal switch combination. The better the processor performance, the more obvious the control performance.

5. Simulation and Results Analysis

To verify the harmonic compensation effect of multistep FCS-MPC on the PV + APF system control, the simulation model as shown in Figure 1 is built in MATLAB/Simulink Toolbox, and the parameters of this paper are shown in Table 1. In this paper, the PV power generation module and inverter grid and harmonic compensation need to be controlled, and the nonlinear load need to be set as an uncontrollable diode rectifier bridge. To verify the dynamic performance of the control method, the illumination intensity changes from 700 W/m^2 to 1000 W/m^2 in 1.5 s; the reference voltage changes from 550 V to 800 V in 0.25 s; the setting load fluctuates in 0.35 s; and the load changes from 5 Ω to 2.5 Ω.

In this paper, multistep FCS-MPC is used to compare the performance of traditional PV and PV + APF systems in the presence of harmonics. The simulation results are as follows. Figure 8 shows the three-phase harmonics detected by the instantaneous reactive power method. When the load changes, the harmonic content also changes.

As shown in Figure 9, under the condition of light and load fluctuation, the performance of the two systems is the same, and the current of the power grid is distorted, which affects the safe operation of the power grid. After 0.35 s load fluctuation, the load current value also changes.

As shown in Figure 10, when the light intensity changes, the grid current changes slightly; when the DC side voltage changes from 550 V to 800 V, the grid current is increased; and when the load value changes, the grid current fluctuates. In the case of harmonic pollution in the power grid, the current waveform of the grid-connected inverter after power injection is distorted, and the current waveform of the PV + APF system for harmonic control is close to the sine wave. It can be concluded that the method proposed in this paper effectively improves the power quality.

As shown in Figure 11, the total harmonic distortion (THD) dynamic change diagram of the grid-connected current shows the grid distortion rate of the system under various parameter changes. (a) PV grid-connected system without an APF: when THD is 0.61% in the whole process, it is not high. Due to the characteristics of the nonlinear load selected in this paper, the 5th, 7th, 11th, and 13th harmonics

Table 1: Parameters of the simulation model.

Parameter	Value
Grid voltage and f	380 V, 50 Hz
DC voltage	800 V
Capacitors $C1$, $C2$	3000 μF
Inductor	2 mH
Resistor	0.01 Ω
Load resistor	5 Ω

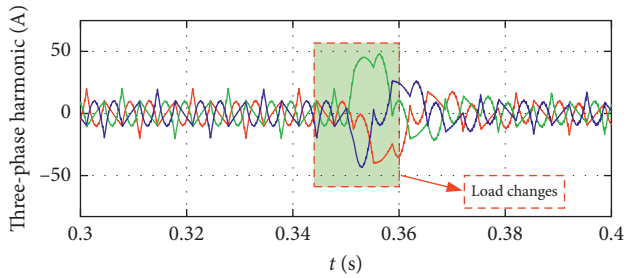

Figure 8: Three-phase harmonic current detected by the instantaneous reactive power method.

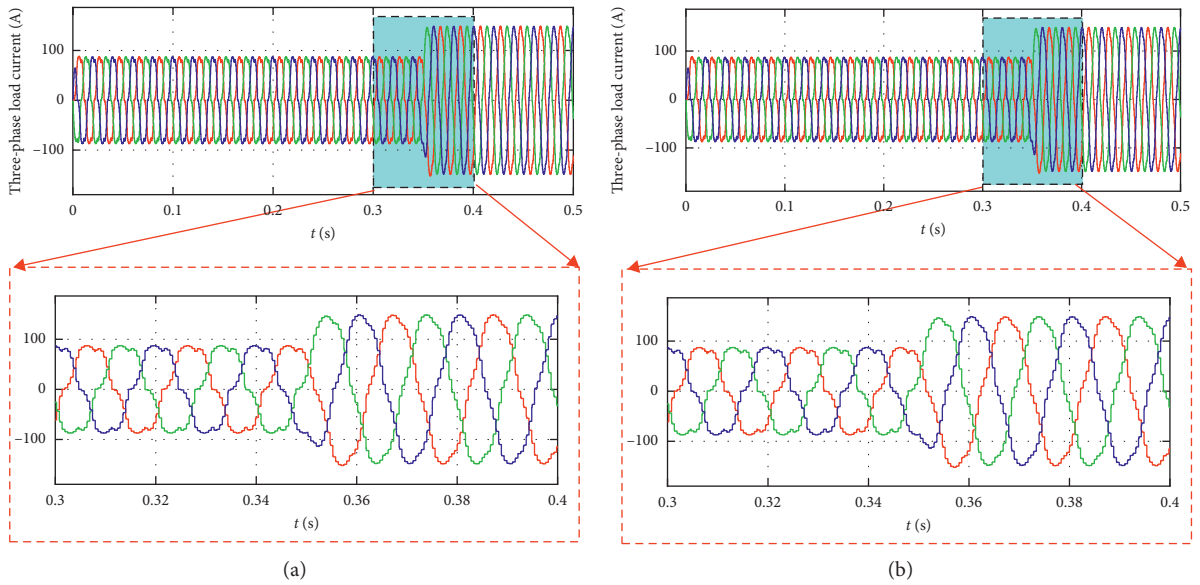

Figure 9: Three-phase load current of the grid-connected system. (a) PV. (b) PV + APF.

are dominant in the power grid. (b) PV + APF system performance: it is found that its THD is lower than that of (a). After treatment, THD is 4.8% in 0.2 S, and the distribution of the harmonic number is decentralized. It can also be found from Figure 11 that THD will fluctuate when the light intensity changes and the DC side reference current changes. After reaching stability, THD will also stabilize.

Figure 12 shows the DC side voltage changes of the two systems. (a) PV grid-connected system without an APF: due to the advantages of FCS-MPC, the DC side voltage value can quickly follow the reference value and recover after fluctuation. (b) PV + APF system: harmonic control is carried out while grid connected. When the load fluctuates in 3.5 s, the harmonic reference also fluctuates, making the DC side voltage fluctuate.

Figure 13 shows the output power of the PV system. When the illumination and DC side reference change, the output power will change accordingly (Figure 13(a)). When the load changes, its output power will not be affected. When the load changes, the harmonic content needs to be compensated, and the output power needs to be consumed to achieve the two-terminal power balance (Figure 13(b)). Hence, the fluctuation occurs at 0.35 s, but the balance is quickly achieved under the FCS-MPC algorithm.

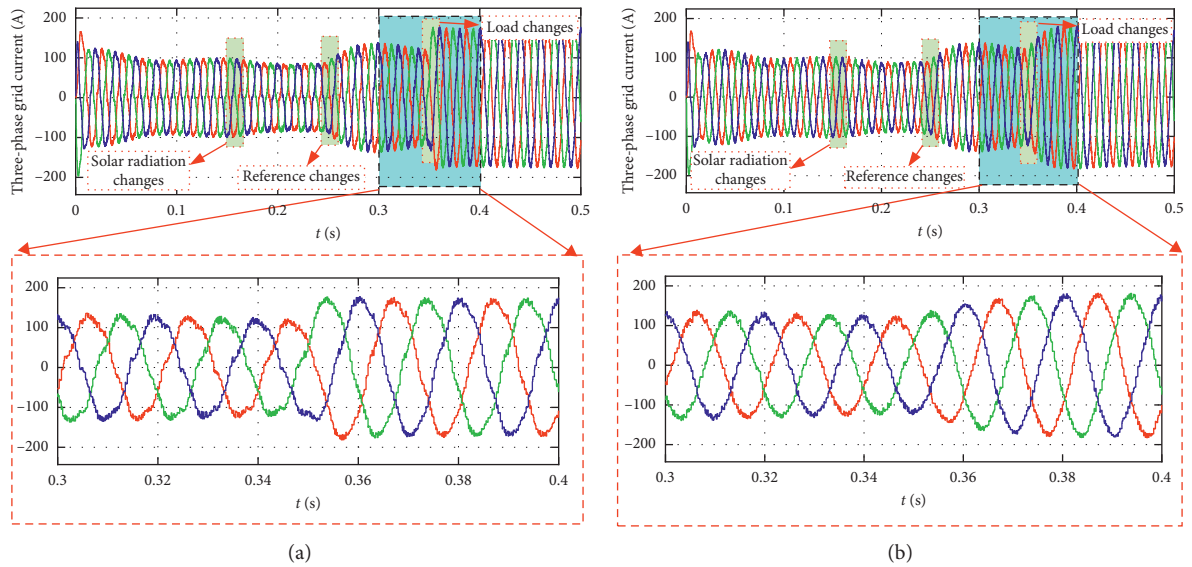

Figure 10: Three-phase grid current of the grid-connected system. (a) PV. (b) PV + APF.

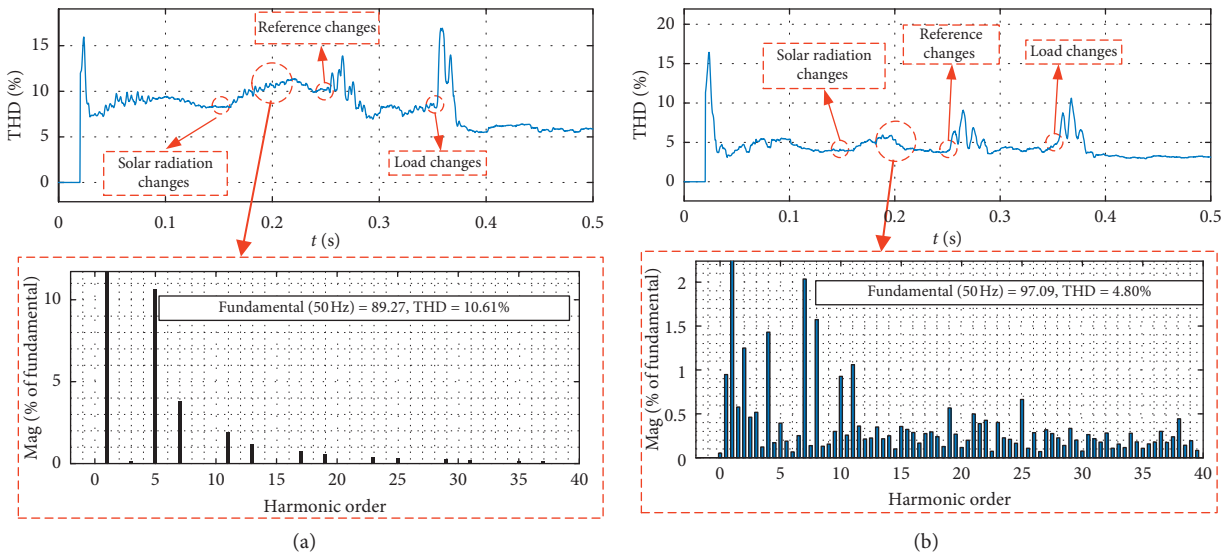

Figure 11: The changes in THD. (a) PV. (b) PV + APF.

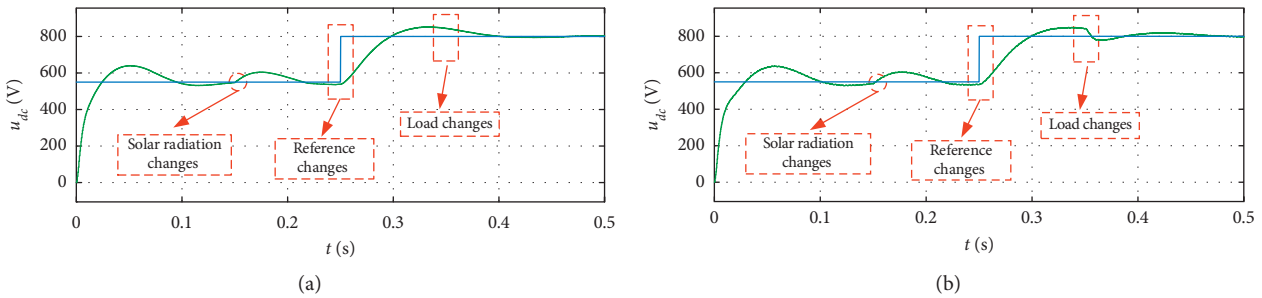

Figure 12: Changes in the DC side voltage. (a) PV. (b) PV + APF.

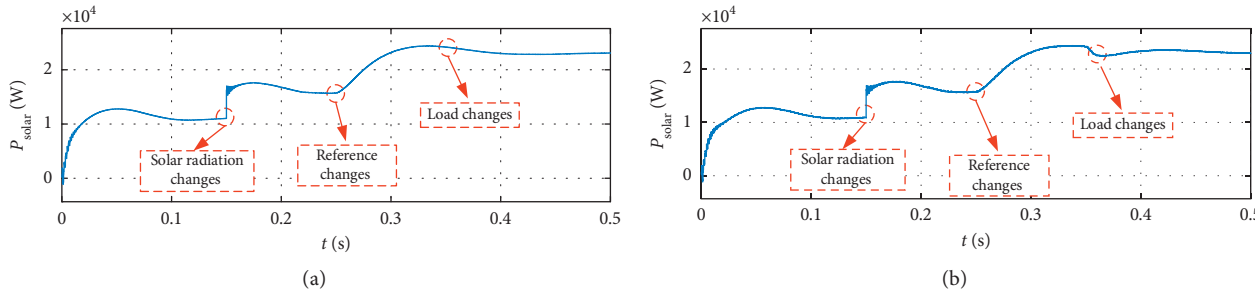

Figure 13: Output power of the PV system. (a) PV. (b) PV + APF.

6. Conclusions

In this paper, a multistep FCS-MPC PV control system combined with an APF is proposed. The system uses solar energy resources, improves power quality simultaneously, and solves the problem of power quality decline caused by the grid-connected systems and loads. It has broad application prospects in the future microgrid system. The scheme proposed in this paper has the following advantages:

(a) From the experimental results, this combined system has little impact on the whole grid when PV power is injected into the grid

(b) Using multistep FCS-MPC, the system has good dynamic performance and steady-state performance

(c) The combination of an APF with a PV system effectively reduces the power grid's THD and improves the power grid's power quality

(d) The whole system does not need additional equipment, as it plays the role of two devices and effectively reduces the input cost.

(e) It has broad prospects in the application of clean energy

Data Availability

No data were used to support this study.

Conflicts of Interest

The authors declare no conflicts of interest.

Authors' Contributions

R.Z. contributed to conceptualization and formal analysis and was responsible for resources and supervision; S.H. investigated the study, validated the data, prepared the original draft, and reviewed and edited the manuscript. All authors have read and agreed to the published version of the manuscript.

Acknowledgments

This project was supported by Natural Science Foundation of Tibet Autonomous Region (XZ202001ZR0093G) and Key Laboratory of Higher Education of Tibet Autonomous Region: Electrical Engineering Laboratory Support Project (2020D-ZN-01).

References

[1] F. Blaabjerg, R. Teodorescu, M. Liserre, and A. V. Timbus, "Overview of control and grid synchronization for distributed power generation systems," *IEEE Transactions on Industrial Electronics*, vol. 53, no. 5, pp. 1398–1409, 2006.

[2] J. M. Carrasco, L. G. Franquelo, J. T. Bialasiewicz et al., "Power-electronic systems for the grid integration of renewable energy sources: a survey," *IEEE Transactions on Industrial Electronics*, vol. 53, no. 4, pp. 1002–1016, 2006.

[3] U. K. Das, K. S. Tey, M. Seyedmahmoudian et al., "Forecasting of photovoltaic power generation and model optimization: a review," *Renewable and Sustainable Energy Reviews*, vol. 81, no. 1, pp. 912–928, 2018.

[4] W. VanDeventer, E. Jamei, G. S. Thirunavukkarasu et al., "Short-term PV power forecasting using hybrid GASVM technique," *Renewable Energy*, vol. 140, pp. 367–379, 2019.

[5] L. Xiong, X. Liu, Y. Liu, and F. Zhuo, "Modeling and stability issues of voltage-source converter dominated power systems: a review," *CSEE Journal of Power and Energy Systems*, 2020.

[6] H. Li, Y. Liu, and J. Yang, "A novel FCS-MPC method of multi-level APF is proposed to improve the power quality in renewable energy generation connected to the grid," *Sustainability*, vol. 13, no. 8, p. 4094, 2021.

[7] T. Esram and P. L. Chapman, "Comparison of photovoltaic array maximum power point tracking techniques," *IEEE Transactions on Energy Conversion*, vol. 22, no. 2, pp. 439–449, 2007.

[8] W. Hayder, E. Ogliari, A. Dolara, A. Abid, M. Ben Hamed, and L. Sbita, "Improved PSO: a comparative study in MPPT algorithm for PV system control under partial shading conditions," *Energies*, vol. 13, no. 8, p. 2035, 2020.

[9] B. Singh, K. Al-Haddad, and A. Chandra, "A review of active filters for power quality improvement," *IEEE Transactions on Industrial Electronics*, vol. 46, no. 5, pp. 960–971, 1999.

[10] H. Akagi, "New trends in active filters for power conditioning," *IEEE Transactions on Industry Applications*, vol. 32, no. 6, pp. 1312–1322, 1996.

[11] J. Rodriguez, M. P. Kazmierkowski, J. R. Espinoza et al., "State of the art of finite control set model predictive control in power electronics," *IEEE Transactions on Industrial Informatics*, vol. 9, no. 2, pp. 1003–1016, 2013.

[12] R. Vargas, P. Cortes, U. Ammann, J. Rodriguez, and J. Pontt, "Predictive control of a three-phase neutral-point-clamped inverter," *IEEE Transactions on Industrial Electronics*, vol. 54, no. 5, pp. 2697–2705, 2007.

[13] Q.-N. Trinh and H.-H. Lee, "An advanced current control strategy for three-phase shunt active power filters," *IEEE Transactions on Industrial Electronics*, vol. 60, no. 12, pp. 5400–5410, 2013.

[14] R. Luo, Y. He, and J. Liu, "Research on the unbalanced compensation of delta-connected cascaded H-bridge multilevel SVG," *IEEE Transactions on Industrial Electronics*, vol. 65, no. 11, pp. 8667–8676, 2018.

[15] S. Devassy and B. Singh, "Modified *pq*-theory-based control of solar-PV-integrated UPQC-S," *IEEE Transactions on Industry Applications*, vol. 53, no. 5, pp. 5031–5040, 2017.

[16] S. Kim, G. Yoo, and J. Song, "A bifunctional utility connected pho-tovoltaic system with power factor correction and UPS facility," in *Proceedings of the Conference Record of the 25th IEEE Photovoltaic Specialists Conference(PVSC)*, pp. 1363–1368, IEEE, Washington, DC, USA, May 1996.

[17] D. R. Chaudhari and S. Gour, "PV-active power filter combination mitigating harmonics using FLC," in *Proceedings of the 2017 Recent Developments in Control, Automation & Power Engineering (RDCAPE)*, pp. 378–381, IEEE, Noida, India, October 2017.

[18] T. Jin, X. Shen, T. Su, and R. C. C. Flesch, "Model predictive voltage control based on finite control set with computation time delay compensation for PV systems," *IEEE Transactions on Energy Conversion*, vol. 34, no. 1, pp. 330–338, 2019.

[19] J. G. L. Foster, R. R. Pereira, R. B. Gonzatti, W. C. Sant'Ana, D. Mollica, and G. Lambert-Torres, "A review of FCS-MPC in multilevel converters applied to active power filters," in *Proceedings of the 2019 IEEE 15th Brazilian Power Electronics Conference and 5th IEEE Southern Power Electronics Conference (COBEP/SPEC)*, pp. 1–6, Santos, Brazil, December 2019.

[20] S. A. Davari, D. A. Khaburi, P. Stolze, and R. Kennel, "An improved finite control set-model predictive control (FCS-MPC) algorithm with imposed optimized weighting factor," in *Proceedings of the 2011 14th European Conference on Power Electronics and Applications*, pp. 1–10, IEEE, Birmingham, UK, August 2011.

[21] M. Et-Taoussi and H. Ouadi, "Power quality control for grid connected Photovoltaic system with Neutral Point Converter," in *Proceedings of the 2016 International Renewable and Sustainable Energy Conference (IRSEC)*, November 2016.

[22] B. Boukezata, A. Chaoui, J. P. Gaubert et al., "Power quality improvement by an active power filter in grid-connected photovoltaic systems with optimized direct power control strategy," *Electric Machines & Power Systems*, vol. 44, no. 16–20, pp. 2036–2047, 2016.

[23] L. Xiong, X. Liu, C. Zhao, and F. Zhuo, "A fast and robust real-time detection algorithm of decaying DC transient and harmonic components in three-phase systems," *IEEE Transactions on Power Electronics*, vol. 35, no. 4, pp. 3332–3336, 2020.

[24] A. S. Shirbhate and P. Jawale, "Power quality improvement in PV grid connected system by using active filter," in *Proceedings of the International Conference on Energy Efficient Technologies for Sustainability*, April 2016.

[25] D. Zong, S. Hu, and X. Yang, "Multi-step finite control set model predictive control for three-level APF," in *Proceedings of the 5th International Workshop on Advances in Energy Science and Environment Engineering (AESEE 2021)*, Xiamen, China, April 2021.

Hindawi
Complexity
Volume 2021, Article ID 2051719, 18 pages
https://doi.org/10.1155/2021/2051719

Research Article

A Resilience Enhancement Model for Complex Distribution Network Coupling with Human Resources and Traffic Network

Biyun Chen, Yumo Shi, and Yanni Chen

Guangxi Key Laboratory of Power System Optimization and Energy Technology, Guangxi University, Nanning 530004, China

Correspondence should be addressed to Yumo Shi; 1812301028@st.gxu.edu.cn

Received 2 May 2021; Accepted 15 May 2021; Published 7 June 2021

Academic Editor: Chun Wei

Resilience is the ability of a system to withstand and recover from deliberate accidents; as to distribution systems, it means the ability to withstand and recover from natural disasters or other serious accidents and ensure electricity supply. Generally, promotion strategies of distribution network resilience mostly focus on electrical topology planning and reinforcement. The operation strategies in emergency repair stage are frequently ignored, especially the complex coupling relationship between distribution network, traffic network, and maintenance teams. A model of resilience improvement for a complicated distribution-traffic-human coupling system under hurricane disasters considering is presented. Firstly, based on the influence spreading mechanism of a hurricane acting on the distribution and traffic part of the system, a fault analysis model of rush repair is constructed. Secondly, according to the function of human resources in shortening the repair time and improving system resilience, an optimization model of emergency repair strategy is proposed. Taking into account the repair demand, traffic cost, and personnel operating and executing ability, the optimized strategy can minimize the social loss in the whole repair and recovery process after hurricane disaster. Furthermore, three indices, including system adaptability, repair rate, and economic loss rate, are proposed to quantify the resilience of distribution network. Finally, case studies on the IEEE33 bus system are implemented to verify the effectiveness of the proposed model.

1. Introduction

Extreme weather events, in particular hurricanes, have a great impact on electric infrastructures, resulting in extensive damages and significant economic and social losses. As a vulnerable part of the electricity infrastructure, distribution network suffers most outages which caused considerable inconvenience for residents living in disaster areas [1]. Therefore, enhancing the distribution network resilience becomes a key task for protecting power systems from extreme weather events.

Resilience, first proposed by Ecologist Holling, describes the ability of species to absorb disturbances and survive. In the context of power system, resilience reflects "the ability of power systems to withstand low-probability high-impact incidents in an efficient manner while ensuring the least possible interruption in supply of electricity, and further enabling a quick recovery and restoration to the normal operation state" [2]. There are various studies of distribution network resilience. In [3], a resilience assessment matrix was put forward to evaluate how the system is suffering and recovering from extreme disturbances, especially natural disasters, from technical, organizational, social, and economic perspectives. Enhancing the resilience of distribution grids from a technical way is the current mainstream approach. A resilience-oriented design (ROD) model was built to obtain the optimal hardening strategy, represented as a two-stage stochastic mixed-integer problem [4]. The first stage was to make the ROD decisions, like hardening lines and installing distributed generations (DGs). Then the second stage evaluated the system operation cost and repair cost. In [5], an optimization configuration model was proposed to improve the disaster resistance of distribution network, considering the impact of automatic switch in addition. The configuration scheme obtained has preferable economic benefits and resilience improvement efficiency. A

two-stage stochastic programming approach was presented to optimize the scheduling of a resilient microgrid (MG), considering the impact of natural disasters and the prevailing uncertainties associated with wind energy, electric vehicles, and real-time market prices [6, 7]. A comprehensive summary of distribution network resilience was presented in [8, 9], including evaluation models such as resilience triangle model and trapezoid model, and introducing several methods to define resilience indicators, such as area definition method, probability definition method, cost definition method, and weighted definition method. Among them, the definition method of power loss area is the most widely used.

With the modernization of cities, some researchers have noticed that the coupling between the important infrastructure systems will affect the distribution network resilience. Considering the interdependence of the urban transportation system (UTS) and power distribution system (PDS), a trilevel optimization model was proposed to improve the coupled system resilience by line hardening and DGs placement [10]. The high penetration of electric vehicles (EVs) further complicates the coupling between the UTS and PDS [11]. The electricity demand uncertainty at each charging/swapping facility depends on the traffic demand of EVs, resulting in the PDS load perturbation and affecting the distribution of traffic flow in turn. A robust dispatch method was proposed to maintain the feasibility of alternating current (AC) power flow constraints considering the impact of road congestion on route choices of VEs [12]. In [13], a two-stage robust optimization model was proposed for expansion planning of coupled active distribution and transportation based on the interaction of roads, distribution lines, DGs, energy storage systems, and charging facilities. A quantitative resilience assessment framework is proposed for the traffic-distribution network, considering both the spatial and temporal impacts of hurricanes [14]. In [15], a resilience enhancement strategy was proposed to improve the load survivability of distribution network under extreme weather events, taking into consideration the interaction between the information system and distribution system. To improve the resilience of distribution network cyber physical system (distribution network CPS) under the network attacks, authors in [16] proposed a method to analyze and evaluate the system risk based on the correlation matrix model of the coupled system.

However, most of the studies improve the distribution network resilience by grid hardening strategy, while paying insufficient attention to the operation measures in postdisaster recovery process. In the postdisaster recovery process, appropriate repair-recovery strategies can shorten the emergency repair time and improve the power supply capacity of critical loads, which significantly enhances the distribution network resilience. Social factors play an important role in the execution of repair-recovery strategies. In [17], a management strategy, considering the impact of social factors, was proposed to reduce postdisaster repair costs and improve comprehensive benefits. A framework was proposed to analyze the human factors and rank error factors for improving system operation reliability [18]. In [19], an emergency repair model was proposed to decrease the repair cost considering the specialty of the repair team and the needs of the faulting task, quantifying the influence of human resources by the utility theory. Soon after, the emergency repair model was strengthened to deal with the multifault in distribution network, considering the cooperation between the repair teams [20]. Moreover, a repair-recovery dynamic model was established to solve the multifault in active distribution network with more layers and scenes based on a multiagent system [21]. These studies focused on the repair-recovery strategy itself and failed to associate repair-recovery strategy with system resilience. In [22], the authors proposed a model to evaluate the distribution network resilience, considering the impact of grid reconstruction and repair-recovery strategy. Unfortunately, the model ignored the impact of human resources in the emergency repair process and simplified the repair process which does not conform to reality.

In this paper, studies focused on the resilience during the emergency repair process after extreme weather events (e.g., hurricane disasters) hit distribution network. The emergency repair environment of distribution network is a complicated distribution-traffic-human coupling system, in which both the distribution and traffic part of the coupling system suffered from the extreme weather events and influenced the repair effect by their physical interdependence. The changes in road conditions under extreme weather will influence the route choices of maintenance staff and increase the transportation cost during the emergency repair stage, which causes the operating cost of the distribution network to increase linearly [13]. Meanwhile, the changes in traffic time will directly affect the repair time which is significant to the system resilience. It is necessary to consider the coupling impact of the distribution-traffic network during the emergency repair stage. Besides, the impact of human resources in emergency repair process also affects the repair effect. For example, repair personnel with different capabilities have significantly different time-consuming and repair results when performing the same repair task. Figuring out and applying the mechanism of human resources in the complicated distribution-traffic coupling system during the emergency repair process could enhance the system resilience.

On these basics, a resilience enhancement strategy is proposed for the complex distribution network coupling with human resources and traffic network against hurricane disasters. First, analyze the characteristics of hurricane disasters and figure out the physical vulnerability of distribution-traffic coupling network related to wind speed. Thus, a fault analysis model is established to generate random failure scenes considering the wind speed, equipment failure probability, and traffic flow speed. Second, according to the postdisaster emergency repair process, determine the mechanism of human resources in improving the complicated distribution-traffic network resilience. An optimization model of emergency repair strategy is proposed, considering repair demands, traffic cost, and the operation ability of the repair team, to minimize the social loss caused by the whole emergency repair process. The obtained repair

strategy has good execution and rapidity which is crucial to resilience. Finally, three indexes, including the adaptive rate of the system, repair rate, and economic loss rate, are proposed for quantitative evaluation on the complex distribution network resilience.

The rest of the paper is organized as follows. Section 2 discusses the process of generating random scenes considering the impact of the hurricane on the complicated distribution-traffic coupling system. Section 3 proposes the mathematical formulation of the emergency repair model considering the human resources. Section 4 presents the general framework and indexes for enhancing and evaluating the complex distribution network resilience. Numerical case studies are presented in Section 5 to demonstrate the effectiveness of the proposed method. Finally, Section 6 concludes the study.

2. Random Scene Model

2.1. Component Failure Model Based on Dynamic Wind Field. Wind speed plays a major role in power system planning, which would determine the design strength of components [23]. In this case, the failure probability of a structure or structural component is closely relevant to the maximum wind speed that it suffers during the hurricane. Thus, in order to obtain the wind speed at a certain point within the disaster area during the entire hurricane and calculate their failure probability, a dynamic wind field model should be established for simulation.

2.1.1. Dynamic Wind Field Model. Assume that the influence range of the hurricane can be approximated as a circle, and the hurricane has no detrimental influence upon the distribution network outside its outer boundary. And within the region that hurricane affected, the wind speed v at each point can be given as a function of the distance d to the eye, i.e., the hurricane center. When d increases from 0 to the maximum wind speed radius, wind speed is monotone increasing; when d increases from the maximum wind speed radius to hurricane coverage radius, wind speed is monotone decreasing [24]. This functional relationship is shown in the following equation:

$$v(d) = \begin{cases} K v_m \left(1 - \exp\left[-\dfrac{d}{r_{mv}} \ln\left(\dfrac{K}{K-1}\right)\right]\right), & 0 \le d < r_{mv}, \\ v_m \exp\left[-\left(\dfrac{\ln \beta}{r_s - r_{mv}}\right)(d - r_{mv})\right], & r_{mv} \le d \le r_s, \\ 0, & d > r_s, \end{cases} \tag{1}$$

where K is an empirical parameter, v_{m} is the maximum sustained wind speed at time t, r_{mv} is the radius to maximum wind speed, r_{s} is the radius of the area affected by the hurricane, and β is the hurricane boundary factor, which represents the ratio of the maximum gradient wind speed to the boundary wind speed.

After the hurricane landed, wind speed would weaken over time by the obstructions on land. Essentially, the wind field is a time-varying field of a concentric circle in translational motion. Capture a certain time section in the process of movement, the static wind field of the hurricane can be modeled as follows:

$$h = \{v_m, r_{mv}, r_s, K, \beta, \varphi, \psi\}, \tag{2}$$

where φ are ψ are the latitude and longitude of the eye location, respectively.

Then the hurricane dynamic wind field can be represented by a series of sequentially static wind field along the hurricane path p_{h} as follows:

$$H = \{h_a, a = 0, 1, \ldots, |H|\}, \tag{3}$$

$$h_a = \Gamma(h_0 \mid \alpha, p_h, v_h, \Delta T_a), \tag{4}$$

where $|\cdot|$ is the number of elements in the set, h_0 is the wind field where the hurricane lands, and h_a is the wind field where hurricane landed at the time sampling point a. $\Gamma(\cdot)$ represents that h_l is a time-varying function of h_0; $\alpha$is the hurricane land decay factor; v_{h} is the hurricane translational speed; ΔT_a is the time elapsed from hurricane landfall (in h_0) to the sampling point a.

2.1.2. Component Failure Model of Distribution Network. The distribution network components mainly include transmission lines, transformers, and switches, including section switches and tie switches. The topological structure of a distribution network could be simplified by making the source-side busbar as the root node, switches and transformers as normal nodes, and transmission lines as edges, separated by switches.

Pole-mounted transformers and switches are vulnerable components when the urban medium-voltage distribution network is invaded and harassed under hurricane scenarios. Furthermore, within some dense vegetation areas, tall vegetation will be toppled over on the line by the gale, causing the collapse or fracture of poles, which leads to the failure of power supply [25]. The outage probability of components in the distribution network is mainly affected by the wind speed of hurricane, and it usually meets the lognormal distribution of wind speed [26]:

$$p_{i,t} = \Phi\left[\frac{\ln(v_{i,t}) - \lambda_i}{\xi_i}\right], \quad \forall i \in \Omega_L, t \in \Omega_T, \tag{5}$$

where $p_{i,t}$ is the outage probability of equipment i at time t, $v_{i,t}$ is the wind speed that equipment i suffers at time t, and λ_i and ξ_i are, respectively, the logarithmic mean and the logarithmic standard deviation of intensity of equipment i. Ω_T is a hurricane-affected moment set which contains the moment from the first outage of the distribution network to the last one. Ω_L is a controller switching equipment set in disaster areas.

2.2. Traffic Network Model of Emergency Repair Process. Hurricane will not only cause part of the distribution network components to fail but also bring adverse effects

to the traffic network, which increases the disaster risk of the complicated distribution-traffic coupling system and the complexity of the emergency repair environment. Research shows that it is mainly caused by the secondary disaster brought by the hurricane itself like strong winds, heavy rain, and storm surge [27]. In the urban traffic network, it is mainly reflected in the phenomenon of bending and collapse of trees on both sides of the road, and the low-lying water accumulation caused by the restricted bearing capacity of the drainage system. Therefore, the carrying capacity of the traffic network in the repair process is mainly affected by terrain features and vegetation.

A typical traffic network model consists of traffic intersections, roads, and signal lights, as shown in Figure 1(a). According to characteristics of the emergency repair, the influence of signal lights is ignored to simplify the model. In this case, its topological structure is shown in Figure 1(b); that is, the roundtrip road between two traffic intersections is regarded as a traffic trunk road, traffic intersections are regarded as nodes, and traffic trunk roads are regarded as edges.

Consequently, based on the topology of the traffic network, adjacency matrix **A** is set up to store the correlation between nodes [28]. **A** is a symmetric matrix of n-order, its diagonal elements are 0, and n is the number of traffic nodes. The meaning of element a_{ij} in **A** is as follows:

(1) $a_{ij} = \omega^T$: there is an adjacency relationship between traffic node i and traffic node j, and the corresponding edge weight is ω^T.

(2) $a_{ij} = \infty$: there is no adjacency relationship between traffic node i and traffic node j, and the corresponding edge weight is infinite.

It is noted that the value ω^T is calculated based on the wind speeds, terrain features, and vegetation, which represents the traffic network vulnerability:

$$\omega^T = \frac{l_{ij}}{\left(1 + d_{ij}\right)}, \tag{6}$$

$$d_{ij} = \frac{e^{h\left(\overline{v}_{ij}|_{\max}\right)}}{1 + e^{h\left(\overline{v}_{ij}|_{\max}\right)}}, \tag{7}$$

$$h\left(\overline{v}_{ij}|_{\max}\right) = \sigma_{ij}\frac{\left(\overline{v}_{ij}|_{\max} - v_o\right)}{v_o}k_{ij}, \tag{8}$$

where l_{ij} is the edge length connecting traffic nodes i and j, d_{ij} is the road traffic difficulty from traffic node i to j, and $\overline{v}_{ij}|_{\max}$ represents the average of the maximum wind speed that traffic nodes i and j suffer during the hurricane. σ_{ij} is the area vegetation density between traffic nodes i and j; k_{ij} is the area terrain parameters between traffic nodes i and j; v_o is the parameter of wind speed scale which takes the minimum wind speed in wind level 8 in the wind scale, that is v_0 = 17.2 m/s [29].

The feature of traffic node i can be modeled by set **I** as

$$\mathbf{I} = \{i, \varphi, \psi, \zeta\}, \tag{9}$$

where φ and ψ are the latitude and longitude of the traffic node i, respectively, and ζ is the parameter set of repair capability.

$$\begin{aligned} \zeta &= \left\{\zeta^{\text{staff}}, \zeta^{\text{resource}}\right\}, \\ \zeta^{\text{staff}} &= \{M_a, a = 0, 1, \ldots, k\}, \\ \zeta^{\text{resource}} &= \left\{N_{a,} a = 0, 1, \ldots, k\right\}, \end{aligned} \tag{10}$$

where ζ^{staff} represents the operation ability of the repair team, ζ^{resource} represents the reserve of repair resources, and k is the number of repair teams stationed at traffic node i.

And the repair path R_o can be described by a set of corresponding nodes:

$$\Gamma_{Ro} = \left\{I_a, a = 0, 1, \ldots, \left|\Gamma_{Ro}\right|\right\}, \quad \forall I \in Ro. \tag{11}$$

2.3. Random Scene. According to the posthurricane environment, the random scene model should take serval factors into consideration, such as the wind field model, the distribution-traffic network fragility model, and the systematic load model. The hurricane field model is established to obtain the wind speed and simulate the failure state of the distribution network and traffic network. A random scene s can be described as

$$s = \left\{t^{\text{land}}, u_{i,t}^{L}, A_t, P_{i,t}\right\}, \quad \forall i \in \Omega_L, t \in \Omega_T, \tag{12}$$

where t^{land} is the hurricane landfall time, $u_{i,t}^{\text{L}}$ is the failure state of the distribution network, A_t is the adjacency matrix of the traffic network, and $P_{i,t}$ is the active power of the distribution network node i at the time t.

Random scene s is generated by the following steps:

(1) The hurricane landing time can be predicted from the relevant meteorological system data. Assume that the probability of hurricane landing obeys a uniform distribution during the predicted period. Sample t^{land} based on its probability density function.

(2) Sample the failure events $z_{i,t}$ in the disaster area ($z_{i,t}$ = 1, the failure event occurrences; $z_{i,t}$ = 0, no failure event) by the component failure probability $p_{i,t}$, which is calculated according to (1) to (5). $u_{i,t}^{\text{L}}$ is the failure state set of all controller switching equipment in the disaster area.

(3) Establish the initial adjacency matrix **A** based on the topology of the traffic network within the disaster area. Calculate ω^T based on (6) to (8) and obtain A_t.

(4) Calculate $P_{i,t}$ according to (13) and (14).

For the transformer node,

$$P_{i,t} = \left(1 - p_{i,t}^{\text{trans}}\right)P_i^{LB}, \quad \forall i \in \Omega_L, t \in \Omega_T. \tag{13}$$

For the nontransformer node, if it is previously in a fault state, $P_{i,t} = 0$; otherwise,

$$P_{i,t} = \tau_i(t) P_i^{LB}, \quad \forall i \in \Omega_L, t \in \Omega_T, \tag{14}$$

where $p_{i,t}^{\text{trans}}$ is the failure rate of transformer node i at time t and $\tau_i(t)$ is a probabilistic factor, which is used to describe random volatility of load and obeys normal distribution [30]. P_i^{LB} is the base value of active power of node i.

3. Emergency Repair Model considering Human Resources

The whole emergency repair process of multiple faults in the distribution network caused by extreme natural disasters can be divided into two stages: network reconfiguration stage and load recovery stage. In the network reconfiguration stage, repair personnel isolates outage components and optimizes the network topology as much as possible to restore the power supply of nonfaulty loads from the transfer channel through switch operation. In the load recovery stage, repair personnel gradually repairs the faults in the distribution network to restore all power supply by the maintenance of repairable faulty equipment and the replacement of spare parts for nonrepairable equipment, according to the repair strategy [31].

Human resources, including repair personnel and repair resources, play an essential role in the whole process of distribution network repair, which mainly reflects on the execution effect of repair strategy. The repair ability preference of repair personnel, the resource allocation and geographic location of repair teams, and the demands of fault tasks will affect the repair effect of fault tasks. Different allocation and maintenance sequences of fault tasks will achieve different repair effects and repair times, which have great significance to improve system resilience. Considering the characteristic of human resources to optimizing repair strategies could obtain a good emergency repair execution effect and shorten the repair time, which finally improve the system resilience.

3.1. Path Planning in Fault Repair Process. The paper divides the repair strategy into three parts: the allocation of repair tasks, maintenance sequence, and path planning. In essence, path planning in emergency repair process is to find the shortest path between two points in the traffic network, so as to achieve the shortest driving time of repair personnel. The construction of the urban distribution network is based on the traffic network frame, which forms a geographically overlapping contrast network. Through the latitude and longitude information, the corresponding points of the distribution network fault node can be identified in the traffic network. Thus, path planning of a single fault task of a repair team can be simplified to a single-source shortest path planning with known traffic network topology. Take into consideration the impact of hurricane and mutual influence of the complicated distribution-traffic coupling system during the emergency repair process, adopting the weight of each topology edge of the traffic network obtained from (6) instead of the geographic length of the road to calculate the driving cost. The minimum programming path solution can be calculated by the Dijkstra algorithm, which is a breadth-first forward search algorithm based on graph theory. Dijkstra algorithm expands to the outer layer with the starting point as the center and constantly looks for the vertex closest to the starting point in each iteration as the starting point of the next iteration until it extends to the endpoint. The set of vertices in the iteration process is the shortest path between two points. Therefore, the minimum driving cost between each node in the repair process would be obtained [28].

3.2. Repair Task Allocation considering Human Resources. In order to realize the numerical evaluation of human resources, this paper adopts utility theory to describe the heterogeneity of fault demand and team repair ability by constructing a utility function $u_j(i)$, which represents the matching degree between the repair team i and repair task j [19]:

$$u_j(i) = \begin{cases} U_j\left(C_i^r, C_j^t\right), & v_{ij} = 1, \\ 0, & v_{ij} = 0, \end{cases}$$

$$U_j\left(C_i^r, C_j^t\right) = \sum_{p=1}^{k} \omega_p \frac{\beta_{ip}}{\alpha_{ip}},$$

$$C_i^r = \begin{pmatrix} \alpha_{i1} & 0 & \cdots & 0 \\ 0 & \alpha_{i2} & \cdots & 0 \\ \vdots & \vdots & & \vdots \\ 0 & 0 & \cdots & \alpha_{ik} \end{pmatrix} \begin{pmatrix} c_1 \\ c_2 \\ \vdots \\ c_k \end{pmatrix}, \tag{15}$$

$$C_j^t = \begin{pmatrix} \beta_{j1} & 0 & \cdots & 0 \\ 0 & \beta_{j2} & \cdots & 0 \\ \vdots & \vdots & & \vdots \\ 0 & 0 & \cdots & \beta_{jk} \end{pmatrix} \begin{pmatrix} c_1 \\ c_2 \\ \vdots \\ c_k \end{pmatrix},$$

where C_i^r is the ability vector of repair team i, C_j^t is the demand vector of repair task j, and v_{ij} is a 0-1 variable which represents the ability to repair faults alone ($v_{ij} = 1$, the repair team i could execute repair task j alone; $v_{ij} = 0$, the repair team i could not execute repair task j alone). α_{ik} is the ability coefficient of the repair team i with ability c_k, β_{jk} is the demand coefficient of the repair team i with ability c_k, and ω_p is the weight of ability c_p which sums to 1, $p = 1, 2, \ldots, k$. In this paper, the value of weight coefficient is determined by expert experience [32].

The larger the $u_j(i)$ value, the better the repair effect. Divide utility value into levels and use the roulette selection method to assign repair tasks; the obtained repair task allocation can ensure meeting the ability preference of each repair team and achieve a good repair effective.

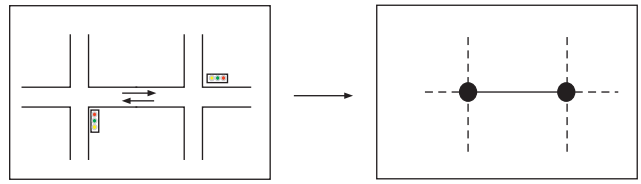

(a) (b)

Figure 1: Traffic network model.

3.3. Repair Strategy Optimization Model

3.3.1. Objective Function. When making repair strategies, decision-makers should give priority to restoring the load of great importance and high power. The purpose of emergency repair is to restore the power supply as soon as possible. In this case, whether the operation is economical during the emergency repair stage or not is not of great importance. Thus, repair strategies of the complex distibution network should aim to decrease social loss caused by outages. And previously, the complex coupling relationship between distribution network, traffic network, and repair teams was partly modeled into the optimization model of repair task allocation and path planning, whose results will be called parameters in the following model.

The proposed formulation is introduced as follows, which represents the weighted sum of the total social losses in the whole repair process:

$$\min f(X) = \sum_{i=1}^{m+n} t(x_i) \sum_{dj=1}^{3} \omega_{dj}(x_i) L_{dj}(x_i),$$

$$t(x_i) = \frac{T_B(x_i)}{\sum_{j=1}^{k} \left(\lambda_i(j)\zeta_j^{\text{staff}}\right)} \cdot + \max\left(\lambda_i(j) \cdot \left(T_{R_j}(x_i) + T_{D_j}(x_i)\right) + T_{ij}\right)_{j=1,2,\ldots,k},$$

$$\lambda_i(j) = \begin{cases} 0, & \text{repair team } j, \\ & \text{refuses the task } i, \\ 1, & \text{repair team } j, \\ & \text{accepts the task } i, \end{cases} \tag{16}$$

$$T_R = \begin{cases} 0, & \zeta^{\text{resource}} \text{ astisfies the needs}, \\ \sum_{\Gamma} \dfrac{\omega^T}{60}, & \zeta^{\text{resource}} \text{ unastisfies the needs}, \\ T_D = \sum_{\Gamma} \dfrac{\omega^T}{60}, & \end{cases}$$

where T_R is the repair resource allocation time, T_D is the drive time to the failure point, T_B is the standard estimated working time of repair task, T_{ij} is the total time spent by repair team j before executing the task i, and $\lambda_i(j)$ is a repair decision variable which indicates whether the repair team j executes the task i. The value of $\lambda_i(j)$ is obtained by the roulette selection method through evaluating the resource demand of repair task, execution capability, and resource allocation of the repair team, and its specific details are included in [19]. ω_{dj} is the weight coefficient of the load in class dj; $L_{dj}(x_i)$ is the outage power of the load in class dj that is restored after the faulty component x_i is repaired. The

system has m failure components, n operable switches, and k repair teams in total. ζ_j^{staff} is the operation ability factor of the repair team j.

Solve the repair strategy optimization model with the discrete bacterial colony chemotaxis algorithm (DBCC) to obtain the sequence of repair tasks [20], where the control variable x_i needs to be discretized:

$$x_i = \frac{a_i}{\sum_{i=1}^{m+n} a_i}, \tag{17}$$

where a_i is a random number between 0 and 1 and represents the fault point label of x_i. The processed $x_i$is no longer the label of the faulty component but represents the position of the bacteria in the solution space. Rearrange x_i from small to large, and then the serial number of x_i in the new sequence represents the order in which the emergency repair is performed. According to the corresponding labela_i of x_i, the fault point label corresponding to the emergency repair sequence can be known.

3.3.2. Constraints

(1) Power flow constraints:

$$\begin{aligned}
&\sum_{(i,j)\in\Omega_D} P_{ij,t} - \sum_{(j,i)\in\Omega_D} P_{ji,t} = P_{i,t}^G - u_{i,t}^L x_{i,t} P_{i,t}, \quad \forall i \in \Omega_L, t \in \Omega_T,\\
&\sum_{(i,j)\in\Omega_D} Q_{ij,t} - \sum_{(j,i)\in\Omega_D} Q_{ji,t} = Q_{i,t}^G - u_{i,t}^L x_{i,t} Q_{i,t}, \quad \forall i \in \Omega_L, t \in \Omega_T,\\
&x_{i,t} \in \{0,1\}, \quad \forall i \in \Omega_L, t \in \Omega_T,\\
&Q_{i,t} = \tau_i(t) Q_i^{LB}, \quad \forall i \in \Omega_L, t \in \Omega_T,\\
&0 \le P_{i,t}^G \le P_i^{G,\max}, \quad \forall i \in \Omega_L, t \in \Omega_T,\\
&0 \le Q_{i,t}^G \le Q_i^{G,\max}, \quad \forall i \in \Omega_L, t \in \Omega_T,\\
&\left|P_{ij}\right| \le P_{ij\max}, \quad \forall (i,j) \in \Omega_D,\\
&\left|Q_{ij}\right| \le Q_{ij\max}, \ \forall (i,j) \in \Omega_D,
\end{aligned} \tag{18}$$

where Ω_D is the set of branch and P_{ij} and Q_{ij} represent the active and reactive power flowing from the distribution network nodes i to j, respectively. $Q_{i,t}$ is the reactive power of the distribution network node i at the time t. $P_{i,t}^G$ and $Q_{i,t}^G$ represent the active and reactive power output of the generation at distribution network node i when the time is t, respectively. $x_{i,t}$ is a 0-1 variable which represents the power supply states of the distribution network node i at the time t ($x_{i,t} = 1$, the node i has power supply; $x_{i,t} = 0$, the node i is in power-off). $P_i^{G,\max}$ and $Q_i^{G,\max}$ represent the maximum active and reactive power output of the generation at distribution network node i, respectively.$P_{ij\max}$ and $Q_{ij\max}$ are the maximum capacity of active and reactive power flowing from the distribution network node i to j.

(2) Voltage constraints: The voltage of each node cannot exceed the limit during the repair process and switching operation.

$$U_{\min} \le U \le U_{\max}. \tag{19}$$

(3) Switching constraints: Taking the switch under operating as a virtual fault point, the repair time is the corresponding switching time, and the switching action is restricted by the principle of gird reconfiguration. The switch state remains unchanged between two repair tasks of the virtual fault point [20]. Besides, the switch will no longer change its state when all loads have been restored to power.

4. Resilience Evaluation

4.1. Indices. Different from reliability, resilience has its newly developing and emerging concept in the area of power systems; it refers to the ability to absorb and rapidly recover from an extraordinary disturbance event [33]. Taking the load performance to represent system performance, Figure 2 shows a conceptual resilience trapezoid, which clearly demonstrates the stages of a power system associated to an external disturbance [34].

In Figure 2, F_0 is the original state of the system; the disturbance hits the system at t_0, which results in the system performance deteriorating; t_1 is the maximum loss moment of the system and F_1 is the corresponding performance level of the system. Following the disturbance, the system will reside in the postdisturbance self-recovery state (t_1-t_2), where grid reconstruction measures would be taken to restore the power supply in the nonfaulty areas; F_2 is the system performance level after reconstruction. Then the grid repair workers apply proper and effective repair measures to make the system fully recover from the disturbance (t_2-t_3) and the system performance level will eventually return to F_3 (the postdisturbance system performance level can be different from the original state).

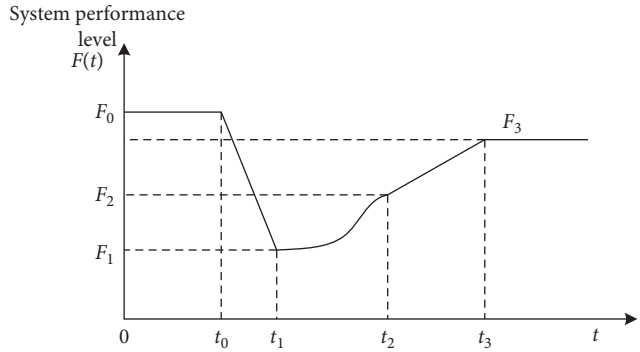

Figure 2: The power system resilience trapezoid model.

Based on the trapezoid model, several different indicators have been put forward to quantitatively analyze the system resilience. These resilience metrics can be divided into two categories in terms of their composition: single indices and composite indices. The single index, such as the integral of the system performance function from the beginning of the disturbance (t_0) to the complete restoration of the system (t_3) or the proportion of system function maintaining the normal state during extreme disasters, is an assessment for the overall process [3, 35]. While the composite index is used to propose several evaluation indices for each stage or capability of resilience and then integrate them through a weighted combination, such as the combination of robustness, rapidity, and performance loss, evaluating resilience from different perspectives [36]. In this paper, considering the impact on system resilience of the complicated coupling relationship of distribution-traffic-human network is mainly reflected in the recovery time, the distribution network resilience R is defined as the time it takes for the system to recover to 95% of its original state after being hit by the extreme weather event, and the 95% of the original state is named the recovery state. To further evaluate the performance of system resilience during the repair process after disasters, the following resilience indexes of the repair process of the distribution network are proposed, which are for a certain disaster scene.

(1) Adaptive rate R1: The probability that the system performance meets the minimum performance requirements and the recovery time does not exceed the longest recovery time limit. The minimum system performance value is 50% of the total system power and the longest recovery time is determined according to the social importance of the load.

$$R_1 = P\left(\min\left(F(t) > \underline{f}, t < \overline{t}\right)\right). \tag{20}$$

(2) Repair rate R2: The recovery speed at which the system can restore to a stable state after the disaster.

$$R_2 = \frac{F_3 - F_1}{t_3 - t_1}. \tag{21}$$

(3) Economic loss rate R3: The ability of the system to decrease economic loss after the disaster.

$$R_3 = \frac{M_\Delta}{M_0},$$
$$M = \sum_{i=1}^{m+n} e_{x_i,k}^{\text{loss}}\left(t\left(x_i\right)\right)L\left(x_i\right), \quad k = 1, 2, 3, 4, 5, \tag{22}$$

where $e_{x_i,k}^{\text{loss}}(t)$ is the economic loss caused by the fault point x_i of load type k with the outage time t and M_Δ and M_0 both represent the economic loss value caused by continuous outages of various loads in the whole repair process; the former adopts the optimization repair strategy in calculation and the latter adopts the same repair sequence but only one repair team to execute all repair tasks, whose repair time for each fault task is the standard repair work time. The load type is divided into 5 categories: industry, business, medicine and health, government, and public utilities. The economic loss function of each type of load is shown in Figure 3 [37].

4.2. Resilience Enhancement Procedure. The resilience enhancement procedure of the complex distribution network under a hurricane disaster coupling with human resources and traffic network is shown in Figure 4.

5. Results and Discussion

In this section, we perform numerical experiments on a IEEE33 bus distribution system. The test system is fitted into an area that covers the range of latitude (28.725°N-29.125°N) and longitude (95.2°W-95.5°W), for demonstration purposes only. There are 37 lines, 5 contract switches, and 33 nodes in the primary network, as shown in Figure 5. The system voltage level is at 12.66 kV and the total load is 3775 kW + j2300kvar [38].

According to the different social importance of each load, the loads are divided into 3 levels and given corresponding weight coefficients and repair time limits to assess the outage loss and the adaptive rate, as shown in Table 1. The load types of each node are shown in Table 2 for evaluating the economic loss. The human resources of emergency repair include repair teams and repair resource reserve, which impact the distribution network resilience. To

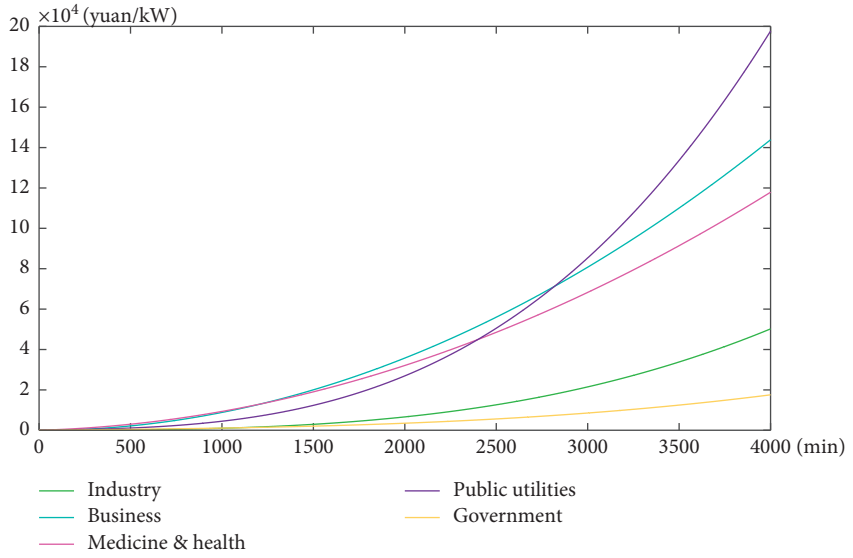

Figure 3: The economic loss function of each load type.

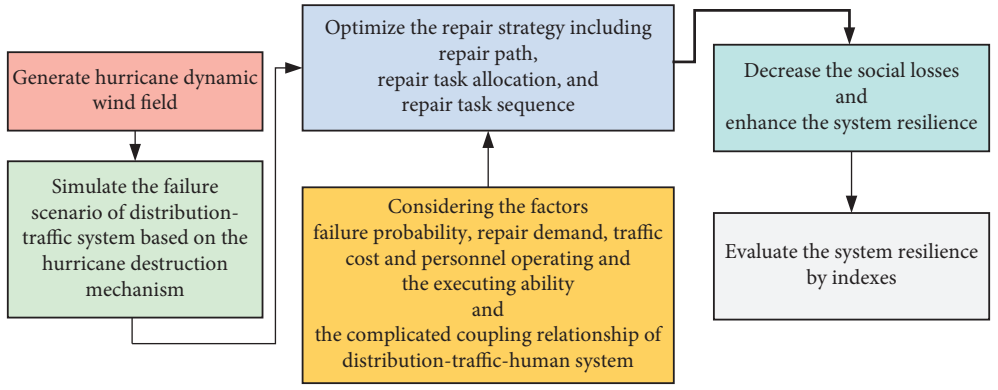

Figure 4: The process of enhancing the complex distribution network resilience coupling with human resources and traffic network under disasters.

consider these effects, it is assumed that the repair teams are stationed at nodes 1, 7, and 12, and the repair resource reserves are placed at nodes 10 and 11, both in the traffic network. The structure of the complicated distribution-traffic-human coupling system is shown in Figure 6.

5.1. Simulation. For illustration, it is assumed that the hurricane lands at the location with latitude 28.9°N and longitude 95.2°W. The hurricane is assumed to be moving with a translational speed of 12.5 mph in the direction of 150°. The test system will be affected by the hurricane for 5 hours. Figure 7 shows the surface wind speed variations of the test system as the hurricane travels along its track with the sample interval of 30 minutes. It is clear to see that the wind speed at most nodes reaches its maximum at the first sample point and then declines over time. Figure 8 shows the specific wind speed of the test system when $T = 30$ min.

Since the damaged state of the complicated distribution-traffic network is related to the suffered wind speed, use the maximum wind speed of each node suffered during the hurricane to calculate the component failure probability, by (1) to (5). The results are shown in Figure 9. Sample the failure events based on failure probability, and the failure scenario of distribution network is obtained as shown in Figure 10. The failed lines are L3-4, L4-5, L10-11, L11-12, and L12-13; the failed switches are installed at L10-11, L11-12, L12-13, and L20-21; the transformer at node 12 is completely damaged and needs to be replaced; the line L20-21 is broken but still repairable; and the nonfault nodes N6-9, N14-17, and N25-32 are affected to outage. Table 3 shows the parameters of each failure event, including the repair resource requirement, the standard repair time, and the load level [39].

5.2. Analysis of the Repair Strategy. There are 3 repair teams in this case and the repair capabilities of each team are shown in Table 4.

The repair capability parameters indicate that none of the single repair teams could meet the resource requirement of failure node N12; and the failed lines L10-11 and L20-21

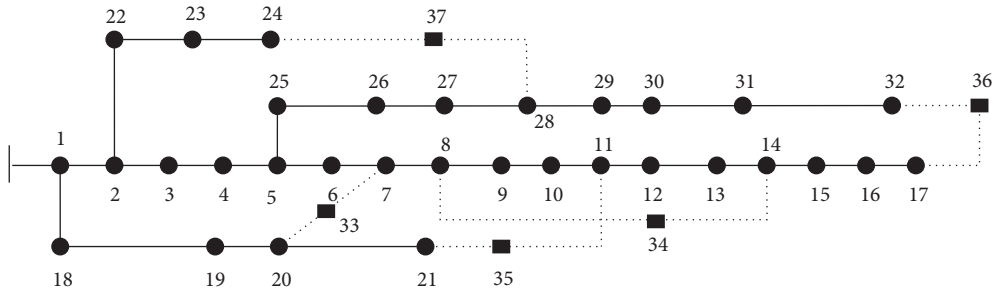

Figure 5: The 33-bus distribution network.

Table 1: The load level parameters.

Level	Node number	The weight coeffcient	$\bar{t}$/h
1	2,3,4,7,8,9,15,16,17,28,29	900	24
2	1,6,10,11,12,21,24,26,27	30	40
3	5,13,14,18,20,22,23,25,30,31,32,33	1	60

Table 2: The load type parameters.

Type	Node number
Industry	1,6,24,26
Business	10,11,12,21,27
Medicine & health	2,3,4,16,17
Government	7,8,9,15,28,29
Public utilities	5,13,14,18,20,22,23,25,30,31,32,33

require a large number of repair resources of which only repair team 1 meets the needs alone. As to repair teams 2 and 3, they need to cooperate or allocate more resources from the reserve point to complete the repair tasks. Considering the repair capability of repair teams and the characteristics of failure events, the repair task assignment scheme is obtained based on the utility value (see Table 5), as shown in Table 6 [19].

It can be noted that, due to the requirements of the repair capability and repair resources, the repair task of node N12 prefers to be assigned to repair teams 1 and 2, followed by repair teams 1 and 3. And to make the high-level load online L3-4 restore as soon as possible, the repair task of line L3-4 prefers to be assigned to repair team 1 alone. The repair task of line L10-11 has never been assigned to repair team 3 due to the resource requirements and geographic distance. While the repair task of line L20-21 prefers to be completed by repair team 3 in cooperation with others for the same reason.

Optimizing the operation sequence of repair plans to minimize the social losses caused during the entire emergency repair process, 3 better repair plans are obtained for reference of the grid workers. Table 7 shows the optimized emergency repair plan, including the repair sequence, the social loss value, and the repair time. Figure 11 particularly demonstrates the social loss variations of each repair plan during the entire emergency repair stage. In order to further illustrate the emergency repair process, take plan 2 as an example to demonstrate the repair sequence, repair team, and the social loss of each repair task, as shown in Figure 12. As a supplement, Figure 13 shows the optimized repair paths of repair team 1 in plan 2. The contribution of the repair teams in each repair task of plan 2 is shown in Figure 14, quantified by the social loss.

It is observed that the switch operation is always executed first in every scheme. This is not only because nodes 36 and 37 are virtual fault points whose repair time is just the response time of switch action, but also the new grid formed by the change of switch state can restore the maximum power supply of the nonfault nodes. The optimized scheme conforms to the rule that the grid reconstruction measures are prioritized during the emergency repair process of distribution network.

Figure 15 shows the resilience and load variations of the test system adopted the repair plans. Evaluate the system resilience under the 3 repair plans by the proposed indexes, and the results are shown in Table 8. It can be noticed that the performances of adaptive rate R_1 and repair rate R_2 are both related to the repair time. The shorter the repair time, the better the index performance, which means indexes R_1 and R_2 are both negatively correlated with the resilience value R. While the economic loss rate R_3 is relatively independent of the resilience R because the different load types have a significant difference in economic loss.

Choose repair plan 3 as an example to demonstrate the relationship between system resilience R and repair rate R_2, which has the best resilience performance. Other parameters remain unchanged, only the operation ability of the repair personnel is gradually increased during the simulation process (a total increase of 30%, with an increase of 5% each time), and the curve of the resilience R and repair rate R_2 is obtained as shown in Figure 16. Besides, the resilience improvement and shortening of repair time brought about by the increase in repair rate R_2 will also increase the adaptive rate R_1 and reduce the economic loss rate R_3 of the test system, as shown in Figure 17.

It is observed that as the repair rate R_2 increases and accumulates to a certain extent, the adaptive rate R_1 of the

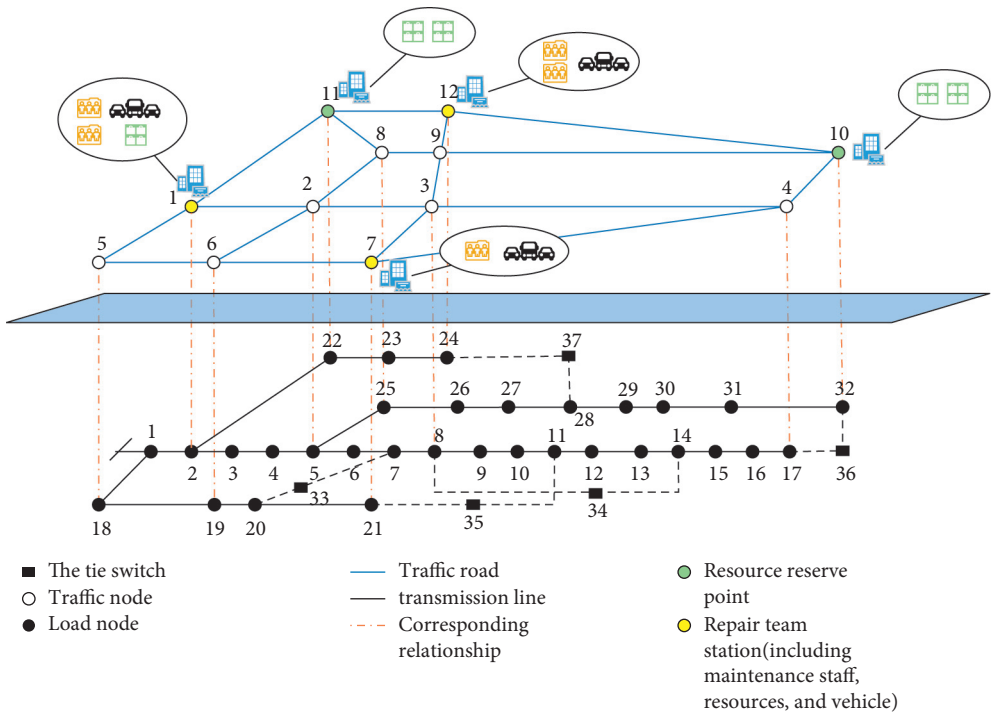

Figure 6: Model of the complicated distribution-traffic-human coupling system.

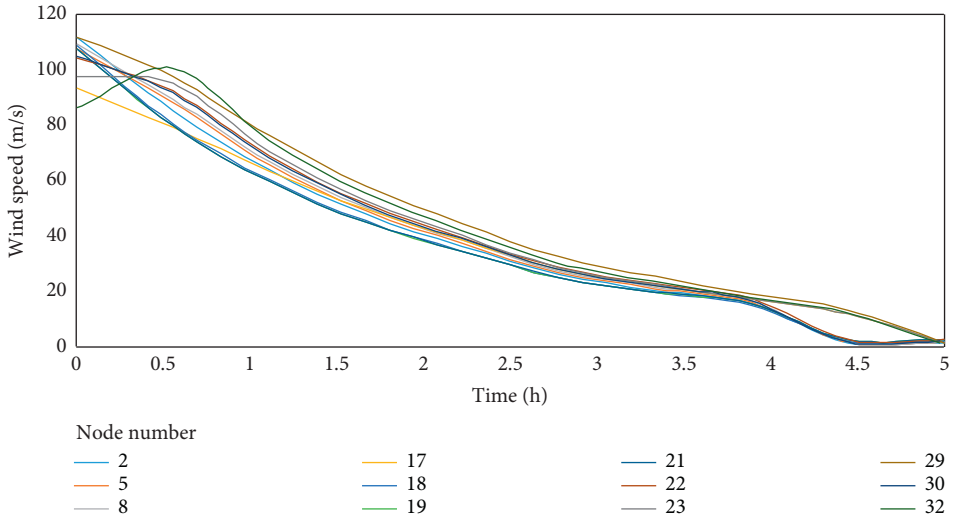

Figure 7: The wind speed attenuation curve. Choose the nodes which are in both the traffic network and the distribution network as a representative, and the node number is corresponded to the distribution network.

system rises stepwise due to the characteristic of the probability. And curves of the R-R_2 and R_3-R_2 have a similar trend which shows that the higher the quality of the human resources involved in the emergency repair process, the higher the corresponding system repair rate R_2, which improves the system resilience and decreases the economic loss. However, the continuous decrease of the slope of the curves indicates that the improved efficiency will gradually level off as the repair rate continues to increase. This is because resilience is related to the time-consuming repair process consisting of the repair task execution time and driving time. Improving the operation ability of the repair

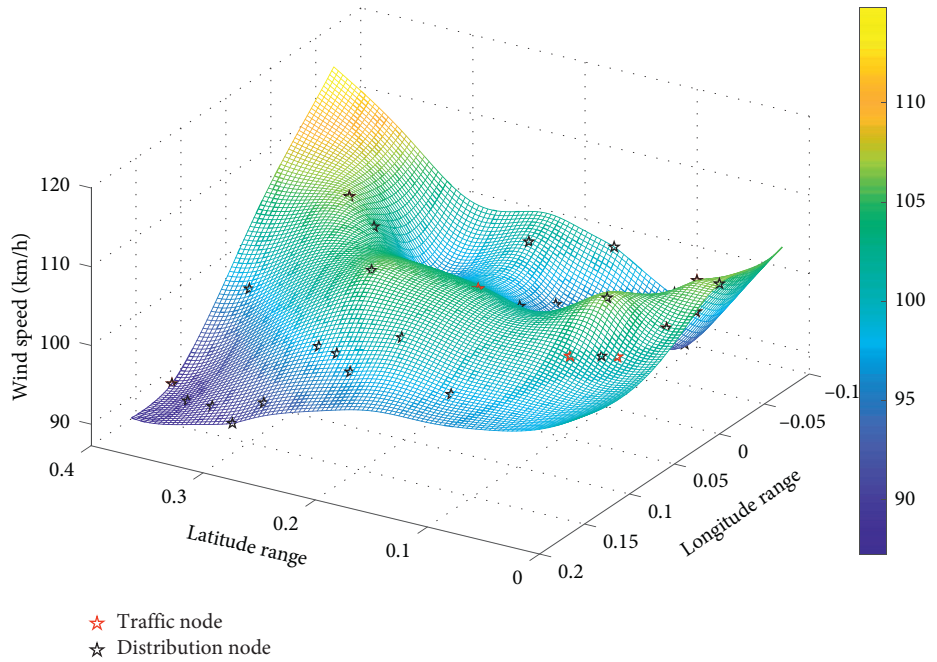

Figure 8: The wind speed at each node of system ($T = 30$ min).

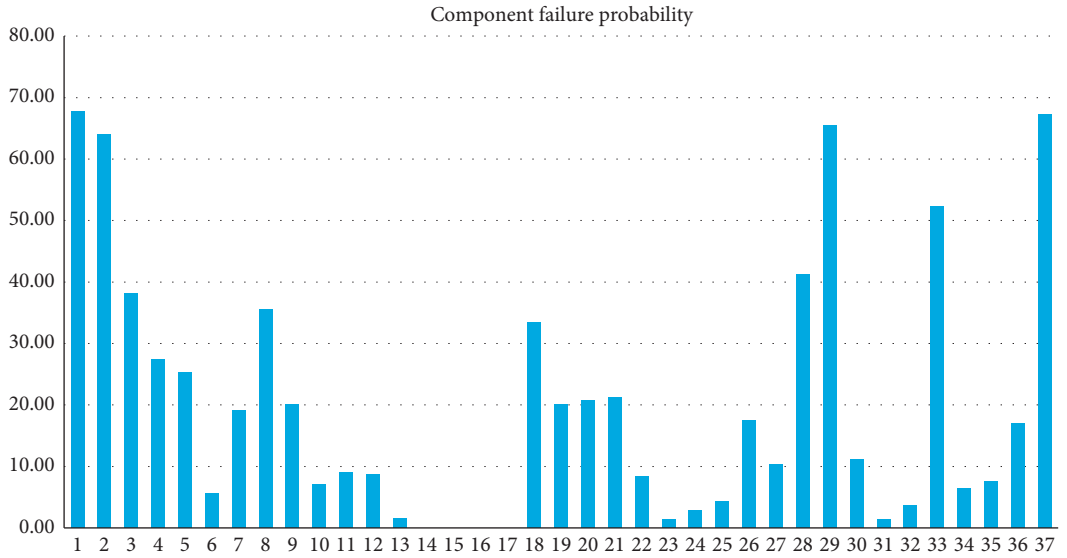

Figure 9: Component failure probability of the distribution network. The Y-axis is the failure probability, and the X-axis is the node label of IEEE33 bus distribution system.

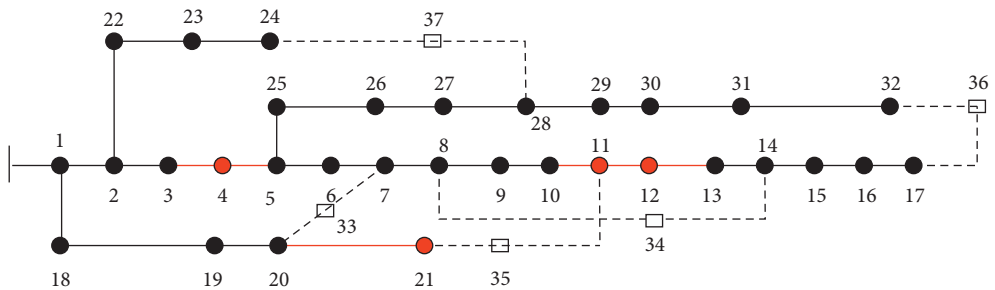

Figure 10: The distribution network failure scenario.

Table 3: Fault event set.

		Fault event						
		3–4	4–5	10–11	11–12	12	12–13	20–21
Resource requirements	Transformer	0	0	0	0	2	0	0
	Backup generation	0	0	0	0	1	0	0
	Line	1.5	1.2	1.5	1.3	0.4	1.2	1.6
	Switch	0	0	1.1	0.5	0.5	0.8	1.8
Operation ability	Mind & body state	1.21	1.07	1.25	1.18	1.34	0.97	1.42
	Repair ability	1	1.14	1.53	1.23	1.65	1.38	1.26
	Working conditions	1	0.76	1.1	0.89	1	1.05	1.31
	Work experience	0.83	1.35	1.48	0.95	1.79	1.24	1.67
The standard repair work time	3	4	7	3	13	4	8	
Load level	1	3	2	2	3	3	2	

Table 4: Repair team parameters.

Repair team		1	2	3
Resource requirements	Transformer	1.5	0.5	1
	Backup generation	1	0.4	0.8
	Line	1.8	1.5	1.3
	Switch	2	0.8	1.4
Operation ability	Mind & body state	1.25	1.32	1.65
	Repair ability	1.57	1.46	1.87
	Working conditions	0.91	1	1.07
	Work experience	1.68	0.89	1.93
Station node	1	12	7	

Table 5: The u_{ij} value of repair teams to each fault event.

Fault event	Repair team					
	1	2	3	1 + 2	2 + 3	1 + 3
3–4	0.95	0.65	0	0.40	0.38	0.37
4–5	0.85	0.63	0.53	0.42	0.40	0.36
10–11	0.74	0	0	0.49	0.54	0.46
11–12	0.64	0.65	0.52	0.33	0.36	0.31
12	0	0	0	0.89	0.65	0.71
12–13	0.60	0.65	0.65	0.42	0.45	0.37
20–21	0.62	0	0	0.67	0.75	0.86

Table 6: Task assignment scheme set.

Plan	Repair team		
	1	2	3
1	3–4,4–5,10–11,12,20–21	10–11,12,12–13,36	11–12,20–21,37
2	3–4,4–5,10–11,12,37	10–11,11–12,12,20–21	12–13,20–21,36
3	3–4,10–11,12,20–21,36	4–5,11–12,12,37	12–13,20–21
4	3–4,4–5,10–11,12,36	11–12,12–13,20–21	12,20–21,37
5	10–11,12,20–21,37	3–4,11–12,36	4–5,12,12–13
6	10–11,12,20–21	3–4,12,36,37	4–5,11–12,12–13

Table 7: Emergency repair sequence and social loss.

Plan	Repair team			Social loss (kWh)	Repair time (h)
	1	2	3		
2	37,3–4,10–11,12,4–5	10–11,12,11–12,20–21	36,12–13,20–21	9631761	63.26
3	36,3–4,12,20–21,10–11	37,4–5,12,11–12	12–13,20–21	9198327	47.83
5	37,10–11,12,20–21	36,3–4,11–12	4–5,12,12–13	8966593	53.15

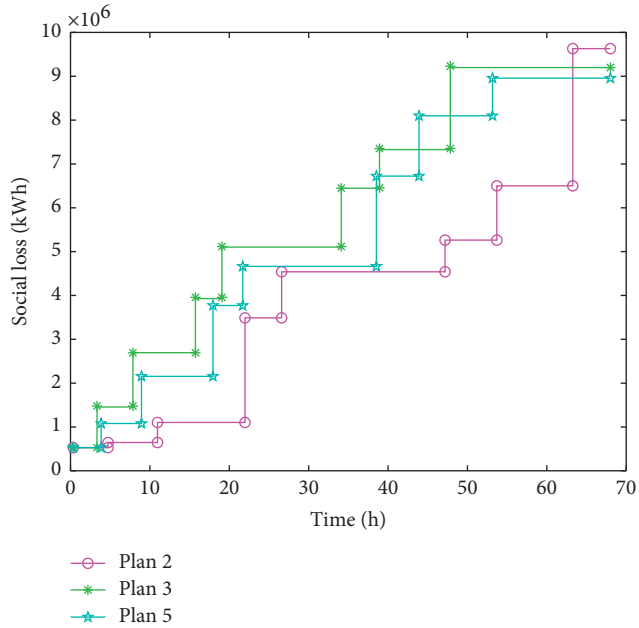

Figure 11: The social loss variations of the test system.

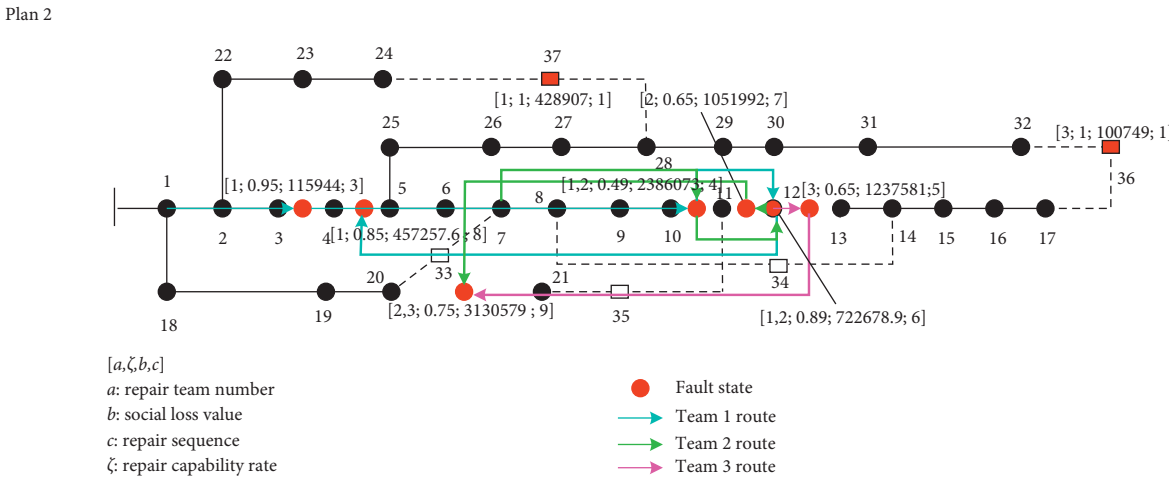

Figure 12: The emergency repair process of plan 2.

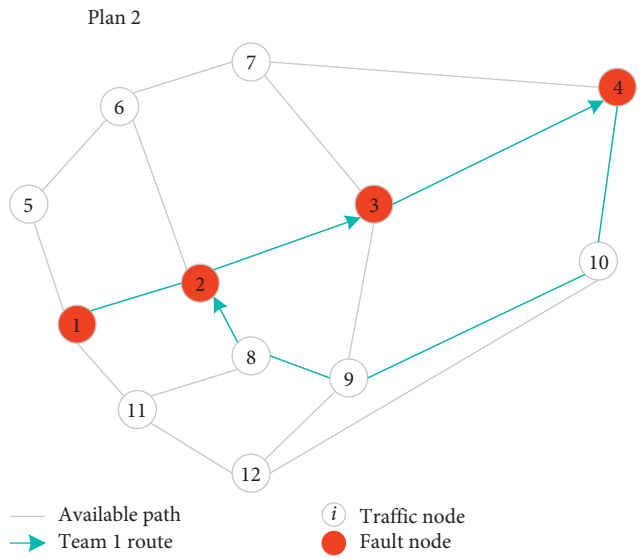

Figure 13: The results of repair path planning.

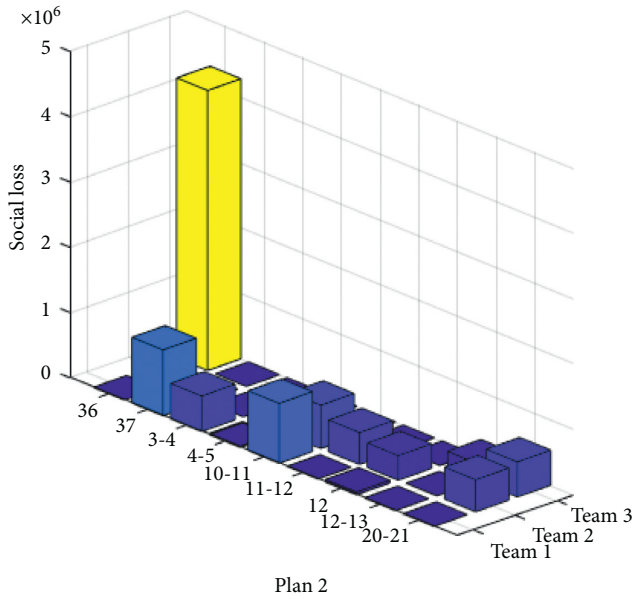

Figure 14: The contribution of repair teams in each repair task.

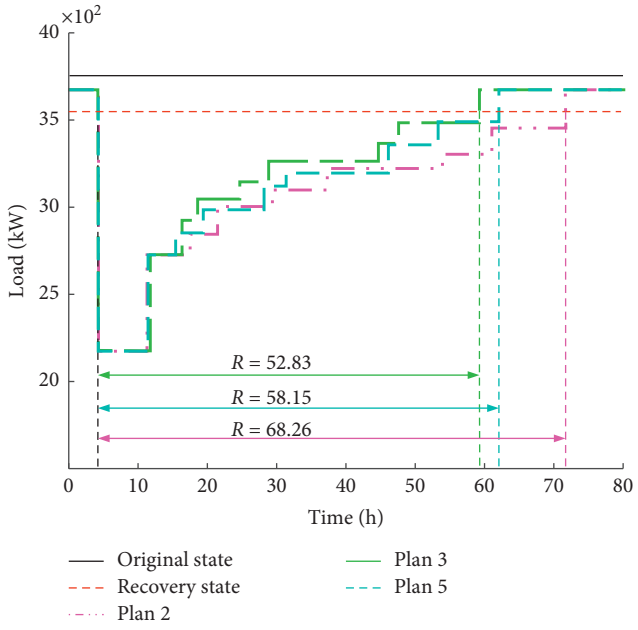

Figure 15: The resilience and load variations of the test system.

Table 8: Distribution network resilience index of different repair plans.

Plan	R	R_1	R_2	R_3
2	68.26	97.11	179.32	80.15
3	52.83	99.01	237.15	85.09
5	58.15	98.12	213.43	81.52

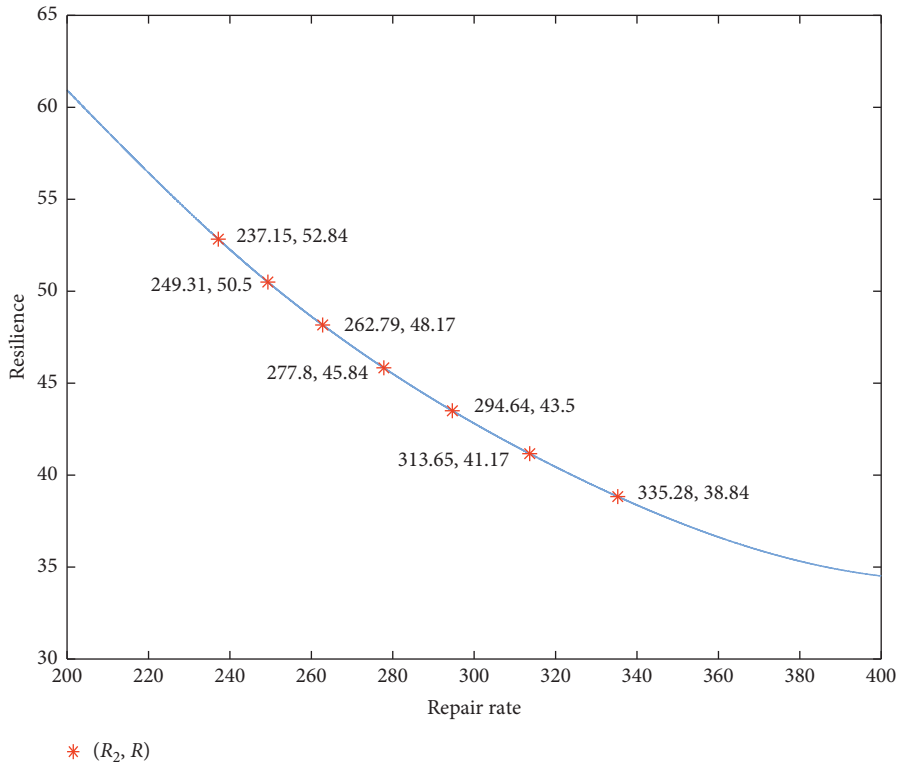

Figure 16: The curve of resilience and repair rate.

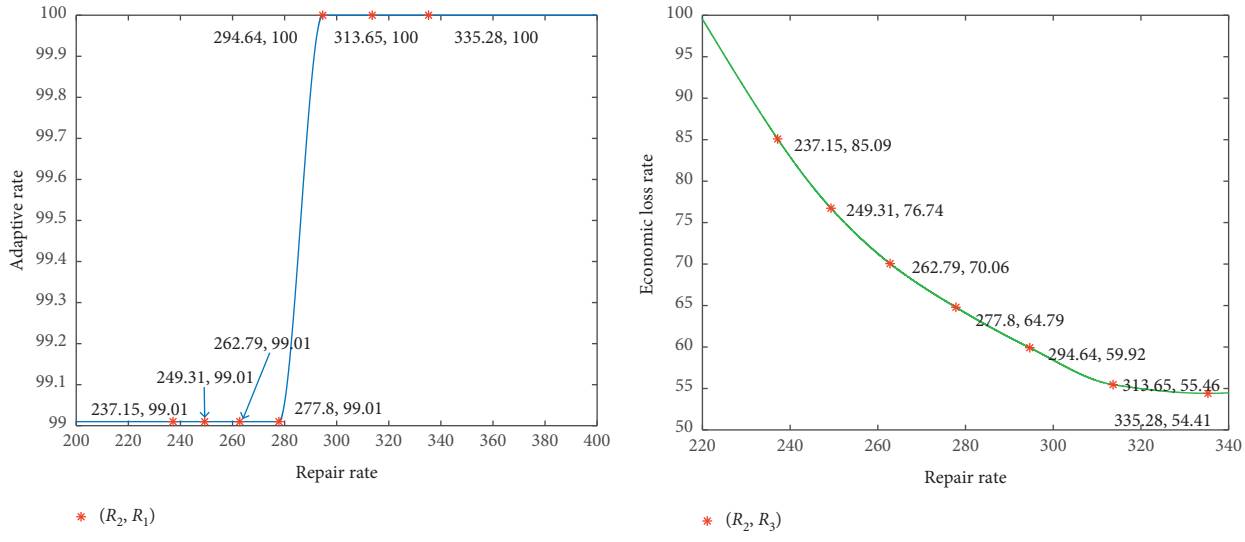

(a) (b)

Figure 17: The curve of three resilience evaluation indices.

personnel can quickly shorten the repair task execution time in the early stage, while it cannot reduce the repair time without limitation.

6. Conclusions

Considering the complex coupling relationship between distribution network, traffic network, and human resources in the emergency repair stage, this paper presents an optimization method to improve the resilience of the complicated distribution-traffic-human coupling system against extreme weather events. Tested on the IEEE33 bus system, the numerical results show that the repair plans, obtained by the proposed model, shorten the execution time of the emergency repair plans and decrease the social and economic losses caused by outages, thereby enhancing the

complex distribution network resilience. The results of evaluation indexes show that the resilience performance is positively correlated with the system adapt and repair abilities. Moreover, improve the quality of human resources by enhancing the operation ability of repair personnel can speed up the system repair rate and increase the system resilience effectively.

Data Availability

The data used to support the findings of this study are available within the article.

Conflicts of Interest

The authors declare that there are no conflicts of interest regarding the publication of this paper.

Acknowledgments

This work was supported in part by the National Natural Science Foundation of China under Grant no. 51767002.

References

[1] A. Arab, A. Khodaei, S. K. Khator, K. Ding, V. A. Emesih, and Z. Han, "Stochastic pre-hurricane restoration planning for electric power systems infrastructure," *IEEE Transactions on Smart Grid*, vol. 6, no. 2, pp. 1046–1054, 2015.

[2] H. Farzin, M. Fotuhi-Firuzabad, and M. Moeini-Aghtaie, "Enhancing power system resilience through hierarchical outage management in multi-microgrids," *IEEE Transactions on Smart Grid*, vol. 7, no. 6, pp. 2869–2879, 2016.

[3] M. Bruneau, S. E. Chang, R. T. Eguchi et al., "A framework to quantitatively assess and enhance the seismic resilience of communities," *Earthquake Spectra*, vol. 19, no. 4, pp. 733–752, 2003.

[4] S. Ma, L. Su, Z. Wang, F. Qiu, and G. Guo, "Resilience enhancement of distribution grids against extreme weather events," *IEEE Transactions on Power Systems*, vol. 33, no. 5, pp. 4842–4853, 2018.

[5] L. B. Chen and H. Chen, "Optimal planning of automatic switches in resilient distribution network against extreme disasters," *Electric Power Automation Equipment*, vol. 11, 2019.

[6] C. Wei, Z. Shen, D. Xiao, L. Wang, X. Bai, and H. Chen, "An optimal scheduling strategy for peer-to-peer trading in interconnected microgrids based on RO and Nash bargaining," *Applied Energy*, vol. 275, 2021.

[7] A. Gholami, T. Shekari, F. Aminifar et al., "Microgrid scheduling with uncertainty: the quest for resilience," *IEEE Transactions on Smart Grid*, vol. 7, p. 1, 2016.

[8] Q. A. Bie Zhaohong and Y. Lin, "Concept and research prospects of power system resilience," *Automation of Electric Power Systems*, vol. 39, no. 22, pp. 1–9, 2015.

[9] C. Y. GAO Haixiang, "Distribution systems resilience: an overview of research progress," *Automation of Electric Power Systems*, vol. 39, no. 23, pp. 1–8, 2015.

[10] X. Wang, M. Shahidehpour, C. Jiang, and Z. Li, "Resilience enhancement strategies for power distribution network coupled with urban transportation system," *IEEE Transactions on Smart Grid*, vol. 10, no. 4, pp. 4068–4079, 2018.

[11] C. Wei, M. Benosman, and T. Kim, "Online parameter identification for state of power prediction of lithium-ion batteries in electric vehicles using extremum seeking," *International Journal of Control, Automation and Systems*, vol. 17, no. 11, pp. 2906–2916, 2019.

[12] W. Wei, S. Mei, L. Wu et al., "Robust operation of distribution networks coupled with urban transportation infrastructures," *IEEE Transactions on Power Systems*, vol. 32, no. 3, pp. 2118–2130, 2017.

[13] S. Xie, Z. Hu, and J. Wang, "Two-stage robust optimization for expansion planning of active distribution systems coupled with urban transportation networks," *Applied Energy*, vol. 261, Article ID 114412, 2020.

[14] Y. Yang, W. Tang, Y. Liu, Y. Xin, and Q. Wu, "Quantitative resilience assessment for power transmission systems under typhoon weather," *IEEE Access*, vol. 6, no. 40, pp. 747–756, 2018.

[15] H. Gao, Y. Chen, S. Mei, S. Huang, and Y. Xu, "Resilience-oriented pre-hurricane resource allocation in distribution systems considering electric buses," *Proceedings of the IEEE*, vol. 105, no. 7, pp. 1214–1233, 2017.

[16] Y. Zhou, "Security analysis and evaluation method of distribution network cyber physical system (CPS) for network attack," Master's Thesis, Nanjing University Of Posts And Telecommunications, Nanjing, China, 2020.

[17] X. L. Liu and C. Yu, "Study on social factors in natural hazard risk management," *Journal of Catastrophology*, vol. 25, no. 4, pp. 120–126, 2010.

[18] M. Tavakoli and M. Nafar, "Human reliability analysis in maintenance team of power transmission system protection," *Protection and Control of Modern Power Systems*, vol. 5, no. 1, pp. 1–13, 2020.

[19] Z. J. Yang and J. Li, "A task allocation strategy of multifault rush repair for distribution network based on optimum utility," *Transactions of China Electrotechnical Society*, vol. 29, no. 6, pp. 263–270, 2014.

[20] Z. Liu and L. Yang, *A rush repair strategy for distribution networks based on improved discrete multi objective bcc algorithm after discretization*, Ph.D. dissertation, 2011.

[21] L. D. Yang and X. Lu, "Dynamic repair recovery strategy of multiple faults for active distribution network based on multi-agent system," *Proceedings of the CSEE*, vol. 37, no. 23, pp. 6855–6865, 2017.

[22] Q. H. Chen and C. Li, "Evaluation of typhoon resilience of distribution network considering grid reconstruction and disaster recovery," *Automation of Electric Power Systems*, vol. 42, no. 6, pp. 47–52, 2018.

[23] M. Madhiarasan, "Accurate prediction of different forecast horizons wind speed using a recursive radial basis function neural network," *Protection and Control of Modern Power Systems*, vol. 5, no. 1, pp. 1–9, 2020.

[24] P. Javanbakht and S. Mohagheghi, "A risk-averse security-constrained optimal power flow for a power grid subject to hurricanes," *Electric Power Systems Research*, vol. 116, pp. 408–418, 2014.

[25] S. M. Quiring, L. Zhu, and S. D. Guikema, "Importance of soil and elevation characteristics for modeling hurricane-induced power outages," *Natural Hazards*, vol. 58, no. 1, pp. 365–390, 2011.

[26] A. M. Salman, Y. Li, and M. G. Stewart, "Evaluating system reliability and targeted hardening strategies of power distribution systems subjected to hurricanes," *Reliability Engineering & System Safety*, vol. 144, pp. 319–333, 2015.

[27] L. Aihua, *Research on the dynamics evolution model of urban disaster chain and the risk assessment method of disaster chain*, Ph.D. dissertation, Central South University, Changsha, China, 2013.

[28] F. Schulz, D. Wagner, and K. Weihe, "Dijkstra's algorithm online: an empirical case study from public railroad transport," *Journal of Experimental Algorithmics (JEA)*, vol. 5, no. 12, 2000.

[29] S. fangfang, *Typhoon damage estimation and prediction of wind vulnerable structures*, Ph.D. dissertation, Harbin Institute of Technology, Harbin, China, 2010.

[30] X. Chen, W. Wu, B. Zhang, and X. Shi, "A robust approach for active distribution network restoration based on scenario techniques considering load and dg uncertainties," in *Proceedings of the 2016 IEEE Power and Energy Society General Meeting (PESGM)*, pp. 1–5, IEEE, Boston, MA, USA, July 2016.

[31] M. Zhou, "Optimal algorithm for system reconstruction (utility theory-based rush repair strategy of post-disaster distribution networks with the real-time adjustment)," *Proceedings of the CSEE*, vol. 23, no. 4, pp. 67–70, 2003.

[32] Z. Jing, "Utility theory-based rush repair strategy of post-disaster distribution networks with the real-time adjustment," Master's thesis, Yanshan University, Qinhuangdao, China, 2014.

[33] R. Francis and B. Bekera, "A metric and frameworks for resilience analysis of engineered and infrastructure systems," *Reliability Engineering & System Safety*, vol. 121, pp. 90–103, 2014.

[34] X. Zhiwen, "Emergency resources from the perspective of resilience," Master's thesis, University of Chinese Academy of Sciences, Beijing, China, 2018.

[35] X. Zhou, S. Ge, T. Li et al., "Research on analysis methods and improvement measures of distribution network resilience under extreme weather conditions," *Proceedings of the CSEE*, vol. 38, no. 2, pp. 505–513, 2018.

[36] C. Nan and G. Sansavini, "A quantitative method for assessing resilience of interdependent infrastructures," *Reliability Engineering & System Safety*, vol. 157, pp. 35–53, 2017.

[37] L. Cong, "Studies on optimal control of power system restoration after blackout," Master's thesis, Beijing Jiaotong University, Beijing, China, 2016.

[38] W. Y. Lu, "Reconfiguration of distribution network after fault based on improved ant colony algorithm," in *Proceedings of the 24th Annual Conference of Power System and Automation in Chinese Universities*, Beijing, China, October 2008.

[39] L. Weijia, *Decision-making and optimization strategies for power system restoration*, Ph.D. dissertation, Zhejiang University, Zhejiang, China, 2016.

Hindawi
Complexity
Volume 2021, Article ID 9936370, 12 pages
https://doi.org/10.1155/2021/9936370

WILEY | Hindawi

Research Article

The Second-Order Differential Equation System with the Controlled Process for Variational Inequality with Constraints

Li Wang, Xingxu Chen, and Juhe Sun

School of Science, Shenyang Aerospace University, Shenyang 110136, China

Correspondence should be addressed to Li Wang; liwang211@163.com

Received 8 March 2021; Revised 29 April 2021; Accepted 21 May 2021; Published 1 June 2021

Academic Editor: Chun Wei

In this paper, the variational inequality with constraints can be viewed as an optimization problem. Using Lagrange function and projection operator, the equivalent operator equations for the variational inequality with constraints under the certain conditions are obtained. Then, the second-order differential equation system with the controlled process is established for solving the variational inequality with constraints. We prove that any accumulation point of the trajectory of the second-order differential equation system is a solution to the variational inequality with constraints. In the end, one example with three kinds of different cases by using this differential equation system is solved. The numerical results are reported to verify the effectiveness of the second-order differential equation system with the controlled process for solving the variational inequality with constraints.

1. Introduction

We consider the variational inequality with constraints, denoted by VIP (K, F): find $x^* \in K$ such that

$$\langle F(x^*), y - x^* \rangle \geq 0, \quad \forall y \in K, \tag{1}$$

where $K = \{x \in \Omega | g(x) \leq 0\}$, F: $\mathfrak{R}^n \longrightarrow \mathfrak{R}^n$ is a monotone mapping, g: $\mathfrak{R}^n \longrightarrow \mathfrak{R}^m$ is a convex and differentiable mapping, and $\Omega \subseteq \mathfrak{R}^n$ is a nonempty closed convex set.

Variational inequality problems arise in physics, mechanics, economics, optimization, control, equilibrium model in transportation, and so forth. The finite dimensional variational inequality is an active field with abundant intension. In the past 30 years, great progress has been made in the study of numerical algorithms for solving the variational inequality problems and many numerical methods have emerged in large numbers, such as nonsmooth equation methods, smoothing methods, projection iteration methods, interior methods, multisplitting methods, homotopy approaches, Tikhonov regularization, and proximal point methods. The book by Facchinei and Pang [1] is the most famous reference to give a detailed numerical treatment of variational inequality problems and complementarity problems in the area of mathematical programming. But this book did not include the differential equation approaches for solving variational inequality problems.

The differential equation method is used to solve constrained nonlinear optimization problems, which was firstly proposed by Arrow and Hurwicz [2]; and the equity-constrained optimization problem was considered. Fiacco and McCormick [3] studied the constraint qualification by using differential equation method. Evtushenko [4] studied the problem of equality constraint earlier. Yamashita [5], Evtushenko et al. [6–10], and Pan [11] developed and improved the differential equation methods. In particular, Evtushenko and Zhadan have carried out a great deal of research on differential equation methods for nonlinear programming problems and constraint problems on general closed sets by using the stability theory of differential equations since 1973, which enriches the differential equation method of nonlinear programming problem. There are other scholars who have done a lot of research work on differential equation methods, and they have established a variety of differential equation systems to solve the optimization problems. Brown et al. [12, 13] proposed the differential equation system based on the penalty function. Zhang and Constantinides [14] presented a differential equation system based on Lagrange function to solve the

equality constraint problem. Since the nonlinear Lagrange function can be used to construct a dual algorithm for solving nonlinear optimization problems and the dual algorithm has no limitation on the feasibility of the original variables, many differential equation systems involved dual variables, such as those in the works of Zhou et al. [15] and Jin et al. [16]. Recently, Jin et al. [17] formulated the differential systems based on the first derivatives and the second derivatives of the approximate augmented Lagrangian. Under suitable conditions, the asymptotic stability of the differential systems and local convergence properties of their Euler discrete schemes are analyzed. Zhang [18] studied the differential equation method for quadratic programming.

At the same time, there are a series of neural network methods for solving variational inequality and complementarity problems. In fact, the model of neural network is often described by the system of differential equations. Zhou et al. [19] transformed the nonlinear complementarity problem into an equivalent optimization problem, and a system of differential equations is constructed to solve the optimization problem. On the basis of projection operator, Gao et al. [20] presented a system of differential equations for solving variational inequality problems with linear and nonlinear constraints. He and Yang [21] studied a new neural network model for nonsymmetric linear variational inequality. The classical neural network model for solving linear variational inequality based on projection operator and compression method is extended. Liao et al. [22] studied the differential equation system of nonlinear complementarity problem. Nazemi and Sabeghi [23] applied a gradient neural network model to efficiently solve the convex second-order cone constrained variational inequality problem. Nazemi and Sabeghi [24] considered a new neural network model to simply solve the convex second-order cone constrained variational inequality problem.

Different from the above results, Antipin [25] considered the first-order and second-order differential equation systems for solving the minimization function on a simple set. The asymptotic and exponential stability of such processes was proved without using Lyapunov function. Furthermore, Antipin [26] studied the differential equation system and the controlled proximal differential equation system for solving the minimization function. The convergence theorems were obtained. Antipin and Antipin [27, 28] established the differential equation system and the controlled proximal differential equation system for solving the saddle problem and proved that the trajectory of the system converges monotonically in norm to one of the equilibrium points. Antipin [29] considered the differential equation system with the controlled process for solving the fixed point of the extremal mapping and proved that the trajectory of the system converges to the solution with exponential rate. Antipin [30] established the differential equation systems and the differential equation system with the controlled process for optimization problem, saddle problem, and the extremal mapping, respectively. The corresponding convergence theorems were also proved. The variational inequality problem with coupled constraints and the fixed point of the extremal mapping with coupled constraints were studied by Antipin and Antipin [31, 32], where symmetric functions were introduced and the differential equation systems with the controlled process for global convergence were proposed. Wang and Wang [33] established the first-order differential equation system to solve the variational inequality with constraints problem (1).

We think that the research of differential equation method for solving variational inequality is not much. In the past, the problem is firstly transformed into a smooth unconstrained optimization problem; then the differential equation method is constructed by using negative gradient for the unconstrained optimization. Inspired by the work of Antipin, our approach is different, which directly starts from the nonsmooth system of equations to establish the differential equation method, which requires relatively weak conditions. At the same time, due to the fact that the differential equation system has mature numerical solution methods, such as Runge-Kutta method, using these pieces of numerical software to solve the problem of variational inequality may achieve good results in practical calculation. It is hoped that our research on the differential equation method for the variational inequality will contribute to the development of the neural network method for solving the variational inequality problem.

In this paper, we will establish the second-order differential equation system with the controlled process for solving the variational inequality with constraints problem (1). The remainder of this paper is organized as follows. In the next section, based on Lagrange function and projection operator, we prove a lemma that gives the equivalent operator equation under certain conditions for problem (1). In Section 3, we establish the second-order differential equation system with the controlled process for the variational inequality with constraints (1) and prove that any accumulation point of the trajectory of the second-order differential equation system is a solution to problem (1). One example with three kinds of different cases is solved by the second-order differential equation system with the controlled process in Section 4, and the transient behaviors of the trajectories of this kind of differential equation system for every case are illustrated.

2. Preliminaries

The projection operator to a convex set is quite useful in reformulating the variational inequality with constraints (1) as an equation.

Let C be a convex closed set; for every $x \in \mathfrak{R}^n$, there is a unique $\widehat{x}$ in C such that

$$\|x - \widehat{x}\| = \min\{\|x - y\| | y \in C\}. \tag{2}$$

The point $\widehat{x}$ is the projection of x onto C, denoted by $\Pi_C(x)$. The projection operator Π_C: $\mathfrak{R}^n \longrightarrow C$ is well defined over $\mathfrak{R}^n$ and it is a nonexpansive mapping.

Lemma 1 (see [34]). *Let H be a real Hilbert space and let $C \subset H$ be a closed convex set. For a given $z \in H$, $u \in C$ satisfies the inequality*

$$\langle u - z, v - u \rangle \geq 0, \quad \forall v \in C, \tag{3}$$

if and only if $u - \Pi_C(z) = 0$.

In order to obtain the second-order differential equation system, we need to transform the variational inequality with constraints problem (1), which can be viewed as the following optimization problem:

$$\begin{aligned} &\min f(y) \\ &\text{s.t.} \quad g(y) \leq 0, \ y \in \Omega, \end{aligned} \tag{4}$$

where $f(y) = \langle F(x^*), y - x^* \rangle$ and $f(y) \geq 0$.

Define the Lagrange function of the minimization problem (4):

$$\mathscr{L}(x^*, y, u) = \langle F(x^*), y - x^* \rangle + \langle u, g(y) \rangle, \quad \forall y \in \Omega, u \in \mathfrak{R}_+^m, \tag{5}$$

where y and u are the primal and dual variables, respectively.

Since x^* is the minimum of $f(y)$, the pair (x^*, u^*) (under certain regularity conditions) is a saddle point of $\mathscr{L}(x^*, y, u)$. That is,

$$\begin{aligned} \langle F(x^*), x^* - x^* \rangle + \langle u, g(x^*) \rangle &\leq \langle F(x^*), x^* - x^* \rangle + \langle u^*, g(x^*) \rangle \\ &\leq \langle F(x^*), y - x^* \rangle + \langle u^*, g(y) \rangle, \end{aligned} \tag{6}$$

$\forall y \in \Omega$ and $u \in \mathfrak{R}_+^m$.

System (6) can be represented in an equivalent manner as

$$\begin{aligned} x^* &\in \arg\min\{\langle F(x^*), y - x^* \rangle + \langle u^*, g(y) \rangle | y \in \Omega\}, \\ u^* &\in \arg\max\{\langle u, g(x^*) \rangle | u \in \mathfrak{R}_+^m\}. \end{aligned} \tag{7}$$

Lemma 2. *Suppose that g: $\mathfrak{R}^n \longrightarrow \mathfrak{R}^m$ is a differentiable mapping and $\Omega \subset \mathfrak{R}^n$ is a nonempty closed convex set. Then the pair (x^*, u^*) is the saddle point of the Lagrange function $\mathscr{L}(x^*, y, u)$ if and only if (x^*, u^*) satisfies the following operator equation:*

$$\begin{aligned} x^* &= \Pi_\Omega\left(x^* - \alpha\left(F(x^*) + \mathscr{J}g(x^*)^T u^*\right)\right), \\ u^* &= \Pi_+(u^* + \alpha g(x^*)), \end{aligned} \tag{8}$$

where $\Pi_+(\cdot)$ and $\Pi_\Omega(\cdot)$ are the operators that project a vector onto the positive octant R_+^m and the set Ω, respectively, and $\alpha > 0$ is a parameter.

Proof. System (4) or system (5) implies that (x^*, u^*) satisfies the following inequalities:

$$\begin{aligned} \langle F(x^*), y - x^* \rangle + \langle u^*, g(y) - g(x^*) \rangle \geq 0, \quad &\forall y \in \Omega, \\ \langle -g(x^*), u - u^* \rangle \geq 0, \quad &\forall u \in \mathfrak{R}_+^m. \end{aligned} \tag{9}$$

If the function g is differentiable, we have

$$\begin{aligned} \langle F(x^*) + \mathscr{J}g(x^*)^T u^*, y - x^* \rangle \geq 0, \quad &\forall y \in \Omega, \\ \langle -g(x^*), u - u^* \rangle \geq 0, \quad &\forall u \in \mathfrak{R}_+^m, \end{aligned} \tag{10}$$

where $\mathscr{J}g(x^*)$ is the Jacobian of the mapping g at x^*.

The variational inequality system (10) can be computed by

$$\begin{aligned} &\langle x^* - x^* + \alpha\left(F(x^*) + \mathscr{J}g(x^*)^T u^*\right), y - x^* \rangle \\ &\langle u^* - u^* - \alpha g(x^*), u - u^* \rangle \geq 0, \quad \forall u \in \mathfrak{R}_+^m, \end{aligned} \tag{11}$$

where $\alpha > 0$ is a parameter.

With the help of projection operators and Lemma 1, the above system of variational inequalities is represented in the form of operator equation as

$$\begin{aligned} x^* &= \Pi_\Omega\left(x^* - \alpha\left(F(x^*) + \mathscr{J}g(x^*)^T u^*\right)\right), \\ u^* &= \Pi_+(u^* + \alpha g(x^*)), \end{aligned} \tag{12}$$

where $\Pi_+(\cdot)$ and $\Pi_\Omega(\cdot)$ are the operators that project a vector onto the positive octant R_+^m and the set Ω, respectively. This completes the proof. □

Furthermore, if g: $\mathfrak{R}^n \longrightarrow \mathfrak{R}^m$ is convex, we have for the second term in the first inequality of the variational inequality (10) that

$$\langle \mathscr{J}g(x^*)^T u^*, y - x^* \rangle = \langle u^*, \mathscr{J}g(x^*)(y - x^*) \rangle \leq \langle u^*, g(y) - g(x^*) \rangle, \tag{13}$$

for all $y \in \Omega$. Thus, we can rewrite the variational inequality (10) as follows:

$$\begin{aligned} \langle F(x^*), y - x^* \rangle + \langle u^*, g(y) - g(x^*) \rangle \geq 0, \quad &\forall y \in \Omega, \\ \langle -g(x^*), u - u^* \rangle \geq 0, \quad &\forall u \in \mathfrak{R}_+^m. \end{aligned} \tag{14}$$

Remark 1. When the function g is convex and differentiable, the relations in (6)–(14) are equivalent to each other.

3. Second-Order Differential Equation System

In this section, we consider the second-order differential equation system for solving the variational inequality with constraints problem (1).

The second-order differential equation system is constructed based on equation (8) as follows:

$$\begin{aligned}\mu_1\frac{d^2x}{dt^2}+\beta_1\frac{dx}{dt}+x&=\Pi_\Omega\left(x-\alpha\left(F(x)+\mathcal{J}g(x)^Tu\right)\right),\quad x(t_0)=x_0,\ \dot{x}(t_0)=\dot{x}_0,\\ \mu_2\frac{\mathrm{d}^2u}{\mathrm{d}t^2}+\beta_2\frac{\mathrm{d}u}{\mathrm{d}t}+u&=\Pi_+(u+\alpha g(x)),\quad u(t_0)=u_0,\dot{u}(t_0)=\dot{u}_0,\end{aligned}\tag{15}$$

where $\mu_1>0,\beta_1>0,\mu_2>0,\beta_2>0$, and $\alpha>0$ are parameters.

In order to provide the convergence of the trajectory of the second-order differential equation system to a saddle point (x^*,u^*) of the Lagrange function $\mathscr{L}(x^*,y,u)$, we introduce the following second-order differential equation system with the controlled process inspired by Antipin et al. [25–32] and Wang and Wang [33].

$$\begin{aligned}\mu_1\frac{\mathrm{d}^2x}{\mathrm{d}t^2}+\beta_1\frac{\mathrm{d}x}{\mathrm{d}t}+x&=\Pi_\Omega\left(x-\alpha\left(F(\overline{x})+\mathcal{J}g(\overline{x})^T\overline{u}\right)\right),\quad x(t_0)=x_0,\dot{x}(t_0)=\dot{x}_0,\\ \mu_2\frac{\mathrm{d}^2u}{\mathrm{d}t^2}+\beta_2\frac{\mathrm{d}u}{\mathrm{d}t}+u&=\Pi_+(u+\alpha g(\overline{x})),\quad u(t_0)=u_0,\dot{u}(t_0)=\dot{u}_0,\end{aligned}\tag{16}$$

where

$$\begin{aligned}\overline{x}&=\Pi_\Omega\left(x-\alpha\left(F(x)+\mathcal{J}g(x)^T\overline{u}\right)\right),\\ \overline{u}&=\Pi_+(u+\alpha g(x)).\end{aligned}\tag{17}$$

If $\mu_1=\mu_2=0$ and $\beta_1=\beta_2=1$, then system (16) coincides with (8) in the work of Wang and Wang [33].

For simplicity, we denote $\ddot{x}=(\mathrm{d}^2x/\mathrm{d}t^2)$ and $\ddot{u}=(\mathrm{d}^2u/\mathrm{d}t^2)$. Similarly, the second-order differential equation system with the controlled process (16) can be represented in the form of variational inequalities as follows:

$$\langle\mu_1\ddot{x}+\beta_1\dot{x}+\alpha\left(F(\overline{x})+\mathcal{J}g(\overline{x})^T\overline{u}\right),y-x-\mu_1\ddot{x}-\beta_1\dot{x}\rangle\geq0,\quad\forall y\in\Omega,\tag{18}$$

$$\langle\mu_2\ddot{u}+\beta_2\dot{u}-\alpha g(\overline{x}),v-u-\mu_2\ddot{u}-\beta_2\dot{u}\rangle\geq0,\quad\forall v\in\mathfrak{R}_+^m,\tag{19}$$

$$\langle\overline{x}-x+\alpha\left(F(x)+\mathcal{J}g(x)^T\overline{u}\right),y-\overline{x}\rangle\geq0,\quad\forall y\in\Omega,\tag{20}$$

$$\langle\overline{u}-u-\alpha g(x),v-\overline{u}\rangle\geq0,\quad\forall v\in\mathfrak{R}_+^m.\tag{21}$$

Subsequently, we assume that g, F, and $\mathcal{J}g^T$ are Lipschitz continuous with the constants $|g|$, $|F|$, and $|\mathcal{J}|$, respectively. In addition, we suppose that $\|\overline{u}\|\leq C_0$ and C_0 is a constant.

With regard to these conditions and (16), it is easy to show the following inequalities since the projection operator is a nonexpansive mapping.

$$\begin{aligned}\left\|u+\mu_2\ddot{u}+\beta_2\dot{u}-\overline{u}\right\| &= \left\|\Pi_+(u+\alpha g(\overline{x}))-\Pi_+(u+\alpha g(x))\right\| \\ &\le \|u+\alpha g(\overline{x})-u-\alpha g(x)\| \le \alpha|g|\|\overline{x}-x\|,\end{aligned} \tag{22}$$

$$\begin{aligned}\left\|x+\mu_1\ddot{x}+\beta_1\dot{x}-\overline{x}\right\| &= \left\|\Pi_\Omega\left(x-\alpha\left(F(\overline{x})+\mathcal{J}g(\overline{x})^T\overline{u}\right)\right)-\Pi_\Omega\left(x-\alpha\left(F(x)+\mathcal{J}g(x)^T\overline{u}\right)\right)\right\| \\ &\le \left\|x-\alpha\left(F(\overline{x})+\mathcal{J}g(\overline{x})^T\overline{u}\right)-x+\alpha\left(F(x)+\mathcal{J}g(x)^T\overline{u}\right)\right\| \\ &= \alpha\left\|F(x)-F(\overline{x})+\mathcal{J}g(x)^T\overline{u}-\mathcal{J}g(\overline{x})^T\overline{u}\right\| \\ &\le \alpha\|F(x)-F(\overline{x})\|+\alpha\left\|\mathcal{J}g(x)^T\overline{u}-\mathcal{J}g(\overline{x})^T\overline{u}\right\| \\ &\le \alpha\left(|F|+C_0|\mathcal{J}|\right)\|x-\overline{x}\| = \alpha C\|x-\overline{x}\|,\end{aligned} \tag{23}$$

where $C = |F| + C_0|\mathcal{J}|$.

Now we discuss the convergence of the trajectories $x(t)$, $u(t)$, $\dot{x}(t)$, and $\dot{u}(t)$ of the second-order differential equation system (16).

Theorem 1. *Suppose that the set of solutions Ω^* of problem (1) is nonempty, F is monotone and Lipschitz continuous with the constant $|F|$, and g is convex, differentiable, and Lipschitz continuous with the constant $|g|$. Suppose that $\|u(t)\| \le C_0$ for all $t \longrightarrow \infty$, $\|\dot{u}(t)\|$ is bounded for all $t \longrightarrow \infty$, $\mathcal{J}g^T$ is Lipschitz continuous with the constant $|\mathcal{J}|$, and $\Omega \subseteq \mathfrak{R}^n$ is a convex closed set. Then the accumulation point of the trajectory $x(t)$ of the second-order differential equation system (16) with $1 < \beta_1 < \mu_1 < (1/2)\beta_1^2$, $0 < \mu_2 < (1/2)\beta_2^2$, and $\alpha^2\left((|F| + C_0|\mathcal{J}|)^2 + |g|^2\right) < (1/2)$ is the solution to the variational inequality with constraints problem (1).*

Proof. Setting $y = x^* \in \Omega^*$ in the variational inequality (18), we have

$$\left\langle \mu_1\ddot{x}+\beta_1\dot{x}+\alpha\left(F(\overline{x})+\mathcal{J}g(\overline{x})^T\overline{u}\right), x^*-x-\mu_1\ddot{x}-\beta_1\dot{x}\right\rangle \ge 0. \tag{24}$$

Let $y = x + \mu_1\ddot{x} + \beta_1\dot{x}$ in the variational inequality (20); we obtain

$$\left\langle \overline{x}-x+\alpha\left(F(x)+\mathcal{J}g(x)^T\overline{u}\right), x+\mu_1\ddot{x}+\beta_1\dot{x}-\overline{x}\right\rangle \ge 0, \tag{25}$$

which implies that

$$\begin{aligned}&\langle \overline{x}-x, x+\mu_1\ddot{x}+\beta_1\dot{x}-\overline{x}\rangle + \alpha\langle F(\overline{x}), x+\mu_1\ddot{x}+\beta_1\dot{x}-\overline{x}\rangle \\ &\quad -\alpha\langle F(\overline{x})-F(x), x+\mu_1\ddot{x}+\beta_1\dot{x}-\overline{x}\rangle + \alpha\langle \mathcal{J}g(\overline{x})^T\overline{u}, x+\mu_1\ddot{x}+\beta_1\dot{x}-\overline{x}\rangle \\ &\quad -\alpha\langle \mathcal{J}g(x)^T\overline{u}-\mathcal{J}g(x)^T\overline{u}, x+\mu_1\ddot{x}+\beta_1\dot{x}-\overline{x}\rangle \ge 0.\end{aligned} \tag{26}$$

Summing inequalities (24) and (26), we infer that

$$\begin{aligned}&\langle \mu_1\ddot{x}+\beta_1\dot{x}, x^*-x-\mu_1\ddot{x}-\beta_1\dot{x}\rangle + \alpha\langle F(\overline{x}), x^*-\overline{x}\rangle + \alpha\langle \mathcal{J}g(\overline{x})^T\overline{u}, x^*-\overline{x}\rangle \\ &\quad +\langle \overline{x}-x, x+\mu_1\ddot{x}+\beta_1\dot{x}-\overline{x}\rangle + \alpha\langle F(x)-F(\overline{x}), x+\mu_1\ddot{x}+\beta_1\dot{x}-\overline{x}\rangle \\ &\quad +\alpha\langle \mathcal{J}g(x)^T\overline{u}-\mathcal{J}g(\overline{x})^T\overline{u}, x+\mu_1\ddot{x}+\beta_1\dot{x}-\overline{x}\rangle \ge 0.\end{aligned} \tag{27}$$

By using inequality (23), we compute the above inequality as follows:

$$\begin{aligned}&\langle \mu_1\ddot{x}, x^*-x-\mu_1\ddot{x}-\beta_1\dot{x}\rangle + \langle \beta_1\dot{x}, x^*-x-\mu_1\ddot{x}-\beta_1\dot{x}\rangle + \langle \overline{x}-x, x+\mu_1\ddot{x}+\beta_1\dot{x}-\overline{x}\rangle \\ &\quad +\alpha\langle F(\overline{x}), x^*-\overline{x}\rangle + \alpha\langle \mathcal{J}g(\overline{x})^T\overline{u}, x^*-\overline{x}\rangle + (\alpha C)^2\|\overline{x}-x\|^2 \ge 0,\end{aligned} \tag{28}$$

where $C = |F| + C_0|\mathcal{J}|$.

Since g is convex, we transform the above inequality by using inequality (14) as follows:

$$\begin{aligned}&\langle \mu_1\ddot{x}, x^* - x - \mu_1\ddot{x} - \beta_1\dot{x}\rangle + \langle \beta_1\dot{x}, x^* - x - \mu_1\ddot{x} - \beta_1\dot{x}\rangle + \langle \overline{x} - x, x + \mu_1\ddot{x} + \beta_1\dot{x} - \overline{x}\rangle \\ &\quad + \alpha\langle F(\overline{x}), x^* - \overline{x}\rangle + \alpha\langle \overline{u}, g(x^*) - g(\overline{x})\rangle + (\alpha C)^2\|\overline{x} - x\|^2 \geq 0.\end{aligned} \tag{29}$$

Letting $y = \overline{x}$ in the first inequality of (14), we have

$$\alpha\langle F(x^*), \overline{x} - x^*\rangle + \alpha\langle u^*, g(\overline{x}) - g(x^*)\rangle \geq 0. \tag{30}$$

Adding the above inequality into (29), we have

$$\begin{aligned}&\langle \mu_1\ddot{x}, x^* - x - \mu_1\ddot{x} - \beta_1\dot{x}\rangle + \langle \beta_1\dot{x}, x^* - x - \mu_1\ddot{x} - \beta_1\dot{x}\rangle + \langle \overline{x} - x, x + \mu_1\ddot{x} + \beta_1\dot{x} - \overline{x}\rangle \\ &\quad + \alpha\langle F(\overline{x}) - F(x^*), x^* - \overline{x}\rangle + \alpha\langle \overline{u} - u^*, g(x^*) - g(\overline{x})\rangle + (\alpha C)^2\|\overline{x} - x\|^2 \geq 0\end{aligned} \tag{31}$$

Setting $v = u^*$ in the variational inequality (19) and $v = u + \mu_2\ddot{u} + \beta_2\dot{u}$ in the variational inequality (21), we deduce that

$$\begin{aligned}&\langle \mu_2\ddot{u} + \beta_2\dot{u}, u^* - u - \mu_2\ddot{u} - \beta_2\dot{u}\rangle - \alpha\langle g(\overline{x}), u^* - u - \mu_2\ddot{u} - \beta_2\dot{u}\rangle \geq 0, \\ &\langle \overline{u} - u, u + \mu_2\ddot{u} + \beta_2\dot{u} - \overline{u}\rangle + \alpha\langle g(\overline{x}) - g(x), u + \mu_2\ddot{u} + \beta_2\dot{u} - \overline{u}\rangle - \alpha\langle g(\overline{x}), u + \mu_2\ddot{u} + \beta_2\dot{u} - \overline{u}\rangle \geq 0.\end{aligned} \tag{32}$$

Summing the above two inequalities and taking into account (22), we obtain

$$\langle \mu_2\ddot{u} + \beta_2\dot{u}, u^* - u - \mu_2\ddot{u} - \beta_2\dot{u}\rangle + \langle \overline{u} - u, u + \mu_2\ddot{u} + \beta_2\dot{u} - \overline{u}\rangle - \alpha\langle g(\overline{x}), u^* - \overline{u}\rangle + (\alpha|g|)^2\|\overline{x} - x\|^2 \geq 0. \tag{33}$$

In view of $\langle \overline{u}, g(x^*)\rangle \leq 0$ and $\langle u^*, g(x^*)\rangle = 0$, we conclude that

$$\begin{aligned}&\langle \mu_2\ddot{u} + \beta_2\dot{u}, u^* - u - \mu_2\ddot{u} - \beta_2\dot{u}\rangle + \langle \overline{u} - u, u + \mu_2\ddot{u} + \beta_2\dot{u} - \overline{u}\rangle \\ &\quad + \alpha\langle g(x^*) - g(\overline{x}), u^* - \overline{u}\rangle + (\alpha|g|)^2\|\overline{x} - x\|^2 \geq 0.\end{aligned} \tag{34}$$

Since F is monotone, we sum (31) and (34) to obtain

$$\begin{aligned}&\langle \mu_1\ddot{x}, x^* - x - \mu_1\ddot{x} - \beta_1\dot{x}\rangle + \langle \beta_1\dot{x}, x^* - x - \mu_1\ddot{x} - \beta_1\dot{x}\rangle \\ &\quad + \langle \overline{x} - x, x + \mu_1\ddot{x} + \beta_1\dot{x} - \overline{x}\rangle + \langle \mu_2\ddot{u}, u^* - u - \mu_2\ddot{u} - \beta_2\dot{u}\rangle + \langle \beta_2\dot{u}, u^* - u - \mu_2\ddot{u} - \beta_2\dot{u}\rangle \\ &\quad + \langle \overline{u} - u, \mu_2\ddot{u} + \beta_2\dot{u} + u - \overline{u}\rangle + \alpha^2\left(C^2 + |g|^2\right)\|\overline{x} - x\|^2 \geq 0.\end{aligned} \tag{35}$$

The above inequality yields that

$$\mu_1\langle \ddot{x}, x - x^* \rangle + \mu_1^2\|\ddot{x}\|^2 + \mu_1\beta_1\langle \ddot{x}, \dot{x}\rangle + \beta_1\langle \dot{x}, x - x^* \rangle + \mu_1\beta_1\langle \dot{x}, \ddot{x}\rangle + \beta_1^2\|\dot{x}\|^2$$
$$-\langle \overline{x} - x, x + \mu_1\ddot{x} + \beta_1\dot{x} - \overline{x}\rangle + \mu_2^2\|\ddot{u}\|^2 + \mu_2\langle \ddot{u}, u - u^* \rangle + \mu_2\beta_2\langle \ddot{u}, \dot{u}\rangle + \beta_2\langle \dot{u}, u - u^* \rangle$$
$$+\mu_2\beta_2\langle \dot{u}, \ddot{u}\rangle + \beta_2^2\|\dot{u}\|^2 - \langle \overline{u} - u, u + \mu_2\ddot{u} + \beta_2\dot{u} - \overline{u}\rangle - \alpha^2\left(C^2 + |g|^2\right)\|\overline{x} - x\|^2 \le 0. \tag{36}$$

Using the relations

$$\langle \overline{x} - x, x + \mu_1\ddot{x} + \beta_1\dot{x} - \overline{x}\rangle = \frac{1}{2}\left\|\mu_1\ddot{x} + \beta_1\dot{x}\right\|^2 - \frac{1}{2}\|\overline{x} - x\|^2 - \frac{1}{2}\left\|x + \mu_1\ddot{x} + \beta_1\dot{x} - \overline{x}\right\|^2,$$
$$\langle \overline{u} - u, u + \mu_2\ddot{u} + \beta_2\dot{u} - \overline{u}\rangle = \frac{1}{2}\left\|\mu_2\ddot{u} + \beta_2\dot{u}\right\|^2 - \frac{1}{2}\|\overline{u} - u\|^2 - \frac{1}{2}\left\|u + \mu_2\ddot{u} + \beta_2\dot{u} - \overline{u}\right\|^2,$$
$$\frac{1}{2}\left\|\mu_1\ddot{x} + \beta_1\dot{x}\right\|^2 = \frac{1}{2}\mu_1^2\|\ddot{x}\|^2 + \mu_1\beta_1\langle \ddot{x}, \dot{x}\rangle + \frac{1}{2}\beta_1^2\|\dot{x}\|^2,$$
$$\frac{1}{2}\left\|\mu_2\ddot{u} + \beta_2\dot{u}\right\|^2 = \frac{1}{2}\mu_2^2\|\ddot{u}\|^2 + \mu_2\beta_2\langle \ddot{u}, \dot{u}\rangle + \frac{1}{2}\beta_2^2\|\dot{u}\|^2, \tag{37}$$

inequality (35) can be transformed into the following:

$$\mu_1\langle \ddot{x}, x - x^* \rangle + \frac{\beta_1^2}{2}\|\dot{x}\|^2 + \beta_1\langle \dot{x}, x - x^* \rangle + \frac{\mu_1^2}{2}\|\ddot{x}\|^2 + \mu_1\beta_1\langle \dot{x}, \ddot{x}\rangle$$
$$+\mu_2\langle \ddot{u}, u - u^* \rangle + \frac{\beta_2^2}{2}\|\dot{u}\|^2 + \beta_2\langle \dot{u}, u - u^* \rangle + \mu_2\beta_2\langle \dot{u}, \ddot{u}\rangle + \frac{\mu_2^2}{2}\|\ddot{u}\|^2$$
$$+\frac{1}{2}\|\overline{u} - u\|^2 + \left(\frac{1}{2} - \alpha^2\left(C^2 + |g|^2\right)\right)\|\overline{x} - x\|^2 \le 0. \tag{38}$$

According to the relations

$$\frac{1}{2}\frac{d^2}{dt^2}\left\|x - x^*\right\|^2 = \|\dot{x}\|^2 + \langle x - x^*, \ddot{x}\rangle,$$
$$\frac{1}{2}\frac{d}{dt}\|\dot{x}\|^2 = \langle \dot{x}, \ddot{x}\rangle,$$
$$\frac{1}{2}\frac{d}{dt}\left\|x - x^*\right\|^2 = \langle \dot{x}, x - x^*\rangle,$$
$$\frac{1}{2}\frac{d^2}{dt^2}\left\|u - u^*\right\|^2 = \|\dot{u}\|^2 + \langle u - u^*, \ddot{u}\rangle, \tag{39}$$
$$\frac{1}{2}\frac{d}{dt}\|\dot{u}\|^2 = \langle \dot{u}, \ddot{u}\rangle,$$
$$\frac{1}{2}\frac{d}{dt}\left\|u - u^*\right\|^2 = \langle \dot{u}, u - u^*\rangle,$$

inequality (38) means that

$$\begin{aligned}&\frac{\mu_1}{2}\frac{\mathrm{d}^2}{\mathrm{d}t^2}\left\|x-x^*\right\|^2+\left(\frac{\beta_1^2}{2}-\mu_1\right)\|\dot{x}\|^2+\frac{\beta_1}{2}\frac{\mathrm{d}}{\mathrm{d}t}\left\|x-x^*\right\|^2+\frac{\mu_1^2}{2}\|\ddot{x}\|^2\\&+\frac{\mu_1\beta_1}{2}\frac{\mathrm{d}}{\mathrm{d}t}\|\dot{x}\|^2+\frac{\mu_2}{2}\frac{\mathrm{d}^2}{\mathrm{d}t^2}\left\|u-u^*\right\|^2+\left(\frac{\beta_2^2}{2}-\mu_2\right)\|\dot{u}\|^2+\frac{\beta_2}{2}\frac{\mathrm{d}}{\mathrm{d}t}\left\|u-u^*\right\|^2\\&+\frac{\mu_2^2}{2}\|\ddot{u}\|^2+\frac{\mu_2\beta_2}{2}\frac{\mathrm{d}}{\mathrm{d}t}\|\dot{u}\|^2+\frac{1}{2}\|u-\overline{u}\|^2+\left(\frac{1}{2}-\alpha^2\left(C^2+|g|^2\right)\right)\|\overline{x}-x\|^2\le 0.\end{aligned}\tag{40}$$

Let $\phi(x)=(1/2)\|x-x^*\|^2$ and $\psi(u)=(1/2)\|u-u^*\|^2$; inequality (40) yields that

$$\begin{aligned}&\mu_1\frac{\mathrm{d}^2}{\mathrm{d}t^2}\phi(x)+\beta_1\frac{\mathrm{d}}{\mathrm{d}t}\phi(x)+\left(\frac{\beta_1^2}{2}-\mu_1\right)\|\dot{x}\|^2+\frac{\mu_1^2}{2}\|\ddot{x}\|^2+\frac{\mu_1\beta_1}{2}\frac{\mathrm{d}}{\mathrm{d}t}\|\dot{x}\|^2\\&+\mu_2\frac{\mathrm{d}^2}{\mathrm{d}t^2}\psi(u)+\beta_2\frac{\mathrm{d}}{\mathrm{d}t}\psi(u)+\left(\frac{\beta_2^2}{2}-\mu_2\right)\|\dot{u}\|^2+\frac{\mu_2^2}{2}\|\ddot{u}\|^2+\frac{\mu_2\beta_2}{2}\frac{\mathrm{d}}{\mathrm{d}t}\|\dot{u}\|^2+\frac{1}{2}\|u-\overline{u}\|^2+\left(\frac{1}{2}-\alpha^2\left(C^2+|g|^2\right)\right)\|\overline{x}-x\|^2\le 0.\end{aligned}\tag{41}$$

Since $\mu_1<(1/2)\beta_1^2$, $\mu_2<(1/2)\beta_2^2$, and $\alpha^2(C^2+|g|^2)<(1/2)$, inequality (41) can be integrated from t_0 to t:

$$\begin{aligned}&\mu_1\frac{\mathrm{d}}{\mathrm{d}t}\phi(x)+\beta_1\phi(x)+\left(\frac{\beta_1^2}{2}-\mu_1\right)\int_{t_0}^{t}\|\dot{x}\|^2\mathrm{d}\tau+\frac{\mu_1^2}{2}\int_{t_0}^{t}\|\ddot{x}\|^2\mathrm{d}\tau+\frac{\mu_1\beta_1}{2}\|\dot{x}\|^2\\&+\mu_2\frac{\mathrm{d}}{\mathrm{d}t}\psi(u)+\beta_2\psi(u)+\left(\frac{\beta_2^2}{2}-\mu_2\right)\int_{t_0}^{t}\|\dot{u}\|^2\mathrm{d}\tau+\frac{\mu_2^2}{2}\int_{t_0}^{t}\|\ddot{u}\|^2\mathrm{d}\tau+\frac{\mu_2\beta_2}{2}\|\dot{u}\|^2\\&+\frac{1}{2}\int_{t_0}^{t}\|\overline{u}-u\|^2\mathrm{d}\tau+\left(\frac{1}{2}-\alpha^2\left(C^2+|g|^2\right)\right)\int_{t_0}^{t}\|\overline{x}-x\|^2\mathrm{d}\tau\le B,\end{aligned}\tag{42}$$

where $B=\mu_1(\mathrm{d}/\mathrm{d}t)\phi(x_0)+\beta_1\phi(x_0)+(\mu_1\beta_1/2)\|\dot{x}_0\|^2+\mu_2(\mathrm{d}/\mathrm{d}t)\psi(u_0)+\beta_2\psi(u_0)+(\mu_2\beta_2/2)\|\dot{u}_0\|^2$.

Since $\|u(t)\|$ and $\|\dot{u}(t)\|$ are all bounded for all $t\longrightarrow\infty$, we deduce that $|(\mathrm{d}/\mathrm{d}t)\psi(u)|$ has the lower bound because

$$\left|\frac{\mathrm{d}}{\mathrm{d}t}\psi(u)\right|=\left|\langle\dot{u},u-u^*\rangle\right|\le\|\dot{u}\|\left\|u-u^*\right\|.\tag{43}$$

Thus, there exists a constant B_1 such that

$$\mu_1\frac{\mathrm{d}}{\mathrm{d}t}\phi(x)+\beta_1\phi(x)\le B_1,\tag{44}$$

which implies that

$$\mu_1\exp\left(-\frac{\beta_1}{\mu_1}t\right)\frac{\mathrm{d}}{\mathrm{d}t}\left(\exp\left(\frac{\beta_1}{\mu_1}t\right)\phi(x)\right)\le B_1.\tag{45}$$

That is,

$$\frac{\mathrm{d}}{\mathrm{d}t}\left(\exp\left(\frac{\beta_1}{\mu_1}t\right)\phi(x)\right)\le B_1\frac{1}{\mu_1}\exp\left(\frac{\beta_1}{\mu_1}t\right).\tag{46}$$

By integrating (45), we have

$$\exp\left(\frac{\beta_1}{\mu_1}t\right)\phi(x)\le\frac{B_1}{\beta_1}\exp\left(\frac{\beta_1}{\mu_1}t\right)+C_1,\tag{47}$$

where C_1 is a constant. We conclude that

$$\phi(x)\le\frac{B_1}{\beta_1}+C_1\exp\left(-\frac{\beta_1}{\mu_1}t\right),\tag{48}$$

which means that $\phi(x)$ is bounded for all $t\longrightarrow\infty$.

The function $\phi(x)$ is strongly convex, and it is well known that each of its Lebesgue sets is bounded. Thus, the trajectory $x(t)$ is bounded. That is, there exists a constant B_2 such that

$$\left\|x(t)-x^*\right\| \le B_2. \tag{49}$$

Now we claim that $\int_{t_0}^{t}\|\dot{x}\|^2 d\tau < \infty$, $\int_{t_0}^{t}\|\ddot{x}\|^2 d\tau < \infty$, $\int_{t_0}^{t}\|\dot{u}\|^2 d\tau < \infty$, $\int_{t_0}^{t}\|\ddot{u}\|^2 d\tau < \infty$, $\int_{t_0}^{t}\|\overline{u}-u\|^2 d\tau < \infty$ and $\int_{t_0}^{t}\|\overline{x}-x\|^2 d\tau < \infty$.

We firstly show that $\|\dot{x}\|$ is bounded. It follows from inequality (42) that

$$\frac{d}{dt}\phi(x) + \frac{\beta_1}{\mu_1}\phi(x) + \frac{\beta_1}{2}\|\dot{x}\|^2 \le B_3, \tag{50}$$

where B_3 is a constant. From $\phi(x) = (1/2)\|x-x^*\|^2$, the above inequality means that

$$\langle \dot{x}, x-x^*\rangle + \frac{\beta_1}{2\mu_1}\left\|x-x^*\right\|^2 + \frac{\beta_1}{2}\|\dot{x}\|^2 \le B_3. \tag{51}$$

In the light of $\langle \dot{x}, x-x^*\rangle = -(1/2)\|\dot{x}\|^2 - (1/2)\|x-x^*\|^2 + (1/2)\|\dot{x}+x-x^*\|^2$, the above inequality infers that

$$\frac{1}{2}\left(\frac{\beta_1}{\mu_1}-1\right)\left\|x-x^*\right\|^2 + \frac{1}{2}(\beta_1-1)\|\dot{x}\|^2 \le B_3. \tag{52}$$

Noting that $1 < \beta_1 < \mu_1$, we conclude that $\|\dot{x}\|^2$ is bounded in the following:

$$\frac{1}{2}(\beta_1-1)\|\dot{x}\|^2 \le B_3 + \frac{1}{2}\left(1-\frac{\beta_1}{\mu_1}\right)\left\|x-x^*\right\|^2 \le B_3 + \frac{1}{2}\left(1-\frac{\beta_1}{\mu_1}\right)B_2, \tag{53}$$

which means that $\|\dot{x}\|^2$ is bounded. It follows, from

$$\left|\frac{d}{dt}\phi(x)\right| = \left|\langle \dot{x}, x-x^*\rangle\right| \le \|\dot{x}\|\left\|x-x^*\right\|, \tag{54}$$

that $(d/dt)\phi(x)$ also has lower bound. Thus, there exists a constant B_5 such that

$$\begin{aligned}&\left(\frac{\beta_1^2}{2}-\mu_1\right)\int_{t_0}^{t}\|\dot{x}\|^2 d\tau + \frac{\mu_1^2}{2}\int_{t_0}^{t}\|\ddot{x}\|^2 d\tau + \left(\frac{\beta_2^2}{2}-\mu_2\right)\int_{t_0}^{t}\|\dot{u}\|^2 d\tau + \frac{\mu_2^2}{2}\int_{t_0}^{t}\|\ddot{u}\|^2 d\tau \\ &+\frac{1}{2}\int_{t_0}^{t}\|\overline{u}-u\|^2 d\tau + \left(\frac{1}{2}-\alpha^2\left(C^2+|g|^2\right)\right)\int_{t_0}^{t}\|\overline{x}-x\|^2 d\tau \le B_5,\end{aligned} \tag{55}$$

which yields that the integrals,

$$\begin{aligned}&\int_{t_0}^{t}\|\dot{x}\|^2 d\tau < \infty, \int_{t_0}^{t}\|\ddot{x}\|^2 d\tau < \infty, \int_{t_0}^{t}\|\dot{u}\|^2 d\tau < \infty, \int_{t_0}^{t}\|\ddot{u}\|^2 d\tau < \infty, \\ &\int_{t_0}^{t}\|\overline{u}-u\|^2 d\tau < \infty, \int_{t_0}^{t}\|\overline{x}-x\|^2 d\tau < \infty,\end{aligned} \tag{56}$$

converge as $t \longrightarrow \infty$.

Assuming that there exists $\varepsilon > 0$ such that $\|\ddot{x}(t)\| \ge \varepsilon$, $\|\ddot{u}(t)\| \ge \varepsilon$, $\|\dot{x}(t)\| \ge \varepsilon$, $\|\dot{u}(t)\| \ge \varepsilon$, $\|\overline{u}(t)-u(t)\| \ge \varepsilon$, and $\|\overline{x}(t)-x(t)\| \ge \varepsilon$ for all $t \ge t_0$, we obtain a contradiction to the convergence of integrals. Hence, there exists a subsequence of time moments $t_i \longrightarrow \infty$ such that $\|\ddot{x}(t_i)\| \longrightarrow 0$, $\|\dot{x}(t_i)\| \longrightarrow 0$, $\|\ddot{u}(t_i)\| \longrightarrow 0$, $\|\dot{x}(t_i)\| \longrightarrow 0$, $\|\overline{u}(t_i)-u(t_i)\| \longrightarrow 0$, and $\|\overline{x}(t_i)-x(t_i)\| \longrightarrow 0$. Since $x(t)$ and $u(t)$ are bounded, we know that $x(t_i)$ and $u(t_i)$ are bounded. We choose the subsequences $x(t_{i_j})$ and $u(t_{i_j})$ of $x(t)$ and $u(t)$. Then there exist x' and u' such that $x(t_{i_j}) \longrightarrow x', u(t_{i_j}) \longrightarrow u'$, $\|\ddot{x}(t_{i_j})\| \longrightarrow 0$, $\|\dot{x}(t_{i_j})\| \longrightarrow 0$, $\|\ddot{u}(t_{i_j})\| \longrightarrow 0$, $\|\dot{u}(t_{i_j})\| \longrightarrow 0$, $\|\overline{u}(t_{i_j})-u(t_{i_j})\| \longrightarrow 0$, and $\|\overline{x}(t_{i_j})-x(t_{i_j})\| \longrightarrow 0$ as $j \longrightarrow \infty$.

Let us consider inequality (16) for all t_{i_j} and take the limit as $j \longrightarrow \infty$; we have

$$\begin{aligned}x' &= \Pi_{\Omega}\left(x' - \alpha\left(F(x') + \mathcal{J}g(x')^T u'\right)\right), \\ u' &= \Pi_{+}\left(u' + \alpha g(x')\right),\end{aligned} \tag{57}$$

which means that $x' \in \Omega^*$ is a solution of variational inequality with constraints (1) by using Lemma 2. This completes the proof. □

4. Numerical Results

In this section, we test the example with three kinds of different cases by our differential equation system (16). The

transient behaviors of the proposed differential equation systems are demonstrated in each case. The numerical implementation is coded by Matlab R2019a running on a PC with Intel i5 9400F of 2.9 GHz CPU and the ordinary differential equation solver adopted is ode45, which uses a Runge-Kutta (4, 5) formula.

Example 1. Consider the variational inequality with constraints problem with F: $\Re^5 \longrightarrow \Re^5$ given by $F(x) = Mx + \rho C(x) + q$ and $K = \left\{x \in \Re_+^5 | g(x) = 10 - \sum_{i=1}^5 x_i \leq 0\right\}$, where M is an asymmetric positive definite matrix and $C_i(x) = \arctan(x_i - 2)$, $i = 1, 2, \ldots, 5$. The parameter ρ is used to vary the degree of asymmetry and nonlinearity, and the data of the example are illustrated as follows:

$$M = \begin{pmatrix} 0.726 & -0.949 & 0.266 & -1.193 & -0.504 \\ 1.645 & 0.678 & 0.333 & -0.217 & -1.443 \\ -1.016 & -0.225 & 0.769 & 0.934 & 1.007 \\ 1.063 & 0.567 & -1.144 & 0.550 & -0.548 \\ -0.259 & 1.453 & -1.073 & 0.509 & 1.026 \end{pmatrix}, \quad (58)$$

and $q = (5.308, 0.008, -0.938, 1.024, -1.312)^T$, which have been considered in the work of Dang et al. [35]. Its solution is $x^* = (2, 2, 2, 2, 2)^T$.

Since the parameter ρ is used to vary the degree of asymmetry and nonlinearity, we apply the second-order differential equation system (16) to solve the variational inequalities in three cases of $\rho < 1$, $\rho = 1$, and $\rho > 1$.

Case 1. When $\rho < 1$, we take $\rho = 0.1$, which means that the degree of asymmetry of $F(x)$ is higher than that of the nonlinearity of $F(x)$. In this experiment, we set $\mu_1 = \mu_2 = 2.02$, $\beta_1 = \beta_2 = 2.01$, and $\alpha = 0.5$ in the second-order differential equation system with the controlled process (16). Figure 1 describes the convergence behaviors of $x(t)$, $u(t)$, $\dot{x}(t)$, and $\dot{x}(t)$ of the second-order differential equation system with the controlled process (16) from the given initial points for the example with $\rho = 0.1$.

Case 2. We take $\rho = 1$, which means that the degree of asymmetry of $F(x)$ is the same as the degree of the nonlinearity of $F(x)$. In this experiment, we let $\mu_1 = \mu_2 = 2.02$, $\beta_1 = \beta_2 = 2.01$, and $\alpha = 0.4$ in the second-order differential equation system with the controlled process (16). The solution trajectories $x(t)$, $u(t)$, $\dot{x}(t)$, and $\dot{x}(t)$ of the second-order differential equation system with the controlled process (16) from the given initial points for the example with $\rho = 1$ are shown in Figure 2.

Case 3. When $\rho > 1$, we take $\rho = 10$, which means that the degree of asymmetry of $F(x)$ is lower than that of the nonlinearity of $F(x)$. In this experiment, we set $\mu_1 = \mu_2 = 2.02$, $\beta_1 = \beta_2 = 2.01$, and $\alpha = 0.06$ in the second-order differential equation system with the controlled process (16). Figure 3 describes the convergence behaviors of $x(t)$, $u(t)$, $\dot{x}(t)$, and $\dot{u}(t)$ of the second-order differential equation system with the controlled process (16) from the given initial points for the example with $\rho = 10$.

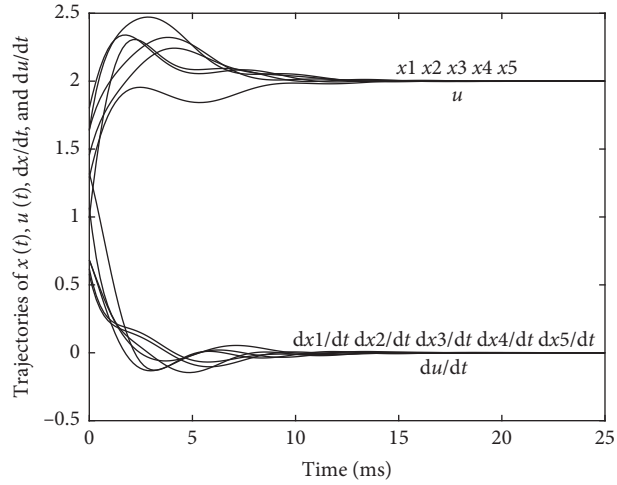

Figure 1: Transient behavior of $x(t)$ and $u(t)$ of the second-order differential equation system (16) in the example with $\rho = 0.1$.

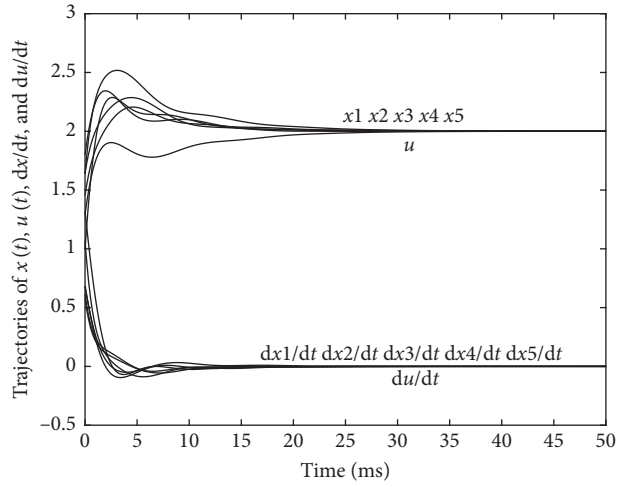

Figure 2: Transient behavior of $x(t)$ and $u(t)$ of the second-order differential equation system (16) in the example with $\rho = 1$.

Remark 2. In Theorem 1, the conditions of the parameters $\mu_1, \beta_1, \mu_2, \beta_2$, and α with $1 < \beta_1 < \mu_1 < (1/2)\beta_1^2$, $0 < \mu_2 < (1/2)\beta_2^2$, and $\alpha^2((|F| + C_0|\mathcal{F}|)^2 + |g|^2) < (1/2)$ are sufficient but not necessary for the convergence of the trajectory of the second-order differential equation system with the controlled process (16) for solving the variational inequality with constraints problem (1). The following lists are given to illustrate the influence on the rate of convergence of trajectory of the second-order differential equation system with the controlled process (16) for solving the variational inequality with constraints problem in the above example. From the condition with $1 < \beta_1 < \mu_1 < (1/2)\beta_1^2$, we have that $2 < \beta_1 < \mu_1$. Hence, we give a discussion in the following and take the first case as an example; that is, $\rho = 0.1$ in our example.

Fixing $\mu_2 = 2.02, \beta_2 = 2.01$, and $\alpha = 0.5$, the convergence time will be changed as follows when μ_1 and β_1 are changed (Table 1). In this experiment, when μ_2, β_2, and α were fixed, we found that the smaller μ_1 and β_1 are, the shorter the

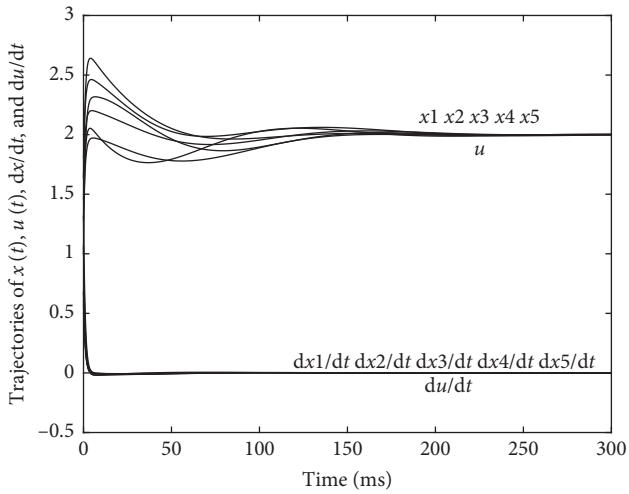

Figure 3: Transient behavior of $x(t)$ and $u(t)$ of the second-order differential equation system (16) in the example with $\rho = 10$.

Table 1: Convergence time of $x(t)$ by the second-order differential equation system (16).

μ_1	β_1	Time (ms)	$x(t)$
2.02	2.01	18.3691	$(2.0000, 2.0000, 2.0000, 2.0000, 2.0000)^T$
2.12	2.11	22.0502	$(2.0000, 2.0000, 2.0000, 2.0000, 2.0000)^T$
2.22	2.21	22.5589	$(2.0000, 2.0000, 2.0000, 2.0000, 2.0000)^T$
2.32	2.31	23.2263	$(2.0000, 2.0000, 2.0000, 2.0000, 2.0000)^T$
2.42	2.41	23.5676	$(2.0000, 2.0000, 2.0000, 2.0000, 2.0000)^T$

Table 2: Convergence time of $x(t)$ by the second-order differential equation system (16).

μ_2	β_2	Time (ms)	$x(t)$
2.02	2.01	18.3691	$(2.0000, 2.0000, 2.0000, 2.0000, 2.0000)^T$
2.12	2.11	18.4430	$(2.0000, 2.0000, 2.0000, 2.0000, 2.0000)^T$
2.22	2.21	21.7473	$(2.0000, 2.0000, 2.0000, 2.0000, 2.0000)^T$
2.32	2.31	21.7503	$(2.0000, 2.0000, 2.0000, 2.0000, 2.0000)^T$
2.42	2.41	21.9388	$(2.0000, 2.0000, 2.0000, 2.0000, 2.0000)^T$

Table 3: Convergence time of $x(t)$ by the second-order differential equation system (16).

α	Time (ms)	$x(t)$
0.2	74.4480	$(2.0000, 2.0000, 2.0000, 2.0000, 2.0000)^T$
0.3	40.5888	$(2.0000, 2.0000, 2.0000, 2.0000, 2.0000)^T$
0.4	23.4882	$(2.0000, 2.0000, 2.0000, 2.0000, 2.0000)^T$
0.5	18.3691	$(2.0000, 2.0000, 2.0000, 2.0000, 2.0000)^T$
0.55	39.5863	$(2.0000, 2.0000, 2.0000, 2.0000, 2.0000)^T$

convergence time is. Furthermore, we also found that the change of β_1 had a great influence on the rate of the convergence when μ_1 is fixed; meanwhile the change of μ_1 has a little effect on the rate of the convergence when β_1 is fixed.

Fixing $\mu_1 = 2.02, \beta_1 = 2.01$, and $\alpha = 0.5$, the convergence time will be changed as follows when μ_2 and β_2 are changed (Table 2). In this experiment, when μ_1, β_1, and α were fixed, we found that the smaller μ_2 and β_2 are, the shorter the convergence time is. Furthermore, we also found that the change of β_2 had a great influence on the rate of the convergence when μ_2 is fixed; meanwhile the change of μ_2 has a little effect on the rate of the convergence when β_2 is fixed.

Fixing $\mu_1 = 2.02, \beta_1 = 2.01, \mu_2 = 2.02$, and $\beta_2 = 2.01$, the convergence time will be changed as follows when α is changed (Table 3). In this experiment, when μ_1, β_1, μ_2, and β_2 were fixed, we found that the convergence time is the shortest at about $\alpha = 0.5$.

5. Conclusions

In this paper, based on the Lagrange function and projection operator, the second-order differential equation system with the controlled process is established for solving the variational inequality with constraints problem (1). The convergence of the trajectories for this kind of differential equation system is proved. Furthermore, we test one example with three kinds of different cases by the second-order differential equation system with the controlled process and illustrate the transient behaviors of the trajectories for this differential equation system in each case, which verify the effectiveness of the second-order differential equation system with the controlled process for solving the variational inequality with constraints.

It is an interesting issue that the second-order differential equation systems are used to solve the optimization problems.

Data Availability

The data used to support the findings of this study are available from the corresponding author upon reasonable request.

Disclosure

Some of the results in this paper were presented at the Proceeding of the 11th World Congress on Intelligent Control and Automation, 2014 (see https://ieeexplore.ieee.org/document/7052904).

Conflicts of Interest

The authors declare that they have no conflicts of interest.

Acknowledgments

The research was supported by the National Natural Science Foundation of China under Project no. 11801381.

References

[1] F. Facchinei and J.-S. Pang, *Finite-Dimensional Variational Inequalities and Complementarity Problems*, Springer-Verlag Inc, New York, NY, USA, 2003.

[2] K. J. Arrow and L. Hurwicz, "Reduction of constrained maxima to saddle point problems," in *Proceedings of the 3rd Berkeley Symposium on Mathematical Statistics and Probability*, J. Neyman, Ed., pp. 1–26, University of California Press, Berkeley, CA, USA, 1956.

[3] A. V. Fiacco and G. P. McCormick, *Nonlinear Programming: Sequential Unconstrained Minimization Techniques*, John Wiley, New York, NY, USA, 1968.

[4] Y. G. Evtushenko, "Two numerical methods of solving nonlinear programming problems," *Soviet Mathematics Doklady*, vol. 15, pp. 420–423, 1974.

[5] H. Yamashita, "A differential equation approach to nonlinear programming," *Mathmatical Programming*, vol. 18, pp. 115–168, 1980.

[6] Y. G. Evtushenko, *Numerical Optimization Techniques*, Optimization Software, Inc. Publication Division, New York, NY, USA, 1985.

[7] Y. G. Evtushenko and V. G. Zhadan, "Barrier-projective methods for nonlinear programming," *Computational Mathematics and Mathematical Physics*, vol. 34, pp. 579–590, 1994.

[8] Y. G. Evtushenko and V. G. Zhadan, "Stable barrier-projection and barrier-Newton methods in nonlinear programming," *Optimization Methods and Software*, vol. 3, no. 1–3, pp. 237–256, 1994.

[9] Y. G. Evtushenko and V. G. Zhadan, "Stable barrier-projection and barrier-Newton methods for linear and nonlinear programming," in *Algorithms for Continuous Optimization*, E. Spedicato, Ed., Kluwer Academic Publishers, Berlin, Germany, pp. 255–285, 1994.

[10] Y. G. Evtushenko and V. G. Zhadan, "Space-transformation technique: the state of the art," *Nonlinear Optimization and Applications*, vol. 320, pp. 101–123, 1996.

[11] P. Q. Pan, "New ODE methods for equality constrained optimization (1)-equations," *Journal of Computational Mathematics*, vol. 10, pp. 77–92, 1992.

[12] A. A. Brown and M. C. Bartholomew-Biggs, "ODE versus SQP methods for constrained optimization, the hatfield polytechnic optimization center," Technical report No. 179, Hatfield Polytechnic, England, UK, 1987.

[13] A. A. Brown and M. C. Bartholomew-Biggs, "ODE versus SQP methods for constrained optimization," *Journal of Optimization Theory and Applications*, vol. 62, no. 3, pp. 371–386, 1989.

[14] S. Zhang and A. G. Constantinides, "Lagrange programming neural networks," *IEEE Transactions on Circuits and Systems II: Analog and Digital Signal Processing*, vol. 39, no. 7, pp. 441–452, 1992.

[15] L. Zhou, Y. Wu, L. Zhang, and G. Zhang, "Convergence analysis of a differential equation approach for solving nonlinear programming problems," *Applied Mathematics and Computation*, vol. 184, no. 2, pp. 789–797, 2007.

[16] L. Jin, L.-W. Zhang, and X.-T. Xiao, "Two differential equation systems for equality-constrained optimization," *Applied Mathematics and Computation*, vol. 190, no. 2, pp. 1030–1039, 2007.

[17] L. Jin, H. Y. Huang, and H. Huang, "Differential equation method based on approximate augmented Lagrangian for nonlinear programming," *Journal of Industrial & Management Optimization*, vol. 16, no. 5, pp. 2267–2281, 2020.

[18] L. F. Zhang, "Based on differential equation method for solving quadratic programming modelling," *WIT Transactions on Modelling and Simulation*, vol. 60, pp. 259–267, 2014.

[19] L. M. Zhou, L. W. Zhang, and S. X. He, "A differential equation approach to solving nonlinear complementarity problems," *OR Transactions*, vol. 9, no. 3, pp. 8–16, 2005.

[20] X.-B. Gao, L.-Z. Liao, and L. Qi, "A novel neural network for variational inequalities with linear and nonlinear constraints," *IEEE Transactions on Neural Networks*, vol. 16, no. 6, pp. 1305–1317, 2005.

[21] B. He and H. Yang, "A neural network model for monotone linear asymmetric variational inequalities," *IEEE Transactions on Neural Networks*, vol. 11, no. 1, pp. 3–16, 2000.

[22] L.-Z. Liao, H. Qi, and L. Qi, "Solving nonlinear complementarity problems with neural networks: a reformulation method approach," *Journal of Computational and Applied Mathematics*, vol. 131, no. 1-2, pp. 343–359, 2001.

[23] A. Nazemi and A. Sabeghi, "A novel gradient-based neural network for solving convex second-order cone constrained variational inequality problems," *Journal of Computational and Applied Mathematics*, vol. 347, pp. 343–356, 2019.

[24] A. Nazemi and A. Sabeghi, "A new neural network framework for solving convex second-order cone constrained variational inequality problems with an application in multi-finger robot hands," *Journal of Experimental & Theoretical Artificial Intelligence*, vol. 32, no. 2, pp. 181–203, 2020.

[25] A. S. Antipin, "Controlled proximal differential systems for saddle problems," *Differential Equations*, vol. 28, no. 11, pp. 1498–1510, 1992.

[26] A. S. Antipin, "On differential prediction-type gradient methods for computing fixed points of extremel mappings," *Differential Equations*, vol. 31, no. 11, pp. 1754–1763, 1995.

[27] A. S. Antipin, "Feedback-controlled saddle gradient processes," *Automation and Remote Control*, vol. 55, no. 3, pp. 311–320, 2003.

[28] A. S. Antipin, "Minimization of convex functions on convex sets by means of differential equations," *Differential Equations*, vol. 30, no. 9, pp. 1365–1375, 1994.

[29] A. S. Antipin, "On finite convergence of processes to a sharp minimimum and to a smooth minimium with a sharp derivative," *Differential Equations*, vol. 30, no. 11, pp. 1703–1713, 1994.

[30] A. S. Antipin, "From optim to equilibria, dynamics of nonhomogeneous systems," *Proceedings Fo ISA*, vol. 3, pp. 35–64, 2000.

[31] A. S. Antipin, "Solving variational inequalities with coupling constraints with the use of differential equations," *Differential Equations*, vol. 36, no. 11, pp. 1587–1596, 2000.

[32] A. Antipin, "Differential equations for equilibrium problems with coupled constraints," *Nonlinear Analysis: Theory, Methods & Applications*, vol. 47, no. 3, pp. 1833–1844, 2001.

[33] L. Wang and S. Wang, "The differential equation method for variational inequality with constraints," *ICIC Express Letters*, vol. 9, no. 10, pp. 2787–2794, 2015.

[34] U. Mosco, "Implicit variational problems and quasi variational inequalities," *Lecture Notes in Mathematics*, Springer-Verlag, vol. 543, pp. 83–156, , Berlin, Germany, 1976.

[35] C. Dang, Y. Leung, X.-b. Gao, and K.-z. Chen, "Neural networks for nonlinear and mixed complementarity problems and their applications," *Neural Networks*, vol. 17, no. 2, pp. 271–283, 2004.

Hindawi
Complexity
Volume 2021, Article ID 1155443, 11 pages
https://doi.org/10.1155/2021/1155443

Research Article

Studying the Effect of Stray Capacitance on the Measurement Accuracy of the CVT Based on the Boundary Element Method

Chuan Xiang[1], **Xinwei Chen**[2], **Hongge Zhao**[1], **Zejun Ren**[1] and **Guoqing Zhao**[3]

[1]*College of Marine Electrical Engineering, Dalian Maritime University, Dalian 116026, China*
[2]*State Grid Shandong Electric Power Company, Jinan 250001, China*
[3]*Dalian North Instrument Transformer Group Co., Ltd., Dalian 116200, China*

Correspondence should be addressed to Chuan Xiang; cxiang@dlmu.edu.cn

Received 17 April 2021; Accepted 18 May 2021; Published 31 May 2021

Academic Editor: Xiaoqing Bai

The capacitive voltage transformer (CVT) is a special measuring and protecting device, which is commonly applied in high-voltage power systems. Its measurement accuracy is affected seriously by the stray capacitances of the capacitance voltage divider (CVD) to ground and other charged parts. In this study, based on the boundary element method, a mathematical model was established firstly to calculate the stray capacitance. Then, the voltage distribution of the CVD was obtained by the CVD's equivalent circuit model. Next, the effect of stray capacitance on the voltage distribution and the voltage difference ratio (VDR) of CVD was analysed in detail. We finally designed three types of shield and optimized their structure parameters to reduce VDR. The results indicated that the average deviation rate between calculated and experimental measured voltages is only 0.015%; that is to say, the method has high calculation precision. The stray capacitance of the CVD to ground is far larger than that of the CVD to the high-voltage terminal. It results in the inhomogeneous distribution of voltage and the increase of VDR. For the test CVT, its VDR exceeds the requirement of class 0.2. Among all of the three types of shield, the C type reduced the VDR of the test CVT the most. After optimizing the structure parameters of C-type shield, the VDR is further reduced to 0.08%. It is not only in accord with the requirement of class 0.2 but also has an adequate margin.

1. Introduction

The Capacitor Voltage Transformer (CVT) has high dielectric strength, fast transient response, wide dynamic range, low power consumption, and nonferromagnetic resonance with power systems. It also can reduce the head steepness of lightning shock and be used as a coupling capacitor for the power carrier communication [1–4]. Thus, it is widely applied in power systems from 35 to 1000 kV. Especially, in the high voltage of 110 kV and above, its market share is over 90%. The measurement accuracy of CVT is one of the key parameters for ensuring the safe and stable operation of the power system. The IEC-60044-5:2004 standard defines the measurement accuracy classes of a single-phase CVT are 0.2, 0.5, 1.0, and 3.0 [5]. It means that, for the highest class 0.2, the measurement accuracy of CVT, which is generally equivalent to the voltage difference ratio (VDR), must be below 0.2%. Stray capacitance affects the performance of high-voltage devices seriously, such as voltage dividers, insulator strings, modular power supplies, and measuring instruments [6]. Thus, it must be considered in the design of high-voltage devices. The stray capacitances of the CVT to ground and other charged parts play an important role in causing the VDR of the CVT [7]. Especially for the CVT applied in the ultra-high-voltage level, the effect of stray capacitance on its VDR is more serious [8]. For instance, the VDR of CVT which applied in the 750 kV power system caused by the stray capacitor is larger than 0.2% [9]. It exceeds the requirement of class 0.2. Therefore, it is urgent to study the influence of stray capacitance on the VDR of CVT and explore solutions to reduce the adverse effect of stray capacitance, so as to ensure the safe and stable operation of the power system.

In recent years, various works have already been carried out for studying the effect of stray capacitance on the electric performance of a high-voltage device. The stray capacitor and the impulse voltage distributions of the HVDC converter valve are calculated by the field-circuit coupling method [10]. The difference between the calculated and experimental voltages is less than 0.1%. Some researchers study the influence of stray capacitance on the voltage distribution of the insulator string [11–13]. The results show that stray capacitance caused the inhomogenous distribution of insulator string voltage. The electric stress on the insulator close to the power line is obviously higher than that close to the tower. A grading ring [14] and metal electrodes [15] can homogenize the voltage distribution effectively. The stray capacitance can also affect the voltage distribution of breaks for the multibreak vacuum circuit breaker [16, 17]. For a three-break circuit breaker, the partial voltage of high-voltage break exceeds 60% due to the effect of stray capacitance of the low-voltage break to ground. It may result in the breaking failure for the short current. Paralleling capacitances across breaks can improve the uniformity of break voltage distribution effectively. The effects of the stray capacitor on the performance of a high-voltage arrestor are studied in [18–20]. JLi et al. [18] calculated the stray capacitance, total leakage current, resistive leakage current, and phase angle difference of arresters by the finite-element method. The interphase interference from stray capacitance can be eliminated by the iterative algorithm based on the resistance-capacitance network model. He et al. [20] analysed the electric potential distribution of the 1000 kV MOV based on an idea of field-circuit combination, i.e., the 3D finite-element method and circuit-analytic method. The nonuniform coefficient of potential distribution can be reduced to within ±5% by installing the grading ring and parallel capacitors.

But, up to now, there are few studies about the effect of stray capacitance on the CVT. For the CVT applied in the 750 kV voltage level and above, the stray capacitance of the CVT to the high-voltage terminal increases the VDR of the CVT more than 0.1% [21]. Installation of a grading ring for a new UHV equipotential shielding CVT can improve the voltage distribution and compensate for the adverse effect caused by stray capacitance [3]. Furthermore, the rated bulk capacitances of this UHV CVT are derived under the interference of stray capacitances [7]. They are much less than those of the traditional CVT without a grading ring for the same accuracy class. The research results can reduce the manufacturing difficulty and cost. The measurement precision of the CVT is affected by stray capacitance and temperature [22]. It can be reduced to 0.1% by choosing large bulk capacitances and resistances with low temperature coefficient. The influence of stray capacitance on the VDR of the CVT is analysed by the field-circuit coupling method with the assumption of the homogenous distribution of stray capacitance [2, 23]. However, the distribution of stray capacitance is inhomogenous in fact. The abovementioned analysis results are not accurate. Reference [24] reviews the calculation methods of the stray capacitance of the CVT, but due to the complex structure of the CVT, it is a failure to solve the stray capacitance by the surface charge method.

Although great progress has been made for the research of the CVT, it is still hard to analyse the effect of stray capacitance on the VDR of the CVT accurately and quantitatively due to the complex configuration of the CVT [25], the difficulty in the experimental measurement of stray capacitance directly [26], and the variation of stray capacitance with the installation location of the CVT [27].

The purpose of this paper is to present a new calculation method of stray capacitance and further analyse the effect of stray capacitance on the VDR of the CVT. In this context, a model based on the boundary element method (BEM) is established to calculate the stray capacitance of the capacitance voltage divider (CVD). The voltage distribution of the CVD is obtained by the equivalent circuit model of the CVD. The reliability of the method is confirmed by comparing the calculated voltage with experimental measured results. Then, the effect of stray capacitance on the VDR of the CVT is analysed. Finally, the structure and parameters of the shield are optimized to further reduce the VDR of the CVT. The research results can contribute to design the high-precision CVT more efficiently.

2. Structure and Operation Principle of the CVT

Currently, the most widely applied of CVT in the power system has a column structure as shown in Figure 1. It consists of two parts: a capacitance voltage divider (CVD) and electromagnetic unit (EMU).

The CVD is mainly composed of a high-voltage capacitor, a medium-voltage capacitor, an external metal expander, and a porcelain insulator. Both of the high- and medium-voltage capacitors consist of dozens or hundreds of capacitance units in series. Each capacitance unit is made of aluminum foil and insulating film which are stacked together and immersed in insulating oil [28–32]. The CVD converts a primary high voltage into a medium voltage ranging from 10~25 kV as the input voltage of the EMU. The EMU is made up of a compensation reactor, a medium-voltage transformer, and a damper. It is used to convert the medium voltage, i.e., the output voltage of the CVD, into a standard secondary voltage as the inputs of power meters and relay protection devices.

In general, the total VDR of the CVT depends on the CVD, EMU, the temperature shift, power frequency variation, and proximity effects. Among them, it is believed that the CVD and EMU are the main factors [7]. The EMU is poured in an aluminum alloy box as a whole, so it is hardly affected by the external electromagnetic interference (EMI). However, the CVD does not have any electromagnetic shield. It is easily affected by EMI. Therefore, in this paper, it is reasonable to ignore the EMU and only take the effect of the CVD on the VDR of the CVT into account. The VDR of the CVD is assumed to be approximately equal to that of the CVT. Besides, the VDR of the CVD depends mainly on the bulk capacitance, the stray capacitance of the CVD to ground and the high-voltage terminal [33–36]. Thus, in order to analyze of the effect of stray capacitance on the VDR of the CVD, it is necessary to calculate the stray capacitance of the CVD accurately first.

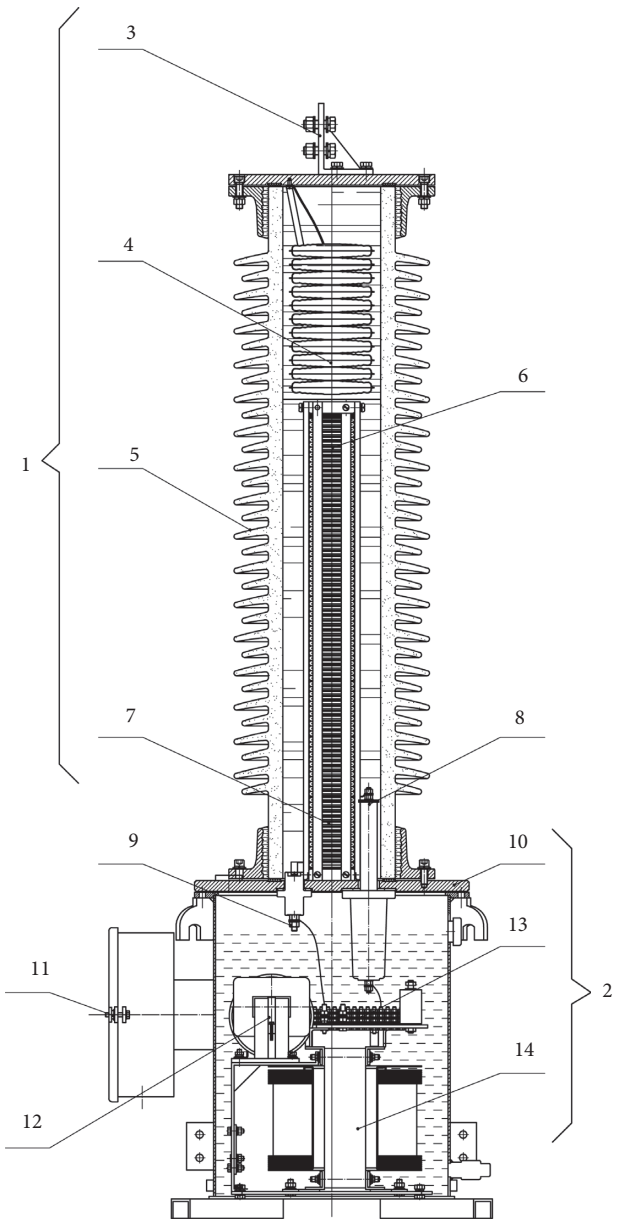

Figure 1: Column CVT structure. 1- CVD, 2- EMU, 3- high-voltage terminal, 4- metal expander, 5- porcelain insulator, 6- high-voltage capacitor, 7- medium-voltage capacitor, 8- medium-voltage tap, 9- low-voltage terminal, 10- EMU box, 11- secondary terminal box, 12- compensation reactor, 13- damper, and 14- medium-voltage transformer.

3. Calculation of Stray Capacitance and Voltage Distribution

3.1. Calculation of Stray Capacitance Based on the BEM. Firstly, the CVD is divided into n capacitance units. Then, the electric potential and the quantity of surface charges on unit i are set as φ_i and Q_i, $i = 1, 2, 3, \ldots, n$, respectively. The low-voltage terminal of the CVD is usually connected to ground directly or via a drain coil with negligible impedance at rated frequency. So, it is assumed as the reference ground with 0 V electric potential. The surface charge, electric potential, and capacitance of all units satisfied the following relationship:

$$\begin{bmatrix} Q_1 \\ Q_2 \\ \vdots \\ Q_n \end{bmatrix} = \begin{bmatrix} C_{11} & -C_{12} & \cdots & -C_{1n} \\ -C_{21} & C_{22} & \cdots & -C_{2n} \\ \vdots & \vdots & \vdots & \vdots \\ -C_{n1} & -C_{n2} & \cdots & -C_{nn} \end{bmatrix} \begin{bmatrix} \varphi_1 \\ \varphi_2 \\ \vdots \\ \varphi_n \end{bmatrix}. \tag{1}$$

The abbreviation of equation (1) is $Q = C\Phi$, where Q and Φ are the column vectors of surface charge and electric potential of all units, respectively. C is the capacitance coefficient matrix of the CVD. The off-diagonal element C_{ij} or C_{ji} ($i, j = 1, \ldots n$, and $i \neq j$) is the mutual capacitance of unit i to unit j.

The diagonal element C_{ii} is the sum of the stray capacitance of unit i to ground C_{ig} and the mutual capacitances of unit i to other units. Hence,

$$C_{ig} = C_{ii} - \sum_{j-1}^{n} C_{ij} \, (i \neq j). \tag{2}$$

The absolute value of the element in the first column of matrix C, i.e., C_{i1} ($i = 2, 3, \ldots, n$, $i \neq 1$), is the stray capacitance of unit i to the high-voltage terminal.

The main calculation methods of electrostatic field are the finite-element method (FEM) and the BEM. The BEM describes the mathematical and physical problems with boundary integral equations and solves them by the discrete technique of the FEM. It has higher accuracy than the FEM [37, 38]. Hence, this article adopted the BEM to calculate the stray capacitance of the CVD.

Firstly, the electric potentials of unit i and other units were assumed to be 1 V and 0 V, respectively. From equation (1), if the total quantity of surface charges on each unit was known, the elements in column i of C can be obtained. In this case,

$$C_{ji} = Q_j, \quad j = 1, 2, \ldots, n. \tag{3}$$

Secondly, the lateral surface of all capacitance units were divided into m patches. The total charges on each unit were assumed to be scattered homogeneously on its patches. Hence, the electric potential φ_k at the center position x_k of patch k ($k = 1, 2, \ldots, m$) is as follows:

$$\varphi_k = \varphi_{kl} + \varphi_{k0}, \tag{4}$$

where φ_{k0} and φ_{kl} are the electric potentials at point x_k generated by the charges on patch k and patch l ($l = 1, 2, \ldots, m$ and $l \neq k$), respectively.

$$\varphi_{ko} = \frac{0.2821\sigma_k}{\varepsilon_0} \sqrt{A_k} = \frac{0.2821}{\varepsilon_0 \sqrt{A_k}} q_k, \tag{5}$$

where ε_0 is the vacuum permittivity, A_k is the area of patch k, and σ_k and q_k are the density and quantity of charges on patch k, respectively.

$$\phi_{kl} = \sum_{l-1,l\neq k}^{m} \frac{1}{4\pi\varepsilon_0}\int_{s_l}\frac{\sigma_l}{r_{kl}}\mathrm{d}s_l = \sum_{l-1,l\neq k}^{m} \frac{q_l}{4\pi\varepsilon_0 A_l}\int_{s_l}\frac{1}{r_{kl}}\mathrm{d}s_l = \sum_{l-1,l\neq k}^{m} P_{kl}q_l, \tag{6}$$

where r_{kl} is the distance between the center positions of patch l and patch k, A_l is the area of patch l, and σ_1 is the density of charges on patch l.

For all patches, equation (6) can be rewritten in the following matrix form:

$$pq = \varphi, \tag{7}$$

where p is a parameter matrix $(m \times m)$, q is the column vector $(m \times 1)$ of the quantity of charges on all patches, and φ is the column vector $(m \times 1)$ of the electric potential of all patches.

Then, the electric potential of all patches of unit i and that of other units was set to be 1 V and 0 V, respectively. Referring to equation (7), the charges on each patch q_k can be obtained. Next, substituting q_k into equation (3), the elements in column i of C were obtained as follows:

$$C_{ji} = Q_j = \sum_{k\in j} q_k, \quad j = 1, 2, \ldots n. \tag{8}$$

By repeating the abovementioned processes, the capacitance coefficient matrix C can be solved. Then, the stray capacitances of units to ground and the high-voltage terminal were obtained correspondingly.

3.2. Calculation of Voltage Distribution of the CVD. After obtaining the stray capacitance, the voltage distribution of the CVD was calculated in this part. Each capacitance unit was regarded as a voltage node. The electric potential of the node at the high-voltage terminal was assumed to be U_1, and the low-voltage terminal was grounded directly. Taking the stray capacitance of units to ground and the high-voltage terminal into account, the equivalent circuit of the CVD was obtained, as shown in Figure 2. Here, C_i is the capacitance of unit i, C_{ig} is the stray capacitance of unit i to ground, and C_{ih} is the stray capacitance of unit i to the high-voltage terminal, and it replaced the parameter C_{i1} in Section 3.

The node voltage equation of the CVD is as follows:

$$Y_B U = I, \tag{9}$$

where $\dot{U}$ is the node voltage column vector, $\dot{U} = [\dot{U}_1, \dot{U}_2, \ldots, \dot{U}_n]^T$. $\dot{I}$ is the current column vector, $\dot{I} = [\dot{I}_1, \dot{I}_2, \ldots, \dot{I}_n]^T$.

From Figure 2, any element $\dot{I}_i$ of $\dot{I}$ can be derived:

$$I_i = \begin{cases} I_i, & i = 1, \\ j\omega\left[(U_{i-1} - U_i)C_{i-1} + (U_1 - U_i)C_{ih}\right], & i = 2, 3 \ldots n. \end{cases} \tag{10}$$

Also, the node admittance matrix Y_B can also be derived:

$$Y_B = \begin{bmatrix} y_1 + y_{1g} + \sum_{j-2}^{n} y_{jh} & -(y_1 + y_{2h}) & -y_{3h} & -y_{nh} \\ -(y_1 + y_{2h}) & y_1 + y_2 + y_{2h} + y_{2g} & -y_{c2} & 0 \\ -y_{3h} & -y_{c2} & \ddots & -y_{n-1} \\ -y_{nh} & 0 & -y_{n-1} & y_{n-1} + y_n + y_{nh} + y_{ng} \end{bmatrix}, \tag{11}$$

where y_n is the self-admittance of unit n, $y_n = j\omega C_n$, $\omega = 100\pi$. y_{nh} is the admittance of unit n to the high-voltage terminal, $y_{nh} = j\omega C_{nh}$. y_{ng} is the admittance of unit n to ground, $y_{ng} = j\omega C_{ng}$.

Substituting equations (10) and (11) into equation (9), the column vector of node voltage $\dot{U}$ was solved, and then, the voltage distribution of the CVD was obtained correspondingly.

3.3. Method Verification. The previous two sections presented the calculation method for the stray capacitance and the voltage distribution of the CVD. Next, we verify the proposed method by comparing the calculated result with the experimentally measured result.

The experimental schematic diagram of CVT voltage measurement is shown in Figure 3. U_1, the high-power-frequency input voltage of the CVT, is generated by using a frequency series resonance device, U_i is the power grid voltage, T_1 is the excitation transformer, U is the output voltage of T_1, R is the current limiting resistor, and L_1 is the adjustable reactor. The output voltage of the CVD is measured by using the voltage transformer calibrator.

The test platform of the CVT is shown in Figure 4. The voltage transformer calibrator model is PT101 with the following parameters: the measuring accuracy is up to 0.002%, and the measuring range is 0~60 kV. The frequency series resonance device model is MEXB-108. Its main structure and electrical parameters are as follows: the input voltage of the excitation transformer is 400 V, the output voltage is 6 kV, and L_1 is an adjustable reactor with an adjustable range of 0~110 H. C_f is a series resonant capacitance with 1000 pF. The test CVT model is TYD110/0.01H. Its main structure and electrical parameters are as follows: the height of the CVD is 1.15 m, the output voltage of the CVD must be within the range of 15 kV to 25 kV to prevent damage to the insulation of the EMU, thus the adjustable position of the medium-voltage tap from ground is 0.162 m to 0.253 m (default position is 0.24 m), the average radius of

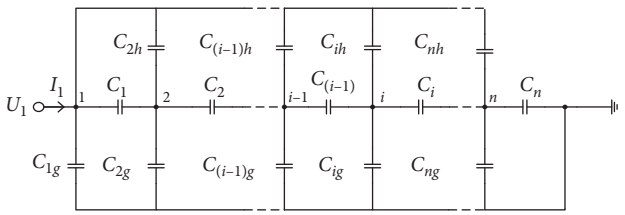

Figure 2: Equivalent circuit of the CVD.

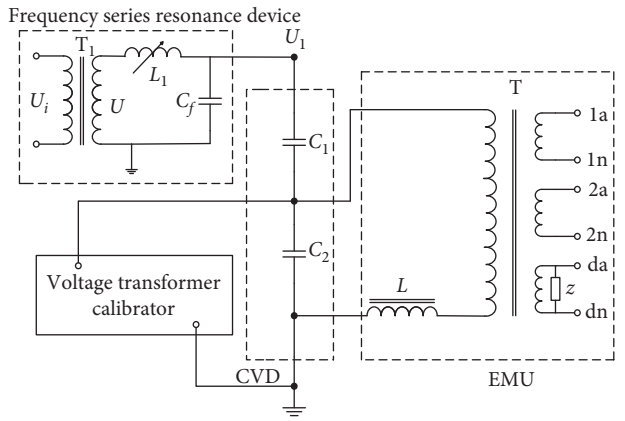

Figure 3: Schematic diagram of voltage measurement of the CVT.

the CVD is 0.30 m, the CVD is made up of 50 capacitance units in series (i.e., $n = 50$), and its total capacitance value is 10000 pF (where the high-voltage capacitor $C_1 = 12574$ pF and medium-voltage capacitor $C_2 = 48853$ pF).

When $U_1 = 110$ kV and the total number of patches of all units $m = 1000$, the voltage distribution of the test CVD is calculated and shown in Figure 5. Adjusting the position of the middle-voltage tap, the measured voltages at four different positions are also illustrated in Figure 5.

The comparison of calculated voltages, measured voltages, and their maximum deviation rates at four different positions is shown in Table 1. The measured voltage is the average value of six measurements. When the measurement number is six and the confidence probability is 0.95, the measurement uncertainty is 1.5×10^{-3} kV. As can be seen from Table 1, at the default position of the medium-voltage tap, the calculated and measured voltages are 22.459 kV and $22.461 \pm 1.5 \times 10^{-3}$ kV, respectively. The maximum voltage difference is 0.0034 kV, and the deviation rate of voltage is as low as 0.0015%. For the four selected measurement positions, the maximum deviation rate of voltage is only 0.021%, and the average deviation rate of voltage is as low as 0.015%. Therefore, the method proposed in this paper had high accuracy, and it is suitable for calculating the stray capacitance and the voltage distribution of the CVD.

4. Results and Discussion

4.1. Effect of Stray Capacitance on Voltage Distribution and VDR of the CVD. Figure 6 presents the stray capacitances of each unit to ground and the high-voltage terminal. As we can see from this, from the high-voltage terminal to ground, C_g increases rapidly from 28 pF to 123 pF and C_h decreases

Figure 4: Test platform of the CVT.

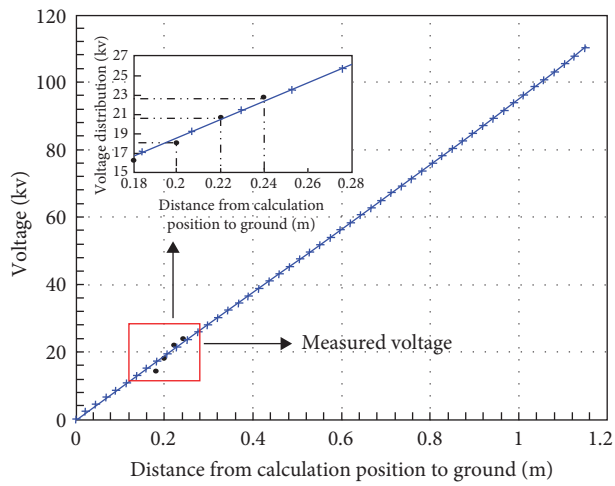

Figure 5: Voltage distribution of the test CVD.

Table 1: Comparison of calculated and measured voltages at four different medium-voltage tap positions.

Position (m)	Measured voltage (kV)	Calculated voltage (kV)	Maximum deviation rate of voltage (%)
0.18	$16.840 \pm 1.5 \times 10^{-3}$	16.842	0.021
0.20	$18.706 \pm 1.5 \times 10^{-3}$	18.707	0.013
0.22	$20.582 \pm 1.5 \times 10^{-3}$	20.581	0.012
0.24	$22.461 \pm 1.5 \times 10^{-3}$	22.459	0.015

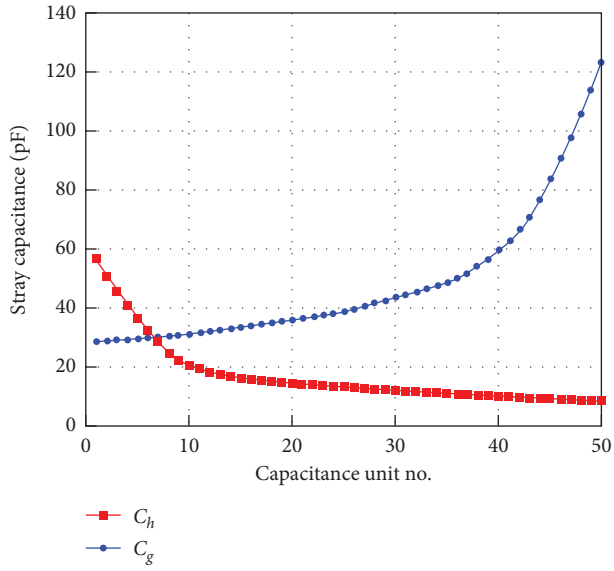

Figure 6: Distributions of C_g and C_h.

slowly from 56 pF to 8 pF. Near the low-voltage terminal, C_g is much larger than C_h. But, near the high-voltage terminal, the difference between C_g and C_h is not obvious. This may result in the inhomogeneous distribution of CVD voltage.

The voltage drop on each capacitance unit of the test CVD is illustrated in Figure 7.

As shown in Figure 7, the voltage drop on the capacitance unit of the test CVD is not uniform. From the high-voltage terminal to the low-voltage terminal, it decreases rapidly from 2.36 kV to 2.12 kV. This is mainly attributed to the large C_g near the low-voltage terminal.

The expression of VDR is as follows [2]:

$$\mathrm{VDR} = \frac{K_N U_{\mathrm{out}} - U_1}{U_1} \times 100\%, \tag{12}$$

where U_{out} is the output voltage of the CVD and k_N is the ideal partial voltage ratio of the CVD.

U_{out} can be changed by adjusting the position of the medium-voltage tap. Within the adjustable range of the medium-voltage tap (0.162 m to 0.253 m from ground), the VDR of the CVD is shown in Figure 8. As we can see, the VDR reduces linearly from 0.292% to 0.273% with the increase of the medium-voltage tap position. At the default position of the medium-voltage tap, the VDR is 0.276%. Although the VDR of the CVD can be reduced by adjusting the position of the medium-voltage tap, it is still higher than the requirement of class 0.2 which specified in the IEC-60044-5:2004 standard.

4.2. Effect of the Shield on the VDR of the CVD. As stated above, due to the effect of stray capacitance, the VDR of the test CVD exceeded the requirement of class 0.2 even adjusting the position of the medium-voltage tap. Some studies indicate that the metal shield and grading ring can compensate for the effect of stray capacitance, improve the distribution of electric field, and boost the voltage endurance and insulation strength of the high-voltage apparatus accordingly [14,15,39]. In this section, we analyze the effect of the shield on the VDR of the test CVD and optimize the structure parameters of the shield to reduce VDR further.

Three types of shield are designed for the test CVT in this study. They are A type (only one shield installed on the high-voltage terminal), B type (only one shield installed on the low-voltage terminal), and C type (two shields installed on both of the high- and low-voltage terminals), as shown in Figure 9. L and l are the lengths of the shield on the high- and low-voltage terminal, respectively. D and d are the distances from the shield on the high- and low-voltage terminal to the axis of the CVD, respectively. The default parameters of the shield are $L = 230$ mm, $D = 75$ mm, $l = 430$ mm, and $d = 100$ mm. The shields are metallic cylindrical layers made of copper, and their thickness is 2 mm.

Figure 10 illustrates the effects of the shield with default parameters on the voltage distribution and VDR of the CVD. It is shown that, for all of the CVDs with the shield, the voltage distributions are more uniform and VDR is smaller than the CVD without shield. Among the three types of

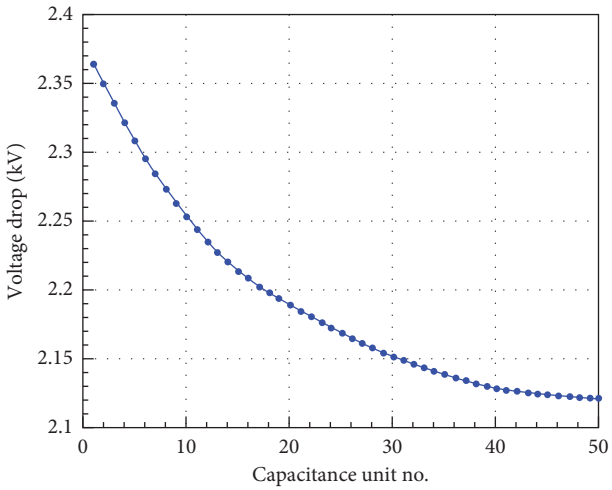

Figure 7: Voltage drop on each capacitance unit of the test CVD.

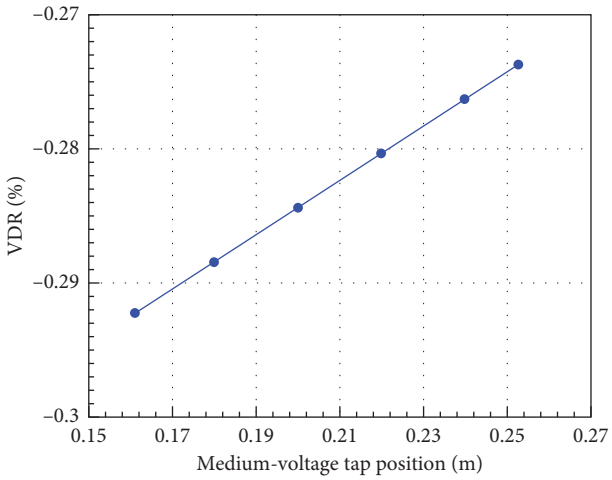

Figure 8: VDR of the CVD at different medium-voltage tap positions. The "+" and "−" before the value on the vertical axis represent the positive deviation and the negative deviation, respectively.

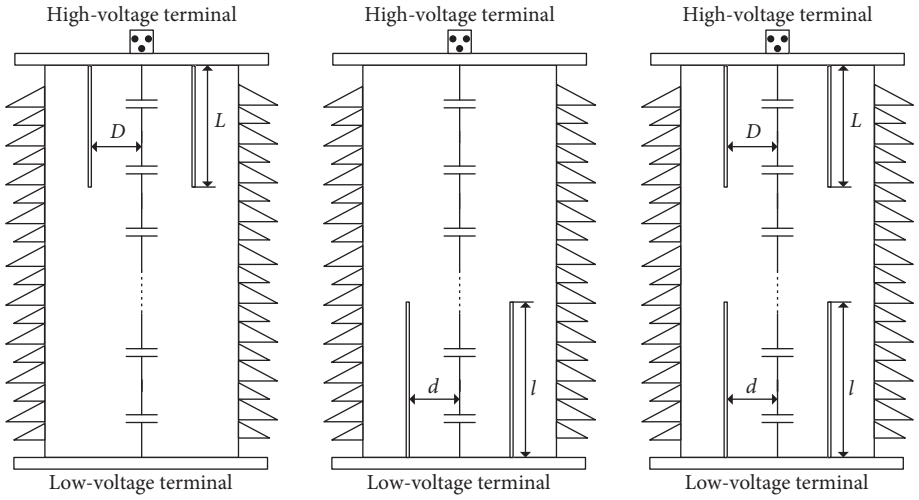

Figure 9: Three types of shield.

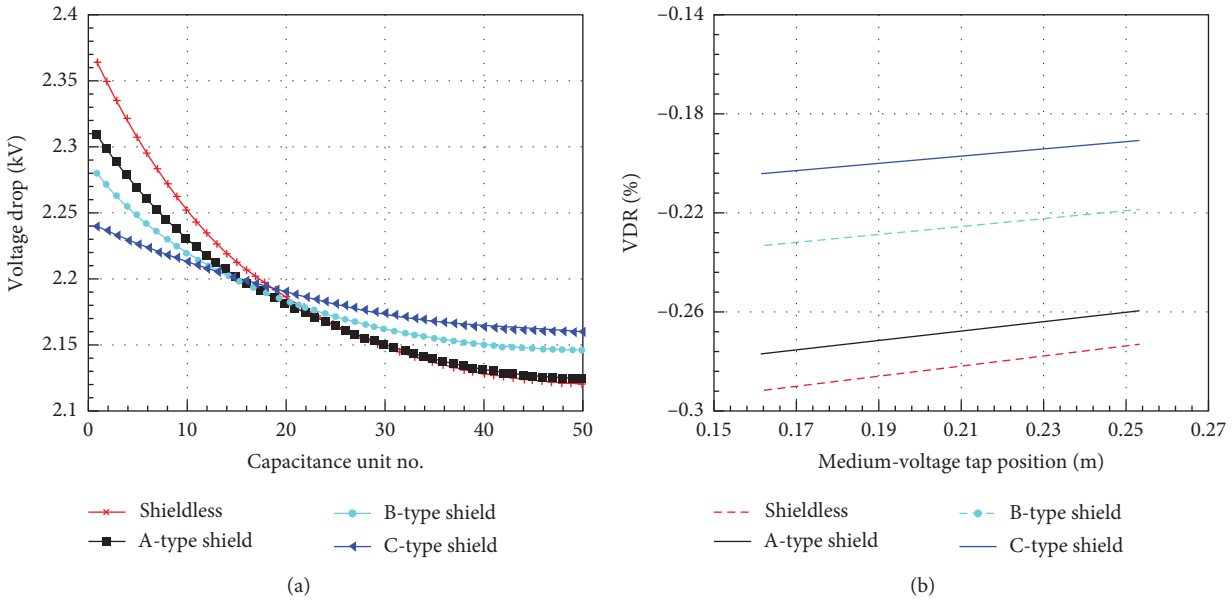

Figure 10: Effect of the shield type on the voltage drop and VDR of the CVD. (a) Voltage drop. (b) VDR.

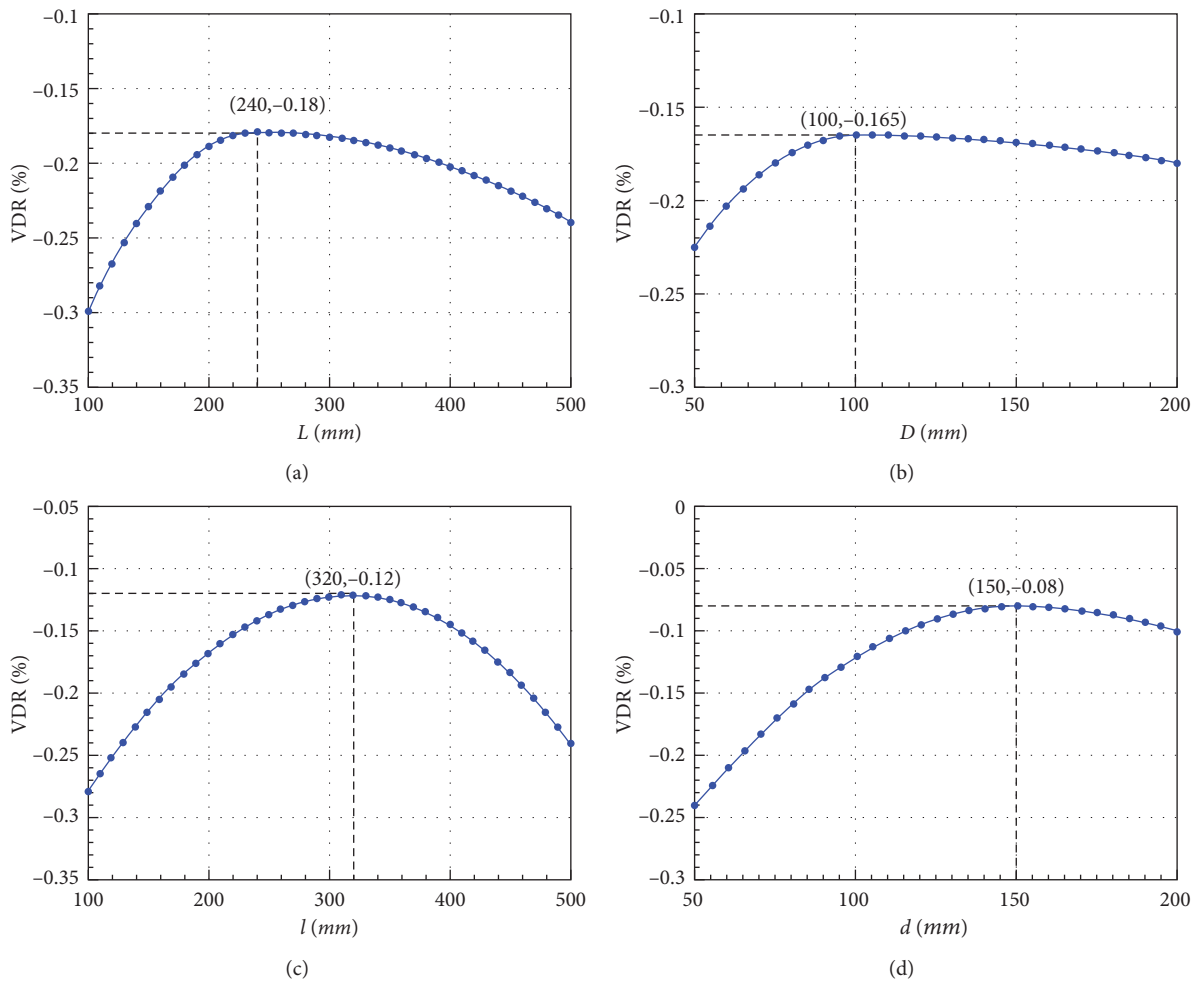

Figure 11: Effect of shield parameters on VDR. (a) L varies from 100 mm to 500 mm, $D = 75$ mm, $l = 430$ mm, and $d = 100$ mm. (b) D varies from 50 mm to 200 mm, $L = 240$ mm, $l = 430$ mm, and $d = 100$ mm. (c) l varies from 100 mm to 500 mm, $L = 240$ mm, $D = 100$ mm, and $d = 100$ mm. (d) d varies from 50 mm to 200 mm, $L = 240$ mm, $D = 100$ mm, and $l = 320$ mm.

shield, the C-type shield is the best choice. As shown in Figure 10(a), the voltage drop on the capacitance unit of the CVD with the C-type shield is the most uniform. Specifically, the maximum voltage drop reduces from 2.31 kV (A type) to 2.24 kV (C type) while the minimum voltage drop increases from 2.12 kV (A type) to 2.16 kV (C type). In addition, Figure 10(b) shows that, for the CVD with a C-type shield, its VDR is the smallest. For instance, the VDR decreases from 0.261% (A type) to 0.192% (C type) at the default position of the medium-voltage tap. As we can also see from Figure 10(b), the VDR of the CVD with a C-type shield varies from 0.204% to 0.191% within the adjusting range of the medium-voltage tap position. Moreover, the VDR is less than 0.2% within the range of 0.20 m to 0.25 m from ground. It satisfies the requirement of class 0.2. But, it does not have an adequate margin.

To reduce the VDR of the CVD further, the optimization of structure parameters of the C-type shield is performed. Due to the internal insulation requirement and technology limitations of the CVT, the adjustable ranges of L and l are limited within 100~500 mm, D and d are limited within 50~200 mm.

The minimum VDR is the optimization goal. The optimization strategy is to optimize one of the parameters L, D, l, and d in turn. During each optimization, the previous optimization results are used as default parameters, and the unoptimized parameters are defaults. The optimization results of parameters are shown in Figure 11.

As can be seen from Figure 11, all parameters L, D, l, and d affect the VDR of the CVD. But, compared with D and L, the effects of l and d are more obvious. Specifically, from Figure 11(a), when L varies from 100 mm to 500 mm, other parameters are defaults, the minimum VDR = 0.18%, and here, $L = 240$ mm. As shown in Figure 11(b), when D varies from 50 mm to 200 mm, $L = 240$ mm; meanwhile, other parameters are defaults, the minimum VDR = 0.165%, and here, $D = 100$ mm. As illustrated in Figure 11(c), when l varies from 100 mm to 500 mm, $L = 240$ mm and $D = 100$ mm; while other parameters are defaults, the minimum VDR = 0.12%, and here, $l = 320$ mm. As shown in Figure 11(d), when d varies from 50 mm to 200 mm, $L = 240$ mm, $D = 100$ mm, and $l = 320$ mm, the minimum VDR = 0.08%, and here, $d = 150$ mm.

According to the analysis mentioned above, the optimization of parameters for the C-type shield improves VDR greatly. The VDR of the CVD was reduced from about 0.2% before optimization to only 0.08% after optimization. Compared with the requirement of class 0.2 (0.2%), it has an adequate margin.

5. Conclusions and Future Work

This paper proposed a method based on the boundary element method and the equivalent circuit of the CVD to calculate the stray capacitance and voltage distribution of the CVD. Then the effect of stray capacitance on the VDR of the CVD was studied. At last, the structure and parameters of the shield were optimized to reduce the VDR of the CVT further. The following conclusions can be drawn:

(1) The proposed method has high precision. The average deviation rate between calculated voltage and experimental measured voltage was only 0.015%. It is a useful and reliable tool for the calculation of stray capacitance and the voltage distribution of the CVD.

(2) For the test CVT, although its VDR was reduced from 0.292% to 0.273% by adjusting the position of the medium-voltage tap, it still did not satisfy the requirement of class 0.2.

(3) All of the three types of shield reduced the VDR of the CVD effectively, in particular the C-type shield. After the optimization of structure parameters for the C-type shield, the VDR was reduced from about 0.2% to only 0.08%. The optimization results of shield parameters were $L = 240$ mm, $D = 100$ mm, $l = 320$ mm, and $d = 150$ mm.

The research work in this paper can be used as a reference for studying the effect of stray capacitance on the performance of the CVD and is helpful to the optimal design of a high-precision CVT. However, the measurement accuracy of the CVT is affected by numerous and complex factors, and only the key factor of stray capacitance was considered in this paper. In future, we will focus on the effects of other factors on the measurement accuracy of the CVT, such as the phase-to-phase interference, the dielectric loss of the capacitor unit, the temperature shift, and the variation of power frequency.

Data Availability

The data used to support the findings of this study are available from the corresponding author upon request.

Conflicts of Interest

The authors declare that there are no conflicts of interest regarding the publication of this paper.

Acknowledgments

This work was financially supported by the National Science Foundation of China (No. 51507025) and Fundamental Research Funds for the Central Universities (No. 3132019014).

References

[1] Q. Y. Wang, J. T. Liao, H. Li et al., "The application of voltage transformer simulator in electrical test training," in *Proceedings of the 3rd International Conference on Advances in Energy Resources and Environment Engineering ICAESEE*, Harbin, China, December 2017.

[2] Z.-h. Li and S. Zhao, "High accuracy optical voltage transformer with digital output based on coaxial capacitor voltage divider," *Transactions of the Institute of Measurement and Control*, vol. 40, no. 13, pp. 3824–3833, 2018.

[3] L. D. Xie, J. C. Zheng, Z. Q. Li et al., "Optimization of grading ring design for a new UHV equipotential shielding capacitor voltage transformer," in *Proceedings of the 2011 Annual*

Report Conference on Electrical Insulation and Dielectric Phenomena, pp. 748–751, Cancun, Mexico, October 2011.

[4] Z. H. Li, Y. Wang, Z. T. Wu, and Z. X. Li, "Research on electronic voltage transformer for big data background," *Symmetry-Basel*, vol. 10, no. 7, pp. 11–27, 2018.

[5] IEC, *IEC 60044-5 International Standard on Instrument Transformers - Part 5: Capacitor Voltage Transformers*, IEC - International Electrotechnical Commission, Geneva, Switzerland, 2004.

[6] J. R. Riba and F. Capelli, "Analysis of capacitance to ground formulas for different high-voltage electrodes," *Energies*, vol. 11, no. 5, 2018.

[7] W. Dong, K. Zha, C. Gao, F. Ji, and Z. He, "Rated capacitance determination of a new 1000 kV equipotential shielding capacitor voltage transformer under the interference of stray capacitance," *IEEE Transactions on Power Delivery*, vol. 33, no. 5, pp. 2078–2086, 2018.

[8] J. Klüss, J. Hällström, and A.-P. Elg, "Optimization of field grading for a 1000 kV wide-band voltage divider," *Journal of Electrostatics*, vol. 73, pp. 140–150, 2015.

[9] X. Wang, G. Ye, K. Guo, X. Li, and S. Wu, "Design points and test of 1000 kV column-type capacitive voltage transformer," *High Voltage Engineering*, vol. 33, no. 11, pp. 37–42, 2007.

[10] H. Guo, G. F. Tang, K. P. Zha, and X. G. Wei, "Calculation on stray capacitances and impulse voltage distribution of HVDC converter valve," *Proceedings of the Chinese Society of Electrical Engineering*, vol. 31, no. 10, pp. 116–122, 2011.

[11] E. Izgi, A. Inan, and S. Ay, "The analysis and simulation of voltage distribution over string insulators using Matlab/Simulink," *Electric power components and system*, vol. 36, no. 2, pp. 109–123, 2008.

[12] M. Ashouri, M. Mirzaie, and A. Gholami, "Calculation of voltage distribution along porcelain suspension insulators based on finite element method," *Electric Power Components and Systems*, vol. 38, no. 7, pp. 820–831, 2010.

[13] D. B. Payne and J. R. Stern, "The effect of controlling stray and disc capacitance of ceramic string insulator in the case of clean and contaminated conditions," in *Proceedings of the 2016 International Electrical Engineering Congress, iEECON 2016*, pp. 333–336, Chiang Mai, Thailand, March 2016.

[14] Q. Y. Wang, J. T. Liao, H. Li et al., "Voltage sharing characteristics of V-type suspension ceramic insulator strings for UHV AC substation," in *Proceedings of the 2015 IEEE 11th International Conference on the Properties and Applications of Dielectric Materials (ICPADM)*, pp. 580–583, Sydney, Australia, July 2015.

[15] C. Zhao, H. Mei, M. Zhu, H. Dai, L. Wang, and Z. Guan, "Influence on voltage distribution of composite insulator by inserting metal electrodes in weather sheds," *IEEE Transactions on Dielectrics and Electrical Insulation*, vol. 22, no. 3, pp. 1623–1629, 2015.

[16] D. C. Huang, G. b. Wu, and J. J. Ruan, "Study on static and dynamic voltage distribution characteristics and voltage sharing design of a 126-kV modular triple-break vacuum circuit breaker," *IEEE Transactions on Plasma Science*, vol. 43, no. 8, pp. 2694–2702, 2015.

[17] S. G. Ai, X. Yu, Y. N. Huang et al., "Voltage distribution design of a novel 363 kV vacuum circuit breaker," in *Proceedings of the 2018 IEEE International Conference on High Voltage Engineering and Application (ICHVE)*, Athens, Greece, September 2018.

[18] J. L. Li, J. J. Ruan, Z. Y. Du et al., "Analysis of interference current for high-voltage arresters based on resistance-capacitance network," in *Proceedings of the 16th IEEE Conference om Electromagnetic Field Computation CEFC*, Annecy, France, May 2014.

[19] C. A. Christodoulou, V. Vita, V. Mladenov, and L. Ekonomou, "On the computation of the voltage distribution along the non-linear resistor of gapless metal oxide surge arresters," *Energies*, vol. 11, no. 11, Article ID 3046, 2018.

[20] J. He, J. Hu, S. Gu, B. Zhang, and R. Zeng, "Analysis and improvement of potential distribution of 1000-kV ultra-high-voltage metal-oxide arrester," *IEEE Transactions on Power Delivery*, vol. 24, no. 3, pp. 1225–1233, 2009.

[21] S. P. Wu, X. X. Wu, Y. Li et al., "Study on error test technology for 1000 kV CVT under operation condition," *Power System Protection and Control*, vol. 46, no. 3, pp. 122–1247, 2018.

[22] C. T. Yang, M. W. Wu, C. W. Jian, and J. Yu, "The stray capacitance on precision of high-voltage measurement," in *Proceedings of the 2009 IEEE Instrumentation and Measurement Technology Conference*, pp. 239–244, Singapore, May 2009.

[23] H. X. Wang, G. Q. Zhang, X. G. Cai, Z. Z. Guo, and Z. Li, "Simulation on influence of external electric field on error characteristics of CVT," in *Proceedings of the 2016 IEEE International Conference on High Voltage Engineering and Application (ICHVE)*, Chengdu, China, September 2016.

[24] Z. H. Zhen, S. Zhao, W. Z. Hu, and Z. X. Li, "Review of the study of high voltage measurement technology," *High Voltage Engineering*, vol. 44, no. 12, pp. 3910–3919, 2018.

[25] J. R. Riba, F. Capelli, and M. Moreno-Eguilaz, "Analysis and mitigation of stray capacitance effects in resistive high-voltage dividers," *Energies*, vol. 12, no. 12, Article ID 2278, 2019.

[26] D. Permata and N. Nagaoka, "Modeling method of fast transient for unsymmetrical stray capacitance to ground," *IEEJ Transactions on Electrical and Electronic Engineering*, vol. 10, no. S1, pp. S28–S33, 2015.

[27] V. T. Kontargyri, I. F. Gonos, and I. A. Stathopulos, "Measurement and simulation of the electric field of high voltage suspension insulators," *European Transactions on Electrical Power*, vol. 19, no. 3, pp. 509–517, 2009.

[28] K. Wang, C. Liu, J. Sun et al., "State of charge estimation of composite energy storage systems with supercapacitors and lithium batteries," *Complexity*, vol. 2021, Article ID 8816250, 15 pages, 2021.

[29] K. Wang, W. Wang, L. Wang, and L. Li, "An improved SOC control strategy for electric vehicle hybrid energy storage systems," *Energies*, vol. 13, no. 20, p. 5297, 2020.

[30] K. Wang, F. Xiao, J. Ren, D. Changxiong, and L. Li, "State of charge (SOC) estimation of lithium-ion battery based on adaptive square root unscented kalman filter," *International Journal of Electrochemical Science*, vol. 15, no. 9, pp. 9499–9516, 2020.

[31] C. Wei, Z. Shen, D. Xiao, L. Wang, X. Bai, and H. Chen, "An optimal scheduling strategy for peer-to-peer trading in interconnected microgrids based on RO and Nash bargaining," *Applied Energy*, vol. 275, 2021.

[32] C. Wei, M. Benosman, and T. Kim, "Online parameter identification for state of power prediction of lithium-ion batteries in electric vehicles using extremum seeking," *International Journal of Control, Automation and Systems*, vol. 17, no. 11, pp. 2906–2916, Nov. 2019.

[33] M. Davarpanah, M. Sanaye-Pasand, and F. Badrkhani Ajaei, "Compensation of CVT increased error and its impacts on distance relays," *IEEE Transactions on Power Delivery*, vol. 27, no. 3, pp. 1670–1677, 2012.

[34] M. Aghaei and S. Kaboli, "On the effect of disorder on stray capacitance of transformer winding in high-voltage power

supplies," *IEEE Transactions on Industrial Electronics*, vol. 64, no. 5, pp. 3608–3618, 2017.

[35] Z. Li, Q. Li, Z. Wu, and Z. Li, "Research into an online calibration system for the errors of voltage transformers based on open-closed capacitor," *Energies*, vol. 11, no. 6, pp. 1455–1466, 2018.

[36] T. Wu, Y. Q. Zhou, Z. H. Cao, and H. H. Peng, "A new type of electronic voltage transformer and its error analysis," *Power System Technology*, vol. 34, no. 4, pp. 209–213, 2010.

[37] P. K. Banerjee and R. Butterfield, *Boundary Element Methods in Engineering Science*, McGraw-Hill, London, UK, 1981.

[38] G. Beer, I. Smith, and C. Duenser, *The Boundary Element Method with Programming: For Engineers and Scientists*, Springer Wien, New York, NY, USA, 2008.

[39] X. Q. Wu, Z. R. Peng, P. Liu, and Z. Yu, "Calculation of electric-field distribution and research on characteristics of shielding ring along the long-rod post porcelain insulators used in 1000 kV system," in *Proceedings of the 2006 IEEE 8th International Conference on Properties & applications of Dielectric Materials*, pp. 603–607, Bali, Indonesia, June 2006.

Hindawi
Complexity
Volume 2021, Article ID 4941966, 13 pages
https://doi.org/10.1155/2021/4941966

Research Article

Data-Driven Fault Diagnosis for Rolling Bearing Based on DIT-FFT and XGBoost

Chuan Xiang, Zejun Ren, Pengfei Shi, and Hongge Zhao

College of Marine Electrical Engineering, Dalian Maritime University, Dalian 116026, China

Correspondence should be addressed to Chuan Xiang; cxiang@dlmu.edu.cn

Received 17 April 2021; Accepted 18 May 2021; Published 29 May 2021

Academic Editor: Chun Wei

The rolling bearing is an extremely important basic mechanical device. The diagnosis of its fault play an important role in the safe and stable operation of the mechanical system. This study proposed an approach, based on the Fast Fourier Transform (FFT) with Decimation-In-Time (DIT) and XGBoost algorithm, to identify the fault type of bearing quickly and accurately. Firstly, the original vibration signal of rolling bearing was transformed by DIT-FFT and divided into the training set and test set. Next, the training set was used to train the fault diagnosis XGBoost model, and the test set was used to validate the well-trained XGBoost model. Finally, the proposed approach was compared with some common methods. It is demonstrated that the proposed approach is able to diagnose and identify the fault type of bearing quickly with almost 99% accuracy. It is more accurate than Machine Learning (89.88%), Ensemble Learning (93.25%), and Deep Learning (95%). This approach is suitable for the fault diagnosis of rolling bearing.

1. Introduction

Rolling bearing is an extremely important basic mechanical component of rotating machinery. It is widely used in various fields of national economy and defense due to its high efficiency, easy assembly, and lubrication [1]. The health state of rolling bearing is directly related to the performance and service life of mechanical equipment. According to an incomplete statistic, about 30% of rotating machinery faults are caused by rolling bearing [2]. Therefore, it is necessary to diagnose and identify the fault of rolling bearing timely.

Over the years, some methods and techniques have been used to monitor the health state of equipment [3–7]. For the fault diagnose of bearing, most of them are based on the analysis of the vibration signal of bearing [8–13]. Generally, most of these methods consist of two stages: data processing and fault state determination [11]. For data processing, most methods extract the fault parameters of vibration signal from the amplitude spectrum, amplitude-frequency diagram, power spectrum, or wavelet spectrum in the time domain and frequency domain and then constitute eigenvector with these parameters for signal analysis. Signal analysis methods mainly include the time domain analysis, frequency domain analysis, and time-frequency domain analysis [12, 13]. Time domain analysis approaches analyze the vibration signal as a function of time [14], such as the spike energy method [15] and the signal enveloping method [16]. Frequency domain analysis, based on the availability of the Fourier transform technology, extracts the vibration signal features more easily than the time domain analysis [16]. The Fourier transform includes short-time Fourier Transform, Fast Fourier Transform (FFT), and Discrete Fourier Transform (DFT). Among them, FFT can perform DFT on finite sequence quickly. Thus it has an excellent performance in the feature extraction of fault diagnosis [14, 17, 18]. Time-frequency domain analysis approaches combine both the time and frequency domain information to study the inner features of signal, such as the Gabor transform [19], continuous wavelet transform [20], and the Wigner–Ville distribution [21]. There are also some other signal processing methods used to construct feature sets, such as sample entropy, fuzzy entropy, and amplitude spectral entropy [11].

For fault state determination, some different Machine Learning (ML) approaches are used to construct a classifier,

for instance, traditional ML, Deep Learning (DL), and Ensemble Learning (EL). In aspect of traditional ML, Chouri et al. [8] applied SVM to automate the fault diagnosis procedure. It extracted the feature of the vibration signal of faulty bearing with Alpha-stable distribution. Bu et al. [22] proposed a method combining LS-SVM and Local Mean Decomposition (LMD) to diagnose the bearing fault. The original vibration signal was decomposed by LMD and trained to constitute the feature vectors. LS-SVM was used to determine the health state of bearing. However, the diagnosis accuracies of these traditional methods were only about 90%. In aspect of DL, Yang et al. [10] constructed a data set after extracting the features of vibration signal in the frequency domain. The data set was used to train a deep neural network (DNN) to classify the fault types. Jiang et al. [23] presented a method based on the convolutional neural network (CNN). The feature parameters of Mel-frequency cepstral coefficients and delta cepstrum were extracted to train the diagnosis model. However, parameter adjustment of these DL methods is difficult and the training time is usually very long. In aspect of EL, Hu et al. [24] proposed a method combining kernel principle component analysis with random forest (RF); a group of classifiers were trained in high dimensional kernel space with RF method. But the overfitting occurs for RF when the data has much noise. A new algorithm of EL called eXtreme Gradient Boosting (XGBoost) was proposed by Chen [25]. This method has many advantages, such as regularization, parallel processing, and missing value processing. It has excellent performance on regression and classification issues [26, 27]. Rao et al. [28] applied the XGBoost algorithm to detect anomalies of the steam turbine based on learning historical data and got a promising result.

This study is to propose an approach based on FFT with Decimation-In-Time (DIT) and XGBoost to diagnose and identify the rolling bearing faults. The experimental data is provided by the Case Western Reserve University Bearing Data Center (CWRU). The DIT-FFT is used to process vibration signal, and the XGBoost model is used as a classifier to diagnose the faults of rolling bearing.

2. Related Algorithms

2.1. DIT-FFT. FFT is a fast computation method of DFT. This section starts with an introduction of DFT. Assuming $x(n)$ is a typical N-points finite sequence, then its DFT is defined as

$$X(k) = \sum_{n=0}^{N-1} x(n) W_N^{nk}, \tag{1}$$

where k is the normalized digital frequency, $k = 0, 1, \ldots, N-1$, $W_N^{nk} = e^{-j2\pi nk/N}$. Unfolding equation (1) into the matrix form, we can obtain

$$\begin{bmatrix} X(0) \\ X(1) \\ \vdots \\ X(N-1) \end{bmatrix} = \begin{bmatrix} W_N^{0\cdot 0} \\ W_N^{1\cdot 0} \\ \vdots \\ W_N^{(N-1)\cdot 0} \\ W_N^{0\cdot 1} \\ W_N^{1\cdot 1} \\ \vdots \\ W_N^{(N-1)\cdot 1} \\ \cdots \\ \cdots \\ \vdots \\ \cdots \\ W_N^{0\cdot (N-1)} \\ W_N^{1\cdot (N-1)} \\ \vdots \\ W_N^{(N-1)\cdot (N-1)} \end{bmatrix} \begin{bmatrix} x(0) \\ x(1) \\ \vdots \\ x(N-1) \end{bmatrix}. \tag{2}$$

Its abbreviated matrix form is

$$X = Fx, \tag{3}$$

where **X** is the DFT matrix, **x** is the sequence matrix, and **F** denotes the transformation matrix. It can be seen from **F** that the computational complexity is $N \times N$ recorded as $(O(N^2))$ for a N-point DFT. It includes N^2 times multiplication and $N \times (N-1)$ times addition. Thus, it will consume a lot of computing time and memory space to process data directly by this method. This study adopted the radix-2 FFT algorithm [29] to improve computational efficiency and reduce computational complexity. In practical applications, there are many different radix-2 FFT algorithms. Among them, the radix-2 FFT algorithm with DIT (radix-2 DIT-FFT) is the most important one. Its flow diagram of the butterfly operation theorem is shown in Figure 1.

As can be seen from Figure 1, the output of the upper branch equals the sum of the inputs of the upper branch and the lower branch, that is, $X(k) = X_0(k) + W_N^k X_1(k)$. The output of the lower branch equals the difference between the inputs of the upper branch and the lower branch, that is, $X(k + (N/2)) = X_0(k) - W_N^k X_1(k)$. With the upper form, for $N = 2^l$ (l is a positive integer), the lengths of the subsequence after the first, the second, ..., and the last decompositions are 2^{l-1}, 2^{l-2}, ..., and $2^0 = 1$, respectively. Therefore, the total number of decompositions is $l = \log_2 N$. For each decomposition, the times of multiplication and addition of the corresponding butterfly operations are $N/2$ and N, respectively. Thus, the total multiplication times M_c (i.e., computational complexity) and addition times A_c are as follows:

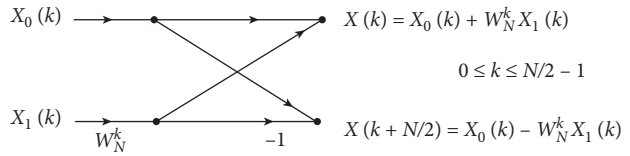

Figure 1: Flow diagram of butterfly operational theorem.

$$M_c = \frac{N}{2} l = \frac{N}{2} \log_2 N,$$
$$A_c = Nl = N \log_2 N. \tag{4}$$

The ratio of multiplications of DIT-FFT and DFT α_M (i.e., the ratio of computational complexity) and the ratio of additions α_A are

$$\alpha_M = \frac{M_c}{N^2} = \frac{(N/2)\log_2 N}{N^2} = \frac{1}{2N} \log_2 N,$$
$$\alpha_A \approx \frac{A_c}{N^2} = \frac{N \log_2 N}{N^2} = \frac{1}{N} \log_2 N. \tag{5}$$

For the radix-2, DIT-FFT and DFT algorithm with different N, α_M, and α_A were illustrated in Figure 2. As we can see from Figure 2, both of α_M and α_A decrease rapidly with the increase of N. In other words, the DIT-FFT method accelerates the calculation speed and improves the calculation efficiency obviously when N is large enough. But when N is greater than 2^{11}, α_M and α_A decrease slowly. Therefore, this paper chose $N = 2^{11}$ as the length of each group sample to reduce the computational complexity.

2.2. XGBoost. XGBoost is an algorithm of EL, which is based on Classification and Regression Tree (CART) [25]. Its objective function is defined as

$$\text{Obj}^{(t)} = \sum_{i=1}^{n} L\left(y_i, \hat{y}_i^{(t-1)} + f_t(x_i)\right) + \Omega(f_t) + \text{constant}, \tag{6}$$

where L is a differentiable convex loss function that measures the difference between the prediction $\hat{y}_i$ and the target y_i. $f_t(x_i)$ is the final score function of the sample in the t^{th} round and x_i is the i^{th} input of the sample. It can be expressed as

$$f_t(x) = \omega_{q(x)}, q: \quad R^m \longrightarrow \{1, 2, \ldots, T\}, \omega \in R^T, \tag{7}$$

where ω is the leaf vector, q is the structure of the tree, and T represents the number of leaf nodes.

The second term Ω on the right side of equation (6) penalizes the complexity of the model. It is defined as

$$\Omega(f) = \gamma T + \frac{1}{2} \lambda \left\| \omega^2 \right\|, \tag{8}$$

where λ and γ are two model parameters used to control the proportion of Ω. ω^2 represents L_2 regularization processing on ω, it can also be expressed as $\sum \omega^2$. If the value of $\Omega(f)$ is small, the complexity of the tree is low while the generalization ability is strong.

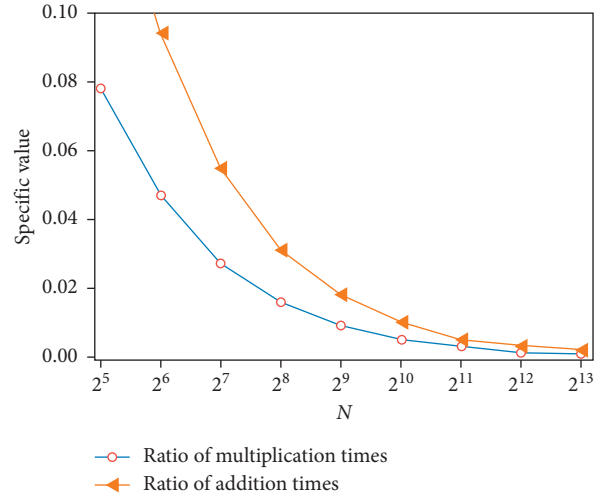

Figure 2: The variation of α_M and α_A with N.

After the second-order Taylor expansion of equation (6), a new objective function is obtained:

$$\text{Obj}^{(t)} \cong \sum_{i=1}^{n} \left[L\left(y_i, \hat{y}_i^{(t-1)}\right) + g_i f_t(x_i) + \frac{1}{2} h_i f_t^2(x_i) \right] + \Omega(f_t) + \text{constant}, \tag{9}$$

where $g_i = \partial_{\hat{y}_i^{(t-1)}} L(y_i, \hat{y}^{(t-1)})$, $h_i = \partial^2_{\hat{y}_i^{(t-1)}} L(y_i, \hat{y}^{(t-1)})$ are the first- and second-order gradient statistics on the loss function L, respectively.

The final objective function only depends on the first-order and the second-order derivative of the error of each data point. Removing the constant term and expanding $\Omega(f)$, the objective function is updated to

$$\text{Obj}^{(t)} \cong \sum_{i=1}^{n} \left[g_i \omega_{q(x_i)} + \frac{1}{2} h_i \omega_{q(x_i)}^2 \right] + \gamma T + \lambda \frac{1}{2} \sum_{j=1}^{T} \omega_j^2,$$
$$= \sum_{j=1}^{T} \left[\left(\sum_{i \in I_j} g_i \right) \omega_j + \frac{1}{2} \left(\sum_{i \in I_j} h_i + \lambda \right) \omega_j^2 \right] + \gamma T, \tag{10}$$

where $I_j = \{i | q(x_i) = j\}$ is defined as the instance set of leaf j.

For the sake of simplicity, we define $G_j = \sum_{i \in I_j} g_i$ and $H_j = \sum_{i \in I_j} h_i$; then,

$$\text{Obj}^{(t)} = \sum_{j=1}^{T} \left[G_j \omega_j + \frac{1}{2} \left(H_j + \lambda \right) \omega_j^2 \right] + \gamma T. \tag{11}$$

Next computing partial derivatives of ω_j and bringing the results back to equation (11), the following formula can be obtained:

$$\text{Obj} = -\frac{1}{2} \sum_{j=1}^{T} \frac{G_j^2}{H_j + \lambda} + \gamma T. \tag{12}$$

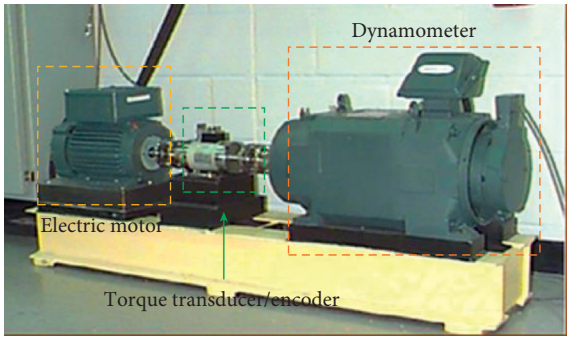

Figure 3: The test bench of SKF rolling bearing fault in CWRU.

It can be used as a scoring function to measure the quality of a tree structure q. The smaller Obj is, the well-structured the tree will be. This score is like the impurity score for evaluating decision trees, except that it is derived for a wider range of objective functions. Generally, it is impossible to enumerate all possible tree structures q. A greedy algorithm that starts from a single leaf and iteratively adds branches to the tree is used instead [25]. Let I_L and I_R be the instance sets of left and right nodes after the split, respectively. Define $I = I_L \cup I_R$, the loss reduction after the split is given by

$$L_{\text{split}} = \frac{1}{2}\left[\frac{G_L^2}{H_L + \lambda} + \frac{G_R^2}{H_R + \lambda} - \frac{G^2}{H + \lambda}\right] - \gamma. \quad (13)$$

This formula is usually used in practice for the evaluation of the split candidate node.

3. Bearing Fault Test Bench

In this paper, the proposed DIT-FFT-XGBoost method is tested by the SKF rolling bearing data sets of CWRU which are standard data for testing diagnosis methods of bearing fault. Figure 3 illustrates the bearing fault test bench of CWRU. It consists of a 2 hp electric motor, a torque transducer/encoder, a dynamometer, and the control electronics. Generally speaking, the rolling element (RE), inner race (IR), and outer race (OR) of the rolling bearing of the electric motor are easily damaged. The test bench can simulate these fault types, that is, RE fault, IR fault, and OR fault. For the OR fault, the damage positions are located at 3 o'clock, 6 o'clock, or 12 o'clock. In this test bench, there are three acceleration sensors used to record the vibration acceleration signals of the rolling bearing. They are placed on the rack with a magnetic base (BA), the bearing seat of the fan end (FE), and the drive end (DE), respectively. The vibration acceleration signals are collected by a 16-channel data recorder. The sampling frequency of FE is 12 kHz, and the fault sampling frequency of DE is 12 kHz or 48 kHz. The bearing speed is 1730, 1750, 1772, or 1797 rpm.

The test bench of CWRU has recorded huge amounts of data. This paper only chose the data of 12 k DE and 1772 rpm for fault diagnosis. There are 9 types of bearing fault and one normal state. The 9 fault types are the RE fault, IR fault, and OR fault with 0.007-, 0.014-, and 0.021-inch damage diameter, respectively. The data of OR fault is only taken from the damage position at 6 o'clock. The data used in this paper is listed in Table 1.

Table 1: Bearing data at DE under the conditions of 12 kHz and 1772 rpm

Damage diameter (inches)	Fault type	Data length
0.007	RE	121410
	IR	121991
	OR	122426
0.014	RE	122136
	IR	121846
	OR	122136
0.021	RE	121410
	IR	121991
	OR	122426
0	Normal state	483903

4. Bearing Fault Diagnosis

4.1. Fault Diagnosis Procedure. The fault diagnosis procedure of rolling bearing with the DIT-FFT-XGBoost method is shown in Figure 4. It mainly includes two stages: data processing and fault state determination. There are two steps in the data processing stage. Step 1: calculate the standard deviation and average value of input data and then standardize the data to be normal distribution to eliminate the impact of the abnormal samples on the data processing. It is suitable for complicated big data. Step 2: process the standardized data with DIT-FFT, and then divide them into the training set and test set. In the fault state determination stage, feed the training set into the XGBoost model. The XGBoost model trains the negative gradient of loss function each time to adjust its parameters. Finally, the well-trained model identifies the fault type of bearing. Analysis was performed with the Python system for computing on a laptop with Intel (R) Core (TM) i5-7200 CPU @ 2.70 GHz.

4.2. Data Processing. The original data of RE fault, IR fault, and OR fault with the 0.007-inch damage diameter collected by the recorder at DE under the conditions of 12 kHz and 1772 rpm are shown in Figure 5.

After fitting and standardizing the data of the above three fault types to be a normal distribution, the standardization results are shown in Figure 6.

Next, transform the standardization results by DIT-FFT; the absolute values of them are shown in Figure 7.

The processing results of the normal state and 9 fault types with 0.014- and 0.021-inch damage diameters are illustrated in Figures 8–14, respectively.

For each of the above figures, the waveforms from top to bottom are original data, standardization result, and transformation result, respectively. As mentioned above, $N = 2^{11} = 2048$ data length was chosen as a group sample for the radix-2 DIT-FFT algorithm in this paper. Data length is 2048 for all of the above data processing figures. According to the data lengths of the 12 k DE bearing data as listed in Table 1 and the above data length selection rule of sample, we

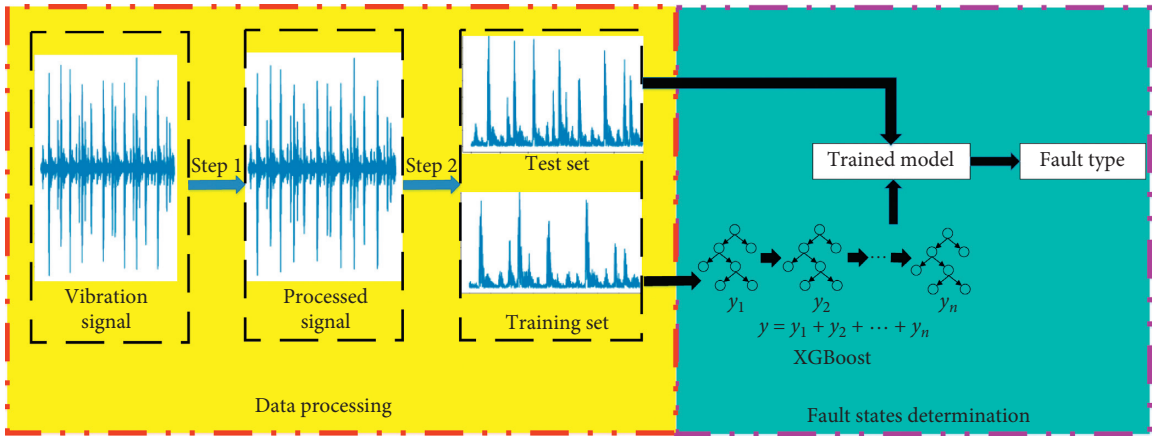

Figure 4: Diagnosis procedure of DIT-FFT-XGBoost.

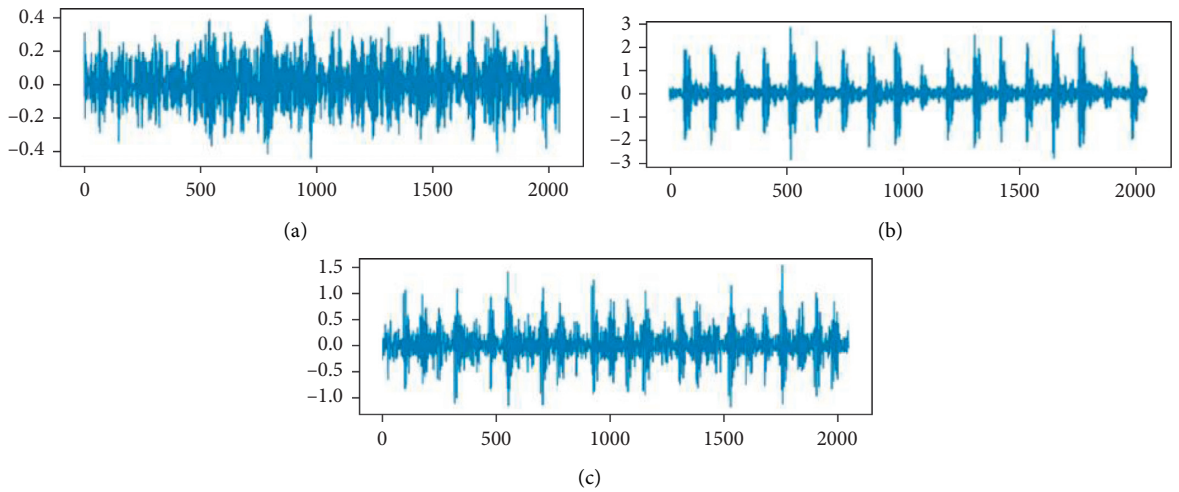

Figure 5: The original data of (a) RE fault, (b) IR fault, and (c) OR fault with 0.007-inch damage diameter.

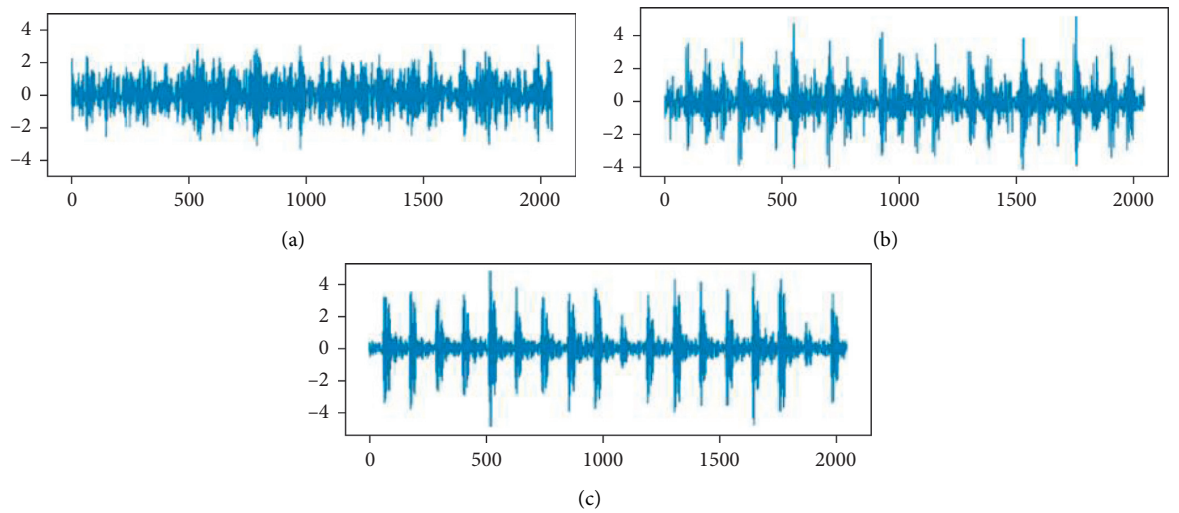

Figure 6: The standardization results of RE fault (a), IR fault (b), and OR (c) with 0.007-inch damage diameter.

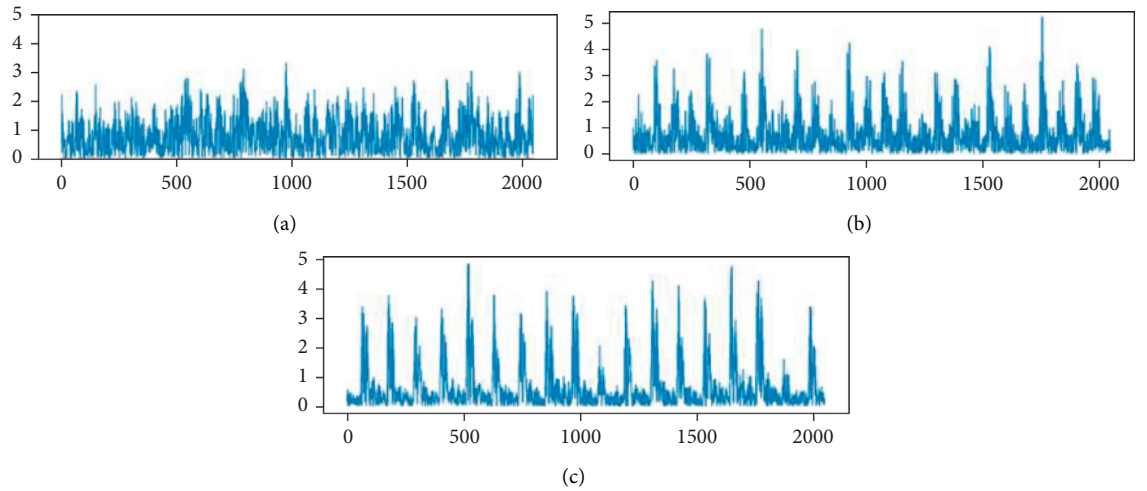

Figure 7: The transformation results of RE fault (a), IR fault (b), and OR fault (c) with 0.007-inch damage diameter.

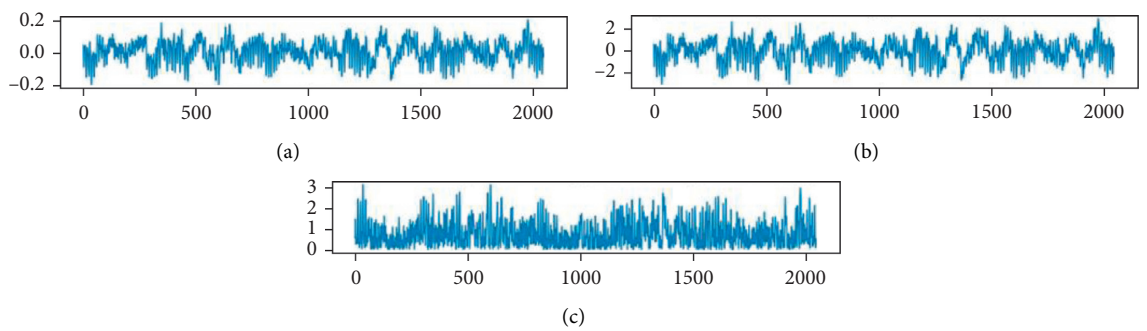

Figure 8: Normal state.

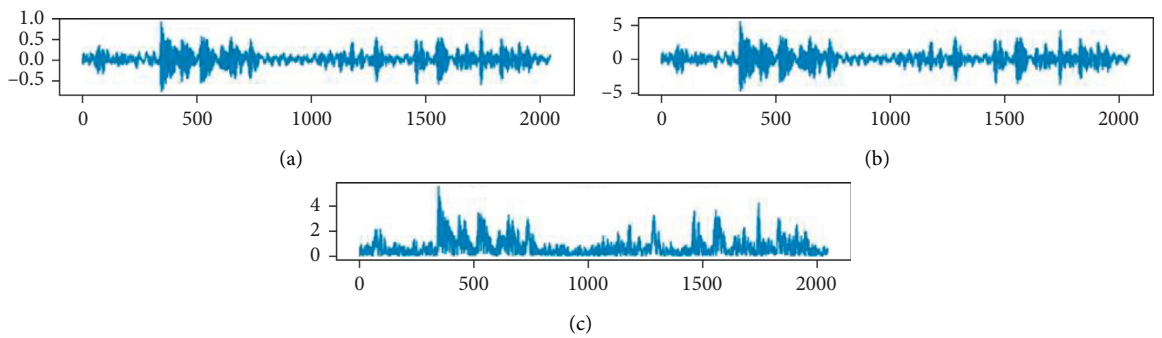

Figure 9: 0.014-inch RE fault.

constructed the training set and test set as illustrated in Table 2. For each bearing fault type and the normal state, 50 group samples were taken from original data as the training set, that is, data length of 102,400. The remaining data was used to construct the test set. Thus, there were 9 group samples as test set for each fault type (i.e., data length of 18,432), and 186 group samples as the test set for the normal state (i.e., data length of 380,928). Therefore, the training set and test set were composed of 500 and 267 group samples, respectively.

4.3. Fault State Determination. In order to make full use of the training set to improve the diagnosis accuracy of the

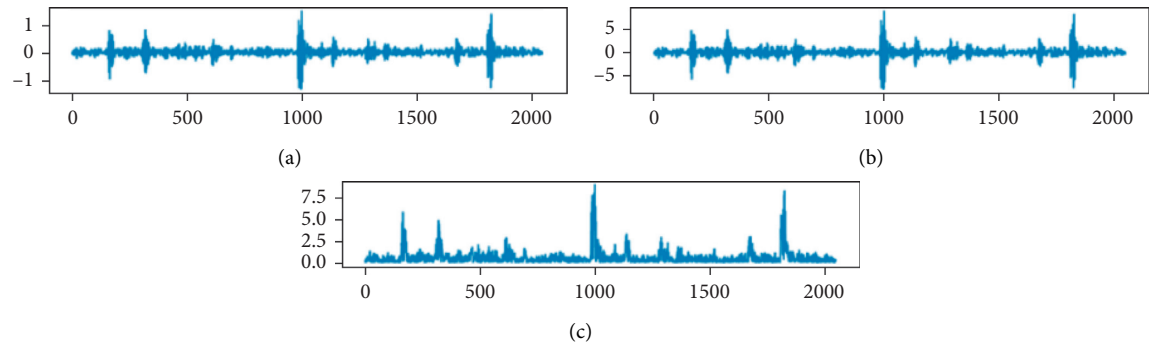

Figure 10: 0.014-inch IR fault.

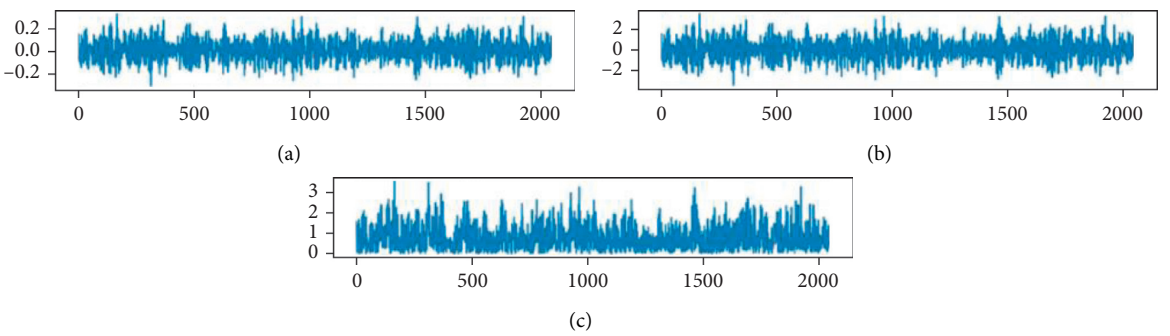

Figure 11: 0.014-inch OR fault.

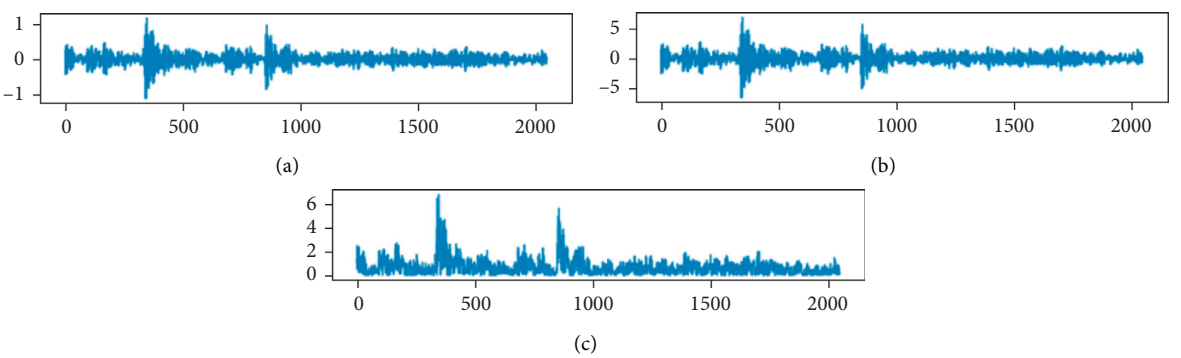

Figure 12: 0.021-inch RE fault.

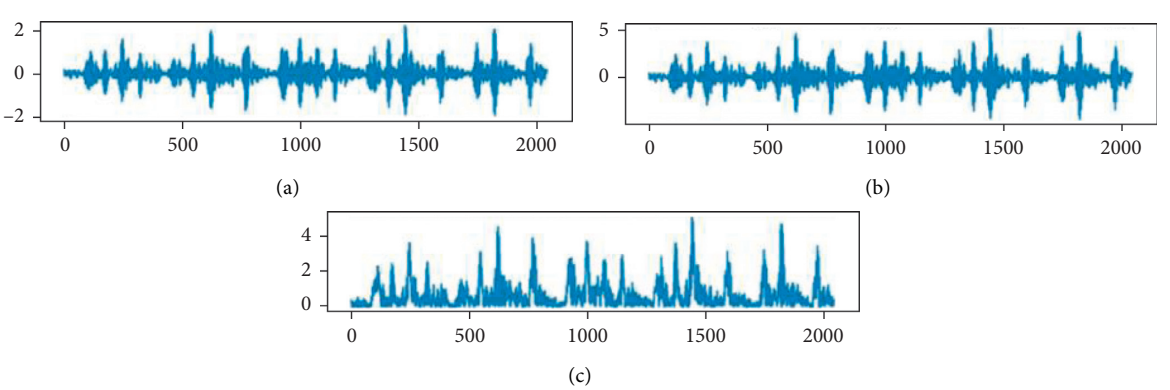

Figure 13: 0.021-inch IR fault.

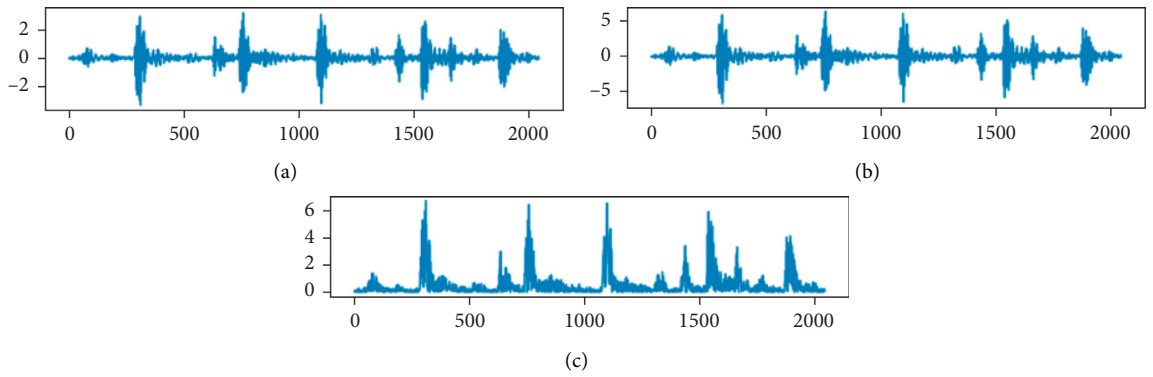

Figure 14: 0.021-inch OR fault.

Table 2: Training set and test set.

Damage diameter (inches)	Fault type	Training set		Test set		Label
		Group	Length	Group	Length	
0.007	RE fault	50	102400	9	18432	0
	IR fault	50	102400	9	18432	1
	OR fault	50	102400	9	18432	2
0.014	RE fault	50	102400	9	18432	3
	IR fault	50	102400	9	18432	4
	OR fault	50	102400	9	18432	5
0.021	RE fault	50	102400	9	18432	6
	IR fault	50	102400	9	18432	7
	OR fault	50	102400	9	18432	8
0	Normal state	50	102400	186	380928	9

XGBoost model, the k-fold cross-validation was introduced to divide the training set into k folds. Among them, $k-1$ folds were used for the training model each time, and the remaining one was used for the testing model. When the parameters of the XGBoost model were default values, the influence of k on the training time and diagnosis accuracy of the model is illustrated in Figure 15. With the increase of k from 3 to 7, the training time gradually increases from 31.91 s to 89.62 s, but the diagnosis accuracy increases firstly and then decreases. When $k = 5$, the diagnosis accuracy is the highest; meanwhile, the training time is not too long. Therefore, the training set is divided into 5 folds.

There are several parameters of the XGBoost model that affect the accuracy of fault diagnosis. Their detailed information is listed in Table 3.

Among them, the most important parameters are the max_depth, min_child_weight, and gamma. The max_depth, that is, the maximum depth of a tree, is a parameter that needs to be adjusted when building a tree. If it is too large, the model will be more complicated and easier to overfit [30]. The test value of this parameter was selected from 3 to 6 in this paper. Min_child_weight, that is, minimum sum of instance weight needed in a child (H_j in (15)), is used to avoid overfitting. If the tree partition step results in a leaf node with the sum of instance weight less than min_child_weight, the building process will give up further partition [30]. The larger the min_child_weight is, the more conservative the model will be. Its range was from 1 to 5. The influence of these two parameters on the diagnosis accuracy of the XGBoost model is shown in Figure 16.

As can be seen from Figure 16, on the whole, the diagnosis accuracies of the XGBoost model for different max_depths decrease with the increase of min_child_weight from 1 to 5. The diagnosis accuracy is the highest when max_depth = 4. In particular, the model has the highest diagnosis accuracy (up to 100%) when min_child_weight = 1.

The last important parameter gamma (γ) represents the minimum loss reduction required to make a further partition on a leaf node of the tree (γ in equation (8)). The larger γ is, the more conservative the algorithm will be [30]. So, its range was from 0 to 0.5 in this study. The influence of γ on the diagnosis accuracy of the XGBoost model is shown in Figure 17.

As can be seen from Figure 17, the diagnosis accuracy of the XGBoost model decreases slightly with the increase of γ from 0 to 0.5. When $\gamma = 0$ or 0.1, the model has the highest accuracy, up to 100%. Moreover, compared with $\gamma = 0.1$, the calculation of the model is small when $\gamma = 0$; thus, $\gamma = 0$ is the better choice for the XGBoost model.

4.4. Result and Analysis. T-distributed stochastic neighbor embedding (T-SNE) is a ML algorithm for dimensionality reduction. It is convenient for the visualization of data. This paper adopted this algorithm to reduce each group sample to

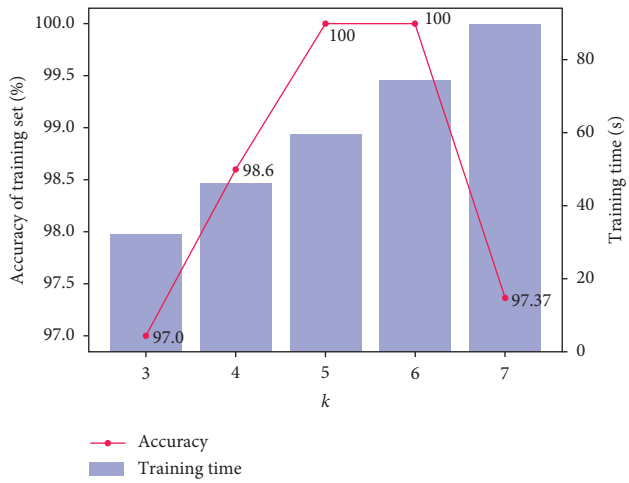

Figure 15: The influence of k on training time and diagnosis accuracy of the model.

Table 3: Main parameters information of XGBoost

Number	Parameter	Implication	Default value
1	max_depth	Maximum depth of a tree	6
2	gamma (γ)	Minimum loss function decline value	0
3	max_delta_step	Maximum delta step we allow each leaf output to be	0
4	lambda (λ)	$L2$ regularization term on weights	1
5	alpha (α)	$L1$ regularization term on weights	0
6	min_child_weight	Minimum sum of instance weight needed in a child	1
7	Eta	Step size shrinkage used in update to prevent overfitting	0.3
8	Subsample	Subsample ratio of the training instances	1

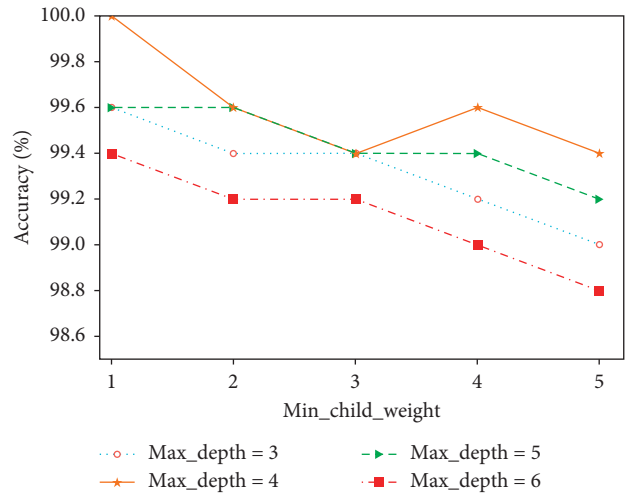

Figure 16: The influence of max_depth and min_child_weight on diagnosis accuracy.

2D and visualize the effect of data processing with DIT-FFT. Figure 18 shows the outcome of dimensionality reduction of processed data. It can be seen that the effect of data processing with DIT-FFT is very obvious. Each type of fault clusters together after the data processing.

When the parameter values of the XGBoost model are default in Table 3, the original data and processed data with DIT-FFT are used to train the XGBoost model and diagnose the test set, respectively. The comparisons of training time of model and diagnosis accuracy of test set between the above two cases are listed in Table 4.

It can be seen from Table 4 that, using the original data as the input of the XGBoost model, the training time is 52.65 s. But it is drastically reduced to 31.91 s using the data processed by DIT-FFT. The diagnosis accuracy of the test set has also greatly improved from about 55% to 93%.

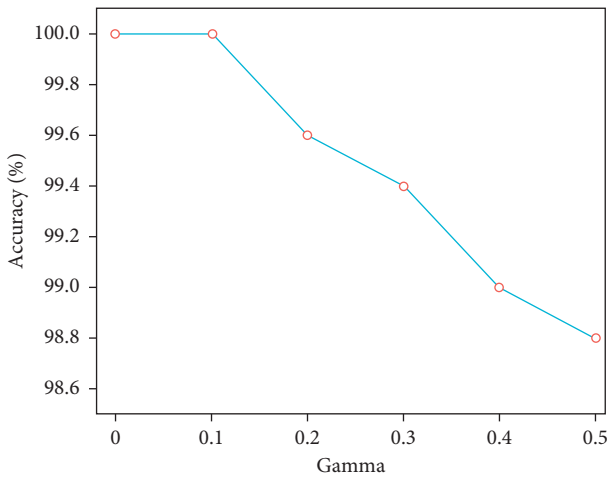

Figure 17: The influence of γ on the diagnosis accuracy of the model.

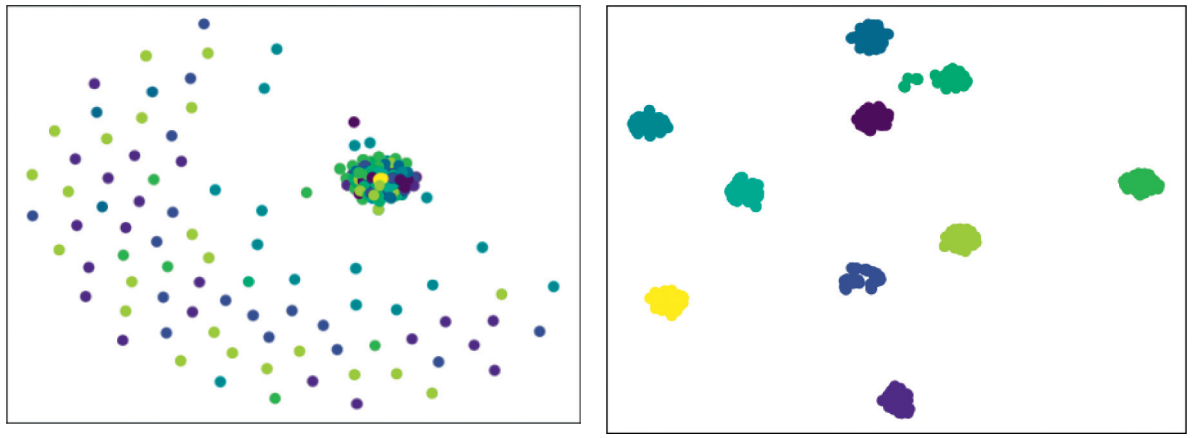

(a) (b)

Figure 18: Visualizations of dimensionality reduction of (a) original data and (b) processed data.

Table 4: Impact of DIT-FFT data processing on fault diagnosis

Item	Original data	Processed data
Training time (s)	52.65	31.91
Accuracy of test set (%)	55.05	93.63

Next, the diagnosis accuracy of the XGBoost model without parameter adjustment for each fault type is further analyzed. The confusion matrixes associated with the obtained results above are illustrated in Figure 19.

As can be seen from Figure 19(a), when the XGBoost model is trained with the original data, it only has high accuracy for the OR fault with a 0.021-inch damage diameter (i.e., label 8). But when the model is trained with the data processed by DIT-FFT, it has high accuracies for 7 fault types (i.e., labels 0, 1, 2, 3, 5, 8, and 10), as shown in Figure 19(b). Thus, it further shows that data processed by DIT-FFT can greatly improve the diagnosis accuracy of bearing.

To further improve the accuracy of model diagnosis, the parameters of the XGBoost model are adjusted to the best values, that is, max_depth = 4, min_child_weight = 1, and $\gamma = 0$. Both the train set and test set are processed by DIT-FFT previously. The confusion matrix for the test set is shown in Figure 20.

We can see from Figure 20 that the XGBoost model with the best parameter values has high accuracies for 9 fault types (i.e., labels 0, 1, 2, 3, 4, 5, 7, 8, 9, and 10). The total diagnosis accuracy of the test set is up to 98.12%. But the model has a low diagnosis accuracy for the RE fault with 0.021-inch damage diameter (i.e., label 6). It misidentifies this fault as the RE fault with a 0.014-inch damage diameter (i.e., label 3). Analyzing the vibration signals of these two faults, we find that they are very similar so that the model cannot identify them accurately. This problem will be further solved in future work.

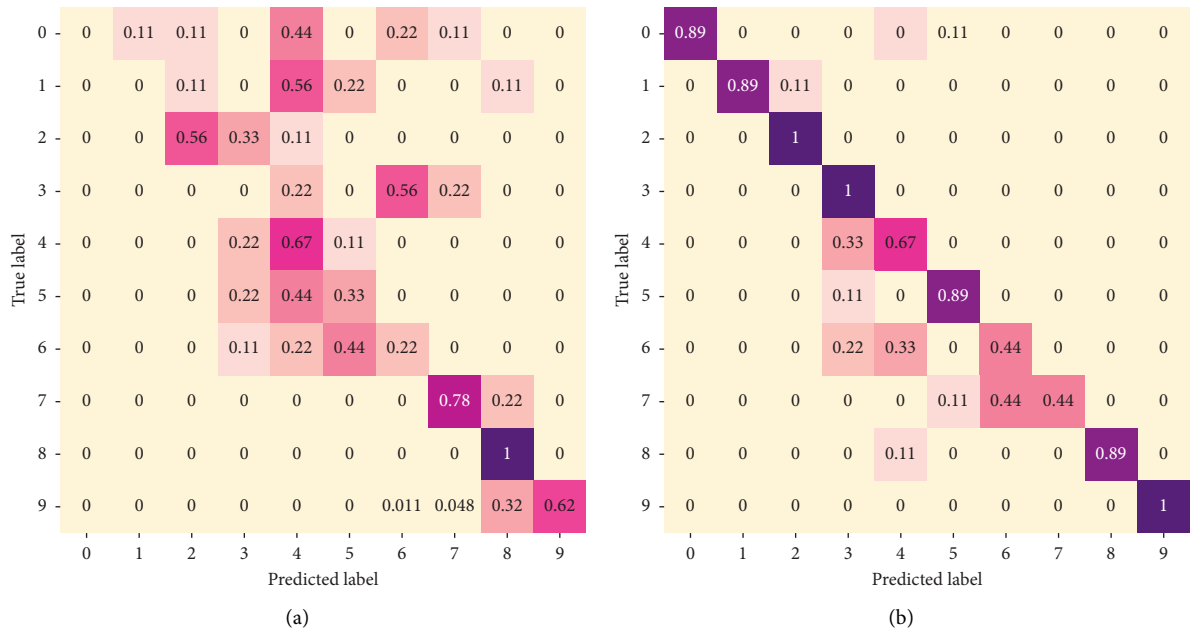

Figure 19: Confusion matrixes obtained from (a) original data and (b) processed data.

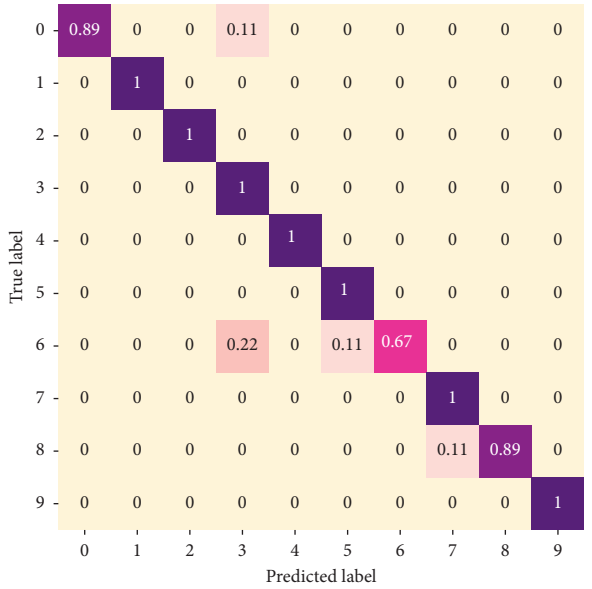

Figure 20: Confusion matrix for the test set.

5. Method Comparison

In this part, the proposed method DIT-FFT-XGBoost is compared with other methods from two aspects, for example, data processing and fault state determination. In aspect of data processing, the Empirical Mode Decomposition (EMD) method was chosen to compare with the DIT-FFT method. EMD has a very good performance in dealing with nonstationary and nonlinear data [17, 27]. It decomposes signal based on the time scale characteristics of the data itself. Taking the RE fault with 0.007-inch damage diameter (i.e., label 0) as an example, the decomposition result of vibration signal by EMD method is illustrated in Figure 21.

After the analysis of the kurtosis of Intrinsic Mode Function (IMF) components shown in Figure 21, four components IMF1 ~ IMF4 are chosen to build a new data set as the input data to train the XGBoost model. The diagnosis accuracy of this well-trained model for the label-0 fault is only 82.40%. As a comparison, when using the vibration signal of the label-0 fault processed by DIT-FFT to train the XGBoost model, the diagnosis accuracy increases up to 88.9%, which is higher than that of EMD.

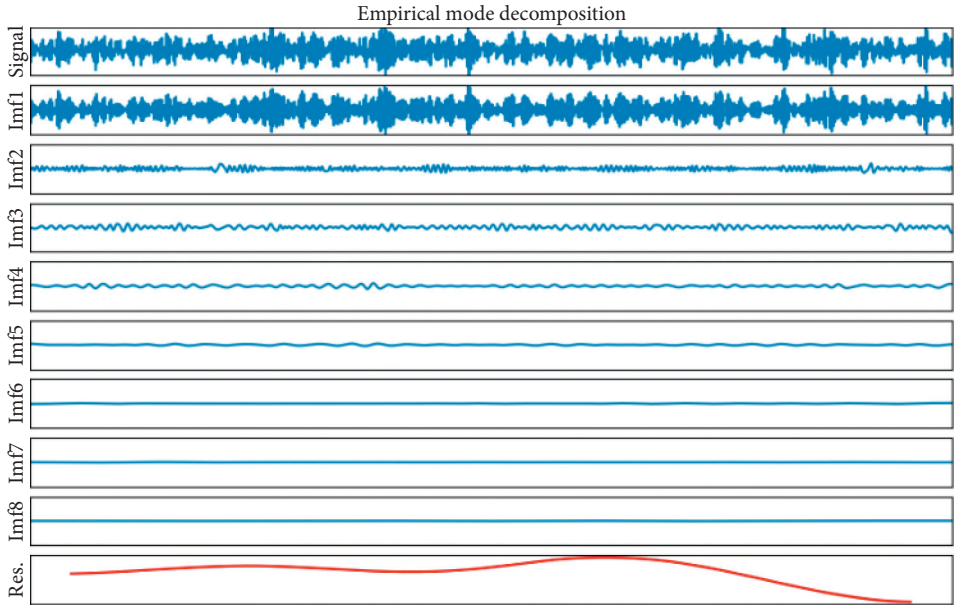

Figure 21: Data processing with EMD.

Table 5: Comparison of different models for fault diagnosis

Item	Machine Learning	EL		DL		XGBoost
	SVM	GBDT	RF	DNN	CNN	
Training time (s)	10.16	48.21	52.17	132.56	50.11	59.53
Accuracy (%)	89.88	11.23	93.25	83.52	95.13	98.12

In aspect of fault state determination, the SVM method in ML; GBDT and RF method in EL; and DNN and CNN in DL are chosen to compare with XGBoost. All of the input training data of these models are preprocessed by DIT-FFT. The comparisons of these models in terms of training time and diagnosis accuracy are shown in Table 5.

As we can see from Table 5, the training time of SVM is the shortest, but its diagnosis accuracy is lower than 90%. It does not satisfy the requirements of the high diagnosis accuracy of bearing faults. Compared with other methods, XGBoost has the highest diagnosis accuracy (up to 98.12%) without a significant increase in training time (59.53 s). Therefore, it is the best choice for the diagnosis of bearing faults.

6. Conclusion

This paper proposed an approach based on DIT-FFT and XGBoost for the fault diagnosis of rolling bearing. The DIT-FFT was used to process vibration signal, and the XGBoost model was used as a classifier for fault identification. The proposed approach was tested with CWRU bearing data and compared with some common methods. The following conclusions can be drawn:

(1) After the vibration signal was processed by DIT-FFT, both of the training time and diagnosis accuracy of the XGBoost model had a significant improvement. The training time reduced from 52.65 s to 31.91 s; meanwhile, the diagnosis accuracy of the test set improved from about 55% to 93%.

(2) After the parameters of the XGBoost model were adjusted to the best values, the model had high accuracies for 9 fault types and the total diagnosis accuracy of the test set was further up to 98.12%.

(3) Compared with the data processing method of EMD, DIT-FFT can extract more fault features and had higher diagnosis accuracy.

(4) Compared with other traditional ML, EL, and DL methods, XGBoost had the highest diagnosis accuracy (up to 98.12%) without a significant increase in training time (59.53 s).

There is no doubt that the combination of DIT-FFT and XGBoost can be used to diagnose bearing faults quickly and accurately.

Data Availability

The data used to support the findings of this study are available from the corresponding author upon request.

Conflicts of Interest

The authors declare that they have no conflicts of interest.

Acknowledgments

This work was supported in part by the National Natural Science Foundation of China under Grant 51507025, Natural Science Foundation of Liaoning Province under Grant 20180550822, and Fundamental Research Funds for the Central Universities under Grant 3132019014.

References

[1] R. B. Randall, *Vibration-based Condition Monitoring: Industrial, Aerospace and Automotive Applications*, John Wiley & Sons, Hoboken, NJ, USA, 2011.

[2] F. Immovilli, C. Bianchini, M. Cocconcelli, A. Bellini, and R. Rubini, "Bearing fault model for induction motor with externally induced vibration," *IEEE Transactions on Industrial Electronics*, vol. 60, no. 8, pp. 3408–3418, 2013.

[3] C. Wei, Z. Shen, D. Xiao, L. Wang, X. Bai, and H. Chen, "An optimal scheduling strategy for peer-to-peer trading in interconnected microgrids based on RO and Nash bargaining," *Applied Energy*, vol. 275, 2021.

[4] C. Wei, M. Benosman, and T. Kim, "Online parameter identification for state of power prediction of lithium-ion batteries in electric vehicles using extremum seeking," *International Journal of Control, Automation and Systems*, vol. 17, no. 11, pp. 2906–2916, 2019.

[5] L. Wang, R. Yan, F. Bai, T. Saha, and K. Wang, "A distributed inter-phase coordination algorithm for voltage control with unbalanced PV integration in LV systems," *IEEE Transactions on Sustainable Energy*, vol. 11, no. 4, pp. 2687–2697, 2020.

[6] F. Xiao, Q. Li, and K. Wang, "Waste plastic triboelectric nanogenerators using recycled plastic bags for power generation," *ACS Applied Materials & Interfaces*, vol. 13, no. 1, pp. 400–410, 2021.

[7] F. Xiao, Y. Zhang, L. Kang et al., "Integrated energy storage system based on triboelectric nanogenerator in electronic devices," *Frontiers of Chemical Science and Engineering*, vol. 15, no. 2, pp. 238–250, 2021.

[8] B. Chouri, M. Fabrice, A. Dandache, M. E. L. Aroussi, and R. Saadane, "Bearing fault diagnosis based on Alpha-stable distribution feature extraction and SVM classifier," in *Proceedings of the International Conference on Multimedia Computing and Systems (ICMCS)*, pp. 1545–1550, Marrakesh, Morocco, April 2014.

[9] W. Mao, W. Feng, and X. Liang, "A novel deep output kernel learning method for bearing fault structural diagnosis," *Mechanical Systems and Signal Processing*, vol. 117, pp. 293–318, 2019.

[10] Y. Yang, P. Fu, and Y. He, "bearing fault automatic classification based on deep learning," *IEEE Access*, vol. 6, pp. 71540–71554, 2018.

[11] Y. Tian, Z. Wang, and C. Lu, "Self-adaptive bearing fault diagnosis based on permutation entropy and manifold-based dynamic time warping," *Mechanical Systems and Signal Processing*, vol. 114, pp. 658–673, 2019.

[12] F. Q. Li, Y. G. Fan, and Y. X. Zhang, "Rolling bearing fault detection method based on wavelet packet energy spectrum-PLS," *Advanced Materials Research*, vol. 971–973, pp. 697–700, 2014.

[13] N. Wang and X. Liu, "bearing fault diagnosis method based on hilbert envelope demodulation analysis," *IOP Conference Series: Materials Science and Engineering*, vol. 436, no. 1, 2018.

[14] A. Issam, B. Nadir, F. Nadir, B. Oudjani, and A. Deliou, "Vibration-based bearing fault diagnosis by an integrated DWT-FFT approach and an adaptive neuro-fuzzy inference system," in *Proceedings of the 2015 3rd International Conference on Control, Engineering & Information Technology (CEIT)*, pp. 1–6, Tlemcen, Algeria, May 2015.

[15] M. Xu, "Spike EnergyTM and its applications," *The Shock and Vibration Digest*, vol. 27, no. 3, pp. 11–17, 1995.

[16] D. Laha and P. Mandal, *Handbook of Computational Intelligence in Manufacturing and Production Management*, Information Science Reference, New York, NY, USA, 2007.

[17] V. K. Rai and A. R. Mohanty, "Bearing fault diagnosis using FFT of intrinsic mode functions in Hilbert-Huang transform," *Mechanical Systems and Signal Processing*, vol. 21, no. 6, pp. 2607–2615, 2007.

[18] J. Xie, G. Du, C. Shen, N. Chen, L. Chen, and Z. Zhu, "An end-to-end model based on improved adaptive deep belief network and its application to bearing fault diagnosis," *IEEE Access*, vol. 6, pp. 63584–63596, 2018.

[19] J. Luo, G. Liu, Z. Huang, and S. S. Law, "Mode shape identification based on Gabor transform and singular value decomposition under uncorrelated colored noise excitation," *Mechanical Systems and Signal Processing*, vol. 128, pp. 446–462, 2019.

[20] A. Maamar, G. P. Bevan, P. A. Wallace, D. K. Harrison, and K. P. Ramachandran, "Fault diagnosis of a centrifugal pump using MLP-GABP and SVM with CWT," *Engineering Science and Technology*, vol. 22, no. 3, pp. 854–861, 2019.

[21] Y. Wu, X. Li, and Y. Wang, "Extraction and classification of acoustic scattering from underwater target based on Wigner-Ville distribution," *Applied Acoustics*, vol. 138, pp. 52–59, 2018.

[22] Y. Bu, J. Wu, J. Ma, X. Wang, and Y. Fan, "The rolling bearing fault diagnosis based on LMD and LS-SVM," in *Proceedings of the 26th Chinese Control and Decision Conference (2014 CCDC)*, pp. 3797–3801, IEEE, Changsha, China, May-June 2014.

[23] Q. Jiang, F. Chang, and B. Sheng, "Bearing fault classification based on convolutional neural network in noise environment," *IEEE Access*, vol. 7, pp. 69795–69807, 2019.

[24] Q. Hu, C. Sun, and L. Du, "Transformer fault diagnosis method using random forests and kernel principle component analysis," *High Voltage Engineering*, vol. 36, no. 7, pp. 1725–1729, 2010.

[25] T. Chen and C. Guestrin, "XGBoost: A scalable tree boosting system," in *Proceedings of the 22nd acmsigkdd international conference on knowledge discovery and data mining*, pp. 785–794, San Francisco, CA, USA, August 2016.

[26] J. Nobre and R. F. Neves, "Combining principal component analysis, Discrete wavelet transform and XGBoost to trade in the financial markets," *Expert Systems With Applications*, vol. 125, pp. 181–194, 2019.

[27] Y. Zhang and J. Zhu, "Atrial fibrillation detection based on EEMD and XGBoost," *Journal of Physics: Conference Series*, vol. 1229, no. 1, 2019.

[28] K. R. Rao, D. N. Kim, and J. J. Hwang, *Fast Fourier Transform-Algorithms and Applications*, China Machine Press, Beijing, China, 2016.

[29] C. J. W. Tukey, "An algorithm for the machine calculation of complex Fourier series," *Mathematics of Computation*, vol. 19, pp. 297–301, 1965.

[30] "XGBoost parameters," https://xgboost.readthedocs.io/en/latest/parameter.html.

Hindawi
Complexity
Volume 2021, Article ID 5634274, 10 pages
https://doi.org/10.1155/2021/5634274

Research Article

Parameter Optimization of Droop Controllers for Microgrids in Islanded Mode by the SQP Method with Gradient Sampling

Peijie Li,[1] **Ziyi Yang**,[1] **Shuchen Huang**,[2] **and Jun Zhang**[3]

[1]*School of Electrical Engineering, Guangxi University, Nanning 530004, China*
[2]*Nanning Power Supply Bureau, Guangxi Power Grid Corporation, Nanning 530031, China*
[3]*Guangxi Power Grid Dispatch and Control Center, Guangxi Power Grid Corporation, Nanning 530023, China*

Correspondence should be addressed to Peijie Li; lipeijie@gxu.edu.cn

Received 8 April 2021; Accepted 14 May 2021; Published 25 May 2021

Academic Editor: Chun Wei

For enhancing the stability of the microgrid operation, this paper proposes an optimization model considering the small-signal stability constraint. Due to the nonsmooth property of the spectral abscissa function, the droop controller parameters' optimization is a nonsmooth optimization problem. The Sequential Quadratic Programming with Gradient Sampling (SQP-GS) is implemented to optimize the droop controller parameters for solving the nonsmooth problem. The SQP-GS method can guarantee the solution of the optimization problem globally and efficiently converges to stationary points with probability of one. In the current iteration, the gradient of the nonsmooth function can be evaluated on a set of randomly generated nearby points by computing closed-form sensitivities. A test on the microgrid system shows that the optimality and the efficiency of the SQP-GS are better than those of the heuristic algorithms.

1. Introduction

Microgrid is an alternative solution to integrate distributed energy resources (DERs). It concludes a cluster of loads, distributed generation (DG), and energy storage systems, just like a small-scale power supply network [1, 2]. Due to the negligible physical inertia of power-electronic converters, the microgrid operation is susceptible to random disturbances, such as variability of DG and random load fluctuations [3], like charging for electric vehicles [4], especially in an islanded mode. The small-signal stability of an islanded microgrid is critical for its reliable operation. In an islanded microgrid, droop control, following a predefined droop coefficient, is widely used to maintain the proportional load sharing between DERs [5]. The small-signal stability of the microgrid in islanded mode is strongly affected by the droop controller parameters. Therefore, it is essential to optimize the controller parameters to enhance the small-signal stability of an islanded microgrid.

Particle swarm optimization (PSO) method is often used to optimize the controller parameters of the microgrid [6–9]. In [6], the maximum of the real part of eigenvalues, also called the spectral abscissa, was minimized to enhance the stability in grid-connected mode. On the other hand, a nonlinear time-domain simulation-based objective function was employed to minimize the error in measure power in islanded mode. The study in [7] proposed a method for optimizing the controller parameters of dynamic droop control for a microgrid in islanded mode and used a spectral abscissa objective function to consider small-signal stability. The study in [8] tried to optimize proportional-integral (PI) current controller parameters considering three design criteria and multiple operating conditions which include grid-connected mode and different islanded modes by a weighted sum of multiple objective functions. The work in [9] proposed an optimization model with a nonlinear time-domain simulation-based objective function for a microgrid in islanded mode. In addition to PSO methods, the study in [10] used the Genetic Algorithms (GA) method to optimize the controller parameters by minimizing the power difference-integrating during the changing process between grid-connected mode and islanded mode.

All the studies above adopt the heuristic algorithms to optimize the control parameters of the microgrid due to the nonsmooth property of the optimization model. Although those algorithms can obtain fast and feasible solutions, they are hard to deliver an optimal solution to the vast majority of cases [11, 12]. The solutions derived by the heuristic algorithms are not deterministic and reproducible. These disadvantages will make the debugging and correctness checking difficult, impeding the industrial application. Concerning the optimization model, the study in [6] did not consider the small-signal stability in islanded mode. As for considering stability, the small-signal stability analysis was performed in [8–10] to obtain the optimum ranges of the controller parameters, while the study in [7] employed spectral abscissa as an objective function to enhance small-signal stability better. The study in [8] considered multiple operating conditions in the optimization model, which may cause the certain index of the design criteria to be poor due to the considering way.

To tackle the weakness mentioned above, this paper proposes an optimization model considering the spectral abscissa in multiple islanded mode operating conditions. Besides, an SQP method combined with GS (SQP-GS) [13] is presented to solve the proposed optimization model. Therefore, droop controllers with optimized parameters can enhance the small-signal stability of the microgrid in islanded mode. As for the SQP-GS method, it had been adopted to optimize the parameters of PSSs and PODs [14].

The major contributions can be summarized as follows:

(1) Based on SQP-GS, a mathematical programming method is presented to solve the proposed nonsmooth optimization model and obtain an optimal and deterministic solution without any convergence problem.

(2) The small-signal stability in different operating conditions is enhanced using a nonsmooth objective function in the optimization model. It can ensure that optimized parameters are robust under multiple operating conditions.

The remainder of this paper is organized as follows: Section 2 presents the small-signal stability model of the microgrid. Section 3 proposes the optimization model for optimizing the droop controller parameters of the microgrid. Section 4 introduces the SQP-GS method to solve the optimization model. In Section 5, the test on the microgrid system under multiple operating conditions is presented. Conclusions are drawn in Section 6.

2. The Small-Signal Stability Model of the Microgrid

The small-signal stability model of the microgrid can be divided into three parts: inverter, network, and load. These small-signal stability models are deduced in dq reference frame [10, 15].

2.1. The Model of the Inverter. The small-signal stability model of the inverter contains two parts: the droop controller and LC filter and coupling inductor. Moreover, the dynamic model of the droop controller consists of the power controller, voltage controller, and current controller.

2.1.1. The Model of the Power Controller. The real and reactive power can be obtained when the instantaneous active and reactive power, calculated from the measured output voltage and output current in dq frame, passes through the low-pass filters. The small-signal stability model can be given by

$$\Delta\dot{P} = -\omega_c \triangle P + \omega_c\left(I_{od}\Delta u_{od} + I_{oq}\Delta u_{oq} + U_{od}\Delta i_{od} + U_{oq}\Delta i_{oq}\right), \tag{1}$$

$$\Delta\dot{Q} = -\omega_c \Delta Q + \omega_c\left(I_{oq}\Delta u_{od} - I_{od}\Delta u_{oq} - U_{oq}\Delta i_{od} + U_{od}\Delta i_{oq}\right), \tag{2}$$

where $\Delta(\cdot)$ is the state variable with respect to the time, $\Delta(\cdot)$ is the state variable or the algebraic variable after linearization, P, Q are the real and reactive power, respectively, $u_{od}, u_{oq}, i_{od}, i_{oq}$ are the output voltage and current in dq frame, respectively, and ω_c is the cut-off frequency of the low-pass filters.

The frequency and voltage can be set by the droop gain; and the small-signal stability model can be given by

$$\Delta\omega = -m_p \Delta P, \tag{3}$$

$$\Delta u_{od}^{*} = -n_q \Delta Q, \tag{4}$$

$$\Delta u_{oq}^{*} = 0, \tag{5}$$

where ω is the frequency, m_p, n_q are the droop gains related to frequency and voltage amplitude, respectively, and u_{od}^{*}, u_{oq}^{*} are the output voltage reference in dq frame, respectively.

The first dq frame of the inverter is set as the common frame; and all the variables from other inverter frames can be converted to the common frame. The small-signal stability model is given by

$$\Delta\dot{\delta} = \Delta\omega - \Delta\omega_{\text{com}} = -m_p \Delta P - \Delta\omega_{\text{com}}, \tag{6}$$

where ω_{com} is the frequency of the common frame taken by the first inverter and δ is the angle between an inverter frame and the common frame.

2.1.2. The Model of the Voltage Controller. The voltage controller contains the PI regulator and the feed-forward terms; and the small-signal stability model of the voltage controller can be given by

$$\Delta\dot{\phi}_d = \Delta u_{od}^{*} - \Delta u_{od}, \tag{7}$$

$$\Delta\dot{\phi}_q = \Delta u_{oq}^{*} - \Delta u_{oq}, \tag{8}$$

$$\Delta i_{ld}^{*} = K_{iu}\Delta\phi_d + K_{pu}\left(\Delta u_{od}^{*} - \Delta u_{od}\right) - \omega_n C_f \Delta u_{oq} + F\Delta i_{od}, \tag{9}$$

$$\Delta i_{lq}^{*} = K_{iu}\Delta\phi_q + K_{pu}\left(\Delta u_{oq}^{*} - \Delta u_{oq}\right) + \omega_n C_f \Delta u_{od} + F\Delta i_{oq}, \tag{10}$$

where ϕ_d, ϕ_q are $\int (u_{od}^{*} - u_{od})\mathrm{d}t$ and $\int (u_{oq}^{*} - u_{oq})\mathrm{d}t$, respectively, i_{ld}^{*}, i_{lq}^{*} are the output current reference in dq frame, respectively, K_{iu}, K_{pu} are the integral and proportional gains of the PI regulator in voltage controller, respectively, w_n is the nominal frequency, F is the feedforward gain, and C_f is the per-phase capacitance.

2.1.3. The Model of the Current Controller. The current controller includes the PI regulator; and the small-signal stability model of the current controller can be given by

$$\Delta\dot{\gamma}_d = \Delta i_{ld}^{*} - \Delta i_{ld}, \tag{11}$$

$$\Delta\dot{\gamma}_q = \Delta i_{lq}^{*} - \Delta i_{lq}, \tag{12}$$

$$\Delta u_{id}^{*} = K_{ic}\Delta\gamma_d + K_{pc}\left(\Delta i_{ld}^{*} - \Delta i_{ld}\right) - \omega_n L_f \Delta i_{lq}, \tag{13}$$

$$\Delta u_{iq}^{*} = K_{ic}\Delta\gamma_q + K_{pc}\left(\Delta i_{lq}^{*} - \Delta i_{lq}\right) + \omega_n L_f \Delta i_{ld}, \tag{14}$$

where γ_d, γ_q are $\int (i_{ld}^{*} - i_{ld})\mathrm{d}t$ and $\int (i_{lq}^{*} - i_{lq})\mathrm{d}t$, respectively, u_{id}^{*}, u_{iq}^{*} are the output inverter voltage reference in dq frame, respectively, i_{ld}, i_{lq} are the sampled filter current in dq frame, respectively, K_{ic}, K_{pc} are the integral and proportional gains in PI regulator of the current controller, respectively, and L_f is the per-phase inductance.

2.1.4. The Model of the LC Filter and Coupling Inductance. The LC filter and coupling inductance can remove the harmonic wave near the switch frequency; and the small-signal stability model of the LC filter and coupling inductance are given by

$$\Delta\dot{i}_{ld} = -\frac{R_f}{L_f}\Delta i_{ld} + \omega_o\Delta i_{iq} - \frac{1}{L_f}\Delta u_{od} + \frac{1}{L_f}\Delta u_{id} + I_{lq}\Delta\omega, \tag{15}$$

$$\Delta\dot{i}_{lq} = -\frac{R_f}{L_f}\Delta i_{lq} - \omega_o\Delta i_{id} - \frac{1}{L_f}\Delta u_{oq} + \frac{1}{L_f}\Delta u_{iq} - I_{ld}\Delta\omega, \tag{16}$$

$$\Delta\dot{u}_{od} = \frac{1}{C_f}\Delta i_{ld} + \omega_o\Delta u_{oq} - \frac{1}{C_f}\Delta i_{od} + U_{oq}\Delta\omega, \tag{17}$$

$$\Delta\dot{u}_{oq} = \frac{1}{C_f}\Delta i_{lq} - \omega_o\Delta u_{od} - \frac{1}{C_f}\Delta i_{oq} - U_{od}\Delta\omega, \tag{18}$$

$$\Delta\dot{i}_{od} = \frac{1}{L_c}\Delta u_{od} - \frac{R_c}{L_c}\Delta i_{od} + \omega_o\Delta i_{oq} - \frac{1}{L_c}\Delta u_{bd} + I_{oq}\Delta\omega, \tag{19}$$

$$\Delta\dot{i}_{oq} = \frac{1}{L_c}\Delta u_{oq} - \frac{R_c}{L_c}\Delta i_{oq} - \omega_o\Delta i_{od} - \frac{1}{L_c}\Delta u_{bq} - I_{od}\Delta\omega, \tag{20}$$

where u_{bd}, u_{bq} are the bus voltage in dq frame, respectively, u_{id}, u_{iq} are the inverter voltage in dq frame, respectively, $\omega_0, I_{ld}, I_{lq}, U_{od}, U_{oq}, I_{od}, I_{oq}$ are the steady state value at the initial operating point, and R_f, R_c, L_f, L_c, C_f are the resistance, inductance, and capacitance in the microgrid, respectively.

2.1.5. The Model of the Individual Inverter. Through the transformation matrix, other inverter variables can transfer to the common frame. The linearization models of the transformation matrix are obtained:

$$\begin{aligned}\left[\Delta i_{oDQi}\right] = &\begin{bmatrix}\cos\delta_o & -\sin\delta_o\\ \sin\delta_o & \cos\delta_o\end{bmatrix}\left[\Delta i_{odqi}\right]\\ &+\begin{bmatrix}-I_{od}\sin\delta_o - I_{oq}\cos\delta_o\\ I_{od}\cos\delta_o - I_{oq}\sin\delta_o\end{bmatrix}\left[\Delta\delta_i\right],\end{aligned} \tag{21}$$

$$\begin{aligned}\left[\Delta u_{bdqi}\right] = &\begin{bmatrix}\cos\delta_o & \sin\delta_o\\ -\sin\delta_o & \cos\delta_o\end{bmatrix}\left[\Delta u_{bDQi}\right]\\ &+\begin{bmatrix}-U_{bD}\sin\delta_o + U_{bQ}\cos\delta_o\\ -U_{bD}\cos\delta_o - U_{bQ}\sin\delta_o\end{bmatrix}\left[\Delta\delta_i\right],\end{aligned} \tag{22}$$

where $\Delta i_{oDQi}, \Delta u_{bDQi}$ are the output current and bus voltage of the ith inverter converted to the common frame, respectively, and δ_0 is the angle between the inverter frame and the common frame.

Combined by the linearization models (1)-(22), the linearization state equation and the linearization output equation of the ith inverter in the common frame are given by

$$\left[\Delta\dot{x}_{invi}\right] = A_{INV_i}\left[\Delta x_{invi}\right] + B_{INVi}\left[\Delta u_{bDQi}\right] + B_{i\omega com}\left[\Delta\omega_{com}\right], \tag{23}$$

$$\begin{bmatrix}\Delta\omega_i\\ \Delta i_{oDQi}\end{bmatrix} = \begin{bmatrix}C_{INV\omega i}\\ C_{INVci}\end{bmatrix}\left[\Delta x_{invi}\right], \tag{24}$$

where $[\Delta x_{invi}] = [\Delta\delta_i \ \Delta P_i \ \Delta Q_i \ \Delta\phi_{dqi} \ \Delta\gamma_{dqi} \ \Delta i_{ldqi} \ \Delta u_{odqi} \ \Delta i_{odqi}]^T$.

2.2. The Model of the Network and Load. The linearization models of the network and load are obtained:

$$\left[\Delta\dot{i}_{\mathrm{line}DQ}\right] = A_{\mathrm{NET}}\left[\Delta i_{\mathrm{line}DQ}\right] + B_{1\mathrm{NET}}\left[\Delta u_{bDQ}\right] + B_{2\mathrm{NET}}\Delta\omega, \tag{25}$$

$$\begin{aligned}\left[\Delta\dot{i}_{\mathrm{load}DQ}\right] = &A_{\mathrm{LOAD}}\left[\Delta i_{\mathrm{load}DQ}\right] + B_{1\mathrm{LOAD}}\left[\Delta u_{bDQ}\right]\\ &+ B_{2\mathrm{LOAD}}\Delta\omega,\end{aligned} \tag{26}$$

where $\Delta i_{\mathrm{line}DQ} = [\Delta i_{\mathrm{line}DQ1}, \Delta i_{\mathrm{line}DQ2}, \ldots, \Delta i_{\mathrm{line}DQn}]^T$, $\Delta i_{\mathrm{load}DQ} = [\Delta i_{\mathrm{load}DQ1}, \Delta i_{\mathrm{load}DQ2}, \ldots, \Delta i_{\mathrm{load}DQp}]^T$, and n, p are the numbers of the lines and loads, respectively.

2.3. The Model of the Microgrid. To define the node voltage clearly, the virtual resistor R_N is assumed between each node and ground. The small-signal stability model is given by

$$\left[\Delta u_{bDQ}\right] = R_N\left(M_{\mathrm{INV}}\left[\Delta i_{oDQ}\right] + M_{\mathrm{LOAD}}\left[\Delta i_{\mathrm{load}DQ}\right] + M_{\mathrm{NET}}\left[\Delta i_{\mathrm{line}DQ}\right]\right), \tag{27}$$

where $\Delta u_{bDQ} = [\Delta u_{bDQ1}, \Delta u_{bDQ2}, \ldots, \Delta u_{bDQm}]^T$, m is the number of nodes in the microgrid, M_{INV} maps the inverter connection points onto network nodes, M_{LOAD} maps the load connection point onto the network nodes, and M_{NET} maps the connection lines onto nodes.

Combined with (23)-(27), the small-signal stability model of the microgrid is given by

$$\begin{bmatrix} \Delta\dot{x}_{\mathrm{INV}} \\ \Delta\dot{i}_{\mathrm{line}DQ} \\ \Delta\dot{i}_{\mathrm{load}DQ} \end{bmatrix} = A_{mg} \begin{bmatrix} \Delta x_{\mathrm{INV}} \\ \Delta i_{\mathrm{line}DQ} \\ \Delta i_{\mathrm{load}DQ} \end{bmatrix}, \tag{28}$$

where $\Delta x_{\mathrm{INV}} = [x_{\mathrm{INV1}}, x_{\mathrm{INV2}}, \ldots, x_{\mathrm{INV}s}]^T$, s is the number of inverters, and A_{mg} is the state matrix of the microgrid model.

3. The Proposed Optimization Model

The dynamic system is stable in small-signal stability sense when all the real parts of the eigenvalues of A_{mg} are negative. The largest real part of all eigenvalues is called the spectral abscissa η, which stands for the power system's stability margin. The value of the spectral abscissa is smaller, and the rate of decay is faster when the system suffers a small disturbance. Therefore, the dynamic system is more stable in the small-signal stability sense. Based on the above small-signal stability model of microgrid, the eigenvalues of A_{mg} can be obtained. Therefore, the spectral abscissa η can be given by

$$\eta\left(\mathbf{A_{mg}}\right) = \max\left\{\mathrm{Re}(\lambda):\ \lambda \in \lambda\left(\mathbf{A_{mg}}\right)\right\} = \mathrm{Re}\left(\lambda_\eta\right), \tag{29}$$

where $\lambda(\mathbf{A_{mg}})$ represents all eigenvalues of $\mathbf{A_{mg}}$. $\mathrm{Re}(\lambda)$ is the real part of all eigenvalues, and λ_η is the eigenvalue with largest real part.

Since the load model is contained in the small-signal stability model of the microgrid, the variation of the load can affect the spectral abscissa of the microgrid exceedingly. Also, load condition variation, such as random load fluctuation, frequently happens in the microgrid operation. Although the microgrid can work well at one load condition, also called operating conditions, it cannot guarantee the small-signal stability at other operating conditions. Therefore, it is crucial to consider multiple operating conditions in the proposed optimization model to achieve better robustness.

The spectral abscissas of different operating condition can be represented as η_i, which stands for the spectral abscissa of the ith operating conditions, $i = [1, 2, \ldots, l]$, and l is the number of the operating conditions.

In [7, 9, 15], through the eigenvalue analysis, the dominant eigenvalues near the imaginary axis are largely sensitive to m_p, n_q and the eigenvalues of medium frequency are largely sensitive to K_{pu}, K_{iu}, K_{pc}, and K_{ic}. The value of η, even the system stability, will vary with droop controller parameters.

Therefore, the critical droop controller parameters of each inverter are considered as the variables $\mathbf{x}$ to be optimized:

$$x = \left[m_{p1}, n_{q1}, K_{pu1}, K_{iu1}, K_{pc1}, K_{ic1}, \ldots, m_{p2}, n_{q2}, K_{pu2}, K_{iu2}, K_{pc2}, K_{ic2}, \ldots, m_{pN}, n_{qN}, K_{puN}, K_{iuN}, K_{pcN}, K_{icN}\right], \tag{30}$$

where N is the total number of inverters.

According to (29) and (30), the spectral abscissa is actually an implicit function of the controller parameters:

$$\eta_i = f\left(m_p, n_q, K_{pu}, K_{iu}, K_{pc}, K_{ic}, \ldots, m_{pN}, n_{qN}, K_{puN}, K_{iuN}, K_{pcN}, K_{icN}\right). \tag{31}$$

The spectral abscissas of the worst operating condition, also called the largest spectral abscissa, can be represented as $\eta_{\max}$:

$$\eta_{\max} = \max\{\eta_1, \eta_2, \ldots, \eta_l\}. \tag{32}$$

According to (32), the objective function can be given to achieve maximum stability of the microgrid in the worst operating condition. This objective function also ensures the maximum stability of microgrid in other operating conditions:

$$\min \eta_{\max}. \tag{33}$$

The constraints of controller parameters of the kth inverter can be listed as the constraint of optimization model:

$$\begin{aligned} \underline{m}_{pk} \le m_{pk} \le \overline{m}_{pk}, \\ \underline{n}_{qk} \le n_{qk} \le \overline{n}_{qk}, \\ \underline{K}_{puk} \le K_{puk} \le \overline{K}_{puk}, \\ \underline{K}_{iuk} \le K_{iuk} \le \overline{K}_{iuk}, \\ \underline{K}_{pck} \le K_{pck} \le \overline{K}_{pck}, \\ \underline{K}_{ick} \le K_{ick} \le \overline{K}_{ick}. \end{aligned} \tag{34}$$

However, $\eta_{\max}$ is not locally Lipschitz. Fortunately, η_i has been proved to be locally Lipschitz and continuously differentiable on open dense subsets of $\mathbb{R}^n$ [16], which means that it is continually differentiable almost everywhere. Also, its gradient can be obtained by calculating spectral abscissa sensitivities. Besides, the small-signal stability constraint with the spectral abscissa of multiple operating conditions can be added to the optimization model to ensure that the microgrid works well in the multiple operating conditions; and, due to the small-signal stability constraint in the optimization model, minimizing $\overline{\eta}$ is equivalent to minimize $\eta_{\max}$.

Through the above discussion, the complete optimization model can be given by

$$\min \overline{\eta}, \tag{35}$$

where $\overline{\eta}$ is the upper limit of spectral abscissa; and the constraints of the optimization model can be listed as follows:

$$\eta_i \le \overline{\eta}, \tag{36}$$

$$\underline{m}_{pk} \le m_{pk} \le \overline{m}_{pk}, \tag{37}$$

$$\underline{n}_{qk} \le n_{qk} \le \overline{n}_{qk}, \tag{38}$$

$$\underline{K}_{puk} \le K_{puk} \le \overline{K}_{puk}, \tag{39}$$

$$\underline{K}_{iuk} \le K_{iuk} \le \overline{K}_{iuk}, \tag{40}$$

$$\underline{K}_{pck} \le K_{pck} \le \overline{K}_{pck}, \tag{41}$$

$$\underline{K}_{ick} \le K_{ick} \le \overline{K}_{ick}, \tag{42}$$

where $\overline{(\cdot)}$ and $\underline{(\cdot)}$ are the upper and lower limits of controller parameters and $k = [1, 2, \ldots, N]$.

The spectral abscissa of multiple operating conditions moves toward the left as far as possible to ensure maximum stability through the optimization model. Thus, the microgrid with optimized controller parameters can operate stably in multiple operating conditions.

According to (31), the spectral abscissa cannot be deduced as an analytical and nonlinear or linear expression of controller parameters; and the spectral abscissa with respect to the parameters has been proved to be nonsmooth [17]. The optimization model in (35)-(42) is a nonsmooth programming problem, which cannot be tackled by the methods for linear or nonlinear programming. It is hard to solve the nonsmooth programming in mathematical programming until the breakthrough in [13].

4. The SQP-GS Method for Solving the Optimization Problem

4.1. The SQP-GS Method. According to the Clarke theorem, if any subgradient is zero, which belongs to the subdifferential of x_0, there is a stationary point x_0 in this nonsmooth function [18].

The nonsmooth problem is hard to be solved until a GS method was proposed in 2005 [18], which can approximate the subgradients for minimizing a nonsmooth objective function. In [18], if the nonsmooth function or constraints are locally Lipschitz continuous, a series of the independent and random gradients of sample point near the nonsmooth point x can be evaluated as convex hull to express the subgradients of x.

The traditional SQP method can solve a QP subproblem to obtain a descending direction. It only solves the smooth problem but fails for the nonsmooth problem. In 2012, the Sequential Quadratic Programming with Gradient Sampling (SQP-GS) method was proposed in [13]. It can converge globally to stationary points with probability of one when the objective function or constraints are locally Lipschitz and continuously differentiable on open dense subsets of $\mathbb{R}^n$.

The SQP-GS method is developed to solve the optimization model in the following form:

$$\begin{aligned} &\min_{\mathbf{x}} f(\mathbf{x}) \\ &\text{s.t.} \quad \mathbf{g}(\mathbf{x}) \le 0, \end{aligned} \tag{43}$$

where the objective function f: $\mathbb{R}^n \longrightarrow \mathbb{R}$ and the inequality constraint functions $\mathbf{g}$: $\mathbb{R}^n \longrightarrow \mathbb{R}^m$.

The SQP-GS method can compute a search direction $\mathbf{d}_k$ in the kth iteration by solving a QP dual subproblem:

$$\min_{\mathbf{d}_k, \mathbf{y}_f, \mathbf{y}_g} \begin{bmatrix} -f(\mathbf{x}_k) \\ -\mathbf{g}(\mathbf{x}_k) \end{bmatrix}^{\top} \begin{bmatrix} \mathbf{y}_f \\ \mathbf{y}_g \end{bmatrix} + \left[\mathbf{d}_k^{\top}, \mathbf{y}_f^{\top}, \mathbf{y}_g^{\top} \right] \mathbf{H}_k \begin{bmatrix} \mathbf{d}_k \\ \mathbf{y}_f \\ \mathbf{y}_g \end{bmatrix}, \tag{44}$$

$$\text{s.t.} \quad \mathbf{H}_k \mathbf{d}_k + \nabla f\left(\mathbf{x}^f\right)^T \mathbf{y}_f + \nabla \mathbf{g}\left(\mathbf{x}^g\right)^T \mathbf{y}_g = 0,$$

$$\forall \mathbf{x}^f \in \mathscr{B}_{\epsilon,k}^f, \ \forall \mathbf{x}^g \in \mathscr{B}_{\epsilon,k}^g, \tag{45}$$

$$e^T \mathbf{y}_f = \rho, \tag{46}$$

$$e^T \mathbf{y}_g = 1, \tag{47}$$

$$\mathbf{y}_f \ge 0, \tag{48}$$

$$\mathbf{y}_g \ge 0, \tag{49}$$

where $\mathbf{x}_k$ is the vector of variables in the kth iteration, $\mathbf{H}_k$ is the approximate Hessian of the Lagrangian optimization model of (43), ρ is a penalty parameter, and $\mathbf{y}_f = (y_{k,0}^f, y_{k,1}^f, \ldots, y_{k,p}^f)$ and $\mathbf{y}_g = (y_{k,0}^{g_j}, y_{k,1}^{g_j}, \ldots, y_{k,p}^{g_j})$ are the approximated minimum-norm elements of the subdifferential of $f(\mathbf{x}_k)$ and $\mathbf{g}(\mathbf{x}_k)$, respectively, $\mathbf{x}^f$ and $\mathbf{x}^g$ are the vectors of the sample points of $f(\mathbf{x}_k)$ and $\mathbf{g}(\mathbf{x}_k)$, respectively, and

$$\mathscr{B}_{\epsilon,k}^f := \left\{ x_{k,0}^f, x_{k,1}^f, \ldots, x_{k,p}^f \right\}, \quad \text{where } x_{k,0}^f := x_k, \tag{50}$$

$$\mathscr{B}_{\epsilon,k}^{g^j} := \left\{ x_{k,0}^{g^j}, x_{k,1}^{g^j}, \ldots, x_{k,p}^{g^j} \right\}, \quad \text{where } x_{k,0}^{g^j} := x_k, \tag{51}$$

are sets of independent and identically distributed random sample points sampled from the closed ball $\mathbb{B}_\epsilon(\mathbf{x}_k)$ centered at $\mathbf{x}_k$, and

$$\mathbb{B}_\epsilon(\mathbf{x}_k) = \left\{ \mathbf{x} \middle| \left\| \mathbf{x} - \mathbf{x}_k \right\| \le \varepsilon \right\}. \tag{52}$$

For reflecting the iteration process, infeasibility value can be defined as

$$\sigma_k(\mathbf{x}_k) := \max(\mathbf{g}(\mathbf{x}_k), 0). \tag{53}$$

The following model reduction $\Delta \mathbf{q}_k$ is also defined in terms of primal and dual infeasibility:

$$\Delta \mathbf{q}_k = \rho f(\mathbf{x}_k) + \sigma_k(\mathbf{x}_k) - \rho \max_{\mathbf{x}_k \in \mathscr{B}_{\epsilon,k}^{f}} \left\{ f(\mathbf{x}_k) + \nabla f(\mathbf{x}_k)^{\top} \mathbf{d}_k \right\} - \sum_{j=1}^{m} \max_{\mathbf{x}_k \in \mathscr{B}_{\epsilon,k}^{g,k}} \left\{ \max \left\{ g^j(\mathbf{x}_k) + \nabla g^j(\mathbf{x}_k)^{\top} \mathbf{d}_k, 0 \right\} \right\} - \frac{1}{2} \mathbf{d}_k^{\top} \mathbf{H}_k \mathbf{d}_k. \tag{54}$$

When the SQP-GS method converges to the optimal solution, these optimality certificates, such as $\sigma_k(\mathbf{x}_k)$, $\Delta \mathbf{q}_k$, can be 0. The sample size p can be set to 0 when the SQP-GS method is solving a smooth function, in which case the SQP-GS method reduces to the general SQP method [14].

4.2. Gradient Evaluation of Spectral Abscissa Function. The gradient of the spectral abscissa $\nabla f(x)$ is crucial for implementing the SQP-GS method; and the spectral abscissa with respect to the controller parameters, also called the spectral abscissa sensitivity, reflects the variation of the variable $\mathbf{x}$ on the impact of system stability. Therefore, the gradient $\nabla f(x)$ of spectral abscissa can be represented as spectral abscissa sensitivity. The spectral abscissa sensitivity can be calculated by the numerical differentiation method, which is numerical spectral abscissa sensitivity.

The numerical spectral abscissa sensitivity can be obtained by

$$\frac{\partial \eta}{\partial \mathbf{x}} \approx \frac{\eta(\mathbf{A}_{\varepsilon}) - \eta(\mathbf{A})}{\varepsilon}, \tag{55}$$

where $\eta(\mathbf{A})$ is the spectral abscissa of the state matrix at the equilibrium point, ε is the small quantity of the variable variation, $\mathbf{x}$ is the variable, and $\eta(\mathbf{A}_{\varepsilon})$ is the spectral abscissa of perturbed state matrix.

As for different variables, the small quantity range is not defined clearly. It causes the accuracy of numerical spectral abscissa sensitivity to be uncertain. When calculating the spectral abscissa sensitivity for each variable, the eigenvalue of $\mathbf{A}_{\varepsilon}$ needs to be recalculated more than once in each iteration. It decreases the efficiency of the optimization.

Hence, the closed-form eigenvalue sensitivity can be an alternative option [19]. It is a mathematical eigenvalue derived at an equilibrium point; and the eigenvalue sensitivity with respect to variable $\mathbf{x}$ can be expressed as

$$\frac{\partial \lambda_i}{\partial \mathbf{x}} = \frac{\psi_i^{\top} \left(\left(\partial \left(\mathbf{A}_{mg} \right) \right) / \partial \mathbf{x} \right) \phi_i}{\psi_i^{\top} \phi_i}, \tag{56}$$

where $\mathbf{A}_{mg}$ is the state matrix of microgrid at the equilibrium point, $\psi_i^{\top}$ and ϕ_i are the left and right eigenvectors of λ_i at an equilibrium point, respectively, and $(\partial \mathbf{A}_{mg} / \partial \mathbf{x})$ can be obtained on matrix calculus.

The closed-form spectral abscissa sensitivity can be expressed by

$$\frac{\partial \eta}{\partial x} = \mathrm{Re}\left(\frac{\partial \lambda_{\eta}}{\partial x} \right). \tag{57}$$

In (56) and (57), $\psi_{\eta}^{\top}$, ϕ_{η}, and $(\partial \mathbf{A}_{mg} / \partial \mathbf{x})$ are required to calculate only once in each iteration. Besides, the closed-form spectral abscissa sensitivity is more accurate than numerical spectral abscissa sensitivity in each iteration. Therefore, the closed-form spectral abscissa sensitivity is used to compute the gradient of the spectral abscissa.

4.3. Solving the Droop Controller Parameters Optimization Problem by SQP-GS. Before employing the SQP-GS method to solve a QP subproblem to get a descending direction, the gradients of objective function and constraints in the optimization model with respect to variable $\mathbf{x}$ should be obtained. The constraint functions in (37)-(42) are smooth; and the gradient of these constraints can be obtained easily. Therefore, the sample size p reduces to zero when the SQP-GS method solves the smooth function. Objective function (35) and the small-signal stability constraint (36) are nonsmooth. The state matrix A_{mg} in (28) for each point in $\mathscr{B}_{\epsilon,k}^{g^j}$ is established. The most critical eigenvalue λ_{η} and the corresponding left and right eigenvectors $\psi_i^{\top}$ and $\phi_i^{\top}$ for each A_{mg} can be obtained in each iteration. According to (56), the most critical eigenvalue sensitivity $(\partial \lambda_{\eta} / \partial x)$ with respect to the ith variable for each point is calculated. Therefore, the gradient $(\partial \eta / \partial x)$ with respect to the ith variable in (57) for each point can be obtained. The initial values of droop controller parameters need to be set in the range of controller parameters limit. Otherwise, they may not converge. The Algorithm 1 is given as follows [14].

5. Test Variation

The following test system in Figure 1 is used to demonstrate the effectiveness of the proposed SQP-GS method. The simulations are carried out on a computer with a four-core 3.70 GHz processor and 16 GB RAM. Also, the SQP-GS method is implemented in MATLAB R2012a. As for the SQP-GS method, those parameters are selected as follows: $\rho = 5e-4$, $\mu_{\rho} = 0.5$, $\varepsilon = 0.1$, $\mu_{\varepsilon} = 0.1$, $\theta = 0.1$, and $\mu_{\theta} = 0.8$.

5.1. Microgrid System Parameters and Four Operating Conditions. We design four operating conditions of the microgrid to verify the effectiveness of the SQP-GS method. The test system in Figure 1 contains three inverters, two connection lines, and two loads. Load 1 is in bus 1, and the other one is in bus 3; and the microgrid system parameters are given in Table 1. Also, the initial condition of the microgrid system is given in Table 2.

To ensure that the droop controller parameters are robust after optimization, similar to multiple operating conditions in [6], we design different operating conditions. They are shown in Table 3. R_{load} of 25 Ω and 20 Ω per phase is equal to the resistive load of 5.6 kW and 7.3 kW [13]. The objection of this paper is to investigate the optimized

(1) Initialization: set $k = 1, k_{\max} = 200$; Set sample size $p > 0$, sample radius $\varepsilon > 0$, constraint violation tolerance $\theta > 0$, penalty parameter $\rho > 0$, line search constant $\varpi \in (0, 1)$, backtracking constant $\gamma \in (0, 1)$, sampling radius reduction factor $\mu_\varepsilon \in (0, 1)$, constraint violation tolerance reduction factor $\mu_\theta \in (0, 1)$, penalty parameter reduction factor $\mu_\rho \in (0, 1)$, infeasibility tolerance $\nu_{in} > 0$, stationarity tolerance parameter $\nu_s > 0$.
(2) Termination conditions check: while $k < k_{\max}$, if $\max(\triangle \mathbf{q}_k) < \nu_s$ or $\varepsilon < \nu_s$, and $\sigma_k < \nu_{in}$, output solution and stop.
(3) Gradient sampling: generate sample point $\mathscr{B}^f_{\varepsilon,k}$ in (50) and obtain gradient of multiple operating condition $(\partial \eta_i / \partial \mathbf{x})$ from (56) and (57), Generate sample point $\mathscr{B}^g_{\varepsilon,k}$ from (51), and get the gradient of smooth constraint in (37)-(42).
(4) Search direction calculation: set H_k>0, solve (45)-(49) to get $(\mathbf{d}_k, \mathbf{y}_f, \mathbf{y}_g)$.
(5) L-BFGS update: update H_k for next iteration according to Limited-memory Broyden-Fletcher-Goldfarb-Shanno (L-BFGS) method [20].
(6) Parameter update: if $\Delta \mathbf{q}_k > \nu_s \varepsilon^2$, go to Step 7. Otherwise, if $\sigma_k \le \theta$, set $\theta \leftarrow \mu_\theta \theta$; if $\sigma_k > \theta$, set $\rho \leftarrow \mu_\rho \rho$. And set $\varepsilon \leftarrow \mu_\varepsilon \varepsilon$, $\beta_k \leftarrow 0$ and go to step 8.
(7) Line search: set β_k as the largest value in the sequence $\{1, \gamma, \gamma^2, \ldots\}$ such that $\mathbf{x}_{k+1} \leftarrow \mathbf{x}_k + \beta_k \mathbf{d}_k$ satisfies: $\rho f(\mathbf{x}_{k+1}) + \sigma(\mathbf{x}_{k+1}) \le \rho f(\mathbf{x}_k) + \sigma(\mathbf{x}_k) - \varpi \beta_k \Delta \mathbf{q}_k$
(8) Iteration increment: set $k \leftarrow k + 1$ and go to step 2.
(9) **end do**

Algorithm 1: SQP-GS method.

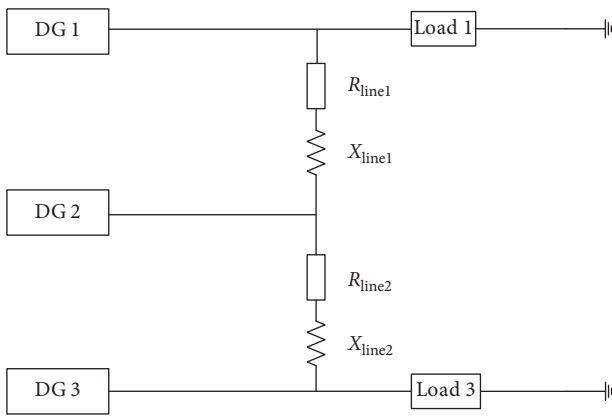

Figure 1: Microgrid structure.

Table 1: The microgrid system parameters.

Parameter	Value
L_f	$1.35e-3H$
C_f	$50e-6F$
R_f	0.1Ω
R_{line1}	0.23Ω
R_{line2}	0.35Ω
L_c	$0.35e-3H$
R_c	0.03Ω
F	0.75
L_{line1}	$3.2e-4H$
L_{line2}	$1.9e-3H$

Table 2: The initial condition of the microgrid system.

Parameter	Value
V_{od}	[380.8, 381.8, 380.4]
I_{od}	[11.4, 11.4, 11.4]
I_{ld}	[11.4, 11.4, 11.4]
V_{bd}	[379.5, 380.5, 379]
w_0	314
$I_{\text{line1}d}$	−3.8
$I_{\text{line2}d}$	7.6
V_{oq}	[0, 0, 0]
I_{oq}	[0.4, −1.45, 1.25]
I_{ld}	[−5.5, −7.3, −4.6]
V_{bq}	[−6, −6, −5]
δ	[0, $1.9e-3$, −0.0113]
$I_{\text{line1}q}$	0.4
$I_{\text{line2}q}$	−1.3

Table 3: The multiple operating conditions.

Case	$R_{\text{load1}}(\Omega)$	$L_{\text{load1}}(H)$	$R_{\text{load3}}(\Omega)$	$L_{\text{load3}}(H)$
Case 1	25	$2.5e-3$	20	$2.2e-3$
Case 2	25	$2.2e-3$	20	$2.5e-3$
Case 3	20	$2.5e-3$	25	$2.2e-3$
Case 4	20	$2.2e-3$	25	$2.5e-3$

parameters in droop controllers that can enhance the small-signal stability of all four operating conditions.

The limit of controller parameters can be shown in Table 4. It is selected based on the trace of the eigenvalues varying with the controller parameters variation [9, 10]. When the droop controller parameters vary in the limit of the variable, the critical eigenvalue will move within the stable region. Meanwhile, the stability of the microgrid operation can be guaranteed. According to the above rule,

Table 4: The limits of controller parameters.

Variable	Lower limit	Upper limit
m_p	$9e-6$	$1e-3$
n_q	$1.3e-5$	$9e-3$
K_{pv}	0.0003	0.1
K_{iv}	200	450
K_{pc}	0.01	15.5
K_{ic}	$10e3$	$16e4$

we can obtain the value domain of the variables from the root locus of the critical eigenvalues with the variable variation.

5.2. Optimization Method Verification. In the last subsection, the four operating conditions have been designed; and we implement the SQP-GS method in MATLAB to optimize the droop controller parameters in microgrid.

From Table 5, we can see the comparison of spectral abscissas between the unoptimized and the optimized values in the four operating conditions. In Case 1 and Case 3, the unoptimized spectral abscissa is 72.3025 and 72.3112, respectively. It stands that the microgrid system is susceptible to encounter oscillation when random load fluctuation occurs. After the optimization, the optimized spectral abscissa is −16.1651 and −16.1212, respectively. It proves that the small-signal stability of the microgrid in four operating conditions is enhanced through SQP-GS method optimization. Therefore, it demonstrated that the SQP-GS method is effective for optimizing the droop controller parameters.

The original parameters and the optimized parameters of the controller are given in Tables 6 and 7. As for the original parameters, the droop controller parameter is designed by the traditional method [15]. Also, the voltage and current controller parameters are selected based on the small-signal stability analysis [9, 10]. For the closed-form spectral abscissa sensitivities of K_{pv}, K_{iv}, K_{pc}, and K_{ic} are fairly small, these controller parameters stay the same nearly in the iteration process.

From Figure 2, there are two eigenvalues with the positive real part in the original system of Case 1. One positive eigenvalue is 72.3025, and the other one is 15.9420. It means that the original system is unstable. After optimizing the controller parameters by the SQP-GS method, all the optimized eigenvalues lie on the left plane. The spectral abscissa of Case 1 is −16.1651. It proves that the stability of the system is improved after the optimization.

In Figure 3, the spectral abscissa of Case 1 decreases in the iteration process with the SQP-GS method. After 83 iterations, the spectral abscissa of Case 1 varies from 72.3025 to −16.1651. It means that the microgrid system with optimized droop controller parameters is stable in the small-signal stability sense.

In Figure 4, the upper limit of the spectral abscissa is varied from −15 to −16.061 in the iteration process. It means that the spectral abscissas of all the cases are less than −16.061. The stability margin of the system is improved.

Figure 5 depicts the sampling radius variation, which is one of the convergence indicators in SQP-GS method. After 83 iterations, the sampling radius decreases from $10e-1$ to $10e-7$; and it proves that the SQP-GS method arrives at convergence.

5.3. Comparison with GA Method. The SQP-GS and GA methods are called nine times, respectively, for optimizing the droop controller parameters; and the mean value of $\overline{\eta}$, spectral abscissa in Case 4, and the computing time are listed in Table 8. As the table shows, the mean value of $\overline{\eta}$ optimized by the GA method is −15.31. Besides, $\overline{\eta}$ optimized by the SQP-GS method is −16.06. In the term of the spectral abscissa, the best value optimized by the GA method is −16.05, while the value optimized by the SQP-GS method is −16.12. As for the computing time, the longest time for the

Table 5: The spectral abscissa of microgrid.

	Spectral abscissa	
	Unoptimized	SQP-GS
Case 1	72.3025	−16.1651
Case 2	72.3024	−16.1647
Case 3	72.3112	−16.1212
Case 4	72.3110	−16.1217

Table 6: The original parameter of controller.

DG	m_p	n_q	K_{pv}	K_{iv}	K_{pc}	K_{ic}
DG1	$6.45e-4$	$2.13e-3$	0.0394	365	6.19	13241
DG2	$6.45e-4$	$2.13e-3$	0.0394	365	6.19	13241
DG3	$6.45e-4$	$2.13e-3$	0.0394	365	6.19	13241

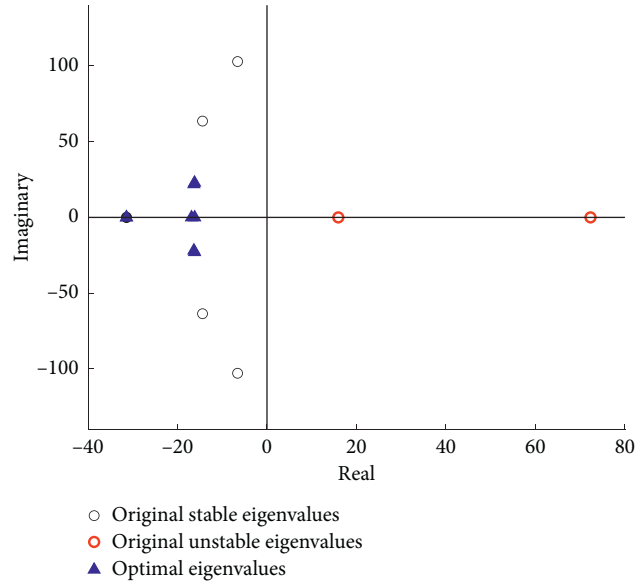

Figure 2: The comparison of eigenvalues of low frequency in Case 1.

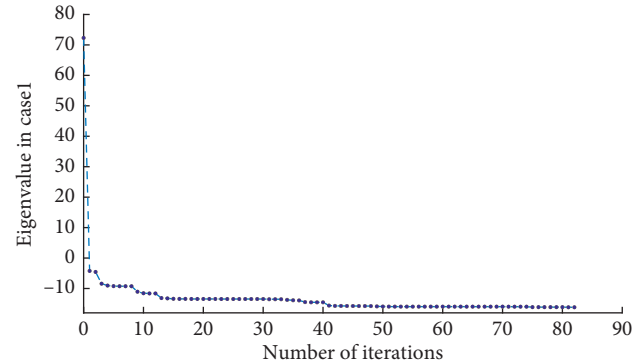

Figure 3: Spectral abscissa variation in the iteration process.

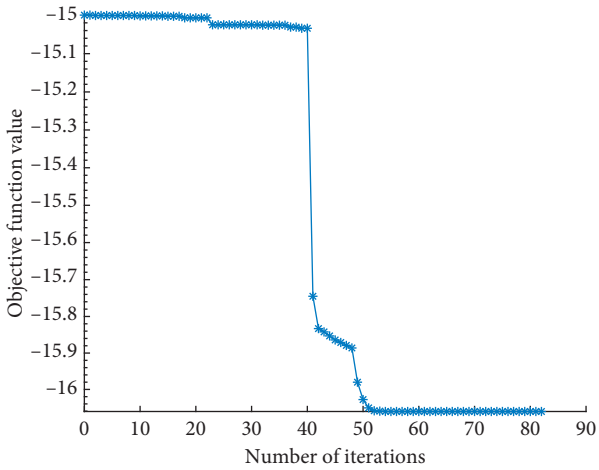

Figure 4: Objective function value variation in the iteration process.

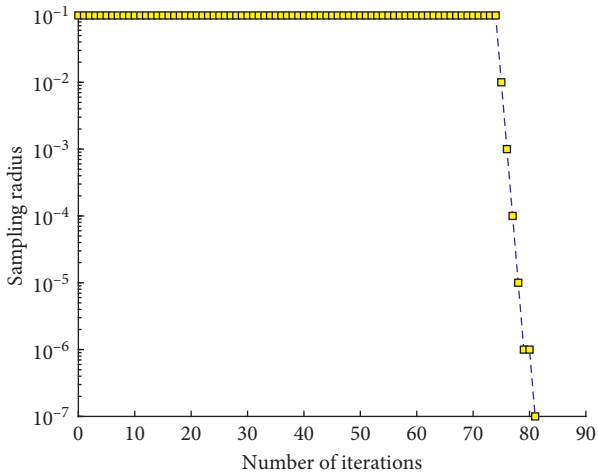

Figure 5: Sampling radius variation in the iteration process.

Table 7: The optimal parameters of controller.

DG	m_p	n_q	K_{pv}	K_{iv}	K_{pc}	K_{ic}
DG1	$7.41e-5$	$1.95e-4$	0.0397	365	6.19	13241
DG2	$1.45e-5$	$1.41e-4$	0.0396	365	6.19	13241
DG3	$1.57e-4$	$7.97e-4$	0.0398	365	6.19	13241

Table 8: Comparison of spectral abscissa and computing time between GA method and SQP-GS method.

		Spectral abscissa			Computing time (h)		
Method	$\overline{\eta}$	Best	Mean	Worst	Min	Mean	Max
GA	−15.28	−16.05	−15.33	−15.09	0.116	0.329	0.709
SQP-GS	−16.06	−16.12	−16.12	−16.12	0.095	0.097	0.102

GA method to converge is 0.709 hours, while the shortest time is 0.116 hours. However, the max computing time of the SQP-GS method is 0.102 hours. These results demonstrate that the optimality and efficiency of the SQP-GS method are better than those of the GA method. Also, Table 8 shows that the SQP-GS can be globally convergent to stationary points with probability of one.

6. Conclusion

This paper proposes the SQP-GS method, which is a mathematical programming method to optimize the spectral abscissa of the microgrid. Combined with the proposed optimization model and SQP-GS method, the microgrid system is better robust in different operating conditions. Moreover, the SQP-GS method's effectiveness and efficiency are better than those of the GA method.

Data Availability

The microgrid system parameters and the initial condition of microgrid system which support the findings of this study are available in [15].

Conflicts of Interest

The authors declare that they have no conflicts of interest.

Acknowledgments

This work was supported in part by the National Natural Science Foundation of China under Grant no. 51967001, in part by the Natural Science Foundation of Guangxi under Grant no. 2018JJA160164, in part by Guangxi Special Fund for Innovation-Driven Development under Grant no. AA19254034, and in part by Guangxi Key Laboratory of Power System Optimization and Energy Technology Research Grant.

References

[1] D. E. Olivares, A. Mehrizi-Sani, A. H. Etemadi et al., "Trends in microgrid control," *IEEE Transactions on Smart Grid*, vol. 5, no. 4, pp. 1905–1919, 2014.

[2] C. Wei, Z. Shen, D. Xiao, L. Wang, X. Bai, and H. Chen, "An optimal scheduling strategy for peer-to-peer trading in interconnected microgrids based on ro and nash bargaining," *Applied Energy*, vol. 295, 2021 https://www.sciencedirect.com/science/article/pii/S0306261921004888, Article ID 117024.

[3] Z. Li and M. Shahidehpour, "Small-signal modeling and stability analysis of hybrid ac/dc microgrids," *IEEE Transactions on Smart Grid*, vol. 10, no. 2, pp. 2080–2095, 2019.

[4] C. Wei, M. Benosman, and T. Kim, "Online parameter identification for state of power prediction of lithium-ion batteries in electric vehicles using extremum seeking," *International Journal of Control, Automation and Systems*, vol. 17, no. 11, pp. 2906–2916, 2019.

[5] T. V. Vu, S. Paran, F. Diaz-Franco, T. El-Mezyani, and C. S. Edrington, "An alternative distributed control architecture for improvement in the transient response of dc microgrids," *IEEE Transactions on Industrial Electronics*, vol. 64, no. 1, pp. 574–584, 2017.

[6] M. A. Hassan and M. A. Abido, "Optimal design of microgrids in autonomous and grid-connected modes using particle swarm optimization," *IEEE Transactions on Power Electronics*, vol. 26, no. 3, pp. 755–769, 2011.

[7] B. K. Unnikrishnan, M. S. Johnson, and E. P. Cheriyan, "Small signal stability improvement of a microgrid by the optimised dynamic droop control method," *IET Renewable Power Generation*, vol. 14, no. 5, pp. 822–833, 2020.

[8] I. Chung, W. Liu, D. A. Cartes, E. G. Collins, and S. Moon, "Control methods of inverter-interfaced distributed generators in a microgrid system," *IEEE Transactions on Industry Applications*, vol. 46, no. 3, pp. 1078–1088, 2010.

[9] V. Naresh Kumar and S. K. Parida, "Parameter optimization of universal droop and internal model controller for multi inverter-fed dgs based on accurate small-signal model," *IEEE Access*, vol. 7, pp. 101 928–101 940, 2019.

[10] K. Yu, Q. Ai, S. Wang, J. Ni, and T. Lv, "Analysis and optimization of droop controller for microgrid system based on small-signal dynamic model," *IEEE Transactions on Smart Grid*, vol. 7, no. 2, pp. 695–705, 2016.

[11] C. Blum and A. Roli, "Metaheuristics in combinatorial optimization," *ACM Computing Surveys*, vol. 35, no. 3, pp. 268–308, 2003.

[12] M. O. Ball, "Heuristics based on mathematical programming," *Surveys in Operations Research and Management Science*, vol. 16, no. 1, pp. 21–38, 2011.

[13] F. E. Curtis and M. L. Overton, "A sequential quadratic programming algorithm for nonconvex, nonsmooth constrained optimization," *SIAM Journal on Optimization*, vol. 22, no. 2, pp. 474–500, 2012, https://doi.org/10.1137/090780201.

[14] P. Li, S. Huang, J. Qi, H. Wei, and X. Bai, "Optimal coordination of PSSs and pods by sequential quadratic programming with gradient sampling," in *Proceedings of the 2020 IEEE/IAS Industrial and Commercial Power System Asia (I & CPS Asia)*, pp. 604–610, Weihai, China, July 2020.

[15] N. Pogaku, M. Prodanovic, and T. C. Green, "Modeling, analysis and testing of autonomous operation of an inverter-based microgrid," *IEEE Transactions on Power Electronics*, vol. 22, no. 2, pp. 613–625, 2007.

[16] J. V. Burke and M. L. Overton, "Variational analysis of non-Lipschitz spectral functions," *Mathematical Programming*, vol. 90, no. 2, pp. 317–351, 2001.

[17] A. S. Lewis and M. L. Overton, "Eigenvalue optimization," *Acta Numerica*, vol. 5, pp. 149–190, 1996.

[18] J. V. Burke, A. S. Lewis, and M. L. Overton, "A robust gradient sampling algorithm for nonsmooth, nonconvex optimization," *Siam Journal on Optimization*, vol. 15, no. 3, pp. 751–779, 2005.

[19] P. Li, Y. Wei, J. Qi, X. Bai, and H. Wei, "A closed-form formulation of eigenvalue sensitivity based on matrix calculus for small-signal stability analysis in power system," *Journal of Modern Power Systems and Clean Energy*, pp. 1–10, 2020.

[20] J. Nocedal, "Updating quasi-Newton matrices with limited storage," *Mathematics of Computation*, vol. 35, no. 151, pp. 773–782, 1980.